Alma Mater Studiorum – Università di Bologna

DOTTORATO DI RICERCA IN

INGEGNERIA CIVILE, CHIMICA, AMBIENTALE E DEI MATERIALI

Ciclo XXXII

Settore Concorsuale di afferenza: 08/B3 Tecnica delle Costruzioni

Settore Scientifico Disciplinare: ICAR 09

EXPERIMENTAL AND NUMERICAL INVESTIGATION ON SHORT AND LONG TERM PERFORMANCE OF MACRO-SYNTHETIC FIBRE REINFORCED CONCRETE MATERIALS

Candidata

Clementina Del Prete

Supervisore

Prof. Ing. Claudio Mazzotti

Coordinatore Dottorato

Prof. Ing. Luca Vittuari

Co-supervisori

Prof. Ing. Nicola Buratti

Prof. Dr. Roman Wan-Wendner

Prof. Dr. Jan Vorel

Esame finale anno 2020

Per Aspera
ad Astra

A mia sorella Francesca

Table of Contents

Abstract I

Introduction III

1. THE FIBRE REINFORCED CONCRETE 1

1.1.CONCRETE AND REINFORCED CONCRETE ORIGIN 3

1.2.FIBRE REINFORCED CONCRETE 5

1.2.1.General 5

1.2.2.Types of concrete and fibre reinforced concrete 7

1.2.3.Fibers reinforcement properties 9

1.2.4.Concrete matrix properties 16

1.2.5.Mix design and rheological parameters 17

1.2.6.Interface characterization 21

1.2.7.Applications 26

2. SHORT TERM BEHAVIOUR: ASPECTS AND CHARACTERIZATION 31

2.1.MICROMECHANICS OF FRCs 33

2.1.1.Interface characterization 34

2.1.2.FRC fibre bridging mechanism 38

2.2.MECHANICAL PROPERTIES 40

2.2.1.Theoretical characterization of FRC tensile properties 40

2.2.2.Uniaxial tensile strength 43

2.2.3.Flexural strength 45

2.2.4.Compressive strength 47

2.3.RECOMMENDATIONS IN FRC DESIGN 48

2.3.1.CNR DT 204/2006 Italian Guidelines 51

2.3.2.fib Model Code 2010 56

3. INTERFACE AND MSFRC BEHAVIOUR CHARACTERIZATION: EXPERIMENTAL ANALYSIS AND RESULTS 61

3.1.FIBRE – MATRIX INTERFACE CHARACTERIZATION WITH PULL-OUT TESTS 63

3.1.1.Outline of the research activity 63

3.1.2.Materials 63

3.1.3.Specimens preparation 65

3.1.4.Pull-out tests 67
3.1.5.Compressive tests 69
3.1.6.Porosity tests 69
3.1.7.Pull-out test results 70
3.1.8.Porosity test results 73
3.1.9.Analysis of experimental results 74
3.1.10.Significance test 79
3.2.FIBRE – MATRIX INTERFACE CHARACTERIZATION: INVERSE ANALYSIS AND NUMERICAL MODEL CALIBRATION 80
3.2.1.Numerical model description 80
3.2.2.Inverse analysis results 82
3.3.MACRO-SYNTHETIC FIBRE REINFORCED CONCRETE: INFLUENCE OF CONCRETE MATRIX AND FIBRE DOSAGE 87
3.3.1.Experimental campaign 87
3.3.2.Materials 87
3.3.3.Specimens preparation 89
3.3.4.Experimental tests 90
3.3.5.Fibre count 92
3.3.6.Three point bending and compressive tests results 93
3.3.7.Analysis of experimental results and significance test 96
3.4.MACRO-SYNTHETIC FIBRE REINFORCED CONCRETE: INVERSE ANALYSIS AND NUMERICAL MODEL CALIBRATION 100
3.4.1.Numerical model description 100
3.4.2.Inverse analysis results 102
3.5.INFLUENCE OF THE MACRO SYNTHETIC FIBRE COMPOSITION 106
3.5.1.Materials 107
3.5.2.Analysis of experimental results 107
4. DEVELOPMENT OF HIGH PERFORMANCE FIBRE REINFORCED CONCRETE WITH SUSTAINABLE WASTE MATERIAL 111
4.1.PROBLEM OF SUSTAINABILITY AND WASTE MATERIAL IN CONCRETE DESIGN 113
4.2.HIGH PERFORMANCE CONCRETE AND FIBRE REINFORCED CONCRETE 114
4.2.1.Silica fume products 119

4.2.2. High Performance Fibre Reinforced Concretes (HPFRC) mechanical behaviour 120
4.3.EXPERIMENTAL INVESTIGATION 125
4.3.1.Preliminary phase 125
4.3.2.Outline of the research activity 126
4.3.3.Materials 127
4.3.4.Mix design optimization 130
4.3.5.Specimens preparation 134
4.3.6.Experimental tests 136
4.3.7.Four point bending test results 138
4.3.8.Analysis and discussion 153
5. EFFECT OF TIME DEPENDENT PHENOMENA ON FIBRE REINFORCED CONCRETE LONG TERM BEHAVIOUR 161
5.1.CREEP AND SHRINKAGE IN CONCRETE 163
5.1.1.Linearity of Creep 166
5.2.CREEP AND SHRINKAGE IN FIBRE REINFORCED CONCRETE 168
5.2.1.Characterization of creep and shrinkage deformations in FRCs 168
5.2.2.Drying shrinkage in FRCs 171
5.2.3.Direct tension in FRCs 171
5.2.4.Pull-out and tensile creep test on single fibre 174
5.2.5.Flexural tests in FRCs 176
5.2.6.Aspects influencing FRCs long term performance 177
6. EXPERIMENTAL INVESTIGATION ON CREEP, SHRINKAGE AND TEMPERATURE EFFECT ON MACRO – SYNTHETIC FIBRE REINFORCED CONCRETE LONG TERM BEHAVIOUR 183
6.1.OUTLINE OF THE EXPERIMENTAL ANALYSIS 185
6.2.PLAIN CONCRETE MECHANICAL CHARACTERIZATION 185
6.2.1.Mix design 185
6.2.2.Preparation of specimens 187
6.2.3.Experimental tests 188
6.2.4.Experimental test results 190
6.3.MSFRC SHORT TERM CHARACTERIZATION WITH TWO DIFFERENT FIBRE DOSAGES 192
6.3.1.Mix design 192
6.3.2.Fibre properties 193

6.3.3.Specimens preparation 193
6.3.4.Experimental test results 195
6.4.EXPERIMENTAL CAMPAIGN ON TIME DEPENDENT PHENOMENA AND TEMPERATURE EFFECT ON MSFRC PERFORMANCE 200
6.4.1.Experimental campaign description 200
6.4.2.Materials 201
6.4.3.Specimens cast 201
6.4.4.Specimens preparation 202
6.4.5.MSFRC compressive strength and elastic modulus 206
6.4.6.Shrinkage test 207
6.4.7.Creep compressive test 209
6.4.8.Flexural creep test 211
6.4.9.Uniaxial tensile creep test 218
6.4.10.Tensile test on single fibre 227
7. NUMERICAL PREDICTIVE MODEL OF SHORT AND LONG TERM PERFORMANCE OF MSFRC 237
7.1.INTRODUCTION 239
7.2.LDPM THEORY 241
7.2.1.LDPM mechanical parameters 244
7.3.LDPM – F THEORY 246
7.4.M – LDPM THEORY 248
7.4.1.Discrete and continuous retardation spectrum 249
7.4.2.Solidification theory 253
7.4.3.Hygro-thermo-chemical model (HTC) 257
7.4.4.Thermal and hygral deformations 258
7.5.M – LDPM – F THEORY 259
7.6.SHORT TERM BEHAVIOUR: MODEL CALIBRATION 262
7.6.1.Specimens modeling 262
7.6.2.Concrete particles generation 263
7.6.3.Concrete parameters calibration 264
7.6.4.Plain concrete calibration results 266
7.6.5.Fibre – Matrix parameters calibration 268
7.6.6.MSFRC fibre count for 0.85% volume fraction of fibers 270
7.6.7.MSFRC calibration results [0.9%] 271

7.7.SHORT TERM BEHAVIOUR: MODEL VALIDATION 278
7.7.1.Influence of the preferential direction parameter 281
7.7.2.Cracking process evolution 283
7.8.LONG TERM BEHAVIOUR: MODEL CALIBRATION 287
7.8.1.LDPM – F mechanical parameters definition 288
7.8.2.Calibration procedure of time dependent phenomena 291
7.8.3.Shrinkage deformation calibration and validation 295
7.8.4.Creep compressive deformation calibration and validation 297
7.8.5.Fibre creep tensile deformation calibration 300
7.8.6.Uniaxial tensile creep deformation calibration 302
7.8.7.Concluding remarks 308
8. ROUND ROBIN OF CREEP TESTS ON STEEL AND MACRO-SYNTHETIC FIBRE REINFORCED CONCRETE 309
8.1.OUTLINE OF THE ROUND ROBIN TEST 311
8.2.EXPERIMENTAL CAMPAIGN 312
8.2.1.Materials 312
8.2.2.Specimens casting 314
8.2.3.Mechanical characterization of Fibre Reinforced Concrete 315
8.2.4.Creep flexural test procedure 317
8.2.5.Differences between laboratories procedure 318
8.2.6.Flexural creep tests results 324
8.3.STATISTICAL ANALYSIS OF THE EFFECT OF TESTS CONDITIONS ON FLEXURAL CREEP RESPONSE 330
8.3.1.Statistical model description 331
8.3.2.Results of the statistical analysis 332
8.3.3.Analysis of the results 338
Conclusions and Future developments 345
References 351
Sitography 365
Acknowledgements 367
Ringraziamenti 369
Appendix A.1 371
Appendix A.2 373
Appendix B 377

Table of Contents

List of Figures

Figure 1.1–(a) Perret: Paris, house in Rue Franklin 1903 (gabrielecherubin.wordpress.com), (b) Le Corbusier:Casa Dom-Ino (domusweb.it). 4
Figure 1.2– (a) Maillart: Schwandbach bridge (pinterest.ru), P. L. Nervi Perret: hangar Orvieto 1937 (pinterest.com). 4
Figure 1.3– (a) E. Freyssinet: Le Veurdre, 1911 (aehistory.wordpress.com). 4
Figure 1.4 –Example of Fibres shape: (a) Crimped; (b) Hooked end; (c) Straight; (d) Monofilament (Plizzari, 2008). 10
Figure 1.5 – Example of Synthetic Fibres: (a) Micro Fibres (indiamart.com); (b) Macro Fibres (danteer.com). 11
Figure 1.6 – Example of cross sectional geometries of fibres. 11
Figure 1.7 .Examples of discrete fibres produced with different materials. 13
Figure 1.8 – Relation between fibres dosage and consistence classes (based on Plizzari, 2008). 18
Figure 1.9 .Tests performed during the production (*valid only for steel fibers), CNR DT 204/2006 20
Figure 1.10 .Single fibre pull-out behaviour (a) slip-hardening (β>0), softening (β<0) and no dependence on slip distance (β=0); (b) output of a pull-out test of PVA fibres from ECC composite (fibre diameter 39μm), (Fiber-Bridging Constitutive Law of Engineered Cementitious Composites, Yang et al. 2007). 22
Figure 1.11 – Examples of hooked end steel fibres with different geometries (Abdallah, 2016). 23
Figure 1.12 – Comparison of pullout response for straight and hooked end steel fibres (Plizzari, 2008). 24
Figure 1.13 – Examples of macro polymeric and micro PVA fibres with different geometries (Abdallah, 2016). 25
Figure 1.14 – Fibres size effect on crack bridging (Betterman, Ouyang, and Shah, 1995). 25
Figure 1.15 – Bending and Shear of inclined fibres crossing matrix crack (Barros and Sena-cruz 2010, Leung and Geng 1995). 26
Figure 1.16– Application of steel reinforced FRC: slabs and industrial floors. 27
Figure 1.17– Application of FRC: shotcrete. 27
Figure 1.18– Application of FRC: precast sewer pipes and tunnel lining. 28
Figure 1.19– Moment Curvature and Load Displacement of beams reinforced with differente fibres dosage and concrete strength FRC (Rinaldi, Grimaldi, and Galli, 2004). 28
Figure 2.1 –Pull-out behaviour: (a) Fibre-Matrix interface zones; (b) Fibre pull-out curve (based on Bentur et al. 1995); (c) Difference between straight and hooked end fibres (based on Löfgren 2005). 35
Figure 2.2 – Pull-out behaviour of inclined fibres: (a) Spalling effect and (b) Cook-Gordon effect (based on Yang et al. 2008). 36

Figure 2.3 – Interface properties described by (a) Linear elastic brittle fracture model; (b) Cohesive strength model; (c) Slip softening fracture model; (d) simplified strength based model (based on Victor C. Li and Stang 1997). 37
Figure 2.4 –FRC cracking process under uniaxial tension: fibres and aggregates bridging effect (based on Choun and Park 2015). 39
Figure 2.5 – Load – Displacement curves for FRC specimens under uniaxial load characterized by (a) Low fibre volume fraction and (b) Higher fibre volume fraction (CNR-DT 204/2006, 2008). 44
Figure 2.6 – Performanced-based classification of fibre reinforced concretes (Naaman and Reinhardt, 2006) 45
Figure 2.7 – FRC stress distribution for a section under flexural load: uncracked and cracked state (based on Robins et al. 2001). 46
Figure 2.8 – FRC and HPFRC compressive behaviour compared with plain concrete compressive response (Löfgren, 2005). 48
Figure 2.9 – Stress-strain constitutive behaviour describing FRC mechanical response under a tensile load advanced by (a) Lim, Paramsivam, and Lee 1987 (b) Lok and Xiao 1998 (c) Dupont and Vandewalle 2002 (d) Kooiman 2000 (e) Barragán BE. 2002 (f) di Prisco et al. 2004 (g) V. C. Li, Stang, and Krenchel 1993 (h) Foote, Mai, and Cotterell 1985 (based on Blanco et al. 2013). 50
Figure 2.10 – FRC tensile behaviour according to the fibre volume content (CNR-DT 204/2006, 2008). 52
Figure 2.11 – FRC average residual strength definition (CNR-DT 204/2006, 2008). 53
Figure 2.12 – FRC simplified constitutive model (a) Linear model and (b) Rigid model (CNR-DT 204/2006, 2008). 53
Figure 2.13 – (a) Three point bending test according to EN 14651 and (b) Load-CMOD output of flexural test for plain concrete (dashed) and FRC (solid) (Di Prisco, Colombo, and Dozio, 2013). 57
Figure 2.14 – Stress-strain relations describing softening and hardening FRC mechanical behaviour (Di Prisco et al., 2013). 59
Figure 2.15 – Stress-strain relation with reference to Serviceability Limit States (SLS) (Di Prisco et al., 2013). 59
Figure 3.1 – Fibre type tested. 64
Figure 3.2 – Sample preparation procedure: (a) Mixing phase; (b) Slump test; (c) Fibers fixed during the specimens vibration. 66
Figure 3.3 – (a) Fibers fixed during the specimens vibration; (b) Samples demoulded after 1 day curing. 67
Figure 3.4 – (a) Pull-out test performed in the servo-hydraulic machine MTS 100kN capacity;(b) Pull-out tests set-up. 68
Figure 3.5 – Cubic specimens, after pull-out tests, used for compressive tests. 69
Figure 3.6 – (a) Extraction of samples from the cubes undamaged core; (b) Samples of approximately 1 cm diameter for porosity tests. 70
Figure 3.7 – Type of failure(a) Fibre Pull-out; (b) Fibre breakage. 71
Figure 3.8 – Three failure types exhibited during pull-out tests. 71

Figure 3.9 – Relation between peak forces of pulled out and ruptured fibers with volume intruded in micropores. 74
Figure 3.10 – 3D regression surfaces correlating the interfacial bond strength with the water-cement and cement-sand ratio for samples cast with (a) CEM I 42.5R and (b) CEM I 52.5R. 75
Figure 3.11 – Linear regression of bond strength and c-s ratio, and confidence interval at 90%, for samples cast with (a) CEM I 42.5R and (b) CEM I 52.5R. 76
Figure 3.12 – Linear regression of bond strength and w-c ratio, and confidence interval at 90%, for samples cast with (a) CEM I 42.5R and (b) CEM I 52.5R. 76
Figure 3.13 – Linear regression of bond strength and mean compressive strength of the corresponding batch, and confidence interval at 90%, for samples cast with (a) CEM I 42.5R and (b) CEM I 52.5R. 78
Figure 3.14 – Linear regression of the rupture failure probability and the mean compressive strength, for samples cast with (a) CEM I 42.5R and (b) CEM I 52.5R. 79
Figure 3.15 – 1D numerical model simulating the interaction of the single fibre with the cementitious matrix: nonlinear springs (Abaqus numerical Software). 81
Figure 3.16 – Local bond shear-slip constitutive models (a) proposed by (Cosenza et al., 2002) in case of FRP reinforcing bars and (b) the constitutive model adopted for the single fibre pull-out process. 82
Figure 3.17 – Example of numerical model calibration by inverse analysis procedure for sample with the code 2G10B_P2. 83
Figure 3.18 – (a) Polypropylene fibers used as reinforcement; (b) Fibre Reinforced concrete mixed; (c) Slump test; (d) Prismatic and cubic specimens. 90
Figure 3.19 – Three point bending flexural test according to Standard Code EN 14651. 92
Figure 3.20 – (a) Prismatic specimens broken at middle section; (b) Subdivision of the cracked area for fibre counting. 93
Figure 3.21 – Nominal Stress-crack opening curves for (a) B1 33 MPa 2 kg/m^3; (b) B2 37 MPa 2 kg/m^3; (c) B3 51 MPa 2 kg/m^3; (d) B7 36 MPa 4 kg/m^3; (e) B5 41 MPa 4 kg/m^3; (f) B6 54 MPa 4 kg/m^3; (g) B8 34 MPa 6 kg/m^3; (h) B9 43 MPa 6 kg/m^3; (i) B10 55 MPa 6 kg/m^3; (l) B11 37 MPa 8 kg/m^3; (m) B14 43 MPa 8 kg/m^3; (n) B15 46 MPa 8 kg/m^3. 95
Figure 3.22 – Mean nominal stress-CMOD curves for (a) 2kg/m^3 fibre dosage; (b) 4kg/m^3 fibre dosage; (c) 6kg/m^3 fibre dosage; (d) 8kg/m^3 fibre dosage. 97
Figure 3.23 – Mean nominal stress-CMOD curves for (a) lower compressive strength class; (b) medium compressive strength class. 98
Figure 3.24 – Mean nominal stress-CMOD curves for the high compressive strength class. 98
Figure 3.25 – Linear regression of the residual flexural strength nominal parameters, f_{R1}, f_{R2} with the mean compressive strength of each batch. 98
Figure 3.26 – Linear regression of the residual flexural strength nominal parameters, f_{R3}, f_{R4} with the mean compressive strength of each batch. 99
Figure 3.27 – Linear regression on the residual flexural strength nominal parameters, f_{R1}, f_{R2}, with the number of fibres included in A_1 and A_2 middle cross section areas. 99
Figure 3.28 – Linear regression on the residual flexural strength nominal parameters f_{R3}, f_{R4} with the number of fibres included in A_1 and A_2 middle cross section areas. 100

Figure 3.29 – Numerical model reproducing half of the prismatic specimen with nonlinear springs placed along the cracked surface. 102
Figure 3.30 – Stress – crack opening constitutive relation describing the local behaviour of the spring. 102
Figure 3.31 – Example of numerical model calibration for a specimen of the group B7 36 MPa 4 kg/m^3. 103
Figure 3.32 – Mean Nominal stress – crack opening flexural behaviour for the five fibres type tested. 108
Figure 3.33 – Mean Nominal stress – crack opening flexural behaviour for the modified fibers compared with the mean flexural trend of the B9 batch (43 MPa and 6kg/m^3 of fibres). 109
Figure 3.34 – Linear regression on the residual flexural strength nominal parameter f_{R1} with the number of fibres included in A_1 and A_2 middle cross section areas and compared with the residual strength values for the reference batch B9 (43 MPa and 6kg/m^3 of fibres). 109
Figure 3.35 – Linear regression on the residual flexural strength nominal parameter f_{R3} with the number of fibres included in A_1 and A_2 middle cross section areas and compared with the residual strength values for the reference batch B9 (43 MPa and 6kg/m^3 of fibres). 110
Figure 4.1 – Concrete matrix phases (based on Saeed 2012). 116
Figure 4.2 – Fibre Reinforced and Highe Performance Fibre reinforced Concrete mechanical behaviour (Jansson, Löfgren, Gylltoft, and Thomas, 2008). 121
Figure 4.3 – Concrete mechanical behaviour in compression, Normal Strength Concrete, High strength concrete and Normal strength concrete (Tue, Simsch, Schneider, and Schmidt, 2004). 122
Figure 4.4 – JSCE recommendations: compressive stress-strain curve (JSCE, 2004). 123
Figure 4.5 – Tensile stress – crack opening relation and bending tensile stress – crack opening relation for ultra high performance concrete (UHPC) materials (Fehling, E., Bunje, K., and Leutbecher, 2007). 124
Figure 4.6 – Flexural behaviour of an Ultra-High Performance Concrete (Yoo and Banthia, 2016). 125
Figure 4.7 – Materials adopted for High Performance Fibre Reinforced Composites realization: (a) Porcelain tiles; (b) Waste material producted by their grinding; (c) CEM I 52.5R; (d) Sand 0-5 mm; I Silica fume products; (f) PVA fibres. 129
Figure 4.8 – Percentages (%) of fines constituents adopted. 130
Figure 4.9 – Stages of the HPFRC casting procedure: (a) Mixing phase; (b) Fibers addition. 135
Figure 4.10 – Stages of the HPFRC casting procedure: (c) Admixture placed in moulds; (d) Cover with plastic sheets; (e) Specimens demoulded. 135
Figure 4.11 – Four point bending tests set-up. 137
Figure 4.12 – Four point bending tests (a) Specimen equipped with the allumium frame where LVDTs are placed; (b) Specimen before the test; (c) Example of localized crack generated by a flexural load; (d) Example of multi – crack pattern. 137

Figure 4.13 – Compressive tests performed on (a) both end of the prismatic specimens; (b) Failure of the sample under compressive load. 138
Figure 4.14 – Nominal Stress – Mean Deflection curves for specimens of H1 – H5 admixtures. 140
Figure 4.15 – Nominal Stress – Mean Deflection curves for specimens of H6 – H9 admixtures. 140
Figure 4.16 – Nominal Stress – Mean Deflection curves for specimens of H10 – H14 admixtures. 141
Figure 4.17 – Nominal Stress – Mean Deflection curves for specimens of H16 – H18 admixtures. 141
Figure 4.18 – Nominal Stress – Mean Deflection curves for specimens of H19 – H23 admixtures. 142
Figure 4.19 – Nominal Stress – Mean Deflection curves for specimens of H24 – H27 admixtures. 142
Figure 4.20 – Nominal Stress – Mean Deflection curves for specimens of H28 – H32 admixtures. 143
Figure 4.21 – Nominal Stress – Mean Deflection curves for specimens of H33 – H36 admixtures. 143
Figure 4.22 – Nominal Stress – Mean Deflection curves for specimens of H37 – H40 admixtures. 144
Figure 4.23 – Nominal Stress – Mean Deflection curves for specimens of H41 – H45 admixtures. 144
Figure 4.24 – Nominal Stress – Mean Deflection curves for specimens of H46 – H49 admixtures. 145
Figure 4.25 – Nominal Stress – Mean Deflection curves for specimens of H50 – H54 admixtures. 145
Figure 4.26 – Nominal Stress – Mean Deflection curves for specimens of H55 – H59 admixtures. 146
Figure 4.27 – Nominal Stress – Mean Deflection curves for specimens of H60 – H63 admixtures. 146
Figure 4.28 – Nominal Stress – Mean Deflection curves for specimens of H64 – H68 admixtures. 147
Figure 4.29 – Nominal Stress – Mean Deflection curves for specimens of H69 – H72 admixtures. 147
Figure 4.30 – Nominal Stress – Mean Deflection curves for specimens of H73 – H77 admixtures. 148
Figure 4.31 – Nominal Stress – Mean Deflection curves for specimens of H78 – H81 admixtures. 148
Figure 4.32 – Compressive peak strength for two specimens of H1 – H9 admixtures. 149
Figure 4.33 – Compressive peak strength for two specimens of H10 – H18 admixtures. 149
Figure 4.34 – Compressive peak strength for two specimens of H19 – H27 admixtures. 149
Figure 4.35 – Compressive peak strength for two specimens of H28 – H36 admixtures. 150
Figure 4.36 – Compressive peak strength for two specimens of H37 – H45 admixtures. 150
Figure 4.37 – Compressive peak strength for two specimens of H46 – H54 admixtures. 150
Figure 4.38 – Compressive peak strength for two specimens of H55 – H63 admixtures. 150

Figure 4.39 – Compressive peak strength for two specimens of H64 – H72 admixtures. 151
Figure 4.40 – Compressive peak strength for two specimens of H73 – H81 admixtures. 151
Figure 4.41 – Histograms representing the indexes in table 4.16 for compressive strength highlighting the admixtures with higher values. 159
Figure 4.42 – Histograms representing the indexes in table 4.16 for nominal flexural strength highlighting the admixtures with higher values. 160
Figure 5.1 – Strain components of shrinkage in (a) normal and (b) high-strength concrete (Sakata and Shimomura, 2004). 164
Figure 5.2 – Strain-time relation of concrete under sustained load (Babafemi, 2015). 165
Figure 5.3 – Isochrones of creep at high stress (Jiràsek and Bazant, 2002). 167
Figure 5.4 – Creep strain component (Babafemi, 2015). 169
Figure 5.5 – Schematic representation of the Creep test with (a) softening and (b) hardening post peak behaviour (Arango, Taungua, Vargas, and Serna Ros, 2012; Babafemi, 2015). 170
Figure 5.6 – Shrinkage test perfomed proposed by Babafemi (Babafemi, 2015) 171
Figure 5.7 – Uniaxial tensile test set-up based on a lever arm principle (G. Zhao et al., 2013) 172
Figure 5.8 – Stress – crack opening displacement and crack opening – time relations observed in long term tests of cracked softening FRC. 173
Figure 5.9 – Set-up proposed by (Mouton, 2012) in the (a) pre-cracking phase and (b) creep phase. 174
Figure 5.10 – Set-up of pull-out creep tests illustrated by Babafemi (Babafemi, 2015). 175
Figure 5.11 – Preliminary short term pull-out and tensile tests proposed by Babafemi (Babafemi, 2015) 176
Figure 5.12 – Flexural creep test set-up proposed by Babafemi (Babafemi, 2015) 177
Figure 5.13 – Influence of core direction on uniaxial tensile response of FRCs (Barragan et al., 2003) 181
Figure 6.1 – Granulometry curves of admixture constituents and Bolomey – Fuller grading envelope. 186
Figure 6.2 – Aggregates used: (a) Sand 0-1 mm; (b) Sand 0-5 mm; (c) Gravel 5-15mm. 186
Figure 6.3 – Specimens cast procedure: (a) Mixing phase; (b) Water addition; (c) Cylindrical and cubic moulds; (d) Prismatic moulds. 187
Figure 6.4 – Experimental tests for plain concrete mechanical characterization: (a) Three point bending test; (b) Cylindrical compression test; (c) Cube compression test; (d) Brazilian test. 189
Figure 6.5 – (a) Testing procedure to obtain the elastic modulus on concrete cylindrical specimens (UNI EN 12390-13); (b) Strain-gauges to measure the strain and consequently the elastic modulus. 189
Figure 6.6 – Nominal stress – strain relation for cylindrical compression tests. 191
Figure 6.7 – Tensile stress – LVDT displacement relation for Brazilian tests. 191
Figure 6.8 – Nominal stress – CMOD relation for three point bending tests. 192
Figure 6.9 – Polypropylene crimped macro-fibers used. 193
Figure 6.10 – Preparation of specimens: (a) Cement addition; (b) Super plasticizer; (c) Slump test; (d) Prismatic samples cast and refining. 194

Figure 6.11 – Nominal stress – CMOD relation for three point bending test on the FRC with dosage of 8 kg/m^3 of fibers. 196
Figure 6.12 – Nominal stress – CMOD relation for three point bending test on the FRC with dosage of 10 kg/m^3 of fibers. 196
Figure 6.13 – Nominal stress – CMOD relations for both dosages. 197
Figure 6.14 – Linear regression of residual strength values f_{R1} with the number of fibers contained in A_1 and A_2 strips, for FRC reinforced with 8 kg/m^3 dosage. 197
Figure 6.15 – Linear regression of residual strength values f_{R3} with the number of fibers contained in A_1 and A_2 strips, for FRC reinforced with 8 kg/m^3 dosage. 198
Figure 6.16 – Linear regression of residual strength values f_{R1} with the number of fibers contained in A_1 and A_2 strips, for FRC reinforced with 10 kg/m^3 dosage. 198
Figure 6.17 – Linear regression of residual strength values f_{R3} with the number of fibers contained in A_1 and A_2 strips, for FRC reinforced with 10 kg/m^3 dosage. 199
Figure 6.18 – Batches realized: (a) First batch; (b) Second batch. 202
Figure 6.19 – Preparation of cylindrical specimens for creep compression and elastic modulus tests eliminating a superior and inferior layer. 203
Figure 6.20 – Phases of cylinders coring. 203
Figure 6.21 – Phases of cylinders coring: (a) Prismatic specimens realization; (b) Subdivision of each prism in three parts; (c) Coring of the prisms; (d) Cylinder cored. 204
Figure 6.22 – Phases of cylinders preparation: (a) Geolite Gel adhesive preparation; (b) Thin adhesive layer on steel plate; (c) Steel plates glued on both ends of cylinders; (d) Connection with aluminium bars; (e) Notch produced at cylinder mid height (width 4mm, depth 10mm); (f) Notched cylinders. 205
Figure 6.23 – Creation of the notch at mid span length of the prismatic sample. 206
Figure 6.24 – Compressive tests. 206
Figure 6.25 – Elastic modulus experimentally determined (EN 12390-13). 207
Figure 6.26 – (a) Preparation of cylinders surface and (b) Strain gauges application. 208
Figure 6.27 – Shrinkage deformation [microstrain] – time. 209
Figure 6.28 – Test set-up for creep compression tests 210
Figure 6.29 – Creep compression tests 210
Figure 6.30 – Creep compression deformation [microstrain] – time. 211
Figure 6.31 – (a) Pre-cracking phase in three point configuration; (b) Detail of crack induced. 212
Figure 6.32 – Force versus CMOD for pre-cracked prisms. 212
Figure 6.33 – Flexural creep test set-up based on lever arm of 2° type. 214
Figure 6.34 – (a) LVDT displacement sensor of 2 mm measurement excursion; (b) Coloumn of three prisms under sustained flexural load. 214
Figure 6.35 – Flexural creep test CMOD – time relation. 216
Figure 6.36 – Flexural test creep coefficient (in terms of crack opening) – time relation. 216
Figure 6.37 – Force versus CMOD for prisms failure phase. 217
Figure 6.38 – Load – CMOD curve including the main phases of the flexural creep test. 218
Figure 6.39 – Pre-cracking phase of cylinder under uniaxial tensile load and crack openind measured by COD at 120° radial distance. 219
Figure 6.40 – Force versus CMOD for pre-cracked cylinders. 220

Figure 6.41 – Lever system for creep tensile test on MSFRC cylinders. 222
Figure 6.42 – (a) Calibration of the sustained uniaxial tensile load by a load cell; (c) Chain of three cylinders under uniaxial tensile load. 222
Figure 6.43 – Uniaxial tensile creep test CMOD – time relation 224
Figure 6.44 – Uniaxial tensile test creep coefficient (in terms of crack opening) – time relation. 225
Figure 6.45 – Force versus CMOD for cylinders failure phase. 226
Figure 6.46 – Load – CMOD curve including all pahses of the uniaxial tensile creep test. 226
Figure 6.47 – (a) Set – up of a tensile test on a single fibre; (b) Fibre under tensile load. 228
Figure 6.48 – Stress – strain curve of a fibre direct tensile test. 228
Figure 6.49 – Fibre tensile creep test set-up based on lever arm of 1° type. 230
Figure 6.50 – (a) Calibration of the creep loading frame with a 2 kN capacity load cell; (b) Tensile creep test on a single fibre. 231
Figure 6.51 – Fibre tensile creep test: Strain – time relation for fibers loaded at 20% of the tensile strength. 232
Figure 6.52 – Fibre tensile creep test: Strain – time relation for fibers loaded at 40% of the tensile strength. 233
Figure 6.53 – Fibre tensile creep test: (a) Creep coefficient – time relation for fibers loaded at 20% of the tensile strength. 233
Figure 6.54 – Fibre tensile creep test: Creep coefficient – time relation for fibers loaded at 40% of the tensile strength. 234
Figure 6.55 – Fibre pull-out creep test set-up based on lever arm of 1° type. 235
Figure 7.1 – (a) Probability function for particle size distribution; (b) LDPM tethraedron connecting four particles (Cusatis, Pelessone, et al., 2011). 244
Figure 7.2 – Fibre intersecting the facet (Jin et al., 2016). 247
Figure 7.3 – Kelvin Chain Model (P. Z. Bažant et al., 1995). 252
Figure 7.4 – Retardation spectra at different n values (P. Z. Bažant et al., 1995). 253
Figure 7.5 – Representation of the equivalent rheological model based on strain additivity principle (Abdellatef et al., 2019). 258
Figure 7.6 – Representation of (a) Prisms for flexural tests; (b) Cylinders and (c) Cubes for compressive tests. 264
Figure 7.7– Schematization of the LDPM extension (a) Close to the prism notch (LDPM 200 mm) and (b) extended to the entire length (LDPM 600 mm) 267
Figure 7.8– (a) Plain concrete flexural tests calibration (LDPM 200 mm); (b) Plain concrete compressive tests calibration (LDPM 600 mm) simulated for six aggregates arrangement (Seeds). 267
Figure 7.9– (a) Plain concrete cube compressive tests calibration simulating two seeds; (b) Plain concrete cylinders compressive tests calibration simulating two seeds. 267
Figure 7.10 – (a) Residual flexural strength fR1 and (b) fR3 versus experimental and numerical fiber count for volume fraction of 0.85%. 271
Figure 7.11 – MSFRC flexural tests calibration (LDPM 200 mm). 273
Figure 7.12 – MSFRC flexural tests calibration (LDPM 600 mm). 274
Figure 7.13 – MSFRC flexural tests calibration: influence of LDPM length. 274

Figure 7.14 – MSFRC flexural tests calibration (Higher fibre modulus). 275
Figure 7.15 – MSFRC flexural tests calibration (Lower minimum aggregate size – 5mm). 275
Figure 7.16 – MSFRC flexural tests calibration: comparison of one seed with 5 mm and 8 mm minimum aggregate size. 276
Figure 7.17 – MSFRC compressive tests tests calibration. 276
Figure 7.18 – Fibers generation and schematization of the numerical fibre count. 277
Figure 7.19 – MSFRC Fiber count versus f_{R1} residual flexural strength. 277
Figure 7.20 – MSFRC Fiber count versus f_{R3} residual flexural strength. 278
Figure 7.21 – MSFRC flexural tests validation (LDPM 200 mm). 279
Figure 7.22 – MSFRC flexural tests validation (LDPM 600 mm). 280
Figure 7.23 – MSFRC cube compressive tests validation. 280
Figure 7.24 – MSFRC Fiber count versus f_{R1} residual flexural strength. 281
Figure 7.25 – MSFRC Fiber count versus f_{R3} residual flexural strength. 281
Figure 7.26 – MSFRC flexural tests validation without considering fibers preferential direction [0.9%]. 282
Figure 7.27 – MSFRC flexural tests validation without considering fibers preferential direction [1.1%]. 283
Figure 7.28 – Plain concrete TPB simulation (Seed 1) with LDPM length 600 mm: CMOD values versus computational time steps. 284
Figure 7.29 – MSFRC 0.9% volume fraction TPB simulation (Seed 1) with LDPM length 600 mm: CMOD values versus computational time steps. 285
Figure 7.30 – MSFRC 1.1% volume fraction TPB simulation (Seed 1) with LDPM length 600 mm: CMOD values versus computational time steps. 285
Figure 7.31 – Plain concrete cracking pattern at measured CMOD of 0.5 mm 286
Figure 7.32 – MSFRC 0.9% cracking pattern at measured CMOD of 0.5 mm 286
Figure 7.33 – MSFRC 1.1% cracking pattern at measured CMOD of 0.5 mm 286
Figure 7.34 – MSFRC 0.9% cracking pattern at measured CMOD of 1.5 mm 286
Figure 7.35 – MSFRC 1.1% cracking pattern at measured CMOD of 1.5 mm 287
Figure 7.36 – MSFRC 0.9% cracking pattern at measured CMOD of 2.5 mm 287
Figure 7.37 – MSFRC 1.1% cracking pattern at measured CMOD of 2.5 mm 287
Figure 7.38 – MSFRC pre-loading phase simulation for three samples having three different fiber seeds (LDPM 600 mm). 290
Figure 7.39 – MSFRC compressive tests for concrete characterization. 290
Figure 7.40 – MSFRC crack evolution during the preloading phase until a residual crack opening (LDPM 600mm). 291
Figure 7.41 – (a) Temperature Profile and (b) Relative humidity profile of HTC model simulated. 296
Figure 7.42 – Temperature changes and diffusion in the cylinder over time. 296
Figure 7.43 – Focus on the gradual application of temperature increment at 80 days (considering the curing period of 28 days). 296
Figure 7.44 – Relative humidity evolution and diffusion in the cylinder over time. 297
Figure 7.45 – MSFRC shrinkage strains: calibration and validation. 297
Figure 7.46 – MSFRC cylinders compressive strength estimation on the experimental cube compressive strength. 298

Figure 7.47 – Numerical simulation of compressive test on the MSFRC cylinders. 299
Figure 7.48 – MSFRC creep compressive strains: calibration and validation. 299
Figure 7.49 – MSFRC creep compressive mechanism simulated on the cylinder having real size and stress evolution (expressed in Pa) along the principal direction ZZ. 299
Figure 7.50 – Creep behaviour according to the analytical model (section 6.4.10) of the polypropylene fibre tested under a load equal to the 20% of the maximum experimental tensile strength. 300
Figure 7.51 – Creep behaviour according to the analytical model (section 6.4.10) of the polypropylene fibre tested under a load equal to the 40% of the maximum experimental tensile strength. 301
Figure 7.52 – Analytical model (section 6.4.10) fitting the experimental data of polypropylene fibre deformations under tensile creep load. 301
Figure 7.53 – Comparison between experimental data and numerical model prediction without accounting for temperature variations. 302
Figure 7.54 – MSFRC model of notched specimen for the mechanical and viscoelastic, viscous problem solution and unotched cylinder for the HTC model. 303
Figure 7.55 – MSFRC cylinders non uniform crack evolution during the simulated pre-cracking phase. 304
Figure 7.56 – Force – CMOD curves simulating the pre-cracking phase of MSFRC cylinders under uniaxial tensile load. 304
Figure 7.57 – Uniaxial tensile creep experimental tests (red curves) simulated with elastic fibers behaviour for data of 100 days. 305
Figure 7.58 – Uniaxial tensile creep experimental tests simulated with viscoelastic fibers behaviour for alla data. 306
Figure 7.59 – Uniaxial tensile creep experimental tests simulated with viscoelastic fibers behaviour for alla data and compared with experimental data (red curves). 307
Figure 8.1 –Particle size distribution of concrete mix. 314
Figure 8.2 – Specimens preparation. 315
Figure 8.3 – Main phases of a creep test. 318
Figure 8.4 – Duration of the load application at the beginning of the creep test for all laboratories. 321
Figure 8.5 – Flexural peak strength for all laboratories (a) Macro-synthetic and (b) Steel Fibers. 321
Figure 8.6 – Flexural residual strength at CMOD/Deflection 0.5 mm for all laboratories (a) Macro-synthetic and (b) Steel Fibers. 321
Figure 8.7 – Creep Index for all laboratories (a) Macro-synthetic and (b) Steel Fibers. 322
Figure 8.8 – Classification of the degrees of freedom of supports. 322
Figure 8.9 – Type of supports classified considering (a) All degrees of freedom [I II III]; (b) Only the translation along the the X axis [III]. 322
Figure 8.10 – Type of static configuration during pre-cracking and creep test. 322
Figure 8.11 – Percentages of laboratories controlling Temperature and Relative Humidity. 323
Figure 8.12 – Flexural creep test set-up adopted by LAB 1. 323
Figure 8.13 – Flexural creep test set-up adopted by LAB 3. 323

Figure 8.14 – Flexural creep test set-up adopted by LAB 5. 324
Figure 8.15 – Flexural creep test set-up adopted by LAB 12. 324
Figure 8.16 – Creep coefficient versus time for specimens with MS fibres for all laboratories. 325
Figure 8.17 – Creep coefficient versus time for specimens with ST fibres for all laboratories. 326
Figure 8.18 – Creep coefficient versus time for specimens with MS fibres for LAB 11 (University of Bologna). 326
Figure 8.19 – Creep coefficient versus time for specimens with ST fibres for LAB 11 (University of Bologna). 327
Figure 8.20 – Creep coefficient for MSFRC beams at t = 360 days considering $t_0 = t_E$. 327
Figure 8.21 – Creep coefficient for MSFRC beams at t = 360 days considering $t_0 = t_E$ + 10’. 328
Figure 8.22 – Creep coefficient for MSFRC beams at t = 360 days considering $t_0 = t_E$ + 30’. 328
Figure 8.23 – Creep coefficient for SFRC beams at t = 360 days considering $t_0 = t_E$. 329
Figure 8.24 – Creep coefficient for SFRC beams at t = 360 days considering $t_0 = t_E$ + 10’. 329
Figure 8.25 – Creep coefficient for SFRC beams at t = 360 days considering $t_0 = t_E$ + 30’. 330
Figure 8.26 – Standardized residuals obtained from nonlinear regression on MS-FRC considering all data of the dataset and creep coefficient at $t_0 = t_E$. 333
Figure 8.27 – Prediction of the creep coefficient of MSFRC specimens for each laboratory, considering $t_0 = t_E$. 334
Figure 8.28 – Standardized residuals obtained from nonlinear regression on S-FRC considering all data of the dataset and creep coefficient at $t_0 = t_E$. 334
Figure 8.29 – Prediction of the creep coefficient of SFRC specimens for each laboratory, considering $t_0 = t_E$. 335
Figure 8.30 – Prediction of the creep coefficient of MSFRC specimens without outliers for each laboratory, considering $t_0 = t_E$. 335
Figure 8.31 – Prediction of the creep coefficient of MSFRC specimens without outliers for each laboratory, considering $t_0 = t_E$ + 10’. 336
Figure 8.32 – Prediction of the creep coefficient of MSFRC specimens without outliers for each laboratory, considering $t_0 = t_E$ + 30’. 336
Figure 8.33 – Prediction of the creep coefficient of SFRC specimens without outliers for each laboratory, considering $t_0 = t_E$. 337
Figure 8.34 – Prediction of the creep coefficient of SFRC specimens without outliers for each laboratory, considering $t_0 = t_E$ + 10’. 337
Figure 8.35 – Prediction of the creep coefficient of SFRC specimens without outliers for each laboratory, considering $t_0 = t_E$ + 30’. 338
Figure 8.36 – Creep coefficient ($t_0 = t_E$) prediction versus residual strength for all laboratories for MSFRC. 342
Figure 8.37 – Creep coefficient ($t_0 = t_E$) prediction versus residual strength for all laboratories for SFRC. 342

Figure 8.38 – Random factors for all laboratories, for creep coefficients at $t_0 = t_E$, $t_0 = t_E$ + 10', $t_0 = t_E$ + 30' – MS and S fibers. 343
Figure 8.39 – Creep coefficients ($t_0 = t_E$) versus fibers density and linear regressions for MS and ST fibers. 343

List of Tables

Table 1.1– Geometrical properties for structural and no structural steel fibres (Coppola and Buoso, 2013). 12
Table 1.2 – Mechanical properties of fibres made of different materials (Collepardi and Troli, 2013). 14
Table 1.3 – Consistence classification according to UNI EN 206-1 (2016). 19
Table 1.4 – Consistence classification according to UNI EN 206-1 (2016). 19
Table 3.1 –Fibres properties. 64
Table 3.2 – Mortar matrix admixtures. 64
Table 3.3 – Mean values of peak forces for all batches distinghuished into pulled out and ruptured fibres. 72
Table 3.4 – Maximum values of intruded Hg volume according to the IUPAC classification pore size. 73
Table 3.5 – Significance test results of the regression parameters correlating bond strength and c-s, w-c and mean compressive strength. 80
Table 3.6 – Inverse analysis results reporting the local parameters values. 83
Table 3.7 – Significance test results of the regression parameters correlating numerical bond strength values and c-s, w-c and mean compressive strength. 87
Table 3.8 – Concrete classes mix design. 88
Table 3.9 – Fibre properties and dosages. 88
Table 3.10 – Outlined and identification code for alla batches. 89
Table 3.11 – Mean compressive strength values outcome of compressive tests. 93
Table 3.12 – Significance test on regression parameters results. 100
Table 3.13 – Local constitutive model parameters calibrated by an inverse analysis procedure. 103
Table 3.14 – Significance test on regression coefficients correlating the local mechanical parameter with concrete compressive strength and number of fibres. 106
Table 3.15 – Composition of the fibre types adopted and batch identification code. 107
Table 4.1 – Sustainability assessment: calculation of SI (sustainability index) for different concrete coloumns processes (Aguado et al., 2016). 114
Table 4.2 – Sustainability assessment: evaluation of requirements, criteria and indicators for the SI calculation (Aguado et al., 2016). 114
Table 4.3 – Mix design differences between Plain Concrete, HPC (High Performance Concrete) and UHPC (Ultra High Performance Concrete), (Spasojević, 2008). 115
Table 4.4 – Matrix mix design of Ultra High Performance Concrete (UHPC) containing basalt constituent (P.P. Li, Q.L. Yu, C.P. Chung, 2017). 118
Table 4.5 – Chemical constituents (%) of waste from rectified porcelain tile. 127
Table 4.6 – Grain size (μm) of waste from rectified porcelain tile. 128
Table 4.7 – PVA fibres used to reinforce the HPC matrix: mechanical and geomatric features. 129
Table 4.8 – Combinations (%) of fine aggregates adopted. 131

Table 4.9 – Fine aggregates and W/F ratio values adopted for the admixtures design. 131
Table 4.10 – Fine aggregates and W/F ratio values adopted for the admixtures design. 132
Table 4.11 – Density of mix design materials. 132
Table 4.12 – Admixtures designed (81). 133
Table 4.13 – Nominal peak, post peak flexural strength and mean compressive strength of all admixtures after 28 days. 151
Table 4.14 – Nominal peak flexural strength of all admixtures after 28 and 60 days. 153
Table 4.15 – Nominal peak flexural strength of all admixtures after 28 and 60 days. 155
Table 4.16 – Indexes as ratio of cement content (kg/m^3) and peak flexural and compressive strength. 158
Table 6.1 – Plain concrete mix design specifications. 186
Table 6.2 – Compressive tests result for plain concrete. 191
Table 6.3 – Elastic modulus measured on cylindrical specimens. 191
Table 6.4 – Mix design specifications for concrete reinforced with 8kg/m^3 and 10 kg/m^3 of polypropylene fibres. 192
Table 6.5 – Macro-synthetic fibre properties. 193
Table 6.6 – Compressive peak strength of MSFRC with dosage of 8 kg/m^3 of fibres. 199
Table 6.7 – Compressive peak strength of MSFRC with dosage of 10 kg/m^3 of fibres. 199
Table 6.8 – Concrete mix design and fibre dosage of the MSFRC tested under long term conditions. 201
Table 6.9 – Outline of the number and specimens type, their dimensions and the type of test realized. 202
Table 6.10 – Compressive strength at 28 days of MSFRC tested under sustained load. 207
Table 6.11 – Elastic modulus at 28 days of MSFRC tested under sustained load. 207
Table 6.12 – Flexural creep test: pre-cracking load at 0.5 mm CMOD, creep load applied and load ratio of specimens tested under sustained creep load. 215
Table 6.13– Signals monitored during the uniaxial tensile pre-cracking phase test. 219
Table 6.14 – Uniaxial tensile creep test: pre-cracking load at 0.3 mm CMOD, creep load applied and load ratio of specimens tested under sustained creep load. 223
Table 6.15 – Fibre tensile strength and elastic modulus evaluated by direct tensile tests on a group of 11 fibres. 228
Table 6.16 – Load applied during the creep test on the fibers. 230
Table 7.1 – Cement-based materials mechanical properties (based on Löfgren 2005). 266
Table 7.2 – Estimation of the tensile characteristic length from tensile strength and elastic modulus experimentally and analytically determined for Plain concrete. 266
Table 7.3 – Set of parameters calibrated on flexural and compressive plain concrete response. 266
Table 7.4 – Estimation of the tensile strength and elastic modulus experimentally and analytically determined for MSFRC [8 kg/m^3]. 269
Table 7.5 – LDPM mechanical parameters calibrated on MSFRC flexural and compressive tests. 270
Table 7.6 – LDPM – F mechanical parameters calibrated on MSFRC flexural and compressive tests. 270
Table 7.7 – Fibre count values evaluated for experimental and numerical simulations. 271

Table 7.8 – LDPM mechanical parameters used for the validation of the MSFRC model. 279
Table 7.9 – LDPM – F mechanical parameters used for the validation of the MSFRC model. 279
Table 7.10 – LDPM mechanical parameters re-calibrated for the MSFRC viscoelastic model. 289
Table 7.11 – LDPM – F mechanical parameters for the MSFRC viscoelastic model. 289
Table 7.12 – Calibration procedure of undamaged behaviour, adapted by (Abdellatef et al., 2019). 293
Table 7.13 – Parameters used to simulate the chemical reactions, heat transfer and moisture transport in concrete. 294
Table 7.14 – Parameters calibrated to simulate creep and hygro-thermal deformations. 294
Table 7.15 – Parameters calibrated to simulate creep deformations of the fibre. 294
Table 7.16 – Experimental and numerical fibre count of cylinders tested under uniaxial sustained load. 305
Table 8.1 – Round Robin Test partecipants. 311
Table 8.2 – Mix design specifications. 313
Table 8.3 – Fibre geometry and mechanical properties. 313
Table 8.4 – Specimens number produced. 315
Table 8.5 – Compressive strength and elastic modulus characterization. 316
Table 8.6 – Flexural peak and residual strength characterization for all batches. 316
Table 8.7 – Type of test and number of specimens for each laboratory. 317
Table 8.8 – Differences between all laboratories for properties and flexural creep test procedure. 320
Table 8.9 – Values of the model [8.1] parameters and their p-values for MSFRC. 341
Table 8.10 – Values of the model [8.1] parameters and their p-values for SFRC. 341
Table 8.11 – Coefficient of Variation of the residual strength for MSFRC and SFRC. 343

Abstract

Fibre Reinforced Concretes are innovative composite materials whose applications are growing considerably during the last decades. As composite materials, their performance depends on the mechanical properties of both components, fibre and matrix. What plays an important role is the behaviour at interface responsible of the crack-bridging activation during the concrete cracked state. Thus, the FRC performance cannot be desumed by the properties of the single constituents, so the experimental analysis represents one of the proper way of investigation. The variables to account for could be proper of the material itself, i.e. fibre and concrete type, or external factors, i.e. environmental conditions. They need to be considered for the mechanical behaviour characterization under short and long term conditions: many aspects are not standardized, above all those regarding the long term behaviour.

The experimental analysis is supported by numerical approaches that, on one side, are aimed at formulating constitutive models on which the structural design involving FRCs is based, on the other, at describing the hetereogeneity of concrete and randomness in fibre distribution which are the aspects that make the model reliable.

In this framework, the present work has the purpose of examining some of the aspects still under investigation, from an experimental and numerical point of view.

The first part of the research is focused on the experimental and numerical characterization of the interface properties and short term response of fibre reinforced concretes with macro-synthetic fibers. The principal aim would be to point out the elements affecting the behaviour at the scale of the single fibre and how they are reflected on the performance of the MSFRC. The experimental database produced represents the starting point for numerical models calibration and validation with two principal purposes: the calibration of a local constitutive law and calibration and validation of a model predictive of the whole material response. In the perspective of the design of sustainable admixtures, the optimization of the matrix of cement-based fibre reinforced composites is realized with partial substitution of the cement amount.

In the second part of the research, the effect of time dependent phenomena on MSFRCs response is studied. An extended experimental campaign of creep tests is performed emphasizing the peculiarities of the material mechanical behaviour and the innovative aspects of the test methodology adopted. The effect of time and temperature variations are analysed in both loaded and unloaded conditions: shrinkage, compressive, uniaxial tensile and flexural creep tests for what concern the whole material and characterization of the polymeric fibre viscoelastic deformations for what concern the reinforcement. The principal aim would be to decouple the phenomena occurring in the flexural state.

On the results achieved, a numerical model able to account for the viscoelastic nature of both concrete and reinforcement, together with the environmental conditions, is calibrated.

Different type of regression models are also elaborated to correlate the mechanical properties investigated, bond strength and residual flexural behaviour, regarding the short term analysis and creep coefficient on time, for what concerns the time dependent behaviour, with the variable investigated.

The experimental studies carried out emphasize the several aspects influencing the material mechanical performance allowing also the identification of those properties that the numerical approach should consider in order to be reliable.

Introduction

Fibre reinforced concretes are defined as composite materials characterized by a cementitious matrix, either normal or high strength, with discrete fibrous reinforcement, made of different materials. They have several applications, either alone or in combination with ordinary or prestressed reinforcement. Their structural application requires a minimum dosage of 0.3%. The fibers addition aims at overcoming the weak aspects of concrete, connected to its limited tensile strength and little resistance to crack propagation. The composite nature of the materials suggests the identification of the mechanical performance of both components whose interaction should assure the load transmission: when concrete starts cracking, the reinforcement is so responsible of the residual strength gained. The knowledge from this point of view is considerable, since lot of researches are focused above all on the macroscopic FRC behaviour. From a numerical point of view, the complexity in describing their behaviour lies in the simulation of the interaction between the two materials, fibre and matrix, and their hetereogeneity. These aspects represent the sources of the scatter in results and one of the main element that a model should be able to reproduce.

The mechanical characterization is the subject of many official regulations infact, during this year, thanks to the Decree n.208 of 9th April 2019, the Italian guidelines named *'Linee Guida per l'identificazione, la qualificazione, la certificazione di valutazione tecnica ed il controllo dei calcestruzzi fibrorinforzati'* are approved (2019).

However, the characterization of the long term behaviour of the FRCs is still an open topic on both for the experimental and numerical point of view.

In this framework, the present work has the purpose of analysing the mechanical performance of different type of macro-synthetic fibers used as reinforcement of normal strength and high strength concretes. In addition, a novel numerical approach is developed in order to simulate the short and long term behaviour of the composite material. The importance of the research is represented by the analysis of those

aspects fundamental in the applications of the MSFRCs as a structural material. First of all the identification of the constitutive relations, at a small scale for the interface properties between the fibre and the matrix and, at the material scale, for the behaviour in cracked state. Moreover, the support of the numerical approach might help to reduce the experimental burden in this field above all concerning the material mechanical characterization.

The thesis is divided into two main sections dealing with respectively the short and long term characterization of macro-synthetic fibre reinforced concretes.

Chapter 1 describes the general aspects of the FRCs regarding the possible type of fibrous reinforcement and matrix design and how the interface fibre-matrix is affected.

In Chapter 2 the mechanics of FRCs are described: starting from the interface mechanical characterization to the bridging mechanism activated during the cracked phase of the material. The crack opening activates the fibre contribution making possible to bear loads when concrete is already cracked. This chapter also describes the compressive, flexural and tensile properties of FRCs and the constitutive models proposed referring to the Standard regulations.

Chapter 3 presents an experimental campaign of pull-out tests on single fibres in order to characterize their interface mechanical behaviour. Based on the experiments a numerical model is calibrated aimed at characterizing a bond-slip law to describe the fibre-concrete interface. The same fibre is used as reinforcement of different concretes: the mechanical behaviour is so characterized by flexural test. The experimental results are the basis for the calibration of the stress-crack opening local constitutive law.

In Chapter 4 the performance of high strength concretes is experimentally analysed with the aim of designing different admixtures where the cement is partially substituted with waste material.

The second part of the thesis regards the long term behaviour of FRC. In Chapter 5 the main time dependent phenomena and their effect on the material performance are described.

Chapter 6 exposes the results of an experimental campaign performed on a macro-synthetic fibre reinforced concrete tested under sustained load in different loading and environmental conditions.

Chapter 7 presents numerical models developed in collaboration with Boku University in Vienna where I spent my period of research abroad. The short and long term behaviour of the MSFRC material is simulated using the Lattice Discrete Particle Model constitutive law implemented in a powerful numerical software, MARS. The numerical models are calibrated and validated on the basis of the experiments performed at the University of Bologna.

Chapter 8 presents a statistical analysis of the results of a round robin experimental campaign con the creep behaviour of cracked FRC beams in bending, with the aim of highlighting the most relevant experimental factors.

CHAPTER 1

1. THE FIBRE REINFORCED CONCRETE

1.1. CONCRETE AND REINFORCED CONCRETE ORIGIN

The use of concrete is dated back to the II century a.C. although it had existed before but with unaware usage: the reactions proper of the material, i.e. the hydration process with water, are something from which has been taken advantage but it was not completely investigated. Around the 200 a.C. the mix design, as we consider it, in terms of mortar and concrete was coded by Marco Porcio Catone. From this moment, the importance in granulometry assortment was considered. During the period of the Industrial revolution the scientific field was developed: Germany, France, England and Italy advanced many innovative ideas. English engineers started to study the behaviour of the flexural structural elements realized with cast-iron. The first use of reinforced concrete was associated with P. W. Barlow, in 1847, who advanced the proposal of using the first reinforced beam in the structural history, to build a small railway bridge. Before being used in the structural engineering sector, the reinforced concrete material found its application in many fields, from strange objects, to ships cast with mortar reinforced with steel reticular reinforcement.

The first region who regulated the use of concrete was the Germany in 1877 for unreinforced concrete. In 1880 the constructor Coignet improved noticeably the mix design techniques through laboratory research aimed at pointing out the best water/cement ratio, mixing time, fresh concrete vibration. Twenty years later, the American Jackson elaborated the first prestressed procedure only to reduce cracks in the concrete subjected to tensile stress. The complete knowledge about the static meaning of the prestressing technique was not still achieved. This century ends with other aspects discovered, about the difference of volume during the curing concrete period, the increment of volume of concrete if put in water, until the publication of the first base for concrete reinforced theory (*'Principi dei calcoli statici per gli edifici in calcestruzzo e in calcestruzzo armato'*, M. Koenen). The French engineer F. Hennebique developed a structural system according which each substructural element of the entire structure is reinforced for a static purpose. Auguste Perret, understood the potentialities of the structural reinforced concrete frames, eliminating the heavy components: bearing walls and archs. (Ghersi, 2012).

Below are reported pictures where the relevant structural realizations, that will lead to the present engineering techniques, are depicted.

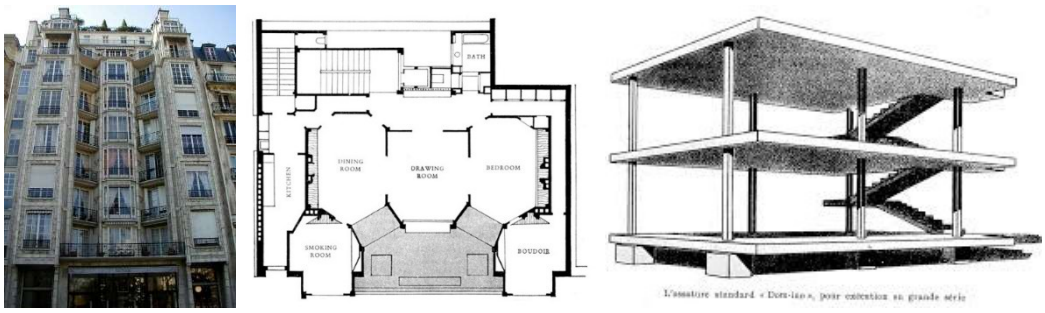

Figure 1.1–(a) Perret: Paris, house in Rue Franklin 1903 (gabrielecherubin.wordpress.com), (b) Le Corbusier:Casa Dom-Ino (domusweb.it).

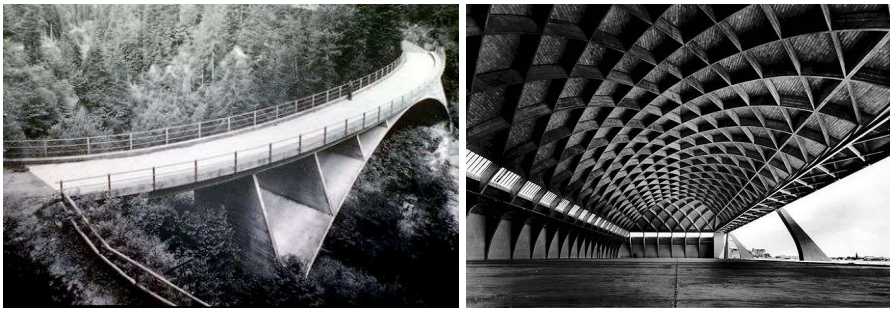

Figure 1.2– (a) Maillart: Schwandbach bridge (pinterest.ru), P. L. Nervi Perret: hangar Orvieto 1937 (pinterest.com).

Figure 1.3– (a) E. Freyssinet: Le Veurdre, 1911 (aehistory.wordpress.com).

Concrete is still a material widely used in the construction sector all over the world, but it appears to be characterized by a brittle fracture, consequently it has little ductility, and also poor tensile strength compared with its compressive strength (Ghersi, 2012). Furthermore, due to the cracking problem, it is necessary to use steel as reinforcement in order to bear load despite the cracked state of concrete (Taheri, Barros, and Salehian, 2012). Despite the use of steel as reinforcement, several cracks

continue to appear and propagate causing the entry of corrosive agents that could affect its durability. It is compromised by two main mechanisms, the carbonation-induced corrosion and the chloride-induced corrosion (Böhni, 2005): the carbonation is caused by CO_2 concentration in the atmosphere, its penetration in concrete pores and the chemical reactions with the cement hydrates. The phenomena are strictly correlated because the carbonation allows the initialization of many other processes such as the chloride ingress and salts attack (Yoshida, Matsunami, Nagayama, and Sakai, 2010).

The scientific progress in the structural fiels covers many centuries, and it is still active trying to overcome the limits of the structural engineering materials adding new technologies.

1.2. FIBRE REINFORCED CONCRETE

1.2.1. General

An alternative to the use of steel reinforcement is represented by the inclusion of fibers: this technology is becoming strongly diffused since the possibility of increasing the toughness of the brittle material allowing the cracking control (Löfgren, 2005). The use of two different materials working together makes possible to take advantage of the mechanical properties of both constituents, that are different, so that the performance of the final material is better than that exibhited when they are used separately (Ramous, Festa, and Bernardo, 2010).

Nowadays the use of fibers is highly promoted, steel or synthetic or natural fibers, because they are able to reduce the crack propagation activating the cracking bridging mechanism (Easley, Faber, and Shah, 2010), when concrete starts cracking. This mechanism is responsible of the improvement of several mechanical properties, the increment of the residual tensile flexural strength and, consequently, the toughness proper of the fibre reinforced concrete (Di Prisco, Plizzari, and Vandewalle, 2011). Moreover, the impact resistance and the control of the rheological properties during the fresh state are improved (Rossi and Pascale, 2007).

The final performance is the result of (a) physical properties of fibres and matrix, (b) bond behaviour between the two components, (c) fibres dosage and (d) the randomness in distribution (Löfgren, 2005).

It should be underlined that the mechanical performance is strongly dependent on the fibre type used since the difference in the energy dissipated during the failure process (Plizzari, 2008). Thus, a good fiber-matrix adhesion should be guaranteed because it is responsible of the load bearing capacity during the matrix cracked state.

The fibre can be produced with many materials and so the final composite material is classified, according to the ACI, American Concrete Instiute (ACI Committee 544, 2002), as:

a. SFRC, FRC with steel fibres;
b. GFRC, FRC with glass fibres;
c. SNFRC, FRC with synthetic fibre (MSFRC in case of macro-synthetic);
d. NFRC, FRC with natural fibres.

The mix design of a fibre reinforced material consists of binder, fine and coarse aggregates, water and inclusion of short or long fibers randomly distributed: the workability of the FRC could be compromised by the fibres addition, in particular if they present a high aspect ratio or complex shape (CNR-DT 204/2006, 2008). It can be improved or modified by using additives or increasing the fine aggregates amount in the matrix.

Depending on the type of fiber, their volume and geometry, the post cracking behavior can be classified as hardening or softening. Those characterized by hardening behavior are defined high performance composite materials: SHCC (strain hardening cementious composite), HPFRC (high performance fibre reinforced concrete) and UHPFRC (ultra-high performance fibre reinforced concrete); typically used for tunnels or irrigation canals.

An important aspect to be mentioned regards the characterization of the FRCs behaviour during the serviceability states: in this perspective, many research studies have been carried out with the aim of understanding how creep and shrinkage deformations can be modified by the fibers inclusion.

1.2.2. Types of concrete and fibre reinforced concrete

The development in the technologies regarding the concrete production has not only the goal of increasing the material strength but optimizing other properties, i.e. workability, ductility and permeability. For this reason, according to the performance needed, a different composition of the material could be adopted:

- HSC – High Strength Concrete;
- SCC – Self Compacting Concrete;
- FRC – Fibre Reinforced Concrete or FRCC – Fibre Reinforced Cement composites;
- HPFRC – High Performance Fibre Reinforced Concrete;

All the composites listed can be classified as high performance materials (concretes or cement composites), characterized by several properties improved if compared with the normal plain concrete (Löfgren, 2005).

High Strength Concrete characterized by w/c < 0.35 and $75<R_{ck}<115$ MPa, are designed using hydraulically active inorganic materials, i.e. ground granulated blast-furnace slag, or constituents reactive with calcium hydroxide (fly ash, micro-silica, calcined clays, silica precipitated) that affect the physical and mechanical properties and concrete durability. Since the high cement dosage, varying from 400 to 500 kg/m^3, and the low water – fines ration, the adoption of a proper superplasticizer is required. Moreover, the optimization of the constituents dosage needs experimental tests to find out the compatibility of ingredients: this property is identified by the compressive strength reached and slump test results indicating the workability and consistence (Bozza M.).

Self-compacting Concrete exhibits its high performance at fresh, early age and hardened state. It has been shown how its adoption is able to rationalize the production gaining several advantages as faster construction, better working conditions and health problems reduction and easier casting since the ability of filling every mould shape during the fresh state (Grauers, 2000).

Fibre Reinforced Concrete is characterized by a cementitious matrix mixed with discrete fibers showing good performance in terms of ductility, direct tensile and flexural tensile strength, impact resistance, if compared to ordinary concrete materials (Collepardi and Troli, 2013). This type of reinforcement is randomly distributed while the ordinary steel reinforcement is placed where necessary according to the stress state. One of the improved aspect is the control during the cracked state, phenomenon that affects an ordinary reinforced concrete structure for what concerns the durability and their static behaviour. For this reason, steel grid or small diameter bars, are used to reinforced concrete structures (Coppola and Buoso, 2013). The strategy of fibers addition makes possible to create a three dimensional reinforcement able to absorb tensile stress in all directions developing a stitching action that allows also to resist to impulsive loads, i.e. cyclic loads, hits and crashes. Nowadays, fibers are used with structural and non-structural purpose, in this case to control plastic and drying shrinkage in industrial pavements.

High-Performance Fibre Reinforced Concrete (or cement composite) is classified as the material exhibiting a post-peak hardening behaviour, so reaching a higher post-peak strength and characterized by a multiple cracking evolution according to the classification proposed by Naaman and Reinhardt 2006. The low water-fines ratio and the high amount of cement used for matrix design gives the high performance: generally the use of fine aggregates with filler function is optimal because a homogeneous and compact matrix is created, i.e. silica fume. The optimization of the mix design for high and ultra high performance concretes is a topic widely investigated: the shape of fine aggregates added seems to affect the material properties. For example the addition of metakaolin, with irregular grains, or silica fume, with rounded grains, has a different influence: the former increases the plastic viscosity at any age of test, even if the fibre content and paste content decreases, while the latter increments the flowability so that plastic viscosity is not so improved (Amanjean, Mouret, and Vidal, 2019).

1.2.3. Fibers reinforcement properties

The fibres addition, as already explained, mitigates the cracking phenomenon increasing the energy absorbed during the cracking process, improves the durability and, partly, substitutes the ordinary reinforcement. The use of steel rebars, sometimes, requires a wider concrete cover to avoid the corrosion phenomena that, using fibres, is reduced. From a production point of view, the fibre itself could be continuous or discontinuous: in the first case they are aligned creating a texture or long tapes, in the second case they are shorter and, for this reason, with a random distribution in the matrix (Alvaro, Pascale, and Di Tommaso, 2007).

Fibres reinforcement can be different in (a) size and shape, (b) material and (c) dosage.

Size and Shape characterize the geometry of the fibrous reinforcement. It is identified by:

- Length, distance between fibre ends;
- Diameter (or equivalent diameter computed when the cross section is neither circular or square), the diameter of the single fibre or that of a circle with equal fibre cross section;
- Aspect ratio, ratio between the length and the equivalent diameter to evaluate the slenderness of the filament;
- Shape, the fibre could be straight or shaped, in longitudinal or transversal direction.

However, these properties influence the flexural toughness of FRCs. For instance hooked-end steel fibers show better performance than straight but also twisted elements can be adopted in this sense. The curved shape influences the behavior of material at the interface fiber-matrix enhancing the crack resistance of the whole material and so its flexural strength (Yoo, Kim, Park, Park, and Kim, 2017). Many studies have revealed that the aspect ratio has an influence on the material toughness, load bearing capacity and fracture energy but this value has to be chosen according to the maximum aggregate size in order to not influence the crack bridging mechanism (Hameed, Turatsinze, Duprat, and Sellier, 2009).

The reinforcement commonly used has a length between 1 and 80 mm and the aspect ratio ranging from 50 and 400. In Figure 1.4 are reported some examples of different fibre profiles, this property can affect significantly the bond properties. They can be produced with crimped shape (Figure 1.4a), straight shape (Figure 1.4c-d) with superficial treatments, with hooked ends (Figure 1.4b).

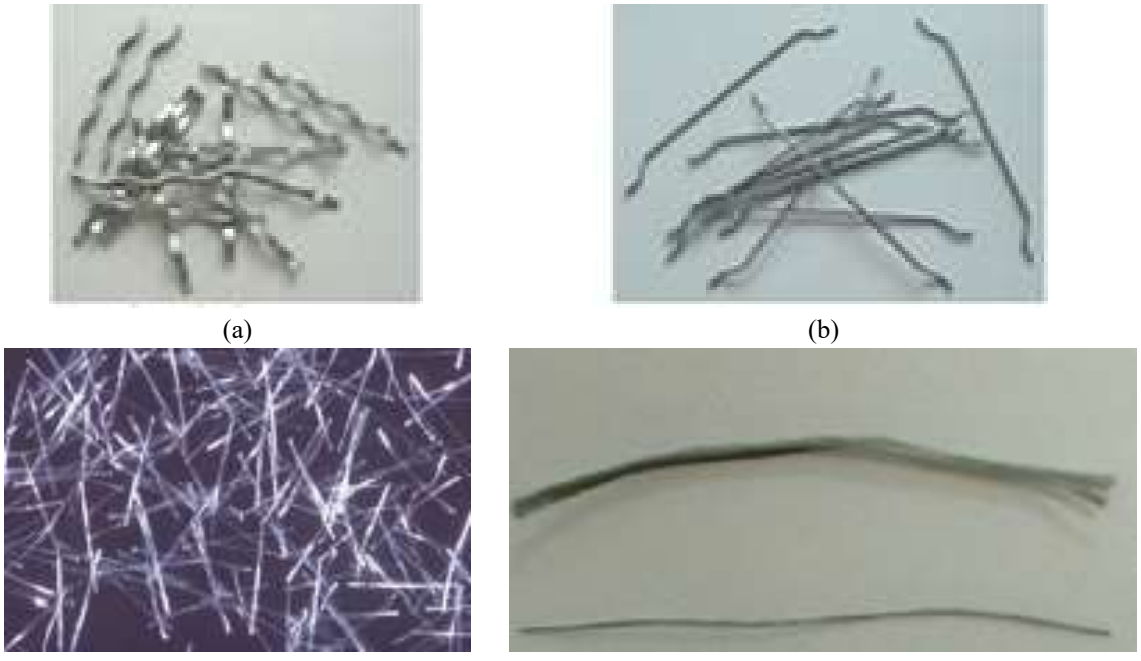

(a) (b)

(c) (d)

Figure 1.4 –Example of Fibres shape: (a) Crimped; (b) Hooked end; (c) Straight; (d) Monofilament (Plizzari, 2008).

The fibre length, or aspect ratio, that is commonly used to characterize the geometry of the macro fibers, plays an important role in the workability of the admixture and also modifies the reinforced concrete performance in both short and long term behaviour. The fibre shape modifies the interface properties: crimped fibres, for example, have a high specific surface in contact with concrete, so this shape is able to face good bond properties.

Moreover fibres can be divided into two large categories, micro and macro fibres: monofilament and fibrillated micro-synthetic fibers are characterized by a length of 12 – 38 mm lengths with typical dosage rates varying from 0.3 – 0.9 kg/m^3 depending on the application. On one hand micro fibers assure a superior resistance to the cracks induced by plastic shrinkage if compared to a welded wire reinforcement, on the other

hand they are unable to contrast the crack width increment over time, caused by drying shrinkage or other stress states.

Macro-synthetic fibers keep the positive aspect of the plastic shrinkage cracks control but also increase the durability, toughness and structural capacity if a proper design is carried out. They have typically a length of 38 – 50 mm with dosages from 1.8 to 9 kg/m^3 (Euclid Chemical, 2018).

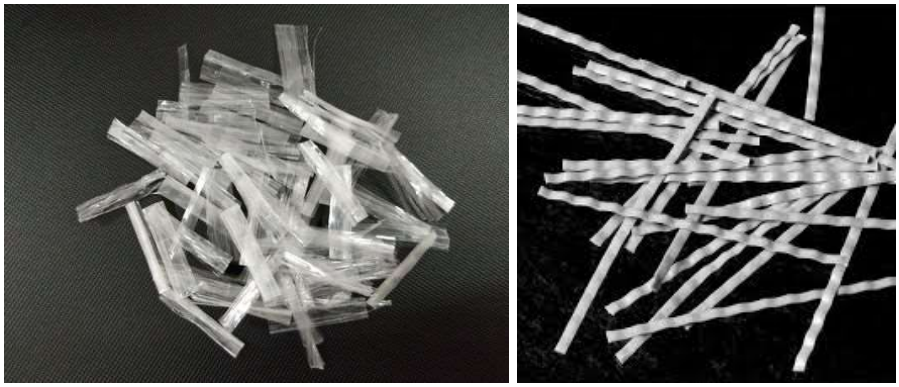

Figure 1.5 – Example of Synthetic Fibres: (a) Micro Fibres (indiamart.com); (b) Macro Fibres (danteer.com).

The cross section shape can vary, from circular to rectangular, elliptical, triangular and irregular (Figure 1.6): this difference implies a different ratio between their surface area and their length. Fibers with rectangular shape are adopted for industrial pavements, different treatment are provided to make them suitable for many applications: during the cast, the rectangular shape drives their placement along the direction parallel to the element surface.

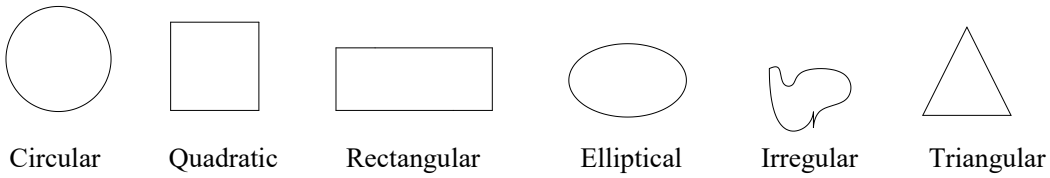

Figure 1.6 – Example of cross sectional geometries of fibres.

The fibre Material represents a further variable. They can be made of steel, polymers, glass, natural materials. They can be classified according the structural and non structural applications (Table 1.1):

Table 1.1– Geometrical properties for structural and no structural steel fibres (Coppola and Buoso, 2013).

STEEL FIBRES		NO STEEL FIBRES		
Shape	Needle	STRUCTURAL	Equivalent diameter	0.4-0.8 mm
Section	Circular / Squared		Length	20-60 mm
Geometry	Crimped / Hooked		Dosage	1.5-6.0 kg/m^3
Equivalent diameter	0.4-1.2 mm	NO STRUCTURAL	Equivalent diameter	0.013-0.2 mm
Length	25-80 mm		Length	10-30 mm
Dosage	25-150 kg/m^3		Dosage	0.6-1.2 kg/m^3

The international standard UNI EN 14889-1 (2006) specifies the properties of steel fibers in case of structural and no structural applications, adopted for concrete, mortar and mortar for injections.

The International code ASTM A 820 (1996) proposes a classification of steel fibers according to the product or the process used:

a. Type I, cold-drawn wire
b. Tipe II, cut sheet
c. Type III, melt-extracted
d. Type IV, mill cut
e. Type V, modified cold-drawn wire.

For each fibre the way to consider the cross-sectional are is specified in order to calculate the tensile strength, indicated to not be less than 345 MPa.

Macro-synthetic fibers are covering plenty of applications since they are easy to handle and not affected by corrosion although time dependent phenomena, creep, environmental conditions and temperature, might reduce their effectiveness (N. Buratti and Mazzotti 2015). They can be produced with several plastic materials, acrylic, aramid, carbon, nylon, polyester, polyethylene, polypropylene, also recycled (Yin et al., 2015). Polypropylene fibers are produced by homopolymer polypropylene resin and present relatively low melting point and elastic modulus compared to other

types. Moreover, polypropylene fibres are used for early strength enhancement and thermal and moisture changes control as they disappear at high temperatures (ACI Committee 544, 2002). The aramid fibers have high tensile strength and tensile modulus, with no changes in properties up to a temperature of 160 °C. Carbon fibers are typically used in aerospace industry sector, produced in tows and spread prior to incorporation in the CFRC to facilitate cement matrix penetration and to maximize fiber effectiveness. Glass fibres are covering many structural applications, above all they are used in exterior building façade panels. GFRC composites possess noticeably load and strain capacity faced during the matrix cracked phase: the additional strength and ductility are attributed to the fibre pull-out mechanism (ACI Committee 544, 2002).

Some examples of fibres produced with steel, carbon, polypropylene with different shape and length are depicted in Figure 1.7.

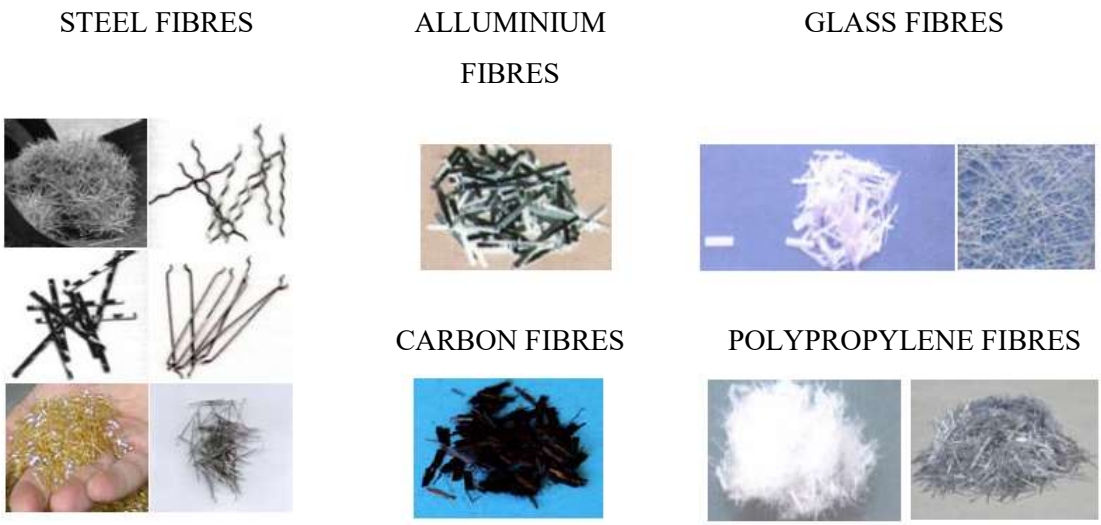

Figure 1.7 .Examples of discrete fibres produced with different materials.

An overall classification based on the elastic modulus of fibres, that is the mechanical property driving the load transfer when concrete starts cracking, divides fibers into two categories: those with elastic modulus lower than the concrete matrix (cellulose, nylon, polypropylene) and those with higher elastic modulus (steel, glass, carbon, kevlar). The organic fibres, with low elastic modulus, suffer more from viscous deformations and, in a concrete matrix cracked state, can exhibit a high deformation. At the same time, the high poisson coefficient causes a decrement of the

cross section diameter with the elongation, inducing the slippage and, so, the failure of the fibre from the matrix. Fibers with higher elastic modulus can improve the present aspect. Thus, using a grid made of fibers or a different surface shape and geometry, able to exhibit a high anchorage, this mechanism can be improved and evolve differently (Collepardi and Troli, 2013). In Table 1.2 the material constituents the fibres commonly used in fibre reinforced concrete field are listed, with the typical diameter, length, density, elastic modulus and tensile strength.

Table 1.2 – Mechanical properties of fibres made of different materials (Collepardi and Troli, 2013).

Fibre	Diameter [μm]	Length [mm]	Density [kg/m^3]	Elastic Modulus [MPa]	Poisson Modulus [-]	Tensile Strength [MPa]	Volume used [%]
Carbon	8	10	1900	380000	0.35	1800	2-12
Polyvinyl alcohol	10	6-12	1300	20000	-	1500	10
Cellulose	-	-	1200	1000	-	300-500	10-20
Glass	8-10	10-50	2540	72000	0.25	3500	2-8
Braided glass	110x650	10-50	2700	70000	-	1250	2-8
Kevlar PRD 49	10	6-65	1450	133000	0.32	2900	<2
Polyacrylo nitrile	10-20	8-40	1180	13500	-	600	0.5-1.5
Nylon	>4	5-50	1140	<4000	0.40	750-900	0.1-6
Polypropy lene	500-4000	20-75	900	<8000	0.46	400	0.2-1.2
Steel	10-330	10-60	7860	160000	0.28	2100	0.5-2

Sometimes also hybrid reinforcements are used, micro and macro steel fibers for example, to optimize the performance of the composite material, taking advangate of the different geometry and properties of the reinforcement (Sorelli, Meda, and Plizzari, 2005). The simoultaneous use of steel, polymeric and carbon fibers might generate a composite with enhanced properties of toughness, impact resistance, permeability, durability plastic shrinkage control, thermal expansion and electrical conductivity joint integrity (Plizzari, 2008).

Dosage of fibers for FRCs design influence the post peak strength. The amount adopted can lie in three different categories:

- Low, 0.1-1%
- Medium, 1-3%
- High, 3-12%.

Their amount, together with the single fibre mechanical properties, tensile strength and elastic modulus, drive the cracking process: the matrix will show a crack corresponding to a deformation much lower than that of fibre who will carry the load until its slippage or breakage that will happen for a deformation much higher than that of concrete.

Since the crack opening is hindered by the reinforcement, the fibres dosage and, indirectly the number of fibres crossing the cracked surface are responsible of the load bearing capacity in concrete matrix cracked state (Buratti, Mazzotti, and Savoia, 2011).

Typically, the FRCs residual flexural strength mechanical parameters (characterized in Chapter 2) are correlated with the effective number of fibres counted on the cracked surface. Cavalaro and Aguado extensively discussed this correlation and how it is reflected on FRCs tensile strength, its variability and fibers distribution, observing that as their volume increases the scatter in reinforcement distribution rises and consequently the curves describing their mechanical response (Cavalaro and Aguado, 2015).

However, the randomness in distribution determines the fibre position close to the crack: an inclined fibre crossing the crack needs a higher load to pull-out. Thus, considering the whole FRC material, this property is reflected in the enhancement of the residual strength. (Li, Wang, and Backer, 1990; Yang, Wang, Yang, and Li, 2007). The International Standard UNI EN 14721:2007 reports the verification of the steel fibres distribution inside the matrix, for both concrete in fresh and hardened state.

It is important to underline that the reinforcement distribution is responsible of the creation of fibrous entanglement that can affect in a negative way the material

behaviour, i.e. the load transferring. The combined use of shorter and longer fibres helps to gain higher residual strength and drive differently the cracking process (Markovic, Walraven, and Mier, 2004).

1.2.4. Concrete matrix properties

The matrix is considered the continuum element of the composite material able to transmit the stress to the reinforcement during the cracked state. The concrete itself needs to be resistent, tough, workable, resistent to shrinkage cracks, impact and fatigue (Plizzari, 2008).

FRCs are designed using the same mix of constituents as the ordinary concrete with the same cement type used, the most used is the Portland (Rossi and Pascale, 2007). Regarding the concrete mix, the water-cement ratio should be designed with particular attention in order to not create voids inside the matrix partly already due to the fibers addition. The presence of voids can generate contractions and, so, the presence of induced stress state with consequent deterioration. When a high dosage is required, the coarse aggregate percentage should be reduced increasing the fine aggregate obtaining a more viscous mix. The CNR-DT 204/2006 prescribes that the maximum aggregate size, d_a, must be lower than 0.5 times the fibre length l_f, assuring uniform and efficient distribution of the fibers inside. To reduce the creation of groups of fibres, a continuum granulometry assortment for concrete should be prescribed and the length of the fibrous reinforcement should be related to the minimum width of the structural element (t):

- Local minimum value: $t \geq 2.0\ d_a$;
- Section without steel reinforcement or single reinforced: $t \geq 2.4\ d_a$;
- Section with more than one reinforcement layer: $t \geq 4.0\ d_a$.

According to reinforcement type, the relations between the spacing, i, d_a, the bars diameter ϕ, l_f, are reported.

1.2.5. Mix design and rheological parameters

Concrete needs to be classified also during its fresh state, measuring the consistence and resistance while, after at a certain curing age (typically 28 days), compression strength and cracking force are characterized. The fibers addition gives the mixture properties of toughness, required for structures subjected to many and repeated blows, i.e. highway joints and industrial slabs, and this capacity is experimentally tested applying repeated multiple blows in the middle of the specimen until the breakage is reached. As mentioned in the general aspects, the fibres addition modifies the concrete workability. On one hand, their use does not reduce the drying shrinkage deformations and those produced by iperstatic stresses inside the material. On the other hand, the fibres addition avoids the propagation of the cracking pattern generated by the drying shrinkage and limitates the deformations induced by the plastic shrinkage for those elements exposed to the water evaporation prematurely: this purpose is fulfilled above all by polymeric fibres (CNR-DT 204/2006, 2008). The workability reduction depends on the reinforcement aspect ratio and dosage: as they increase, the concrete shows less workability. The aim is the improvement of the reinforcement efficency calibrating their amunt.

Figure 1.8, proposed by Plizzari, indicates the change of consistence from plain to fibre reinforced concrete as the dosage increased, the quantities indicated for steel and polymeric are the typical dosages adopted to not modify significantly the admixture consistence. This problem can be solved modyfing the granulometry of the matrix choosing a different maximum aggregate size, mantaining a constant water cement ratio increasing the cement dosage to help the fibres dispersion or adding superplasticizer, the last solution is the most adopted solution (Plizzari, 2008).

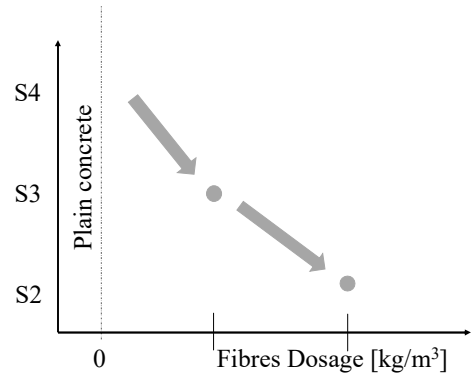

POLYMERIC FIBRES DOSAGE:

> 0.8 – 1 kg/m^3

STEEL FIBRES DOSAGE:

≈ 25 kg/m^3

Although the slump class can be reduced

Figure 1.8 – Relation between fibres dosage and consistence classes (based on Plizzari, 2008).

An aspect to be born in mind is that the fibrous reinforcement has to be added after the other constituent are mixed according to the prescribed velocity. The mixing process of a fibre reinforced concrete with polymeric fibres influences the single fibre performance, especially for flat geometries (Lerch, Rooyen, and Boshoff, 1999). Generally, they are added to the mixture during the mixing phase, after which the admixture mixing goes on for about 5 minutes.

The fibre and aggregate are linked by geometric relations:

- Maximum aggregate size $\leq$ 0.5 fibre length;
- Minimum thickness of the structural element $\geq$ 1.5 fibre length;
- Maximum aggregate size $\leq$ 1/3 minimum structural element thickness.

The rheological material properties are those characterizing the fresh state. Their declaration is a relevant aspect since their influence on the material performance during the hardened state. Moreover, the workability of concrete matrix is declared according to the regulation UNI EN 206-1 (2016), specifying the consistence of the mixture obtianed through the slump test: this is used for characterization of both plain and fibre reinforced concrete at fresh state. The test procedure is regulated by UNI EN 12350-2 (2019).

The classification and consistence class attribution follows what collected in Table 1.3:

Table 1.3 – Consistence classification according to UNI EN 206-1 (2016).

CONSISTENCE CLASS	MIXTURE LOWERING [mm]	DENOMINATION
S1	From 10 to 40	Wet
S2	From 50 to 90	Plastic
S3	From 100 to 150	semi-fluid
S4	From 160 to 210	Fluid
S5	More than 210	Superfluid

The same regulation, UNI EN 206-1, apart from this test, points out other tecniques to classify the fresh state of concrete:

- Vebè classes;
- Classes of compactability;
- Spreading classes.

The fibre reinforced concrete workability is mostly represented by the Vebè test since it represents the conditions of the concrete cast in the reality. The parameter describing the property is the time necessary to compact the concrete after its vibration at a prescribed velocity. The regulation indicates the following classification:

Table 1.4 – Consistence classification according to UNI EN 206-1 (2016).

CONSISTENCE CLASS	VEBE' TIME [s]
V0	≥ 31s
V1	From 30 to 21s
V2	From 20 to 11s
V3	From 10 to 6s

It accounts for the size and volume of aggregates, the air content, the superplasticizer percentage and the superficial fibre friction, aimed also at computing the critical fibre volume exceeded which the compactation needs to be performed with other tecqniques. The referring regulation is UNI EN 12350-3 (2019). The flow test is described in UNI EN 12350-5 (2019) dividing the consistence classes according to the spreading diameter and the compactability. What can modify the ordinary concrete workability are the ambiental conditions and the type and dosage

of ingredients used to cast it. On the other side, the FRC workability is influenced mostly by the fibres volume in the matrix, as stated before, in particular it decreases with the volume increment. The constituent fibre material modifies also the consistence, propylene material, mostly with high aspect ratio tend to create tangles during the mixing phase. In addition, the high aspect ratio could lead to the same mixing conditions. The fiber size combinated with the aggregate size drive the internal arrangement and the reinforcement contribution (CNR-DT 204/2006, 2008). For this reason, it is preferible the usage of fibres with low aspect ratio and a high volume fraction, so as to not compromise the post peak ductility of the material.

If the aspect ratio is less than 100 and a medium dosage is adopted, the superplasticizer usage is adviced in order to obtain plastic concrete with a good consistence. It is remarkable that a high plasticizer content can cause the segregation of the aggregates. A good compromise is the adoption of a percentage of silica fume that gives a good workability and high viscous consistence avoiding the segregation problem. The mixture stability is compromised by this phenomenon that is controlled by a test perfomed throwing a portion of concrete and measuring the amount of aggregates before and after the test as indicator of segregation state, the higher aggregates amount remaining the less segregation tendency of the material.

Apart from the tests described, the realization of structural elements with FRCs need further ispections to assure the compatibility of the structure with the requirements in terms of function, durability and resistance properties (CNR-DT 204/2006, 2008). Regarding the FRC fresh state, a correct mixing procedure is verified also by a visual ispection (Figure 1.9).

Oggetto	Proprietà	Metodo	Frequenza	Registrazione
FRC fresco	corretta miscelazione	ispezione visiva [v. UNI EN 206-1 2001]	ogni giorno di getto di miscela omogenea	apposito modulo
FRC fresco	contenuto di fibre	*peso dopo separazione fibre-matrice [v. CEN prEN 14721 2004]	ogni 50 m^3 di getto di miscela omogenea o almeno due controlli al giorno	apposito modulo
FRC indurito	resistenza prima fessurazione	Appendice A	Appendice B	apposito modulo
FRC indurito	resistenze equivalenti	Appendice A	Appendice B	apposito modulo

Figure 1.9 .Tests performed during the production (*valid only for steel fibers), CNR DT 204/2006

1.2.6. Interface characterization

The strength of concrete is limited by internal defects, microcracks and holes (Roumaldi and Batson, 2008) and this lead to a brittle failure in tension. This weakness is overcome with steel reinforcement opportunely spaced so to reduce cracks formation. The fibers addition sees the improvement of the material performance in terms of fracture toughness, tensile and flexural strength and ductility (Lin, Kanda, and Li, 1999) and the random distribution of short fibres in a concrete matrix allows to not concentrate the reinforcement strength along one preferential direction resulting almost weak in the other directions (Imechanica.org). This evaluation is expressed also referring to the unidirection of composites materials where the fibres are arranged only along one principal direction (Tuberosa, Troiani, Sangiorgi, Scafè, and Marabini, 2012)

Different bond fibre-matrix conditions generated influence the post-cracking phase due to a different failure mode triggered by the fiber. The mechanism activated in the fibre surroundings close to the matrix has been the subject of several investigations. Bentur et al. observed the interface conditions of fibrillated polypropylene fibres trough SEM analysis finding out that the bonding is strictly controlled by interfacial adhesion and mechanical anchoring (Bentur, Mindess, and Vondran, 1989). The first researches were aimed at understanding the mechanisms of load transfer at the fibre-matrix interface and the optimal methods to evaluate the bond strength in a composite material (Chamis, 1972). The first steps towards the study of mechanical phases characterizing the fibre slippage assumed that at a critical embedded length value, the debond from the matrix starts at a stress level depending on the yield stress and work-hardening rate of the wire, its surface conditions, i.e. its roughness (Bowling and Groves, 1979). The stages characterizing the pull-out failure, pointing the critical length whitin which the failure mode changes, were studied on the hypothesis of homogeneous material with small variation in properties of their interface (Bartoš, 1980). The first attemps in formulating theoretical models that could describe the failure at interface materials and the aspects that mostly influence it are described in (Bartos, 1981; Hsueh, 1992; Naaman, 1992; Wang, Li, and Backer,

1988b) until the crack bridging phenomenon description, for FRC materials, by means of an analytical model where the stress is function of the crack width, concrete, fibre and interface parameters (Li, Stang, and Krenchel, 1993). Later, the slip-hardening interface behaviour started to be investigated (Lin and Li, 1997): it represents the background of an analytical model then formulated where a new parameter β accounting the slip-hardening effect was introduced. This model (Yang et al., 2007) describes the behaviour of a single fibre subjected to pullout force as divided into two phases: debonding and pull-out (Figure 1.10). The debonding process is concurrent with the crack propagation that develops along the interface. The representation suggests a direct proportion between force and slip until the peak after that, despite the drop of the force, the crack formed in the concrete grows after having reached the critical width and the only contribution is given by the fibre.

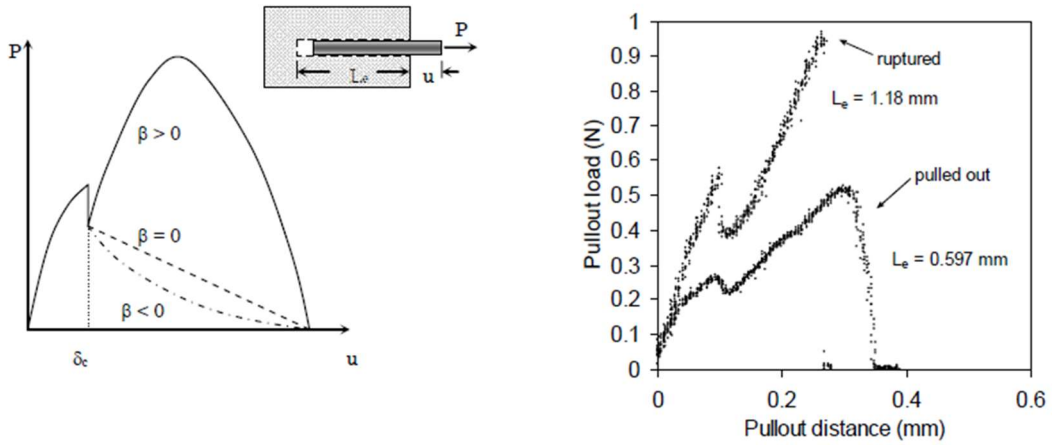

Figure 1.10 .Single fibre pull-out behaviour (a) slip-hardening (β>0), softening (β<0) and no dependence on slip distance (β=0); (b) output of a pull-out test of PVA fibres from ECC composite (fibre diameter 39μm), (Fiber-Bridging Constitutive Law of Engineered Cementitious Composites, Yang et al. 2007).

According to the interface condition, the single fibre can slip out, gaining more ductility or break in case of a very high bond strength. Intermediate bond values, for which most fibres pull out without breaking represent the most desirable behaviour because it will correspond to the highest apparent ductility of FRC elements (Jewell, Mahboub, Robl, and Bathke, 2015). The maximum force the single fiber is able to bear is named pull-out force, whose value is measured by means of pull-out tests: this

has been considered as the best way to characterize the fibre bond strength (Chamis, 1972).

The perfect adhesion between matrix and reinforcement is required if a good performance would be prescribed to the FRC. The combination of concrete and fibres give optimal properties to the composite material if a perfect bond is activated. Interface properties are so responsible of the performance of FRC materials because the bond between fibers and matrix determines the crack bridging mechanism and the capacity of sustaining load during the matrix cracked state. This is the reason why fibers are subjected to some treatments on surface to improve their bond properties (Di Maida, Radi, Sciancalepore, and Al., 2015).

The main factors influencing the fibre-matrix interaction can be summarized as:

- Chemical adhesion;
- Surface roughness;
- Fibre material properties;
- Shape of fibres;
- Strength and stifness of the matrix.

Steel fibres, for example, need to be characterized by a high friction on the surface that, combined with a hooked shape, increase the confinement of the single element by the concrete and, consequently, the bond strength (Abdallah, Fan, and Zhou, 2016) depending also on the shaped fibre edge. A hooked fiber creates an anchorage with the matrix requiring more energy to be pulled out as the increment of the matrix confinement (Figure 1.12).

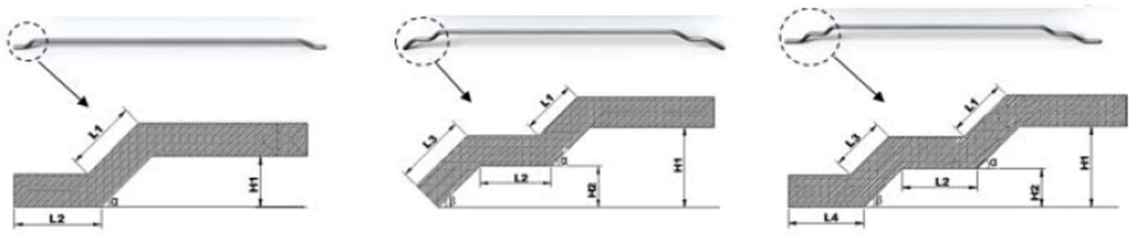

Figure 1.11 – Examples of hooked end steel fibres with different geometries (Abdallah, 2016).

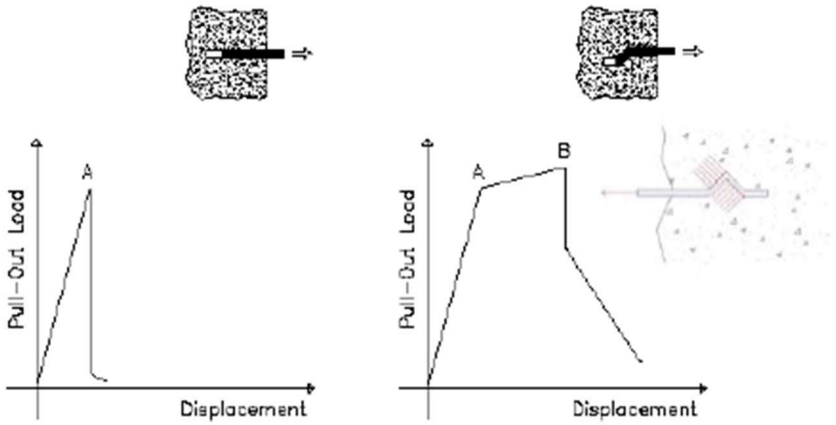

Figure 1.12 – Comparison of pullout response for straight and hooked end steel fibres (Plizzari, 2008).

Zaho et all studied the bond slip mechanism comparing hooked-end and straight shape of steel fibres by means of pull-out tests using acoustic emission techniques to investigate deeply the interfacial bond (G. Zhao, Verstrynge, Di Prisco, and Vandewalle, 2012). This research has revealed a better adhesion for hooked-end fibres that present a stronger anchorage with the matrix, as already explained. In addition, the mechanical process dominating the pull-out behaviour is different according to their profile: for straight fibres the dominating process is the residual friction existing between the two phases of the material; for hooked fibres, the pull-out curve has a linear trend followed by a non-linear trend after which both frictional and debonding processes are triggered.

Regarding the matrix strength, it plays an important role in the pull-out mechanism, a higher concrete strength involves a greater pull-out force for steel fibres that, during the slippage, shows microcracks close to the interface (Markovich, Van Mier, and Walraven, 2001).

Comparing the interface properties in the field of synthetic fibres, micro PVA fibres (Figure 1.13) face better interfacial properties than polypropylene fibres. They are mostly produced using various blends of polypropylene that does not feature a hydrophilic nature. Therefore, chemical adhesion is weaker compared to PVA fibres (Liu, Li, Liu, Yang, and Cui, 2012). The pull-out response, in terms of load displacement is strongly influenced by shape of fibres: in particular a wave-shaped profile assures higher bond strength if compared to that straight, being characterized

also by a multi-peaks pattern (Tang, Li, Wang, and Shi, 2016). The enahcement in bond strength due to a shaped fibre morphology, is associated with the increment of energy required to be pulled out. The load decrement observed during the slippage phase is due to the filament diameter reduction (Redon et al., 2001) with the elongation, especially true for polymeric materials because of the Poisson effect governing the transversal deformation.

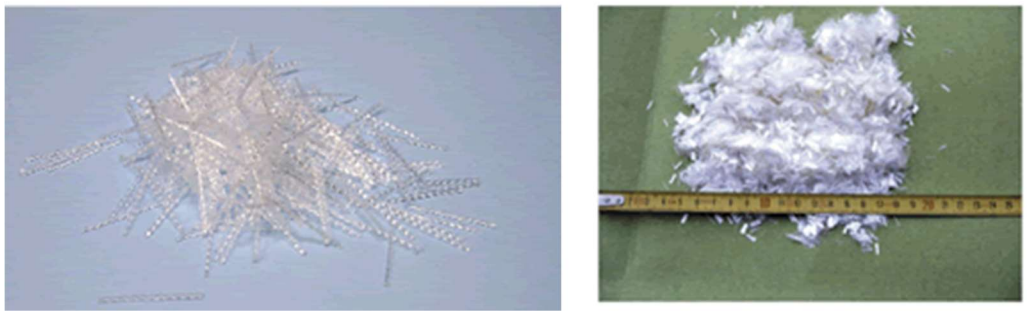

Figure 1.13 – Examples of macro polymeric and micro PVA fibres with different geometries (Abdallah, 2016).

Figure 1.14 shows how the fibre length can affect the post peak trend, due to the ability in connecting completely the two sides of the crack, that, according to the length can lead to an increment of the residual strength and a more ductile behaviour in case of longer fibres (Chasioti and Vecchio, 2017).

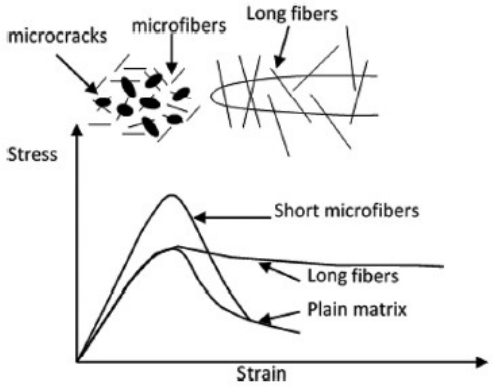

Figure 1.14 – Fibres size effect on crack bridging (Betterman, Ouyang, and Shah, 1995).

The material energy in the cracking process evolution is handled by means of many phenomena; the fibre breakage, its pull-out, the debonding from the matrix, the bridging phenomenon and the crisis of the matrix around the single fibre (Zollo, 1997). What needs to be considered is the local inflection of the fibre due to their random position that induces a stress higher than that absorbed in case of a fiber

completely perpendicular to the crack. The concentrated stresses in the fibre sorroundings might cause local concrete spalling that is proposed as one of the mechanism responsible of the pullout increment (Morton and Groves 1974, Brandt 1985).

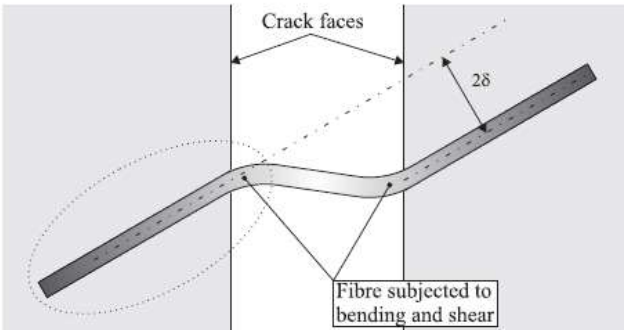

Figure 1.15 – Bending and Shear of inclined fibres crossing matrix crack (Barros and Sena-cruz 2010, Leung and Geng 1995).

1.2.7. Applications

The enhancement of the mechanical properties of concrete by the fibres addition makes FRC materials suitable for applications in those fields where concrete might face problems due to cracking, durability and low tensile capacity. Industrial floors, tunnels, structural foundations and precast elements are extensively interested by fibre reinforced concrete applications.

Industrial floors designed using FRCs are becoming widespread, since the reduction of joints representing the weak element in this type of contruction (Figure 1.16). Sometimes, they are designed combining steel and fibrous reinforcement, or with local reinforcement. Tipically joints are sawn at 6-10 m or in case of jointless floors, the dilation joints are designed with a distance < 50 m. The depth spaces between 120-250 mm and the element is designed with a concrete classes C30/37 or C35/45 with a steel fibres amount of 20-40kg/m^3.

The structural capacity of these structures is examined by applying the yielding line theory tracing the preferential directions of the crack diffusion and pattern.

Figure 1.16– Application of steel reinforced FRC: slabs and industrial floors.

Shotcrete or spritzbeton is a special kind of concrete sprayed onto surfaces of tunnels, walls to strengthen them. Shotcrete linings, in a temporary and final configuration, are designed used only fibres as concrete reinforcement, or comining it with mesh and steel arches. The layer realized covers a width of 100-200 mm for temporary linings and 50-100 mm for final structures. The concrete used in the design belongs to a class C25/30-C30/37 reinforced with an amount of 25-35 kg/m^3 of steel fibres in the first case and C35/45-C50/60 with a medium-high dosage of 30-50 kg/m^3 for final linings. The shotcrete performance is identified by flexural toughness and energy absorption, testing centrally loaded round panels, according to the ASTM C1550-08 (2012).

Figure 1.17– Application of FRC: shotcrete.

Precast sewer pipes are also designed with steel fibres reinforced concrete, according to the European regulation EN 1916 (2004), for a thickness of 5-12 mm and a diameter ≤ 1.2 m only the fibres reinforcement could be used, while for larger diameter a combined reinforcement is designed. In this application the range of fibers amount lies in a medium-high range of 15-40 kg/m^3. Tunnels realization sees also the application of concrete reinforced with steel fibres to realize segmental tunnel lining

for a diameter of 4-16 m, relized with concrete C40/50-C50/60 and a fibre amount of 30-40 kg/m^3.

Figure 1.18– Application of FRC: precast sewer pipes and tunnel lining.

The use of fibers could substitute completely the traditional steel reinforcement reducing the construction time typical of traditional concrete casting, guaranteeing the uniform reinforcement, increasing the fire resistance, reducing the cracks deriving from the shrinkage and increasing the toughness of the concrete.

Some special applications regard the use of the composite material for underwater concrete slabs, structures in hydraulic engineering and pre-stressed beams, roof panels.

Reinforcing material is believed to be another potential application of fibre reinforced concretes with the aim of increasing the ductility of a structural element applying a layer of FRC in the bottom part of a reinforced concrete beam (Figure 1.19).

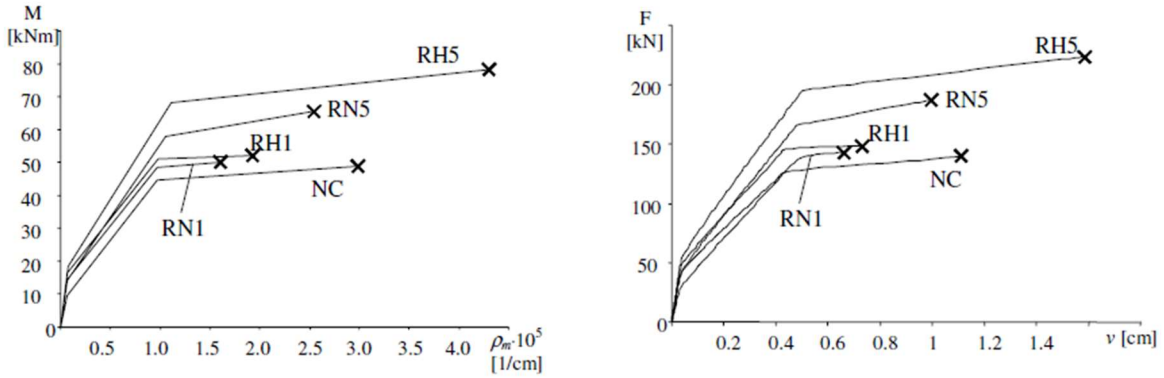

Figure 1.19– Moment Curvature and Load Displacement of beams reinforced with differente fibres dosage and concrete strength FRC (Rinaldi, Grimaldi, and Galli, 2004).

The research carried out by Rinaldi et al. (2004) revealed an increment of ductility, characterized in terms of moment-curvature relation, for a concrete beam reinforced

with high dosage of FRC (5%) with fibre having a plastic behaviour (RH5 in figure 1.19) (Rinaldi et al., 2004).

This application involves also the use of FRC with high performance.

In the perspective of the reinforcement of a structual element with FRCs, the adhesion between support and reinforcement material is crucial because of the load transmission. The nature of the adhesion is physical, chemical and mechanical. Some preliminary threatments can be necessary to improve the adhesion, for example filling the cracks or removing portion of damaged material to not create discontinuities and stress concentration.

When the support consists of traditional reinforced concrete, the steel condition need to be checked in case carbonation phenomena are triggered.

CHAPTER 2

2. SHORT TERM BEHAVIOUR: ASPECTS AND CHARACTERIZATION

2.1. MICROMECHANICS OF FRCs

The FRCs mechanical performance is dominated by internal micromechanical processes activated. Concrete exhibits microcracks due to shrinkage, thermal expansion of mortar even if the load is not applied. Since the interface mortar-concrete represents the weakest part of the admixture, microcracks appears in loading conditions because of the difference in stiffness. Concrete material is characterized by low tensile strength, and above all by a brittle mechanical behaviour.

The fibres inclusion makes possible to overcome the concrete weakness achieving the cracking control during the cracked state of concrete gaining residual tensile strength (Easley et al., 2010). The nonlinear fibre reinforced concrete mechanical behaviour derives from damage mechanisms involving the matrix cracking and the progressive debonding and slippage of the fibre (Marfia, 2007). Thus, it is important to study how the interface properties can slow down the FRC cracking process. The composite toughness increment is due to the energy dissipated by friction between the materials: this purpose is fulfilled by using different fibers shape and designing the concrete matrix opportunely, as described in section 1.2.2.

The interaction between the debonding, slippage process and the matrix cracking, has been widely studied above all for continuous fibres in brittle matrix (Aveston, Cooper, and Kelly A. 1971, Budiansky, Hutchinson, and Evans 1986). Then, some micromechanical models have been proposed to determine the relation between the cohesive tension and the progressive FRC crack opening, taking into account the crack control opered by aggregates and fibres (Stang and Krenchel 1993, Stang, Li, and Krenchel 1995). The hetereogeneity of concrete and so the aggregate size assortment generates many voids inside the cementitious matrix: this is a characterizing aspect of the cementitious based materials.

2.1.1. Interface characterization

Different conditions might drive the cracking pattern of concrete, aggregates characteristics, grains assortment, stiffness and strength, surface conditions, texture and the additional type of materials used in the design admixture. Many researches have been carried out aimed at understanding the aggregate and matrix grade effects (Darwin, Barham, Kozul, and Luan, 2001; Karihaloo, 2001; Otsuka and Date, 2000; Vasanelli, Micelli, and Aiello, 2014; Wu, Chen, Yao, and Zhang, 2001) added to micromechanical model of the fracture process proposed (Tijssens, Sluys, and Giessen 2001, Mier and Vliet 1999). Generally the cracking process evolution in concrete starts with existing microcracks before the loading phase, due to internal state of stress; when load is applied, cracks start at interface mortar aggregates propagating till the peak strength is reached: the softening behaviour is governed by crack bridging and branching.

The micromechanics of FRCs, in terms of cracking process evolution, is correlated with:

- Fibre geometry;
- Fibre mechanical properties (bond strength, tensile strength, elastic modulus);
- Fibre orientation respect to the crack

The fibers contribution starts when concrete reaches its tensile strength and cracks appear: the debonding and subsequently the load transferred to the fibre might lead to the fibre slippage or breakage, correspondent with respectively lower and higher bond strength, at a certain critical opening width. These actions are responsible of the FRC toughness increment.

According to the fibre type and shape, the cracking process is handled differently with a different fracture energy required. In Figure 2.1b-c a typical pull-out curve characterizing the single fibre performance is reported: first an initial elastic bond is assured until the fibre starts debonding, after full debonding the pull-out stage is controlled by the friction contribution during the softening branch due to the progressive decrement of the embedded length and the slip-decaying friction. The

fibre profile exhibits a different mechanical interlock with concrete and so, the pull-out process is handled differently if a hooked end shape is compared to a straight or crimped/corrugated fibre. The deformations of the hooked end help to dissipate more energy. For a crimped or corrugated form, adopted mostly for plastic fibres, is possible to increase the length and so their bond strength (Khabaz, 2016): in this case, while the fibre pulls out, it is subjected to an elongation making it loosing its original shape and its profile drives the post-peak trend. For indented fibres, the friction stage is characterized by a waved shape due to the particular geometry (Groth, 2000).

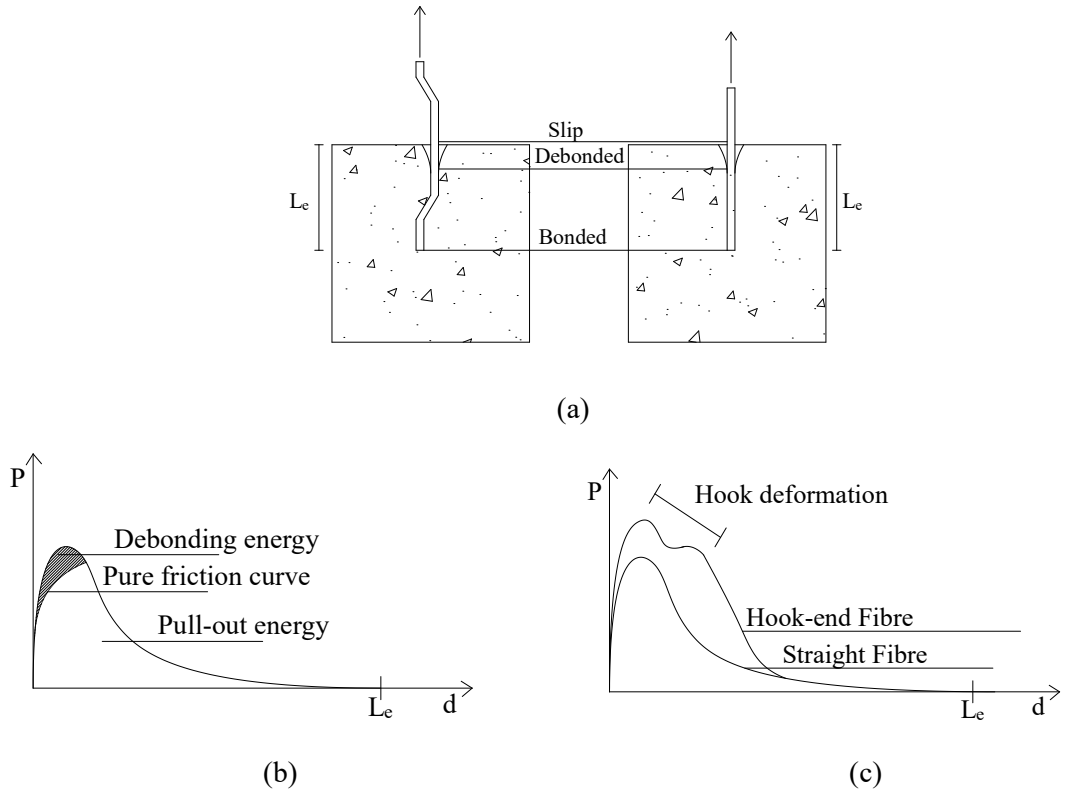

Figure 2.1 –Pull-out behaviour: (a) Fibre-Matrix interface zones; (b) Fibre pull-out curve (based on Bentur et al. 1995); (c) Difference between straight and hooked end fibres (based on Löfgren 2005).

Within the plastic fibers, PVA and polypropylene face different bond strength properties due to their different hydrophilic nature, the former are characterized by a higher bond strength and require more debonding fracture energy in pulling out. Polypropylene fibres feature a weaker chemical adhesion, as already mentioned in the previous section.

An element playing an important role is the fibre orientation that is driven mostly by the coarse aggregates arrangement in concrete (Ostrowski et al., 2018): the

phenomena activated by a inclined fibre bridging a crack are studied by performing pull-out tests with angles different from 90° between the fibre and the surface: the pull-out resistance of fibre with an angle > 45° is higher than aligned fibres (Brandt 1985) because of the mechanism associated with the vertical component in which the pull-out load is divided. During the fibre slippage, the matrix spalling (Figure 2.2a), might occour and, in this case, its strength results of great importance. This phenomenon is associated with the stress concentration coming up by the deviation between the portion of embedded fibre and the pull-out force applied. Load has two components, parallel to the fibre, responsible of the pull-out mechanism and perpendicular (Cunha, Barros, and Sena-cruz, 2010b). The snubbing effect is attributed to the frictional contribution of the matrix cone during the slippage phase generating a load increment. An additional effect, known as Cook-Gordon effect (Figure 2.2b), is due to the crack propagation towards the fibre that generates its elongation. Basically, with the increment of the inclination of the fibre, the pull-out force increases since the confinement action of concrete towards the fibre, applying a normal force higher than in the case of zero inclination.

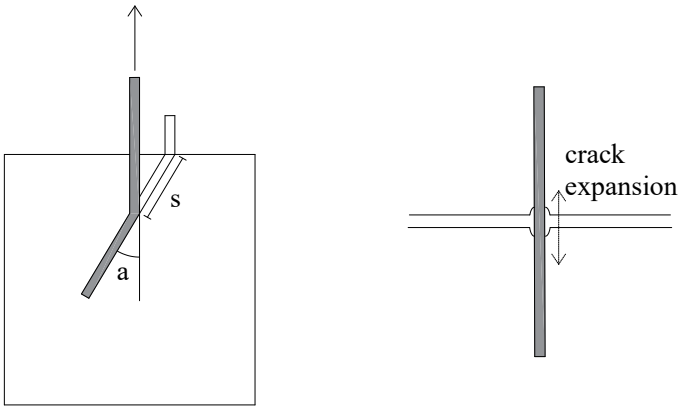

Figure 2.2 – Pull-out behaviour of inclined fibres: (a) Spalling effect and (b) Cook-Gordon effect (based on Yang et al. 2008).

The mechanical constitutive law that describes the fibre matrix interaction can be included in one of two categories: relations assuming that, considering the interface, there is a bonded and debonded zone and those relations considering the interface as a cohesive zone at each instant during the pull-out process. The former category is based on a criterion driving the progressive increment of the debonded zone: the

fracture energy and the resistance are the mechanical parameters on which the criterion is formulated (Stang, Li, and Shah, 1990). In Figure 2.3c, it is assumed that the bond strength at the end of the debondend zone has an infinite value and an adequate fracture energy has to be triggered to extend the debonded length. This is the so defined characteristic interfacial fracture energy (Stang and Shah, 1991). The constitutive model in Figure 2.3a, assumes a resistance criterion: as the maximum bond strength for the matrix or fibre is reached, that is equal in the bonded zone, the debonding is activated. The constant value of the bond strength τ_f refers to the friction bond strength causing slippage in this part. The model in Figure 2.3d sees a gradual decrement of the bond strength in the transition zone between the bonded and debonded fibre length (slip-weaking models): the breakdown zone is thought to be associated with the local microstructure at fibre-matrix interface.

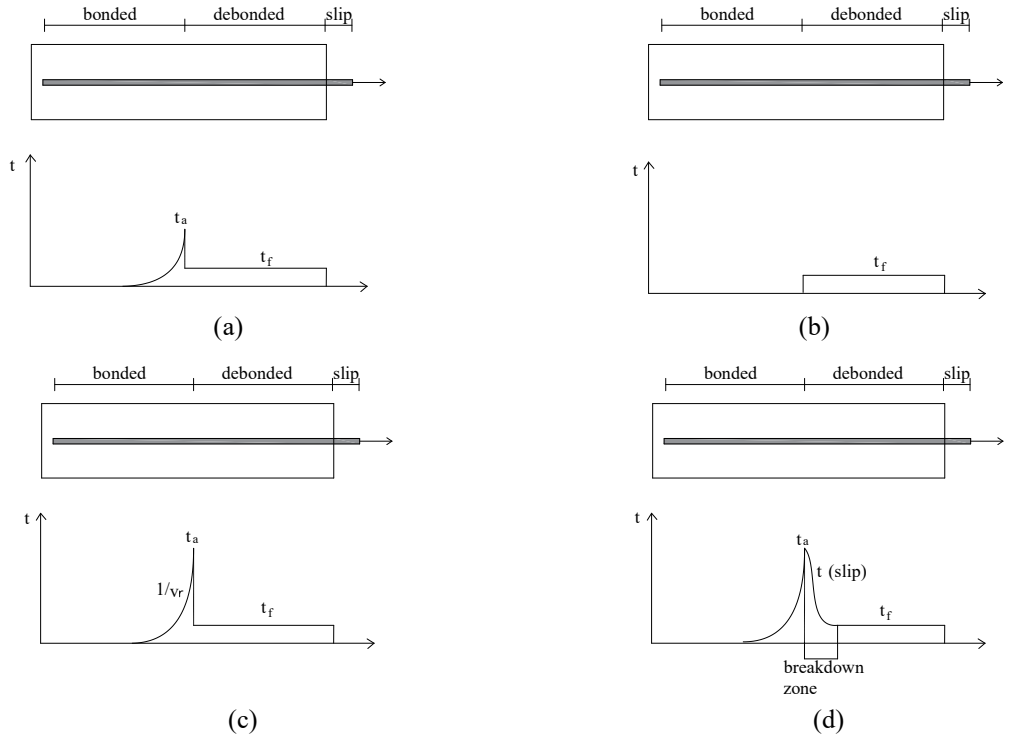

Figure 2.3 – Interface properties described by (a) Linear elastic brittle fracture model; (b) Cohesive strength model; (c) Slip softening fracture model; (d) simplified strength based model (based on Victor C. Li and Stang 1997).

The second type of models describe the entire interface with one constitutive relationship assuming that the relative displacement between fibre and matrix are responsible of the load transferring mechanism. Any cohesive models propose a

linear relation between bond strength and slippage for low displacements, while generally the stress due to a friction contribution is characterized by a softening or hardening trend. The most difficult aspect to investigate is the adhesion modulus and the initial stifness of the interface: the phenomena interacting at the interface during the initial stage are attributed to either fibre and matrix, since the matrix closer to the interface is weaker than in the other part of the composite. Many investigations have been carried out but succeeding only in the determination of the constitutive relation of the descending branch (Y. and Shah, 1993). For this reason, it is common to assume τ_s the slippage stress as a material constant, for example Wang et al. (Wang, Li, and Backer, 1988a) introduced the relation:

$$\tau_s = \tau_0 + a_1 \Delta v + a_1 \Delta v^2 \qquad [2.1]$$

Where the parameters τ_0 a_1 a_2 are dependent on the fibre type: τ_0 is quantified differently if a lateral pressure is applied. For example, Leung and Geng suggested a Coulomb law dependent on the friction coefficient μ (Li and Stang, 1997), while the other coefficients can be either positive or negative accounting the local interfacial damage with a reduction of the bonded zone between fibre and matrix. Nammur and Naaman (1986) proposed a constitutive law that describes the interface stress slip law by a monotonous linear model in the two stages, assuming a constant value of τ_s and so neglecting the interface fracture energy and the hardening or softening stress trend.

2.1.2. FRC fibre bridging mechanism

According to the mechanisms described before, the FRC mechanical performance is the result of the combination of both fibre properties, regarding material and geometry, their placement and orientation and aggregates particles contribution. The tensile strength of the material is not strongly affected by the fibres addition while the residual strength, if compared to that of plain concrete, grows significantly. For brittle materials, i.e. plain concrete, a localized crack and, consequently failure, drives the post peak behaviour leading to a load decrement as the concrete matrix starts cracking (Figure 2.4). Examing the fibre reinforced concrete behaviour during the

cracked state, fibres and aggregates are combined to give their bridging contribution. Considering the cracking process evolution four different zones can be distincted: a zone of microcracking (A-C) and macrocracking growth (C-D), the zone where the load is transferred trough fibres and aggregates (D-E) and traction free zone achieved for large crack openings (Choun and Park, 2015).

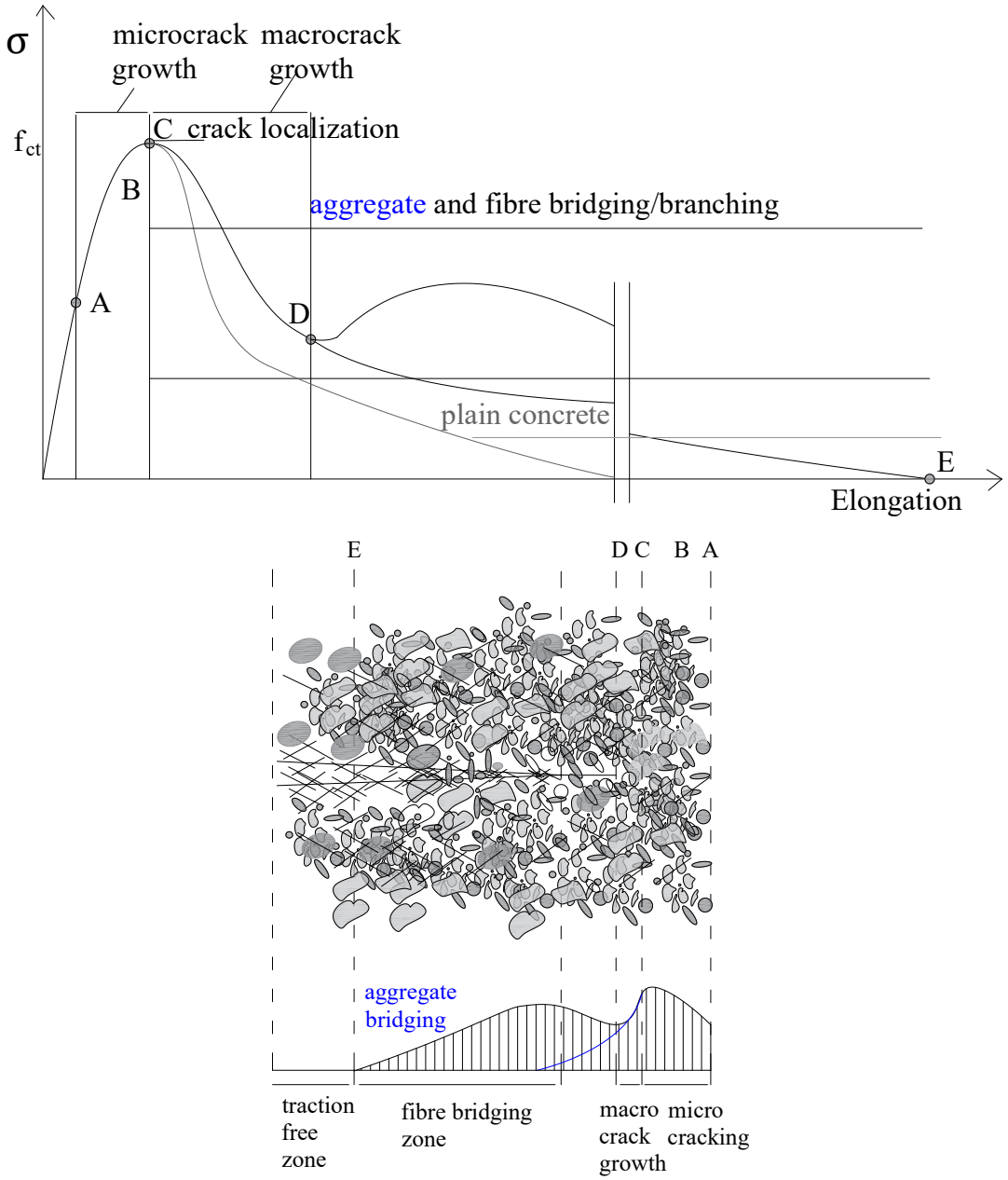

Figure 2.4 –FRC cracking process under uniaxial tension: fibres and aggregates bridging effect (based on Choun and Park 2015).

Basically, the contribution of fibres occurs gradually, and their geometry drives differently the cracking state evolution, for example, for hooked end or shaped fibres, the stress could increase due to its deformation during the pull-out phase.

Since the fracture process depends on the aggregate size compared to that of fibre, micro and macro fibers work at a different scale because, given the same dosage, they are less spaced and, so, a greater amount is added.

Thus, the number of fibres connecting the cracked surface is a variable that could reflect better the differences also in terms of fibre geometry and, how, they influence the residual strength capacity. The simulation of the bending capacity of structural element starts from the behaviour of the single fibre in terms of constitutive law since the strict connection of the fibre failure mechanism with the crack-bridging activation and evolution.

2.2. MECHANICAL PROPERTIES

2.2.1. Theoretical characterization of FRC tensile properties

The definition of the mechanical properties for fibre reinforced concretes cannot follow the same characterization of ordinary concrete, typically identified by its compressive strength, although the other mechanical properties are considered. The main difference presented by the two materials is the constitutive behaviour, linear for conventional concrete, until the peak load and then characterized by a softening behaviour. On the other side, FRCs exhibit an almost elasto-plastic behaviour.

The residual strength gained thanks to the fibers addition is the factor that distinguishes the FRCs mechanical performance from that exhibited by the unreinforced concrete. Due to this, the residual tensile strength is the property mechanically characterized.

Many theoretical models have been formulated with the principal aim to highlight the ductility achieved by the fibres addition, starting from many assumptions that simplify the problem discussion.

The first model was proposed by Romualdi and Batson (Shah, 1988) applying the concepts of linear elastic fracture mechanics, assuming the crack bridging capacity operated by fibres when the material is subjected to a triaxial tensile load, avoiding the crack propagation. This assumption finds a discrepancy because in the reality there is no perfect bond between the two materials: the slippage along the interface

fibre-matrix was neglected. As this model did not find any experimental applications was not adopted.

The prediction of the tensile strength for a composite material is addressed also to an alternative theory to that proposed by Romualdi and Batson, the role of mixture. The initial assumptions of the present theory are:

- The fibers alignment along the loading direction;
- Perfect bond between the two components, fibre and matrix;
- Poisson's modulus equal to zero for both materials.

Considering fibre, V_f and matrix V_m volumes as ratio of the unitary volume is possible to express the stress state of the composite as:

$$\sigma_c = V_f \sigma_f + (1 - V_f)\sigma_m \quad [2.2]$$

$$E_c = E_f V_f + (1 - V_f)E_m \quad [2.3]$$

where:

E_c, E_f, E_m elastic moduli of material composite, fibre and matrix;

σ_c, σ_f, σ_m stress of material composite, fibre and matrix.

Imposing the equality of strain $\varepsilon_m = \varepsilon_f$:

$\sigma_f = n \cdot \sigma_m$ (n coefficient of homogenization) [2.4]

$$\sigma_m = \frac{\sigma_c}{1 + (n-1)V_f} \quad [2.5]$$

Defing:

- ε_{mu} strain correspondent to the matrix cracking;
- σ_c matrix cracking stress;
- V_{fcrit} fibres critical volume;
- σ_{mu} matrix ultimate stress;

- σ_{fu} fibre strength, in case of breakage failure, or bond strength, in case of pull-out failure;
- $n = \frac{E_f}{E_m}$ homogenization coefficient.

The global stress of the composite material results:

$$\sigma_c = \sigma_m[1 + V_f(\frac{E_f}{E_m} - 1)] \quad [2.6]$$

This relation highlights the limitated influence of the fibers addition to the cracking stress of the composite, although in the initial approaches, the contribution was supposed to be associated with a delay of the composite material cracking process. Considering, for example, an elastic modulus of 30 GPa for concrete, reinforced with 2% of steel fibres with modulus of 210 GPa, the composite stress results 1.12 higher than the matrix strength. As a concluding remark, the fibres inclusion does not modifies significantly the pre-cracking mechanical behaviour. In case of lower elastic modulus, 0.5% of polypropylene fibres with 8 GPa modulus of elasticity, the composite strength is almost equal to that characterizing the concrete matrix. An observation should be exposed about the influence of the fibers addition during the fresh state of concrete during which the matrix modulus of elasticity is lower than that characterizing the reinforcement. Therefore, the tensile strength of the composite is incremented by the fibers insertion and this leads to a better control of additional stress in concrete due to the plastic shrinkage in this phase.

The hypothesis listed before simplify the problem, not accounting the random fibres placement and the interface strength between the two materials: these effects can be included considering two factors, η_Φ considers the fibres placement efficiency and η_l the fibre length influence (Balaguru and Shah 199, Maidl 1995):

$$\sigma_c = \sigma_m \cdot V_m + \eta_\Phi \cdot \eta_l \cdot \tau_{av} \cdot \frac{L_f}{d_f} \cdot V_f \quad [2.7]$$

Where τ_{av} is the average bond strength and L_f / d_f the fibre aspect ratio.

The orientation factor is different during the elastic and cracked stage of the composite: regarding the elastic state, when the composite deforms only in the load applied direction, the efficiency factors are assumed by Cox (Cox, 1952), as equal to 1/3 for random 2-D dispersion and equal to 1/6 to random 3-D arrangement. In case of deformations also in the other directions, the efficiency factor is equal to 3/8 and 1/5 respectively for random 2-D and 3-D placement (Krenchel, 1964).

During the cracked state, the stress is transferred from the matrix to the fibre, this phenomenon can be described by the shear-lag theory, originally introduced by Cox to describe the behaviour of fibrous paper. The theory is based on the equilibrium between the fibre stress σ_f and the interfacial shear stress τ_i that is the mechanical process on which is based the crack bridging mechanism (section 2.1.2).

2.2.2. Uniaxial tensile strength

The failure processes activated in the composite materials with a cementitious matrix follow more a ductile behaviour: this difference can be highlighted by a tensile test on a fibre reinforced concrete sample.

An ordinary concrete, when tested under uniaxial tensile load configuration, shows a softening post-peak behaviour. The fibre addition does not modify substantially the tensile strength, although during the first loading stage both cementitious matrix and fibers carry the load: this is due to the increment of porosity caused by the reinforcement addition. The main role of the fibrous reinforcement is the increment of the residual stress driving the post-peak material response. According to the volume fraction added to the cementitious matrix, the FRC could be still characterized by a descending post-peak behaviour, as in Figure 2.5a considering a volume of approximately 0.2-2% of fibre, but gaining residual tensile strength and increasing the toughness. The post-peak behaviour can follow a hardening trend as in Figure 2.5b if a volume ranging from approximately 2% to 8% is considered. The cracking pattern is, for softening FRC, featured by a localized failure, inducing the ‘softening’ behaviour, while, the higher amount of fibres handles the cracking process generating a multi cracking pattern dissipating more energy and exhibiting a more

ductile behaviour. Moreover, the formation of many cracks reduces the problems connected to the penetration of aggressive external substances since the increment of number of cracks involves smaller opening width. It is important to underlined that the hardening mechanical behaviour could be achieved either with a high fibre dosage or by designing the cementitious matrix with high performance.

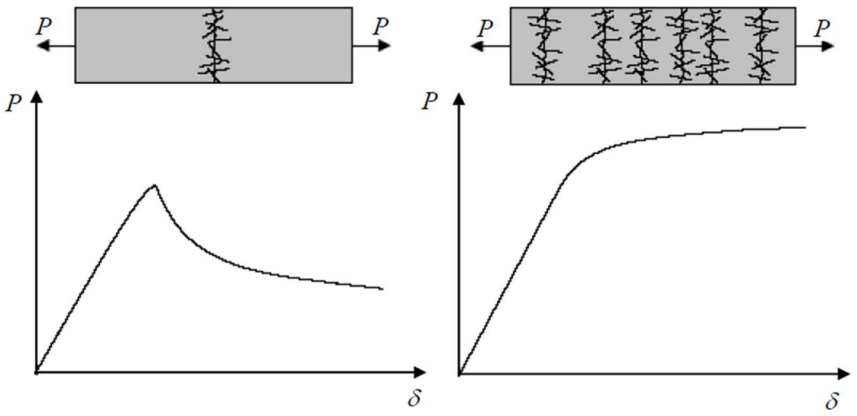

Figure 2.5 – Load – Displacement curves for FRC specimens under uniaxial load characterized by (a) Low fibre volume fraction and (b) Higher fibre volume fraction (CNR-DT 204/2006, 2008).

The uniaxial tensile tests present many difficulties in performing, for this reason the tensile strength on fibre reinforced concretes is characterized by means of flexural tests on notched specimens. The aspect to be born in mind is that a uniaxial softening behaviour does not implies the same response under a flexural load because the flexural stress state sees a compressive zone where the deformation increases linearly with the stress helping a more stable crack propagation: for this reason the post-peak behaviour under flexural load could present some differences.

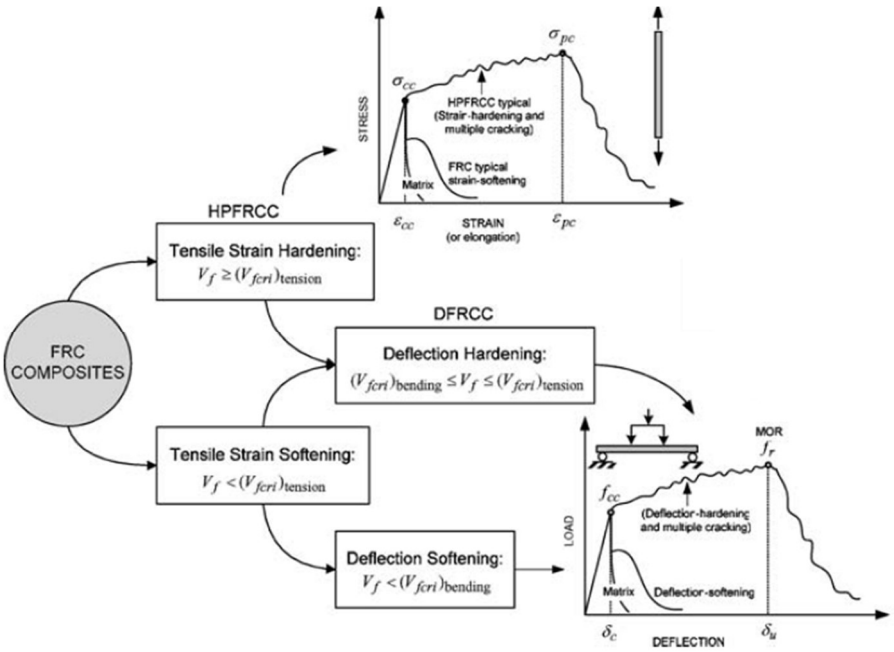

Figure 2.6 – Performanced-based classification of fibre reinforced concretes (Naaman and Reinhardt, 2006)

2.2.3. Flexural strength

As stated before, the flexural behaviour of FRC materials is considerably different from the response under uniaxial tensile load. Besides, the present material is strongly adopted for those structural applications with a predominant flexural load state. Thus, it is necessary to characterize the flexural mechanical behaviour. Examing the section of a beam under a flexural load, during the uncracked state the stress has a linear distribution along the height of the section.

As the matrix cracks, the load bearing capacity is attributed first to both aggregate and fibers, then only to fibers: the stress distribution along the cracked part of the section is not linear anymore (Figure 2.7).

The trend can be approximated by a constant stress distribution (Collepardi and Troli, 2013).

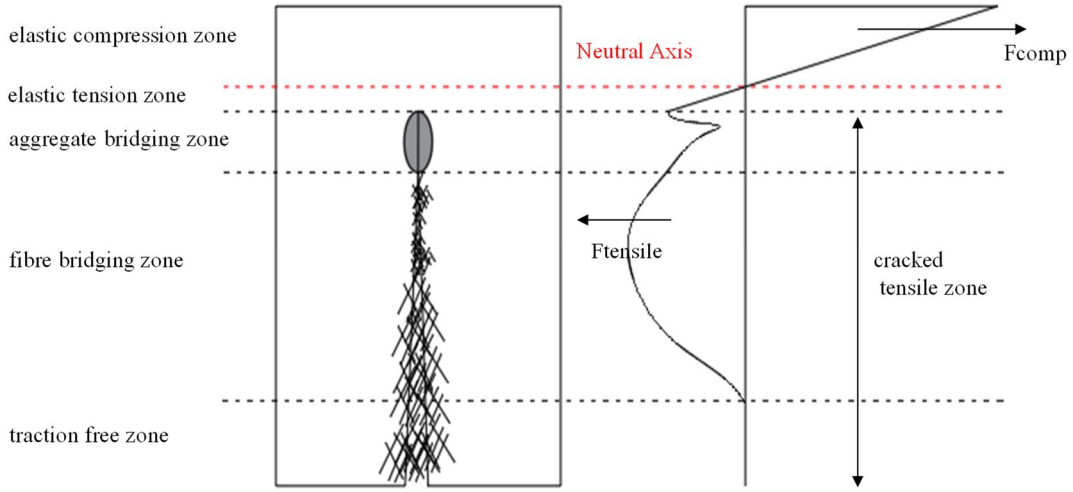

Figure 2.7 – FRC stress distribution for a section under flexural load: uncracked and cracked state (based on Robins et al. 2001).

At this point, it is important to estimate the minimum volume of fibres able to bear the load: the mixture theory could be used for the calculation considering the maximum load of the single fibre σ_{fu}. As specified before, this parameter represents the fibre strength itself in case of fibre breakage or the maximum bond strength in case of pull-out failure, so:

$$\sigma_c = V_{fcrit} \cdot \sigma_{fu} \qquad [2.8]$$

and considering the composite strength as calculated before [2.6] is possible to write the following expression:

$$V_{fcrit} = \frac{\sigma_m}{(\sigma_{fu} - E_f \varepsilon_m + \sigma_m)} \qquad [2.9]$$

indicating the minimum fibre volume needed to absorb the load when the matrix is cracked and the load is transferred. The increment of fibre strength makes possible to reduce the volume fraction adopting fibers with lower elastic modulus. Moreover, the present theory demonstrates how the bond strength is strongly responsible of the material performance during the cracked state: using fibres with low bond strength implies an increment of the volume fraction to make possible the load absorption.

It is necessary to state that the real volume fraction needed will be higher than the quantity output of the expression just analysed because this theory idealizes the

mechanical behaviour since the hypothesis do not verifies in the reality, i.e. perfect bond. The difficult aspect lies in the mixing phase that could be compromised by a high volume fraction insertion (CNR-DT 204/2006, 2008).

The volume fraction, the effective number of fibres crossing the cracked surface and the bond strength are the parameters most influencing the FRCs mechanical behaviour: it is possible to increase the ductility of the material with a proper consideration of these parameters.

The flexural test is the most significant test to mechanically characterize the energy dissipated and so the material toughness, the equivalent flexural strength and other parameters identifying the post-peak behaviour.

2.2.4. Compressive strength

The cementitious materials are characterized by a good compressive strength: in case of fibre reinforced concretes this property is not remarkably affected by the fibres addition because, although the role of the reinforcement is to connect the crack sides, assuring a strength increment, the absence of perfect bond between the two materials do not make possible to achieve an increment of compressive load. Thus, the relative slippage between concrete and fibres is considered as partly responsible.

On the other hand, the bridging action operated by the fibrous reinforcement in the direction perpendicular to the cracks formation under compressive load, is reflected on the failure mechanism that appears different from that exhibited by conventional concrete (Sarbini, Ibrahim, and Saim, 2012). For this reason, the descending branch is characterized by a less softening trend given the increment of the ultimate strain, so the mechanical behaviour appears more ductile, as indicated in Figure 2.8.

From the design point of view, the constitutive relation regulating the compressive behaviour and the compressive strength itself can be considered as those proper of concrete without fibres. Thus, the compressive strength is determined following the International standard test regulations indicated in UNI EN 12390-3 (2019) as for plain concrete.

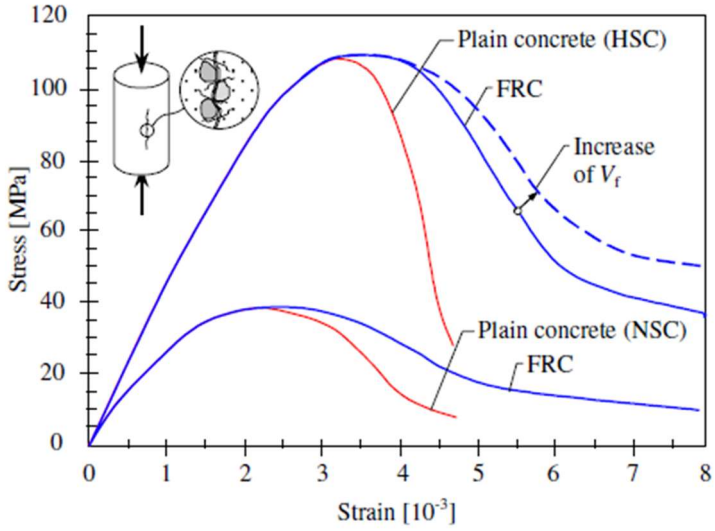

Figure 2.8 – FRC and HPFRC compressive behaviour compared with plain concrete compressive response (Löfgren, 2005).

2.3. RECOMMENDATIONS IN FRC DESIGN

The design of FRC structures requires reliable models reproducing the materials constitutive behaviour. In the previous section the evolution of the cracking process is described referring to the phenomena activated during the cracked state: in this framework the constitutive model adopted should reflect the mechanical processes.

The constitutive relation describes the FRC behaviour by a stress versus crack opening curve that could be used in a cohesive crack model, for example the fictitious crack model proposed by Hillerborg (Hillerborg, Modéer, and Petersson, 1976) or a crack band model (Z. P. Bažant and Oh, 1983). The σ – w diagram is based on the Hillerborg FCM (Fictitious Crack Model) that divides a stress – displacement curve into the σ – ε constitutive relation describing the concrete behaviour outside the crack and a stress – crack opening relation describing the softening of the cracked section. On one hand, the stress deformation relation describes the elastic behaviour of the material while the crack opening parameter can describe better the real mechanism of FRCs.

The different attempts in formulating a constitutive model are aimed at combining the concrete and fibers contributions by an intermediate phase when the load is transferred from a material to the other. A constant post peak (Lim, Paramsivam, and

Lee, 1987) can be assumed in case of low fibres content that does not influence also the pre-cracking stage (WA, JM, and EP., 2004), Figure 2.9a; a non linear elastic trend is also proposed followed by an intermediate branch before achieving the fibres contribution (Lok and Xiao, 1998) to describe better the transferring of load from the matrix to the reinforcement, Figure 2.9b. An important step towards the full understanding of the FRC behaviour was made by Dupont and Vanderwalle (2002) who proposed a double stress levels to describe the post peak response accounting for a primarly deformation of the fibre followed by the crack bridging action. The present model assumes =2.5 and =1.5 so not dependent on the concrete tensile strength (Figure 2.9c).

Other approaches relate the stress with the crack opening to describe the post peak mechanical behaviour: in Figure 2.9d a bilinear trend with zero residual strength whose parameters identifying the two stages of the response are obtained by an inverse analysis (Kooiman, 2000). In Figure 2.9e the model indicated by Barragán (2002) considers a hardening post-cracking behaviour with an increment of the residual strength until a 2.0 mm crack opening. After several studies carried out by Di Prisco (Di Prisco, Ferrara, Colombo, and Mauri, 2004), the $\sigma - w$ model in Figure 2.9f was advanced: the constitutive model consists of a bilinear curve with a first softening part that describes the cracked concrete behaviour, followed by the fibers contribution where two residual strength values are reported correspondent to precise values of crack opening.

These models described are classified as indirect approaches while the direct elaboration considers experimental data or material properties. The variables need to be determined are: the softening plain concrete behaviour, the number of fibres crossing the cracked area, fibre pull-out behaviour and their arrangement in the matrix. However, this model is not largely used since the limitation on the crack opening value, 0.3 mm, until which it can be applied.

These models are aimed at estimating and predicting the flexural capacity of the material, combining the contributions of the constituents.

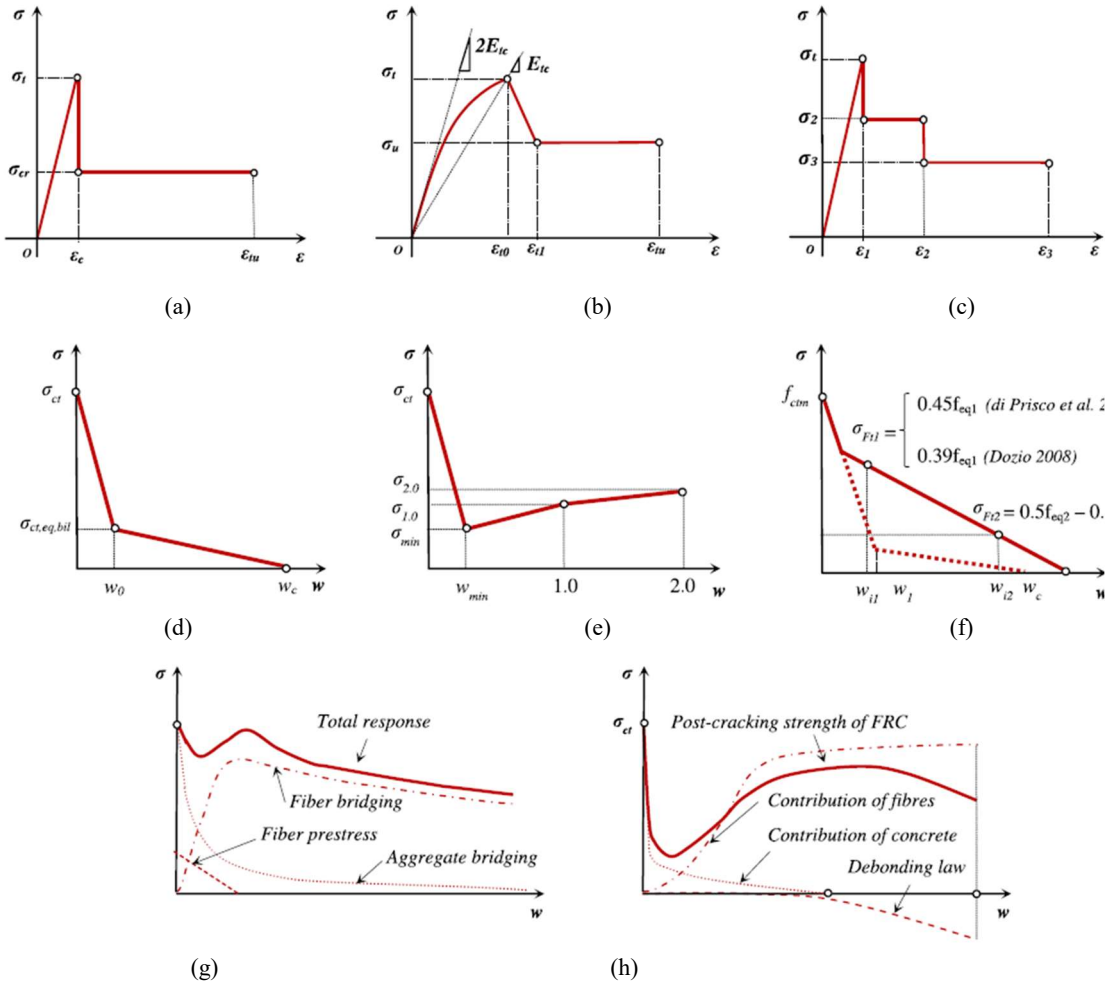

Figure 2.9 – Stress-strain constitutive behaviour describing FRC mechanical response under a tensile load advanced by (a) Lim, Paramsivam, and Lee 1987 (b) Lok and Xiao 1998 (c) Dupont and Vandewalle 2002 (d) Kooiman 2000 (e) Barragán BE. 2002 (f) di Prisco et al. 2004 (g) V. C. Li, Stang, and Krenchel 1993 (h) Foote, Mai, and Cotterell 1985 (based on Blanco et al. 2013).

The identification of the constitutive model simulating the tensile post cracking behaviour, is one of the aspects more addressed in the last decades. The innovative aspect is the model formulation with distinction between structural and no structural reinforcement, while in the initial formulations only steel fibres were accounted. A difference to point out is that some standard indications identify the tensile properties indicating the equivalent flexural tensile strength f_{eq}, while others the residual flexural strength f_R. The difference is based on the mechanical property on which their calculation is performed: the equivalent strength is associated with the energy absorption while the residual strength capacity in terms of stress the material owns in correspondence of precise deflection or crack opening values. In addition, the general aspects that the regulations specify are: the precise values of the ultimate strain, the

relation between strain and crack opening through the characteristic length, the specification of the safety coefficients, the fibers involved in the cracking spacing and their orientation. It is possible to state general recommendations or official regulations on the basis of plenty of experimental results and numerical analysis performed: the fibre reinforced concrete mechanical characterization is still an opened topic of many research projects, but the background concerning its short term behaviour has increased noticeably during the last decades.

The following sections 2.3.1 and 2.3.2 focus on the recommendations given by two guidelines in the field of FRC design and characterization, CNR DT 204/2006 and Model Code 2010, although some concepts have been already mentioned in the previous sections.

2.3.1. CNR DT 204/2006 Italian Guidelines

The Italian National Research Council (CNR) published the *Guidelines for the design, execution and control of FRC structures* with the purpose of regulating the structural applications that make use of the innovative composite material, the fibre reinforced concrete. The CNR-DT document indicates two different type of properties evaluation: nominal and structural properties. The first have to be determined by means of standard laboratories tests, the latter have to be performed on structures with the same significative size of the real structural element.

Regarding the material mechanical performance, the compressive strength is not affected by the fibrous reinforcement and it can be assumed as plain concrete strength. The elastic modulus is not affected by the presence of the fibrous reinforcement, for this reason it is assumed as the normal concrete one.

The instructions identify two main mechanical behaviour of the material, according to the volume fraction contained, for V_f ranging from 0.3 and 2% a softening behaviour, while for volume fraction greater than 2%, a hardening post-cracking response associated with a multicracking phenomenon. The peak uniaxial tensile strength is assumed as the composite material matrix tensile strength, f_{ct}, while the residual capacity can be estimated, according to the CNR-DT indications,

multiplying the extraction force of the single fibre with their number, obtaining the residual load. The equation [2.10] relates the specific extraction force with the volume fraction of fibers, V_f, the aspect ratio, l_f/d_f, and the bond between the fibre and the matrix:

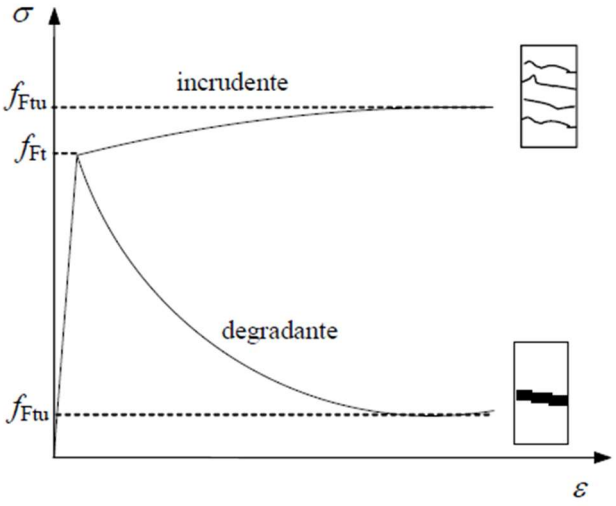

Figure 2.10 – FRC tensile behaviour according to the fibre volume content (CNR-DT 204/2006, 2008).

$$Q = \alpha \cdot V_f \cdot l_f/d_f \cdot \tau_m \qquad [2.10]$$

where α is a coefficient accounting for the fiber orientation.

It is easy to note that this procedure does not consider the condition of the single fibre element, inclination, interface conditions, fibres arrangement in the matrix. From this, the necessity of performing uniaxial or flexural experimental tests so to characterize the effective material performance. The uniaxial test follows the procedure of the International code UNI U73041440 returning the stress-crack opening constitutive law but in case of softening material behaviour it is not easy to perform due to the material instability. Alternatively the constitutive behaviour in tension can be characterized indirectly performing bending tests according to the International code UNI 11039, on notched specimens. The un-notched specimen is tested in case of thin elements accounting for cast direction, mixture procedure and wall effect, calculating more precisely the sectional ductility. In both cases the

nominal stress evaluation considers the elastic behaviour of the material, dividing the bending moment with the resistance modulus:

$$\sigma_N = \frac{6Pl}{bh^2} \qquad [2.11]$$

The output of the flexural test is a stress – crack opening relation, where the post-peak behaviour could be identified by the residual strength at precise crack opening values or adopting the equivalent strength calculated on a range of crack openings. The differential displacement between the two points at the notch tip is defined as Crack Tip Opening Displacement.

According to the characterization of the material, two simplified stress-strain laws (σ-w) are proposed, one considering the hardening or softening behaviour and the residual service and ultimate strength (Figure 2.12a), the other a rigid plastic behaviour (Figure 2.12b). Both of them describe only the post-peak behaviour.

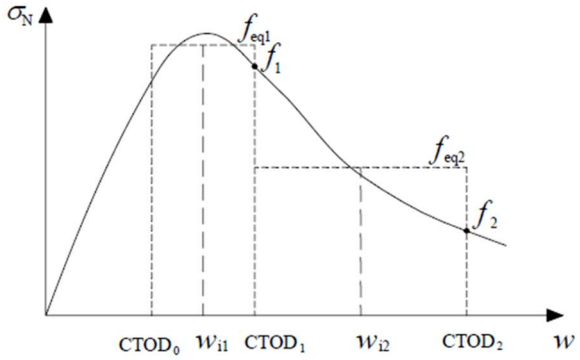

Figure 2.11 – FRC average residual strength definition (CNR-DT 204/2006, 2008).

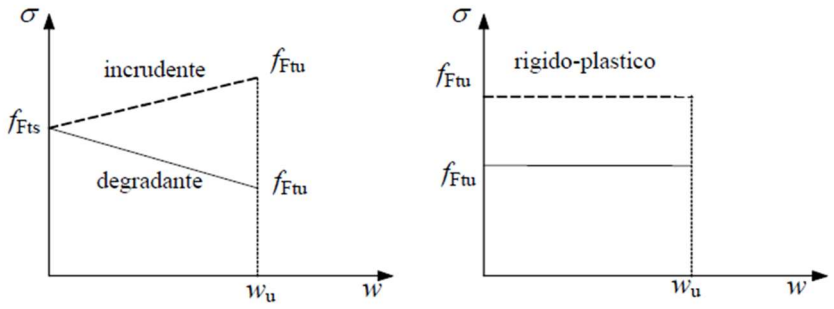

(a) (b)

Figure 2.12 – FRC simplified constitutive model (a) Linear model and (b) Rigid model (CNR-DT 204/2006, 2008).

The strength values, f_{Fts}, f_{Ftu}, w_u define the constitutive models and are calculated according to values output of the corresponding flexural test, where f_{eq1} and f_{eq2} are

related respectively to the SLS and ULS conditions. For a notched beam, f_{eq1} is the mean value over a CTOD range of 0 mm-0.6mm, while f_{eq2} over a range 0.6 mm-3mm. In case of unotched beam, f_{eq1} is evaluated on a range of $3w_I$-$5w_I$, where w_I is the opening displacement correspondent to the load peak, f_{eq2} considers the range $0.8w_u$-$1.2w_u$ with w_u the smallest value between $0.02l_{cs}$ and 3 mm.

Once the equivalent strengths are calculated, the linear constitutive relation is determined by computing the references values:

$$f_{Fts} = 0.45 f_{eq1} \quad [2.12]$$

$$f_{Ftu} = k \cdot [f_{Fts} - \frac{w_u}{w_{i2}} \cdot (f_{Fts} - 0.5 f_{eq2} + 0.2 f_{eq1})] \geq 0 \quad [2.13]$$

where k value is assumed equal to 0.7 for uncracked sections under tension and equal to 1 in the other situations. For the rigid-plastic model:

$$f_{Ftu} = \frac{f_{eq2}}{3} \quad [2.14]$$

Nevertheless, it is possible to relate the stress – crack opening constitutive model to stress – deformation relation, considering the ratio between the crack opening and the characteristic length of the structural element.

$$l_{cs} = \min\{s_{rm}, y\} \quad [2.15]$$

$$\varepsilon = w / l_{cs} \quad [2.16]$$

with s_{rm} spacing between cracks and y neutral axis position.

The present guidelines give also recommendations in case of structural elements design with fibre reinforced concretes.

The definition of the durability is described, it is of noticeable importance since the capacity of reducing the crack opening given by the fibres, until a crack opening value of 60 μm the concrete is considered uncracked. This document provides the fibres type suitable with each concrete type with reference only to steel fibres.

The procedure to compute the capacity of the structural element at ultimate limit state is described, in case of flexural load, shear in presence or absence of traditional

longitudinal and shear reinforcement, buckling, and torsion for one dimensional element, i.e. beams, using the constitutive models for the material in tension, described before. Plates loaded perpendicular and along the section are treated, showing the procedure for the resistance verification based on the values of the fibre reinforced concrete. Limitations for stress and crack opening are given for the serviceability limit states conditions, providing the prescription of the minimum reinforcement amount controlling the cracking.

Fibres

The document gives indications about the geometrical properties of the fibres, the aspect ratio, the length and the calculation of the equivalent diameter according to the cross section shape. Concerning the material, the steel fibres can be classified according to the tensile strength and the production process. Polymeric and carbon fibres can be classified in macro fibres, for a length up to 80 mm and micro fibres for length of few millimetres. Their minimum dosage in structural applications is 0.3%.

Matrix

The matrix is designed according to specific rules, for example increasing the fine aggregate ratio and assuring a good workability to have good adhesion properties. The characterization of the concrete and mortar matrix are performed according to the regulations for normal concrete in case no specific indications are given.

The polymeric fibres can reduce the shrinkage cracks during the plastic stage.

The CNR DT 204 specifies the following international regulations as available in the field of the design with FRC materials:

- RILEM, 2001, “Test and design methods for steel fibre reinforced concrete: uniaxial tension test for steel fibre reinforced concrete”, RILEM TC 162-TDF Recommendations, *Materials and Structures*, 34: 3-6;
- RILEM, 2000, “Test and design methods for steel fibre reinforced concrete: beam test”, RILEM TC 162-TDF Recommendations, *Materials and Structures*, 33: 3-5;

- ACI Committee 544, 1999, “Measurement of properties of Fiber Reinforced Concrete”, ACI 544.2R-98, *American Concrete Institute*, ACI Farmington Hills, MI;
- ACI Committee 544, 1996, “Design considerations for steel Fiber Reinforced Concrete”, ACI 544.4R-88, *American Concrete Institute*, ACI Farmington Hills, MI;
- ACI Committee 544, 1996, “State of the art Report on Fiber Reinforced Concrete”, ACI 544.1R-96, *American Concrete Institute*, ACI Farmington Hills, MI;
- JCI, 1984, “Method of tests for flexural strength and flexural toughness of fiber reinforced concrete”, JCI Standard SF-4, JCI Standards for test methods of fiber reinforced concrete, *Japan Concrete Institute*.

2.3.2. fib Model Code 2010

Making a focus on the Model Code 2010, one of the most innovative aspects regards the classification of the fibre reinforced concrete composites based on the residual strength values, derived from experimental stress-crack opening curves.

The residual strength values marked in Figure 2.13b are function of the mechanical parameters identifying the residual flexural strength, f_{R1} and f_{R3}, output of the characterization flexural test performed according to European standard reference UNI EN 14651. The specimen has 150x150x600 mm^3 dimensions and presents a notch at mid-span with 25 mm height and 4 mm width, it is tested in a three point bending test configuration monitoring the crack opening mouth displacement (CMOD). The test is carried out in displacement control with rates of 0.05 mm/min for CMOD<0.1 mm and 0.1 mm/min for larger CMOD values. The experimental test characterizes the FRC performance by means of 5 nominal flexural tensile strengths f_L, f_{R1}, f_{R2}, f_{R3} and f_{R4}, corresponding to the peak nominal strength for CMOD < 0.05 mm and the residual flexural tensile strengths at CMODs of 0.5 mm, 1.5 mm, 2.5 mm and 3.5 mm respectively.

It is recommended to characterize the material according to the UNI EN 14651, also other tests can be accepted in case of correlations with the UNI EN mechanical parameters.

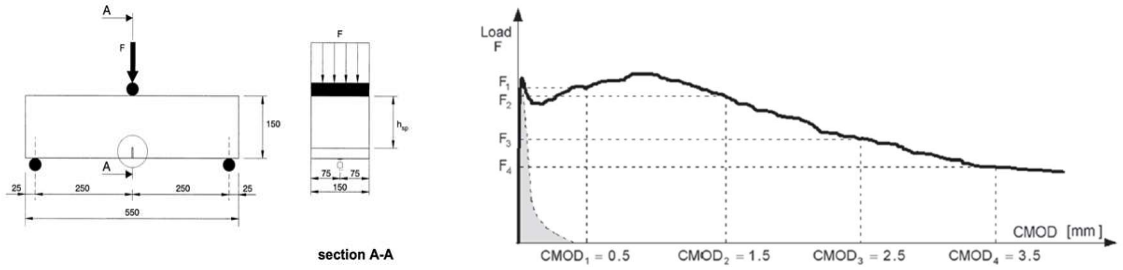

(a) (b)

Figure 2.13 – (a) Three point bending test according to EN 14651 and (b) Load-CMOD output of flexural test for plain concrete (dashed) and FRC (solid) (Di Prisco, Colombo, and Dozio, 2013).

The stress values of f_{R1} and f_{R3} are respectively the reference values for the serviceability limit states (SLS) and ultimate limit states (ULS) and their calculation follows the same concept explained before:

$$f_{R,j} = \frac{3F_j L}{2bh_{sp}^2} \qquad [2.17]$$

dividing the maximum bending moment by the resistance modulus of the section.

The fib (Fédération Internationale du Béton) introduced the FRC design guidelines by elaborating two simplified constitutive models: the rigid-plastic and the linear-elastic relations represented in stress-crack opening form for softening and hardening post peak behaviour as already described by the CNR DT 204 (section 2.3.1).

The Model Code indicates also more complex constitutive law describing the mechanical behaviour of plain concrete under tensile loads and the post peak propagation of strength for three different cases (Figure 2.14). In the first case, CASE I, for softening materials the post peak follows the relation:

$$\frac{\sigma - f_{ct}}{0.2 f_{ct} - f_{ct}} = \frac{\varepsilon - \varepsilon_P}{\varepsilon_Q - \varepsilon_P} \qquad [2.18]$$

for $\varepsilon_P \leq \varepsilon \leq \varepsilon_C$ and

$$\varepsilon_Q = \frac{G_f}{f_{ct} \cdot l_{cs}} + (\varepsilon_P - \frac{0.8 f_{ct}}{E_c}) \qquad [2.19]$$

where G_f is the fracture energy of plain concrete.

The structural characteristic length is adopted to obtain the deformation correspondent to the SLS and ULS respectively dividing the crack opening value $CMOD_1$ and the ultimate crack opening by characteristic length value l_{cs} and the minimum between $\{\varepsilon_{Fu}, 2.5/l_{cs}\}$. When f_{Fts} is larger than f_{ct} the cases II and III are defined. For CASE II the branch follows the equation:

$$\frac{\sigma - f_{ct}}{f_{Fts} - f_{ct}} = \frac{\varepsilon - \varepsilon_P}{\varepsilon_{SLS} - \varepsilon_P} \qquad [2.20]$$

for $\varepsilon_P \le \varepsilon \le \varepsilon_{SLS}$

The third case, CASE III, sees the definition of the $\overline{\text{A'D}}$ branch as:

$$\frac{\sigma - \sigma_{A'}}{f_{Fts} - \sigma_{A'}} = \frac{\varepsilon - \varepsilon_{A'}}{\varepsilon_{SLS} - \varepsilon_{A'}} \qquad [2.21]$$

where $\sigma_{A'} = 0.9 \cdot f_{Fts}$.

It is also specified that, in case of structural elements having a no homogeneous crack distribution across the section, the FRC is described with reference to different portions of the cross-section since the different crack spacing presented.

The Model Code suggests a simplified relationship for the serviceability limit states adopting the same curve of the plain concrete response and so taking into account the peak strength contribution, and a bilinear relation for the post-cracking stage. The two points $(\varepsilon_{SLS}, f_{Fts} = k_a \cdot f_{R1})$ and $(\varepsilon_{ULS}, f_{Ftu})$ describe the residual strength due to the fibre pull-out mechanism (Figure 2.15).

Regarding the long term performance, for structural fibers used as reinforcement and influenced by creep phenomena, the behaviour of cracked FRC in tension state need to be analysed. The possibility of partially or totally substitution of the reinforcement using fibres can be accepted if any requirements regarding residual and peak strength are satisfied.

The Model Code 2010 introduces also safety factors and the orientation fiber factors accounting for phenomena that can increase (>1) or decrease (<1) the post

cracking strength: this is an innovative aspect. Due to this, it is the first regulation to recommend the determination of the fiber orientation effect as representative of the material state in structural elements.

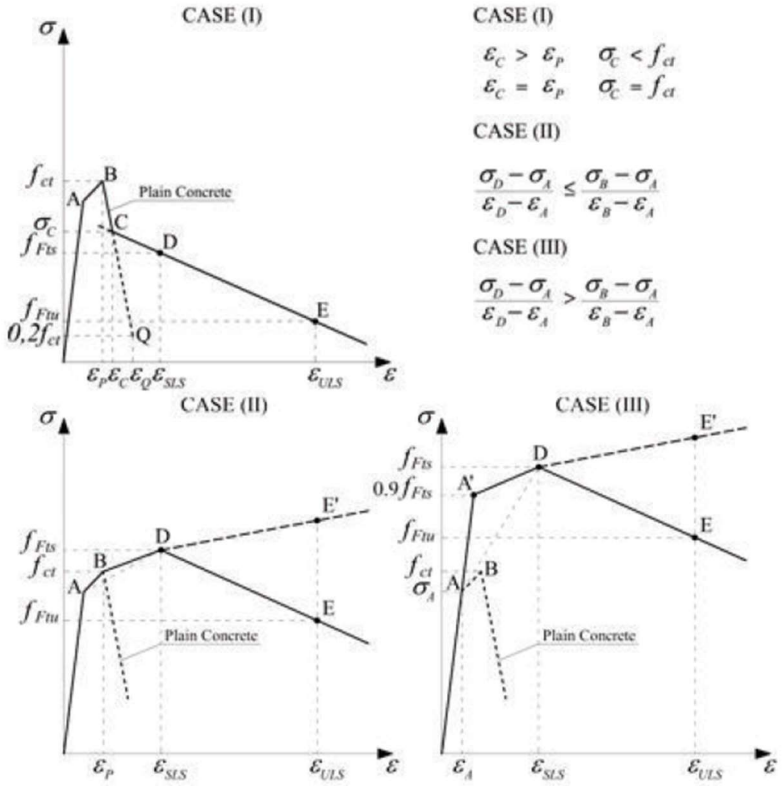

Figure 2.14 – Stress-strain relations describing softening and hardening FRC mechanical behaviour (Di Prisco et al., 2013).

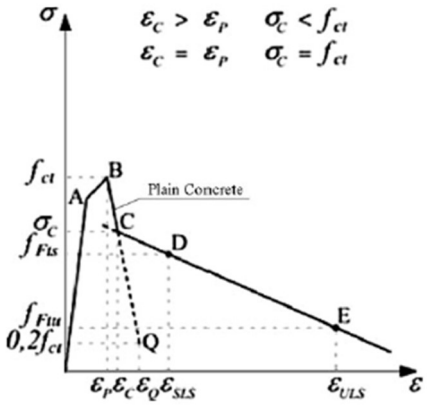

Figure 2.15 – Stress-strain relation with reference to Serviceability Limit States (SLS) (Di Prisco et al., 2013).

CHAPTER 3

3. INTERFACE AND MSFRC BEHAVIOUR CHARACTERIZATION: EXPERIMENTAL ANALYSIS AND RESULTS

3.1. FIBRE – MATRIX INTERFACE CHARACTERIZATION WITH PULL-OUT TESTS

3.1.1. Outline of the research activity

The study of the interface properties between fibres and matrix is carried out developing an experimental campaign of pull-out and compressive tests on mortar admixtures designed with different combinations of the components choosing four water-cement ratios, three cement-sand ratios and two different cement strength classes of Portland cement.

The choice of using no coarse aggregates is based on the effective role covered by the cement paste and the fine aggregates to surround completely the reinforcement representing the phase of the mix design more responsible of the matrix strength. On the other side, bigger aggregates represent the element that drive more the fibre orientation in concrete matrix (Ostrowski et al., 2018).

3.1.2. Materials

The specimens are prepared realizing 22 different mortar admixtures: they are characterized by four water-cement (w/c) ratios ranging from 0.4 to 0.6, three cement sand (c/s) ratios, between 0.25 and 0.5 and two cement strength classes, CEM I 42.5R and CEM I 52.5R. These values have been chosen as typical proportions used for the conventional design of concrete. The real amount of each ingredients, cement, sand, water is calculated by setting the three following equations, the third is based on the equilibrium of volumes, considering ρ_s=2.65 t/m^3 and ρ_c=3.1 t/m^3:

$$w / c = \text{value} \quad [3.1]$$

$$c / s = \text{value} \quad [3.2]$$

$$\frac{s}{\rho_s} + \frac{c}{\rho_c} + H_2O = 1000 \quad [3.3]$$

All admixtures are so characterized, whose specifications in terms of water (kg), cement (kg) and sand (kg) are reported in Appendix A.1. The total amount of water

includes also the absorbed water that represents the 1.3% of the amount of sand, since the aggregates are used in dry conditions. The interface behaviour is characterized by means of pull-out tests, considering a polypropylene crimped fibre with two different embedded lengths: 20 mm and 25 mm. Table 3.1 lists the mechanical and geometrical fibre properties where the tensile strength and the elastic secant modulus have been estimated performing tensile tests on single fibers. In addition, the value of the diameter in table has been obtained weighing many groups of fibres, with a different length for each group, to obtain a more accurate value. Each admixture is identified with a code composed by a number (2 referred to 20 mm embedded length and 5 referred to 25 mm embedded length), a letter (G referred to samples cast with CEM I 42.5 R and H for those cast with CEMI 52.5 R), and a progressive number indicating the batches according to the codes in

Table 3.2. For each admixture six specimens are cast with three different batches.

Figure 3.1 – Fibre type tested.

Table 3.1 –Fibres properties.

Fibre property	Value
Fibre length [mm]	39
Fibre diameter [mm]	0.92
Fibre Aspect ratio [-]	43
Fibre material	PP
Fibre tensile strength [MPa]	391
Elastic secant modulus [GPa]	2.25
Shape	crimped

Table 3.2 – Mortar matrix admixtures.

Mix code	Cement	w/c	c/s	Mix code	Cement	w/c	c/s
(2/5)G1	42.5R	0.4	0.5	(2/5)H1	52.5R	0.4	0.5
(2/5)G2	42.5R	0.4	0.3	(2/5)H2	52.5R	0.4	0.3
(2/5)G3	42.5R	0.45	0.5	(2/5)H3	52.5R	0.45	0.5
(2/5)G4	42.5R	0.45	0.3	(2/5)H4	52.5R	0.45	0.3
(2/5)G5	42.5R	0.45	0.25	(2/5)H5	52.5R	0.45	0.25
(2/5)G6	42.5R	0.5	0.5	(2/5)H6	52.5R	0.5	0.5
(2/5)G7	42.5R	0.5	0.3	(2/5)H7	52.5R	0.5	0.3
(2/5)G8	42.5R	0.5	0.25	(2/5)H8	52.5R	0.5	0.25
(2/5)G9	42.5R	0.6	0.5	(2/5)H9	52.5R	0.6	0.5
(2/5)G10	42.5R	0.6	0.3	(2/5)H10	52.5R	0.6	0.3
(2/5)G11	42.5R	0.6	0.25	(2/5)H11	52.5R	0.6	0.25

3.1.3. Specimens preparation

The experimental campaign sees the preparation of cubic samples 100 x 100 x 100 mm^3 dimension with a single fibre inserted at the middle of one of their faces for a depth of 20 mm and 25 mm in order to consider, aside from the mortar matrix effect, the embedded length influence on the interface properties. The admixtures are realized, using a planetary mix, (Figure 3.2a) with cement, dry sand of 0-4 mm grains assortment, water and superplasticizer according to the mixture workability, maintaining a value ranging from 1% to 3% of the cement quantity. The procedure followed is regulated by the UNI EN 197-1 (2011) that specifies the mixing time and procedure according to the following phases:

1. An amount of 70% of water and cement mixed for a time of 30 s at velocity 1;
2. Addition of sand and mix for 30 s at velocity 1;
3. Addition of all water remaining and mix for 30 s at velocity 2;
4. Stop the mix for 1:30 min;
5. Mix the whole admixture, with additive if necessary, for 60 s at velocity 2.

The idea is to maintain almost the same workability among the same batches to reduce the scatter, already remarkable in case of bond tests; the consistence of the mixes so realized is measured by means of slump tests, reaching values contained in

the range from 20 to 50 mm (Figure 3.2b). After the mixing phase, the mortar is cast into polyurethane moulds and vibrated. A special technique is used to hold the fibre positioned in the middle of the upper face of each cube: an aluminium bar is screwed at both edges to the mould walls (Figure 3.2c). During the vibration, by mans of this procedure, is possible to remove the entrapped air assuring a good adhesion between fibre and matrix eliminating the voids in its sorroundings. The specimens are then wrapper with plastic sheets to avoid the formation of cracks onto the surface, due to moisture exchange with the environment. After two days the samples are demoulded (Figure 3.3) and cured in water at a constant temperature of 20°C for 26 days. The experimental campaign aims at studying the interface mechanical properties by performing pull-out tests and characterizing the mortar matrix by compressive tests, that are executed on the same cubic specimens used for the fibre pull-out since no noticeabily high forces are registered so to affect the compressive strength of the material.

(a) (b)

Figure 3.2 – Sample preparation procedure: (a) Mixing phase; (b) Slump test; (c) Fibers fixed during the specimens vibration.

(a) (b)

Figure 3.3 – (a) Fibers fixed during the specimens vibration; (b) Samples demoulded after 1 day curing.

3.1.4. Pull-out tests

The pull-out tests on single plastic fibres are not standardized. The experimental test procedure adopted has been carefully studied because the difficulty in handling with plastic fibres is related to possibility of damaging the surface so compromising the test results and, on the other hand, their surface is preliminary treaded after the industrial production so indirect methods to grip the fibre, i.e. glue, are not effective.

In the present investigation the pull-out tests are performed using a servo-hydraulic MTS Landmark loading frame of 100kN capacity, controlled by the MTS Flextest 40 controller. Specimens are placed between two square steel plates blocked with four threaded bars positioned in the corners in order to realize a contrast system. The upper plate horizontality is verified by a level in case the external surface presents some irregularities, the fibre is gripped by means of two aluminium plates with sand paper glued onto their surface taking care of the fibre positioning in the center of the gripping system. The system used makes sure to not damage the fibre during the gripping phase, infact a very low pressure of 1 MPa is applied and the aluminium plates are used to not grip directly the fibre with the mechanical grips with which the machine test is equipped, assuring the pressure and load transmission (Figure 3.4). Many attempts have been made in inserting a load cell with lower capacity in the present loading frame but the only effective solution has been to use the gripping

system and the measurement system proper of the machine. Despite the capacity of the load cell used (100kN), might result high for this kind of test, the load measured is accurate (maximum error of 0.05%).

The test is carried out in displacement control, monitoring the stroke displacement: in a first attempt two LVDTs were placed close to the fibre but the displacement measured was very consistent with that of the actuator and, therefore, they were removed in order to not damage the fibre state, simplifying the test setup. The rate of the experimental test has been choosen according to some preliminary tests aimed at stating the rate influence on the entire test output, the peak force value and the post-peak behaviour: a rate of 0.06 mm/sec is adopted.

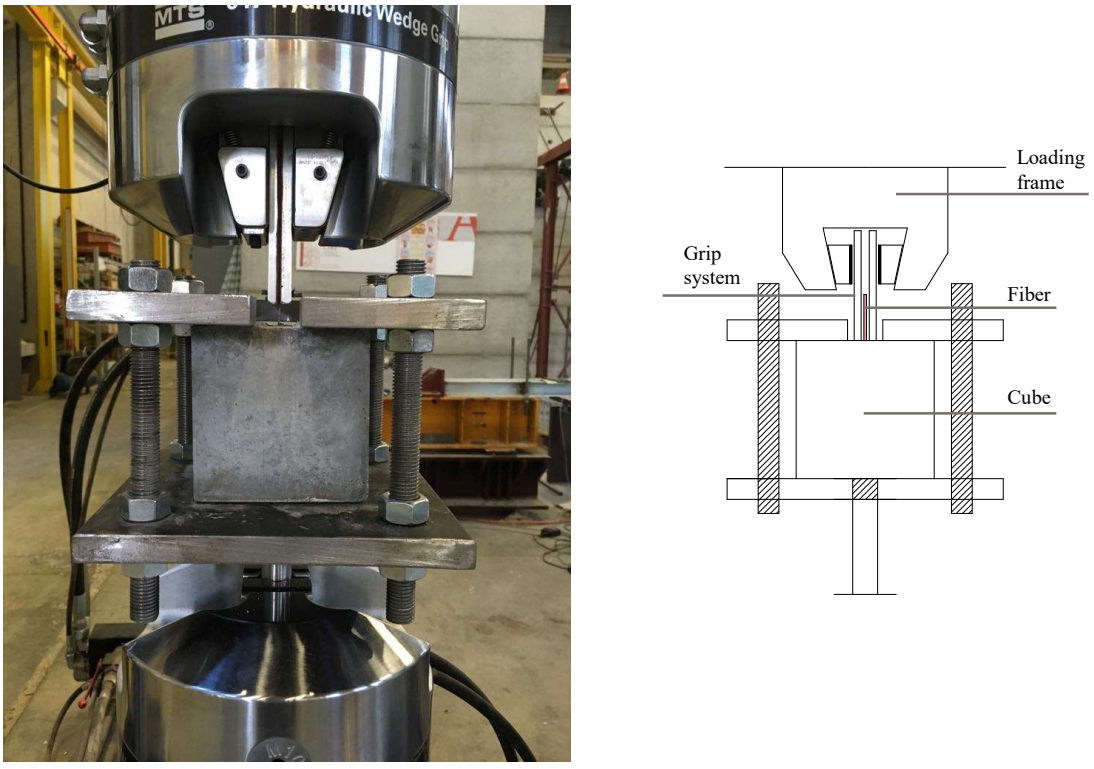

(a) (b)

Figure 3.4 – (a) Pull-out test performed in the servo-hydraulic machine MTS 100kN capacity;(b) Pull-out tests set-up.

3.1.5. Compressive tests

The admixture mix design defines its strength properties and an additional variable to examine is its compressive strength, analysing possible correlations with the bond strength. Compressive tests are performed applying the pressure on the face perpendicular to the cast surface that appears more regular.

Figure 3.5 – Cubic specimens, after pull-out tests, used for compressive tests.

3.1.6. Porosity tests

Since the matrix microstructure is thought to have an influence on the bond strength property, the porosity could be a variable reflecting this aspect.

Thus, a preliminar evaluation of the matrix internal state is performed trough Mercury Intrusion Porosimetry (MIP) tests as a good predictor of the concrete state (Claisse, Cabrera, and Hunt, 2001). These tests use the properties of mercury (Hg), making it penetrate inside the voids of the matrix samples with pressure that increases as the pores size decreases.

The porosity is thought to have an effect on the bond properties in terms of bond strength and failure type. These tests need samples of about 1 cm^3 representative of the mortar internal microstructure, so they were extracted from the undamaged core of cubes after the compression tests.

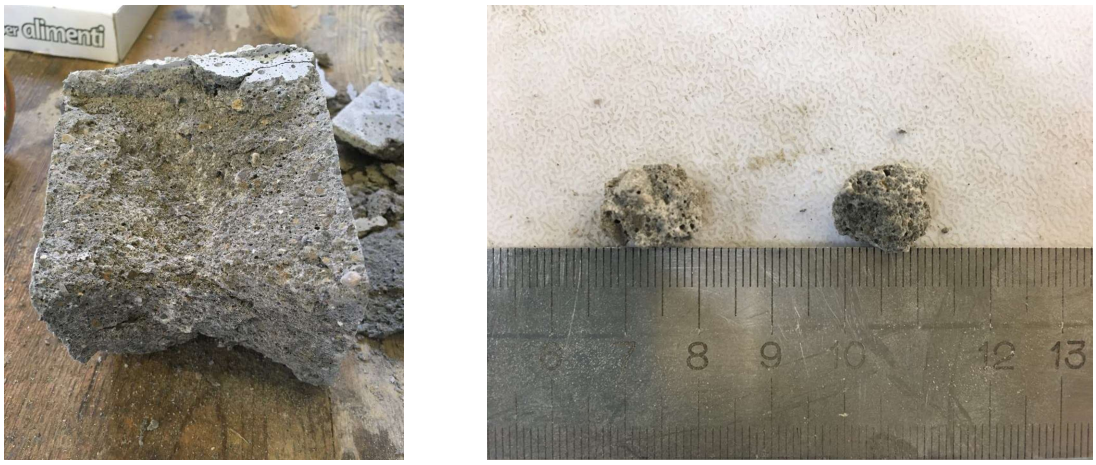

(a) (b)

Figure 3.6 – (a) Extraction of samples from the cubes undamaged core; (b) Samples of approximately 1 cm diameter for porosity tests.

3.1.7. Pull-out test results

A fibre embedded in a cementitious matrix, according to the theory explained before, when subjected to a pull-out load, exhibits a first ascending branch until the peak force and then a discending phase leading to the full fibre slippage.

During the first stage, the fibre starts debonding and then the pull-out load decreases until the fibre is completely out of the matrix at a displacement corresponding to the embedded length. Figure 3.7a depicts this type of failure. It can also happen that, in case of high bond strength, the fibre breaks instead of pulling out (Figure 3.7b), in this case the corresponding load might be comparable with its tensile strength.

The experimental campaign performed pointed out three different failure type: slippage and breakage of the fibre and a combined failure (Figure 3.8). Considering the pull-out failure, the post peak stage is driven by a frictional interlock between fibre and matrix. The descending branch is characterized by a waved shape, according to the fibre crimped profile (Figure 3.8, blue curve). In case the fibre breaks, after the peak, the descending branch presents some steps which follow the gradual fibre fibrillation (Figure 3.8, orange curve). It is interesting to note that, in some cases, after the debonding phase, at a lower load, the fibre breaks while its pull-out load results higher than the failure load. This result could be addressed to a damage of the

fibre during the debonding phase, and so, the entire slippage does not take place. The failure load associated to the behaviour described has almost an intermediate value between the fibre pull-out and breakage (Figure 3.8, yellow curve).

(a) (b)

Figure 3.7 – Type of failure(a) Fibre Pull-out; (b) Fibre breakage.

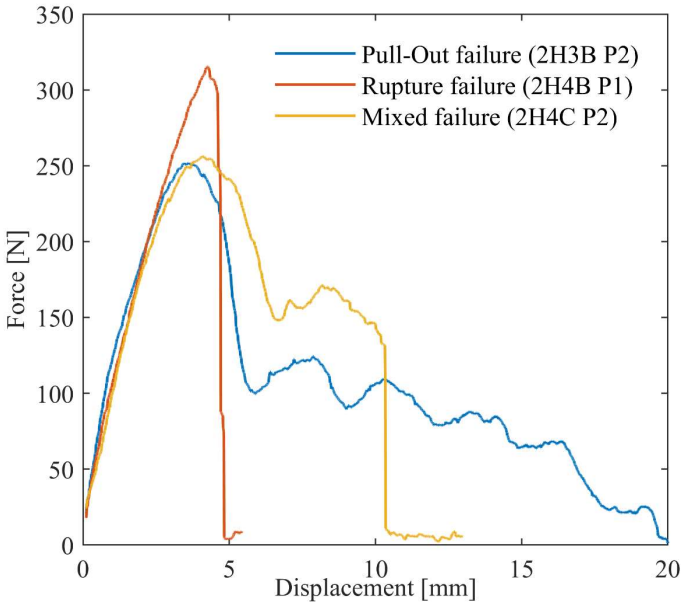

Figure 3.8 – Three failure types exhibited during pull-out tests.

In Table 3.3 the results of pull-out tests are reported in terms of mean peak force for pulled-out and ruptured fibers, indicating the respective number of fibers and the coefficient of variation. In addition in Appendix A.2 the whole database of results and the corresponding failure type for each specimen are reported.

Table 3.3 – Mean values of peak forces for all batches distinghuished into pulled out and ruptured fibres.

Mix Code	Pulled out fibres			Ruptured fibres		
	$F_{p,m}$ [N]	COV [%]	n°	$F_{p,m}$ [N]	COV [%]	n°
2G1	269	0	1	271	9	4
2G2	0	0	0	259	4	4
2G3	249	0	1	264	4	4
2G4	255	1	2	261	5	4
2G5	276	2	3	287	3	2
2G6	249	11	3	286	15	3
2G7	258	8	4	300	8	2
2G8	252	8	6			
2G9	176	14	5			
2G10	225	6	5	232	0	1
2G11	244	9	3	274	12	3
2H1	0	0	0	299	2	6
2H2	253	9	4	302	0	1
2H3	251	3	2	297	10	3
2H4	259	0	1	311	3	4
2H5	259	0	1	285	13	4
2H6	271	3	3	305	5	3
2H7	0	0	0	271	7	4
2H8	252	2	3	269	2	2
2H9	207	7	4	0	0	0
2H10	212	4	4	0	0	0
2H11	233	16	2	259	3	2
5G1	251	7	2	294	7	4
5G2	249	0	1	273	6	5
5G3	224	9	4	264	5	2
5G4	172	27	2	253	12	4
5G5	282	13	2	277	8	4
5G6	225	11	5	281	0	1
5G7	233	15	4	302	0	1
5G8	213	10	2	260	8	4
5G9	169	24	6	0		0
5G10	200	17	6	0		0
5G11	195	9	5	290		1

5H1	0	0	0	288	9	6
5H2	234	0	1	293	6	5
5H3	0	0	0	298	5	6
5H4	266	0	1	283	4	5
5H5	228	14	2	309	1	3
5H6	236	0	1	280	7	5
5H7	245	10	2	284	8	4
5H8	275	0	1	297	7	5
5H9	258	7	4	261	4	2
5H10	268	14	6	0	0	0
5H11	291	9	3	248	9	3

3.1.8. Porosity test results

The output of the porosity tests is a relation between the volume of mercury intruded in the pores and their size. In Table 3.4 the amount of Hg inside the pores is reported according to the IUPAC pore size classification but considering only the maximum value of this quantity. The samples tested are extracted by specimens having the same cement type, CEM I 42.5R, and the same fibre embedded length but different mix design. The specimens selected are those presenting singularities in the load values and the failure type, i.e. some of them exhibited a pull-out failure at high load or the opposite situation. In Figure 3.9 the peak forces measured by pull-out tests are correlated with the Specific Intruded Hg volume in micropores, where the linear regression reported is evaluated only on the pull-out forces. As expected, with the increment of mercury amount and, therefore the increment of porosity, the bond strength decreases.

Table 3.4 – Maximum values of intruded Hg volume according to the IUPAC classification pore size.

ID sample	Macropores [mm^3/g]	Mesopores [mm^3/g]	Micropores [mm^3/g]	ID sample	Macropores [mm^3/g]	Mesopores [mm^3/g]	Micropores [mm^3/g]
2G1A_P1	0.82	26.06	102.48	2G7C	0.99	17.61	79.01
2G1B_P1	0.69	5.29	67.16	2G7C	0.69	6.73	68.91
2G2B_P1	0.71		75.92	2G8C	0.65	35.14	108.79
2G2B_P2	0.59	29.16	82.44	2G9C	0.84	9.16	85.90
2G3C_P1	0.66	6.23	84.81	2G10C	0.82	3.65	84.47
2G4C_P2	0.67	46.38	108.76	2G11C	0.66	25.94	96.98
2G5C	0.61	7.74	74.70	2G11C	0.64	26.06	102.48
2G6C	0.8	9.55	85.80				

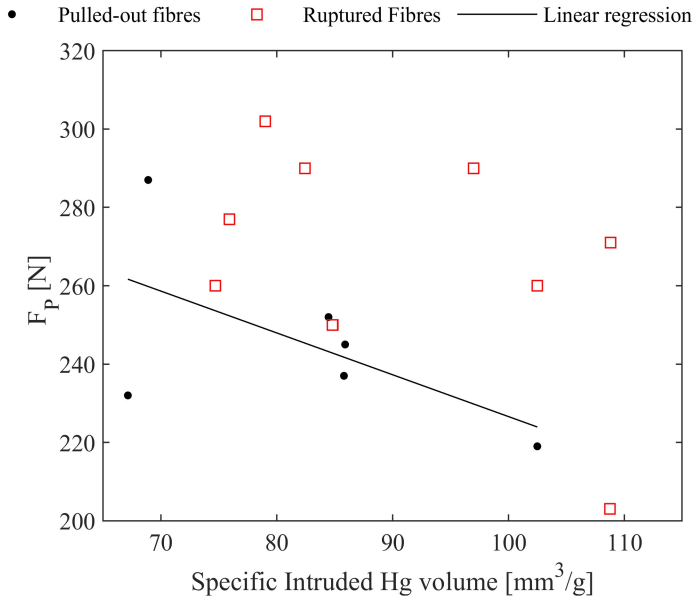

Figure 3.9 – Relation between peak forces of pulled out and ruptured fibers with volume intruded in micropores.

3.1.9. Analysis of experimental results

In a first analysis, comparing the results within the same embedded length, it is possible to observe how the number of fibres exhibiting a pull-out failure decreases with the water cement ratio and the cement sand ratio. On the other hand examining the two embedded lengths, 20 and 25 mm, an increment of fibres characterized by the mixed failure type and also the pull-out failure can be denoted but not a remarkable difference in the peak load, thought to be influenced by the fibre embedded length. For this reason, considering only the two lengths examined, the matrix mix design appears to be the variable most responsible of the failure type and, obviously, of the value associated. In order to better investigate the relations existing, the bond strength value is considered so that both embedded lengths can be included in the same examination.

This consideration is built on the assumption of a uniform distribution of the bond strength along the fibre debonded length. Moreover, the results are separated according to the cement strength that strongly influences the failure load and failure type. A first visualization is proposed in a three dimensional (Figure 3.10) space, relating the bond strength values of pulled out fibres with water-cement and cement-

sand ratio: the scatter plot includes also the values associated to the mixed failure mode.

The curvature characterizing the surfaces is in accordance for both cement strength but resulting flatter for the second cement type as the less data of pulled out fibre, nevertheless a higher bond strength is measured.

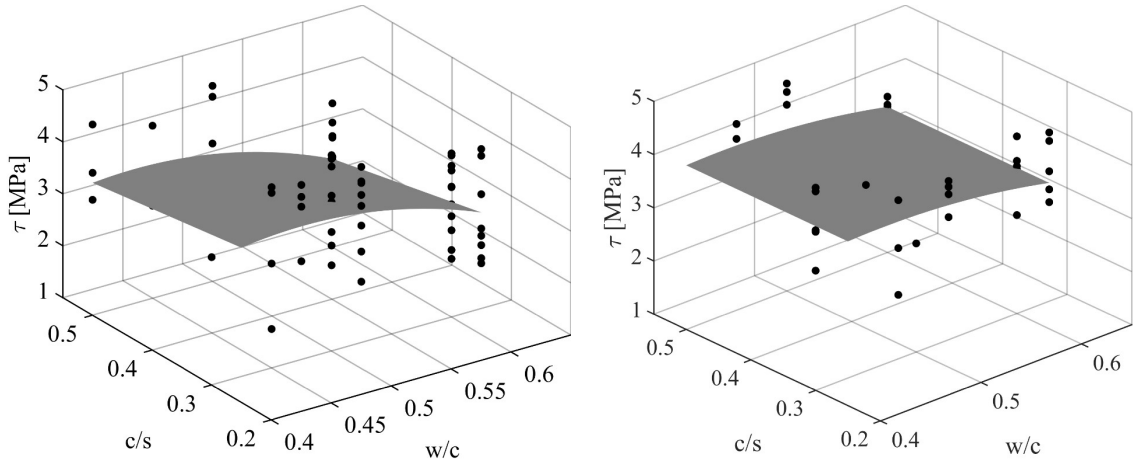

Figure 3.10 – 3D regression surfaces correlating the interfacial bond strength with the water-cement and cement-sand ratio for samples cast with (a) CEM I 42.5R and (b) CEM I 52.5R.

In order to separate the contributes, a two dimensional view is used, correlating the bond strength with the w/c ratio, keeping the c/s ratio constant for each curve and the opposite case, following the subdivision according to the cement type.

The chart in Figure 3.11b does not contain data referred to a w/c ratio of 0.4 since all fibers broke instead of pulling out. The correlations below report the single bond strength values and the linear regression evaluated for those samples having the same water-cement ratio (Figure 3.11) and cement sand ratio (Figure 3.12).

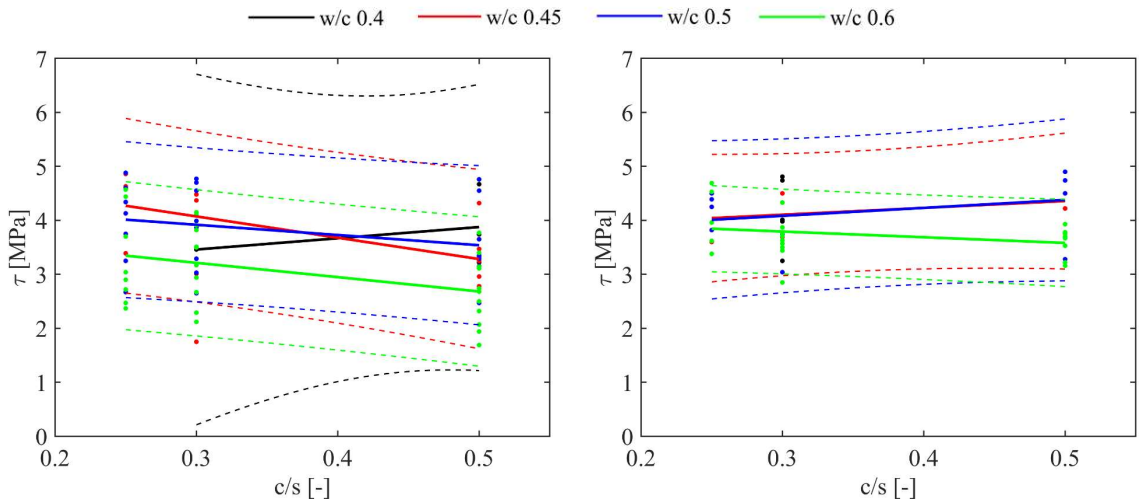

Figure 3.11 – Linear regression of bond strength and c-s ratio, and confidence interval at 90%, for samples cast with (a) CEM I 42.5R and (b) CEM I 52.5R.

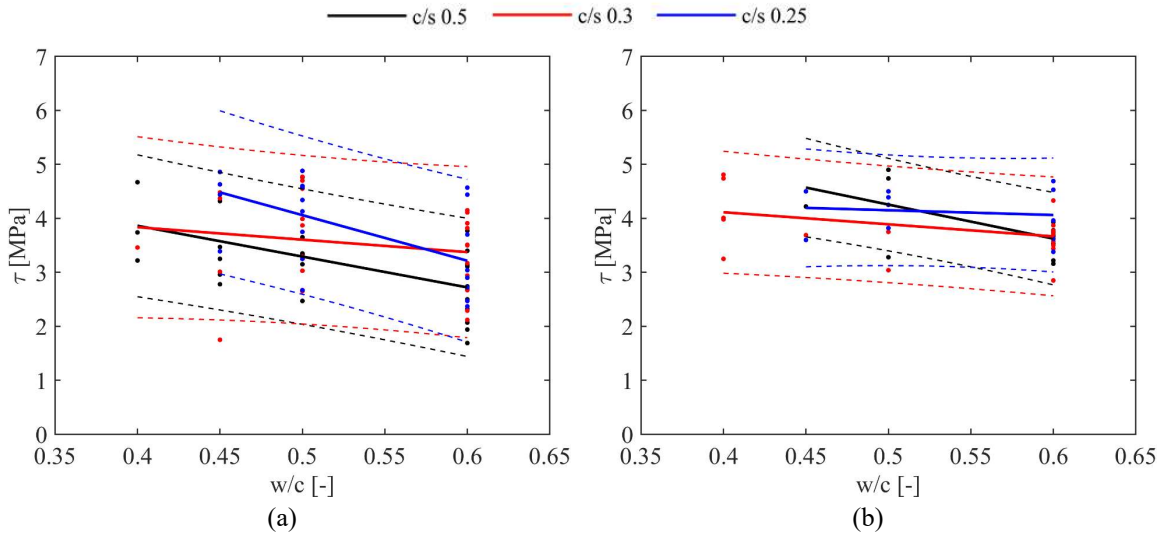

Figure 3.12 – Linear regression of bond strength and w-c ratio, and confidence interval at 90%, for samples cast with (a) CEM I 42.5R and (b) CEM I 52.5R.

It results clearly visible that the bond strength decreases with the higher water-cement ratio, although the slope of the regression lines is reduced in case of a higher strength cement: it gives its contribution reducing the correlation.

It should be underlined that, apart from the strength class, the CEM I 52.5R has a different granulometry resulting finer and, for this, supposed to increase the bond strength. The effect of the cement sand ratio is not clearly visible, for specimens cast

with 42.5 cement class, the increment of cement quantity and decrement of sand in the mixture lead to a lower bond strength, for specimens cast with the second cement type the trend is not defined, only for mixes with 0.6 water cement ratio is compatible with the previous relation. Since the mix design reflects the matrix strength, the mean compressive strength for each batch (R_{cm}) is calculated and related to the bond strength faced by each specimen. Since the effect of the cement types appears significant, the results are divided according to CEM I 42.5R and CEM I 52.5R.

The elaborations relate the compressive strength with the bond strength resulting by those fibres exhibiting a pull-out and mixed type failure and also those related to the fibre breakage: in this case the bond strength value does not characterize the effective capacity because its breakage is generated by high bond, so the real bond strength is supposed to be higher than that reported.

Hovewer, the linear regression is done on data of pulled out and mixed mode failure fibers, highlighting how a high compressive strength involves higher bond strength leading to a different failure type (Figure 3.13).

This aspect is examined more explicitly evaluating the probability of failure occurring with the matrix compressive strength increment: a breakage failure is more likely to happen rather than a pull-out behaviour since the increment of bond strength. The values reported in the chart refer to the mean compressive strength for each batch (Figure 3.14).

The analysis of results presented suggests that the matrix mix design influences the interface properties but it is not easy to state clearly which variable has a stronger effect. This partly due to the scatter of results for this type of test and the impossibility of uncoupling the variables as the matrix strength is determined by their combined effect.

The present analysis aimed at finding out the possible correlation between the interfacial property fiber – matrix, i.e. bond strength, and the mix design parameters, i.e. ratio of the components and compressive strength. In addition, on the dataset generated a predictive model can be elaborated, basing on the ANN – approach

(Artificial Neural Networks), with the purpose of predicting the mechanical properties for other admixtures and at embedded lengths different from those tested. The technique mentioned is based on a network structure organized in nodes having input, hidden and output layers, where each connection has a proper weight (McKinley, 1996): if an input of data is given, trough an iterative system of initialisation and training, the ANNs give back the resulting output then compared with the experimental data (to be fitted). This approach, in the enginnering field, is adopted for example by Cascardi et al. to predict the strength of concrete confined with FRP where the parameters involved were mechanical, for example Young Modulus of FRP and ultimate strength, and geometric, height/diameter of the coloumn (Cascardi, Micelli, and Aiello, 2017).

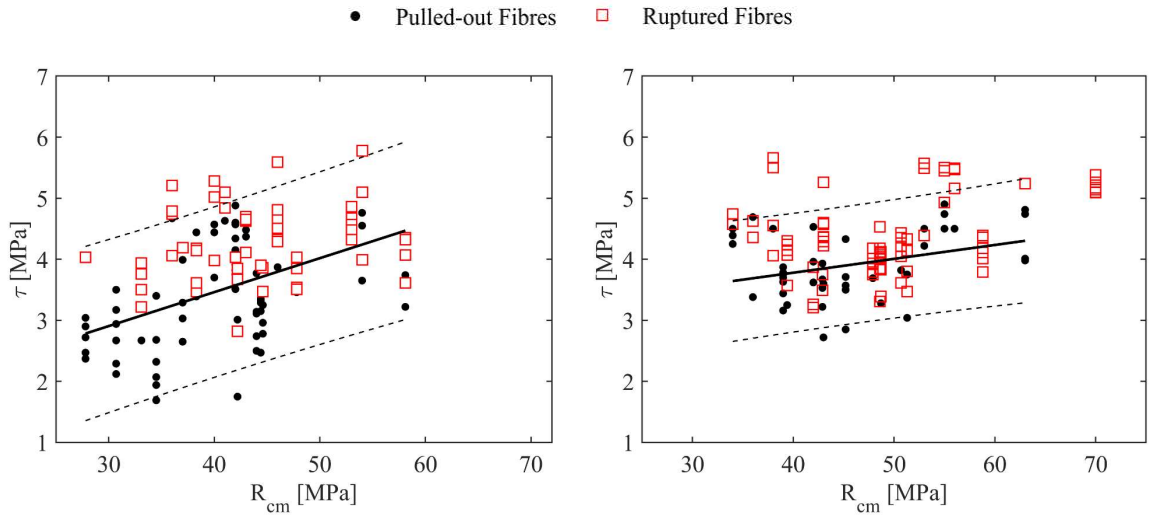

Figure 3.13 – Linear regression of bond strength and mean compressive strength of the corresponding batch, and confidence interval at 90%, for samples cast with (a) CEM I 42.5R and (b) CEM I 52.5R.

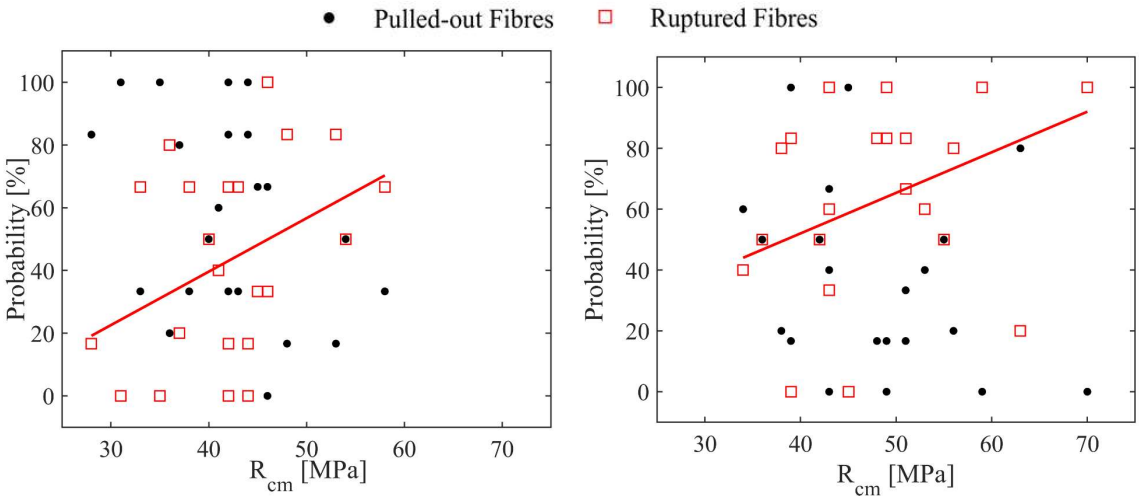

Figure 3.14 – Linear regression of the rupture failure probability and the mean compressive strength, for samples cast with (a) CEM I 42.5R and (b) CEM I 52.5R.

3.1.10. Significance test

In the framework of the parameters analysis and those influencing the interfacial fibre-matrix behaviour, a statistical evaluation is proposed. The relation of the bond strength is expressed by a multi regression model that considers the variables analysed of w/c, c/s and compressive strength (related to each specimen) in also mixed and quadratic form. Indicating:

$$p = w/c$$
$$t = c/s$$
$$z = R_c$$

the model has the expressions:

$$\tau = b_1 + m_1 \cdot (p) + m_2 \cdot (t) + m_3 \cdot (z) + m_4 \cdot (t)^2 + m_5 \cdot (p)^2 + m_6 \cdot (z)^2 + m_7 \cdot (t) \cdot (p) + m_8 \cdot (z) \cdot (p) + m_9 \cdot (z) \cdot (t) \quad [3.4]$$

where b_1 and $m_1 \ldots m_9$ are the regression coefficients on which the significance test is performed computing their p-values and using a threshold value of 0.05: in Table 3.5 are reported the values of the regression parameters and their statistical significance. The results suggest a statistic significance of the mixed parameter containing the

compressive strength and the w/c ratio, for CEM I 42.5R, and no parameters for higher strength cement, CEM I 52.5R. This might be attributed to a mixed effect of the parameters and to the low amount of data on which the test is performed, since many fibers broke.

Table 3.5 – Significance test results of the regression parameters correlating bond strength and c-s, w-c and mean compressive strength.

Coefficient	CEM I 42.5R		CEM I 52.5R	
	Value	Significant	Value	Significant
m_1 (w/c)	-	-	-	-
m_2 (c/s)	-	-	-	-
m_3 (R_c)	-	-	-	-
m_4 (c/s^2)	-	-	-	-
m_5 (w/c^2)	-	-	-	-
m_6 (R_c^2)	-	-	-	-
m_7 (w/c c/s)	-	-	-	-
m_8 (w/c R_c)	3.03	Yes	-	-
m_9 (c/s R_c)	-	-	-	-
b	2.27	Yes	-	-

3.2. FIBRE – MATRIX INTERFACE CHARACTERIZATION: INVERSE ANALYSIS AND NUMERICAL MODEL CALIBRATION

3.2.1. Numerical model description

When a stress-bond slip law is determined, many models are based on the assumption that slip and bond shear are constant along the embedded length. This concept might be coincident with the reality in case of steel bars, but in other interface conditions, i.e. FRP and FRC, the local distribution has to be considered (Focacci, Nanni, Fellow, ASCE, and E. Bakis, 2000). According to this, the elaboration of a numerical model able to describe the relation between the local bond strength and the fibre slippage is performed to simulate the experimental results.

The embedded fibre portion is modelled by means of many truss elements (80 for 20 mm embedded length and 100 for 25 mm embedded length), each of them presenting at its both ends nonlinear springs with the aim of simulating the bond behaviour with the matrix (Figure 3.15). The boundary conditions are applied in order

to allow the translation along the direction of the load that is applied at one end of the element, as in the experimental results where the fibre is gripped close to the part where it is embedded in the mortar matrix. This means that the length of the fibre modelled is only that embedded. The spring insertion makes possible to describe the local behaviour characterizing them by a cohesive nonlinear constitutive law: the debonding phase until the peak strength is described by a power-law relation while the pull-out stage, dominated by a friction mechanism, by a bilinear trend.

Figure 3.15 – 1D numerical model simulating the interaction of the single fibre with the cementitious matrix: nonlinear springs (Abaqus numerical Software).

The constitutive law has been properly developed starting from the studies carried on by Cosenza et al. (Cosenza, Manfredi, and Realfonzo, 2002) regarding the reinforcement with FRP bars and the problem of the rebar pull-out: in their work the model adopted accounts for the debonding phase until the peak strength followed by a descending branch. The equation regulating the debonding phase is related to a set of parameters: the peak strength, τ_m, and the corresponding slip , s_m, and the shape parameter α, based on the constitutive law adopted by Eligehausen, Popov and Bertero to describe the debonding stage of FRP (1983).

$$\tau = \tau_m \left(\frac{s}{s_m} \right)^{\alpha} \qquad [3.5]$$

The model adopted by Cosenza et al. has been modified according to the post-peak friction behaviour exhibited by the fibre tested characterized by sudden drop of the load after the peak and a friction phase with a waved shape that the model is not able to fully simulate.

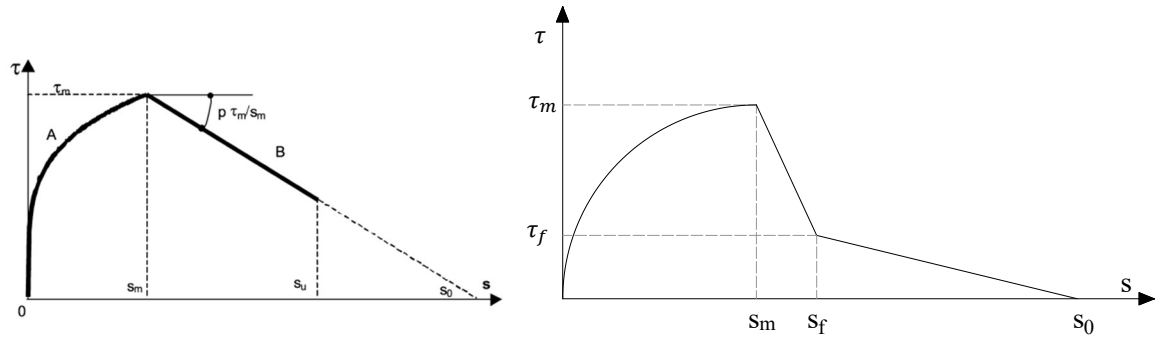

Figure 3.16 – Local bond shear-slip constitutive models (a) proposed by (Cosenza et al., 2002) in case of FRP reinforcing bars and (b) the constitutive model adopted for the single fibre pull-out process.

The parameters describing the bond-slip law are determined by an inverse analysis procedure that makes use of the Matlab™ Pattern Search algorithm: it minimizes the cost function defined as a linear combination of the difference between experimental and numerical results in correspondence of many reference points and quantities, i.e. the ares under the load-displacement curve, the peak force and several points of the curve.

$$C = \gamma_T \left(\frac{A_n - A_e}{A_e} \right)^2 + \gamma_{LOP} \left(\frac{f_{peak,n} - f_{peak,e}}{f_{peak,e}} \right)^2 + \sum \gamma_i \left(\frac{f_{i,n} - f_{i,\mathrm{e}}}{f_{i,\mathrm{e}}} \right)^2 \qquad [3.6]$$

The analysis uses as input the experimental load-displacement curves for each specimen exhibiting a pull-out failure and calibrating the bond-slip law by reducing the differences between experimental and the generated numerical model.

3.2.2. Inverse analysis results

In Figure 3.17 is reported the output of the inverse analysis, the orange line represents the experimental result on which the numerical model (blue line) is calibrated: the comparison shows a good agreement between the two curves so the model is able to capture the real bond behaviour except for the waved shape driven by a purely frictional behaviour.

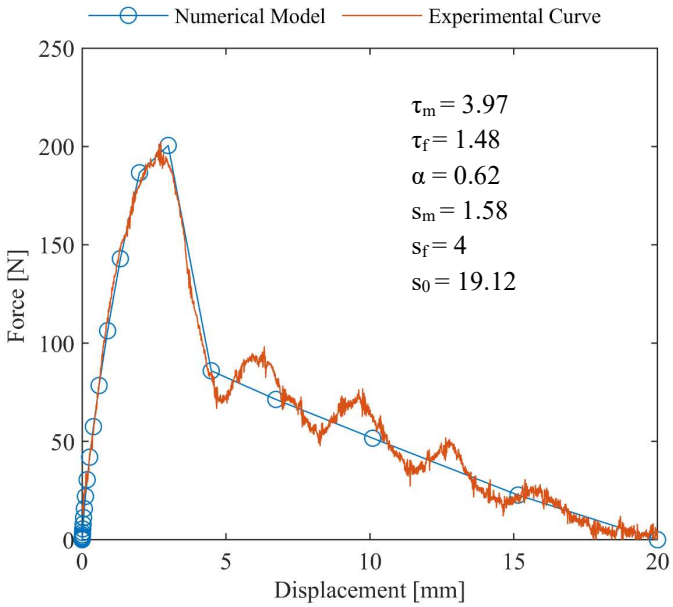

Figure 3.17 – Example of numerical model calibration by inverse analysis procedure for sample with the code 2G10B_P2.

The set of parameters is calibrated on the experimental results of pulled out fibres and collected in Table 3.6 and the maximum bond strength is correlated with the parameters analysed before.

Table 3.6 – Inverse analysis results reporting the local parameters values.

Specimen ID	τ_m	τ_f	α	s_m	s_f	s_0
2G3C_P1	4.5893	1.731	0.37646	1.8609	7.3086	18
2G6A_P1	4.9449	2	0.79788	1.6102	6.5234	20
2G6C_P2	4.0189	1.9539	0.83789	1.367	4.7811	20
2G7A_P2	3.4984	1.9383	0.48932	1.025	10	20
2G7B_P2	4.3234	1.9999	0.56129	1.3336	10	20
2G7C_P1	3.9359	1.9988	0.30589	1.0406	9.9961	20
2G8A_P2	4.7276	0.6	0.20886	5	6.8899	18
2G8B_P2	4.8343	1.9999	0.60986	1.9825	6.3291	20
2G8C_P1	4.1117	1.9998	0.56349	1.4488	8.9785	20
2G8C_P2	3.9616	1.9999	0.48834	1.3496	5.99	20

2G9B_P1	2.6005	0.84459	0.79719	1.1105	4	18.012
2G9B_P2	2.9015	1.1961	0.79248	0.91514	4	19.332
2G9C_P1	3.4027	1.2839	0.23144	3.3327	4.0001	20
2G9C_P2	4.3705	1.8016	0.60082	1.1805	4	19.951
2G9E_P2	2.869	0.60039	0.43653	0.90098	8.4454	18
2G10B_P1	3.6684	1.9989	0.71094	1.4038	9.9999	20
2G10B_P2	3.9702	1.4783	0.61916	1.5787	4	19.116
2G10C_P1	4.4568	1.9999	0.8125	2.4309	6.0491	20
2G10C_P2	4.1943	1.785	0.55359	2.0483	5.1132	20
2G10D_P2	4.227	1.9999	0.36853	1.2918	6.5898	20
2G11A_P1	3.9164	1.9998	0.56812	1.6076	5.3027	20
2G11A_P2	3.6879	1.9998	0.72533	1.7224	10	20
2G11B_P2	4.8666	2	0.33545	2.4575	6.2501	20
5G1B_P2	2.8227	1.6773	0.81055	2.0672	5	25
5G3A_P1	3.7465	1.6832	0.99799	1.5789	5	25
5G3A_P2	3.3188	1.1344	1.2637	1.6512	5	25
5G3B_P1	3.85	1.325	0.7188	3.65	4.5	24
5G4B_P1	2.0001	0.6	0.81638	1.3214	4.0002	23
5G4B_P2	2.5922	2.1424	0.30891	1.6917	12	25
5G5B_P2	3.0219	1.9999	0.1001	0.90024	10	25
5G6A_P1	3.6156	1.5855	0.38153	1.8714	5	25
5G6B_P1	3.3642	1.3304	0.27148	3.4723	4.8723	25
5G6B_P2	3.7252	1.6969	0.82959	1.407	5	25
5G6C_P1	2.001	0.90012	0.10147	0.6	5	20
5G6C_P2	3.7416	1.5738	0.32813	1.1375	5	22.145
5G7A_P1	3.1059	1.6766	0.45021	1.141	4.469	25
5G7B_P1	3.09	1.4742	0.94922	0.98125	5.002	25
5G7B_P2	3.5355	1.7525	0.50098	1.5066	5	25
5G7C_P2	4.2016	1.3375	0.43616	2.1448	5	25
5G8B_P2	3.85	1.6688	0.2969	3.6344	4.4531	23.5
5G9A_P1	2.5692	0.78984	1.277	1.0416	4	24.999
5G9A_P2	2.9983	0.6	0.327	1.9054	4	23

5G9B_P1	2.0063	1.0718	0.5939	0.60197	5	20
5G9B_P2	2.0001	0.90024	0.74445	0.60002	5	20
5G9C_P1	4.0218	0.60002	0.66138	2.0543	5.9364	23
5G9C_P2	2.2719	1.0133	0.39648	0.60234	5	20
5G10A_P1	3.3695	0.60002	0.70508	2.5641	4	23
5G10A_P2	3.4691	1.45	0.94531	2.3607	4.7813	25
5G10B_P1	2.0325	1.3082	0.43671	0.60001	5	20.536
5G10B_P2	2.0326	0.60002	0.28662	0.90024	4	23
5G10C_P1	3.9027	1.619	0.5072	1.4676	5	25
5G10C_P2	3.0297	2.8609	1.3	1.607	5	25
5G11A_P1	3.0961	1.3836	0.75336	1.5152	4.4219	25
5G11A_P2	3.1273	1.5145	0.53046	1.0873	4.5938	25
5G11B_P1	2.5653	0.87578	0.72614	1.0326	4	23
5G11B_P2	2.8678	2.0299	1.2999	0.82305	5.499	20.589
2H3A_P2	4.2741	1.9999	0.54283	1.3904	7.1484	20
2H3B_P2	5.0658	2	0.59399	2.2652	5.9944	20
2H6A_P1	5.6522	2	0.71484	2.5387	6.1879	20
2H6C_P1	4.0082	1.9998	0.47997	0.93122	10	20
2H6C_P2	4.3051	1.9998	0.44141	0.95859	10	20
2H8B_P2	4.4347	1.5281	0.60352	2.1715	9.9999	18
2H9A_P1	4.5922	1.8152	0.76514	2.774	4.3672	19.877
2H9A_P2	4.4262	1.7054	0.61816	2.7672	4.1602	18.344
2H9B_P1	3.1352	0.8445	0.5495	1.7067	7.047	20
2H9B_P2	4.4232	1.909	1.0098	2.6773	5.0898	20
2H10A_P1	3.7035	1.4822	0.57715	1.8355	4.9336	18
2H10A_P2	3.8172	1.6685	0.77098	2.1949	6.1172	20
2H10B_P1	4.0225	1.9964	0.45642	2.2047	5.9204	20
2H10B_P2	4.0062	1.5906	0.43352	2.0562	6.0313	20
2H11A_P1	3.7025	1.7742	0.37158	1.9479	4.3452	20
2H11A_P2	4.0805	1.9998	0.82275	1.3216	10	20
5H6A_P1	3.21971023	1.9	0.11714	2.0245	6.1836	25
5H7C_P1	3.08	1.3375	0.499967	1.8885	9.15	25

5H9A_P1	4.0761	1.3453	0.40919	2.5909	5	25
5H9C_P1	3.85	1.4002	0.31223	1.9317	5	25
5H9C_P2	3.5303	1.0023	0.125	1.7105	5.0002	25
5H10A_P1	3.0473	0.90024	0.1001	1.7449	11.939	25
5H10A_P2	3.6273	1.3685	0.125	2.1307	5.005	25
5H10B_P1	4.3344	1.4391	0.65015	2.0641	5	25
5H10B_P2	3.9086	1.9999	0.34497	1.6615	4.6797	25
5H10C_P1	3.4242	1.1012	0.48535	2.3719	12	25
5H10C_P2	2.7211	0.90488	0.10999	1.5008	5	25
5H11A_P2	3.0043	0.90195	0.10065	2.266	12	25
5H11B_P1	3.9437	1.9999	0.32813	1.0465	10	25
5H11B_P2	3.0199	1.4	0.12494	2.45	7.874	25

The significance test in section 3.1.10 is repeated on the regression parameters of the model correlating the bond strength values calibrated by the inverse analysis and the variables investigated according to the expression [3.4].

Examining the values in Table 3.9 it is possible to find out the consistence with the significance test performed on the experimental results apart from the significance of the Rc^2 parameter.

This might be motivated by two main reasons: the model is not calibrated on the curves of mixed type failure and, for any samples, the numerical peak strength is not completely coincident with the experimental.

According to this, the analysis is developed on a lower number of data and some maximum bond strength values are not the same for experiments and numerical model.

Table 3.7 – Significance test results of the regression parameters correlating numerical bond strength values and c-s, w-c and mean compressive strength.

Coefficient	CEM I 42.5R		CEM I 52.5R	
	Value	Significant	Value	Significant
m_1 (w/c)	-	-	-	-
m_2 (c/s)	-	-	-	-
m_3 (R_c)	-	-	-	-
m_4 (c/s^2)	-	-	-	-
m_5 (w/c^2)	-	-	-	-
m_6 (R_c^2)	2.43	Yes	-	-
m_7 (w/c c/s)	-	-	-	-
m_8 (w/c R_c)	2.82	Yes	-	-
m_9 (c/s R_c)	-	-	-	-
b	-	-	-	-

3.3. MACRO-SYNTHETIC FIBRE REINFORCED CONCRETE: INFLUENCE OF CONCRETE MATRIX AND FIBRE DOSAGE

3.3.1. Experimental campaign

In the perspective of investigating the behaviour of the composite fibre reinforced concrete, the idea would be to identify the properties that might influence the overall material response and then investigate the influence of the variables on the mechanical behaviour. According to the present purpose, an experimental analysis is developed considering a macro-synthetic fibre reinforced concrete designed with different concrete classes, fibre dosage and fibre type.

3.3.2. Materials

The cement-based material is designed with three different concrete classes, varying the composition with a water-cement ratio ranging from 0.53 to 0.43, CEM II/A-LL 42.5 R content and, so, fine and coarse aggregate amount (Table 3.8). According to the mixes, a lower, medium and higher strength classes are produced. In order to study the effect of the fibrous reinforcement on the residual flexural strength capacity, four dosages of the same fibre type tested before, macro-synthetic

crimped fibers (Figure 3.18a), are adopted: 2, 4, 6, 8 kg/m^3. The mechanical and geometrical properties are listed in Table 3.9.

Table 3.8 – Concrete classes mix design.

Concrete component	Lower strength (L)	Medium strength (M)	Higher strength (H)
CEM II/A-LL 42.5 R [kg/m^3]	368	398	433
Sand 0-5 mm [kg/m^3]	819	807	793
Gravel 5-15 mm [kg/m^3]	547	539	530
Gravel 15-22 mm [kg/m^3]	423	416	409
Water [l/m^3]	195	195	195
W/C	0.53	0.49	0.45

Table 3.9 – Fibre properties and dosages.

Fiber geometrical property	Value
Fiber length [mm]	39
Fiber diameter [mm]	0.92
Fiber Aspect ratio	43
Fiber material	PP
Fiber tensile strength [Mpa]	391
Elastic secant modulus [Gpa]	2.25
Dosages [kg/m^3]	2 – 4 – 6 – 8

Combining the classes of concrete designed and the fibres dosages, 12 batches are cast and each of them is identified by a code composed by a letter, B, a progressive number, a letter, L, M, H indicating the concrete strength class and a number associated with the dosage of ofibres contained. In Table 3.10 is presented the outline of the experimental campaign.

Table 3.10 – Outlined and identification code for alla batches.

Batch ID	Concrete admixture	Fibers dosage [kg/m^3]
B1_L_2	L	2
B2_M_2	M	2
B3_H_2	H	2
B5_M_4	M	4
B6_H_4	H	4
B7_L_4	L	4
B8_L_6	L	6
B9_M_6	M	6
B10_H_6	H	6
B11_L_8	L	8
B14_M_8	M	8
B15_H_8	H	8

3.3.3. Specimens preparation

The experimental campaign characterizes the MSFRC material testing its compressive strength and residual flexural strength. According to this aim, for each batch, 4 cubic samples 150 x 150 x 150 mm^3 dimension and 8 prismatic specimens of 150 x 150 mm^2 cross section and 600 mm length are cast. All samples are produced using a concrete mixer with a vertical axis having a nominal capacity of 300 litres and the aggregates have been dried in the oven at a temperature of 120°C for 24h before the cast realization. The mixing phase follows the procedure described:

1. An amount of 50% of water is added in the mixer with all aggregates and mixed for 5 min;
2. Cement and remaining water are added;
3. Fibres are added and mixing for 3 min adjusting the admixture with an amount of superplasticizer in order to reach a slump value of at least 170 mm (Figure 3.21b).

The admixture is inserted in polyurethane prismatic and cubic moulds (Figure 3.21c) and then vibrated embedding the vibrator only in the parts close to the ends so

as to not modify the fibres arrangement generated during the cast, above all in the central part. Then all specimens are covered by nylon sheets to prevent moisture exchange with the surrounding environment that could generate shrinkage cracks. After two days the specimens are demoulded and cured in a climate room with humidity controlled, 99 %, and temperature of 20°C. According to the standard code EN 14651, the specimens have been notched, after 25 days, at the mid-span section in order to control the crack location and development during the experimental tests.

(a) (b)

(c) (d)

Figure 3.18 – (a) Polypropylene fibers used as reinforcement; (b) Fibre Reinforced concrete mixed; (c) Slump test; (d) Prismatic and cubic specimens.

3.3.4. Experimental tests

According to the European regulation, EN 14651, the prisms are tested in a three point bending configuration, during which the crack opening in the middle section is monitored characterizing the MSFRC performance with a stress – crack opening

relation. The flexural tests are realized through a servohydraulic machine with a capacity of 500kN and loading frame 370.50 produced by MTS: the machine is regulated by an electrical controller, Flextest 40. The opening of the central crack corresponding to the notch is measured by a Crack Opening Displacement transducer while the load applied with a load cell having a capacity of 50kN: they are both connected to the mentioned controller. The tests are performed in displacement control with a rate of 0.05 mm/min until a CMOD of 0.1 mm and then with a rate of 0.2 mm/min for values of crack opening higher than 0.1 mm. The FRC behaviour is characterized by the nominal residual flexural strength values corresponding to crack opening of 0.5 mm, 1.5 mm, 2.5 mm, 3.5 mm. These values are calculated from the load measured at each crack opening, assuming an elastic material behaviour:

$$\sigma = \frac{3}{2}\frac{FL}{bh_{sp}^2} \qquad [3.7]$$

where F is the load measured, L is the distance between the supports, b is the base section dimension and h_{sp} is the notched section height.

The concrete matrix is characterized testing cubic specimens under compressive load according to the procedure reported in UNI EN 12390-3 Standard.

Figure 3.19 – Three point bending flexural test according to Standard Code EN 14651.

3.3.5. Fibre count

A further analysis includes the evaluation of the effective number of fibers crossing the cracked surface, shown to be responsible of the residual flexural strength. For this reason, the prismatic specimens, after the flexural tests, are broken into two parts and the fibers are counted, separating pulled-out and broken whose part is contained in both specimen half and, therefore, the amount of broken fibres should result the same on both section sides. The cracked area is divided into three equal parts: the fibres included in A_1 and A_2 areas (Figure 3.20) are thought to be most involved in the cracking process observing the crack development and, for this reason, only those belonging to the mentioned areas are considered in the analysis and correlated to the residual strength parameters.

(a) (b)

Figure 3.20 – (a) Prismatic specimens broken at middle section; (b) Subdivision of the cracked area for fibre counting.

3.3.6. Three point bending and compressive tests results

The concrete compressive strength determined ranges from a value of 33 MPa to 55 MPa (Table 3.11): it is possible to notice that the concrete cast with a high dosage of fibres, 8 kg/m^3, is characterized by a lower strength than expected. Regarding the flexural tests, the output is represented in nominal stress-crack opening relation: for each batch the results are showed in Figure 3.21 where the black curves represent the single specimen behaviour while the mean trend is marked with a red solid line. A first visual analysis highlights how the residual strength rises noticeably with the fibre dosage and, also, an increment of the scatter between the single flexural curves is observed.

Table 3.11 – Mean compressive strength values outcome of compressive tests.

Batch name	Rc_m [MPa]	Batch name	Rc_m [MPa]
B1_L_2	33	B8_L_6	34
B2_M_2	37	B9_M_6	43
B3_H_2	51	B10_H_6	55
B5_M_4	41	B11_L_8	37
B6_H_4	54	B14_M_8	43
B7_L_4	36	B15_H_8	45

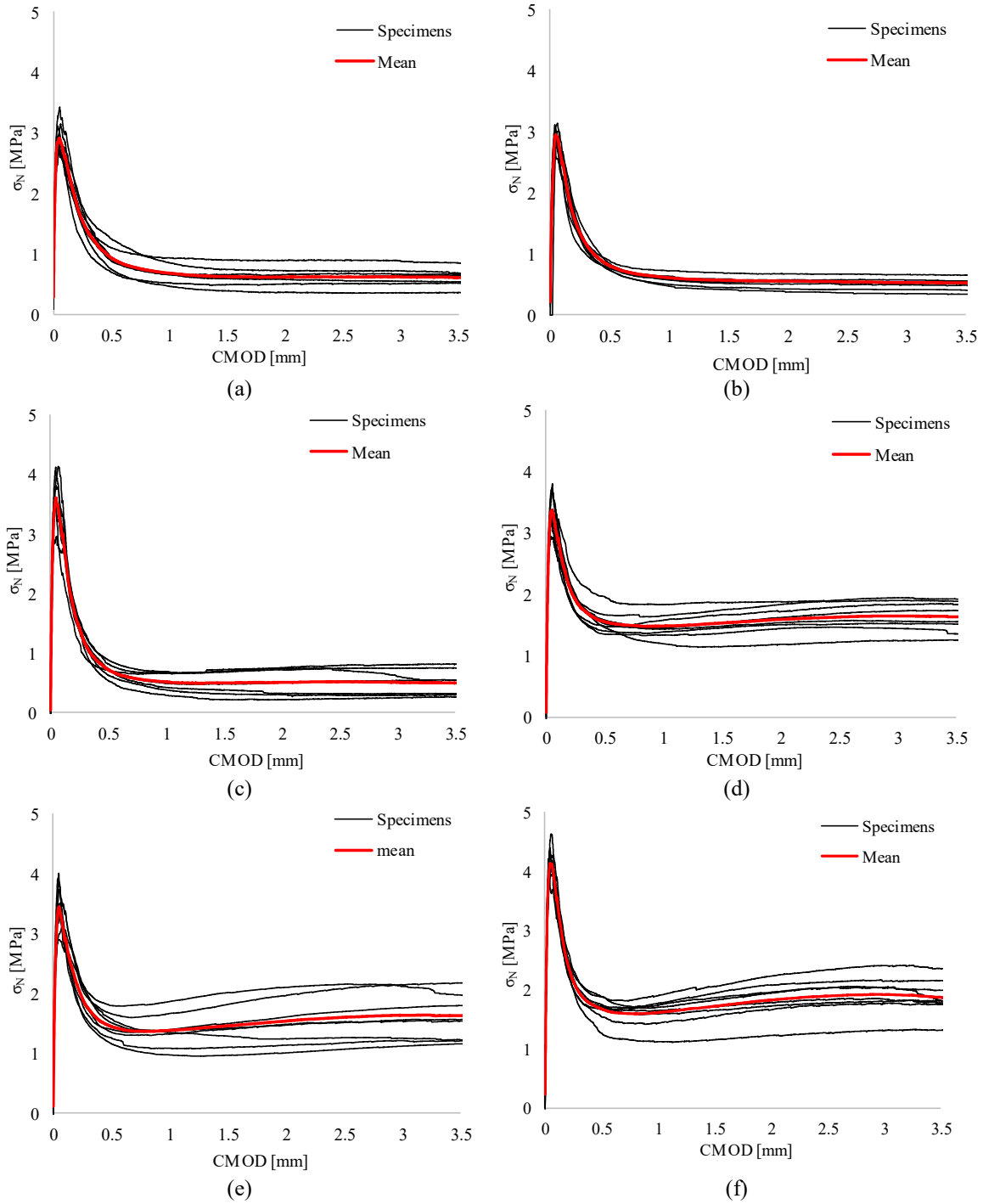
Specimens
Mean
σN [MPa]
CMOD [mm]
(a)
(b)
(c)
(d)
mean
(e)
(f)

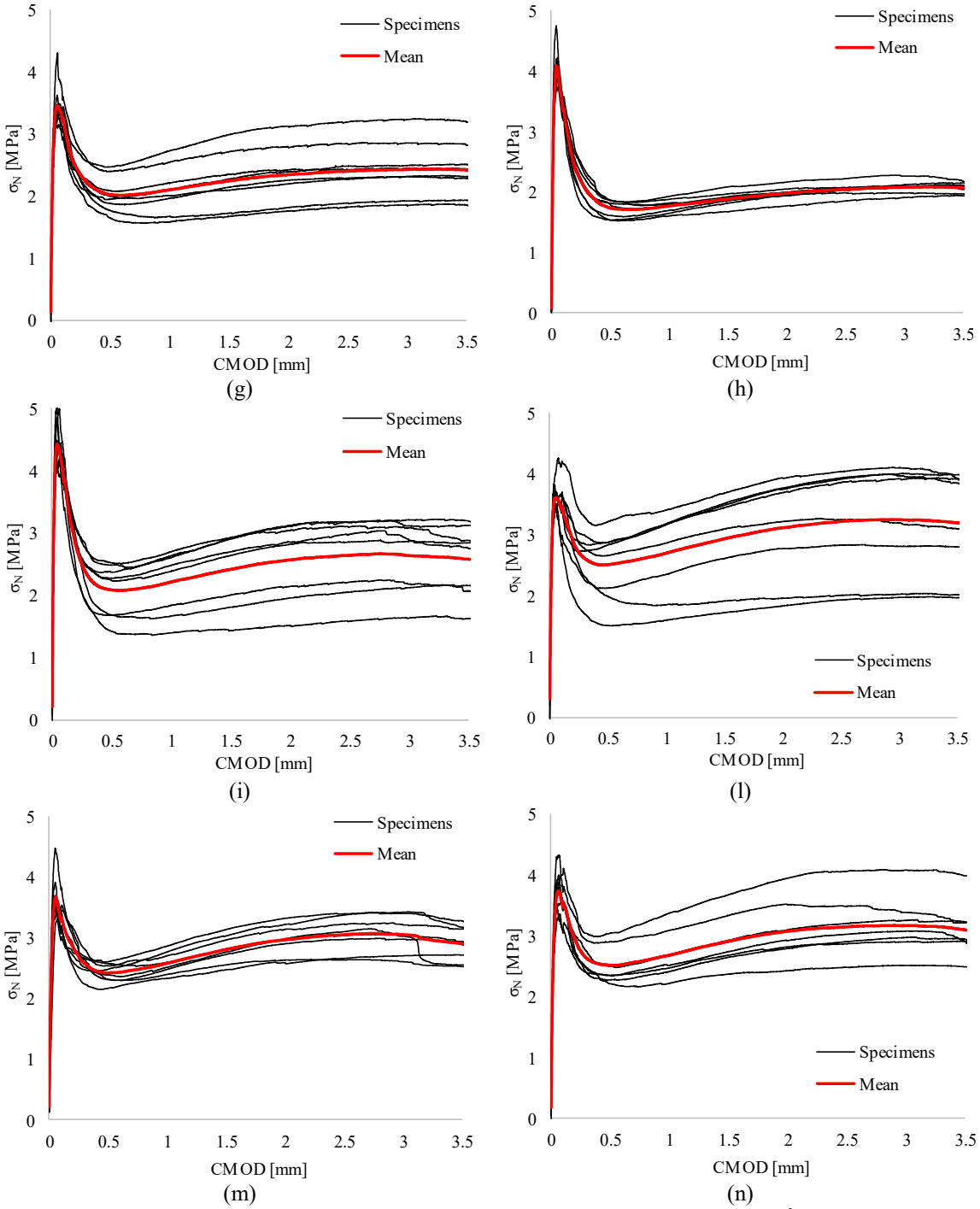

Figure 3.21 – Nominal Stress-crack opening curves for (a) B1 33 MPa 2 kg/m^3; (b) B2 37 MPa 2 kg/m^3; (c) B3 51 MPa 2 kg/m^3; (d) B7 36 MPa 4 kg/m^3; (e) B5 41 MPa 4 kg/m^3; (f) B6 54 MPa 4 kg/m^3; (g) B8 34 MPa 6 kg/m^3; (h) B9 43 MPa 6 kg/m^3; (i) B10 55 MPa 6 kg/m^3; (l) B11 37 MPa 8 kg/m^3; (m) B14 43 MPa 8 kg/m^3; (n) B15 46 MPa 8 kg/m^3.

3.3.7. Analysis of experimental results and significance test

A more detailed analysis of the results can be performed considering the mean flexural behaviour in terms of nominal stress and crack opening displacement for each batch: they are grouped first according to the four dosages and then to the three concrete classes. Whitin the same fibre dosage, the compressive strength does not modify remarkably the post cracking response while the flexural tensile peak strength presents a different value as the concrete strength changes (Figure 3.22). On the contrary, considering the different dosages for each concrete class, it drives in very a different way the post-peak behaviour increasing noticeably the residual strength (Figure 3.23 – Figure 3.24).

Moreover, the flexural residual tensile strength values, f_{Ri}, are described by a linear regression model as function of the mean compressive strength and the effective number of fibres crossing the cracked surface. The choice of evaluating the relation existing with their effective number is motivated by the fact that, although the dosage is the same within a group of specimens, the distribution and, so, the effective number of fibers is the factor more responsible of the MSFRC behaviour during the cracked state.

The linear regression represented in Figure 3.25 – Figure 3.26 and Figure 3.33 – Figure 3.28, correlating the residual flexural strength parameters with, respectively, the mean compressive strength of concrete and the number of fibers, suggest that the latter is the parameter affecting more the MSFRC residual strength.

Furthermore, the statistical significance of the variables analysed is demonstrated trough a significance test on the regression parameters correlating the residual flexural strength values with the compressive strength and fibres number.

$$f_{R,i} = b_i + m_{1,i} \cdot (N_{fibers,A1+A2}) + m_{2,i} \cdot R_{cm} \qquad [3.8]$$

where b_i, $m_{1,i}$, $m_{2,i}$ are the regression coefficients and i=1,…,4. The t-test outcome (Table 3.12) highlights that concrete compressive strength, i.e. m_2 parameters, has no statistical significance for the MSFRC under investigation. The strong correlation

with the number of fibers, already observed, has also a statistic confirmation. The low influence of the concrete compressive strength on the flexural behaviour is specific for the fibers and concrete admixture tested. Moreover, the analysis performed shows that, increasing the fibers dosage from 2 kg/m^3 to 8 kg/m^3, the scatter of results rises. This can be motivated by the less uniform distribution of fibers and also by the entrapped air in concrete that could modify the mechanical performance of the fibre reinforced concrete. This observation can motivate also the peak strength in Figure 3.24 for the curves of the admixture with 8 kg/m^3 of fibers that results lower if compared with the other curves. Besides, observing all the curves for the batches B11, B14, B15, there is a high scatter within the single batch and this might cause the decrement of the peak strength.

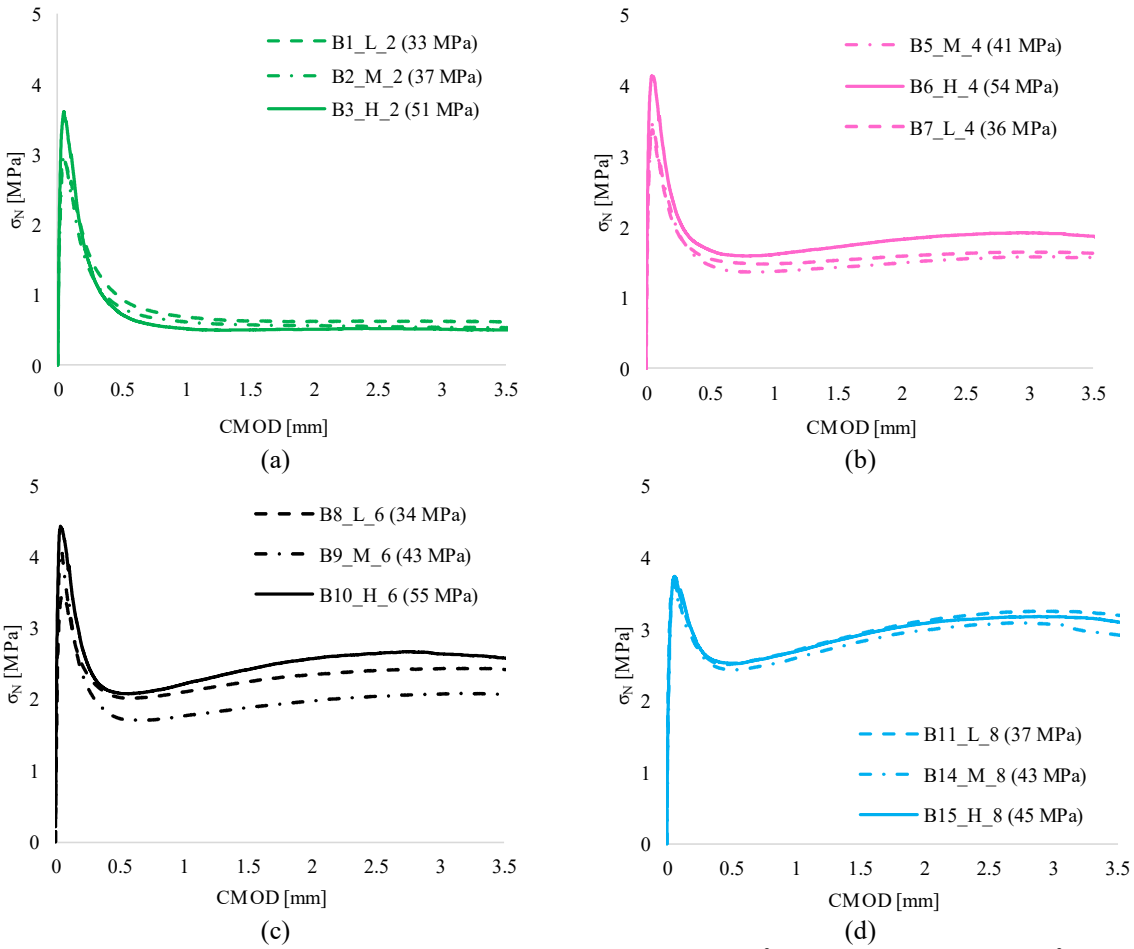

Figure 3.22 – Mean nominal stress-CMOD curves for (a) 2kg/m^3 fibre dosage; (b) 4kg/m^3 fibre dosage; (c) 6kg/m^3 fibre dosage; (d) 8kg/m^3 fibre dosage.

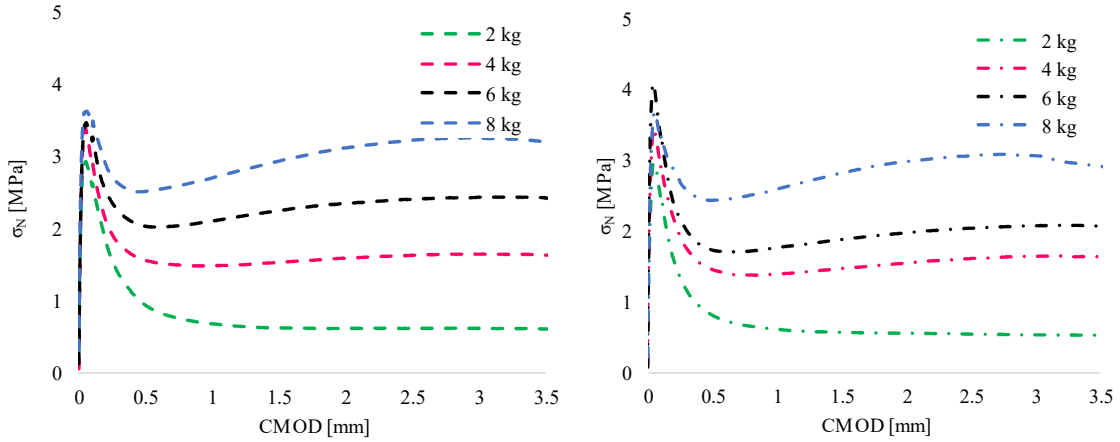

Figure 3.23 – Mean nominal stress-CMOD curves for (a) lower compressive strength class; (b) medium compressive strength class.

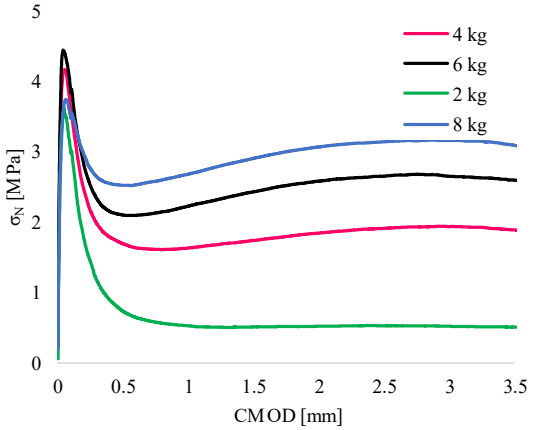

Figure 3.24 – Mean nominal stress-CMOD curves for the high compressive strength class.

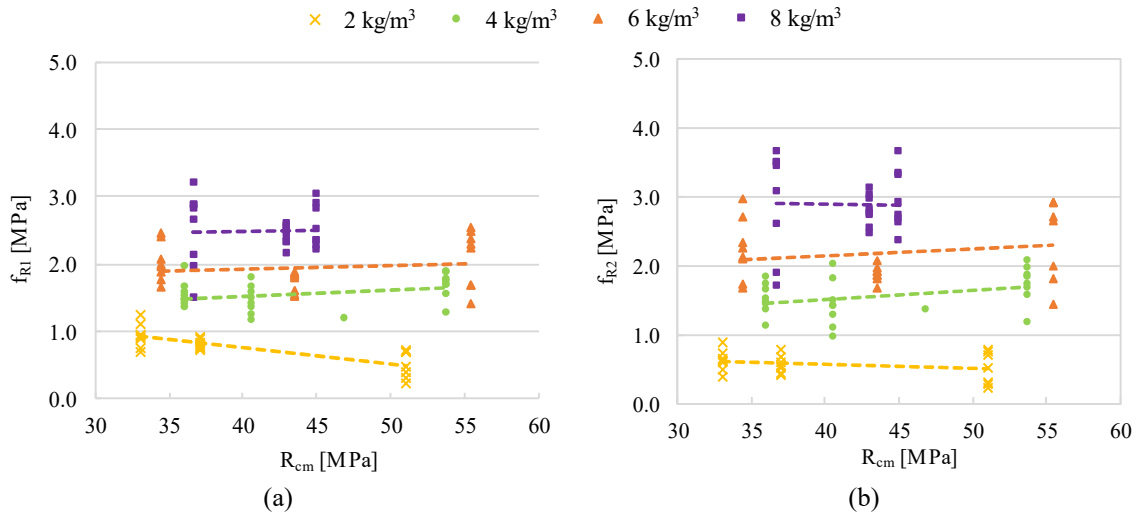

Figure 3.25 – Linear regression of the residual flexural strength nominal parameters, f_{R1}, f_{R2} with the mean compressive strength of each batch.

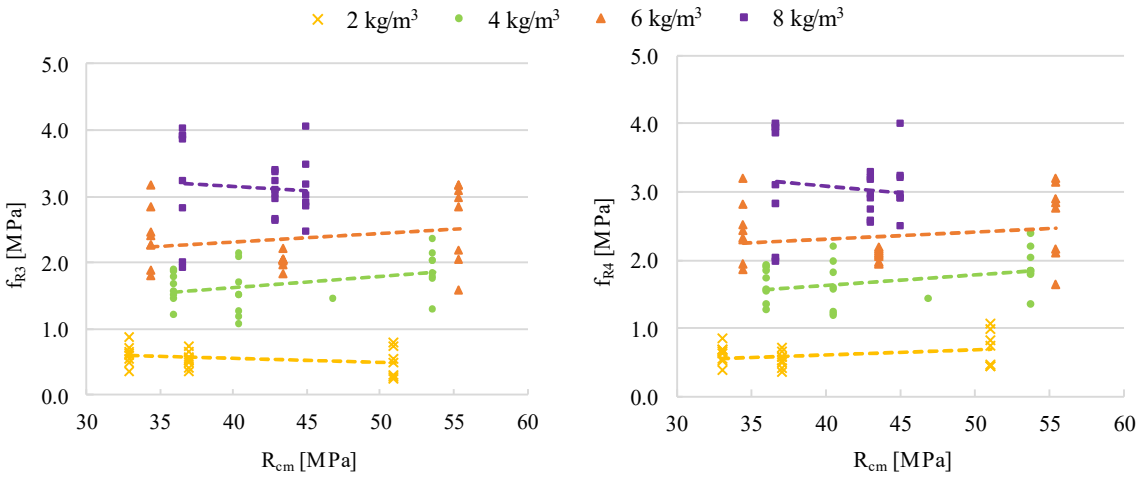

(c) (d)

Figure 3.26 – Linear regression of the residual flexural strength nominal parameters, f_{R3}, f_{R4} with the mean compressive strength of each batch.

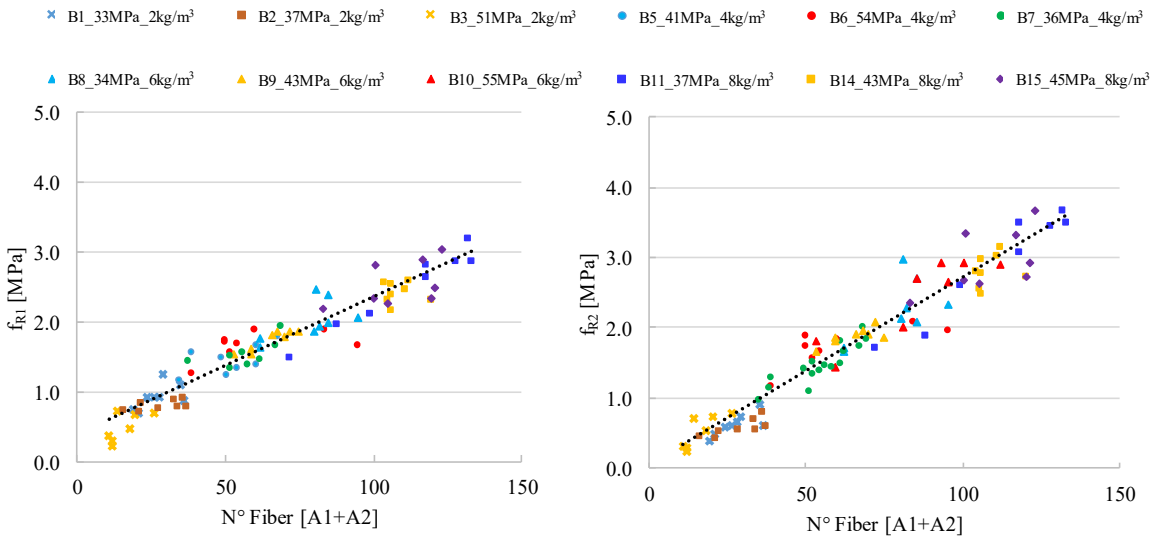

(a) (b)

Figure 3.27 – Linear regression on the residual flexural strength nominal parameters, f_{R1}, f_{R2}, with the number of fibres included in A_1 and A_2 middle cross section areas.

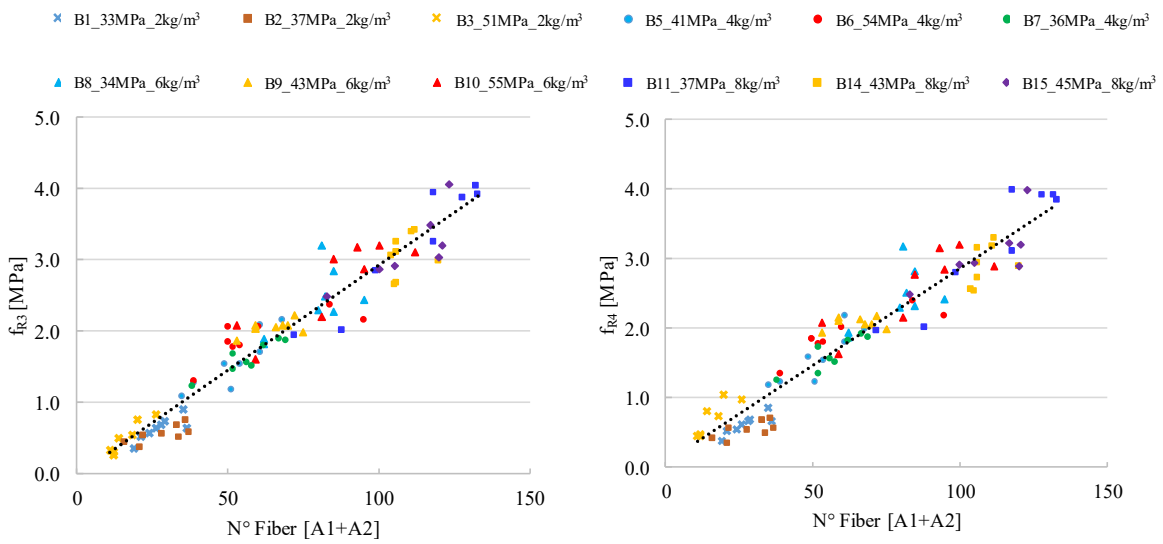

Figure 3.28 – Linear regression on the residual flexural strength nominal parameters f_{R3}, f_{R4} with the number of fibres included in A_1 and A_2 middle cross section areas.

Table 3.12 – Significance test on regression parameters results.

Residual flexural tensile strength parameter	b		m_1		m_2		R^2
	Value [-]	Significant	Value [-]	Significant	Value [-]	Significant	
f_{R1}	0.398	YES	0.020	YES	0.000	NO	0.900
f_{R2}	-0.297	YES	0.027	YES	0.008	NO	0.926
f_{R3}	-0.446	YES	0.030	YES	0.010	NO	0.923
f_{R4}	-0.372	YES	0.029	YES	0.010	NO	0.910

3.4. MACRO-SYNTHETIC FIBRE REINFORCED CONCRETE: INVERSE ANALYSIS AND NUMERICAL MODEL CALIBRATION

3.4.1. Numerical model description

The flexural behavior and the cracking process of the prismatic specimens is simulated by means of a numerical model elaborated by the FEM software ABAQUS. The specimen is modeled in a 2D space, considering half of the entire specimen because of the symmetric shape, in this way the computational time connected to the analysis is also reduced. The cracking process and the progressive crack opening is

modeled placing nonlinear springs on the cracked zone, in particular on each vertex of the squared mesh, whose value is set in order to define the influencing area of each spring (Figure 3.29). The approach used in the model is a homogeneous approach and springs follow a nonlinear cohesive behavior (Figure 3.30). The constitutive law adopted is based on the approaches described in section 2.3 of the thesis where, within the coehesive relations, multilinear relations describe the post-peak behavior.

The constitutive model implemented has been accurately calibrated according to a hypothetical behavior of the single fiber on the cracked surface starting from the previous calibration of the pull-out process. The accuracy in describing the local mechanism triggered during the crack development involving the fibre contribution is motivated also by the fact that, in case of high dosage of the fibre reinforced concrete, the post peak trend calibration needs more parameters to be described. An earlier choice of modeling the local behavior only with six parameters did not give optimal results because the local behavior so modeled did not describe properly the post peak response of the material. The flexural behavior of samples designed with ah high amount of fibers is identified by a curve that rises up during the cracked phase. Due to this, the post peak response is described with a numerical model regulated by 8 parameters, the elastic stage until the peak is not described since the springs start working as the crack starts.

The parameters are calibrated by means of a procedure of inverse analysis based on the Matlab™ Pattern Search algorithm, already mentioned before (section 3.1.10), that minimizes the difference between experimental response, used as reference and the numerical result obtained trough the cost function:

$$C = \gamma_T \left(\frac{A_n - A_e}{A_e} \right)^2 + \gamma_{LOP} \left(\frac{f_{LOP,n} - f_{LOP,e}}{f_{LOP,e}} \right)^2 + \sum \gamma_i \left(\frac{f_{i,n} - f_{i,\mathrm{e}}}{f_{i,\mathrm{e}}} \right)^2 \qquad [3.9]$$

where the reference parameters are the peak strength characterizing the flexural behavior, the area under the mechanical response curve and the strength evaluated at some crack openings values arbitrarily set in the code.

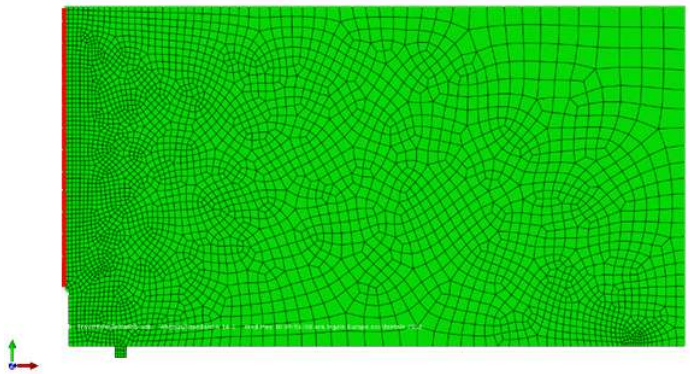

Figure 3.29 – Numerical model reproducing half of the prismatic specimen with nonlinear springs placed along the cracked surface.

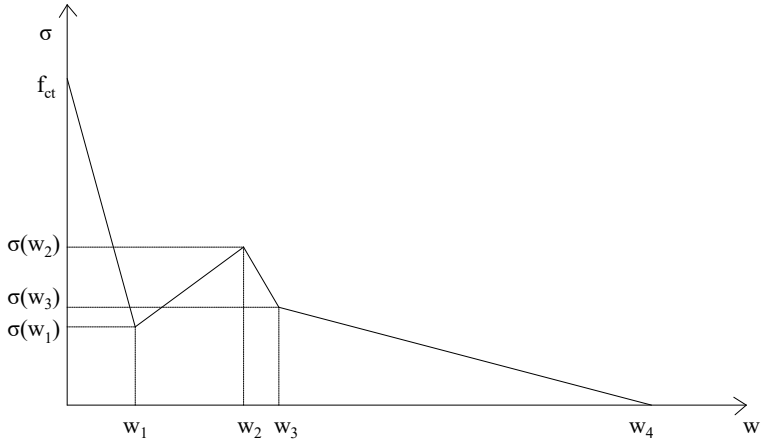

Figure 3.30 – Stress – crack opening constitutive relation describing the local behaviour of the spring.

3.4.2. Inverse analysis results

Figure 3.34 shows an example of calibration procedure output for a sample designed with a dosage of fibers of 4 kg/m^3 and concrete compressive strength of 36 MPa. The comparison between the experimental and numerical behaviour calibrated makes possible to appreciate how the tensile behaviour of the single spring, in terms of parameters driving the cracking evolution and global trend is able to accurately describe the FRC material behaviour.

The parameters calibrated for all specimens are collected in Table 3.13. The regression model proposed before (section 3.3.7) is adopted to correlate the variables of fibre number and concrete strength with the local flexural strength parameters:

$\sigma(w_1)$, $\sigma(w_2)$, $\sigma(w_3)$ identifying the residual flexural strength and f_{ct}, the peak flexural strength. The analysis on the local parameters confirms the influence of the number of fibers on the local residual strength behaviour but not on the peak flexural strength (Table 3.14).

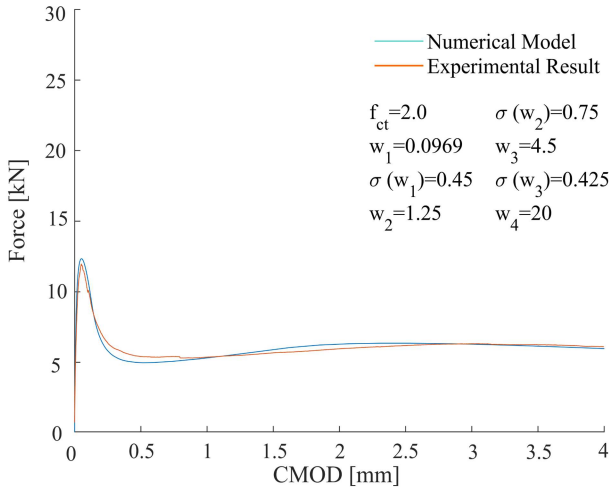

Figure 3.31 – Example of numerical model calibration for a specimen of the group B7 36 MPa 4 kg/m^3.

Table 3.13 – Local constitutive model parameters calibrated by an inverse analysis procedure.

Specimen ID	f_{ct}	w_1	$\sigma(w_1)$	w_2	$\sigma(w_2)$	w_3	$\sigma(w_3)$	w_4
B1_T1	1.75	0.0656	0.7	0.25	0.25	5.75	0.050	18.50
B1_T2	1.50	0.0540	0.7	0.25	0.25	1.5	0.175	20.00
B1_T3	1.50	0.0578	0.825	0.25	0.25	8.75	0.05	18.50
B1_T4	1.25	0.0578	1.2	0.125	0.375	3.5	0.05	20.00
B1_T5	1.25	0.0578	0.7	0.25	0.25	10	0.05	18.50
B1_T6	1.625	0.0969	0.325	5	0.25	6.5	0.05	18.50
B1_T7	1.50	0.0656	0.7	0.25	0.1875	1	0.113	20.00
B1_T8	2.125	0.0656	0.2	5	0.125	6.75	0.05	18.5
B2_T1	1.625	0.0930	0.2	2.375	0.1875	2.5	0.175	5.5
B2_T2	1.5	0.0773	0.575	0.25	0.25	5.75	0.175	18.5
B2_T3	1.375	0.0461	0.95	0.125	0.25	1.25	0.1125	20

B2_T6	2.375	0.0852	0.2	2.375	0.375	2.5	0.05	20
B2_T7	2.125	0.0734	0.2	2.375	0.25	2.75	0.05	3
B2_T8	2	0.0930	0.2	1.375	0.1875	10	0.175	20
B3_T1	2.375	0.0617	0.2	0.5	0.25	10	0.2375	18.5
B3_T2	3.25	0.05	1.2	2.375	1.4375	2.5	0.8	3
B3_T4	1.75	0.0462	1.075	0.125	0.1875	0.75	0.05	20
B3_T5	2.375	0.0617	0.45	0.25	0.25	10	0.2375	18.5
B3_T6	1.5	0.0969	0.2	0.75	0.1875	1	0.05	20
B3_T7	2.25	0.0813	0.2	4.875	0.125	10	0.05	19.5
B5_T1	1.75	0.0813	0.2	0.5	0.5	4.5	0.3	20
B5_T2	1.25	0.0969	0.45	3.25	0.625	3.5	0.3	20
B5_T3	1.75	0.0812	0.2	2	0.5	2.5	0.3	20
B5_T4	2.25	0.0656	0.7	5	0.625	7.5	0.3	19
B5_T5	1.75	0.0969	0.2	1.25	0.75	2.5	0.3	20
B5_T6	1.75	0.0969	0.45	3	1	10	0.925	19
B5_T7	1.75	0.0813	0.2	2.25	0.75	2.5	0.3	5
B5_T8	1.75	0.0813	0.7	0.25	0.5	3.5	0.3	19
B6_T1	2.5	0.0578	0.7	2	0.75	10	0.675	11
B6_T2	2.25	0.0813	0.45	2.5	0.75	3	0.3	19.5
B6_T3	2.25	0.0656	0.7	5	0.5	6.5	0.3	11
B6_T4	2.25	0.0891	0.45	2	0.875	2.5	0.3	20
B6_T5	2.5	0.0813	0.45	1.25	0.75	10	0.675	19
B6_T6	2.5	0.0891	0.45	0.5	0.625	10	0.55	19
B6_T7	2.5	0.0578	0.45	3.25	0.375	3.5	0.05	4
B6_T8	2.25	0.0891	0.45	2.25	0.75	2.5	0.425	20
B7_T1	1.75	0.0969	0.45	2.25	0.625	2.5	0.3	3
B7_T2	1.75	0.05	0.7	0.25	0.5	3	0.3	4
B7_T3	1.5	0.0891	0.7	0.25	0.5	10	0.425	19
B7_T4	2	0.0734	0.7	5	0.5625	6.5	0.3	11
B7_T5	1.5	0.0813	0.45	3	0.625	5.5	0.55	6
B7_T6	1.5	0.0813	0.45	3	0.75	10	0.675	20
B7_T7	2	0.0969	0.45	1.25	0.75	4.5	0.425	20

B7_T8	1.75	0.0734	0.45	1.5	0.75	4.5	0.3	5
B8_T1	1.5313	0.0998	0.6063	1.125	0.7813	10	0.7688	19
B8_T2	1.5938	0.0998	0.575	3.2813	0.6875	3.5	0.05	19
B8_T3	1.375	0.0998	0.7	4	1	6.5	0.3	11
B8_T4	1.5	0.0998	0.5125	2.7188	0.7188	2.75	0.05	18.75
B8_T5	1.5	0.0998	0.6531	1.9063	0.8125	5.25	0.7688	19
B8_T6	1.75	0.0998	0.7625	1.2813	1	4.5625	0.8	15
B8_T7	1.75	0.05	0.825	1.375	1.125	10	0.8625	12
B8_T8	1.5	0.0813	0.45	1.25	1	3.25	0.55	19
B9_T1	2.375	0.0617	0.575	4.75	0.9375	10	0.8	19
B9_T2	2.125	0.0734	0.7	1.875	0.75	9	0.675	19
B9_T3	2	0.0969	0.575	3.375	0.75	6	0.3	20
B9_T4	2	0.0695	0.45	1.25	0.75	10	0.7375	19
B9_T5	2.5	0.0578	0.575	1.75	0.75	10	0.55	17.5
B9_T6	2.125	0.0656	0.7	3.75	0.625	9.5	0.3	19
B9_T7	3.125	0.0539	0.45	2	0.75	3.25	0.55	7
B9_T8	2.125	0.0813	0.45	1.5	0.75	9.75	0.55	20
B10_T1	2.25	0.0827	0.7469	0.9375	1.0469	1.9375	1.0344	6
B10_T2	2.5938	0.0539	0.7625	1.2813	1.0156	9.75	0.9875	14
B10_T3	2.7188	0.0783	0.6844	1.4688	1.1406	2.75	1.7688	3.25
B10_T4	2.6563	0.5391	0.7	1.4063	1.2031	7.3125	0.2063	8
B10_T5	2.3125	0.0813	0.4188	2.5938	0.6875	2.8125	0.081	17.75
B10_T6	2.625	0.05	0.575	5	1	9.5	0.3	19
B10_T7	2.875	0.05	0.825	1.2813	1.125	9.5	0.8625	12
B10_T8	3.2188	0.0578	0.45	0.9688	0.8125	1	0.8	14.25
B11_T1	2.0313	0.0471	0.95	2.125	1.5	3.4375	0.8156	20
B11_T2	1.8438	0.0656	0.45	1.9688	0.75	4.1875	0.3	7
B11_T3	2.0938	0.0344	0.9813	1.8125	1.5	4.1875	0.8	20
B11_T4	1.875	0.0578	0.7	3.375	1.25	4	0.05	17
B11_T5	1.625	0.0813	0.95	1.875	1.5	5	0.8	20
B11_T6	1.5938	0.0998	0.6531	5	0.6563	6.5	0.3	11
B11_T7	1.625	0.0930	0.95	1.625	1.125	4.25	0.8	12

B11_T8	1.875	0.0852	1.075	1.625	1.3125	5	1.175	20
B14_T1	1.25	0.0969	0.95	1.875	1.125	5.5	0.8	12
B14_T2	2.25	0.0969	0.7	1	1	3	0.8	3.5
B14_T3	1.75	0.0617	1.2	0.125	1	6.5	0.8625	8
B14_T4	2.125	0.0461	0.7	1.375	1.25	3	0.8	20
B14_T5	2	0.0773	0.7	1.25	1	8	0.8	14
B14_T6	1.75	0.0891	0.825	1.25	1.25	6	0.8	14
B14_T7	1.5	0.0891	0.95	1.75	1.3125	5.75	0.3	16
B14_T8	1.875	0.0695	0.95	2	1.125	3.5	0.8	20
B15_T1	1.325	0.0969	0.7	1.5	1	2.5	0.8	20
B15_T2	2.375	0.0656	1.075	1.375	1.5	6	1.3	20
B15_T3	1.75	0.0969	0.825	2.5	1.1875	3.25	0.2375	20
B15_T4	1.625	0.0969	0.825	3.75	1.5	9.5	1.425	10
B15_T6	1.875	0.0969	0.7	2	1.25	3.5	0.3	5.5
B15_T7	1.75	0.0969	1.075	4	1.25	7.5	0.8	10
B15_T8	1.75	0.0969	0.7	0.625	1.0625	10	0.9875	12

Table 3.14 – Significance test on regression coefficients correlating the local mechanical parameter with concrete compressive strength and number of fibres.

Local strength parameters value	b		m_1		m_2	
	Value [-]	Significant	Value [-]	Significant	Value [-]	Significant
f_{ct}	0.195	YES	0.000	NO	0.04	YES
σ (w_1)	0.462	YES	0.004	YES	-0.002	NO
σ (w_2)	-0.133	YES	0.01	YES	0.006	NO
σ (w_3)	-0.379	YES	0.007	YES	0.009	NO

3.5. INFLUENCE OF THE MACRO SYNTHETIC FIBRE COMPOSITION

Within the synthetic fibers reinforcement, the fibre type is also responsible of the interfacial properties and, so, of the mechanical performance of the fibre reinforced material. Therefore, a further analysis of five different modification of the

macrosynthetic fibre before considered, in terms of chemical composition and production technique, is developed. The constituents of the material are varied introducing different components and, also, using a different technique of production. These variations determine on one hand a different number of fibers at the same volume and, also, a modification of the interface properties. For this reason, the aim would be to investigate the different performance achieved.

3.5.1. Materials

The fibre types are indicated in Table 3.15, where for each composition the percentage of the methacholine, maleic anhydride and silica fume are reported while the modification for the fibre type F5 consists of an additional preliminar threatment. In order to investigate their effect of the fibre reinforced concrete response, one concrete class of the previous tested, the medium strength class, and one dosage, 6 kg/m^3, are used to produce five batches. They are identified by the codes (F1,...,F5) specified in Table 3.15.

Table 3.15 – Composition of the fibre types adopted and batch identification code.

BATCH ID	FIBRE CHEMICAL COMPOSITION			
	Methacholine	Maleic Anhydride	Silica Fume	Double Stretch
F1	0.20%	/	/	/
F2	0.20%	0.20%	/	/
F3	0.25%	0.25%		Yes
F4		0.425%	0.425%	/
F5			0.25%	/

3.5.2. Analysis of experimental results

The MSFRC mechanical performance is characterized by performing three point bending tests on prismatic specimens according to the procedure described before (European Standard EN 14651) and the mechanical behaviour is analysed in terms of

nominal stress – crack opening relation (Figure 3.32 – Figure 3.33) and nominal residual strength values (Figure 3.34 – Figure 3.35). The relations exposed include the comparison with the mean curve of the reference batch tested in the previous section in order to evaluate if the adoption of a modified fibre type improves the mechanical performance. The comparison reveals a difference in the post peak trend evident for the fibre containing silica fume products.

Examining the residual flexural strength values (Figure 3.34 – Figure 3.35) and comparing them with the values exhibited by the reference batch, it can be seen how the mechanical performance reflects the fibre type and its composition because the technique adopted for their production leads to a different total volume altough the same dosage adopted andinfluencing the residual strength performance. The other fibre type does not significantly improve the material performance.

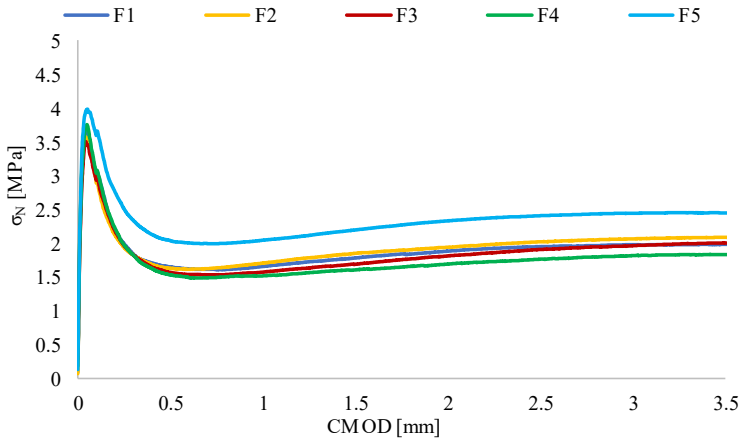

Figure 3.32 – Mean Nominal stress – crack opening flexural behaviour for the five fibres type tested.

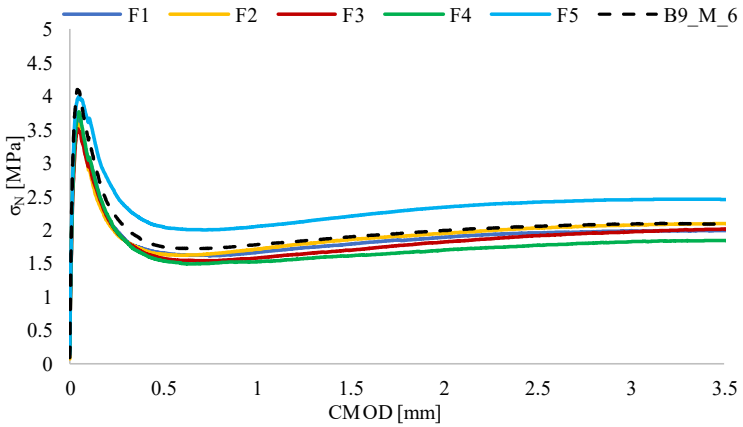

Figure 3.33 – Mean Nominal stress – crack opening flexural behaviour for the modified fibers compared with the mean flexural trend of the B9 batch (43 MPa and 6kg/m^3 of fibres).

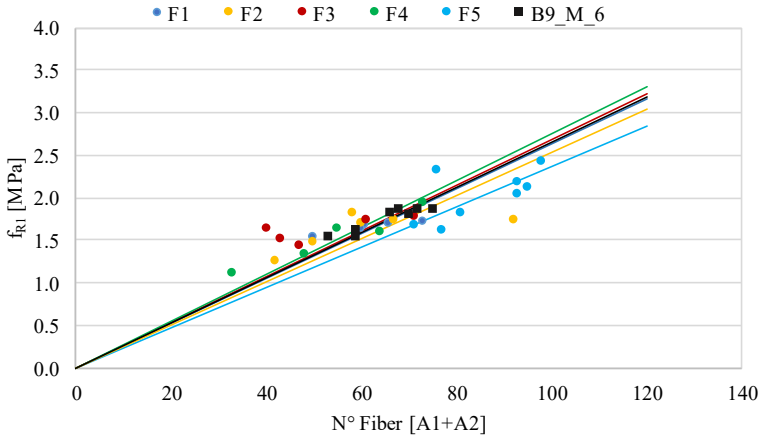

Figure 3.34 – Linear regression on the residual flexural strength nominal parameter f_{R1} with the number of fibres included in A_1 and A_2 middle cross section areas and compared with the residual strength values for the reference batch B9 (43 MPa and 6kg/m^3 of fibres).

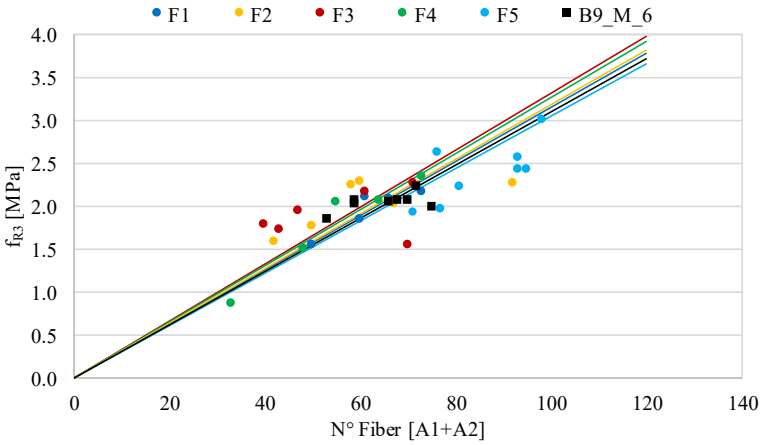

Figure 3.35 – Linear regression on the residual flexural strength nominal parameter f_{R3} with the number of fibres included in A_1 and A_2 middle cross section areas and compared with the residual strength values for the reference batch B9 (43 MPa and 6kg/m^3 of fibres).

CHAPTER 4

4. DEVELOPMENT OF HIGH PERFORMANCE FIBRE REINFORCED CONCRETE WITH SUSTAINABLE WASTE MATERIAL

4.1. PROBLEM OF SUSTAINABILITY AND WASTE MATERIAL IN CONCRETE DESIGN

The high mechanical potentialities of concrete material and the ability in realizing structures resistant and resilient against the extreme environmental conditions and climate effects (Hajek, 2019) make it one of the structural material most used in the engineering construction field. On the other side, the use of natural materials for the production and the dangerous gas emitted by the construction industry, are in contrast with the sustainability problem and the decarbonization project proposed by the European Union (Imbabi, Carrigan, and McKenna, 2012; Jackson et al., 2017). The CO_2 emissions rose by 1.4% in 2017 reaching maximum historic levels (IEA - International Energy Agency, 2018) although the Kyoto protocol targets adopted in 1997 in order to reduce the greenhouse gas concentration in the atmosphere to avoid interferences with the climate system.

Related to the present aim, the sustainability approach is going to be implemented into a new *fib* ModelCode 2020 thanks to the activities carried out by the fib Commission 7 (fib Bulletin 28, 2004; fib Bulletin 71, 2013) and on the work of Commission 10 in preparing the MC2020.

The achievement of sustainable purpose in technologies and developments should consider many aspects in the concrete structures, from the conventional design methods need to be improved, innovations about concrete mix, composite materials and ways of reinforcement and also procedures of maintenance, repair and recycling processes. The structural design would be, in any case, aimed at fullfilling requirements with reference to ultimate limit states and serviceability limit states and, so, structural safety, serviceability and durability.

Important steps are being taken towards the officialization of sustainable approaches by adopting official methods to asses, in an objective way, the sustainability of a concrete structure. In this framework, Aguado et al. proposed the MIVES method, a multi-criteria procedure, where the economic, environmental and social aspects are required and a three levels structure is proposed composed by

requirements, criteria and indicators. A sustainability index is assigned as the sum of dimensionless factors of each requirement multiplied by the weight assigned (Aguado, Gàlvez, Fernandez-Ordònez, and De La Fuente, 2016).The method has been applied, for example, to evaluate the Sustainability contribution different building processes of coloumns realized with three different concretes, two technologies of cast, two different sections and so, dimensions.

Table 4.1 – Sustainability assessment: calculation of SI (sustainability index) for different concrete coloumns processes (Aguado et al., 2016).

Type f_{ck}	Compacting system	Section	Dimensions (cm)	A_c (mm^2)	A_s (mm^2)	Ref.
C25	Vibration	Rectangular	40x40	158743	1257	C25/V/S
		Circular	50	195331	1018	C25/V/C
	Self Compacting	Rectangular	40x40	158743	1257	C25/SC/S
		Circular	50	195331	1018	C25/SC/C
C50	Vibration	Rectangular	30x30	88743	1257	C50/V/S
		Circular	35	96211	792	C50/V/C
	Self Compacting	Rectangular	30x30	88743	1257	C50/SC/S
		Circular	35	96211	792	C50/SC/C
C75	Vibration	Rectangular	25x25	61243	1257	C75/V/S
		Circular	30	70685	679	C75/V/C
	Self Compacting	Rectangular	25x25	61243	1257	C75/SC/S
		Circular	30	70685	679	C75/SC/C

After stating the requirements, criteria and indicators, the SI (sustainability index) is computed.

Table 4.2 – Sustainability assessment: evaluation of requirements, criteria and indicators for the SI calculation (Aguado et al., 2016).

Requirements	Criteria	Indicators
R1. Economic (50%)	C1. Construction costs (67%)	I1. Building costs (85%)
		I2. Non acceptance costs (15%)
	C2. Efficiency (33%)	I3. Maintenance (60%)
		I4. Habitability (40%)
R2. Environmental (33%)	C3. Emissions (67%)	I5. CO_2 Emissions (100%)
	C4.Resources consumption (33%)	I6. Concrete consumption (90%)
		I7. Steel consumption (10%)
R3. Social (17%)	C5. Negative effects on the producer industry (80%)	I8. Workers' inconveniences (20%)
		I9. Workers' safety (80%)
	C6. Effects to third party (20%)	I10. Environment nuisances (100%)

Ref.	SI	Ref.	SI	Ref.	SI
C25/V/S	0.608	C50/V/S	0.662	C75/V/S	0.707
C25/V/C	0,558	C50/V/C	0.716	C75/V/C	0.794
C25/SC/S	0.623	C50/SC/S	0.717	C75/SC/S	0.771
C25/SC/C	0,564	C50/SC/C	0.768	C75/SC/C	0.852

4.2. HIGH PERFORMANCE CONCRETE AND FIBRE REINFORCED CONCRETE

The concepts of sustainability and environmental impact reduction are introduced in fibre reinforced concrete materials with the design of cement based fibre concretes where the constituents are partially substituted optimizing the matrix design.

The concrete matrix can be designed either with traditional mechanical performance of the plain concrete, following the common criteria, or with high performance. The latter is the case of High Performance Fibre Reinforced Concrete. The difference between the two types lies in the selection of the aggregates, i.e. type and size, the high cement content, the low water-cement ratio. Regarding the aggregates used, cement (diameter approximately equal to 15 μm) is mixed with silica fume (diameter having a range between 0.01 and 1 μm) having filler function reducing the porosity, sand (the aggregate with bigger diameter than the other components around 150 – 600 μm), and other aggregates resulted by grinding stones as quartz (medium diameter size 10 μm) and other types. The liquid part is composed by the water and superplasticizer used to increase the low workability of these admixtures since the fine aggregates tend to agglomerate during the mixing phase. The fibres added can be made of steel that increase the tensile strength and ductility, PVA characterized by less mechanical strength but more ductility and polypropylene; in general their size reaches the length of 1 – 2 cm with a diameter of few millimetres. With reference to steel fibers reinforcement, a comparison can be made with ordinary concrete, high performance concrete (HPC) and Ultra High Performance Concrete.

Table 4.3 – Mix design differences between Plain Concrete, HPC (High Performance Concrete) and UHPC (Ultra High Performance Concrete), (Spasojević, 2008).

COMPONENTS [kg/m^3]	PLAIN CONCRETE	HPC	UHPC
Portland Cement	<400	410	700-1000
Coarse Aggregate	≈1000	920	0-200
Fine Aggregate, sand	≈700	620	1000-2000
Silica Fume	-	40	200-300
Superplasticizer	-	5	10-40
Water	>200	100-150	110-200
Fibre	-	-	>150
w/c ratio	>0.35	0.28-0.38	<0.24
aggregate/cement	-	<0.38	<0.22
Density	2000-2800	2000-2800	>2500

This type of material is characterized by a homogeneous and compact internal structure with a low percentage of porosity given the small aggregate size used in the mix design. In general, the cementitious matrix is composed by three phases, the cement, the aggregates and the transition zone where the cracks, according to the mechanical properties of the contituents, are generated. This is the most heterogeneous zone where there is a high pores percentage and calcium hydroxide crystals producted during the hydration phase.

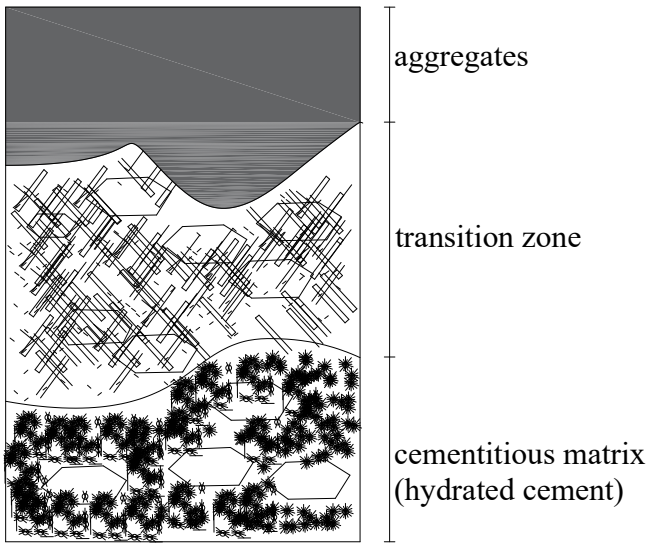

Figure 4.1 – Concrete matrix phases (based on Saeed 2012).

Bigger aggregate size determines more crack opening in the matrix while the internal structure and so the pores size is driven mostly by the water/cement ratio and determines the mechanical properties of the matrix since the stress is concentrated around the voids of the structure generating micro-cracks.

Consequently, the transition zone organization is strictly connected with the mechanical performance of the material. From this point of view, to make the cementitious matrix more homogeneous, the density should be increased adopting a mix design with aggregates and cement more compact. This aim is achieved using fine aggregates leading to a bigger stifness, approximately similar to that of cement, the addition of silica fume products with a pozzolanic and micro-filler action, reducing the internal porosity of the material, a low water/cement ratio that reduces

the space between the cement grains, the transition zone extension decreases on the opposite the cement paste volume increases respect to the volume of the internal voids. The use of fine aggregates involve a decrement of the workability due also to the low water/cement ratio: for this reason it is necessary the addition of plasticizer and superplasticizer and, in some cases, a thermal treatment to optimize the material micro-structure reducing the transition zone.

The type and size of aggregates play an important role in the mechanical performance of the UHPC since the aggregate is a component weaker than the cement paste. In general the aggregates used, apart from the sand, consist of different types of rock: gabbro, basalt, quartz, limestone, sandstone. The concrete compressive strength grows with the strength of the rock type, so it is important to underline how the compressive and flexural strength are related to the aggregate and the transition zone drives the compressive strength of the material. A scientific study developed on mix design realized with percentages of basalt have revealed the best performance in terms of compressive strength since the cracks involve the aggregates and the cement paste (P.P. Li, Q.L. Yu, C.P. Chung, 2017) . The mix design in realized with Portland Cement (CEM I 52.5R), microsilica (mS), limestone powder (LP), sand 0 -2 (S), basalt (BA), water (W) and superplasticizer (SP). The fibre type is made of steel, with a length of 13 mm, diameter of 0.2 mm and tensile strength of 1100 MPa. The mix design is optimized using six combinations of the constituents, keeping the water/powder ratio equal to 0.2, SP equal to 0.8% of the total powder in terms of weight, and consequently mS and LP amount range from 5%, 15%, 30% with reference to the weight (Table 4.4).

Table 4.4 – Matrix mix design of Ultra High Performance Concrete (UHPC) containing basalt constituent (P.P. Li, Q.L. Yu, C.P. Chung, 2017).

Table 2 Recipes of UHPC (kg/m^3)

No.	CEM	mS	LP	S	BA 1-3	BA 2-5	BA 5-8	BA 8-11	BA 8-16	W	SP
3-900	675	45	180	864.5	576.3	0	0	0	0	180	10.8
8-900	675	45	180	588.1	178.6	403.1	313.9	0	0	180	10.8
8-850	637.5	42.5	170	700.1	100.5	435.7	310.4	0	0	170	10.2
8-800	600	40	160	812.2	22.3	468.4	307.0	0	0	160	9.6
8-750	562.5	37.5	150	903.6	0	318.8	453.8	0	0	150	9.0
16-900	675	45	180	304.7	308.3	306.6	247.5	120.9	206.2	180	10.8

The study shows that the addition of aggregates produced by basalt acts on the interface between aggregates and cement but its potential mechanical strength is limited by the cement paste; in addition a bigger aggregate size shows a higher compressive strength. To sum up, an aggregate/cement ratio equal to 1.1 gives back a high compressive strength. Apart from the sand, fine size aggregate powder with a filler function but with no reaction with the cement, generate an increment of the 30% of strength respect to concrete realized with no amount of these constituents. Finally, whatever sand can be used to design the matrix of concrete with high performance.

The UHPC production with the aim of guaranteeing optimal performance during the fresh and hardened state needs:

- Cement with moderate aggregate size and celite amount less than 8% reducing the requirement of water;
- Fine aggregate/cement ratio approximately equal to 1.4 with a maximum grains diameter of 0.8 mm;
- Silica fume with low percentage of carbon (0.5%) as a quantity of 25% of the cement weight and characterized by a bigger grains size (1.2 micron) reducing the specific surface and the water required;
- Silica powders and other reactive powders with an amount of 25% of the cement weight;
- Polycarboxylate water reducers and superplasticizer that allows a good workability of the material releasing the entrapped air during the mixing phase;

- Adoption of a water cement ratio between 0.16 – 0.27 (preferably 0.22);

4.2.1. Silica fume products

Silica fume products are obtained by condensation of silica vapor (SiO_2) and are composed for a higher percentage of 90% by non-crystallized silicon particles having a size varying from 0.5 μm and 5 μm. Their filler function is mostly given by the specific surface they are characterized by, 25-30m^2/g, determined according to ISO 9277 (2010).

The role of the silica fume in the mix design deserves a short explanation. It is characterized by very small particles, with diameters included in a range of 0.01 – 0.1 μm, from a chemical point of view it contains a high amount of amorphous silica with small amounts of steel and magnesium. Its small aggregate size makes possible the creation of a very compact internal structure and fine texture (Russo, 2011) especially because their size is smaller than the cement grains, obtaining a material with higher strength, high density, with a low porosity and so resistant to the penetration of external factors. On the other side, the small aggregate size and the high specific surfaces of the silica fume grains (20-30 m^2/g) requires a high amount of water to agglomerate properly and cast the final product. The optimal dosage of this component is about 20 – 30%, higher amount could affect in a negative way the material mechanical properties. The solution lays in the use of the superplasticizer (2 – 4% of the cement) that allows the adoption of a low water cement ratio, otherwise the use of a higher amount of water could set aside the positive aspect of the silica fume use. They are reflected in the mechanical performance (compressive and flexural strength, elstic modulus, toughness, mortar – aggregates bond and abrasion resistance) and durability aspects. Moreover:

- The addition of SF increases the compressive strength at 28 days;
- The SF addition does not increase the tensile strength but the flexural tensile strength;

- The bond between the fibre and cementitious matrix is improved;
- High percentage of SF increase noticeabily the autogeneous and plastic concrete shrinkage, decreasing the creep deformation.

Moreover, the mechanical aspect of this material is the capacity of developing its strength over time so being still active (Tavano and Berra, 1985), so could be appropriate to evaluate the properties of the material designed with silica fume products also after a curing period longer than 28 days characterization.

4.2.2. High Performance Fibre Reinforced Concretes (HPFRC) mechanical behaviour

The high and ultra-high performance fibre reinforced concretes (HPFRC – UHPFRC) are materials recently developed despite their first application might addressed to the beginning of 90s in France and the in USA. There is a plenty of type of fibres used to reinforce concrete with high performance: typically they are made of steel, polymers, glass, carbon and natural. The fibres mechanical properties themselves influence the final performance of the UHPFRC, in particular their toughness, elastic tensile modulus, and the geometrical aspects, shape, length, diameter and aspect ratio. The optimization of the performance given by tha irregular shape of the fibre and their high aspect ratio is maintained the same as those used in FRCs with 'traditional' performance. The mechanical behaviour of the high performance concrete reinforced with short fibres is the combination of the mechanical aspects given by the cementitious matrix and the fibres addition (connected with the dosage, type and geometry): the compressive strength can reach a value higher than 150 MPa exhibiting higher stifness, and the increment of the tensile strength and ductility of the composite material are remarkable. Figure 4.2 shows a comparison between ordinary and high performance concrete subjected to a compressive and flexural load, underlining the difference in peak and post-peak behaviour.

The mechanical characterization of the material regards the compressive strength and flexural behaviour analysis in terms of peak and post-peak evolution when the elastic resources are completely used. The main difference respect to the fiber reinforced concrete is the creation of a crack pattern characterized by many cracks instead of a localized one: the material exhibits a hardening trend and the final behaviour follows the trend of a typical FRC.

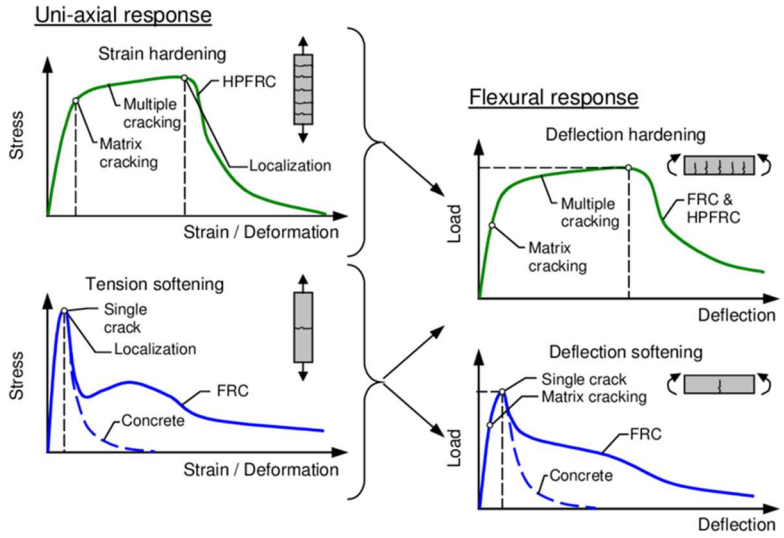

Figure 4.2 – Fibre Reinforced and Highe Performance Fibre reinforced Concrete mechanical behaviour (Jansson, Löfgren, Gylltoft, and Thomas, 2008).

Thus, a UHPFRC is characterized by a hardening behaviour:

$$f_{ct} \geq f_{ct,m} \qquad [4.1]$$

that is, together with the compressive strength and the ultimate tensile strain, the parameter used to characterize and determine the quality and efficence of the fibrous reinforcement. Regarding the compressive performance, it is strictly influenced by the cementitious matrix composition: comparing the mechanical performance of an unreinforced ultra high performance concrete (UHPC), a normal strength concrete (NSC) and high strength concrete (HSC), a UHPC is able to exhibit a compressive strength of 150 MPa sometimes without thermal treatment. In general, the fibres contribution is visible in the post-peak branch that follows a slope depending on the

fibres content, their geometry, their length related to the aggregate size and the fibres arrangement. The peak compressive strength is slightly modified by the fibres content, in particular for a dosage of 2.5%, an increment of approximately 15% of the compressive strength is achieved.

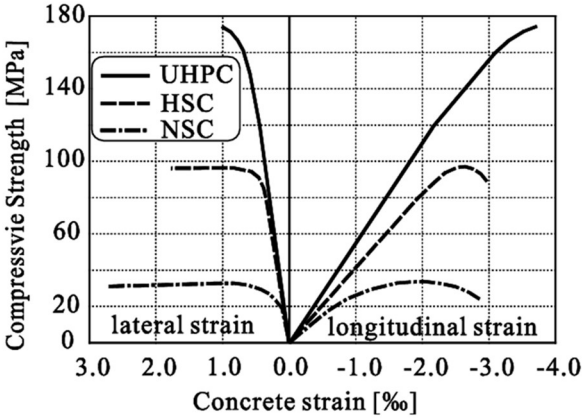

Figure 4.3 – Concrete mechanical behaviour in compression, Normal Strength Concrete, High strength concrete and Normal strength concrete (Tue, Simsch, Schneider, and Schmidt, 2004).

The mechanical response of the material under a compressive load can be divided into three phases:

1. An elastic linear part characterized by an elastic modulus of approximately 50 Gpa and higher, that affect the structural response;
2. A non linear part before the failure load, at approximately 70 – 80% of the peak strength;
3. A descendent behaviour with a trend dependent on the fibers arrangement and properties.

The determination of a constitutive behaviour is not easy since the complex failure mechanism activated inside the matrix. The uniaxial compressive test gives back the constitutive behaviour under compression by which it is possible to obtain the elastic modulus E, the compressive strength f_c, the strain correspondent to the elastic limit $\varepsilon_{c,el}$, the ultimate strain $\varepsilon_{c,u}$. The French regulation, based on the first two parameters elastic modulus and compressive strength, defines the constitutive relation used during the design phase in both ultimate and serviceability limit states assuming:

- A global security coefficient 1.3 and in addition a coefficient for compressive state 0.85 for the design at ULS;
- A reduction coefficient 0.6 for the SLS.

The bilinear relation in Figure 4.4 is so defined, the elastic phase until the constant value used in the design phase is followed by a plastic stage until the ultimate deformation $\varepsilon_{c,u}$ 0.0035 (in the Deutesch regulation the ultimate strain value is the effective value as the limit of the plastic stage). The present relation is easy to adopt for the structural design since only two parameters are considered.

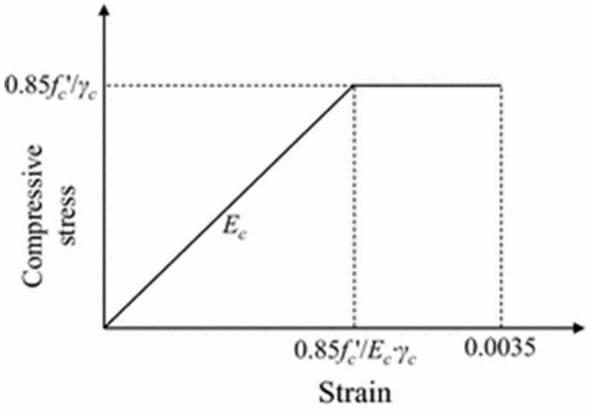

Figure 4.4 – JSCE recommendations: compressive stress-strain curve (JSCE, 2004).

Regarding the performance of the material in terms of tensile strength, on one hand the UHPC material is able to show a tensile strength between 7 – 10 MPa without fibres addition. The fibrous reinforcement, according to the dosage, geometrical properties and orientation, increases noticeably the strength reaching 15 MPa giving, at the same time, a ductile post-peak behaviour, with a final softening branch if related to the crack opening measurement.

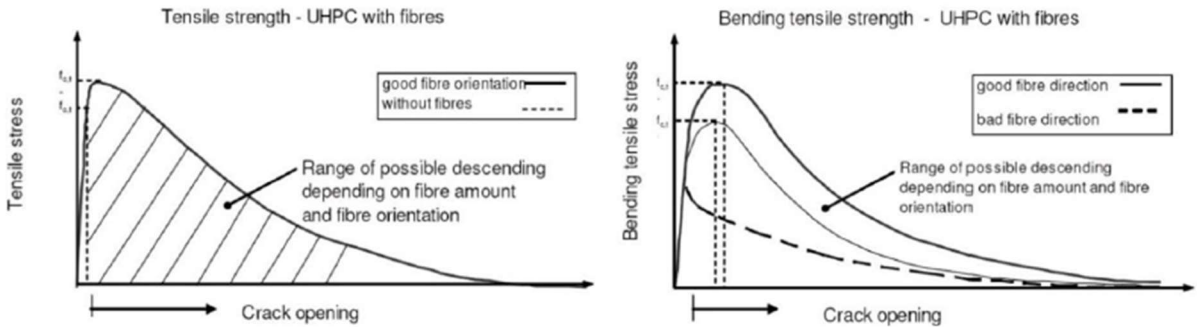

Figure 4.5 – Tensile stress – crack opening relation and bending tensile stress – crack opening relation for ultra high performance concrete (UHPC) materials (Fehling, E., Bunje, K., and Leutbecher, 2007).

The tensile and compressive strength of the material are related, the optimization of the cementitious matrix in combination with the high modulus of fibers added and a good adhesion between the two components, given by the fibres shape, is able to improve the performance of the material in terms of tensile strength. It has been demonstrated that, increasing the compressive strength, also the tensile strength and the ultimate strain increase.

Examining the mechanical behaviour of a UHPC material (Figure 4.6) subjected to a flexural load, two main phases can be identified:

a. The first part follows a linear eastic law, dominated more by the matrix properties rather than the fibres properties. It is described by the elastic modulus E, peak tensile strength of the matrix that represents the elastic limit $f_{t,1st}$;
b. The post – peak phase is approximated by a linear behaviour characterized by a multi cracks pattern until the ultimate strength value reached thanks to the fibrous reinforcement, $f_{t,max}$. After the peak identified by the elastic limit, the rate at which the tensile strength grows is much slower than the elastic part, it can be also maintained constant. Thanks to the fibres, the material exhibits a ductile behaviour.

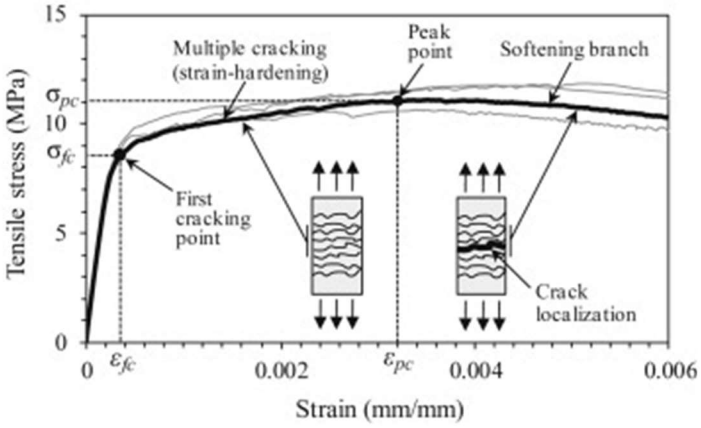

Figure 4.6 – Flexural behaviour of an Ultra-High Performance Concrete (Yoo and Banthia, 2016).

Although the post cracking behaviour evolution, the bridging process activated is similar to that of a normal strength concrete (NSC) reinforced with fibres: the microcracks activate the load transferring process and for a deformation value approximately equal to 0.25% all cracks appear.

The French standard code NF P 18-470 (2016) indicate the determination of the UHPFRCs tensile properties by means of a four point bending test on un-notched specimens where the deflection is monitored and three point bending configuration on notched specimens with the determination of the tensile behaviour class.

The applications of the present material range from the design of parts of structures subjected to particular loading and environmental conditions (Brühwiler and Denarié, 2008), for rehabilitation or new structures and also combined with normal concrete in order to increase the durability of the structure, given its good adhesion properties demonstrated by an important research (Tayeh, Abu Bakar, Megat Johari, and Voo, 2013).

4.3. EXPERIMENTAL INVESTIGATION

4.3.1. Preliminary phase

In the framework of the fibre reinforced concrete materials and according to the properties described before, the optimization of the matrix with different constituents

and the micro-fibres properties lead to an improvement of the mechanical performance for what concern the material strength and the cracking pattern evolution. In addition, attention deserves also the mechanical performance of the material over time.

In order to merge these aspects, studying their combined effect, an experimental analysis is undertaken characterizing the mechanical behaviour of cement based high performance material, designed with porcelain stoneware waste material and reinforced with PVA short fibers. The present analysis is based on a background of results previously achieved: the porcelain stoneware powder obtained from the cold grinding of porcelain stoneware tiles and white and black electric arc furnace slags for partially substitution of respectively cement and sand are examined in both plain and two fibre reinforced composites types. This preliminary analysis revealed the good mechanical properties of the porcelain stoneware powder since its addition did not reduce the material mechanical performance, leading to a high compressive strength for some of the edmixtures tested. On the contrary, the addition of electric arc furnace slag modifies significantly the material fresh state reducing the workability and requiring a higher water content and, so, a decrement of the mechanical strength. The admixture type exhibiting a better mechanical performance where reinforced with either steel and PVA fibres achieving better results for the second fibres reinforcement type. The mechanical characterization sees the execution of bending tests, in three and four point configuration, and compressive tests. Some of the research activities of this preliminary evaluation are part of MATERSOS, a research project funded by the Emilia Romagna Region (Buratti et al. 2018).

4.3.2. Outline of the research activity

On the basis of the preliminary results, an experimental campaign is organized with the aim of understanding how the optimization of the matrix mix design of high performance cement-based material reinforced with PVA fibres might affect the

mechanical behaviour, in terms of flexural strength, compressive strength and post cracking behaviour. The cementitious matrix is designed with cement CEM I 52.5R I, porcelain stoneware powder (P), silica fume products (SF), sand (S) and water with PVA fibers addition. The workability is improved by adding an amount of superplasticizer (SP). In order to separate the components effects, the Design of Experimenta criteria is used to consider nine possible combinations of the fine aggregate quantities, silica fume, porcelain stoneware and cement; these proportions are combined with three values of the total fines amount and three values of the water – fines ratio generating 81 different admixtures. The mechanical responses are tested casting three prismatic specimens having 40x40 mm^2 cross section and 160 mm long for each admixture: two of them are tested after 28 days curing while the third after 60 days curing in order to evaluate the activity of the components on time. The characterization is performed by flexural tests in four point bending configuration and compressive tests. The same specimen, before tested under flexural load, is then subjected to a compression test on both ends applying the load on a surface having the same cross section area, 40x40 mm^2. The procedure is explained in detail in the following section.

4.3.3. Materials

Porcelain stoneware powder

This material, as specified before, consists of a waste product obtained from the cold grinding of porcelain stoneware tiles and it reveals mostly the presence of SiO_2. It is important to underline that this material does not require any preliminary treatment before the usage. The chemical composition is reported in Table 4.5 and the grain size assortment is collected in Table 4.6.

Table 4.5 – Chemical constituents (%) of waste from rectified porcelain tile.

Oxides	%
SiO_2	74.00
Al_2O_3	18.00
TiO_2	0.66
Fe_2O_3	0.92

CaO	1.44
MgO	0.46
K_2O	2.36
Na_2O	1.53
ZrO_2	0.27
SO_3	<0.05
P.F.	0.42
Cl^-	0.002
Organic subst.	0.07
Insoluble res.	2.00

Table 4.6 – Grain size (μm) of waste from rectified porcelain tile.

D_{10}	d_{50}	d_{90}
3.1	22.9	91.4

Cement

The cement used in the present experimental campaign is a Portland cement (CEM I) with a strength of 52.5 MPa and is classified as type R according to the time in which it starts to react with the components, i.e. the water.

Sand

The HPFRC are realized using sand that is a natural siliceous aggregate, with grain size included in the range 0 – 5 mm.

Silica fume

This material belongs to the addition material of type II as indicated in the regulation UNI EN 206 (2016) and it is characterized by pozzolanic activity, as explained before. Its adoption is regulated by UNI EN 13263 (2009) that indicates the limits for SiO_2 content, chlorides SO_3, CaO and SiO, the specific surface and the amount of dry material respect to the declared value.

PVA fibres

The fibrous reinforcement consists of microfibres realized with extruded polyvinyl and its commercial typology is identified as MasterFiber 401; it is a fibre type with high performance with the ability of increasing noticeably the ductility of the material. It is remarkable that their introduction does not modify significantly the

fresh state of concrete. The mechanical and geometrical properties collected in Table 4.7 are declared directly by the company which produces them.

Table 4.7 – PVA fibres used to reinforce the HPC matrix: mechanical and geomatric features.

Fibre property	Value
Fibre length [mm]	12
Fibre diameter [μm]	200
Fibre Aspect ratio [-]	60
Fibre material	PVA
Fibre tensile strength [MPa]	800
Elastic secant modulus [GPa]	8.5
Shape	straight

The admixture is prepared adding the proportioned amount of potable water, in this case further examination about its composition are not needed, and liquid superplasticizer MasterGlenium ACE 300. Its adoption is indicated for precast elements with concrete having low water-cement ratio and high strength with short curing period.

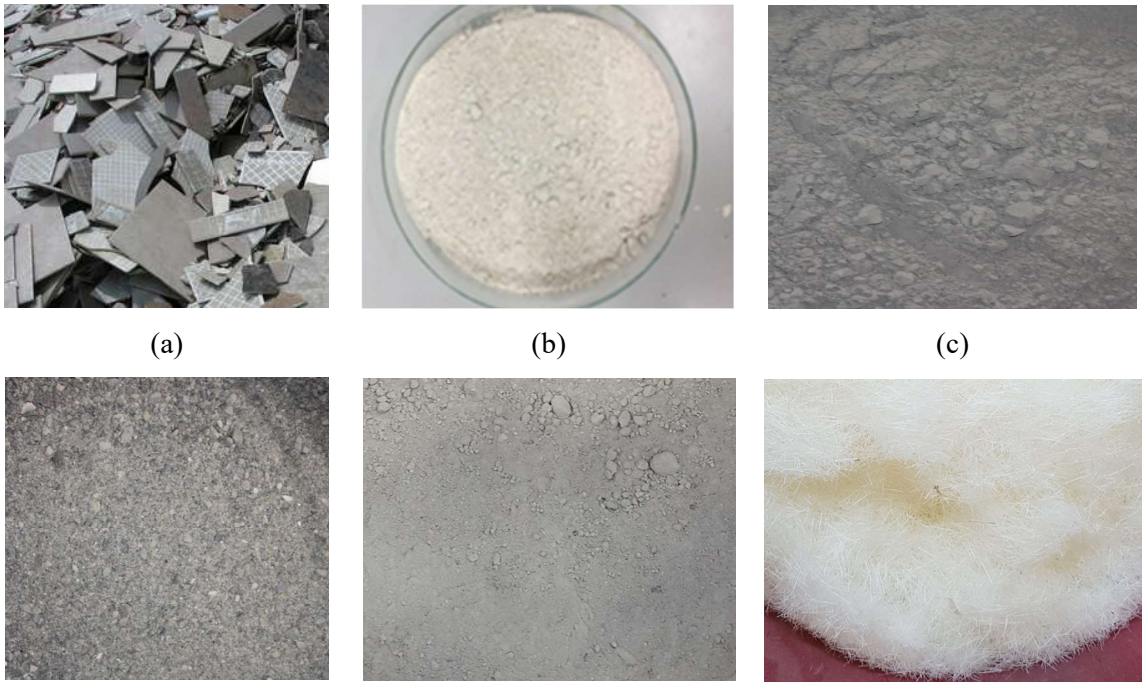

(a) (b) (c)

(d) (e) (f)

Figure 4.7 – Materials adopted for High Performance Fibre Reinforced Composites realization: (a) Porcelain tiles; (b) Waste material producted by their grinding; (c) CEM I 52.5R; (d) Sand 0-5 mm; (e) Silica fume products; (f) PVA fibres.

4.3.4. Mix design optimization

The mix design proportioning is more responsible of the mechanical performance of the material respect to the total amount of the constituents. The adoption of a statistical technique to design the composition of a HPC helps to find out the best proportion since the large suggested value of the ingredients (Mohammad and Ozgur, 2017). In this study the role of three main variable is investigated and, for this reason, they represent the components whose amount is optimized:

- Total fine aggregates amount;
- Proportion of fines;
- Water – fines ratio.

The proportion of fines, silica fume (SF), cement I and porcelain powder (P) are three variables, whose proportions identify a region of interest in two – dimension space. In Figure 4.8 the nine points marked correspond to the combinations of the fines adopted and their percentages are explicated in Table 4.8.

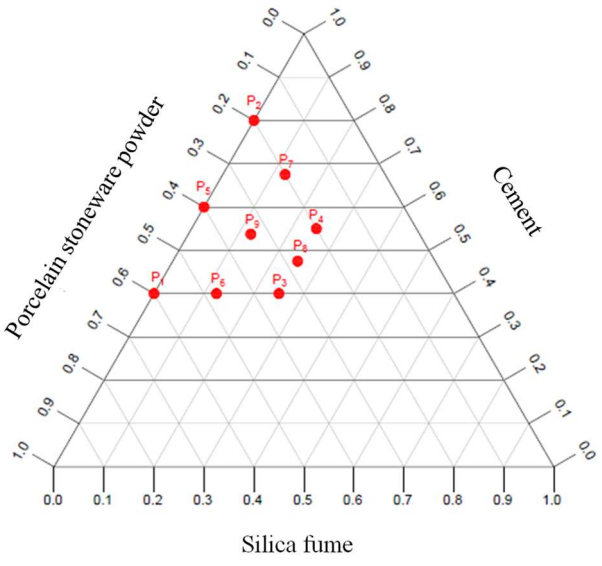

Figure 4.8 – Percentages (%) of fines constituents adopted.

Table 4.8 – Combinations (%) of fine aggregates adopted.

Point ID	%C	%P	%SF
1	0.4	0.6	0
2	0.8	0.2	0
3	0.4	0.35	0.25
4	0.55	0.2	0.25
5	0.6	0.4	0
6	0.4	0.475	0.125
7	0.675	0.2	0.125
8	0.475	0.275	0.25
9	0.5375	0.3375	0.125

According to the proportion within the fines, the total amount fine aggregates and water – fines ratio are combined using the Design Of Experiments criteria, in particular the mixture design procedure. For both properties, their minimum, maximum and mean values are established:

Table 4.9 – Fine aggregates and W/F ratio values adopted for the admixtures design.

Fines Min	900	W/F Min	0.18
Fines Max	1200	W/F Max	0.25
Mean Value	1050	Mean Value	0.215

The statistical mixture methodology declares the normalization of the variable values, Fines and W/F ratio in the present analysis, so that the actual values have a range between ± 1. The normalization coefficients are {-1; -0.7071068; 0; 0.7071068; 1} and the combinations of fines [kg/m^3] and W/F [-] are so calculated:

$$Fines[kg/m^3] = Mean + (Fines_{MAX} - Mean) \cdot Normalized_{Fines} \quad [4.2]$$

$$w/c = Mean + (w/c_{MAX} - Mean) \cdot Normalized_{w/c} \quad [4.3]$$

This procedure generates nine combinations having the values in Table 4.10.

Table 4.10 – Fine aggregates and W/F ratio values adopted for the admixtures design.

Fines	Water/Fines
1050	0.215
1050	0.18
1156.066	0.239749
943.934	0.190251
1200	0.215
943.934	0.239749
900	0.215
1156.066	0.190251
1050	0.25

The respective amount of silica fume, porcelain powder and cement are calculated as the percentage of the total fine aggregate quantity. The water is then computed depending on the correspondent value for each combination, obviously the total water amount will include also the absorbed water calculated as the 1.6% of the sand amount because dry aggregates are used.

The PVA fibres dosage is fixed with a value of 30 kg/m^3 and superplasticizer quantity of 25 l/m^3. By calculating all ingredients amount, the sand quantity for each admixture is obtained considering the total volume and the density of each component:

$$Sand[kg/m^3] = \rho_s \cdot (1000 - (C/\rho_c) - (\mathrm{P}/\rho_P) - (SF/\rho_{SF}) - (PVA/\rho_{PVA}) - H_2O - Plsticiz) \quad [4.4]$$

Table 4.11 – Density of mix design materials.

Density ρ	[t/m^3]
C	3.1
P	2.74
SF	2.7
PVA	1.3
Sand	2.61744

A complete overview of the admixtures design is reported in table, while the specific components and amount of the mix design compounds is reported in Appendix B enclosed.

Table 4.12 – Admixtures designed (81).

MIX ID	Fines [kg/m^3]	W/F	%C	%P	%SF
H1	1050	0.215	0.4	0.6	0
H2			0.8	0.2	0
H3			0.4	0.35	0.25
H4			0.55	0.2	0.25
H5			0.6	0.4	0
H6			0.4	0.475	0.125
H7			0.675	0.2	0.125
H8			0.475	0.275	0.25
H9			0.5375	0.3375	0.125
H10	1050	0.18	0.4	0.6	0
H11			0.8	0.2	0
H12			0.4	0.35	0.25
H13			0.55	0.2	0.25
H14			0.6	0.4	0
H15			0.4	0.475	0.125
H16			0.675	0.2	0.125
H17			0.475	0.275	0.25
H18			0.5375	0.3375	0.125
H19	1156.066	0.239	0.4	0.6	0
H20			0.8	0.2	0
H21			0.4	0.35	0.25
H22			0.55	0.2	0.25
H23			0.6	0.4	0
H24			0.4	0.475	0.125
H25			0.675	0.2	0.125
H26			0.475	0.275	0.25
H27			0.5375	0.3375	0.125
H28	943.93	0.19	0.4	0.6	0
H29			0.8	0.2	0
H30			0.4	0.35	0.25
H31			0.55	0.2	0.25
H32			0.6	0.4	0
H33			0.4	0.475	0.125
H34			0.675	0.2	0.125
H35			0.475	0.275	0.25
H36			0.5375	0.3375	0.125
H37	1200	0.215	0.4	0.6	0
H38			0.8	0.2	0
H39			0.4	0.35	0.25
H40			0.55	0.2	0.25
H41			0.6	0.4	0
H42			0.4	0.475	0.125
H43			0.675	0.2	0.125
H44			0.475	0.275	0.25
H45			0.5375	0.3375	0.125
H46	943.93	0.239	0.4	0.6	0
H47			0.8	0.2	0

H48			0.4	0.35	0.25
H49			0.55	0.2	0.25
H50			0.6	0.4	0
H51			0.4	0.475	0.125
H52			0.675	0.2	0.125
H53			0.475	0.275	0.25
H54			0.5375	0.3375	0.125
H55	900	0.215	0.4	0.6	0
H56			0.8	0.2	0
H57			0.4	0.35	0.25
H58			0.55	0.2	0.25
H59			0.6	0.4	0
H60			0.4	0.475	0.125
H61			0.675	0.2	0.125
H62			0.475	0.275	0.25
H63			0.5375	0.3375	0.125
H64	1156.066	0.19	0.4	0.6	0
H65			0.8	0.2	0
H66			0.4	0.35	0.25
H67			0.55	0.2	0.25
H68			0.6	0.4	0
H69			0.4	0.475	0.125
H70			0.675	0.2	0.125
H71			0.475	0.275	0.25
H72			0.5375	0.3375	0.125
H73	1050	0.25	0.4	0.6	0
H74			0.8	0.2	0
H75			0.4	0.35	0.25
H76			0.55	0.2	0.25
H77			0.6	0.4	0
H78			0.4	0.475	0.125
H79			0.675	0.2	0.125
H80			0.475	0.275	0.25
H81			0.5375	0.3375	0.125

4.3.5. Specimens preparation

The admixture is prepared trough a planetary mixer Hobart N50 (Figure 4.10a-b) and following a specific procedure:

1. Sand and absorbed water are mixed for 2 minutes;
2. Fines and water are added and mixed for 1 minute;
3. The superplasticizer is added and mixed for 4 minutes;
4. Fibers are added and all is mixed for 1 minute.

It should be underlined that, although the superplasticizer amount is supposed to be maintained constant, in case of low workability it has been slightly increased.

The specimens are cast in both polyurethane and steel moulds (Figure 4.10a), each of them accommodates three samples: the blend is manually compacted slightly shaking the mould. Following the common procedure, the specimens are covered by plastic sheets (Figure 4.10b) to isolate them from environmental moisture exchanges. After 24h the samples are demoulded (Figure 4.10c) and cured in water at a controlled temperature of 20 °C for 27 days, two of them for each admixture, and 59 days approximately, the remaining specimen of all admixtures.

(a) (b)

Figure 4.9 – Stages of the HPFRC casting procedure: (a) Mixing phase; (b) Fibers addition.

(a) (b) (c)

Figure 4.10 – Stages of the HPFRC casting procedure: (a) Admixture placed in moulds; (b) Cover with plastic sheets; (c) Specimens demoulded.

4.3.6. Experimental tests

As specified before, the mechanical properties of the admixtures are evaluated by performing flexural tests in four point configuration and compressive tests. The bending tests procedure follows the French regulation NF P18-470 (2018), placing two Linear Variable Differential Transformer (LVDTs) at mid span on both sides of the specimens in order to monitor the vertical displacement during the test (Figure 4.11). The transducers are placed on an aluminium frame shaped according to the specimen cross section realizing a contrast support measuring the vertical displacement on the two sides whose mean value is calculated. The tests are realized with a servohydraulic machine having a capacity of 500 kN, produced by MTS and the test is perfomed in displacement control until a mean deflection of 0.9 mm while the load is recorded using a load cell with a lower capacity, 50 kN. The boundary conditions realized follow the static scheme of a simply supported configuration materialized by four steel cylinders, in the bottom part and upper part of the specimen where the load is applied. The nether supports are placed by a distance of 3/8 of the total sample length, respect to the middle section, while for the load application supports a distance of 1/8.

The flexural mechanical behaviour is represented by a nominal stress-mean deflection curve, where the stress is calculated assuming an elastic behaviour of the material:

$$\sigma_{t,fl} = \frac{3F}{b \cdot a} \qquad [4.5]$$

where F [N] is the load applied and a, b the dimensions of the cross section.

The compressive strength of the material is evaluated using the same sample previously tested but applying the load on both ends where there are no cracks. the present test is performed in force control with a rate of 0.8 MPa/s, using a square steel element with the same specimen cross-section, 40x40 mm^2 to apply the load. The mean compressive strength R_{cm} is so calculated dividing the load measured by the area (Figure 4.13).

Besides the mechanical properties of flexural peak strength and residual strength, the cracking pattern for each sample is examined, inspecting the amount of cracks started in the composite and their position.

Comparing the cracking pattern in Figure 4.12c-d the difference between a single crack and a multi-cracking pattern can be appreciated.

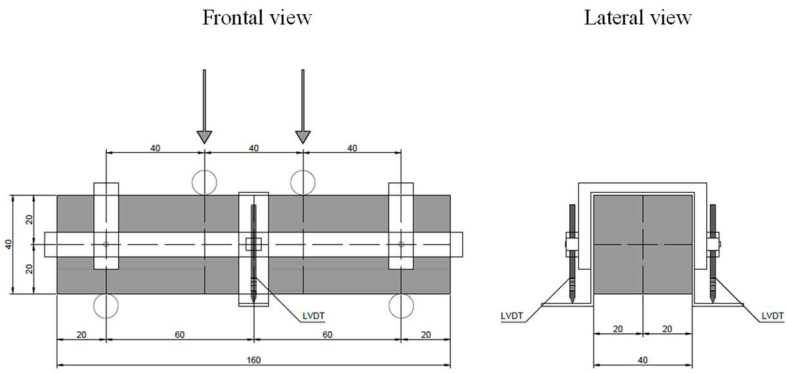

Figure 4.11 – Four point bending tests set-up.

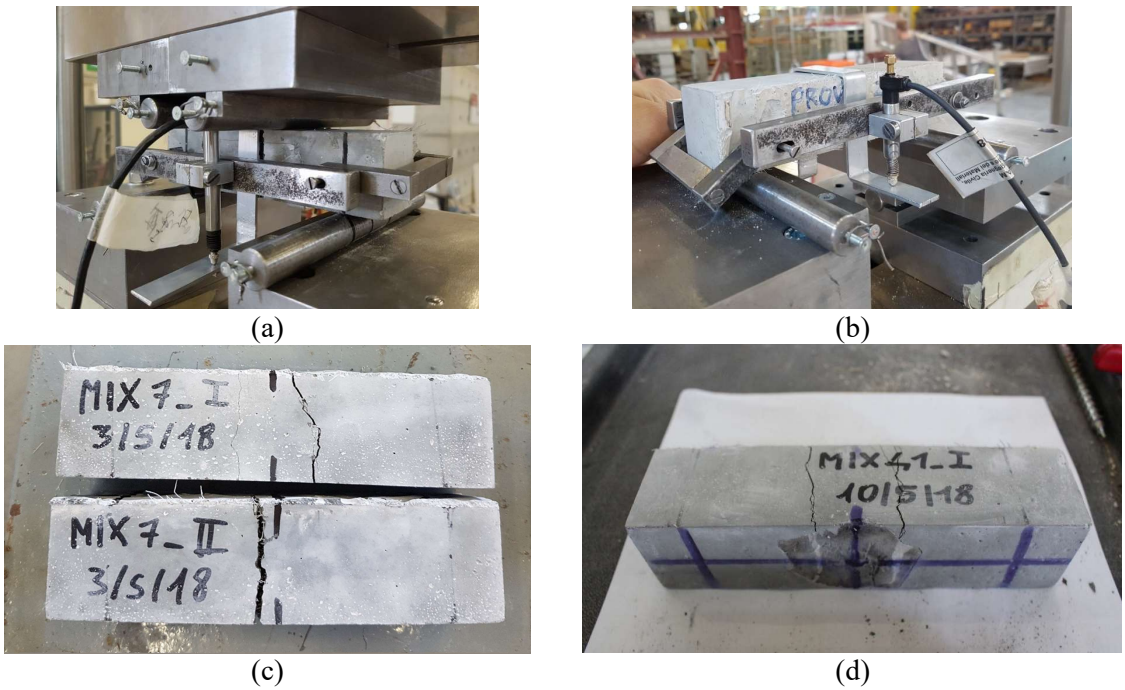

(a) (b)

(c) (d)

Figure 4.12 – Four point bending tests (a) Specimen equipped with the allumium frame where LVDTs are placed; (b) Specimen before the test; (c) Example of localized crack generated by a flexural load; (d) Example of multi – crack pattern.

(a) (b)

Figure 4.13 – Compressive tests performed on (a) both end of the prismatic specimens; (b) Failure of the sample under compressive load.

4.3.7. Four point bending test results

The outcome of the flexural test characterizes the performance of all admixtures relating the nominal stress to the mean deflection. The charts (Figure 4.14-Figure 4.31) collect all curves of all admixtures with reference to 28 days curing, reporting both curves for the two specimens tested of each mix type marked with solid and dashed line. The mean compressive strength is calculated for each prism as the test is performed on both ends and the values are represented in the form of histograms helping, in this way, a visual evaluation (Figure 4.32-Figure 4.40).

Remembering that the mixes can be grouped into nine combinations of fines and water-fines ratio and for each of them the same percentage of fines are repeated, an overall evaluation could be drawn comparing the nine groups: H1 – H9, H10 – H18, H19 – H27, H28 – H36, H37 – H45, H46 – H54, H55 – 63, H64 – H72, H73 – H81. For what concern the flexural behaviour, many aspects can vary:

- Peak strength value;
- Hardening behaviour;

– Cracks formed.

The peak strength is identificatory of the cementitious matrix strength so it depends on the mix design properties, while the cracking state evolution is entrusted to the fibers reinforcement. Their dispersion together with the matrix design and, so, the capacity of assuring a high bond strength determine the post-peak capacity of the material. These factors make possible to develop, in most cases, a multi cracking pattern identified by the presence of many steps in the cracking phase, correspondent to the gradual formation and opening of cracks. This can be confirmed considering the response of the Mix H14, the two samples (Figure 4.16) marked in yellow solid and dashed line feature a hardening behaviour characterized respectively by a single crack and two cracks formation, since the fibres dispersion influence. Observing the curves in Figure 4.15 the trend of all samples is characterized by a multi-fessurative and hardening behaviour. On the opposite, the trend behaviour in Figure 4.19 shows a descending trend after the peak and an increment of the post-peak strength equal or lower than the peak value.

This type of behaviour is indicated by a hardening percentage in Table 4.13 calculated considering the difference between the two values, peak and post-peak. Considering all curves, the peak strength values range from 4 MPa to 11 MPa, considering the mean value of the two samples for each mix, while the post-peak flexural strength in included in a range of 5 MPa to 12 MPa.

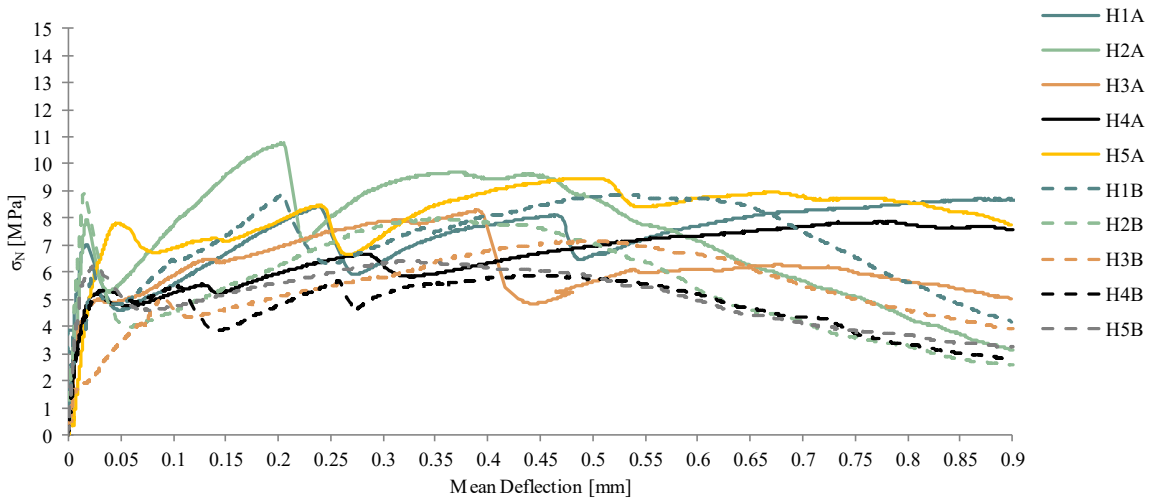

Figure 4.14 – Nominal Stress – Mean Deflection curves for specimens of H1 – H5 admixtures.

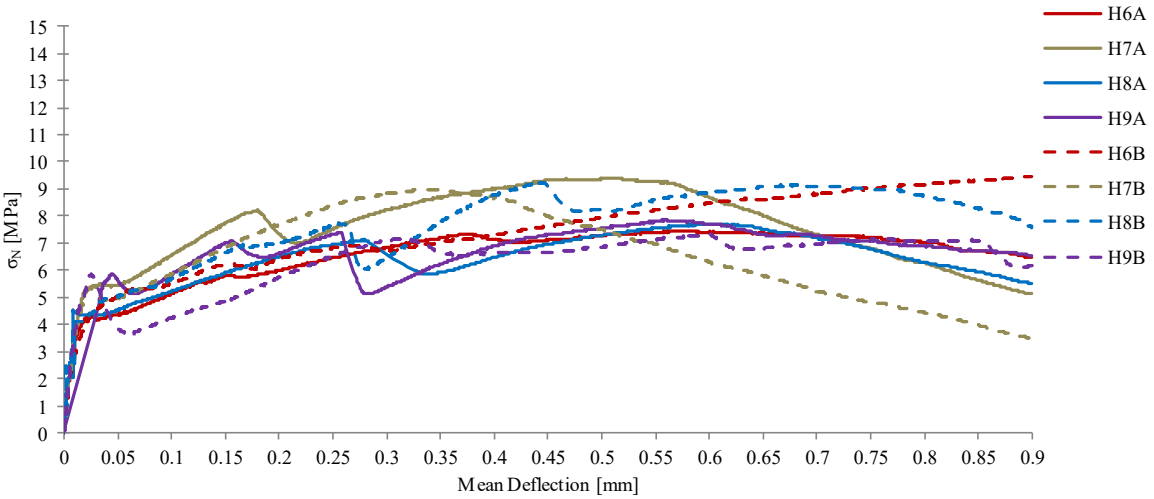

Figure 4.15 – Nominal Stress – Mean Deflection curves for specimens of H6 – H9 admixtures.

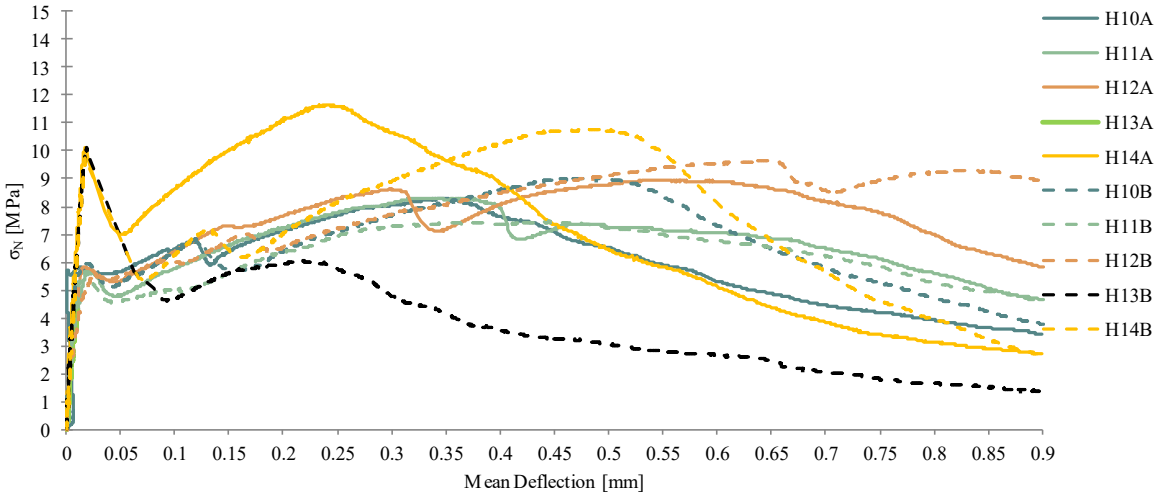

Figure 4.16 – Nominal Stress – Mean Deflection curves for specimens of H10 – H14 admixtures.

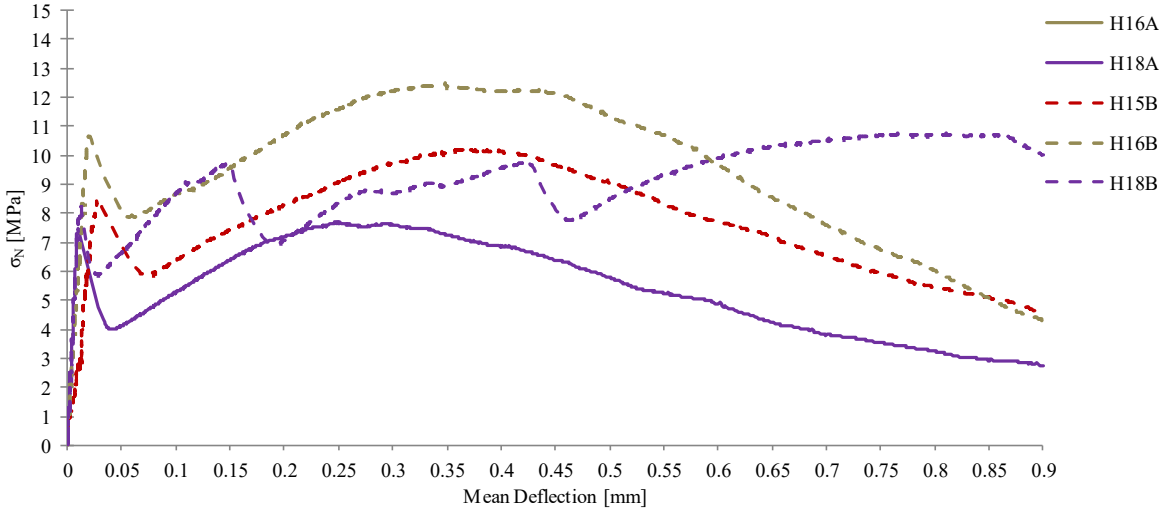

Figure 4.17 – Nominal Stress – Mean Deflection curves for specimens of H16 – H18 admixtures.

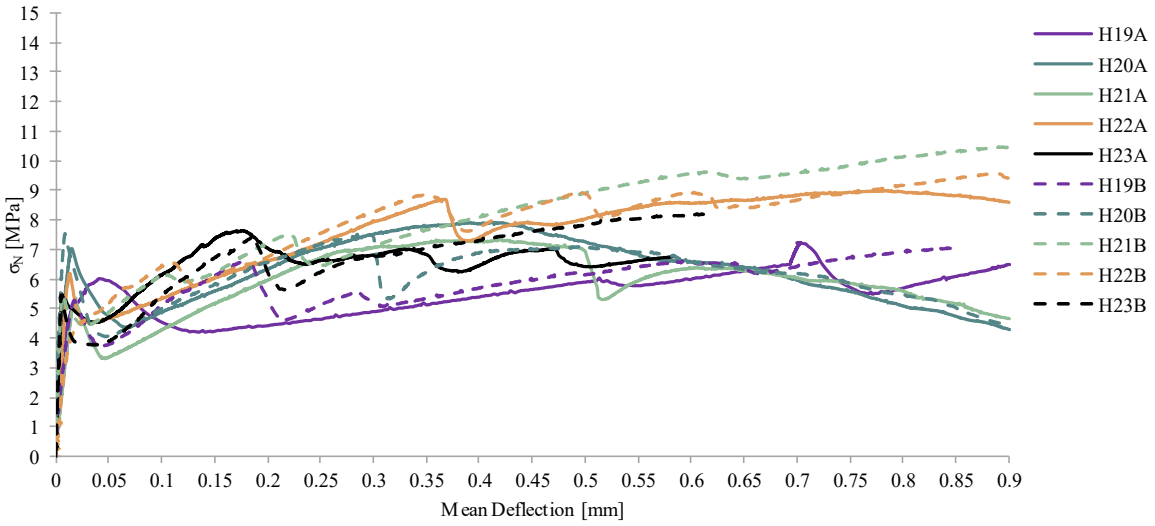

Figure 4.18 – Nominal Stress – Mean Deflection curves for specimens of H19 – H23 admixtures.

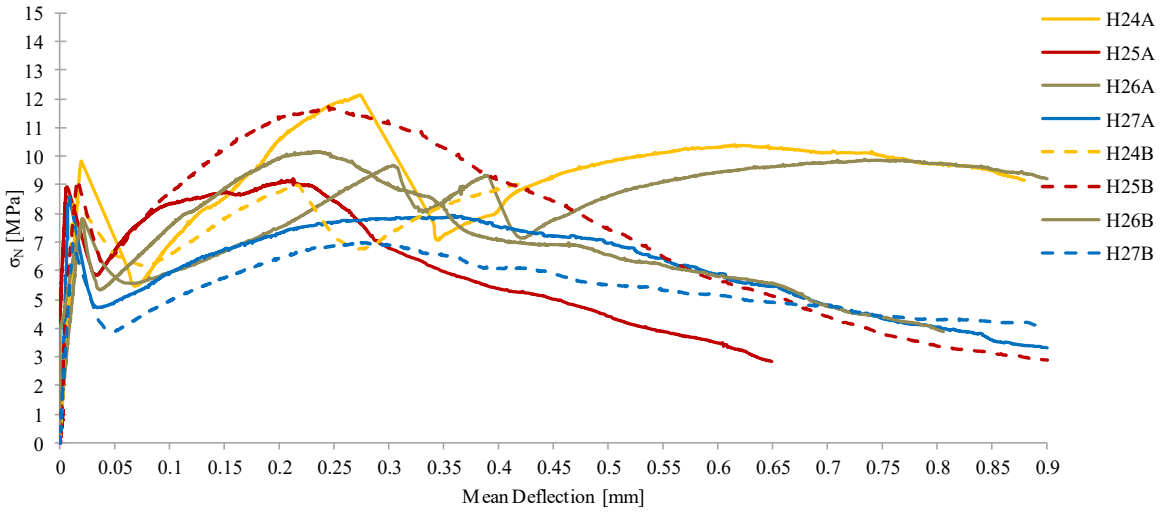

Figure 4.19 – Nominal Stress – Mean Deflection curves for specimens of H24 – H27 admixtures.

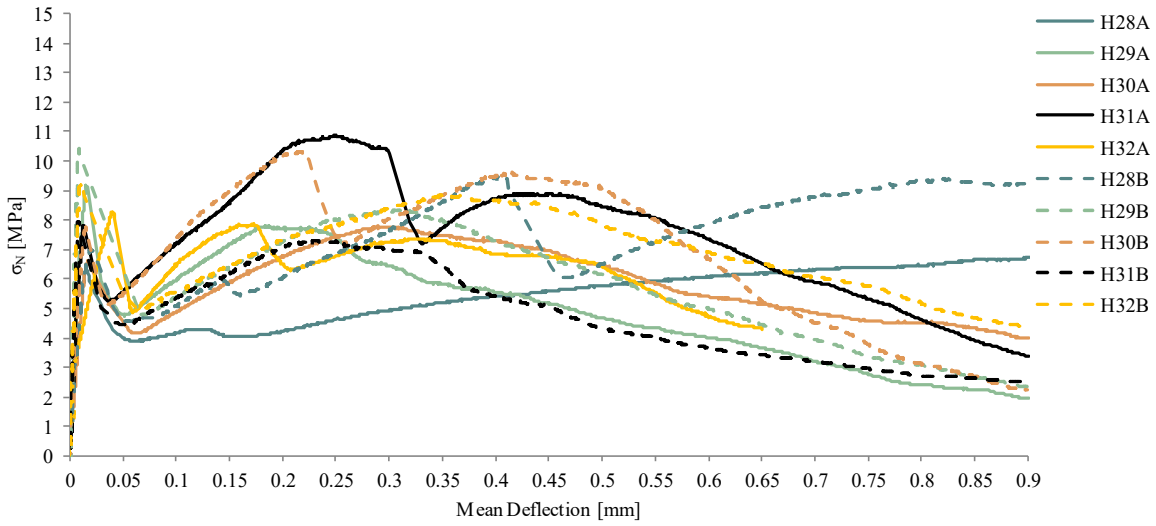

Figure 4.20 – Nominal Stress – Mean Deflection curves for specimens of H28 – H32 admixtures.

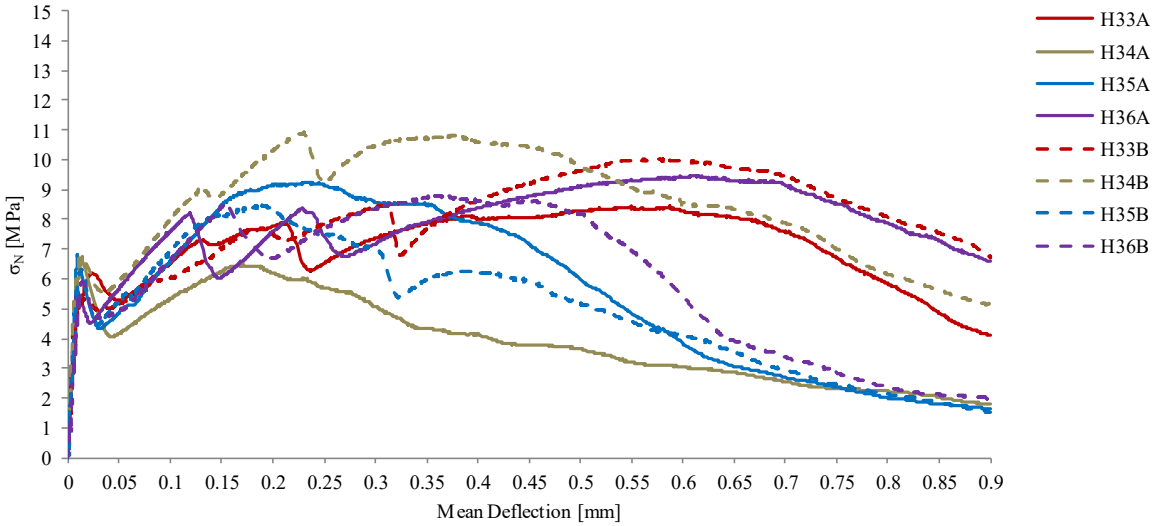

Figure 4.21 – Nominal Stress – Mean Deflection curves for specimens of H33 – H36 admixtures.

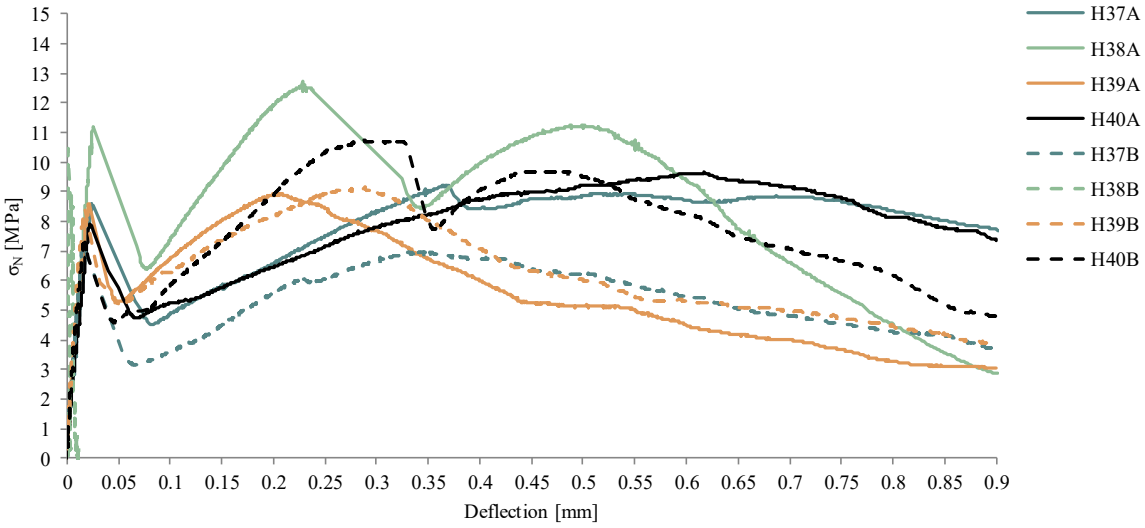

Figure 4.22 – Nominal Stress – Mean Deflection curves for specimens of H37 – H40 admixtures.

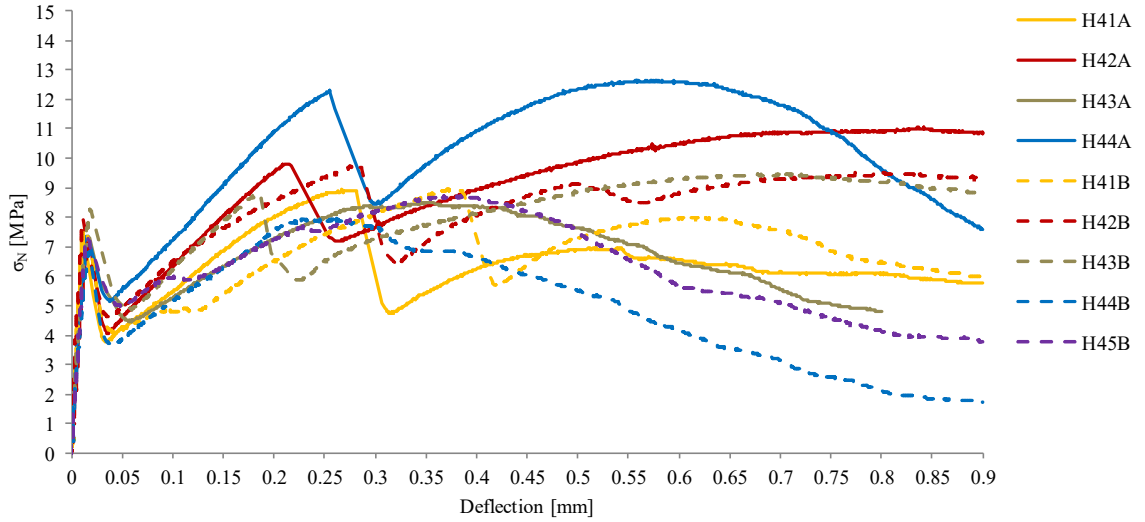

Figure 4.23 – Nominal Stress – Mean Deflection curves for specimens of H41 – H45 admixtures.

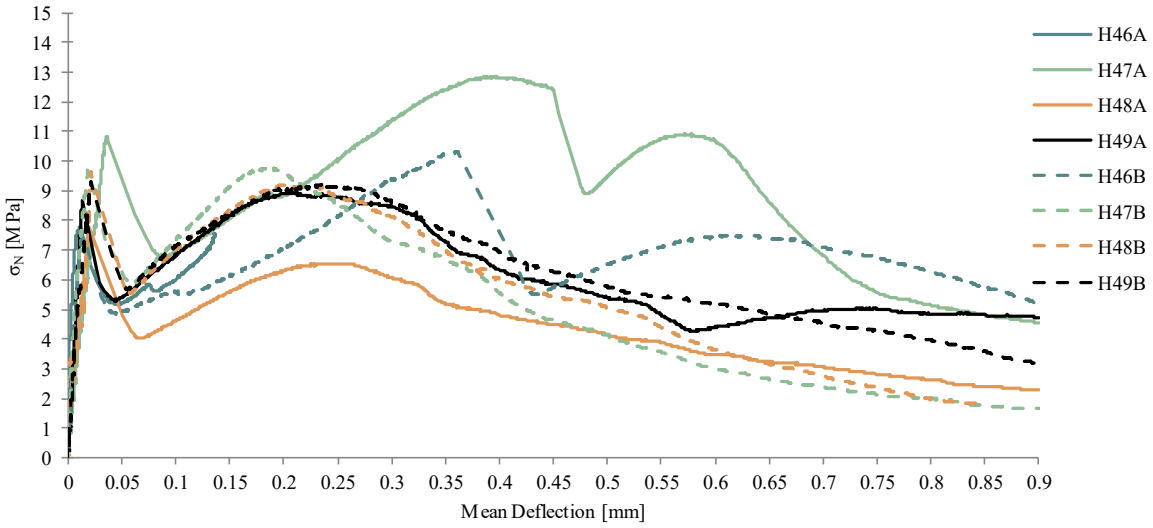

Figure 4.24 – Nominal Stress – Mean Deflection curves for specimens of H46 – H49 admixtures.

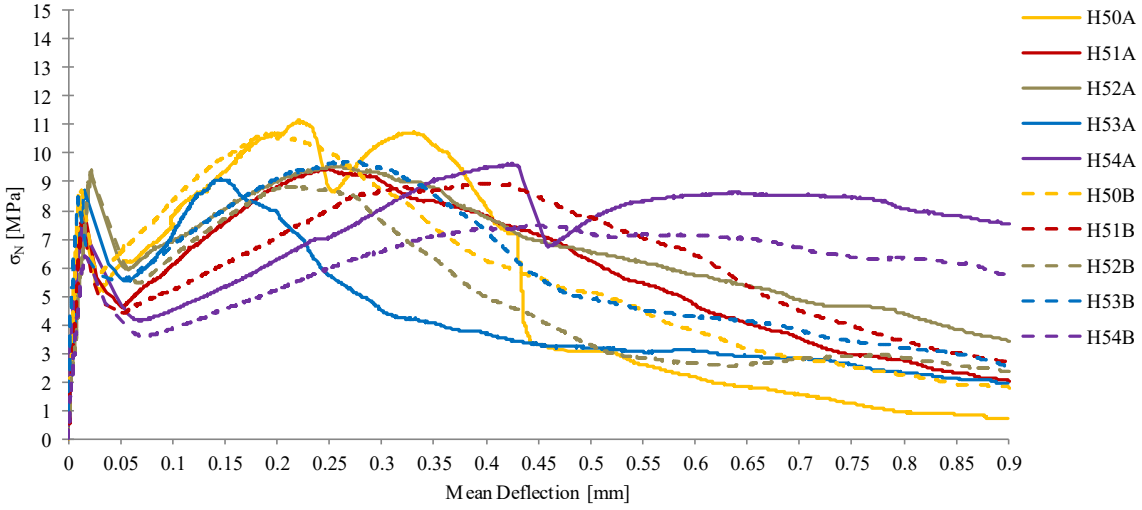

Figure 4.25 – Nominal Stress – Mean Deflection curves for specimens of H50 – H54 admixtures.

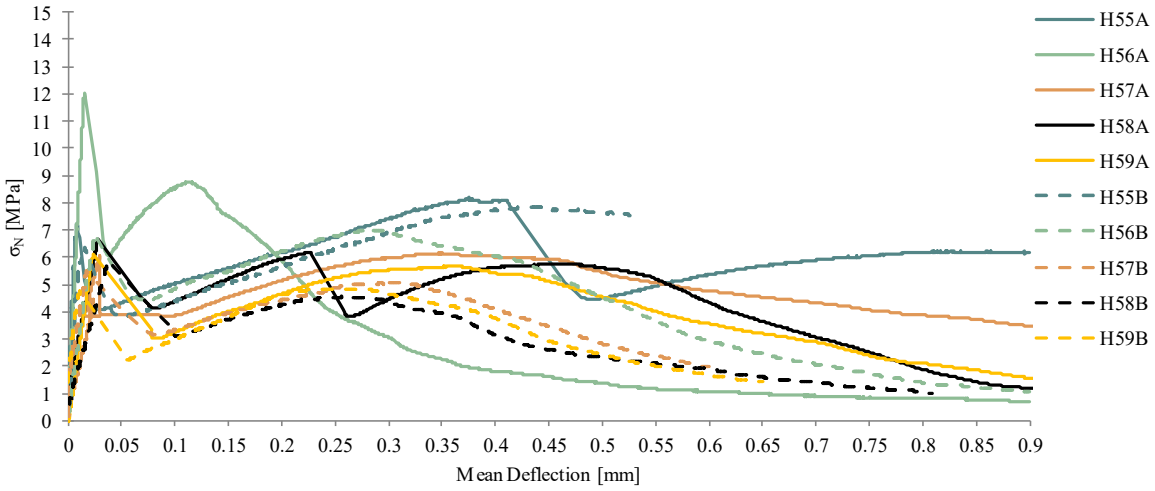

Figure 4.26 – Nominal Stress – Mean Deflection curves for specimens of H55 – H59 admixtures.

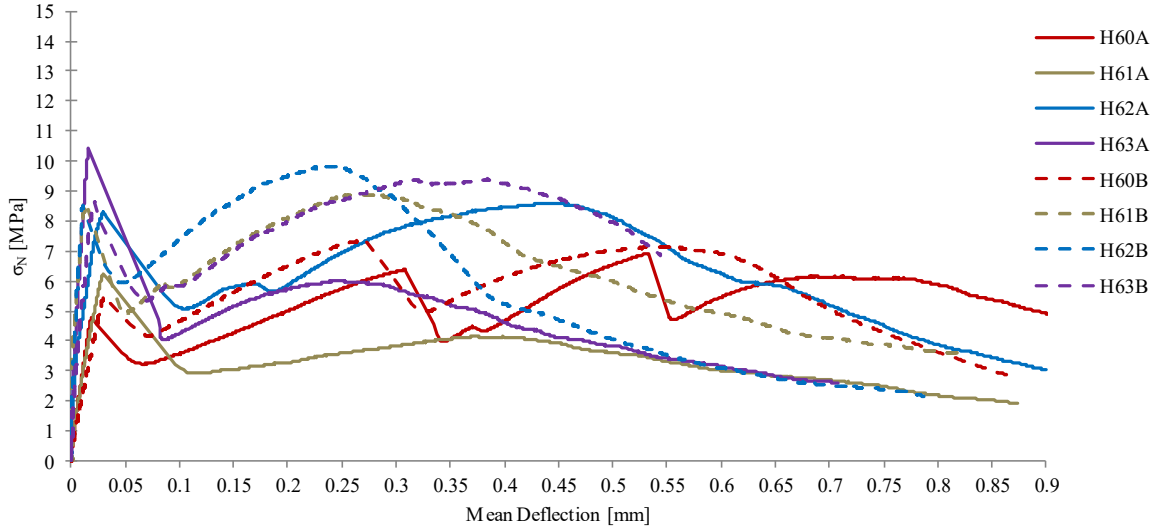

Figure 4.27 – Nominal Stress – Mean Deflection curves for specimens of H60 – H63 admixtures.

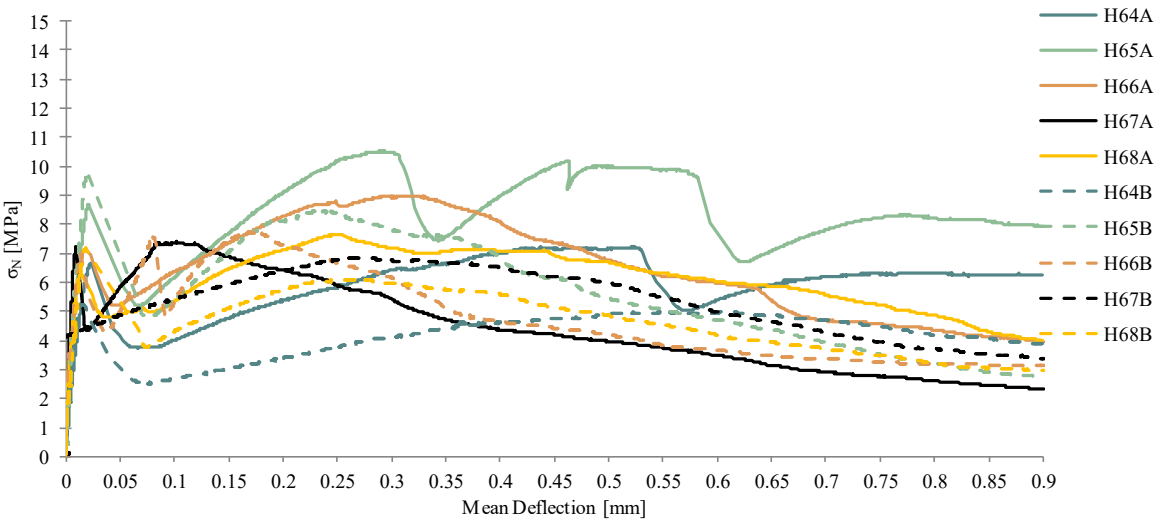

Figure 4.28 – Nominal Stress – Mean Deflection curves for specimens of H64 – H68 admixtures.

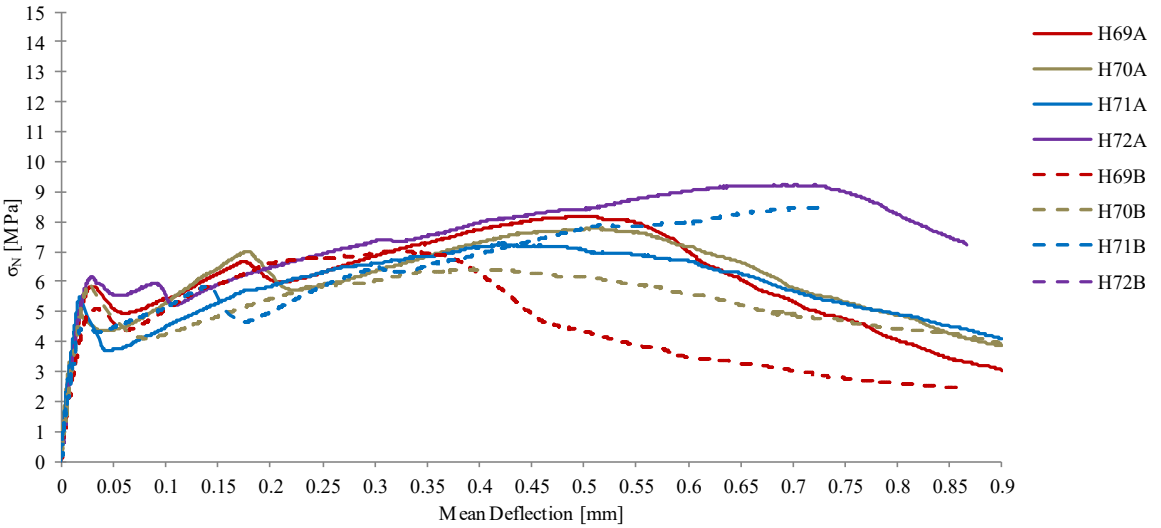

Figure 4.29 – Nominal Stress – Mean Deflection curves for specimens of H69 – H72 admixtures.

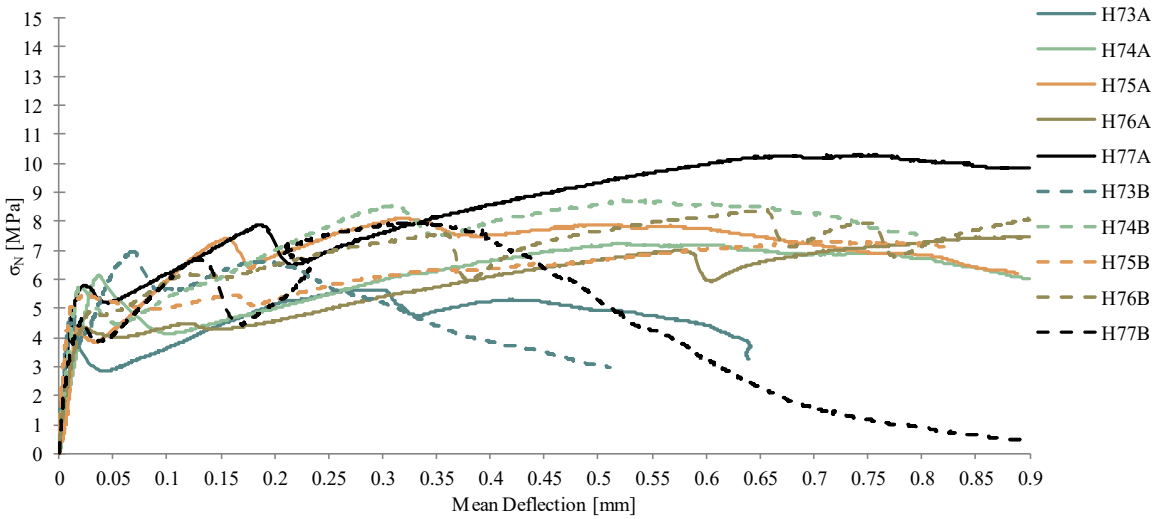

Figure 4.30 – Nominal Stress – Mean Deflection curves for specimens of H73 – H77 admixtures.

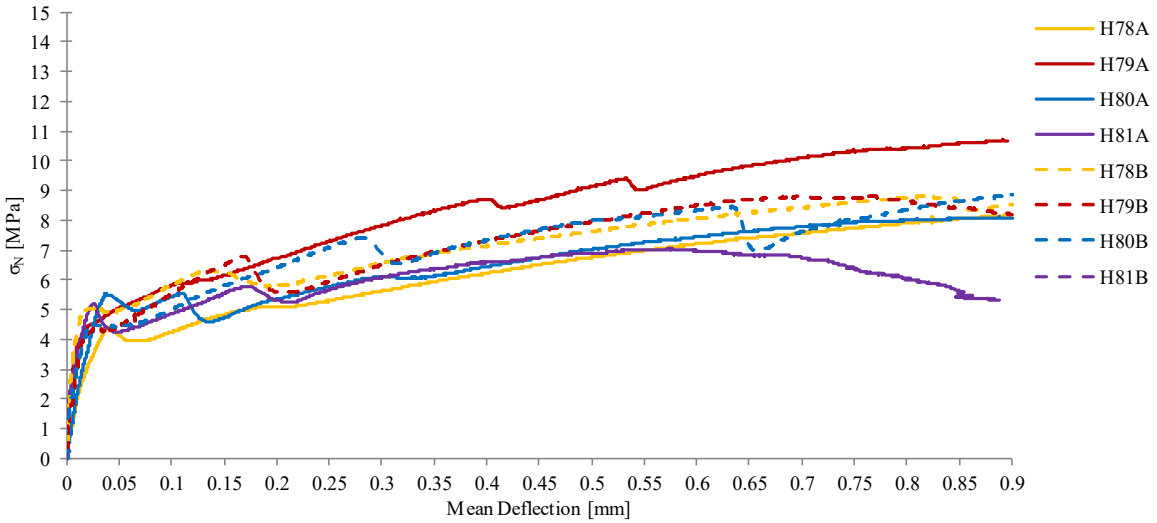

Figure 4.31 – Nominal Stress – Mean Deflection curves for specimens of H78 – H81 admixtures.

The compressive strength value reflects almost completely the matrix design properties, in this case the water – fine ratio and the fine aggregates amount adopted for the design. It is straightforward thinking that the combinations of these variable generates different responses.

An interesting observation can be formulated comparing, within the same group, the strength featured by samples designed with lower cement amount substituted with porcelain stoneware powder. For example, considering the H1 – H9 group (Figure 4.32), the H2 group is the admixture designed with 0.8% cement and 0.2% porcelain powder, the other groups present a partial substitution of the cement quantity with silica fume products or increasing the porcelain powder amount. Comparing their values, i.e. H9 mix, there is no remarkable decrement of the strength. Obviously, the trend is different among all groups since the aforementioned variables, fines and W/F, present different values.

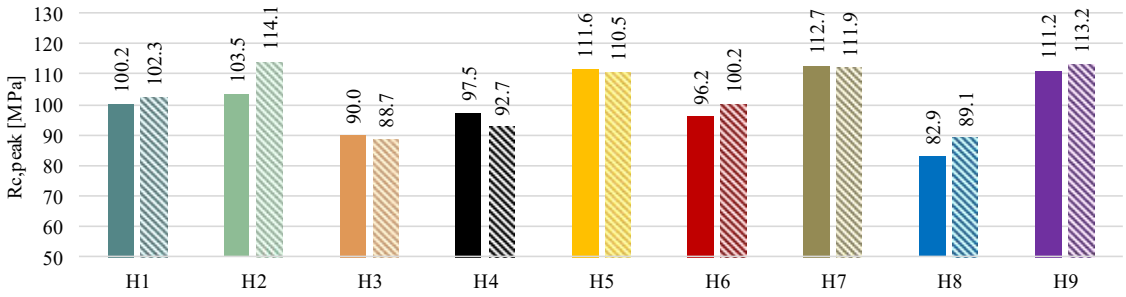

Figure 4.32 – Compressive peak strength for two specimens of H1 – H9 admixtures.

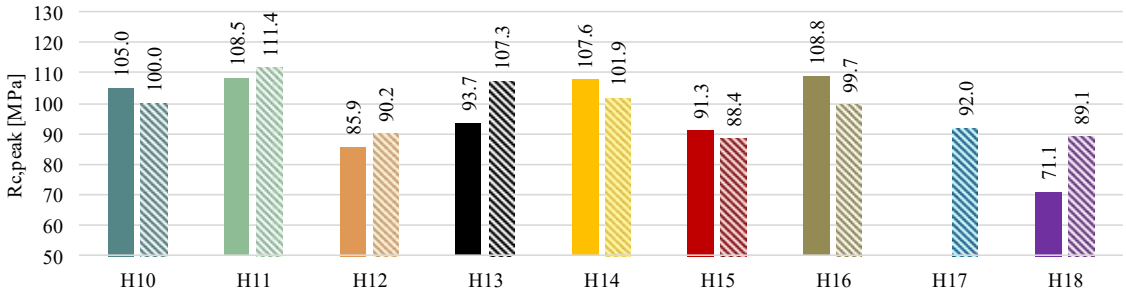

Figure 4.33 – Compressive peak strength for two specimens of H10 – H18 admixtures.

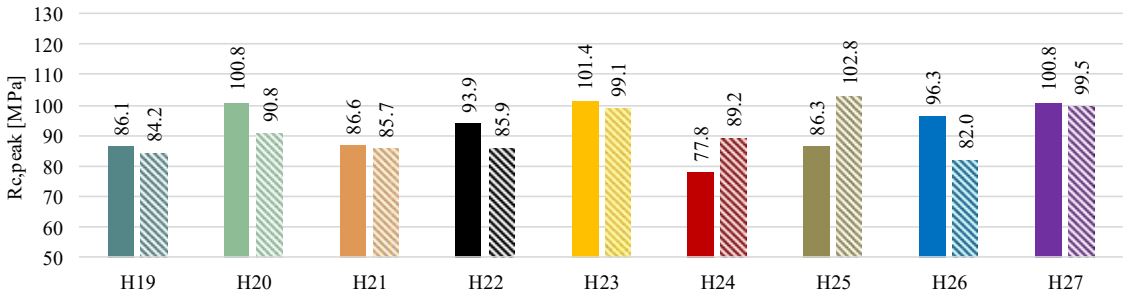

Figure 4.34 – Compressive peak strength for two specimens of H19 – H27 admixtures.

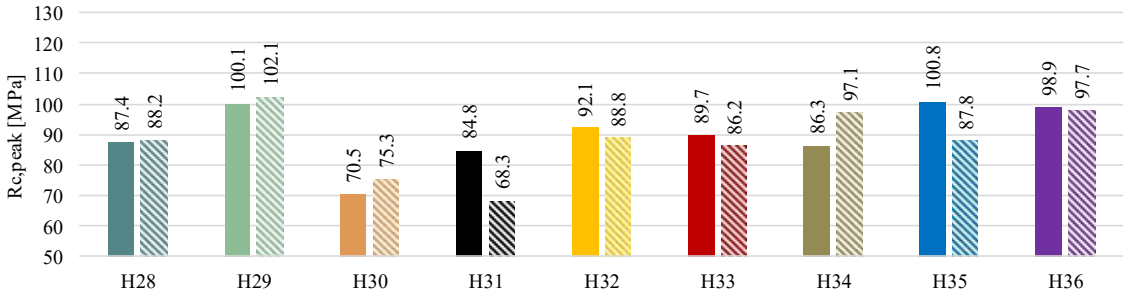

Figure 4.35 – Compressive peak strength for two specimens of H28 – H36 admixtures.

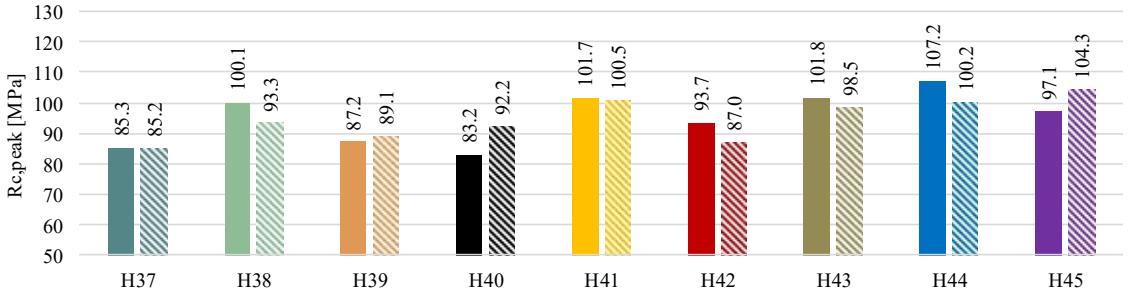

Figure 4.36 – Compressive peak strength for two specimens of H37 – H45 admixtures.

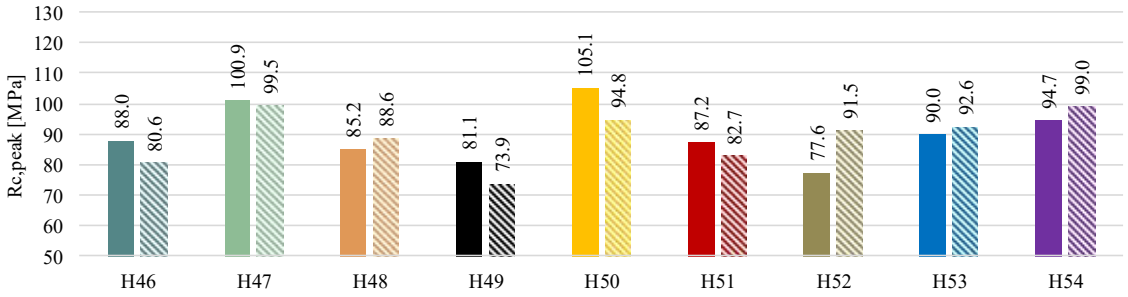

Figure 4.37 – Compressive peak strength for two specimens of H46 – H54 admixtures.

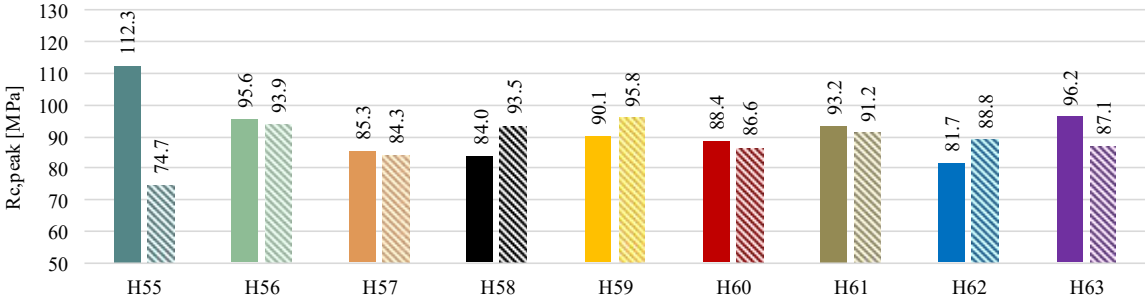

Figure 4.38 – Compressive peak strength for two specimens of H55 – H63 admixtures.

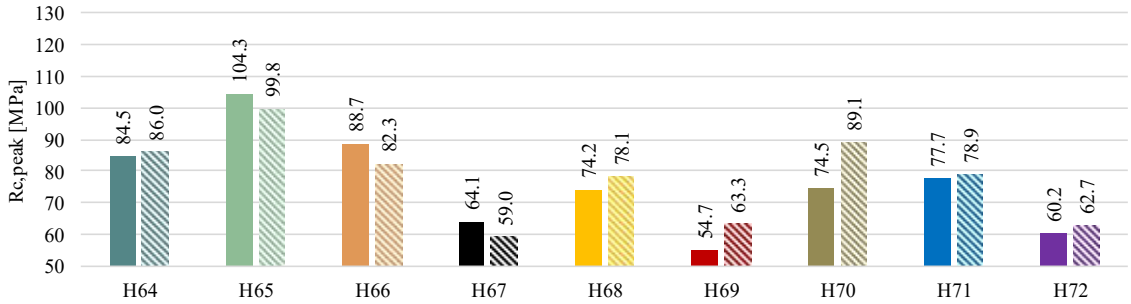

Figure 4.39 – Compressive peak strength for two specimens of H64 – H72 admixtures.

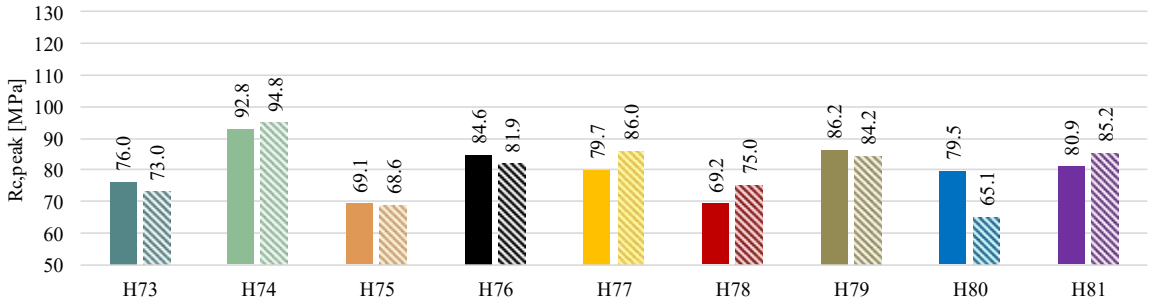

Figure 4.40 – Compressive peak strength for two specimens of H73 – H81 admixtures.

Table 4.13 – Nominal peak, post peak flexural strength and mean compressive strength of all admixtures after 28 days.

MIX ID	28 days			
	$\sigma_{N,peak}$ [MPa]	$\sigma_{N,post-peak}$ [MPa]	Hardening [%]	R_{cm} [MPa]
H1	5.454	8.69	37.24	101.29
H2	8.444	9.38	9.98	108.82
H3	4.784	6.67	28.28	89.38
H4	4.863	6.68	27.20	95.08
H5	6.89	7.824	11.94	111.03
H6	4.075	8.418	51.59	98.16
H7	5.16	9.177	43.77	112.34
H8	4.5	7.9	43.04	86.00
H9	5.54	7.455	25.69	112.18
H10	5.86	8.64	32.18	102.52
H11	5.66	7.816	27.58	109.93
H12	5.488	9.233	40.56	88.04
H13	9.114	6.836	-33.32	100.49
H14	9.9375	11.13	10.71	104.78
H15	6.361	10.148	37.32	89.85
H16	10.662	12.388	13.93	104.21
H17	6.57	6.671	1.51	92.05
H18	7.96	9.133	12.84	80.09
H19	5.474	6.906	20.74	85.15
H20	6.8535	7.684	10.81	95.80
H21	4.775	8.85	46.05	86.15
H22	5.3865	9.213	41.53	89.86
H23	5.595	7.904	29.21	100.23
H24	9.34	10.539	11.38	83.48
H25	9.0405	11.621	22.21	94.54
H26	8.045	9.969	19.30	89.15

H27	7.7425	7.421	-4.33	100.15
H28	6.641	8.04	17.40	87.81
H29	9.7495	8.042	-21.23	101.14
H30	7.1955	8.927	19.40	72.88
H31	7.829	8.954	12.56	76.56
H32	9.265	8.149	-13.69	90.47
H33	5.717	9.178	37.71	87.98
H34	6.76	8.589	21.29	91.73
H35	6.7305	8.649	22.18	94.30
H36	5.815	9.084	35.99	98.32
H37	7.9125	8.004	1.14	85.25
H38	9.269	9.65	3.95	96.71
H39	8.3535	8.947	6.63	88.17
H40	7.293	10.126	27.98	87.73
H41	7.645	8.901	14.11	101.12
H42	7.7085	10.337	25.43	90.35
H43	8.277	8.932	7.33	100.11
H44	7.105	10.272	30.83	103.72
H45	8.05	8.7	7.47	100.71
H46	7.6825	8.959	14.25	84.28
H47	10.202	11.256	9.36	100.19
H48	7.751	7.837	1.10	86.88
H49	8.6525	8.995	3.81	77.48
H50	8.414	10.8	22.09	99.94
H51	7.585	9.095	16.60	84.97
H52	8.748	9.115	4.03	84.52
H53	8.481	9.346	9.26	91.30
H54	6.7005	8.468	20.87	96.86
H55	6.65	6.97	4.59	93.52
H56	9.383	7.84	-19.68	94.75
H57	5.735	5.58	-2.78	84.80
H58	6.17	5.37	-14.90	88.73
H59	5.355	5.235	-2.29	92.92
H60	5.105	7.11	28.20	87.46
H61	7.325	6.49	-12.87	92.20
H62	8.31	9.185	9.53	85.27
H63	9.45	7.675	-23.13	91.65
H64	5.93	6.07	2.31	85.26
H65	9.205	9.465	2.75	102.07
H66	6.9	8.34	17.27	85.47
H67	5.71	7.055	19.06	61.58
H68	6.642	6.84	2.89	76.14
H69	5.47	7.575	27.79	58.98
H70	5.4	7.082	23.75	81.81
H71	4.9	6.515	24.79	78.29
H72	6.13	5.93	-3.37	61.48
H73	4.67	6.285	25.70	74.49
H74	5.88	7.96	26.13	93.77
H75	4.875	6.86	28.94	68.89
H76	4.595	7.135	35.60	83.25
H77	5.195	7.845	33.78	82.83
H78	4.71	5.695	17.30	72.11
H79	4.44	8.68	48.85	85.17
H80	4.915	6.46	23.92	72.28
H81	5.22	5.76	9.38	83.09

4.3.8. Analysis and discussion

As described before, an additional evaluation of the present study is elaborated on the long term effects, by performing flexural and compressive tests after a curing period of 60 days, in water at a temperature of 20 °C, in order to study the matrix components activity on time. The peak flexural strength after the two curing periods is compared evaluating the percentage of increment featured (Table 4.14): most of them exhibited an increment of the peak flexural strength. The same observation can be made analysing the data referred to the compressive strength after 28 and 60 days in Table 4.15.

It is important to underline that the comparison between the data after 28 and 60 days curing is made respectively on two and one samples. Thus, compressive strength reduction, i.e. the negative percentage could represent a strange result.

Table 4.14 – Nominal peak flexural strength of all admixtures after 28 and 60 days.

MIX ID	28 days	60 days	%
	$\sigma_{N,peak}$ [MPa]	$\sigma_{N,peak}$ [MPa]	
H1	5.45	6.57	16.94
H2	8.44	7.66	*-10.28*
H3	4.78	6.53	26.68
H4	4.86	8.00	39.24
H5	6.89	7.80	11.61
H6	4.08	7.18	43.26
H7	5.16	7.90	34.70
H8	4.50	7.56	40.44
H9	5.54	8.07	31.38
H10	5.86	6.42	8.67
H11	5.66	7.88	28.15
H12	5.49	8.50	35.43
H13	9.11	8.82	*-3.30*
H14	9.94	8.25	*-20.41*
H15	6.36	7.57	15.98
H16	10.66	8.14	*-31.05*
H17	6.57	8.45	22.20
H18	7.96	9.07	12.21
H19	5.47	8.10	32.39
H20	6.85	9.58	28.42
H21	4.78	9.73	50.95
H22	5.39	9.15	41.10
H23	5.60	7.26	22.90
H24	9.34	8.09	*-15.45*
H25	9.04	7.73	*-17.01*
H26	8.05	8.41	*4.36*
H27	7.74	7.71	*-0.43*
H28	6.64	7.49	11.30

H29	9.75	8.56	*-13.84*
H30	7.20	8.76	17.86
H31	7.83	8.90	11.99
H32	9.27	7.29	*-27.16*
H33	5.72	7.34	22.11
H34	6.76	9.23	26.74
H35	6.73	7.84	14.12
H36	5.82	7.71	24.53
H37	7.91	7.43	*-6.55*
H38	9.27	9.56	3.07
H39	8.35	6.74	*-23.87*
H40	7.29	6.74	*-8.14*
H41	7.65	8.45	9.51
H42	7.71	7.00	*-10.06*
H43	8.28	7.19	*-15.09*
H44	7.11	7.85	9.51
H45	8.05	7.73	*-4.11*
H46	7.68	7.51	*-2.30*
H47	10.20	9.61	*-6.18*
H48	7.75	9.90	21.72
H49	8.65	9.99	13.35
H50	8.41	8.74	*3.71*
H51	7.59	9.60	21.02
H52	8.75	10.42	16.01
H53	8.48	9.08	6.60
H54	6.70	9.17	26.89
H55	6.65	9.60	30.73
H56	9.38	12.56	25.29
H57	5.74	11.48	50.04
H58	6.17	13.73	55.06
H59	5.36	13.85	61.34
H60	5.11	12.01	57.49
H61	7.33	13.13	44.21
H62	8.31	8.87	6.31
H63	9.45	9.37	*-0.85*
H64	5.93	11.04	46.29
H65	9.21	10.78	14.61
H66	6.90	13.51	48.93
H67	5.71	10.71	46.69
H68	6.64	10.81	38.56
H69	5.47	8.39	34.80
H70	5.40	10.06	46.32
H71	4.90	12.22	59.90
H72	6.13	11.93	48.62
H73	4.67	7.54	38.06
H74	5.88	8.17	28.03
H75	4.88	8.19	40.48
H76	4.60	10.20	54.95
H77	5.20	9.19	43.47
H78	4.71	8.56	44.98
H79	4.44	10.40	57.31
H80	4.92	9.32	47.26
H81	5.22	8.61	39.37

Table 4.15 – Nominal peak flexural strength of all admixtures after 28 and 60 days.

MIX ID	28 days	60 days	%
	R_{cm} [MPa]	R_{cm} [MPa]	
H1	101.29	98.03	*-3.32*
H2	108.82	113.20	3.87
H3	89.38	67.97	*-31.50*
H4	95.08	92.85	*-2.40*
H5	111.03	103.66	*-7.11*
H6	98.16	112.04	12.39
H7	112.34	123.78	9.24
H8	86.00	100.67	14.57
H9	112.18	114.44	1.97
H10	102.52	103.60	1.04
H11	109.93	99.74	*-10.21*
H12	88.04	113.85	22.67
H13	100.49	92.54	*-8.60*
H14	104.78	115.31	9.13
H15	89.85	115.58	22.26
H16	104.21	113.81	8.44
H17	92.05	110.79	16.92
H18	80.09	94.13	14.92
H19	85.15	90.86	6.28
H20	95.80	112.08	14.53
H21	86.15	104.06	17.22
H22	89.86	97.67	8.00
H23	100.23	115.17	12.97
H24	83.48	92.04	9.30
H25	94.54	101.43	6.79
H26	89.15	94.39	5.55
H27	100.15	94.89	*-5.54*
H28	87.81	96.41	8.92
H29	101.14	102.33	1.16
H30	72.88	103.38	29.50
H31	76.56	108.12	29.19
H32	90.47	108.56	16.67
H33	87.98	107.53	18.18
H34	91.73	117.64	22.02
H35	94.30	109.86	14.16
H36	98.32	119.59	17.79
H37	85.25	103.27	17.45
H38	96.71	108.96	11.25
H39	88.17	94.77	6.96
H40	87.73	98.31	10.76
H41	101.12	112.35	10.00
H42	90.35	99.51	9.21
H43	100.11	109.51	8.58
H44	103.72	103.31	*-0.40*

H45	100.71	97.47	*-3.33*
H46	84.28	95.42	11.68
H47	100.19	96.66	*-3.65*
H48	86.88	85.47	*-1.65*
H49	77.48	103.33	25.02
H50	99.94	104.37	4.24
H51	84.97	101.51	16.30
H52	84.52	95.08	11.10
H53	91.30	87.04	*-4.89*
H54	96.86	101.34	4.42
H55	93.52	87.92	*-6.37*
H56	94.75	124.95	24.17
H57	84.80	120.05	29.36
H58	88.73	116.38	23.76
H59	92.92	113.01	17.78
H60	87.46	116.99	25.24
H61	92.20	113.01	18.41
H62	85.27	118.21	27.87
H63	91.65	115.15	20.41
H64	85.26	114.84	25.76
H65	102.07	121.28	15.84
H66	85.47	120.36	28.99
H67	61.58	86.98	29.20
H68	76.14	83.61	8.93
H69	58.98	79.32	25.65
H70	81.81	80.54	*-1.57*
H71	78.29	99.53	21.34
H72	61.48	74.42	17.39
H73	74.49	93.71	20.51
H74	93.77	100.45	6.65
H75	68.89	84.22	18.20
H76	83.25	105.04	20.74
H77	82.83	94.94	12.76
H78	72.11	82.38	12.47
H79	85.17	97.39	12.54
H80	72.28	103.51	30.17
H81	83.09	101.98	18.52

The aim of the present study would be the identification of those admixtures having a good performance with a reduced amount of cement in the framework of realizing also sustainable admixtures with high performance.

A better representation is proposed in form of indexes calculated as the ratio between peak flexural and compressive strength and the cement amount per mix (kg/m^3), multiplied per 100. The higher the index value, the lower the cement

content and the higher the performance achieved. Table 4.16 collects all data calculated for the 81 admixtures.

The indexes are illustrated in form of histograms (Figure 4.41 – Figure 4.42) where the compressive and flexural strength are also reported in order to evaluate the admixtures characterized by high performance and, at the same time, high index. All data are in ascending order according to the strength so, for example, the admixtures H9 and H7 (Figure 4.41) present high compressive strength values and contain respectively 564 kg/m^3 and 709 kg/m^3 of cement: the index has a higher value for the first, H9, as it has been designed with less cement showing a high compressive strength value. H1 admixture has 420 kg/m^3 cement quantity and is characterized by a high index value since the compressive strength results remarkable.

Some considerations can be drawn also on the indexes computed considering the peak flexural strength (Figure 4.42): the admixture identified as H63 contains a low cement amount (484 kg/m^3) if compared to H16 (709 kg/m^3) but exhibits a high strength value (9.45 MPa) so it is characterized by a high index.

Since the considerable number of admixtures tested, each of them characterized by different proportion of constituents, this index has been considered as an indicator of the strength achieved related to the amount of cement used.

In this way it is possible to compare the different admixtures but considering also the value of the strength related.

Table 4.16 – Indexes as ratio of cement content (kg/m^3) and peak flexural and compressive strength.

Mix ID	Index $\sigma_{N,peak}$ [-]	Index R_{cm} [-]	Mix ID	Index $\sigma_{N,peak}$ [-]	Index R_{cm} [-]
H1	1.3	24.1	H42	1.6	18.8
H2	1.0	13.0	H43	1.0	12.4
H3	1.1	21.3	H44	1.2	18.2
H4	0.8	16.5	H45	1.2	15.6
H5	1.1	17.6	H46	2.0	22.3
H6	1.0	23.4	H47	1.4	13.3
H7	0.7	15.9	H48	2.1	23.0
H8	0.9	17.2	H49	1.7	14.9
H9	1.0	19.9	H50	1.5	17.6
H10	1.4	24.4	H51	2.0	22.5
H11	0.7	13.1	H52	1.4	13.3
H12	1.3	21.0	H53	1.9	20.4
H13	1.6	17.4	H54	1.3	19.1
H14	1.6	16.6	H55	1.8	26.0
H15	1.5	21.4	H56	1.3	13.2
H16	1.5	14.7	H57	1.6	23.6
H17	1.3	18.5	H58	1.2	17.9
H18	1.4	14.2	H59	1.0	17.2
H19	1.2	18.4	H60	1.4	24.3
H20	0.7	10.4	H61	1.2	15.2
H21	1.0	18.6	H62	1.9	19.9
H22	0.8	14.1	H63	2.0	18.9
H23	0.8	14.4	H64	1.3	18.4
H24	2.0	18.1	H65	1.0	11.0
H25	1.2	12.1	H66	1.5	18.5
H26	1.5	16.2	H67	0.9	9.7
H27	1.2	16.1	H68	1.0	11.0
H28	1.8	23.3	H69	1.2	12.8
H29	1.3	13.4	H70	0.7	10.5
H30	1.9	19.3	H71	0.9	14.3
H31	1.5	14.7	H72	1.0	9.9
H32	1.6	16.0	H73	1.1	17.7
H33	1.5	23.3	H74	0.7	11.2
H34	1.1	14.4	H75	1.2	16.4
H35	1.5	21.0	H76	0.8	14.4
H36	1.1	19.4	H77	0.8	13.1
H37	1.6	17.8	H78	1.1	17.2
H38	1.0	10.1	H79	0.6	12.0
H39	1.7	18.4	H80	1.0	14.5
H40	1.1	13.3	H81	0.9	14.7
H41	1.1	14.0			

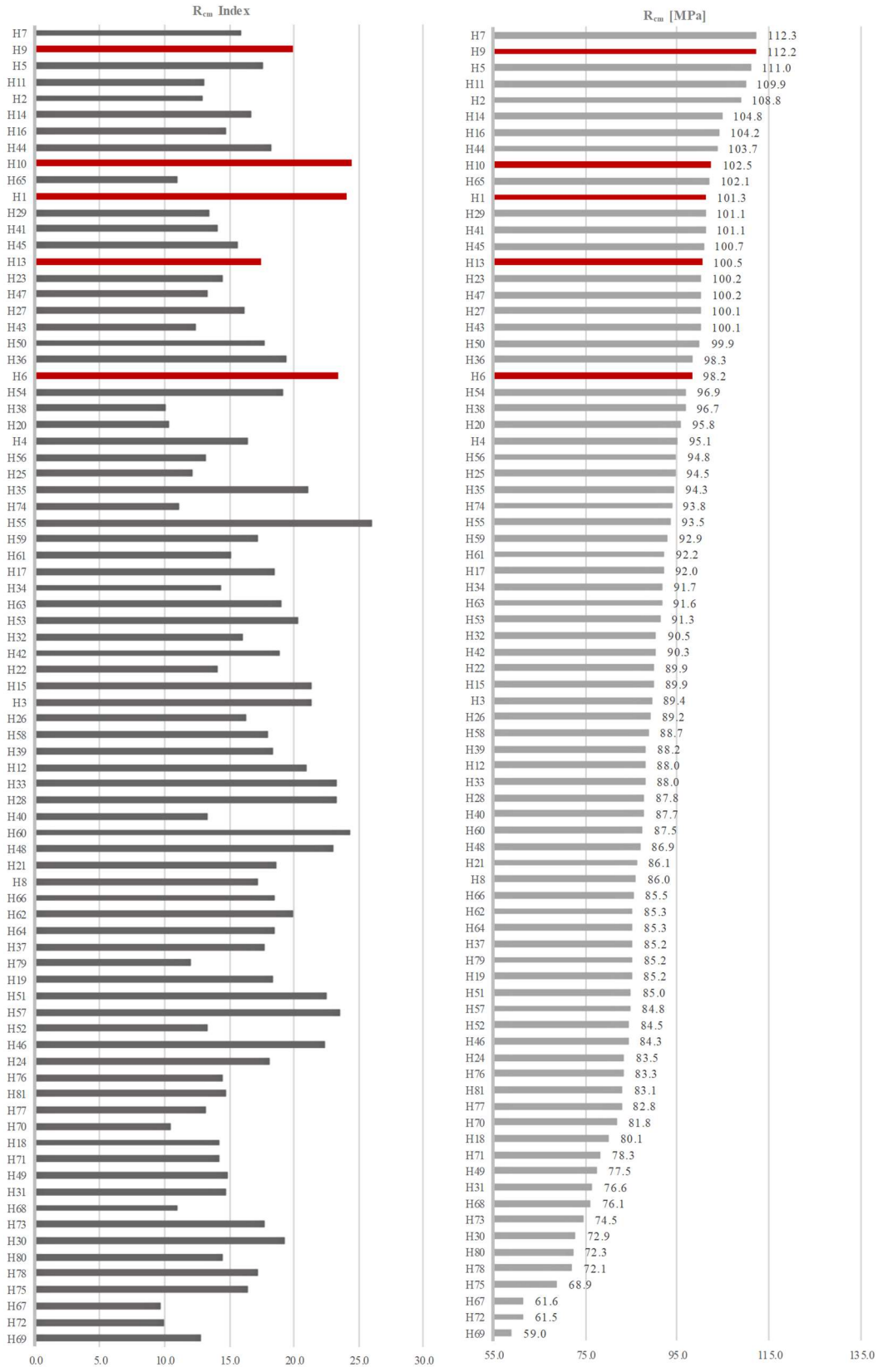

Figure 4.41 – Histograms representing the indexes in table 4.16 for compressive strength highlighting the admixtures with higher values.

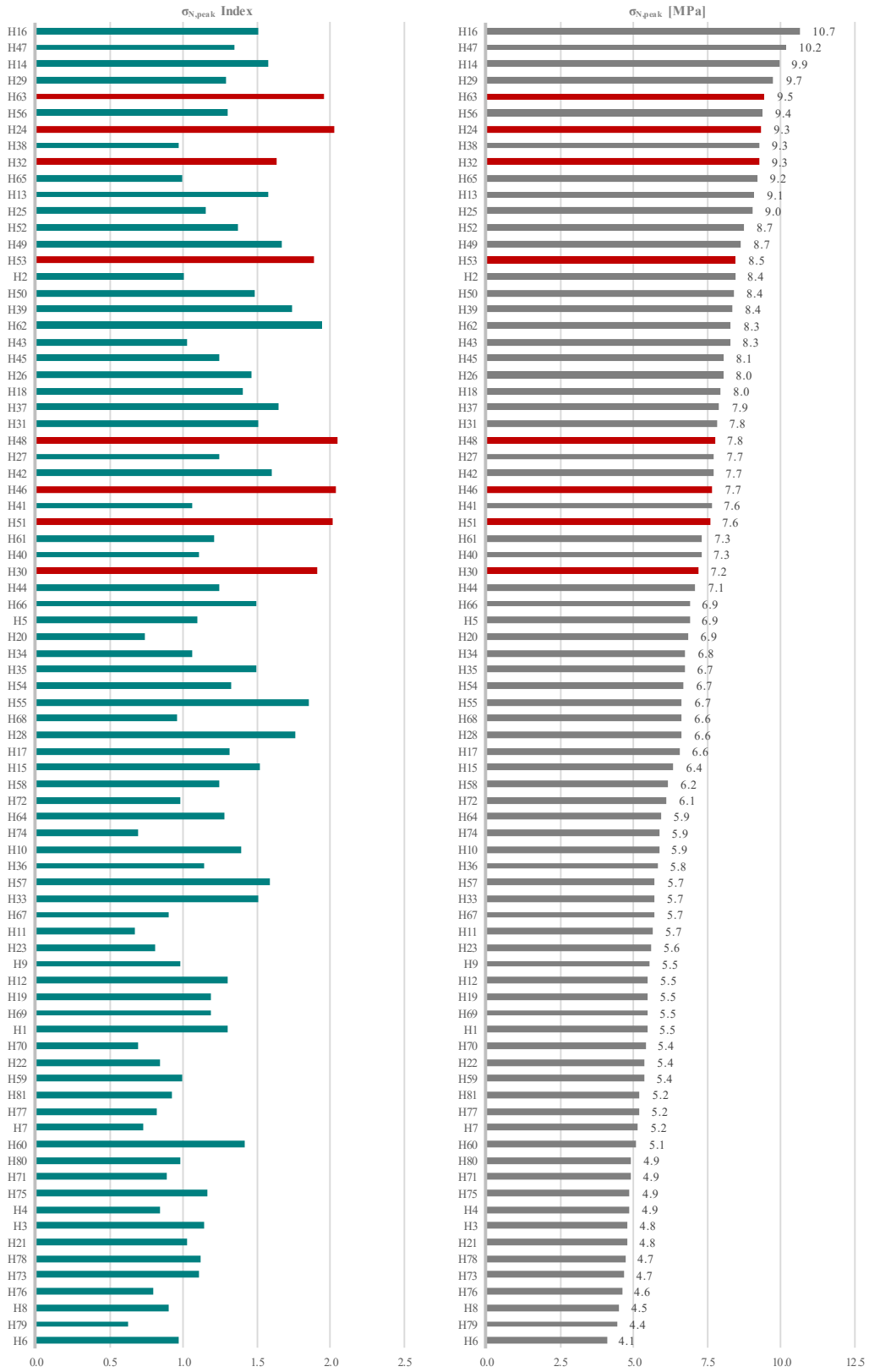

Figure 4.42 – Histograms representing the indexes in table 4.16 for nominal flexural strength highlighting the admixtures with higher values.

CHAPTER 5

5. EFFECT OF TIME DEPENDENT PHENOMENA ON FIBRE REINFORCED CONCRETE LONG TERM BEHAVIOUR

5.1. CREEP AND SHRINKAGE IN CONCRETE

The mechanical performance of concrete material is affected by creep and shrinkage rheological phenomena. Thus, in the engineering applications of reinforced concrete, the cracking problem is ascribed to the present phenomena and, during the time, compressive stresses might be transferred from creeping concrete to steel bars causing buckling or compression failure. The deformations induced are absorbed by concrete although the load applied is lower than the concrete strength leading to an internal cracking process evolution: these mechanisms, triggered during the life of a structure in concrete, could compromise its serviceability and durability (Jiràsek and Bazant, 2002). For this reason, they need to be accounted in the serviceability limit states design of concrete structures.

However, the strain induced by shrinkage and creep present a different nature: the shrinkage phenomenon is not dependent on the load applied while creep deformation depends on the stress level by a linear relation. The deformation induced by shrinkage consists of four contributions: drying shrinkage, hardening shrinkage, autogenous and carbonation shrinkage. The contribution most responsible of the total deformation is the one that generates a difference in volume after the creep test of no sealed specimens. Considering a specimen exposed to dry environmental conditions, the shrinkage deformations gained are the result of the mechanisms triggered: the increment of tension of pore water and the solid surface tension of pore walls generated by the diffusion of water out of the specimen. This contribution is defined as drying shrinkage (Jiràsek and Bazant, 2002). If it is in water, the shrinkage exhibited is much lower than the drying shrinkage and often negligible, the swelling that happens is caused by an increment of water content. The autogeneous shrinkage contribute, visible in sealed specimens, represents the 5% of the drying shrinkage deformation and it is due to the chemical reactions activated during the hydration of cement. As a consequence, for normal concretes it is negligible but for high strength concrete with a low water cement ratio its value can be comparable with the entire drying shrinkage strain so it has to be considered. The strain generated can be

measured by linear measurement systems since the stress induced is linear although the three-dimensions of the specimen. After the complete drying of concrete, the hydration process and, consequentially, the autogeneous shrinkage stop to a humidity amount of 80%. In the mean while humidity is dropping, the drying shrinkage starts so a little autogeneous shrinkage is superimposed on that drying.

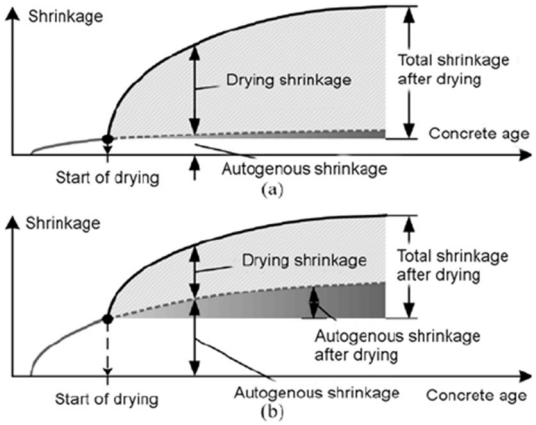

Figure 5.1 – Strain components of shrinkage in (a) normal and (b) high-strength concrete (Sakata and Shimomura, 2004).

The creep strain is defined as the difference between the strain gained by loaded and unloaded elements. The creep strain consists of two constributes: basic creep, featured in the hardened cement paste due to internal arrangement of microstructural bonds, and drying creep. The difference between the deformation induced by shrinkage and creep of a sealed specimen is defined as drying creep or Pickett effect (Zdenek and Yunping, 1994). With drying or high stress levels, concrete creep is nonlinear but the term viscoplasticity is not so realiable because there are not deformations of plastic nature.

When a load is applied on a specimen, the entire behaviour is described by an elastic, instantaneous, strain and creep or viscoelastic strain. At the moment of load application, the specimen will show an elastic deformation and, then, the viscous deformation starts showing an increment over time with a gradually reduced rate, if at some age it is unloaded, it will recover a part of the strain immediately and then it exhibits a progressive recovery over time at a decreasing rate. The complexity is

given by many coexistent phenomena because the specimen drying causes additional creep strains and, at the same time, the non-uniformity of shrinkage leads to a discrepancy between the shrinkage measured on free load specimen, much lower, and the true shrinkage under a loading condition. Drying creep evolves on time similarly to shrinkage, exhibiting a dependence on thickness while the basic creep is not conditioned by this feature (Jiràsek and Bazant, 2002).

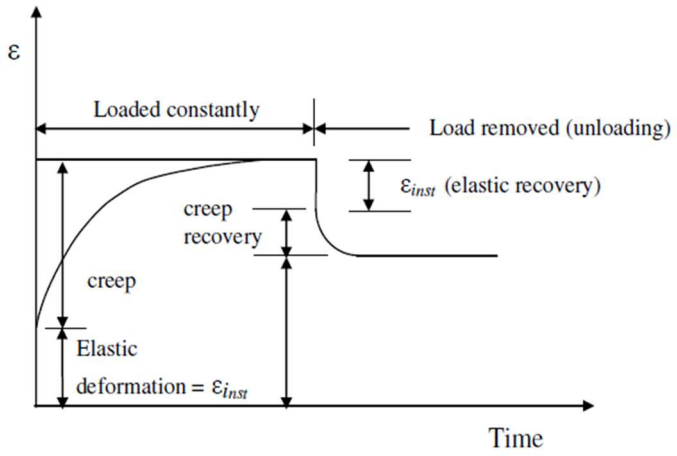

Figure 5.2 – Strain-time relation of concrete under sustained load (Babafemi, 2015).

The ageing of concrete is the peculiar aspect characterizing its mechanical behaviour: the effect produced on concrete is associated with an increment of elastic modulus and strength over time with a decreasing rate. This clearly suggests that creep tends to reduce in concrete loaded at higher age. The ageing endures an increment of stifness and strength of concrete with the time, generated by the gradual pore filling operated by the cement paste hydration products, most of all the tri-calcium silicate hydrate gel. This process lasts many years until the humidity in pores goes under 80 %. In computing the shrinkage and creep deformation, the istant of time when start considering the evolution of the phenomena is the age of concrete or when it has been demoulded since, during the curing period, it has been constrained being not free to exhibits deformation.

5.1.1. Linearity of Creep

The relation between stress and deformation is linear if the stress applied is lower than 50% of the maximum strength: this relation refers principally to basic creep but it is not reliable for drying creep. The linearity makes possible to calculate the strain at each instant of time using the compliance function *J(t',t)*.

$$\varepsilon(t) = \sigma \cdot J(t,t') \qquad [5.1]$$

The linearity involves a strict dependence between the stress and strain during the time: considering two load stress values applied corresponding to a deformation gained, an amount of load equal to the addition of the two considered will generate a strain given by the addition of the two previous strains. This property is defined as principle of superposition, proposed for non-ageing phenomena by Boltzmann and for ageing by Volterra (Jiràsek and Bazant, 2002). Thus, each stress history can be described by various time steps during wich an infinitesimal load amount is applied:

$$\varepsilon(t) = \int_0^t J(t,t')d\sigma(t') + \varepsilon_0(t) \qquad [5.2]$$

at the end the deformation gained is described by the equation 5.2 where the elastic deformation is added. The initial strain includes the thermal strain, the shrinkage strain and the cracking strain. The compliance function in the equation is defined as Kernel parameter of the integral equation. The superposition principle can be written also in the reverse form when a prescribed deformation is applied:

$$\sigma(t) = \int_0^t R(t,t')d[\varepsilon(t') - \varepsilon_0(t')] \qquad [5.3]$$

Where *R(t,t')* represents the relaxation function. In case of no prescribed deformations and stresses, the equations written describe the creep phenomenon and, so, the relation between stress and strain. These equations are the fundament of the aging linear viscoelastic theory, whose key concept is the dependence of creep

deformation evolution on the loading time t'. The strict aging dependence does not make possible to apply the Laplace principle transformation, effective for non-aging materials (as it will be shown for polymers mechanical behaviour). This complication is managed trough numerical solutions by integration step-by-step over time.

This relation will not be considered linear anymore when stress applied is bigger than half of the maximum concrete strength, beyond this limit the behaviour is considered as nonlinear due to the time-dependent growth of micro cracks that will develop in an irreversible way. The nonlinear creep behaviour can be illustrated with the stress-strain isochrones generated by conducting constant load creep tests at different stress levels and connecting points at the same age t.

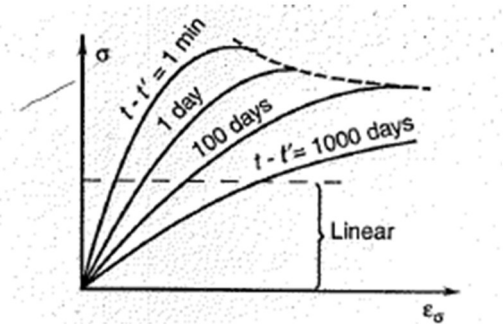

Figure 5.3 – Isochrones of creep at high stress (Jiràsek and Bazant, 2002).

Usually the creep deformations evolution are referred by means of a dimensionless factor, the creep coefficient $\varphi(t,t')$, defined as the ratio between the creep strain at the generic instant of time over the elastic creep strain at age t':

$$\varphi(t,t') = E(t')J(t,t') - 1 = \varepsilon_{creep} / \varepsilon_0 \qquad [5.4]$$

The inclusion of creep in structural analysis is achieved by using the so-called age-adjusted elastic modulus, where elastic and creep strain components are included:

$$E''(t,t_1) = [E(t_1) - R(t,t_1)] / \varphi(t,t_1) \qquad [5.5]$$

t_1 represents the time of load application and $\varphi(t,t_1)$ is creep coefficient defined as the ratio of creep at time t to instantaneous elastic strain. The definition of the effective reduced modulus encloses the effect of the stress relaxation and the influence of the ageing on the elastic modulus value.

5.2. CREEP AND SHRINKAGE IN FIBRE REINFORCED CONCRETE

The mechanical behaviour of fibre reinforced concretes under short term loading conditions is largely investigated but there are plenty of research activities developed in the last decades aimed at estabilishing official regulations concerning their mechanical behaviour characterization over time. On the other hand, the influence of time dependent phenomena and, so, how the deformation can affect the behaviour of the composite material during the service state, is a still opened aspect. The experimental characterization is not officially regulated and the inclusion of creep and shrinkage effects in the material design are aspects still under investigation. The necessity of performing experimental analysis is due to the composite nature of the material and the difficulty in separating the two contributions instead of considering the combined action of both cracked matrix and fibres connecting the cracks and, at the same time, limitating creep strains.

It is well known that the creep mechanism generates a stress redistribution and, so, could represent a positive aspect but the deformations generated, elongation and constractions, modify the mechanical state of the material. The standardization is important also in the perspective of the analysis of several factors modifying the phenomenon evolution, i. e. the influence of fibre type, mix design, pre-cracking and load level. The absence of standardized test methodologies leads to a discrepancy in the experimental outputs and to a difficult comparison.

5.2.1. Characterization of creep and shrinkage deformations in FRCs

Analysing the creep deformation evolution on time (Figure 5.4) three phases can be distinguished (Illston, 1965), the first phase is a sudden increment of the deformation due to the load application, then the specimen gains creep deformations at a lower rate until the failure in the third stage reached when the creep limit is exceeded. For fibre reinforced concretes, two materials suffer from time dependent effects, particularly those concretes reinforced with plastic fibres rather than steel.

Under long term loads, fibers exhibit their viscoelastic properties, i. e. the elasticity of the solids and the viscosity of the fluids, accumulating the viscous deformation, if unloaded, as a plastic part (Houshyar, Shanks, and Hodzic, 2005).

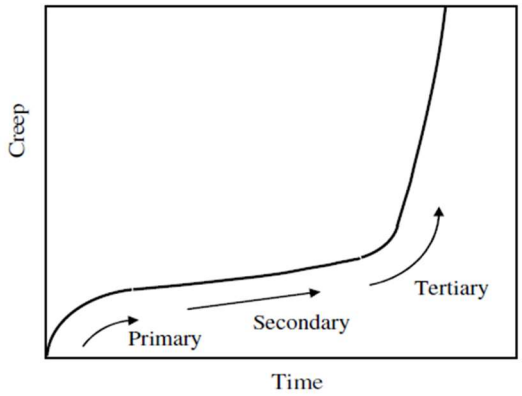

Figure 5.4 – Creep strain component (Babafemi, 2015).

It is important to study how creep and shrinkage affect the FRCs behaviour during the cracked state when fibers start working: as the material cracks, the load exhibits a drop whose magnitude depends on the fibers modulus of elasticity. In case of steel fibers the load decreases less than for plastic fibres since they are characterized by lower elastic modulus. The mechanism activated after the crack opening, and involving the fibre, are different: the single fiber can pull-out, elongate or break under a constant load, as described in Chapter 2 referring to the short term analysis.

The deformation evolution is regulated by the progressive crack opening on time and the single fibre that gradually debonds from the matrix until the final pull-out. Moreover, also the creep of the single fibre needs to be accounted as responsible of the increment of crack opening, remarkable for macro-synthetic fibrers characterized by a viscous nature (Babafemi, 2015).

The FRCs creep behaviour is studied at different levels since the composite nature of the material. However, the load condition most likely to occur is the flexural state where the deformations gained are the result of different loading conditions: concrete compression, concrete cracked in tension, shrinkage deformations (see section 5.1) mitigated by the fibre reinforcement featuring viscoelastic bond and deformation of elongation. This is the reason why, typically, many levels are experimentally

investigated by means of shrinkage tests under free load conditions, compression, uniaxial tensile, flexural tests on the composite material under sustained load; in addition, pull-out and tensile creep tests on the single fibre should be performed to quantify the creep of the fibre and the viscous bond activated at interface with the matrix. In literature there are many proposals of creep tests set-up presenting, obviously, many variations since the lack of standardization. As already specified, the creep test characterizes the cracked FRC mechanical behaviour in service states conditions, returning a relation in terms of load – crack opening. The procedure followed sees the realization of three phases:

1. Pre-cracking: the specimen is tested under short term conditions typically in displacement control until a certain value of crack opening and, then, unloaded;
2. The creep phase: the sustained load, as a ratio of the strength exhibited during the previous phase, is applied;
3. In case no tertiary creep occours leading to the failure of the specimen, it is reloaded according to the static configuration of the phase (1) until the failure.

In Figure 5.5 are reported the load – crack opening relations outcome of a flexural creep test including the three phases described, respectively for softening (in general macro-synthetic fibre reinforced concrete) and hardening (in general with steel reinforcement) FRCs.

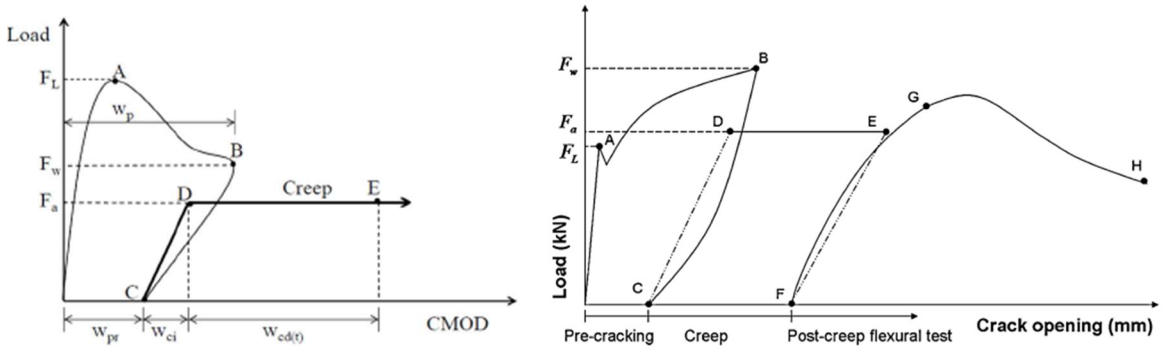

(a) (b)

Figure 5.5 – Schematic representation of the Creep test with (a) softening and (b) hardening post peak behaviour (Arango, Taungua, Vargas, and Serna Ros, 2012; Babafemi, 2015).

5.2.2. Drying shrinkage in FRCs

The shrinkage phenomenon is activated during the plastic and hardened phase, the plastic fibres have the role of mitigating the effect during both states: in particular PVA fibres can mitigate the effect during the hardened state. The water diffusion inside the specimen regulates the shrinkage mechanism in a way depending on the fibres type, elastic modulus, aspect ratio and dosage. The hydraulic shrinkage is associated with the matrix mix design, fibers and their arrangement. In case of microfibres, their addition tends more to reduce the shrinkage deformation rather than macrofibres because of the difference in the distribution: in the first case a denser distribution is achieved. Nevertheless, some studies demonstrated the increment of drying shrinkage when microfibres are added because of the voids in the matrix due to the high number of fibers included (Amin, Kirk, Garo, and Bijan, 2014).

Figure 5.6 – Shrinkage test perfomed proposed by Babafemi (Babafemi, 2015)

5.2.3. Direct tension in FRCs

The RILEM TC 162-TDF (Vandewalle et al. 2001) states the reccomandations to test SFRCs under direct tensile load to mechanically characterize the material properties and, although this test requires extremely care to be performed, it is widely used. The procedure before described is followed in the experimental analysis conducted by Vrijdaghs (Vrijdaghs, Di Prisco, and Vandewalle, 2016) where notched cylinders are pre-cracked to activate the fibre reinforcement during the creep test monitoring the crack opening by three LVDTs in a 120° configuration. The precracking setup used consists of two steel plates glued on both specimen ends and connected with three steel loading bars on which three strain gauges are placed. The

specimen is manually precracked tying the steel rebars and computing the total load applied as the sum of each load recorded in a single bar. The difficulty might be encountered is a not symmetrical crack opening due to the fibers concentration (G. Zhao, Di Prisco, and Vandewalle, 2013). After the unloading phase during which an irreversible strain is registered, the specimen is subjected to sustained load trough a lever arm system. The load is, as specified in the general procedure, a ratio of the residual strength measured during the pre-cracking phase.

Figure 5.7 – Uniaxial tensile test set-up based on a lever arm principle (G. Zhao et al., 2013)

The creep deformations registered under uniaxial load are also comprehensive of the shrinkage strain, for this reason, the tensile contribution is calculated subtracting this part of deformation. An aspect to be born in mind is that the presence of the notch creates a larger specific area in contact with the environmental conditions if compared to the cylinders used for shrinkage tests. Zerguini et al. tested SFRC notched cylinders under uniaxial tensile load varying their diameters: 68 mm, 100 mm and 150 mm, revealing that this varable does not affect significantly the response of the material in terms of post-cracking energy and scatter in results (high dosages are tested: from 54 kg/m^3 to 100 kg/m^3) (Zerguini and Rossi, 2003). A variation of the boundary conditions described before (Vrijdaghs et al., 2016) is proposed by Sorelli et al. that performed uniaxial tensile tests on prismatic specimens with rotations allowed at the specimen ends (Sorelli, Meda and Plizzari 2005).

After the creep test, specimens are unloaded recovering a part of the deformation that is measured; then they are tested in the same uniaxial tensile load conditions until

failure: it might occur also during the creep test. The envelope of the three phases represents the theoretical short term FRC behaviour.

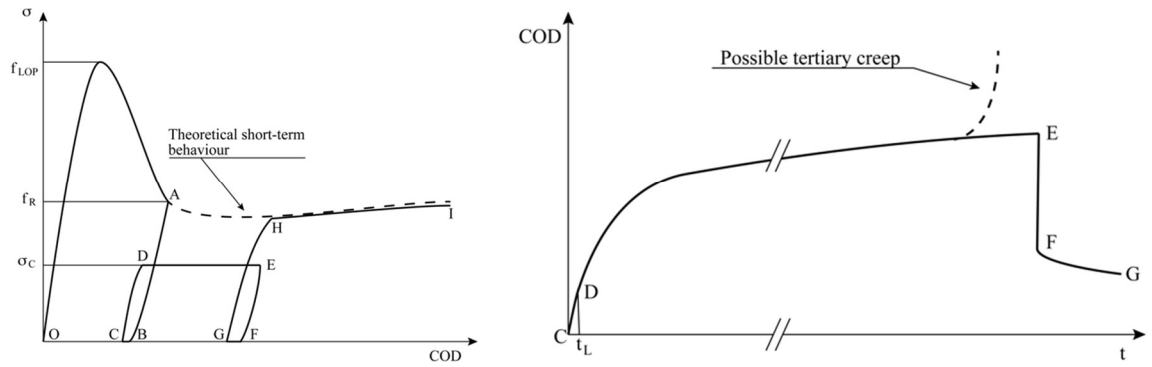

Figure 5.8 – Stress – crack opening displacement and crack opening – time relations observed in long term tests of cracked softening FRC.

A variation is proposed by Plizzari et al. who performed uniaxial tensile tests applying low cycle fatigue loads on notched specimens observing that the damage is partly due to the cyclic conditions and partly to the time effect (Plizzari, Cangiano, and Alleruzzo, 1997).

In Babafemi (Babafemi, 2015) experimental creep tests, characterizing the mechanical behaviour of MSFRCs under sustained load, the uniaxial tensile and creep tests are based on Mouton work (Mouton, 2012). The specimen, before subjected to sustained load, is pre-cracked in short term loading conditions (Figure 5.9a) to simulate the service cracked condition and activate the fibers contribution. The set-up is studied with two connections at both ends: the important aspect is that they should not be rigid constrains so that additional moments are not transferred. The simultaneous crack opening is registered by linear trasducer (LVDT) placed over the notch.

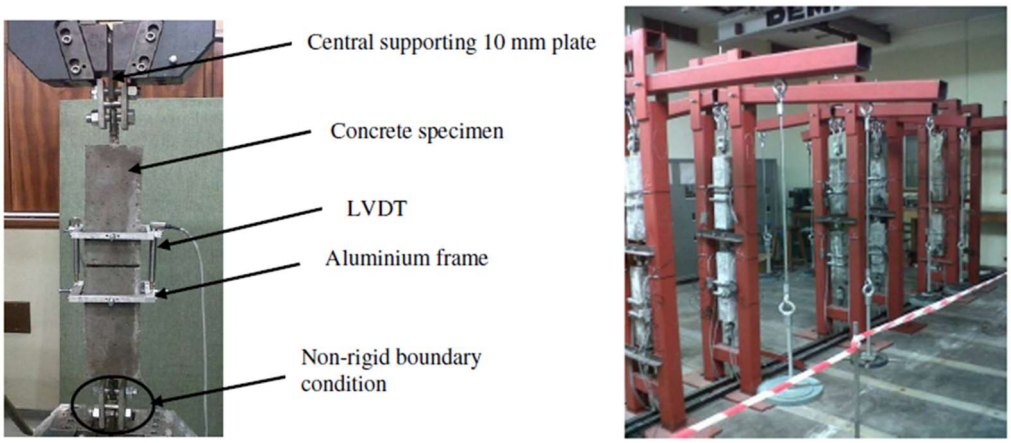

(a) (b)

Figure 5.9 – Set-up proposed by (Mouton, 2012) in the (a) pre-cracking phase and (b) creep phase.

The uniaxial creep test for macro-synthetic FRCs is performed applying the load by means of a lever arm system calibrated according to the residual tensile strength registered during the precracking test. The boundary conditions realized are the same of the previous test setup with a security system in case the specimen breaks under the sustained load. In the computation of the load applied during the creep test, also the steel elements connecting the specimens, are accounted for the total calculation of the weight. The strain recorded contains also the drying shrinkage contribution. For this reason, a shrinkage test is performed where the specimen is free loaded and the strain is recorded by LVDTs placed on the specimen trough aluminium frames.

5.2.4. Pull-out and tensile creep test on single fibre

At a single fibre level, pull-out creep tests and single fibre creep tests are proposed. This type of investigation is not widely performed because of the difficulties inherent the test itself and the details connected, i.e. the deformation acquisition and the set-up arranged. During the loading phase, for example, the fibre should not be damaged to not compromise the test and it is important that the system used to grip the fibre does not slip without extracting the fibre and also the care in the strains measurement has to be guaranteed (Babafemi, 2015). The set-up proposed by Babafemi has a grip system consisting in a hand drill chuck and the deformation is registered taking

pictures with constant time intervals. The present study is also performed by Vrijdaghs et al. for polypropylene macrofibers where it is found out how the load ratio influences the fibre behaviour and, consequently, the failure time (Vrijdaghs, Di Prisco, and Vandewalle, 2017). In addition, creep tests on the single fibre make possible to compute separately the contribution of the fibre to the whole material creep deformation.

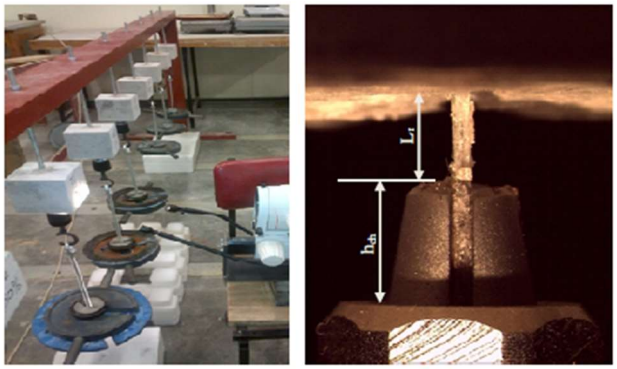

Figure 5.10 – Set-up of pull-out creep tests illustrated by Babafemi (Babafemi, 2015).

Almost the same technology is described by Babafemi to investigate the single fibre viscoelastic deformation of the single fibre. It is gripped on both ends paying attention to not allow the slippage otherwise the test results are not reliable. As in creep tests, the load applied represents a percentage of the maximum bond strength estimated by pull-out short term tests.

The strength percentages applied are 50% and 80% of the bond strength while for tensile tests, the 30% of the fibre tensile strength is applied. Short term tests performed by Babafemi make use of the same setup type described before with the elongation monitored by linear transducers supported by a PVC strip. Particular attention is given to the placing phase during which is necessary to make sure the allignement of the chucks with the fibre. Moreover, the pull-out tests are perfomed with four different rate values to determine its influence on the experimental test results.

Figure 5.11 – Preliminary short term pull-out and tensile tests proposed by Babafemi (Babafemi, 2015)

5.2.5. Flexural tests in FRCs

The structural level concerns the residual flexural strength and toughness property determination of the FRCs. The reference documents are the European Standard EN 14651 (EN 14651-2005) and RILEM TC 162-TDF (RILEM TC 162-TDF, 2000). The material performance is so characterized by a load – crack opening relation characterized by a flexural test in three point bending configuration (see chapter 2, section 2.3.2). The test could be performed also adopting a four point bending configuration measuring the crack opening by two linear transducers placed close to the tip of the notch on both specimen sides. Typically the relation is expressed in terms of crack opening but also the deflection can be monitored: it could be difficult to compare results of creep tests in terms of deflection and crack opening since the former includes also contributes of the uncracked section and, so, it has a bigger value while the second is representative only of the cracked section displacement and so, has a smaller value.

In a flexural state, the deformations induced are the result of many conditions interacting so the idea is to validate the theory calibrated on the different loading conditions realized before, drying shrinkage tests, compression and uniaxial creep tests on MSFRCs and the single fibre creep tests. Babafemi performs flexural creep tests adopting a set-up realized on the basis of Arango et al. (2012) and Zerbino and Barragan (2012) work (Arango et al. 2012; Zerbino and Barragan 2012). The

specimens are organized in a coloumn of three elements on a stiff support base made of longitudinal and trasverse channels section, loaded in a four point configuration and the CTOD is recorded with dial gauges over the midspan notch. The system transmits the load using a lever arm principle, through the lever arm where the weight, before calibrated on the pre-cracking test, is placed. The examples of frames designed for creep tests can contain only one sample or a coloumn of specimens (at least three): in this case they need to be ordered according to the residual strength since the one placed at the bottom will receive a higher load applied. This effect can be balanced organizing the pile of samples according to the residual strength measured during the precracking test phase.

Figure 5.12 – Flexural creep test set-up proposed by Babafemi (Babafemi, 2015)

The creep flexural test is followed by the failure phase during which the specimens are reloaded until an established final crack opening value.

5.2.6. Aspects influencing FRCs long term performance

The long term mechanical performance of FRCs might be affected by different aspects but in a different way if compared to the short term characterization.

The fibre type in terms of elastic modulus, specific surface, handles the creep deformations in a different way: the fibrous reinforcement with a elastic modulus

higher than that of ordinary concrete is able to reduce more the deformations induced by creep while those characterized by lower elastic modulus create a weaker interface with the matrix gaining the opposite effect (Q. Zhao, Y., Guoqing, Jinyang, and Xiaochen, 2016). Although the elastic modulus of PVA is higher than PP fibers and both lower than concrete, they behave differently: PVA fibres addition causes a lower creep resistance of the fibre reinforced concrete. Thus, also the internal defects and the specific surface of the reinforcement play an important role. The comparison could be done also in terms of specific creep, defined as:

$$C_t = \frac{\varepsilon_{ct} - \varepsilon_t}{\sigma} \qquad [5.6]$$

ε_{ct} creep strain at *t*, ε_t shrinkage strain after a time period *t*, recorded under a load equal to σ. The FRC elastic modulus measured at 28 days is a macro scale indicator and a higher value imples a lower specific creep. On the other side, PVA and PP fibres register a specific creep value quite higher than steel fibres addition, but still higher for the first material rather than the second.

The lack of standardization for creep test methodologies for FRCs is confirmed by the fact that there are many proposals of experimental test methods with some differences. Serna et al. (Arango et al., 2012) advanced the proposal for a creep flexural test of cracked FRCs, underlining the importance of some elements, i.e. the set-up designed, that should allow the application of a constant load over time to more than one specimen in the same frame. The creation of additional secondary moments need to be avoided otherwise the creep test could be stopped.

As reported in Chapter 1, section 1.2.7, an example of fibre reinforced concrete application is represented by the shotcrete. Creep behaviour of shortcrete panels is examined by Bernard who examines the creep behaviour of shotcrete panels reinforced with steel and two types of macro-synthetic fibre. The study revealed that the relation between the load ratio and creep coefficient is difficult to state because two different results are achieved: considering steel and one MS fibres type (those

straight) it appears to be insensitive while, considering the creep coefficient trend of FRC reinforced with the other MS fibre type, suggests a dependence on it (Bernard, 2004). Bernard advances the idea that, more than the load ratio, what drives this sensitivity is how the load ratio is defined because the load gained and correspondent maximum deformation cannot be representative of the strength exhibited during the creep test above all if the load lies in a region of rapid strain softening.

Some researches found out that the fibre geometry influences also the creep deformations evolution: in particular geometry, slenderness, dosage of steel fibres (Taengua, Arango, Martì-Vargas, and Serna, 2014). While, regarding the concrete matrix, the variables to consider as influent are: the compressive strength, maximum aggregate size, and load applied on prismatic notched specimens under a flexural load. Among all the variables, the study carried out revealed that fibres slenderness and dosage appear to be significative for the FRC performance. The load applied, indicated by the load ratio parameter, influence the material flexural response increasing the creep deformations as it increases. The fibre content and their slenderness combined with the load factor affect the residual strength gained during the pre-cracking phase while their length is not so mechanically significant. Especially fibre content and the load ratio are connected because, the high dosage increases the load bearing capacity with the possibility of not registering extremely high deformation values when higher loads are applied. At the same time, the increment of slenderness leads to a higher creep deformation control: in this way the effects induced by the application of high load can be mitigated. The creep load ratio is often the 50% of the residual strength exhibit in the precracking stage but, also higher values, 60% and 70%, are found in literature. In particular Kusterle stated that for MSFRC a creep load ratio of 50% makes possible to have good long term performance since this material registers higher deformations (Kusterle, 2009). On the other side, SFRCs are able to bear higher load so a value of 60% can be considered, since the failure is achieved for ratios equal to 75-80%. Moreover, environmental conditions such as temperature and humidity must be controlled

because the temperature variation has been found to be responsible of the terziary creep activation (Buratti and Mazzotti 2015) leading to the failure in MSFRC specimens. Another point of discussion is the duration of creep tests because the terziary creep failure can occur after some years of test: it is suggested for bending tests a duration between 30 and 90 days (R. Zerbino, Monetti, and Giaccio, 2019) while compressive tests have a larger duration of 6 – 12 months. The loading – unloading cycles performed does not help to reduce the duration of tests but their execution during the creep tests could help to monitor the progressive evolution of the material damage measured on the compliance of the specimens.

The flexural creep tests are easier to perform and exhibits less variability in results but it is necessary to understand how tensile and compressive creep strain occour simultaneously and might be studied in a flexural loading state. Recently according to the RILEM Draft Recommendations, the tensile behaviour of SFRC is characterized by tensile tests on notched cylinders in fixed end boundary conditions. Direct tensile creep tests are perfomed to compute the tensile deformation as a separate contribution but the procedure to develop is not easy: the cylindric specimens are cored from a prismatic FRC sample, whose coring direction should be accounted (Figure 5.13), then pre – cracked in an uniaxial tensile load configuration, unloaded and a sustained load is applied to perfom the creep test. First of all, the choice of considering cored samples helps to account more for the random fibres arrangement than in case of moulded cylinders: the research executed by Barragán et al. (Barragan, Gettu, Martin, and Zerbino, 2003) shows the difference in the tensile strength response for specimes cored vertically (the casting direction) or horizontally (perpendicular to casting direction). The latter exhibit a considerably better post-peak performance due to a stronger fibre orientation: this situation is more similar to the real tensile stress application and help to quantify as reliable as possible the contribution of concrete and fibers when loaded in tension. Moreover, the behaviour under sustained load is also analysed on FRC beams (Vasanelli, Micelli, Aiello, and Plizzari, 2013) realized with reinforced concrete and the addition of steel and plastic

fibers. This study has been carried out with the aim of pointing out the effect of the fibrous reinforcement in the reduction of the crack spacing in the perspective of the long term performance characterization.

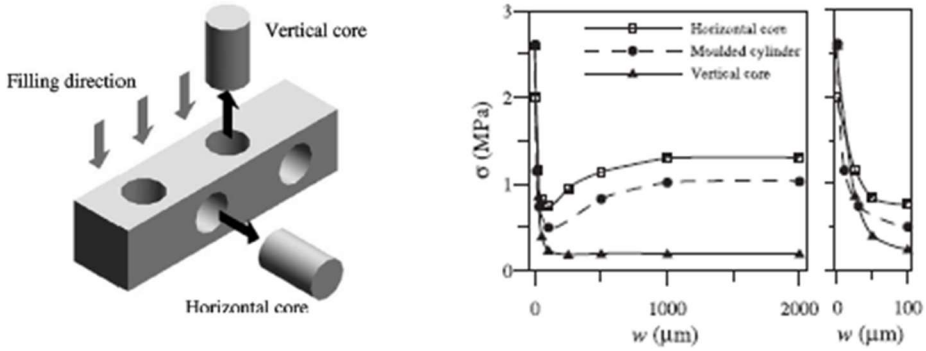

Figure 5.13 – Influence of core direction on uniaxial tensile response of FRCs (Barragan et al., 2003)

CHAPTER 6

6. EXPERIMENTAL INVESTIGATION ON CREEP, SHRINKAGE AND TEMPERATURE EFFECT ON MACRO – SYNTHETIC FIBRE REINFORCED CONCRETE LONG TERM BEHAVIOUR

6.1. OUTLINE OF THE EXPERIMENTAL ANALYSIS

According to the literature research focused on the characterization of FRCs long term performance, the present section deals with the effects of time dependent phenomena on the service state of a concrete reinforced with polypropylene macro fibers. The study is developed by executing tests in unloaded and loaded conditions, shrinkage tests, creep compressive tests, uniaxial tensile and flexural tests at composite material level, in addition to direct tensile tests on single fibers. Beside the analysis of the creep deformation evolution due to the time, the temperature is a further variable studied by carrying out experimental tests not in isothermal conditions but by increasing the temperature at certain time intervals.

The idea would be to quantify the contribution of the deformations induced by time and temperature and to evaluate how they interact in flexural cracked state of the material.

The procedure starts with the characterization of the material used in unreinforced state, referring to the plain concrete, then two fibres dosage are evaluated in order to select the one with which the final admixture would be designed. As a consequence of what discussed in the previous sections, it is not obvious that higher dosage of fibers implies better performance but many factors should be accounted, i.e. the entrapped air due to the highe reinforcement amount, the mixing phase complications.

The final admixture characterizes the MSFRC tested under sustained loads.

6.2. PLAIN CONCRETE MECHANICAL CHARACTERIZATION

6.2.1. Mix design

The mix design of plain concrete is characterized by the granulometry curve in Figure 6.1, indicating the aggregate fractions contained, included in the range identified by the curves of Fuller and Thompson and Bolomey. The material used are cement, CEM I 52.5R, sand with an aggregate size ranging from 0 – 1 mm and 0 – 5

mm, gravel characterized by a grain assortment between 5 and 15 mm (Figure 6.2), potable water and superplasticizer Glenium Sky 542.

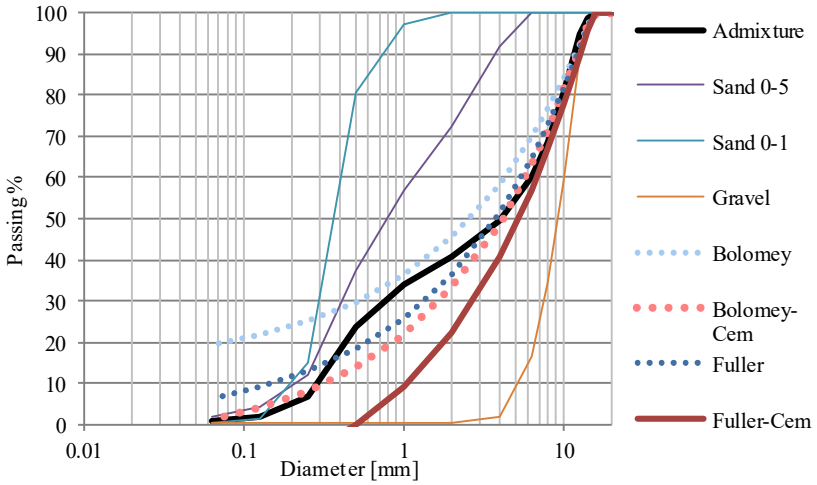

Figure 6.1 – Granulometry curves of admixture constituents and Bolomey – Fuller grading envelope.

(a) (b) (c)

Figure 6.2 – Aggregates used: (a) Sand 0-1 mm; (b) Sand 0-5 mm; (c) Gravel 5-15mm.

The present admixture is designed according to the materials quantities reported in Table 6.1.

Table 6.1 – Plain concrete mix design specifications.

Concrete component	Value
CEM I 52.5 R [kg/m^3]	400
Sand 0-1 mm [kg/m^3]	174
Sand 0-5 mm [kg/m^3]	740
Gravel 5-15 mm [kg/m^3]	848
Water [l/m^3]	184
W/C	0.46

6.2.2. Preparation of specimens

The ingredients are mixed according to the identical procedure described in chapter 3, section 3.3.3, except from the fibres addition phase since plain concrete is cast. The material characterization sees the realization of:

- Four prismatic specimens for flexural tests (150 x 150 x 600 mm^3);
- Four cylinders for compressive tests (diameter 150 mm, height 300 mm);
- Four cylinders for Brazilian tests (diameter 150 mm, height 300 mm);
- Two cylinders for elastic modulus characterization (diameter 150 mm, height 300 mm);
- Two cubes for compressive tests (150 x 150 x 150 mm^3).

(a) (b)

(c) (d)

Figure 6.3 – Specimens cast procedure: (a) Mixing phase; (b) Water addition; (c) Cylindrical and cubic moulds; (d) Prismatic moulds.

The admixture is vibrated inside the moulds trying to not modify the aggregates distribution and then they are covered with plastic sheets preventing moisture exchange and so early shrinkage phenomena. After 48 hours they are demoulded and cured in a climate controlled room at 20°C and relative humidity of 99% for 26 days.

6.2.3. Experimental tests

This phase characterizes the flexural strength of plain concrete trough three point bending tests (Figure 6.4a), according to the standardized methodology exposed for concrete with fibers in section 3.3.4 monitoring the crack opening during the test (BS EN 14651-2005).

The tensile strength is computed by brazilian tests following the procedure regulated by the standard code UNI EN 12390-6:2010. The cylinder is placed between two steel profiles (Figure 6.4d) to create a contact surface with the cylinder realizing a condition of uniform load distribution. The displacement is measured by two linear transducers, LVDTs, placed along the perpendicular direction to the crack formation. The tests are realized with the servohydraulic testing machine used for flexural tests, with a capacity of 500 kN.

The cylindrical compressive strength (Figure 6.4b) is characterized by compression tests on cylinders monitorning the vertical displacement using three potentiometers positioned according to a radial distance of 120°. The test is executed in a loading frame equipped with a square plate whose lowering rate depends on the pressure manually regulated. The ordinary compressive tests on cubes are performed using the same loading frame (Figure 6.4c).

The elastic modulus is obtained performing a compressive test applying preloading and loading cycles at two different stress levels according to the European standard UNI EN 12390-13:2013 (Figure 6.5).The modulus is computed by dividing the stress applied to the strain acquired by two strain-gauges glued vertically on the opposite sides of the cylinder external surface. They present an insulating flexible backing

supporting a metallic foil pattern which is connected, by an electrical cable, to the acquisition system. As the specimen starts deformating, the instrument deforms simultaneously generating a variation of the element resistance obtaining the correspondent strain.

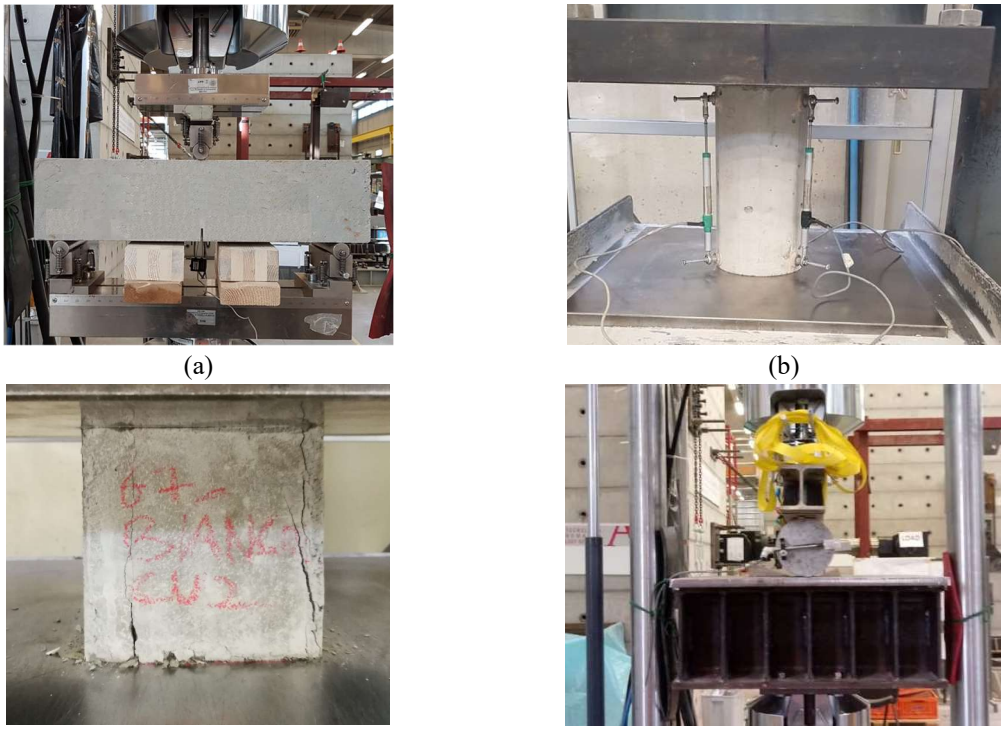

(a) (b)

(c) (d)

Figure 6.4 – Experimental tests for plain concrete mechanical characterization: (a) Three point bending test; (b) Cylindrical compression test; (c) Cube compression test; (d) Brazilian test.

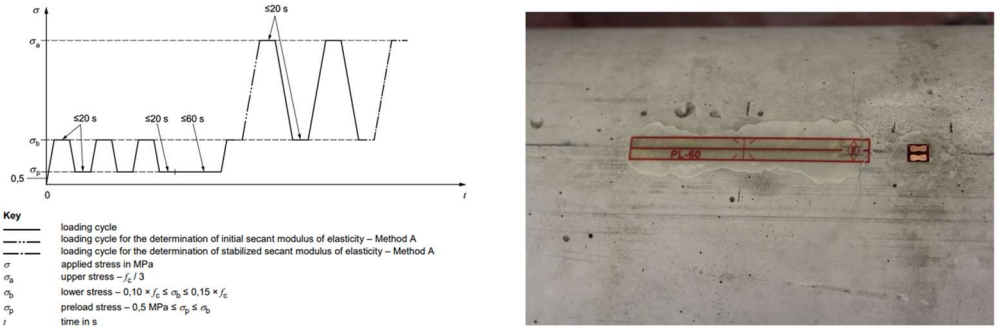

(a) (b)

Figure 6.5 – (a) Testing procedure to obtain the elastic modulus on concrete cylindrical specimens (UNI EN 12390-13); (b) Strain-gauges to measure the strain and consequently the elastic modulus.

6.2.4. Experimental test results

The plain concrete behaviour under compressive load is characterized by compression tests on cylinders and cubes. The output of the first test type is reported in terms of nominal stress, calculating according to the definition dividing the load measured by the circular cross section, and the strain, computed as the mean value of the three potentiometers deformation (Figure 6.6).

During the splitting tests, the load and the relative displacement corresponding to the principal crack are measured. It is possible to obtain the stress value using the standardized formula indicated in UNI EN 12390-6:2010:

$$f_{ts} = \frac{2P}{\pi hd} \qquad [6.1]$$

defining P the maximum load measured, d the base diameter and h the height of the cylinder tested. In case of particular boundary conditions realized for the load application, the tensile strength value is multiplied by correction coefficients (Garcia, Márquez, Zúñiga-Suárez, Zuñiga-Torres, and Villalta-Granda, 2017).

The flexural behaviour is reported in terms of nominal stress, considering the notched mid-span section, related to the crack opening. The Figure 6.8 indicates with a solid red line the mean curve and with the grey area the scatter value among the specimens tested.

The Table 6.2 indicates the compressive strength measured on cubes and in Table 6.3 the experimental values of the elastic modulus are reported.

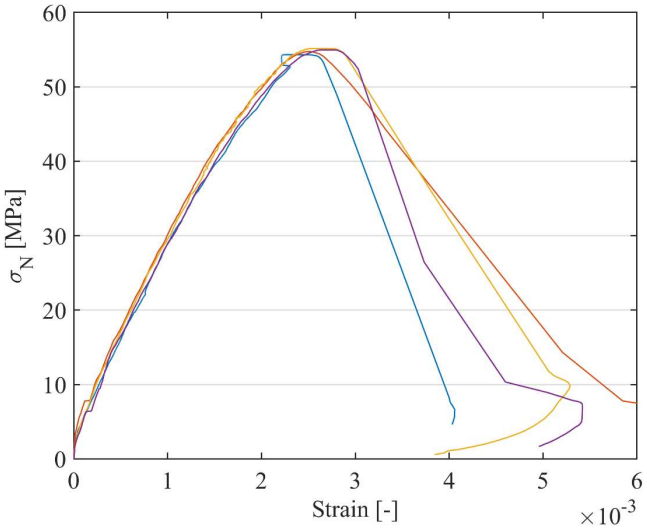

Figure 6.6 – Nominal stress – strain relation for cylindrical compression tests.

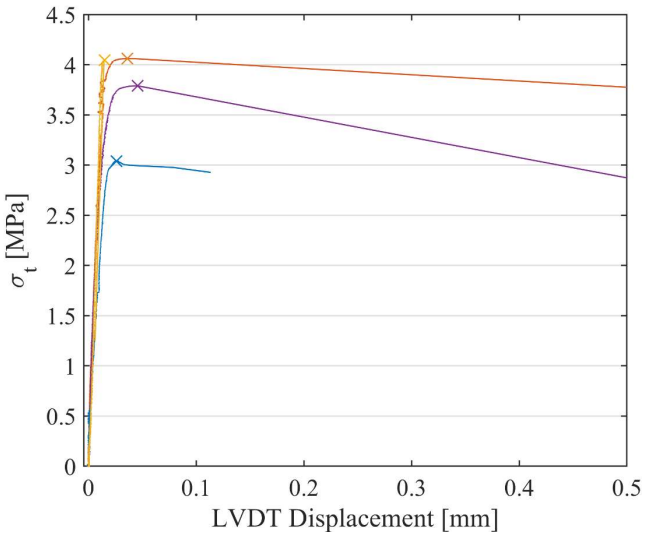

Figure 6.7 – Tensile stress – LVDT displacement relation for Brazilian tests.

Table 6.2 – Compressive tests result for plain concrete.

Sample ID	R_c [MPa]	R_{cm} [MPa]
Cu_1	48.3	51.3
Cu_2	54.3	

Table 6.3 – Elastic modulus measured on cylindrical specimens.

Sample ID	E_c [GPa]	E_{cm} [GPa]
Cy_1	27.8	27.3
Cy_2	26.9	

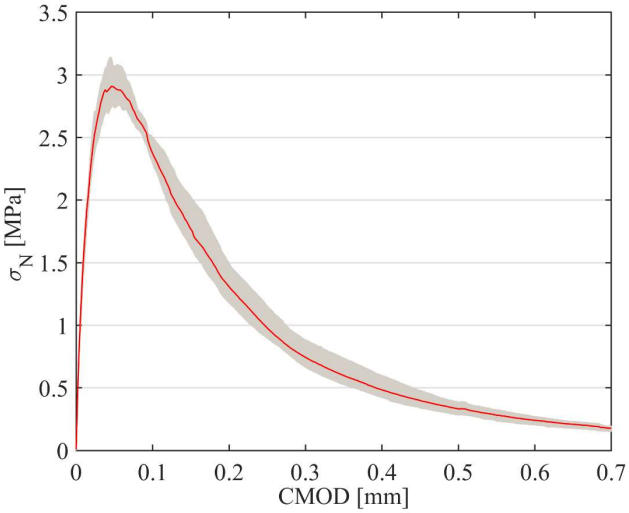

Figure 6.8 – Nominal stress – CMOD relation for three point bending tests.

6.3. MSFRC SHORT TERM CHARACTERIZATION WITH TWO DIFFERENT FIBRE DOSAGES

6.3.1. Mix design

The fibre reinforced concrete is designed using concrete mix specified for the plain concrete and two fibre dosages, 8 kg/m^3 and 10 kg/m^3. The quantities are indicated in Table 6.4 where a light amount of aggregates is substituted by the fibres volume. Considering the polypropylene density of 900 kg/m^3 the modified quantities of sand and gravel are calculated: the difference in volume is very small since the low reinforcement volume.

Table 6.4 – Mix design specifications for concrete reinforced with 8kg/m^3 and 10 kg/m^3 of polypropylene fibres.

Concrete component	Dosage 8 kg/m^3	Dosage 10 kg/m^3
CEM I 52.5 R [kg/m^3]	400	400
Sand 0-1 mm [kg/m^3]	172	171
Sand 0-5 mm [kg/m^3]	730	727
Gravel 5-15 mm [kg/m^3]	837	834
Water [l/m^3]	184	184
W/C	0.46	0.46

6.3.2. Fibre properties

The reinforcement consists of polypropylene crimped macro fibres, different from those adopted in the previous section (Figure 6.9), characterized by the geometrical and mechanical properties reported in Table 6.5. They present almost a rectangular cross section and a high aspect ratio that, according to the research results described in section 5.2.6, should influence the creep deformations.

Figure 6.9 – Polypropylene crimped macro-fibers used.

Table 6.5 – Macro-synthetic fibre properties.

Fibre property	Value
Fibre length [mm]	54
Fibre diameter [mm]	0.81
Fibre Aspect ratio [-]	67
Fibre material	PP
Fibre tensile strength [MPa]	473
Elastic secant modulus [GPa]	2.6
Shape	crimped

6.3.3. Specimens preparation

The mechanical performance characterization of the MSFRC material under investigation is evaluated on the flexural response, as indicated in the Model Code 2010, by analysing the residual strength values, and on compressive tests to characterize the concrete class. Thus, eight prisms with size of 150 x 150 x 600 mm^3

and three cubes of 150 x 150 x 150 mm^3 for both fibre dosages are cast. The procedure followed is coincident with that reported in section 3.3.3 (Figure 6.10a):

1. An amount of 50% of water is added in the mixer with all aggregates and mixed for 5 min;
2. Cement and remaining water are added;
3. Fibres are added and mixed for 3 min adjusting the admixture with an amount of superplasticizer (Figure 6.10b) in order to reach a slump value of at least 170 mm (Figure 6.10c).

The element that could vary among the batches might be the amount of superplasticizer added, since the environmental conditions, i.e. temperature, humidity and consequently the aggregates degree of drying could be different. However, the same conditions are attempted to remain unchanged, specimens are covered with plastic sheets in the meanwhile concrete is passing from fresh to hardened state for 48 hours, after that they are demoulded and cured in a climate room at constant temperature of 20°C and relative humidity of 99%.

(a) (b) (c) (d)

Figure 6.10 – Preparation of specimens: (a) Cement addition; (b) Super plasticizer; (c) Slump test; (d) Prismatic samples cast and refining.

6.3.4. Experimental test results

The experimental tests executed are three point bending tests on prismatic specimens presenting a notch of 25 mm height at mid span length and compression tests on cubes. The residual strength is evaluated starting from the nominal stress – crack opening relations for both dosages (Figure 6.11 and Figure 6.12) and then relating the residual strength f_{R1} and f_{R3} correspondent to crack opening of 0.5 mm and 2.5 mm with the number of fibres contained in the two strips close to the notch. In a first attempt, it should be noticed the increment of scatter in results due to the fibers addition, between plain concrete and fibre reinforced concrete: this is expected since the post peak behaviour is almost totally driven by the arrangement of fibres and their random dispersion in the matrix. The linear regression on the flexural residual strength values with the number of fibres (from Figure 6.14 to Figure 6.17) reveal, as demonstrated by the experimental analysis in chapter 3, section 3.3.6, a strong dependence of the residual capacity on the fibres effectively crossing the cracked surface. As expected the different dosage is reflected in the post peak performance, increasing the residual strength with the higher fibers amount, and obviously in the residual strength parameter values.

Nevertheless, a dosage of 8 kg/m^3 of this fibre type shows optimal mechanical properties and, for this reason, the long term investigation considers the present fibre reinforced concrete properties. The concrete is characterized by the compressive strength reported in Table 6.6 and Table 6.7 respectively for the lower and higher dosage, showing no remarkable difference in values. This is also confirmed by the peak flexural strength values exhibited by the two dosages not having significant differences (Figure 6.13).

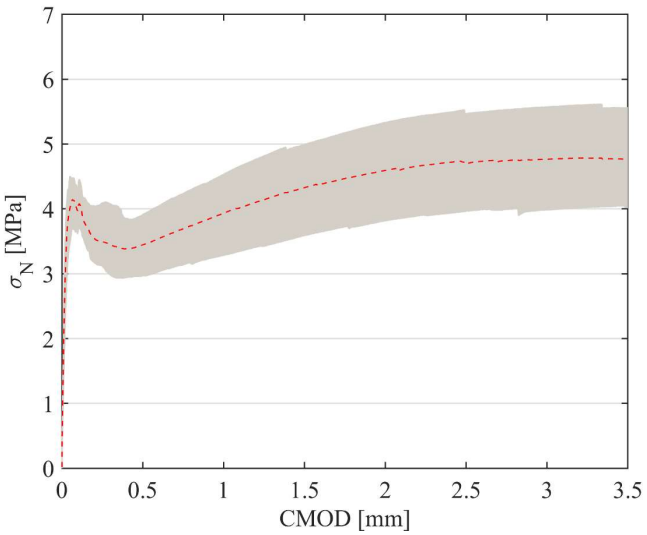

Figure 6.11 – Nominal stress – CMOD relation for three point bending test on the FRC with dosage of 8 kg/m^3 of fibers.

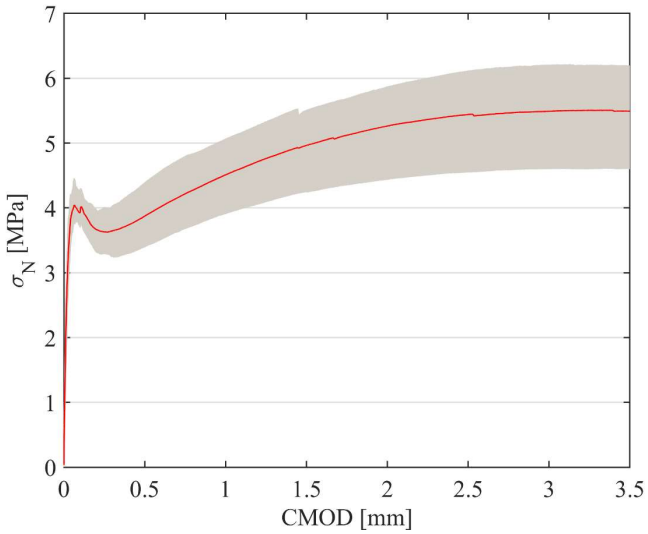

Figure 6.12 – Nominal stress – CMOD relation for three point bending test on the FRC with dosage of 10 kg/m^3 of fibers.

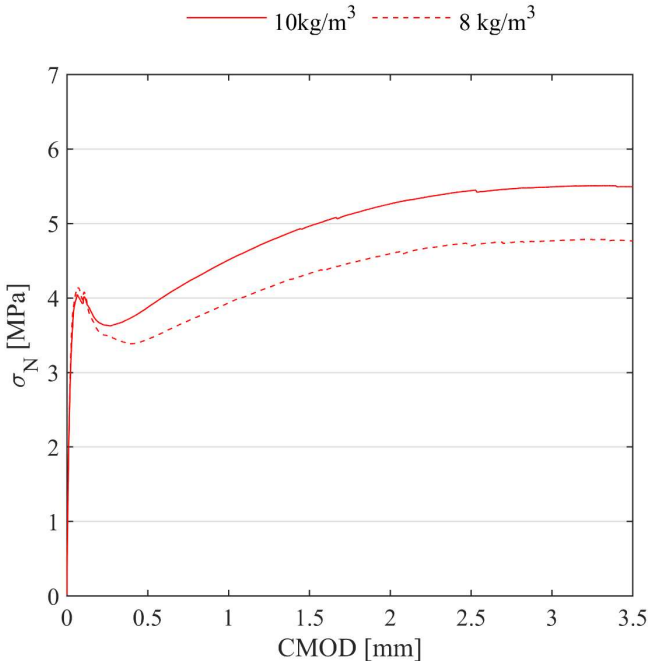

Figure 6.13 – Nominal stress – CMOD relations for both dosages.

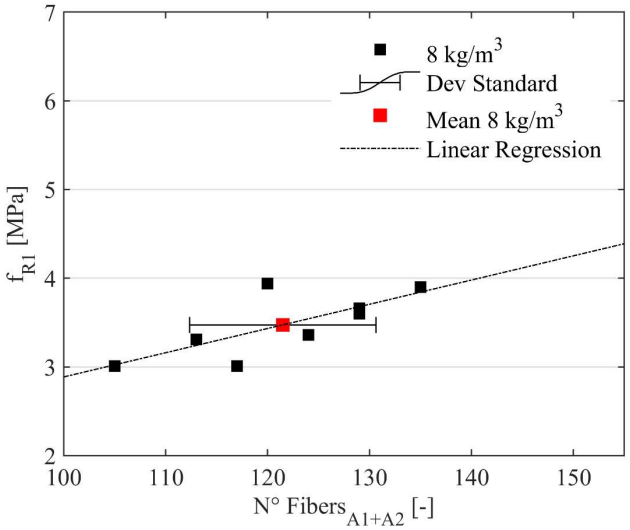

Figure 6.14 – Linear regression of residual strength values f_{R1} with the number of fibers contained in A_1 and A_2 strips, for FRC reinforced with 8 kg/m^3 dosage.

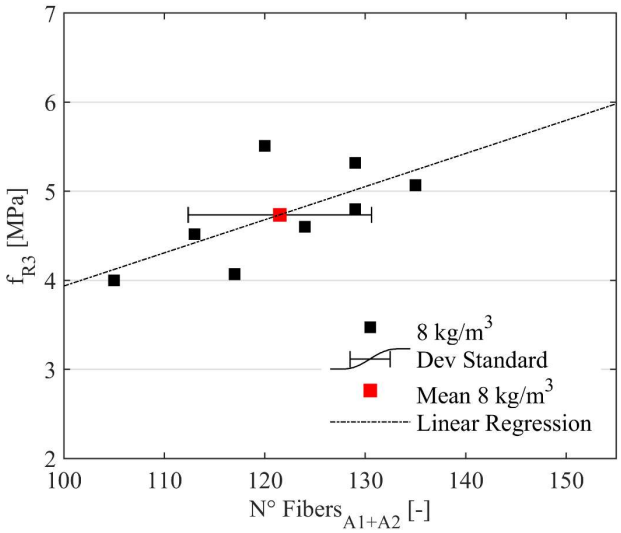

Figure 6.15 – Linear regression of residual strength values f_{R3} with the number of fibers contained in A_1 and A_2 strips, for FRC reinforced with 8 kg/m^3 dosage.

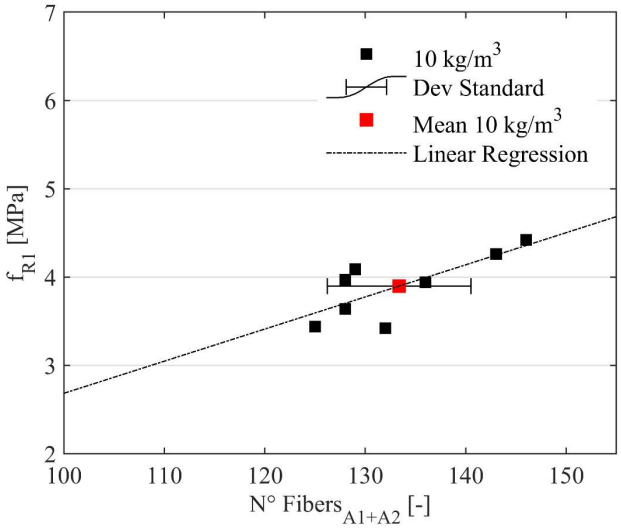

Figure 6.16 – Linear regression of residual strength values f_{R1} with the number of fibers contained in A_1 and A_2 strips, for FRC reinforced with 10 kg/m^3 dosage.

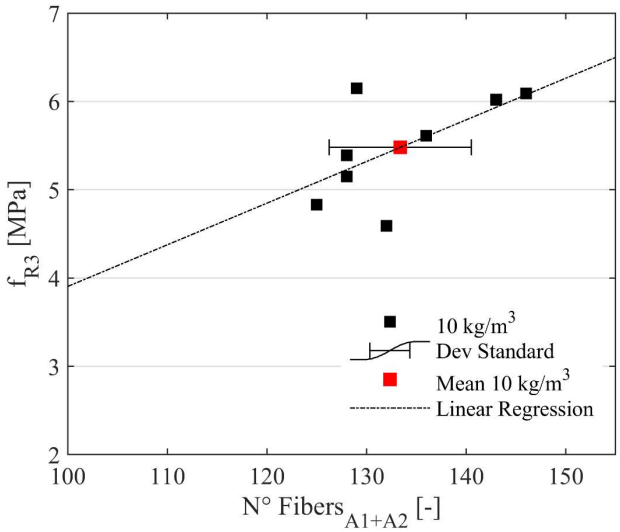

Figure 6.17 – Linear regression of residual strength values f_{R3} with the number of fibers contained in A_1 and A_2 strips, for FRC reinforced with 10 kg/m^3 dosage.

Table 6.6 – Compressive peak strength of MSFRC with dosage of 8 kg/m^3 of fibres.

Sample ID	R_c [MPa]	R_{cm} [MPa]
Cu_1	60.8	58.6
Cu_2	56.4	
Cu_3	58.7	

Table 6.7 – Compressive peak strength of MSFRC with dosage of 10 kg/m^3 of fibres.

Sample ID	R_c [MPa]	R_{cm} [MPa]
Cu_1	61.4	58.9
Cu_2	54.8	
Cu_3	60.5	

6.4. EXPERIMENTAL CAMPAIGN ON TIME DEPENDENT PHENOMENA AND TEMPERATURE EFFECT ON MSFRC PERFORMANCE

6.4.1. Experimental campaign description

The combined effect of time dependent phenomena, creep and shrinkage, and temperature variations on macro-synthetic fibre reinforced concrete in a cracked state is investigated by performing an experimental campaign where the material is tested under sustained load in different loading conditions. As discussed before, during the flexural state, as the most common load condition, concrete is partially compressed, according to the position of the neutral axis, part of the deformation is induced by drying shrinkage and the fibres crossing the cracked surface undergo elongation and slippage at matrix interface. For this reason the experimental campaign sees the realization of:

a. Shrinkage tests
b. Compressive tests
c. Uniaxial tensile tests
d. Flexural tests
e. Tensile tests on single fibers.

All tests are performed in environmental controlled conditions in a chamber with a relative humidity of 55% and initial temperature of 20°C (since it is increased during the tests).

The peculiarity is the accurate and specific design of the different set-up to perform the tests because they should be adapt for the specimens positioning, the optimization of the number of samples to be tested, the application of sustained load, the realization of the boundary conditions, the allocation of instruments to monitor the displacement, the initial calibration of the load and the security in case of tertiary creep and, so, failure of the specimen. It should be underlined that the study of creep deformations in cracked state requires the pre-cracking of specimens applying the same condition of the creep test.

6.4.2. Materials

The fibre reinforced concrete tested is realized according to the mix design previously characterized (Table 6.8) and a dosage of 8 kg/m^{3}of the fibre type previously described (Table 6.5).

Table 6.8 – Concrete mix design and fibre dosage of the MSFRC tested under long term conditions.

Concrete component	Dosage 8 kg/m^3
CEM I 52.5R [kg/m^3]	400
Sand 0-1 mm [kg/m^3]	172
Sand 0-5 mm [kg/m^3]	730
Gravel 5-15 mm [kg/m^3]	837
Water [l/m^3]	184
W/C	0.46

6.4.3. Specimens cast

The mix design is realized using a concrete mixer with vertical axis where the constituents are inserted according to the procedure described in section 3.3.3. Globally two batches are produced, for reason connected to the maximum nominal capacity of the mixer (300 L) and the issues deriving from mixing a huge amount of material. First six cylinders, two cubes and five prisms are realized, the second batch includes eight prisms and two cubes while the fibres are used without previous threatments. All specimens are demoulded after 48 hours and cured in tanks filled with water at a constant temperature of 20°C.

(a) (b)

Figure 6.18 – Batches realized: (a) First batch; (b) Second batch.

6.4.4. Specimens preparation

The experimental campaign sees the realization of different specimen types and size, since many tests are performed, and each of them subjected to a proper preparation procedure.

To make it clear a global outline of the specimens produced and the respective test for what they are intended is presented in Table 6.9.

Table 6.9 – Outline of the number and specimens type, their dimensions and the type of test realized.

Specimen type	N° of specimens	Dimensions	Type of test
Cylinder	2	d=150 mm h=300 mm	Elastic Modulus
Cylinder	2	d=150 mm h=300 mm	Shrinkage
Cylinder	2	d=150 mm h=300 mm	Creep compression
Notched Prism	8	section=150 x 150 mm^2 length=600 mm	Creep flexural
Notched cored cylinder	12	d=125 mm h=150 mm	Creep uniaxial tensile
Cube	4	150x150x150 mm^3	Compression
Fiber	4	Le=23 mm	Creep uniaxial tensile

The specimens undergo a preliminary preparation for the experimental test.

Cylinders. The cylinders tested under creep compression load and used to calculate the elastic modulus are preparared levelling both surfaces, eliminating a part of

thickness equal to 2.5 cm by a disk saw (Figure 6.19), to assure uniform contact with the steel plate where load is applied.

Figure 6.19 – Preparation of cylindrical specimens for creep compression and elastic modulus tests eliminating a superior and inferior layer.

Cylinders for uniaxial tensile creep. The procedure of realization for the cylinders intended for uniaxial tensile creep tests is different because they are not cast directly in a cylindrical mould but they are cored from prismatic samples (Figure 6.20). First prismatic specimens of 150 x 150 x 600 mm^3 dimensions are cast (a), then each of them is divided into three equal parts maintaining the same section 150 x 150 mm^2 and a length 200 mm obtaining 15 partial prisms (b). The final cylinder is cored from each part, using a core drill of 132 mm external diameter and 124 mm internal diameter (c), generating 12 cylinders having a total height of 200 mm and final diameter of 125 mm (d).

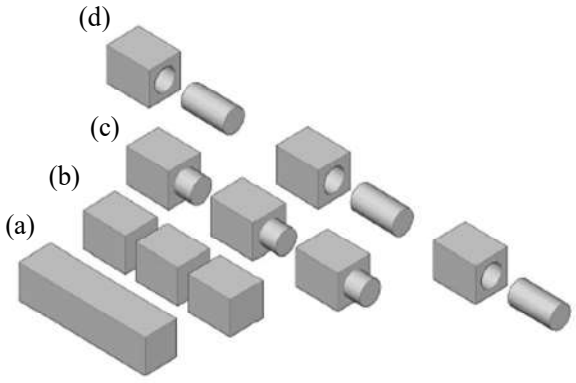

Figure 6.20 – Phases of cylinders coring.

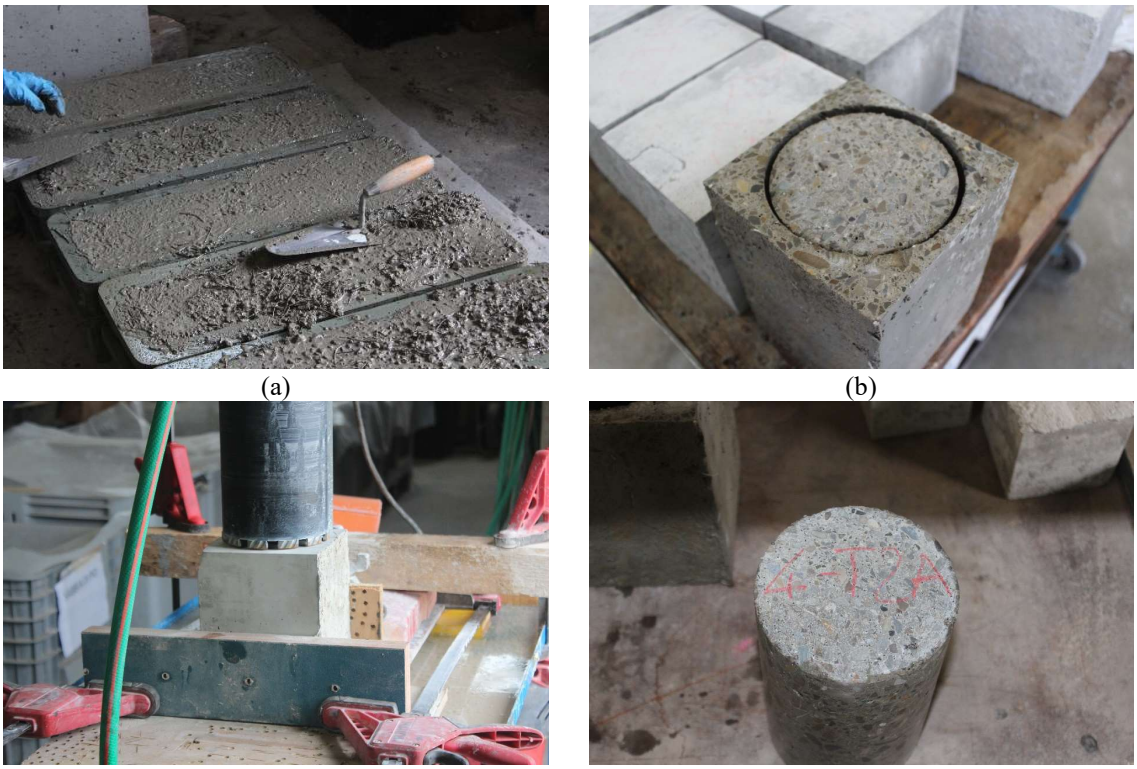

(a) (b)

(c) (d)

Figure 6.21 – Phases of cylinders coring: (a) Prismatic specimens realization; (b) Subdivision of each prism in three parts; (c) Coring of the prisms; (d) Cylinder cored.

The cylinders so obtained have been further levelled on both ends obtaining a final height of 150 mm: for this type of test it is necessary to realize two connections at the ends where the tensile load should be applied. For this reason two circular steel plates realized with the concrete cylinder diameter, 125 mm, and thickness of 40 mm, are glued using an epoxy mineral adhesive Geolite Gel, a bicomponent material (Figure 6.22a). Its complete drying is not immediate so it is possible to place correctly the external plates assuring the flatness of surfaces before preparing them definitely (Figure 6.22b and c). Moreover, the steel plates are connected by three allumium plates placed with a radial distance of 120° (Figure 6.22d) with an initial function of easing the drying of glue maintaining concrete specimen and steel plates together, and then, during the creep test, prevent the complete breakage of the cylinders into two parts compromising the entire test since a chain of three concrete samples will be

placed in the frame (section 5.6.8). Finally a notch is created at mid height of each cylinder with a depth of 10 mm and width of 4 mm (Figure 6.22d and e).

Figure 6.22 – Phases of cylinders preparation: (a) Geolite Gel adhesive preparation; (b) Thin adhesive layer on steel plate; (c) Steel plates glued on both ends of cylinders; (d) Connection with aluminium bars; (e) Notch produced at cylinder mid height (width 4mm, depth 10mm); (f) Notched cylinders.

Prismatic specimens. The prisms preparation consisted of creating a notch at mid span length on the side orthogonal to the cast direction (Figure 6.23), so that the load

is applied along the orthogonal direction. The position of the notch is preliminary drawn to help the accuracy of its realization.

Figure 6.23 – Creation of the notch at mid span length of the prismatic sample.

6.4.5. MSFRC compressive strength and elastic modulus

The elastic modulus, according to the European Standard, EN 12390-13, and the compressive strength are determined for the fibre reinforced concrete under investigation. The results are reported respectively in Table 6.10 and Table 6.11. For the compressive strength determination, two mean compressive strength values are reported because two different batches are realized (Table 6.10).

Figure 6.24 – Compressive tests.

Table 6.10 – Compressive strength at 28 days of MSFRC tested under sustained load.

Sample ID	R_c [MPa]	R_{cm} [MPa]
Cu_1 [1]	57.3	54.9
Cu_2 [1]	52.5	
Cu_1 [2]	55.6	54.5
Cu_2 [2]	53.4	

Figure 6.25 – Elastic modulus experimentally determined (EN 12390-13).

Table 6.11 – Elastic modulus at 28 days of MSFRC tested under sustained load.

Sample ID	E_c [GPa]	E_{cm} [GPa]
Cy_1	29.8	29.5
Cy_2	29.2	

6.4.6. Shrinkage test

Test procedure description

The shrinkage test is executed on two cylindrical specimens: as specified, the shrinkage phenomenon takes place in unloading conditions, so the samples are placed in the climate chamber and their deformation is monitored by means of two 60 mm long strain gauges (Figure 6.26b). They are glued using HBM X60 adhesive, on the later surface, before sanded and threaded with ethanol eliminating the superficial dust and impurities (Figure 6.26a), along the vertical axis of the cylinder that is the

direction where the drying shrinkage deformation should develop more and the sensor presents the higher sensitivity. The glue used has an immediate effect so the procedure should be performed accurately and in a fast way: for this reason the right position of the instrument is before traced with a pencil.

(a) (b)

Figure 6.26 – (a) Preparation of cylinders surface and (b) Strain gauges application.

Test results

The deformations induced by the drying shrinkage phenomenon are represented in Figure 6.27 for the two samples tested, where the intervals of temperature are reported. The temperature increment at 50 days and 175 days first generates an initial decrement of the deformation due to the alteration of the environmental conditions, when temperature increases the strain registered has an opposite direction, due to the expansion, and then the deformations start to increase again with a different rate. Within the test the rate at which the strain develops is different because the specimen gradually reaches an equilibrium with the enrivorment. However, in the reality condition of temperature and humidity are rarely constant.

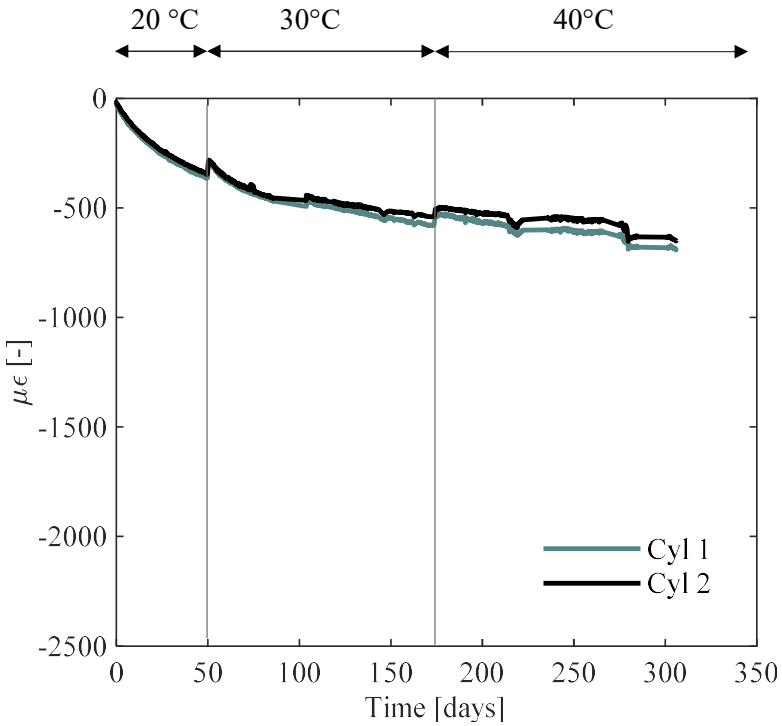

Figure 6.27 – Shrinkage deformation [microstrain] – time.

6.4.7. Creep compressive test

Test procedure description

The phase of preparation follows the same procedure described for the shrinkage test since the deformations, in terms of strain, are measured with the same sensor type, two strain gauges placed with a radial distance of 180°. In this case the strain profile is determined under sustained compressive load recorded during the entire period of the test.

As explained before, the load applied during long term tests is a percentage of the maximum strength to simulate the service conditions. In the present test the 20% of the maximum compressive load is applied: 192 kN. The samples tested are two: first they are accommodate in the loading framework (Figure 6.29) composed by two steel plates connected with four screwed steel bars positioned in the corners, then the load is applied by injecting oil in pressure using a hydraulic jack, whose oil pressure variations are compensated by an oil accumulator. The

calibration of the load is controlled by the load cell located under the top plate with which the specimen is in contact (Figure 6.28).

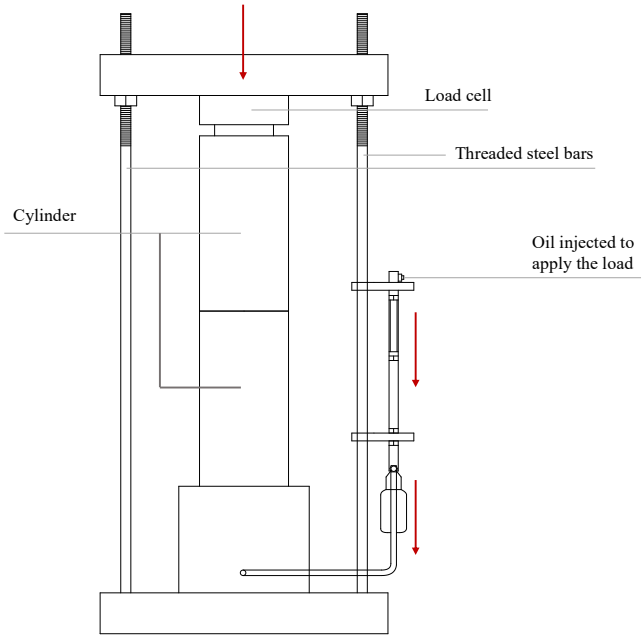

Figure 6.28 – Test set-up for creep compression tests

Figure 6.29 – Creep compression tests

Test results

Figure 6.30 represents the deformations exhibited by the two specimens under creep compression load including the contribution of the drying shrinkage. The temperature increment, during the test, invlolves an increment of the deformation due

to a rate acceleration that gradually decreases infact the trend of the curve becomes flatter as the rate starts to slow down. The specimens are unloaded at 280 days and the residual unrecovered strain is measured. Moreover, comparing the deformation recovered with the initial elastic deformation values, they appear to be consistent.

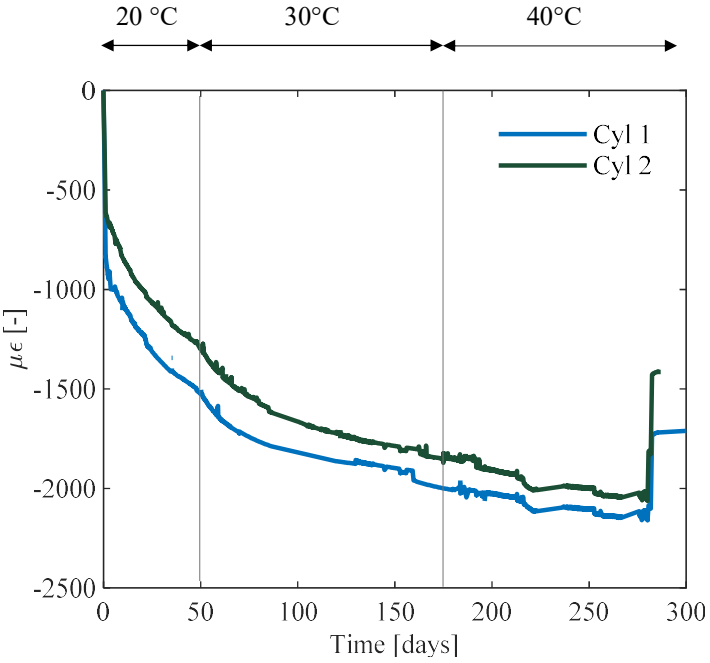

Figure 6.30 – Creep compression deformation [microstrain] – time.

6.4.8. Flexural creep test

Test procedure description

This load condition is simulated on time with the purpose of studying the creep deformations induced during the flexural cracked state of the fibre reinforced material analysed. For this reason, the specimens tested under sustained load are precracked to simulate the service state activating the fibers contribution.

Pre-cracking phase

The notched prisms are pre-cracked in three point bending configuration (Figure 6.31) according to the same testing procedure used to characterize the global material response standardized by the European regulation EN14651 (section 3.3.4). The test is carried out in crack opening displacement control with a rate of 0.05 mm/min for

CMOD < 0.1 mm and 0.2 mm/min until a crack opening value of 0.5 mm, corresponding to the residual flexural strength f_{R1}. Then the specimen is unloaded and the deformation is partially recovered, elastic deformation, showing a residual crack opening.

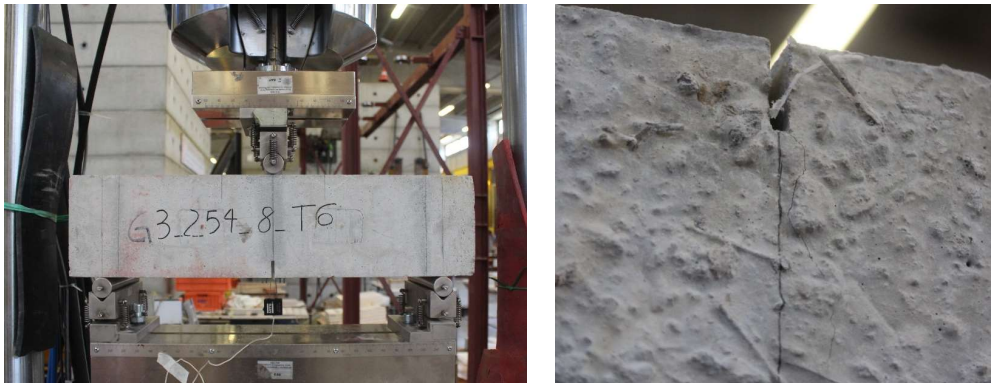

(a) (b)

Figure 6.31 – (a) Pre-cracking phase in three point configuration; (b) Detail of crack induced.

Pre-cracking test results

The curves output of the pre-cracking phase are reported in Figure 6.32 in terms of load – crack mouth opening displacement relation and the prisms exhibiting the higher residual strength are used for the creep test. After the unloading phase, the deformation is still recorded measuring the residual crack opening value.

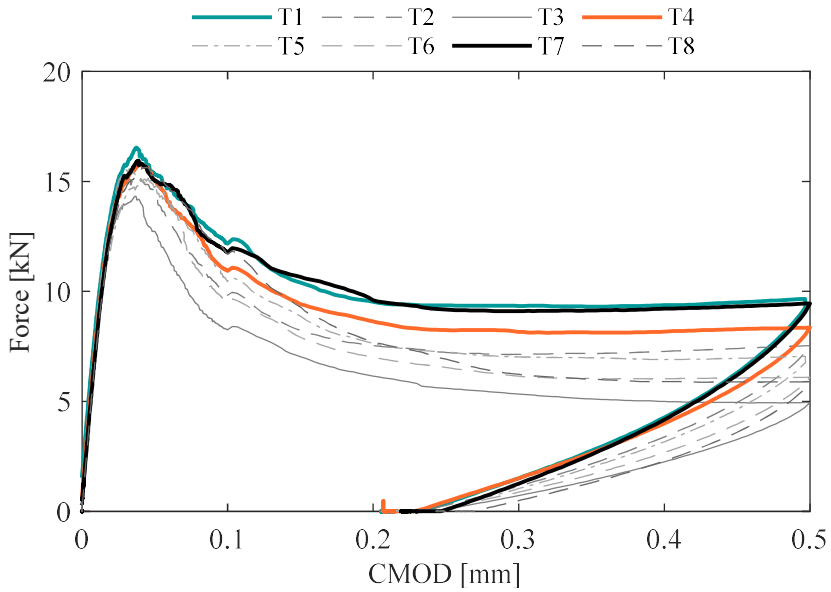

Figure 6.32 – Force versus CMOD for pre-cracked prisms.

Creep flexural test

During the creep flexural test, three specimens are tested at the same time since the loading frame allows the allocation of three samples. The frame functioning is based on the lever mechanism of 2° type characterized by the position of the fulcrum out of the two load application points (Figure 6.33). According to the distance at which the load is applied, the load received by the specimens is amplified: steel plates as dead weight are positioned on the lever arm and the load is transferred to all specimens by a series of steel plates with cylindrical supports (Figure 6.34b). During the creep test, the load is applied with according to four point bending configuration: in this way the maximum bending moment generated is extended to a larger zone than the middle cross section. Base supports are placed at a distance of 225 mm from the middle section while the loading supports have a distance of 75 mm from the centre. The constraint conditions realized by a system of 20 mm diameter cylinders allow the rotations around their longitunal axis and one of the base support allows also the rotation around the longitudinal axis of the prism in order to not create torsional stresses. The samples are ordered according to their residual strength, the prism allocated in the bottom part will be that characterized by the higher strength since it supports a higher load fraction. According to the position of supports in an alternate order and since the load is applied on the side opposite to the notch, the top and bottom prisms have the notched section oriented downwards while only the middle specimen is upward oriented. Table 6.12 shows the order in which the specimens are placed and the respective load ratio calibrated on the bending moment generated since the loading conditions during the pre-cracking and creep phase are different, from three to four point bending.

After the precracking phase, three out of eight specimens are selected according to the residual strength value showed at CMOD=0.5 mm, choosing those exhibiting the higher residual strength capacity. They are identified by the code T1, T4 and T7. The sustained load applied represent the 50 % of the residual strength but the exact percentage is calculated considering also the weight deriving from steel plates and

supports placed between the prisms. After the creep test, whose duration has been about 300 days, the specimens are unloaded continuing to register the deformation for some days, to measure the residual crack opening value.

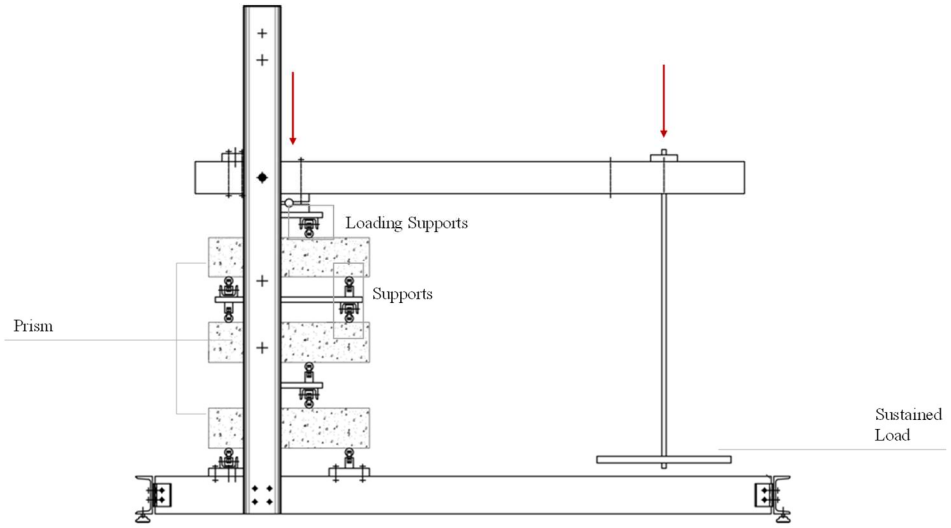

Figure 6.33 – Flexural creep test set-up based on lever arm of 2° type.

(a) (b)

Figure 6.34 – (a) LVDT displacement sensor of 2 mm measurement excursion; (b) Coloumn of three prisms under sustained flexural load.

Table 6.12 – Flexural creep test: pre-cracking load at 0.5 mm CMOD, creep load applied and load ratio of specimens tested under sustained creep load.

Sample ID	Pre-cracking bending moment [kNmm]	Creep bending moment [kNmm]	Load applied [kN]	Load ratio [-]
T4 [1st from the top]	1044.625	522.313	6.91	0.51
T7 [2nd from the top]	1182.125	591.063	6.91	0.49
T1 [3rd from the top]	1207.75	603.875	6.91	0.51

Creep test results

The results of the creep flexural test are reported in terms of crack opening displacement on time (Figure 6.35) and creep coefficient (Figure 6.36) for the prisms under sustained load. The creep deformation registered and the increment due to the change of temperature are both partly attributed to the concrete creep deformation because the section upon the neutral axis is compressed, partly to the fibre elongation in traction, to the gradual slippage deformations at interface fibre – matrix and in small part due to the creep deformation of the concrete under tension.

Observing the evolution of the creep coefficient on time that indicates how the deformation increases, during the first isothermal period, at 20°C, the crack opening increases noticeably at a high rate that during the next stages appears to be reduced and the trend of the curve, as observed before, is flatter.

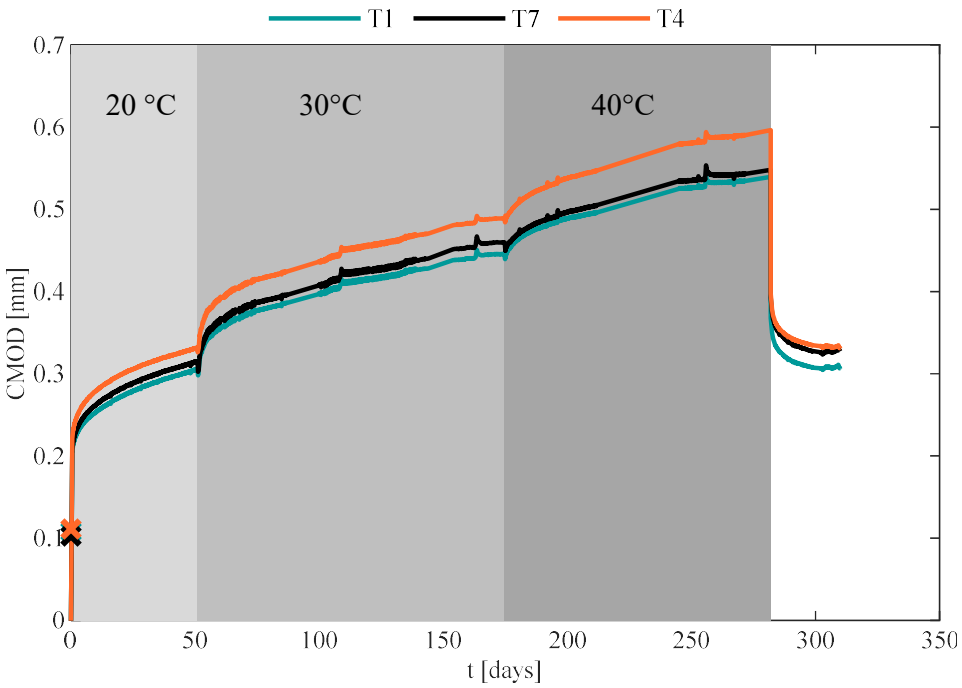

Figure 6.35 – Flexural creep test CMOD – time relation.

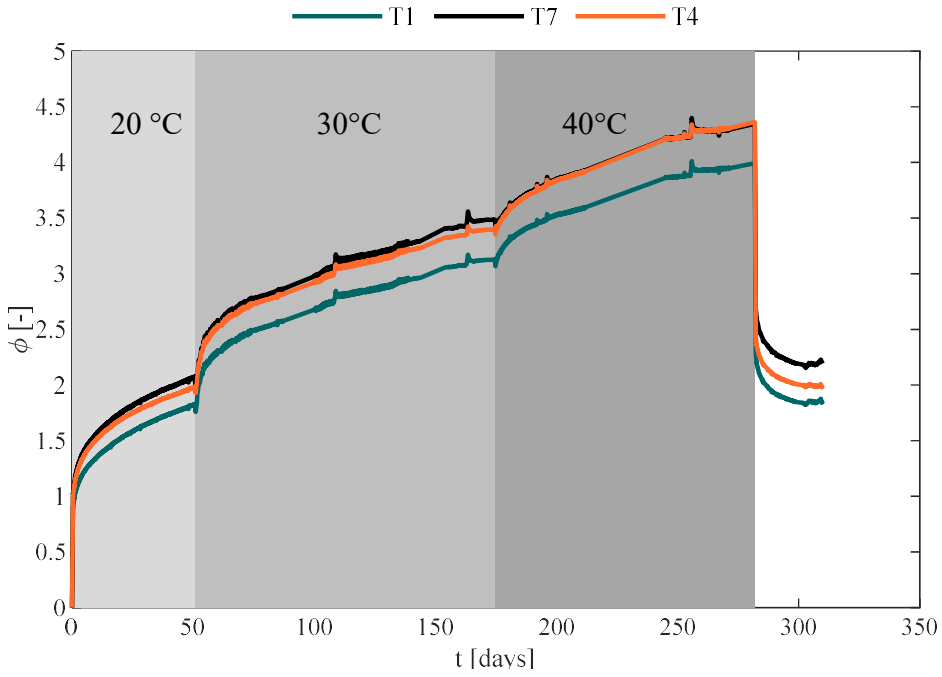

Figure 6.36 – Flexural test creep coefficient (in terms of crack opening) – time relation.

Failure phase

The behaviour of the material in service conditions is characterized by a third phase of test defined as the failure phase during which the deferred deformations influence the residual capacity of the material. It consists on reloading the specimen after the creep phase until a final crack opening value with the same loading configuration and velocity rate followed during the pre-cracking phase. Once the specimens are unloaded and the residual crack opening is measured, they are removed from the creep frame paying extremely attention to not apply strong movements or hit them, and then reloaded according to three point bending configuration. It should be underlined that all precracked specimens, those tested or not under creep load, are reloaded until failure. The envelope of the mechanical behaviour during pre-cracking, creep and failure characterize the flexural cracked capacity of the material under service conditions.

Failure phase results

All specimens are reloaded until the failure (Figure 6.37): the specimens tested under sustained load still exhibit a residual capacity higher than the others, although a creep test has been performed.

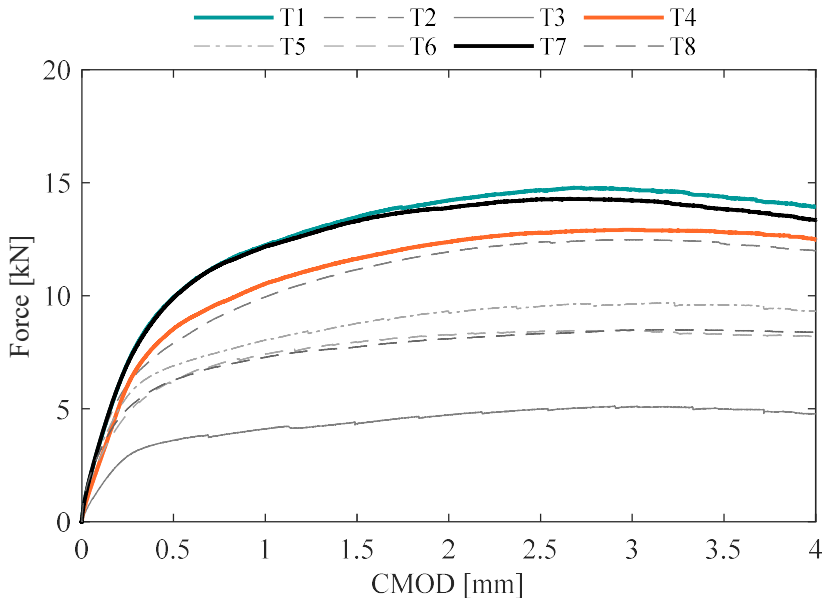

Figure 6.37 – Force versus CMOD for prisms failure phase.

The three phases, in case of prisms tested under sustained load, and two phases for prisms only pre-cracked and then reloaded, are unified (Figure 6.38): the envelope of the curve characterize the flexural behaviour of the material in cracked state.

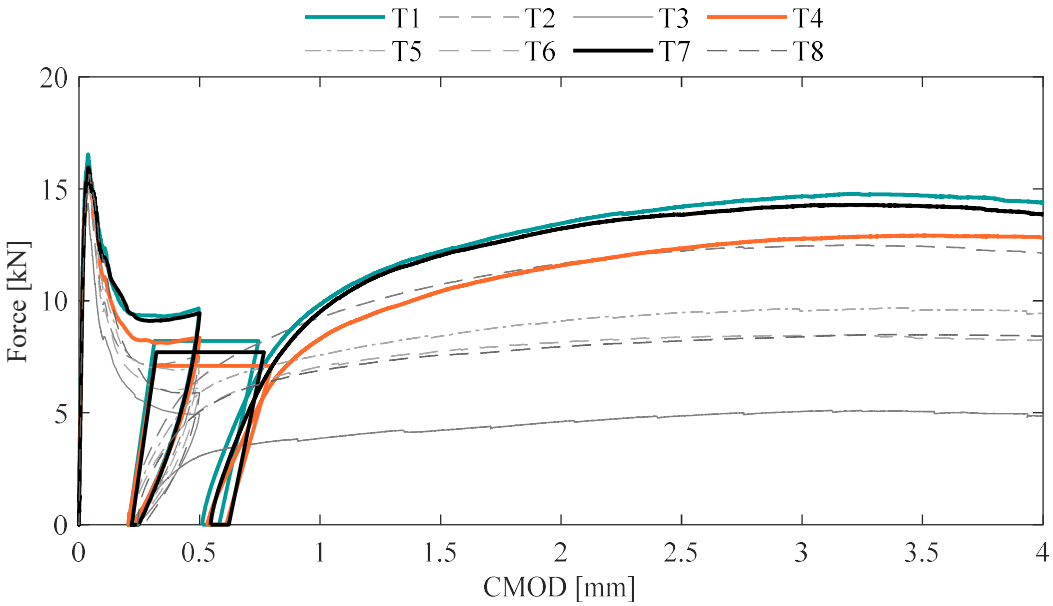

Figure 6.38 – Load – CMOD curve including the main phases of the flexural creep test.

6.4.9. Uniaxial tensile creep test

Test procedure description

The pure tension load condition is simulated on pre-cracked notched cylinders with the purpose of separating the tensile contribution. Actually the creep deformations measured are almost totally due to the viscous bond fibre-matrix and the viscoelasticity of the fibre itself since the creep deformation of concrete under pure tension is not remarkable.

Pre-cracking phase

The pre-cracking phase under pure tension loading conditions is performed using the servohydraulic machine already mentioned, with a capacity of 500 kN. Each cylinder, equipped with steel plates on both ends as described in section 6.2.2, is connected to the upper and lower grip system of the machine through articulated

joints allowing the rotations so that during the application of the vertical displacement no additional stress are induced. On the other side, the complication inherent in the test consists of the no symmetrical crack opening measurements. The displacement control is managed by three COD (Clip On Displacement) sensors placed at equal radial distance of 120° (Figure 6.39) and during the test different signals control are used (Table 6.13) until a final crack opening opening displacement value of 0.3 mm. The crack development is not uniform so the duration of the test is variable, after the maximum crack opening value is reached the cylinder is unloaded. During the test the allumium vertical bars connecting the steel plates are removed and after the test, replaced and saved for the duration of the creep test to preserve the cracked condition of the cylinder and reduce the possible deformation state changes.

Table 6.13– Signals monitored during the uniaxial tensile pre-cracking phase test.

Signal	Rate	Range
COD_{max}	0.005 mm/min.	$COD_{max} < 0.05$ mm
COD_m	0.005 mm/min.	$COD_m < 0.05$ mm
COD_m	0.01 mm/min.	$COD_m < 0.3$ mm

Figure 6.39 – Pre-cracking phase of cylinder under uniaxial tensile load and crack openind measured by COD at 120° radial distance.

Pre-cracking test results

The curves relative to the pre-cracking phase are reported in Figure 6.40 where it is possible to identify the loading until a crack opening value of 0.3 mm and then the unloading branch according to the residual deformation faced by each cylinder.

The solid curves represent those selected and used for the creep tests.

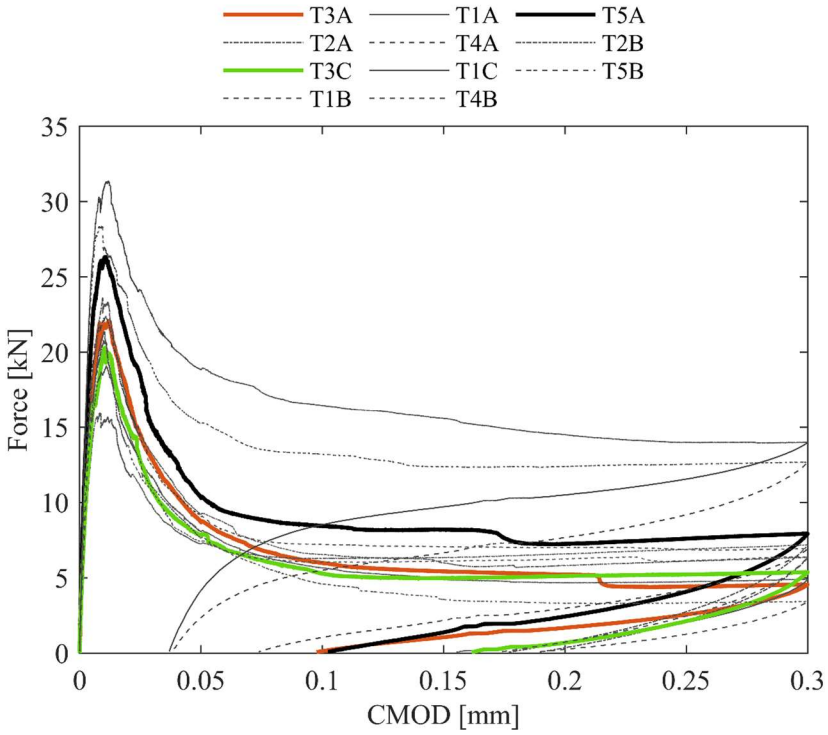

Figure 6.40 – Force versus CMOD for pre-cracked cylinders.

Uniaxial creep tensile test

After the pre-cracking phase, three cylinders out of fifteen are selected according to the higher redisual tensile strength gained and the small scatter that basically results high in this type of test. The cylinders used are indetificated with the codes T3A, T5A, T3C where the number represents the original entire prism while the letter refers to the part from which they are cored A and C are the external 200 mm length parts, B that in the middle. The cylinders are connected creating a chain equipped with steel eyebolts to both ends and connected each other by steel rings: in this way the free rotation boundary condition is realized (Figure 6.42b).

The loading frame has a supporting base realized with two longitudinal channel sections made stiffer with transverse channel sections welded on them and also two vertical channel sections connected to the upper lever arm where the dead weight for the application of the load are placed. In this case the fulcrum is between the two application points so the lever system is of 1° type so the load is applied to transfer a uniaxial tensile force (Figure 6.49). The allocation of the cylinders is preceeded by the load calibration using a load cell screwed to threaded bars inserted in the same position of the cylinders chain (Figure 6.42a). Then, the specimes are connected one by one starting from the first connected to the lever arm that is the one characterized by the higher tensile strength since in this case the order is opposite respect to the flexural case. In Table 6.14 are reported the specifications about the order of specimens in the chain, the pre-cracking load, the creep load and the effective load applied during the creep test. The calculation of the load ratio accounts for the additional weight of the articulated joints connecting the cylinders. During the placement phase, the lever arm is kept horizontally without applying any load by mean of a threaded steel bar, after that the bar is removed so the lever weight is applied and then the calibrated load is added. Figure 6.42b shows the chain of three cylinders under uniaxial tensile sustained load. The crack opening during the creep test is monitored by using LVDTs with 2 mm excursion placed at 120° inserted in steel supports glued on either side of the crack, one of them is holed, the other represents the contrast part for the sensor. The deformations are monitored during all procedure and, abviously, during the test. As for flexural tests, after 300 days the specimens are unloaded and the crack opening is measured until an almost horizontal trend of the deformation is reached: this condition is associated with the elastic crack opening recovering.

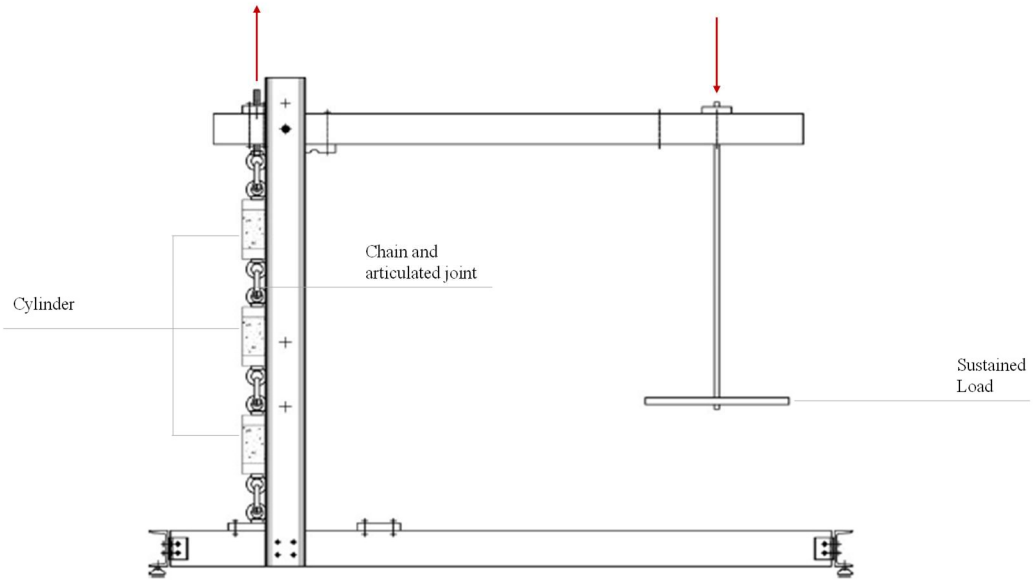

Figure 6.41 – Lever system for creep tensile test on MSFRC cylinders.

(a) (b)

Figure 6.42 – (a) Calibration of the sustained uniaxial tensile load by a load cell; (c) Chain of three cylinders under uniaxial tensile load.

Table 6.14 – Uniaxial tensile creep test: pre-cracking load at 0.3 mm CMOD, creep load applied and load ratio of specimens tested under sustained creep load.

Sample ID	Pre-cracking load [kN]	Creep Load [kN]	Load Applied [kN]	Load ratio [-]
T5A [1st from the top]	7.93	3.97	3	0.38
T3A [2nd from the top]	4.56	2.28	3	0.60
T3C [3rd from the top]	5.38	2.69	3	0.53

Creep test results

The mechanical behaviour of the material under sustained uniaxial tensile load is represented in terms of crack opening displacement on time (Figure 6.43) and creep coefficient (Figure 6.44). The cylinder named T3C exhibits the higher deformation if compared to the others and it exhibits also the higher residual crack opening during the pre-cracking test. This result can be attributed to a particular distribution of fibers on the cracked surface leading to a higher residual crack-opening and, so, higher deformations during the tensile creep test. Moreover, comparing the behaviour of the material under tensile and flexural creep load, what is important to notice is the increment of the deformation and creep coefficient as the temperature increases. The difference might be attributed to the fact that the major contribution of the deformation is given by the fibre elongation and interface slippage and, since polymers suffer a lot creep and temperature phenomena, this test reflects a lot the behaviour of the fibre. Moreover, the gradual elongation of the fibre leads to the reduction of its section due to the poisson effect and so the bond slip is enhanced. The two mechanisms are strictly connected because, considering the pull-out of the single fibre, it will start to debond creating a debonded zone where the fibre starts to creep. The deformation leads to a lateral contraction for the Poisson effect on time. Gradually the bonded length decrases because the creep deformations of the single fiber until the pull-out failure (Vrijdaghs et al., 2017). According to this, the deformations measured during a creep pull-out test include the contribution of the fibre creep itself. The interface between fibre and matrix becomes weaker and, in

particular for the fiber tested, the loss of the crimped profile modifies the bond strength and the elastic modulus on time. It is not easy to quantitatively estimated this change but, in the following section (7.5), an analytical approach to consider the creep deformation for the single fibre will be proposed. The formulation will account for the modification of the fibre elastic modulus on time trough a coefficient contained in the expression presented.

Observing the creep deformations evolution in terms of creep coefficient (Figure 6.44), the difference between the three samples is reduced but still the scatter is higher than in case of flexural creep tests.

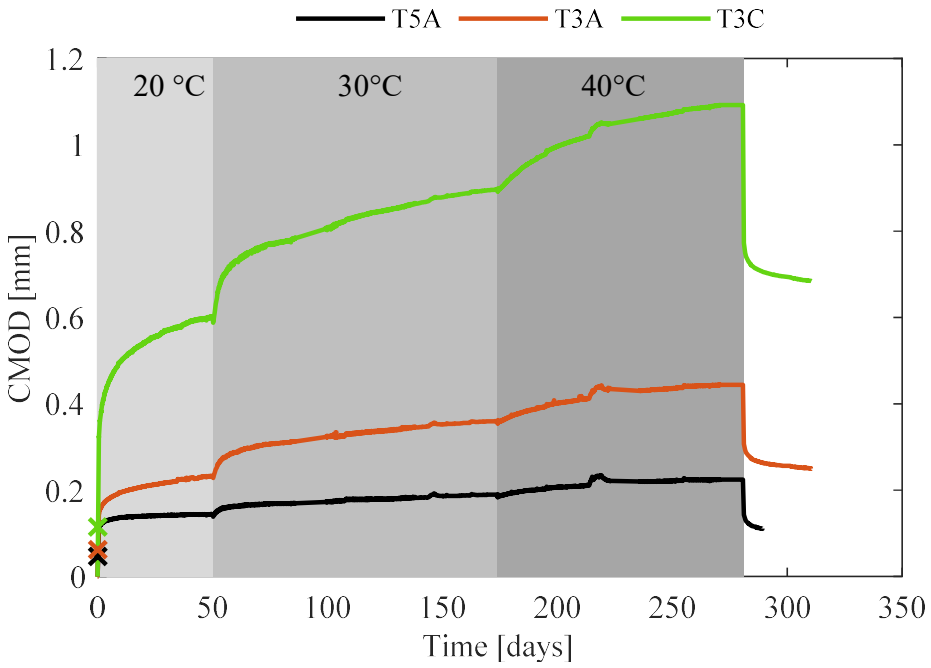

Figure 6.43 – Uniaxial tensile creep test CMOD – time relation

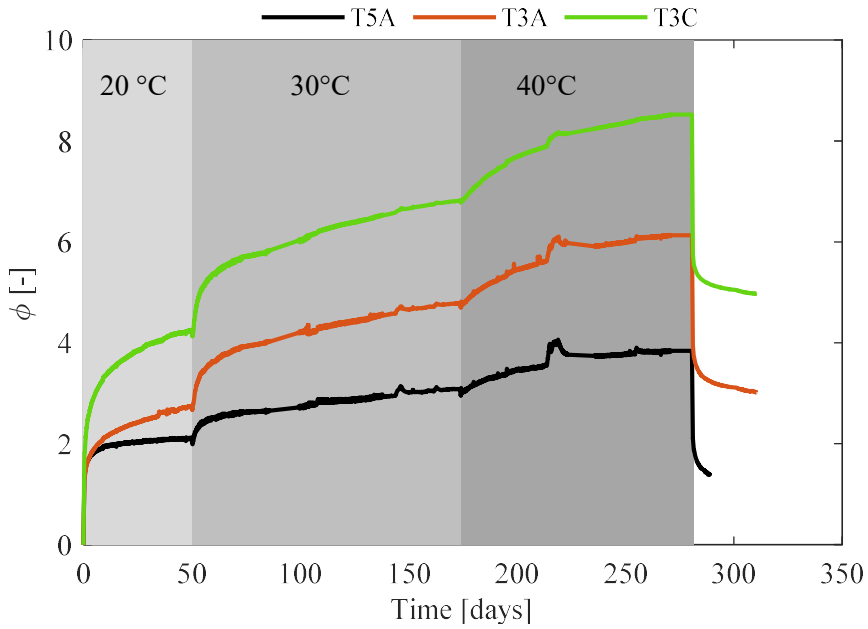

Figure 6.44 – Uniaxial tensile test creep coefficient (in terms of crack opening) – time relation.

Failure phase

After the creep test the cylinders are removed and the reloaded until failure in the same loading and boundary conditions realized during the pre-cracking phase. The crack opening is monitored using three COD at 120° and the test is carried on in mean crack opening displacement control at a constant rate of 0.2 mm/min. The behaviour of the material during the failure phase is different in case of uniaxial tensile load because a uniform load condition is applied and the residual stress has a softening branch more pronounced than in flexural state where the section above the neutral axis is compressed.

Failure phase results

The curves representing the last stage of the creep test are reported in Figure 6.45.

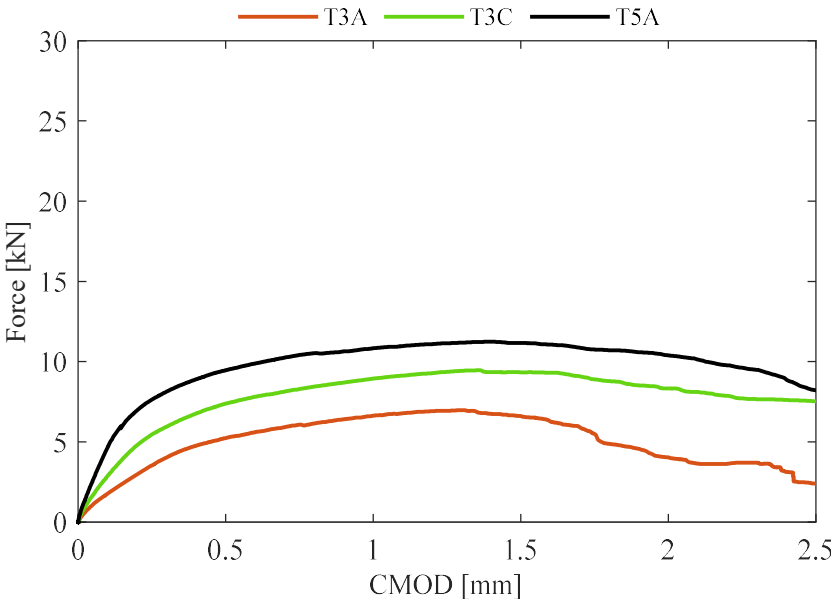

Figure 6.45 – Force versus CMOD for cylinders failure phase.

Considering all phases of the creep test under uniaxial tensile load, the scatter in the behaviour is more pronounced than for the flexural tests bacuase of the type of loading condition.

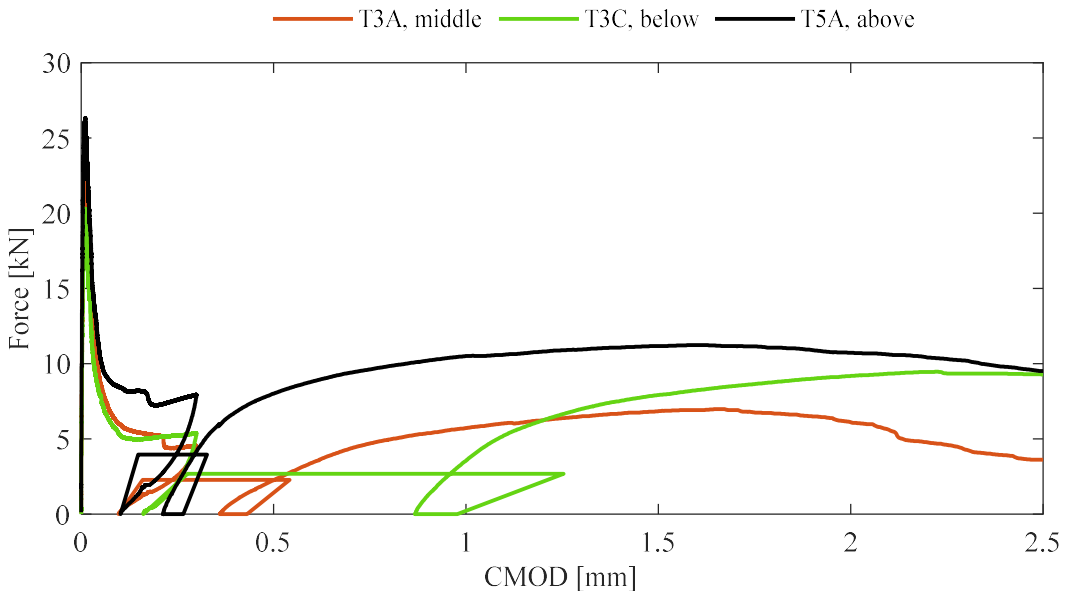

Figure 6.46 – Load – CMOD curve including all pahses of the uniaxial tensile creep test.

6.4.10. Tensile test on single fibre

Test procedure description

The unique contribution of the fibre viscoelasticity to the creep deformation of the macro-synthetic FRC material is measured performing tensile creep tests on the single fibre. The tensile strength is first characterized trough direct tensile tests on a group of fibers under short term behaviour.

Tensile strength characterization

The short term tensile test is performed using the same servohydraulic frame described in section 3.3.4, with an additional load cell of 2kN capacity. During the test the displacement of the stroke is controlled with a feed rate of 5 mm/min and the fibre is gripped on both ends using the same system adopted during the pull-out tests (see section 3.1.4): allumium plates with sand paper glued on their internal sides so that relative displacements between the fibre and the plate are avoided (Figure 6.47). The plates are tightened using the gripsof the servohydraulic machine. The tests are carried out until the breakage of the fibre. The typical output of the test is the curve in Figure 6.48: the tensile strength and elastic secant modulus are so characterized referring respectively to the peak strength calculated on the cross section whose nominal dimension are indicated by the producers and the correspondent strain computed dividing the elongation measured during the test by the fibre free length between the steel plates. The mean tensile strength and elastic modulus are considered on eleven tests (Table 6.15).

(a) (b)

Figure 6.47 – (a) Set – up of a tensile test on a single fibre; (b) Fibre under tensile load.

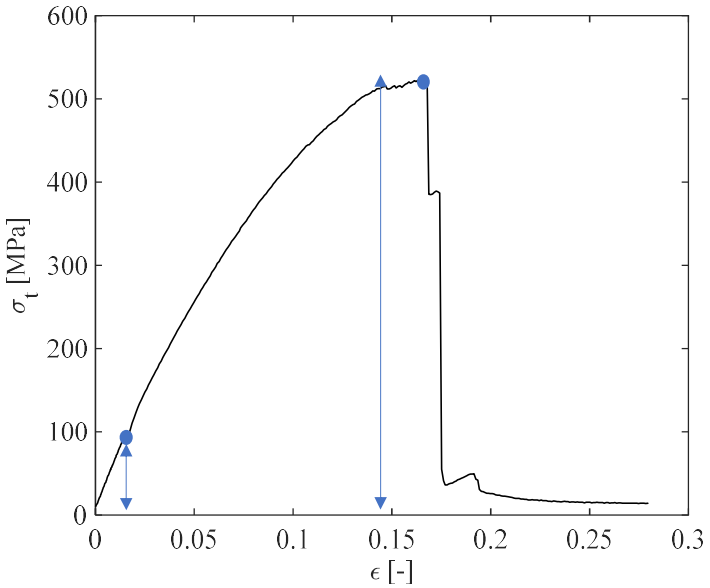

Figure 6.48 – Stress – strain curve of a fibre direct tensile test.

Table 6.15 – Fibre tensile strength and elastic modulus evaluated by direct tensile tests on a group of 11 fibres.

Specimen ID	Tensile strength [N]	Tensile strength [MPa]	Elastic secant modulus [GPa]	Elastic tangent modulus [GPa]
B1	218	422	3.96	4.97
B2	206	400	3.04	3.85
B3	223	432	3.45	5.42
B4	269	522	3.20	5.21
B5	244	473	2.00	3.26
B6	235	456	2.57	3.49

B7	254	492	1.04	1.74
B8	269	522	2.29	3.85
B9	261	506	1.82	2.89
B10	224	436	2.32	3.85
B11	279	541	-	-
Mean Values	244	473	2.6	3.9
COV	0.095	0.095	0.32	0.28

Tensile creep test

After characterizing the tensile strength of the fibre, the 20% and 40% of the maximum load are applied during the creep tests. The frame used to perform the uniaxial tensile creep test is reproduced at a smaller scale to apply a sustained tensile load to the single fibre (Figure 6.49). The system is composed by a steel base where two vertical C-profiles are bolted and the lever arm is connected to them by a passing pin reproducing the fulcrum of the lever. The fibre is allocated between two small steel cylinders: the lower is screwed in the base while the upper is connected first to a system of two cylinders, one screwed into the other and, by a passing pin and these are linked to the lever arm by an additional pin.

The fibre is gripped in two different ways according to the percentage of load applied. For the lower load, the fibre is glued with HBM X60 adhesive injected in the cylinders where the fibre is embedded. For the higher load the cylindrical supports have been previously notched for a depth of 3 mm and width of 3 mm and paper sand is inserted in order to grip perfectly the fibre. The different technique is adopted because of the slippage of the fibre under a higher load: this is supposed to happen because the bond strength with between the fibre and the glue is lower than the tensile strength. It is important to underline that the loading frame and the mutual distances of all set-up components are calibrated so to estimate the fibre free length during the test, in this way the precise placement is achieved.

The procedure followed starts from the frame calibration with the load cell of 2 kN capacity (Figure 6.50a), then the fibre is inserted first in the lower cylinder for an embedded length of 15 mm and then the upper part is connected gluing or gripping

the fibre for a length of 16 mm producing a free length value of 23 mm over 54 mm of total length (Figure 6.50b). During this procedure the lever arm is maintained in horizontal position by a screwed steel bar removed at the beginning of the test.

The elongation of the fibre is monitored during the test with two LVDTs of 10 mm fixed to the upper cylinder with an alluminium support with three holes, the middle accommodating the fibre cylinder and the two externals the linear sensors. The contrast support where the instruments point is fixed to the lower cylinder. The elongation measured is divided by the free length of the fibre obtaining the correspondent strain.

Table 6.16 – Load applied during the creep test on the fibers.

Sample ID	Load ratio [%]	Load applied [N]	Stress applied [MPa]
Fib A 20%	20	48	93
Fib B 20%	20	48	93
Fib A 40%	40	96	186
Fib B 40%	40	96	186

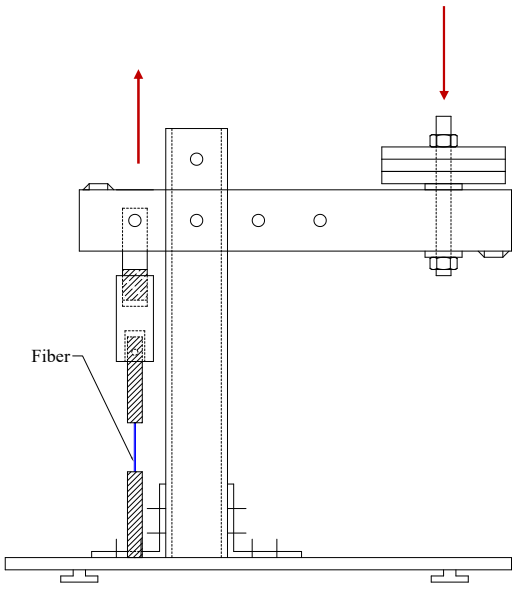

Figure 6.49 – Fibre tensile creep test set-up based on lever arm of 1° type.

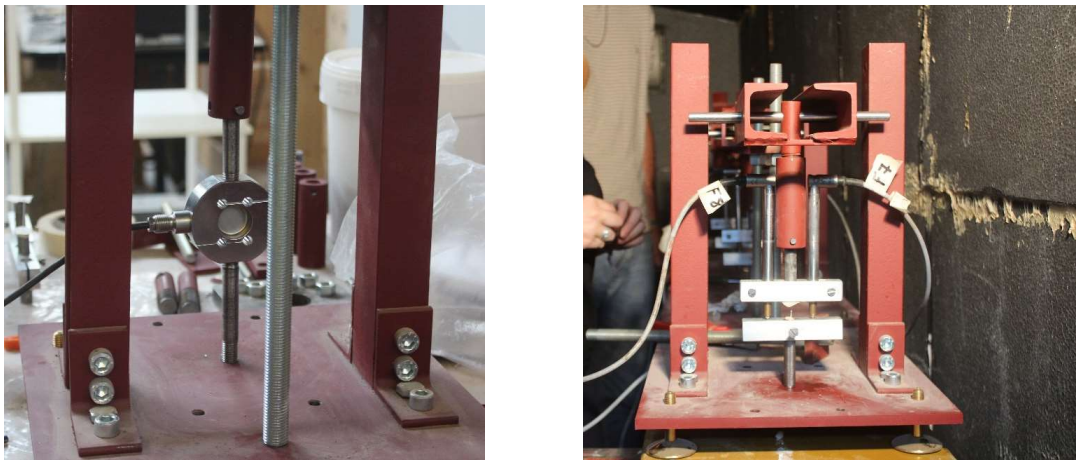

(a) (b)

Figure 6.50 – (a) Calibration of the creep loading frame with a 2 kN capacity load cell; (b) Tensile creep test on a single fibre.

Fibre tensile creep test results

The deformations gained by the fibre under sustained load is represented in terms of strain and creep coefficient on time for the lower load applied in Figure 6.51 and Figure 6.53 and the higher load percentage in Figure 6.52 and Figure 6.54. The data reported for the fibre loaded at 40% refer to a shorter time period as these tests started late due to issues linked to the gripping system that required many initial trials.

Comparing the initial elastic deformation at the loading instant, the values are almost consistent because the value exhibited by the fibre with higher load, 0.082, is approximately four times the value exhibited by the lower load fibre, 0.02, considering the difference of temperature at which the fibre is loaded. Moreover, the difference in the response can be addressed also to the different gripping systems because, although a lower load is applied, the fibre can endure a slight relative displacement at interface with the adhesive. This is also highlighted by the difference between the two responses of the fibre equally loaded, for the higher load the curves of the two specimens are more consistent.

The creep coefficient is an indicator of the long term deformation evolution. for this reason comparing the creep coefficient calculated on the fibre creep tensile test and those measured on the uniaxial test of the MSFRC material, the difference of

values, between 1 – 2 the former, 2 – 4 for the latter, can be explained by the fact that the viscoelastic mechanisms activated during the uniaxial FRC test regard the elongation of the fibre itself but also the viscoelastic deformations developed at interface fibre – matrix that cause the gradual fibre slippage.

It is important to specify that the results are reported for two fibers loaded at each ratio but the scatter in results, within the same load applied, is not so pronounced. Moreover, the use of the same gripping technique might reduce also the dissimilarity in creep coefficient. This condition could be also attributed to the different temperature, 20°C for lower load and 30°C for higher load, at the beginning of the test.

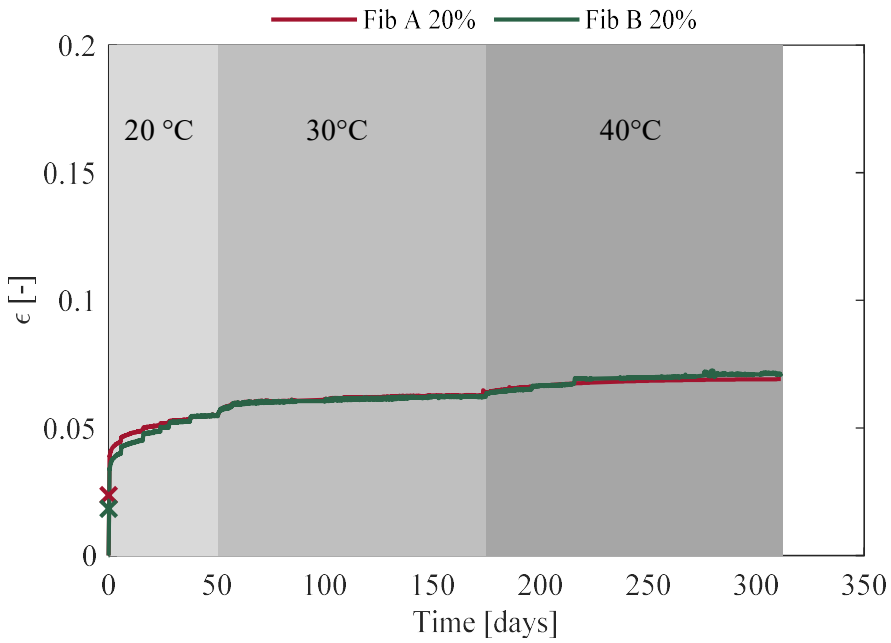

Figure 6.51 – Fibre tensile creep test: Strain – time relation for fibers loaded at 20% of the tensile strength.

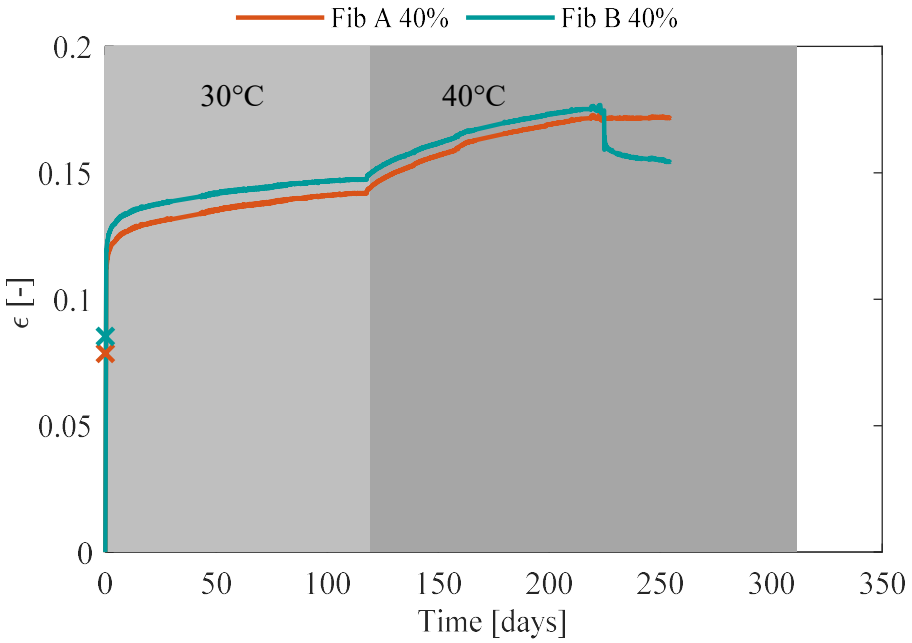

Figure 6.52 – Fibre tensile creep test: Strain – time relation for fibers loaded at 40% of the tensile strength.

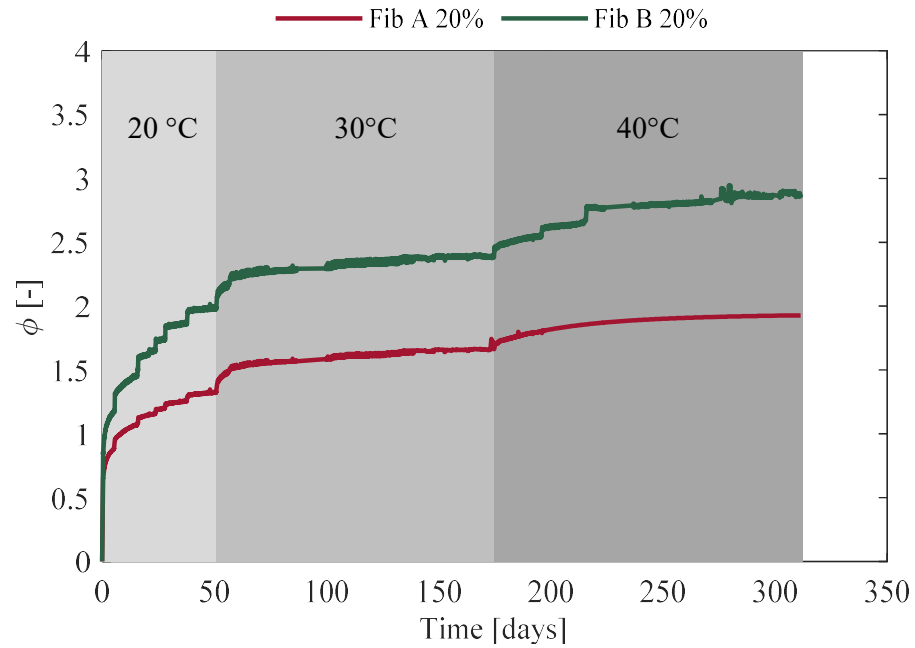

Figure 6.53 – Fibre tensile creep test: (a) Creep coefficient – time relation for fibers loaded at 20% of the tensile strength.

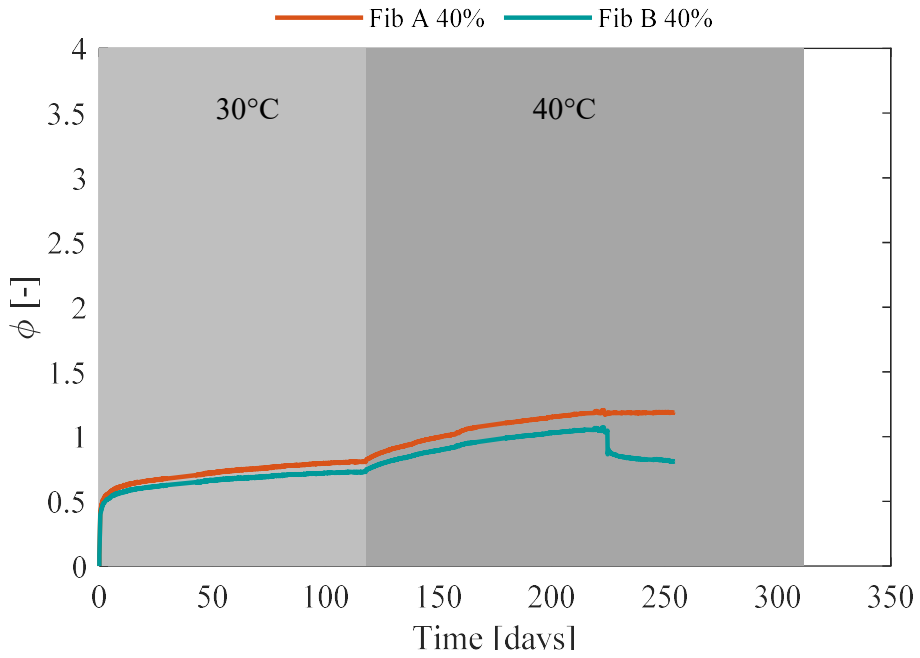

Figure 6.54 – Fibre tensile creep test: Creep coefficient – time relation for fibers loaded at 40% of the tensile strength.

In addition, a further loading frame is proposed to study the pull-out mechanism of the fibre embedded in concrete over time. The external structure and the system of connections are the same presented for the fibre creep tensile test but the concrete cube is blocked by two horizontal steel slats with two external holes each where four threaded bars are screwed on the base.

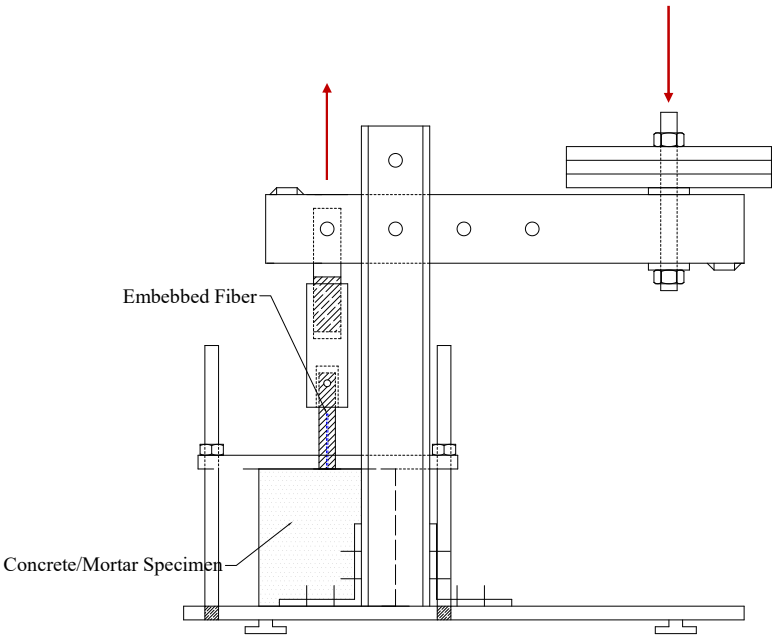

Figure 6.55 – Fibre pull-out creep test set-up based on lever arm of 1° type.

CHAPTER 7

7. NUMERICAL PREDICTIVE MODEL OF SHORT AND LONG TERM PERFORMANCE OF MSFRC

7.1. INTRODUCTION

The complexity in modeling the mechanical behavior of fiber-reinforced concrete lies in the heterogeneity of the concrete and the randomness of the fibers distribution, that are characteristics to be considered in order to elaborate a reliable numerical model.

The fibers orientation is mostly driven by the flow casting direction and influences the mechanical properties (Ferrara, Shyshko, and Mechtcherine, 2012). Many attempts are advanced in literature elaborating numerical models to study the sectional stress distribution or the mechanical behaviour of the entire material. For example Mobasher and Barsby started from the constitutive stress-strain law predicting the flexural tensile behaviour of strain-hardening composite materials performing a parametric study (Mobasher and Barsby, 2011). In the field of finite element approaches, the behaviour of SFRC is proposed by Bernardi et al. with the implementation of a constitutive 2D-PARC relation, used for reinforced concrete elements and extended to account for steel fiber reinforcement (Bernardi, Cerioni, and Michelini, 2012). The approach followed can be included in the field of smeared-fixed crack models and considers the total strain as the superposition of the concrete and the crack itself. Furthermore, in the perspective of studying the cracked behaviour of FRCs, the prediction of the crack width of FRC beams represents also a topic studied (Vasanelli, Micelli, Aiello, and Plizzari, 2014).

In this framework the present work deals with the numerical approach for macro-synthetic fibre reinforced concretes with the lattice discrete particle model (LDPM, LDPM – F) theory. The last twenty years literature have advanced many models describing concrete in mini-scale (less or equal to 10^{-4} m) and meso-scale (10^{-3} m) (Cusatis, Pelessone, and Mencarelli, 2011). In the context of meso-scale theories, the Lattice Discrete Particle Modelling theory is one of the most validated with the ability of describing the aggregates particles interaction simulating the mechanical processes of concrete.

Recently the LDPM theory for concrete has been extended to include the fibers reinforcement contribution to the crack-bridging phenomenon: this approach is named LDPM-F. Cusatis et al. (Jin, Buratti, Stacchini, Savoia, and Cusatis, 2016) calibrated and validated the LDPM-F approach for concretes reinforced with straight synthetic and steel fibres.

The present work starts with the calibration and validation of the LDPM-F theory for a concrete reinforced with polypropylene crimped fibres on the experimental results exposed in chapter 6. The calibration phase is developed in two phases: the calibration of LDPM concrete parameters on experimental results for the plain concrete and consequently the fibre-concrete interaction parameters are calibrated on the experimental results of the same concrete reinforced with 8 kg/m^3 of polypropylene crimped fibres. The validation phase is preceeded by many considerations involving the parameters accounted and calibrated: concrete minimum aggregate size, fibre elastic modulus and fibre count. In addition, the influence of the LDPM approach extended to the entire specimen length or to the part involved in the cracking process, is detected. The constitutive law is then validated on the experimental results of the same concrete reinforced with a higher fibre dosage of 10 kg/m^3. On the basis of the mechanical parameters calibrated for concrete, fibers and matrix – fibre interaction, a numerical model accounting for the viscoelastic behaviour of both constituents, concrete and polymeric fibers, is proposed. The model is based on the extended LDPM theory coupled with HTC model and discrete Microprestress Solidification theory, M-LDPM (Abdellatef, Boumakis, Wan-Wendner, and Alnaggar, 2019). The present formulation is further extended to consider the viscoelasticity of polymeric fibers, M-LDPM-F. The numerical modeling procedure makes use of the experimental creep test results, in particular the viscoelastic behaviour of concrete is calibrated on shrinkage and creep compressive tests, the viscoelastic behaviour of fibers on the tensile creep tests on the single filament while the entire behaviour on the uniaxial creep tests on the MSFRC. This loading condition, in particular if applied to pre-cracked specimens, generates a

deformative state whose major contribute is given by the fibre deformation and the viscoelastic bond so the results can be used for the calibration of both phenomena. The work here exposed includes the viscoelastic behaviour of the polymeric reinforcement but not the viscoelastic bond that represents a further development of the numerical model. Thus, the creep flexural test results will be used as a validation of the model calibrated accounting for both phenomena.

The adoption of the present numerical approach could allow, on one side, the reduction of the experimental effort for the FRCs characterization phase and, on the other side, the analysis of the time dependent deformations whose evolution and prediction is an aspect still under investigation.

The numerical approach proposed in the present chapter is developed in collaboration with the scientific staff of the Institute of structural engineering, Christian Doppler Laboratory of Boku University in Vienna.

7.2. LDPM THEORY

The LDPM theory is the result of the Confinement Shear Lattice (CSL) theory combined with Discrete Particle Model (DPM). This approach takes the capabilities of the first theory in terms of simulation of the concrete mesoscale because concrete aggregates are materialized with particles connected together through the Delaunay tetrahedralization starting in the aggregate centre. The lattice connecting all particles is organized according to polyhedral cells each of them incorporating a piece of aggregate whose internal layout is regulated by the aggregates size. Their interaction occurs with shear or normal stress components; the pure tension and shear-tension behaviour is regulated by a softening meso-scale constitutive law while the pure compressive behaviour and shear compressive by a plastic hardening constitutive law.

LDPM saves also the DPM theory aspects regarding the computational nature of the theory that allows the estimation of the particles trajectories integrating their equilibrium force equation (Bakker, 2006): the most important feature is the

simulation of the particles separation and fragmentation that describes the material failure.

The LDPM formulation keeps these aspects adding new features, a volumetric effect is included because the tetrahedralization involves four vertexes, i.e. the centers of four aggregate pieces; the cracking process can be better described since the stress and strain computation is performed on every single facet of the polyhedral cells; the proper description of phenomena regulating failure in tension and compression makes possible to show better capabilities in prediction of the compressive macroscopic behavior. Finally, cyclic loading conditions can be performed and the effect of a high confinement can be described.

The concrete structure is built on several elements as the number and size of the aggregate particles, located in a specific position, connected to each other and having a surface through which the force transmission is handled. This structure is generated assigning the mix design properties as input parameters: cement content per unit volume (c), water-cement ratio (w/c), maximum (d_a) and minimum (d_0) aggregate size. The following equation describes the aggregate size combination according to the diameter distribution as the typical Fuller curve used in concrete design:

$$F(d) = \left(\frac{d}{d_a} \right)^{n_f} \qquad [7.1]$$

with n_f Fuller coefficient. Then, the real aggregate volume fraction v_a is computed according to the water and cement fraction: the LDPM aggregates volume is calculated as

$$v_{a0} = \left[1 - \left(d_0 / d_a \right)^{n_f} \right] v_a \qquad [7.2]$$

computing the total volume of simulated aggregates V_{a0}. Then the particles are generated following the relation in Figure 7.1a relating P_i a random number between 0 and 1 with d_i the diameter of the single particle:

$$d_i = d_0\left[1 - P_i\left(1 - {d_0}^q \Big/ {d_a}^q\right)^{-1/q}\right] \qquad [7.3]$$

The generation procedure is arrested when the new volume of generated particles is bigger than the total volume computed V_{a0}. The external surface of the simulated concrete specimen is realized with vertexes, edges of L_e length and polyhedral faces of A_p area, so N_e and N_p nodes (particles with zero radius) are associated respectively with each edge e and polyhedral face p. Their dimensions are regulated by the mesh size h_s chosen as $1.5d_0$ the minimum aggregate size so that the external discretization reflects that internal. Afterwards, the particles allocation is generated with a distance between the particles centers of $d_i/2+d_j/2+\zeta d_0$ avoiding overlaps of new particles with the previous generated.

The important aspect to be born in mind is that the Delaunay tetrahedralization connects four particles center creating a surface where the interaction and, consequently the failure, takes place (Figure 7.1b). Each tetrahedron can be subdivided in four subdomains whose displacement components u_i are related to the position of the generic node x_i through the expression:

$$\boldsymbol{u}(\boldsymbol{x}) = \boldsymbol{u}_i + \boldsymbol{\theta}_i \times (\boldsymbol{x} - \boldsymbol{x}_i) = \boldsymbol{A}_i(\boldsymbol{x})\boldsymbol{Q}_i \qquad [7.4]$$

where $\mathbf{Q}_i^{\mathrm{T}}=[\mathbf{u}_i^{\mathrm{T}}\boldsymbol{\theta}_i^{\mathrm{T}}]$ unifies traslational and rotational degree of freedom of the generic node.

Considering the centroid C of each tetrahedron facet and his displacement $\mathbf{u}_{Ck}$ is possible to define the facet strain vector that decomposed along three directions one obtains:

$$\begin{aligned}
\varepsilon_{Nk} &= \frac{\boldsymbol{n}_k^T[\![\boldsymbol{u}_{Ck}]\!]}{l_e} = \boldsymbol{B}_N^{jk}\boldsymbol{Q}_j - \boldsymbol{B}_N^{ik}\boldsymbol{Q}_i \\
\varepsilon_{Mk} &= \frac{\boldsymbol{m}_k^T[\![\boldsymbol{u}_{Ck}]\!]}{l_e} = \boldsymbol{B}_M^{jk}\boldsymbol{Q}_j - \boldsymbol{B}_M^{ik}\boldsymbol{Q}_i \\
\varepsilon_{Lk} &= \frac{\boldsymbol{l}_k^T[\![\boldsymbol{u}_{Ck}]\!]}{l_e} = \boldsymbol{B}_L^{jk}\boldsymbol{Q}_j - \boldsymbol{B}_L^{ik}\boldsymbol{Q}_i
\end{aligned} \qquad [7.5]$$

on which the LDPM formulation for particles compatibility is based.

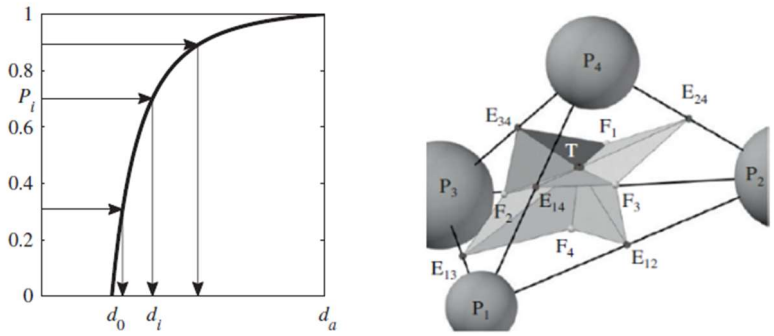

(a) (b)

Figure 7.1 – (a) Probability function for particle size distribution; (b) LDPM tethraedron connecting four particles (Cusatis, Pelessone, et al., 2011).

For what concerns the equilibrium equations to complete the LDPM formulation, these expressions are derived from the equation that equals the internal and external work computed by the Principle of Virtual Work (PVW) equation. The equilibrium expressions are the following:

$$\begin{aligned} \partial W_k &= F_{ik}^T \partial Q_i + F_{jk}^T \partial Q_j \\ \boldsymbol{F}_{ik}^T &= -l_e A_k (\sigma_{Nk} \boldsymbol{B}_N^{ik} + \sigma_{Mk} \boldsymbol{B}_M^{ik} + \sigma_{Lk} \boldsymbol{B}_L^{ik}) \\ \boldsymbol{F}_{jk}^T &= l_e A_k (\sigma_{Nk} \boldsymbol{B}_N^{kj} + \sigma_{Mk} \boldsymbol{B}_M^{kj} + \sigma_{Lk} \boldsymbol{B}_L^{kj}) \end{aligned} \quad [7.6]$$

that relate the forces correspondent to *i* and *j* nodes associated with *k* facet. The global equilibrium of the tetrahedron is set summing all facets contributions and equalling the internal with the external virtual work. The final expression describes the translational and rotational equilibrium of LDPM polyhedral cell.

The present section has described some aspects of the discrete LDPM theory: a more detailed description is reported in *'Lattice Discrete Particle Model (LDPM) for Failure Behavior of Concrete. I: Theory'* (Cusatis, Pelessone, et al., 2011).

7.2.1. LDPM mechanical parameters

The parameters aimed at calibrating the geometrical organization of LDPM particles concern the concrete mix design: the cement content, the water-cement ratio,

the aggregate to cement content, and minimum and maximum aggregate size. The parameters that need to be also calibrated are those related to the meso-scale LDPM constitutive law. The elastic behavior within the LDPM formulation is described by the following equations:

$$\sigma_N = E_N \varepsilon_N ; \sigma_M = E_T \varepsilon_M ; \sigma_L = E_T \varepsilon_L \quad [7.7]$$

where $E_0=E_N$, $E_T=\alpha E_0$; E_0 is the effective normal modulus and α the shear-normal coupling parameter. E_0 and α describe the elastic problem in the meso-scale field and they are the corresponding parameters of the classical elastic theory at macroscopic level, the elastic modulus E and the Poisson's ratio v. The relations connecting them are the following:

$$E_0 = \frac{1}{1-2\nu} E \leftrightarrow E = \frac{2+3\alpha}{4+\alpha} E_0$$
$$\alpha = \frac{1-4\nu}{1+\nu} \leftrightarrow \nu = \frac{1-\alpha}{4+\alpha} \quad [7.8]$$

The inelastic behavior is faced by the LDPM formulation through the fracture behavior under tension and tension/shear loading conditions, the pore collapse under compression and the frictional behavior.

The inelastic part is regulated by a set of parameters needed to be calibrated: the tensile strength σ_t with the characteristic length l_t for what concerns both LDPM and the macroscopic softening tensile behavior and n_t the softening exponent relating shear and tensile behavior with the facets. The macroscopic compressive behavior is mostly governed by the shear strength ratio σ_s/σ_t more influencing the unconfined compression state, yielding compressive stress σ_{c0}, initial hardening modulus H_{c0}, transitional strain ratio k_{c0} and densified normal modulus E_d. The shear boundary set of parameters is defined by μ_0 initial internal friction coefficient, μ_∞ internal asymptotic friction coefficient, and σ_{N0} the transitional stress that are responsible more of the compressive behavior than tensile strength. k_{c1} and k_{c2} define the compressive non-linear evolution of the normal component of stress on the facet in a compressive state. The last parameter k_t regulates the unloading-reloading hysteresis

cycles in terms of size in LDPM and macroscopic approach respectively for tensile fracturing facet and compressive, tensile behavior (Cusatis, Mencarelli, Pelessone, and Baylot, 2011). The optimal calibration of these parameters is performed on experimental results of hydrostatic compression tests, unconfined compression and fracture tests, triaxial compression at low and high confinement.

In the present work the calibration of plain concrete is obtained fitting three point bending tests curves in terms of stress crack-opening, compression tests reporting the peak strength and compression tests on cylinders.

7.3. LDPM – F THEORY

The extension of LDPM approach to include the crack bridging contribution of fibre reinforcement is achieved by a random generation of short fibres in the concrete mesostructure modelled with spherical particles. These elements are geometrically and mechanically described. Their geometry is modelled assigning the fibre length l_f, the diameter d_f, in this work it is assumed the real diameter and not the equivalent one and their volume fraction V_f according which the fibres number is generated (Jin et al., 2016):

$$N_f = \left[4V_f V / (\pi d_f^2 A_f) \right] \qquad [7.9]$$

This system is added to the concrete particles where the facets will intersect the single fiber: the single element will be divided into a smaller L_s and longer L_l length (Figure 7.2).

The intersection defines the fibre orientation identified by the vectors n and n_t respectively normal and parallel to the facet. The mechanical behavior of the single fibre is modeled computing the interaction with the matrix.

In general the bond fiber-matrix is mechanically identified by a pull-out experimental test where the output is a curve showing a peak, the maximum bond

strength, followed by a frictional phase (Del Prete, Buratti, Manzi, and Mazzotti, 2019).

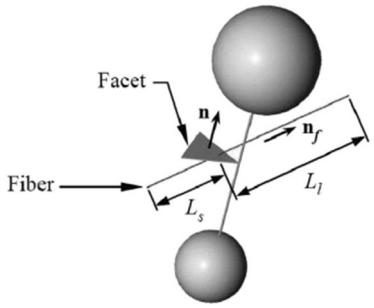

Figure 7.2 – Fibre intersecting the facet (Jin et al., 2016).

The debonding stage until the peak corresponding to the displacement value v_d is described by the bond fracture energy G_d and the frictional stress τ_0 according to the following law (Jin et al., 2016):

$$P(v) = \left[\frac{\pi^2 E_f d_f^3}{2} (\tau_0 v + G_d) \right]^{1/2} \quad [7.10]$$

While the pull-out stage, handled by a frictional mechanism has the expression:

$$P(v) = P_0 \left(1 - \frac{v - v_d}{L_e} \right) \left[1 + \frac{\beta (v - v_d)}{d_f} \right] \quad [7.11]$$

with β dimensionless coefficient and $P_0 = \pi L_e d_f \tau_0$ initial pull-out force.

The LDPM-F needs the geometrical properties as input values for short fibers generation and the calibration of τ_0, β and G_d characterizing their debonding phase. Besides, this approach accounts for other effects that the fiber inclination at interface with matrix can imply: snubbing, spalling and cook-Gordon effects. The snubbing effect is due to the frictional contribution of the matrix cone during the slippage of the fibre inclined that generated a load increment ($P_f > P$) (Jin et al., 2016).

$$P_f = \exp(k_{sn} \varphi_f^{'}) P(v) \quad [7.12]$$

Moreover, the angle between the portion of embedded fiber and the pull-out force applied to the segment edge induces stress concentration and the possibility of concrete matrix failure. This phenomenon is named as spalling effect and affects the concrete matrix for a specific size length defined with the expression:

$$s = \frac{P_{fN} \sin(\theta/2)}{k_{sp}\sigma_t d_f \cos^2(\theta/2)} \qquad [7.13]$$

with P_{fN} the normal component of the total force P_f. The Cook-Gordon effect features when there is a tensile stress concentration that induces a crack propagation towards the fibre that itself endures an elongation. This mechanism generates the crack opening whose value is increased of a quantity v_{cg}:

$$v_{cg} = \frac{4k_{cg}P_f}{\pi d_f^2 E_f} \qquad [7.14]$$

referred to the single fibre.

To sum up, the LDPM-F calibration requires the knowledge of the following additional parameters: k_{sp}, k_{sn}, Cook Gordon feature, σ_{uf}, E_f derived from the mechanical characterization.

The LDPM theory and, consequently the LDPM-F extension, is implemented in MARS (Modeling and Analysis of the Response of Structures) software: it is a powerful and robust object-oriented computational software based on a dynamic explicit algorithm saving the same performance of a finite element code but adding some techniques, i.e. the LDPM theory. The capabilities featured by this code concern the solution of plenty of problems including structural break-ups, fragmentation and post-failure response under extreme loading conditions.

7.4. M – LDPM THEORY

A material is defined viscoelastic if, when the load is applied, shows an elastic behavior followed by a slow and continuous increment of strain at a descreasing rate.

The viscoelastic behaviour is time-dependent and so described by constitutive equations including time in addition to stress and strain variables. The structural design with fiber reinforced concrete materials implies the adoperation of two classes of materials different in terms of mechanical properties and behavior: they exhibit different states of stress and strain according to the load conditions.

The approach of modeling fibers and concrete as a composite material instead of considering two separate constituents helps to reproduce a more reliable behavior since both polymers and concrete suffer from creep phenomena. The viscoelastic matrix behavior is simulated approximating the creep compliance function with a Kelvin chain model while the polypropylene behavior is formulated according to the expression derived from the superposition principle of Volterra and Boltzmann. The reason of treating both components of FRC as viscoelastic materials concerns the redistribution of stress when concrete deforms for creep and shrinkage and, thus the long term performance of the whole materials changes if compared to that of the plain concrete (Findley, J.S., and K., 1976).

The description of the theory adopted to simulate the concrete creep phenomena, M – LDPM, requires the explanation of some concepts here briefly reported: the continuous retardation spectrum, the solidification theory and the hygro-thermo-chemical model.

7.4.1. Discrete and continuous retardation spectrum

The M-LDPM constitutive law accounts for creep, shrinkage and thermal effects in concrete and it is based, as mentioned in the previous section, on the Kelvin Chain constitutive law (Abdellatef et al., 2019). Concrete is an aging viscoelastic material and, considering small time steps, it is right to assume that the material properties are constant over time and so effectively nonaging, for this reason they can be calculated at the time t_{nh} as the center of the time step. The use of the geometric center of the time step agrees with the concentration of the creep deformations in the first part of the time step in the kelvin chain model. It represents a way to transform the

viscoelastic behavior of the material into a rate-type creep law that treats the problem as an elastic problem. This allows to not refer to the entire stress history at each integration point for each time step.

According to the basic creep definition, the aging aspect of the basic creep of concrete can be treated with two different approaches: the first that describes the material as characterized by age-dependent parameters regulated by some equations; the second one is based on an age-indipendent theory but considering the volume fraction of the age-indipendent material growing on time. The second one characterizes the creep behavior using a non-aging model which takes into account the aging property computing the increment of the volume fraction of the solidifying constituent material. This model has to describe the nonaging creep for the numerical purposes, correlating this to the physics of the problem. This correlation is possible only when it is described by firt-order differential equations. The nonaging creep is characterized by a Kelvin chain model composed by different kelvin units in series consisting of coupled spring and dashpot. On the other hand, also the Maxwell model could describe a creep problem using parallel units composed by springs and dashpot. Indeed, the creep tests are simulated properly using a kelvin model while the Maxwell model describes better a relaxation test.

The solidification theory (Zdenek, Fellow, ASCE, and Yunping, 1995), originally described the creep of nonaging constituent with a finite number of Kelvin chain units, *N*, each of them described by its spring modulus E_μ and a retardation time $\tau_\mu = \frac{\eta_\mu}{E_\mu}$ (η_μ dashpot viscosity). Representing $1/E_\mu$ versus τ_μ the retardation spectrum is obtained, that characterizes the material creep properties. The use of a finite number of elements in the Kelvin chain implies a discrete spectrum, whose identification is not univocal because different retardation times can give equal good fits of the measured creep curves. The way to overcome this limitation is to elaborate a continuous retardation spectrum, identified in unambiguous way from arbitrary measured creep curves.

The compliance function *J(t,t')* complete characterizes the linear viscoelastic behaviour describing the strain *ε(t)* of concrete induced by a uniaxial sustained stress *σ* applied at *t'*. Starting from the equation:

$$J(t,t') = q_1 + C(t,t') \qquad [7.15]$$

it describes the behavior of the material by means of the compliance function *J*, representing the strain ε at age *t* of concrete under uniaxial sustained stress equal to 1. For any stress history σ_t, the superposition principle is followed (the poisson ratio is constant, 0.18, and equal to the elastic one). *C(t,t')* is the creep compliance function. The term q_1 is age indipendent and considered as the deformation corresponding to an instantaneous load.

For the nonaging Kelvin chain model with *N* kelvin units, the creep compliance function is described by the Dirichlet series:

$$C(\xi) = \sum_{\mu=1}^{N} A_\mu [1 - e^{-\frac{\xi}{\tau\mu}}] \text{ with } A_\mu = \frac{1}{E_\mu} \qquad [7.16]$$

A_μ has to be calibrated with the experimental results since this parameter regulates the strain increment during the time lag corresponding to the retardation time τ_μ. This compliance is evaluated as $A_j = L_j \ln(10)$. To avoid nonuniqueness problems in the computation of the retardation time, the solution is to use an infinite number of Kelvin units and introducing a continuous retardation spectrum instead of the discrete one. This spectrum can be evaluated using the viscoelastic theory:

$$C(\xi) = \int_0^\infty L^*(\tau)(1 - e^{-\frac{\xi}{\tau}})d\tau \text{ with } L^*(\tau) = \frac{L(\tau)}{\tau} \qquad [7.17]$$

$$C(\xi) = \int_{-\infty}^{\infty} L(\tau)(1 - e^{-\frac{\xi}{\tau}})d(\ln \tau) \qquad [7.18]$$

$L(\tau)$ is the continuous retardation spectrum obtained from the expression below:

$$L(\tau) = \lim_{k\to\infty} \frac{(-k\tau)^k}{(k-1)!} C^{(k)}(k\tau) \qquad [7.19]$$

Using a finite value of k ($k \geq 1$), generally a retardation spectrum of order 3 represents a good approximation. The purpose is to deduce the continuous retardation spectrum given the compliance of the material. The term $C^{(k)}$ includes the information regarding the material compliance and, now, the problem consists in finding out which kind of compliance function has to be adopted. Since the short term creep data, for concrete, follow the power curve while the long term data the logarithmic curve, the combination in log-power law could be a reliable presentation of the compliance function for concrete. The expression approximating better creep results is:

$$C(\xi) = q_2 \ln[1 + \left(\frac{\xi}{\lambda_0}\right)^n] \qquad [7.20]$$

where q_1 and q_2 are related to the concrete strength and its composition. The retardation spectrum $L(\tau)$ is obtained using the compliance function as input behavior. The detailed formulation is reported in *'Continuous Retardation Spectrum for Solidification Theory of Concrete Creep'* (P. Z. Bažant, Fellow, ASCE, and Xi, 1995)

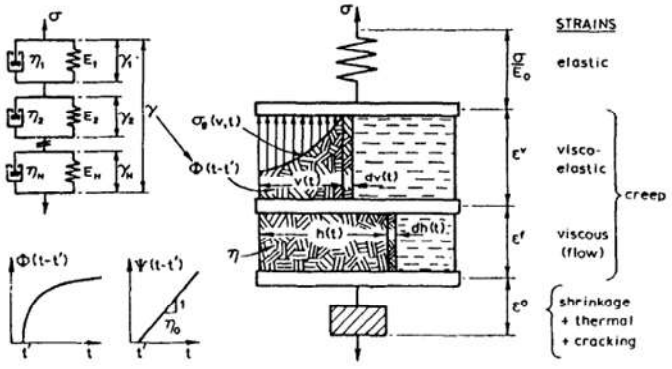

Figure 7.3 – Kelvin Chain Model (P. Z. Bažant et al., 1995).

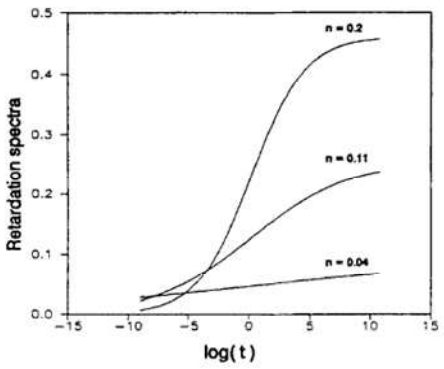

Figure 7.4 – Retardation spectra at different n values (P. Z. Bažant et al., 1995).

7.4.2. Solidification theory

The creep behaviour of concrete is described by the Microprestress Solification Theory. According to the present theory, the aging property of concrete basic creep is taken into account by the growth of the volume fraction of concrete over time, in other words it is caused by the processes of hydration and polymerization of cement. Concrete matrix consists of three parts: liquid that cannot bear load, and two load-bearing parts, the solid parts of concrete, exhibiting viscous flow and viscoelastic deformation. Therefore, the total creep strain is composed of two terms, viscoelastic strain ε_v and the viscous flow strain ε_f. In this theory the properties of the load-bearing matter are aging-indipendent so the viscoelastic standard theories can be applied. Consequently, the creep strain rate for the viscoelastic solid part can be expressed as the product between the age-indipendent property strain rate, $\dot{\gamma}$, and the increment of volume fraction *v(t)* of the solid.

$$\dot{\varepsilon}^{v}(t) = \frac{1}{v(\alpha_b)}\dot{\gamma} \qquad [7.21]$$

with

$$\gamma = \int_0^t \Phi(t_r(t) - t_r(\tau))\boldsymbol{G}\dot{\boldsymbol{\sigma}}d\tau \text{ and } v(\alpha_b) = (\alpha_b / \alpha_b^{\infty})^{n_\alpha} \qquad [7.22]$$

The term γ represents the binder viscoelastic micro-strain rate and $v(\alpha_b)$ is a function representing the volume fraction of the binder that is produced by the early-age chemical reactions, $\Phi(t-t_0)=\xi_2 \ln[1+(t-t_0)^{0.1}]$ is the non-aging micro-compliance function of C-S-H gel and the time interval is the loading interval. ξ_2 and α are model parameters. The use of t_r reduction time accounts for the effect of change in relative humidity and temperature:

$$t_r(t)=\int_0^t \psi(\tau)d\tau \qquad [7.23]$$

with

$$\psi(t)=[0.1+0.9h^2]\exp\left[\frac{Q_v}{R(\frac{1}{T_0}-\frac{1}{T})}\right] \qquad [7.24]$$

where h, T are the relative humidity and temperature (Kelvin) at time t, R the universal gas constant and Q_v the activation energy for the creep processes ($Q_v / R \approx 5000K$). In addition, **G** is a tensor depending on α the shear-normal coupling parameter. In the vectorial form we have the following relation

$$\varepsilon^* = 1/E_0 \boldsymbol{G}\sigma \qquad [7.25]$$

where

$$G=\begin{bmatrix}1 & 0 & 0\\ 0 & 1/\alpha & 0\\ 0 & 0 & 1/\alpha\end{bmatrix} \qquad [7.26]$$

The purely viscous strain rate represents the permanent strain of creep deformation due to the long term creep, drying creep effect and transitional thermal creep. This contribute is equal to:

$$\dot{\varepsilon}^f(t)=\xi_4 k_0 \psi(t) S\boldsymbol{G}\sigma \qquad [7.27]$$

Where *S* is the microprestress computed solving the differential equation

$$\dot{S} + \psi_s(t) k_0 S^2 = k_1 \left| \dot{T} \ln(h) + \frac{T\dot{h}}{h} \right| \quad [7.28]$$

with k_0, k_1, ξ_4 model parameters.

$$\psi_s(t) = [0.1 + 0.9h(t)^2] \exp\left[\frac{Q_s}{R(\frac{1}{T_0} - \frac{1}{T(t)})} \right] \quad [7.29]$$

With $Q_s / R \approx 3000K$. S_0 at time $t=t_0$ must be defined as a parameter of the model. The three parameters k_0, k_1, ξ_4 are not indipendent in computing the viscous strain. Basic creep viscous strain depends on ξ_4 while drying and transitional thermal creep depend on both ξ_4 and the product $k_0 k_1$. This is easily demonstrated setting the auxiliary variable $\bar{S} = k_0 S$ so:

$$\dot{\varepsilon}^f(t) = \xi_4 k_0 \psi(t) S \boldsymbol{G\sigma} \quad [7.30]$$

and

$$\dot{\bar{S}} + \psi_s(t) k_0 S^2 = k_0 k_1 \left| \dot{T} \ln(h) + \frac{T\dot{h}}{h} \right| \quad [7.31]$$

A correct extimation of k_0 requires experimental data on the microprestress evolution.

As stated before, the constitutive equations are solved considering different time steps, so the strain calculation is computed in an incremental form:

$$\Delta\varepsilon^* = \Delta\varepsilon - (\Delta\varepsilon^s + \Delta\varepsilon^t + \Delta\varepsilon^v + \Delta\varepsilon^f) \quad [7.32]$$

where the total strain increment $\Delta\varepsilon$ is obtained multiplying the facet strain rate, computed with the nodal velocities on each LDPM facet, for the time step.

Considering N kelvin chain units and computing the strain for every time step Δt the viscoelastic strain increment is:

$$\Delta\varepsilon^{v} = \sum_{j=1}^{N}(\boldsymbol{G}A_j\sigma^{i} - \gamma_j^{i})(1-\mathrm{e}^{-\frac{\psi^{i}\Delta t}{\tau_j}})\frac{1}{v(\alpha_b^{i})} \qquad [7.33]$$

The purely viscous strain increment at of the facet level is computed considering the quantities σ^{i}, ψ^{j}, $\psi^{i}{}_{s} = \psi_s(t^{i})$ constant over the time step Δt. This leads to:

$$\Delta\varepsilon^{f} = \Delta t\xi_4 k_0 \psi^{i} S^{i}\boldsymbol{G}\boldsymbol{\sigma}^{\boldsymbol{i}} \qquad [7.34]$$

The microprestress value is updated every time step according to the following expression:

$$\Delta S^{i} = -\psi_s{}^{i} k_0 S^{i2}\Delta t + k_1 \mid \Delta T^{i}\ln(h^{i}) + T^{i}\frac{\Delta\dot{h}}{h^{i}} \mid \qquad [7.35]$$

Considering these strain increments for every time step and subtracting them to the initial $\Delta\varepsilon$, $\Delta\varepsilon^{*}$ the term of the equation [7.32] is computed representing the strain increment used by the LDPM constitutive law to compute the corresponding facet stress vector increment $\Delta\sigma$ updating the stress vector at the end of each time step. It is important to underline that the *E* modulus to which the LDPM constitutive equations refer to is the apparent normal modulus $\overline{E_0}(t)$ defined as:

$$\overline{E_0}(t) = \frac{1}{\xi_1 + \dfrac{A_0}{v(\alpha_b(t))}} \qquad [7.36]$$

This means that at every time step the elastic effective LDPM stress is calculated according to this elastic modulus while the nonlinear part of the LDPM constitutive equations is imposed by a vertical return algorithm (Abdellatef et al., 2019).

Summarizing, in the solidification theory is possible to use a continuous retardation spectrum for the Kelvin chain model despite the aging of concrete. The spectrum can be obtained by the asymptotic transformation method that leads to an

unique spectrum given the compliance function. The spectrum can be simplified using an order 3, especially for smaller values of time exponent that are typical of concrete. This theory is based on the discretization of the continuous retardation spectrum that solves the creep problem for concrete with a rate-type formulation which is combined with the solidification theory for aging: this represents a complete model for basic creep description.

7.4.3. Hygro-thermo-chemical model (HTC)

The HTC model (hygro-thermo-chemical) describes the multiphysics of transport mechanisms in concrete, i.e. moisture and heat. In agreement with the definition of the solidification theory, the spatial and temporal fields of temperature, *T*, relative humidity, *h*, and overall binder reaction degree, α_b, have to be defined to describe the deformations. For this reason the HTC model is adopted for the description of the evolution of the three parameters. According to this model, *h* and *T* distributions can be determined regulating the mass balance and enthalpy balance throught the following equation specific for concrete mixes containing Portland cement and silica fume, and temperatures less than 90°C.

$$\nabla \cdot (D_h \nabla h) - \frac{\partial w_e}{\partial h}\frac{\partial h}{\partial t} - \frac{\partial w_e}{\partial \alpha_c}\dot{\alpha}_c - \frac{\partial w_e}{\partial \alpha_s}\dot{\alpha}_s - \dot{w}_n = 0 \qquad [7.37]$$

And

$$\nabla \cdot (\lambda_t \nabla \mathrm{T}) - \rho c_t \frac{\partial T}{\partial t} + \dot{\alpha}_c c \tilde{Q}_c^{\infty} + \dot{\alpha}_s s \tilde{Q}_s^{\infty} = 0 \qquad [7.38]$$

Where *c* is the cement content, *s* silica content, D_h moisture permeability, w_e evaporable water, α_c cement hydratation degree, α_s silica-fume reaction degree, $\dot{w}_n = 0.253\dot{\alpha}_c c$ rate of non-evaporable water change, ρ mass density of concrete, c_t isobaric heat capacity, λ_t heat conductivity, $\tilde{Q}_c^{\infty}$ cement hydration enthalpy (≈

450kJ/kg) and $\tilde{Q}_s^{\infty}$ latent heat of silica-fume reaction per unit mass of reacted silica-fume ($\approx$ 780kJ/kg). The moisture permeability D_h is defined as a nonlinear function of *h* and *T*; the evaporable water w_e is a function of the relative humidity in the pores and the aging of the cementitious material paste. Cement hydration can be characterized by the hydration degree α_c, the fraction of cement fully reacted with water; also the silica-fume reaction can be characterized by the reaction degree, α_s. Since we have the binder, it is convenient to merge into only one reaction degree α_b both hydration degrees: it can be defined as the ratio between the released heats of hydration from both reactions divided by the sum of the total heat of hydration of full reactions. Therefore it can be defined as:

$$\alpha_b(t) = \frac{\alpha_c(t) c\tilde{Q}_c^{\infty} + \alpha_s(t) s\tilde{Q}_s^{\infty}}{c\tilde{Q}_c^{\infty} + s\tilde{Q}_s^{\infty}}. \qquad [7.39]$$

7.4.4. Thermal and hygral deformations

The strain rate of thermal and shrinkage phenomena are described by the following relations where the coefficients α_T and α_h are considered average properties of the material.

$$\dot{\varepsilon}^t = [\alpha_T \dot{T} \quad 0 \quad 0]^T \qquad [7.40]$$

$$\dot{\varepsilon}^s = [\alpha_h \dot{h} \quad 0 \quad 0]^T \qquad [7.41]$$

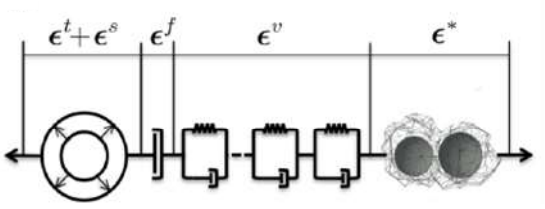

Figure 7.5 – Representation of the equivalent rheological model based on strain additivity principle (Abdellatef et al., 2019).

7.5. M – LDPM – F THEORY

The M-LDPM theory has been extended to include the viscoelastic behaviour of polypropylene fibers, whose viscoelastic nature cannot be neglected when dealing with time dependent phenomena. The polypropylene is basically a plastic material: in general wood, natural, plastics and synthetic fibers are treated as viscoelastic materials. They result significantly influenced by the straining or stressing rate, if stress is applied for longer time, they will gain more strain on time. Their mechanical behavior is characterized using creep, stress relaxation and constant rate stressing (Findley et al., 1976).

The numerical approach here adopted to describe the creep deformations of polymers is based on the exponential Kernel functions. The formulation proposed is easier than that used for concrete creep description since the non aging nature of the plastic material. On the other hand, simple models such as Maxwell and Kelvin-Voight in terms of single units are not so flexible to describe the real behavior of the material (Sorzia, 2016). The fractional derivative model (FDM) is more flexible and needs a small number of parameters to be calibrated, the flexibility is associated with the derivatives order that make possible to obtain a good description. Rabotnov in 1948 suggested to use fractional-exponential operators describing the experimental data of real materials (Rabtnov, 1948). Fraction-exponential functions in viscoelastic operators are widely used in the last decades to describe very well the viscoelastic behavior of real materials. A viscoelastic viscoplastic model for polypropylene uniaxial behavior is proposed by Tscharnuted, Jerabek, Major and Pinter (Tscharnuter, Jerabek, Major, and Pinter, 2012). Their paper proposed the Schapery viscoelastic and Perzyna viscoplastic methods to strain recovery data of polypropylene materials as the load histories can activate irreversible deformation mechanisms.

The description of creep polypropylene behavior of the fibers reinforcement is developed using the model proposed by Golub, Fernati and Lyashenko (Golub,

Fernati, and Lyashenko, 2008). It starts from the Boltzamm and Volterra principle and is aimed at determining the kernel parameters using a mathematical processing of the experimental data available. The mathematical function used to determine these parameters is the Rabotnov fractional exponential function that approximates the fractional exponential kernel by the Mittag-Leffler function, the Laplace-Carson transform and the approximation of a bounded creep function. Given the difficulties about the converging in the analytic expression of kernel function it is necessary to approximate the functions using some mathematical expressions. The goal in using this model is the description of an experimental creep function to unlimited test duration that has been one of the discriminating aspects in selecting the method to be used. Among the different approximation methods, the Mittag-Leffler function (Rozovskii, 1961) was choosed since the analogy in the material, the polypropylene, tested and described by Andrea Sorzia (Sorzia, 2016). The Boltzmann-Volterra theory of hereditary viscoelasticity describes the long term deformation of linear viscoelastic materials under uniaxial tension:

$$\varepsilon(t)=\frac{1}{E}\left(\sigma(t)+\lambda\int_0^t K(t-\tau)\sigma(\tau)d\tau\right) \quad [7.42]$$

$$\sigma(t)=E\left(\varepsilon(t)+\lambda\int_0^t R(t-\tau)\varepsilon(\tau)d\tau\right) \quad [7.43]$$

$\varepsilon(t)$, $\varepsilon(\tau)$ are the total strain including elastic and creep strain at times *t,* τ and $\sigma(t)$, $\sigma(\tau)$ are stresses at times *t,* τ. $K(t-\tau)$ and $R(t-\tau)$ are the creep and relaxation kernel, *E* is the elastic modulus and λ the rheological parameter; *t* the observation time and τ the time preceding the time of observation. The kernel parameters are calculated for different stress levels: $\sigma(t)=\sigma_k h(t)$ with $(k=\overline{1,m})$. So it is possible to write:

$$\varepsilon(t)=\frac{\sigma_k}{E}h(t)\left(1+\lambda\int_0^t K(t-\tau)d\tau\right) \quad [7.44]$$

where $h(t)$ is the Heaviside function.

It is possible to approximate the kernel creep parameter with the Rabotnov fractional exponential function:

$$K(t-\tau)=\sum_{n=0}^{\infty}\frac{(-\beta)^n(t-\tau)^{\alpha+(1+\alpha)n}}{\Gamma[(1+\alpha)(1+\mathrm{n})]} \qquad [7.45]$$

where $\alpha(0<\alpha<1)$ and $\beta(\beta>0)$ are the kernel parameters need to be determined from the creep tests and Γ gamma function. Substituting this expression in the integral equation considering σ_k constant and $\tau=0$:

$$\varepsilon(t)=\frac{\sigma_k}{E}h(t)\left(1+\lambda\int_0^t\sum_{n=0}^{\infty}\frac{(-\beta)^n(t-\tau)^{\alpha+(1+\alpha)n}}{\Gamma[(1+\alpha)(1+\mathrm{n})]}d\tau)\right) \qquad [7.46]$$

The results of the integral is:

$$\varepsilon(t)=\frac{\sigma_k}{E}h(t)[1+\lambda\sum_{n=0}^{\infty}\frac{(-\beta)^n(t-\tau)^{\alpha+(1+\alpha)n}}{\Gamma[(1+\alpha)(1+\mathrm{n})]}] \qquad [7.47]$$

The sum of series in equation [7.46] is approximated with the Rabtnov operator:

$$э_{\alpha}^{*}(-\beta)=\frac{1}{\beta}\{1-\exp[-(1+\alpha)^{1+\alpha}\beta\,\mathrm{t}^{1+\alpha}]\} \qquad [7.48]$$

and defining the Mittag-Leffler function as:

$$E_{\mu}(z)=\sum_{n=0}^{\infty}\frac{(-1)^n z^n}{\Gamma(1+\mu n)} \qquad [7.49]$$

the following expression can be written:

$$E_{1+\alpha}(-\beta t^{1+\alpha})=\exp[-(1+\alpha)^{1+\alpha}\beta\,\mathrm{t}^{1+\alpha}] \qquad [7.50]$$

Thus, substituting the [7.48] in [7.47] the creep function is obtained:

$$\varepsilon(t)=\frac{\sigma_k}{E}h(t)\{1+\frac{\lambda}{\beta}[1-\exp(-(1+\alpha)^{1+\alpha}\beta\,\mathrm{t}^{1+\alpha})]\} \qquad [7.51]$$

The present expression has been implemented as a module of the software used in an incremental form. The unknown constants describing the model are λ rheological parameter, α and β the fractional exponential kernel parameters, where λ has the following expression (Sorzia, 2016):

$$\lambda = \frac{E_0 - E_\infty}{E_0}\beta \qquad [7.52]$$

That correlates the elastic modulus of polypropylene fibre assumed on time as half of the instantaneous elastic modulus.

7.6. SHORT TERM BEHAVIOUR: MODEL CALIBRATION

7.6.1. Specimens modeling

The calibration of the MSFRC material under examination is decoupled in two phases: first the parameters of the concrete matrix are calibrated on the plain concrete experimental response and, then, the fibers contribution on the reinforced concrete exprimental results. In detail, the response of concrete reinforced with lower dosage, 8kg/m^3 of polypropylene crimped fibres, is used for the model calibration. Then, the validation is performed on the MSFRC with higher dosage (10kg/m^3). The LDPM approach used in the numerical model elaboration could be also combined with a finite element method approach with the aim of reducing the computational time. Cubes, cylinders and prismatic specimens are modelled applying the LDPM constitutive approach to the entire sample since the failure involves the whole element. On the other hand, in case of notched FRC prismatic specimens, the failure is almost concentrated in that part of concrete close to the notch. For this reason, the flexural response is calibrated on a prism modelled with LDPM length of 600 mm, the prism full length, and a small extension of 200 mm, reporting a comparison between the responses. The numerical models reproduce the same geometrical and boundary conditions of the experimental tests. The cubic specimens have size of 150 mm x 150 mm x 150 mm, the prisms are characterized by 150 mm x 150 mm cross

section, 600 mm length, deflection length (distance between the bottom supports) of 500 mm and a central notch of 4 mm width and 25 mm high. The cylinders have the height of 300 mm and a diameter of 150mm[1]. The compressive test is simulated applying a pressure on the upper face of the element, cylinder and cube, blocking rotations and translations in the bottom face allowing the vertical translation and the rotation in correspondence of the upper face. The simulation of flexural tests is performed modelling three steel supports with square section, two placed at the bottom of the sample and one in the upper where the load is applied. In the inferior part the translation and rotation along the X axis and the rotation around the Y axis are allowed, while the vertical translation and rotation around the Y axis are set as free at the top. This aspect has a great importance in the evolution of the cracking process that, in case of stiff connections, might cause the cracks at the interface between specimen and supports.

7.6.2. Concrete particles generation

The particles depicted in Figure 7.6 are generated with the assignement of concrete mix design properties: w/c and a/c ratios, cement content and aggregate range size. Actually the smaller diameter (d_0) is approximately 1 mm while, for computational time issues, the particles in LDPM approach are generated assigning a range of 8 – 15 mm covering almost the 30% of the Fuller curve generated with the real aggregate size (Marangi, 2010).

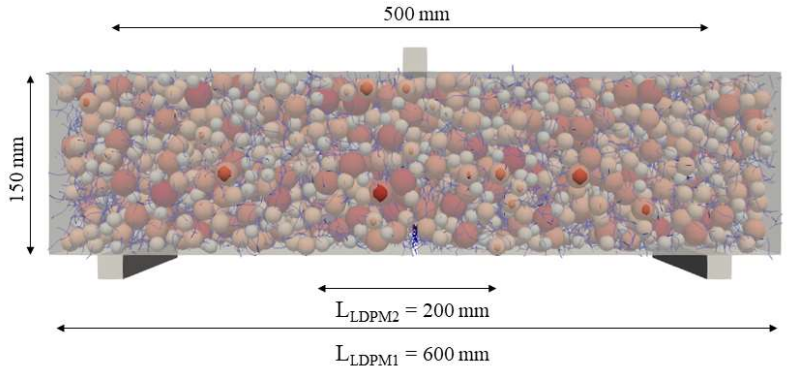

[1] The figure depicts the prisms and cubes with fibres while the cylinders as plain concrete: the cubes and cylinders compression with the flexural tests are used for plain concrete calibration while only compressive and flexural tests are used for fibre reinforced concrete calibration. The figure is only representative because the specimens have been modelled without fibres for the plain concrete but the geometry remains the same.

(a)

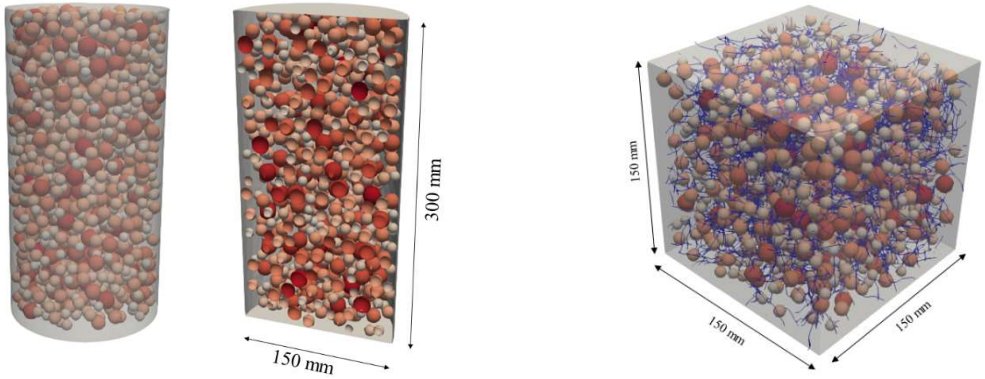

(b) (c)

Figure 7.6 – Representation of (a) Prisms for flexural tests; (b) Cylinders and (c) Cubes for compressive tests.

7.6.3. Concrete parameters calibration

The parameters calibrated on the flexural responses are:

- Normal modulus (as it is identified by LDPM parameter)
- Tensile strength
- Tensile characteristic length
- Softening exponent.

The calibration should assume an initial set of parameters from which the procedure starts. This phase is preceded by a previous examination of the effect of the mechanical parameters on the numerical response revealing that, the tensile strength affects the peak strength, the tensile characteristic length the peak strength and the area under the curve, since it is an indicator of the toughness of the material, the softening exponent the descending post-peak branch.

The formula indicated [7.8] is used to estimate the mesoscale elastic modulus, where α is the equivalent of the poisson ratio at a macroscopic scale. The tensile strength is determined on brazilian test results: the value determined experimentally is 3.7 MPa, this is compared with the tensile strength calculated by the compressive strength and the flexural strength (starting from the experimental results) with the formula [7.53 – 7.54] (Section 11.2.10.2, D.M. 17 Gennaio 2018):

$$f_{ctm}=0.3(f_{ck}^{2/3}) \quad [7.53]$$

$$f_{cfm}=1.2\,f_{ctm.} \quad [7.54]$$

The final value is so estimated (Table 7.2).

The characteristic length estimation is based on the fracture mechanics theory applied on the experimental flexural response in terms of stress-crack opening (Chiu, Panchmatia, and Sivaram, 2011). The specific fracture energy considers the area under a load-deflection curve (indirect method for Hillerborg's model application), so the relation reported below [7.55] is used to correlate the crack opening to the vertical displacement with the hypothesis of rigid small displacements (Chiu et al., 2011):

$$\delta = \frac{CMOD \cdot l}{4h} \quad [7.55]$$

$$l_{ch} = \frac{E \cdot G_f}{f_t^2} \quad [7.56]$$

the tensile characteristic length is so calculated [7.56] (Hillerborg, 1985).

Since the plain concrete calibration is the first phase of the fibre reinforced mechanical behavior calibration, one one hand it should assume the concept that the tensile characteristic length, as also implemented in the computational code, is an indicator of the material toughness and so, for the reinforced material has a value considerably higher than that characterizing the plain concrete response (l_{ch}>1000 mm). On the other hand, the tensile characteristic length value is computed according to the mesoscale parameters of elastic modulus (normal modulus as it is defined by LDPM) and tensile strength: this explains the high value assumed for the calibration. The shear strength ratio is calibrated on the compression tests since its less influence on the flexural response. The parameters so calibrated are reported in Table 7.3.

As specified before, the calibration of the other parameters is based on values reported in literature for concrete having in principle the same mix composition and approximately the same performance since the several experimental tests type required to calibrate all parameters.

Table 7.1 – Cement-based materials mechanical properties (based on Löfgren 2005).

Material	f_c [MPa]	f_t [MPa]	E [GPa]	G_F [Nm/m^2]	l_{ch} [mm]
Cement paste	10 – 25	2.0 – 10.0	10 – 30	≈ 10	5 – 15
Mortar		1.0 – 10.0	10 – 30	10 – 50	100 – 200
Normal-strength concrete	20 – 80	1.5 – 5.0	25 – 40	50 – 150	200 – 400
High-strength concrete	> 80	4.0 – 5.5	40 – 50	100 – 150	150 – 250
Fibre-reinforced concrete	20 – 80	1.5 – 5.0	25 – 40	> 500	> 1 000

Table 7.2 – Estimation of the tensile characteristic length from tensile strength and elastic modulus experimentally and analytically determined for Plain concrete.

$f_{ct,1}$ [MPa]	$f_{ct,2}$ [MPa]	$f_{ct,3}$ [MPa]	$f_{ct,m}$ [MPa]	$E_{c,1}$ [GPa]	$E_{c,2}$ [GPa]	$E_{c,m}$ [GPa]	l_{ch} [mm]
3.2*	2.4*	3.7**	3.11	34.0*	27.3**	30.7	373

*Calculated from Eurocode
**Experimental values

Table 7.3 – Set of parameters calibrated on flexural and compressive plain concrete response.

E_0 [GPa]	α [-]	σ_t [MPa]	l_t [mm]	σ_s/σ_t [-]	n_t [-]	σ_{C0} [MPa]
34	0.25	1.55	600	5.5	1.	190
H_{c0}/E_0 [-]	k_{c0} [-]	k_{c1} [-]	k_{c2} [-]	μ_0 [-]	μ_∞ [-]	σ_{N0} [MPa]
0.4	2	1	5	0.35	0	600
d_0 [mm]	d_a [mm]	c [kg/m^3]	w/c [-]	n_F [-]	ρ_c [kg/m^3]	a/c [-]
8	15	400	0.46	0.5	2400	4.34

7.6.4. Plain concrete calibration results

The numerical model calibrated is reported in terms of flexural response in Figure 7.8, cube and cylinders compressive tests, where the peak strength is calibrated (Figure 7.9). For each model different seeds are simulated: a seed represents a different arrangement of the aggregates, in case of plain concrete, obtained by setting a different sequence of numbers in the input file. A further observation is added simulating the flexural behaviour with LDPM approach extended to the entire specimen (Figure 7.8b): the curves present no remarkable differences. However, the trend is not identical as the different arrangement of particles in two different volumes.

The cylindrical compressive strength simulated results lower than the experimental results, nevertheless it is reliable since has a value lower than the compressive strength simulated on cubes.

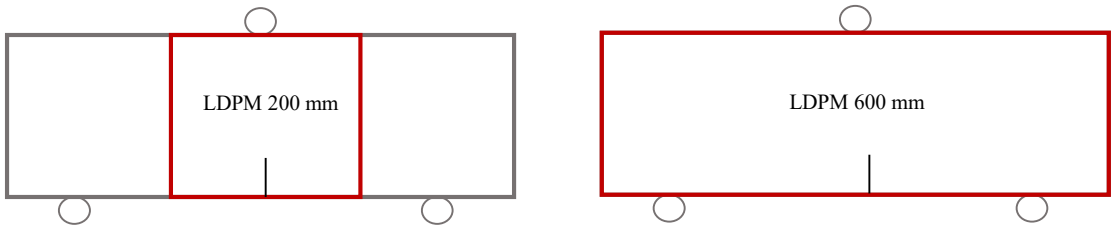

(a) (b)

Figure 7.7– Schematization of the LDPM extension (a) Close to the prism notch (LDPM 200 mm) and (b) extended to the entire length (LDPM 600 mm)

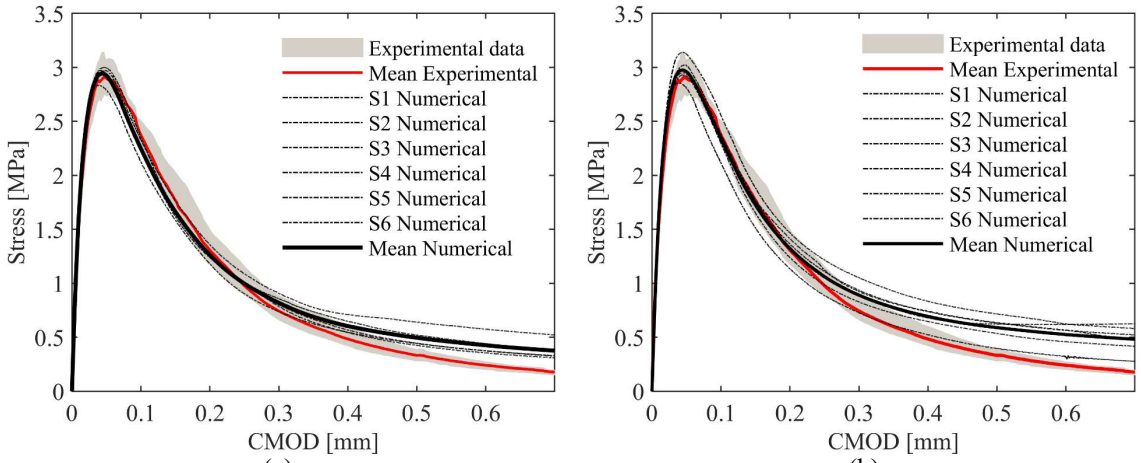

(a) (b)

Figure 7.8– (a) Plain concrete flexural tests calibration (LDPM 200 mm); (b) Plain concrete compressive tests calibration (LDPM 600 mm) simulated for six aggregates arrangement (Seeds).

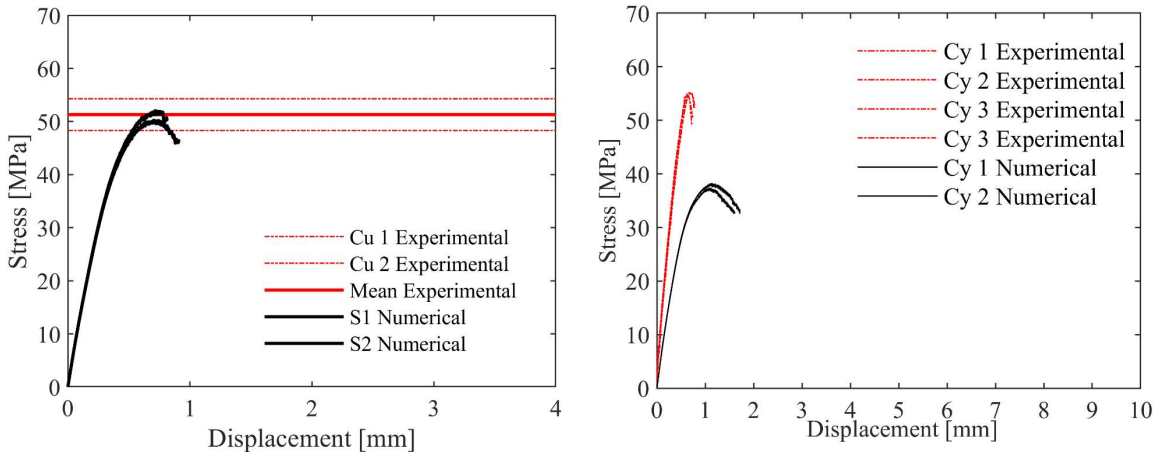

(a) (b)

Figure 7.9– (a) Plain concrete cube compressive tests calibration simulating two seeds; (b) Plain concrete cylinders compressive tests calibration simulating two seeds.

7.6.5. Fibre – Matrix parameters calibration

Comparing the experimental results for plain and fibre reinforced concrete, the former shows lower values than the latter, so the parameters calibrated on the plain concrete are readjusted on the basis of MSFRC flexural and compressive response increasing the tensile strength, tensile characteristic length, softening exponent and decreasing the shear strength ratio.

The fibrous reinforcement is modelled assigning the fibre geometry for the single element generation and the mechanical properties to describe the fibre – bridging mechanism.

The fibers are randomly generated inside the LDPM concrete portion according to the geometrical properties described in section 7.3: in the case at issue, the specification of a high number of edges per fibre has been demonstrated to better describe the crimped shape of the filament together with the tortuosity and preferential direction value. It is important to accurately describe the fibre shape because a crimped profile features a different interfacial behavior if compared to those straight. The pull-out experimental campaign exposed before (chapter 3), although considers a different fibre, has revealed how the post peak trend is influenced by the fibre shape influencing the flexural response. Even for fibre reinforced concrete calibration, the influence of the parameters to be assigned is examined. The debonding fracture energy influences the value and position of the peak of a pull-out curve (Marangi, 2010) and it represents a portion of the whole area under the load – displacement curve: its calibration is based on values reported in literature mostly for PVA fibres. Since polypropylene has a lower chemical adhesion than the previous material, values of $G_d < 5$ N/m are used in the calibration procedure. β is a parameter affecting the post-peak slope of a pull-out response curve (see section 1.2.6) if softening, constant or hardening trend. The tensile strength and elastic modulus assigned are those proper of the fibre, resulted from direct tensile experimental tests performed on a group of fibers (see section 6.4.10).

A consideration should be expressed on the polypropylene density, its value determines the number of fibers generated and the post peak response of the material is strongly conditioned by this element. For this reason, using ρ=946 kg/m^3 proper of the polypropylene material, the volume fraction obtained is 0.85% while, considering the density declared by the company for this type of fibre ρ=910 kg/m^3, a volume fraction of 0.9% is obtained. The determination of the right volume fraction is based on the fibre count comparison between the experimental and numerical number. Moreover, before the validation of the model, many considerations are elaborated on the d_0 value, the lower aggregate size, the estimation of the fibre elastic modulus E_f, that regulates the load transmission from the matrix to the fibrous reinforcement in the cracked state and a comparison between numerical and experimental fibres count crossing the cracked surface, as a verification of the right volume fraction to be assigned.

Table 7.4 collects the mechanical parameters calculated on the experimental compressive and flexural strength results using the expressions [7.53 – 7.54]: these values are used as reference in order to calibrate the mesoscale parameters. It is important to underline that the mesoscale elastic modulus, as already specified, is calculated as a function of α = 0.25.

Table 7.5 and Table 7.6 indicate respectively the mechanical parameters calibrated on three point bending and compressive tests regulating the LDPM (concrete) and LDPM-F (fibre reinforcement) constitutive behaviour.

Table 7.4 – Estimation of the tensile strength and elastic modulus experimentally and analytically determined for MSFRC [8 kg/m^3].

$f_{ct,1}$ [MPa]	$f_{ct,2}$ [MPa]	$f_{ct,3}$ [MPa]	$f_{ct,m}$ [MPa]	$E_{c,1}$ [GPa]	$E_{c,2}$ [GPa]	$E_{c,m}$ [GPa]
3.5*	3.4*	-**	3.45	35.4*	-**	35.4

*Calculated from Eurocode
**Experimental values

Table 7.5 – LDPM mechanical parameters calibrated on MSFRC flexural and compressive tests.

E_0 [GPa]	α [-]	σ_t [MPa]	l_t [mm]	σ_s/σ_t [-]	n_t [-]	σ_{C0} [MPa]
40	0.25	2.0	800	4.0	1.5	190
H_{c0}/E_0 [-]	k_{c0} [-]	k_{c1} [-]	k_{c2} [-]	μ_0 [-]	μ_∞ [-]	σ_{N0} [MPa]
0.4	2	1	5	0.35	0	600
d_0 [mm]	d_a [mm]	c [kg/m^3]	w/c [-]	n_F [-]	ρ_c [kg/m^3]	a/c [-]
8	15	400	0.46	0.5	2400	4.34

Table 7.6 – LDPM – F mechanical parameters calibrated on MSFRC flexural and compressive tests.

G_d [N/m]	τ_0 [MPa]	β [-]	k_{sp} [-]	k_{sn} [-]	σ_{uf} [MPa]	k_{rup} [-]
1.0	4.0	0.5	6.2	1.0	473	0.0
E_f [GPa]	l_f [mm]	d_f [mm]	V_f [%]	Tortuosity	Shape [-]	ρf [kg/m3]
2.6	54	0.81	0.85/0.9	0.6	crimped	946/910

7.6.6. MSFRC fibre count for 0.85% volume fraction of fibers

The experimental investigation revealed the correlation between the residual flexural strength and the effective fibers number present in the cracked cross section of the beam.

For this reason, the number of fibers generated by the code is considered for two volume fractions: 0.85% and 0.9%. Figure 7.10 presents the comparison between the experimental and numerical fibre count: the procedure will be explained in detail in section 7.6.7. Besides any singularities the results appear consistent. Moreover, the volume fraction of 0.9% is adopted since the numerical mean value and the standard deviation are closer to those experimental (Table 7.7).

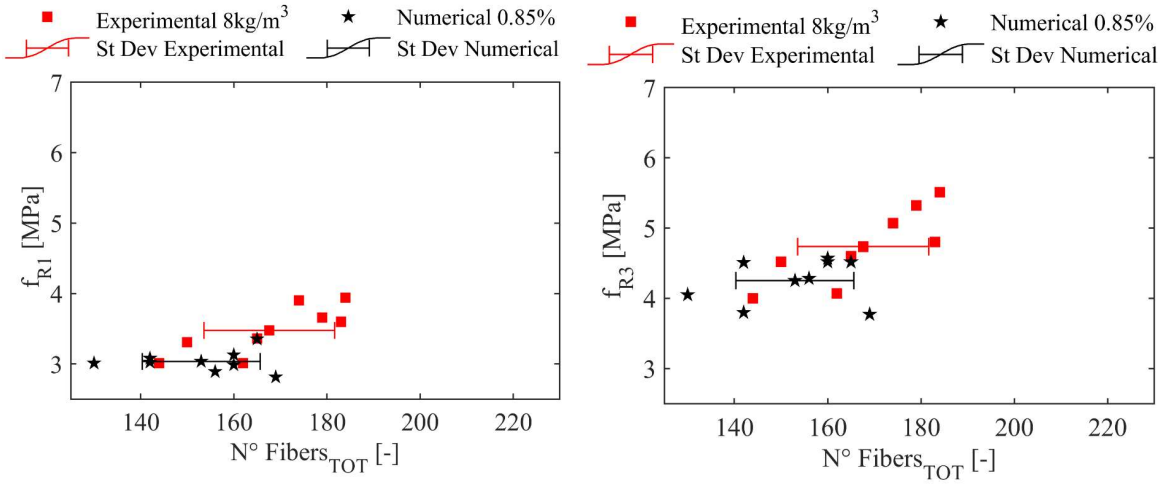

(a) (b)

Figure 7.10 – (a) Residual flexural strength fR1 and (b) fR3 versus experimental and numerical fiber count for volume fraction of 0.85%.

Table 7.7 – Fibre count values evaluated for experimental and numerical simulations.

Specimen ID	Fiber Count [-]		
	Experimental	Numerical (0.85%)	Numerical (0.9%)
T1	174	156	160
T2	165	142	147
T3	179	165	175
T4	184	160	165
T5	183	169	180
T6	150	142	147
T7	144	130	136
T8	162	160	156
Mean	168	153	158
St Deviation	14.1	12.6	14.0

7.6.7. MSFRC calibration results [0.9%]

The numerical model is calibtaed on the experimental flexural response simulating eight seeds and extended the LDPM approach for a length of 200 mm close to the notched section (Figure 7.11). Moreover, the same parameters are used to simulate

the flexural behaviour but extending the LDPM approach to the entire length of 600 mm. The response is reported in Figure 7.12 where four seeds are generated whose mean curve, solid black line, is compared to the mean trend of four seeds of the previous approach (LDPM length 200 mm) in Figure 7.13. The difference is more pronounced in the post-peak trend rather than in the peak value: this was expected since the fibers generation involves a different volume and, so, their position changes.

A further observation involves the fibre elastic modulus. The first set of elastic parameters for the reinforcement considers the secant elastic modulus of 2.6 GPa and, observing the flexural trend in Figure 7.11, the descending branch reaches a minimum value lower than the experimental response. Since the load transferring mechanism drives this phase and depends on the elastic modulus of the reinforcement which carries the load in the cracked section, a higher fibre elastic modulus of 3.3 GPa, closer to the tangent elastic modulus of 3.9 GPa (see section 6.4.10). The simulation considers four seeds Figure 7.14 and the value adopted appears to describe better the contribution of the fibre reinforcement in the post-peak. Thus, the present value will be adopted for the model validation.

In addition, the cracked phase simulated by the model presents many ‘jumps’ that, according to the several calibrations performed on MFRCs with different fibers type and dosages, it has been found to increase with the amount of fibers. In order to investigate the numerical feature responsible, the numerical model is simulated with a lower value of the minimum aggregate size, 5 mm. Figure 7.15 shows the flexural response of the numerical model simulated with the same parameters but with a minimum aggregate size of 5 mm. A first visual comparison suggests a reduction of the ‘jumps’ confirmed by comparing one single seed with 8 mm grain size (black solid line) and 5 mm size (dashed line) in Figure 7.16. In light of this, the jumps are thought to be associated with the breakage of the particle crossed by the neutral axis that rises towards the up edge of the section that is going to be fully cracked. However, this is a further observation but all simulations consider an aggregate size range between 8 – 15 mm.

The compressive tests are also simulated in order to calibrate the shear-strength ratio parameter (Figure 7.17).

As in the experimental analysis, the number of fibers is estimated also for the numerical model extracting their coordinates (Figure 7.18) and counting them using a code elaborated with Matlab™: the fibers included in the middle cross section are counted and related to the residual flexural strength at 0.5 mm crack opening, f_{R1}, and 2.5 mm crack opening, f_{R3}. The linear regression in Figure 7.19 - Figure 7.20, is elaborated on the experimental and numerical data obtained from the numerical flexural response simulated with LDPM extension of 200 mm, 2.6 GPa fibre elastic modulus and respectively 5 mm d_0 (grey points) and 8 mm d_0 (black stars). The number of fibers generated with the volume fraction assigned agrees with the experimental results. Moreover, considering the results of the simulations with 5 mm aggregate size, the fibers number and the residual strength present a smaller scatter, this might be due to the higher volume of aggregates that causes a more 'ordered' dispersion.

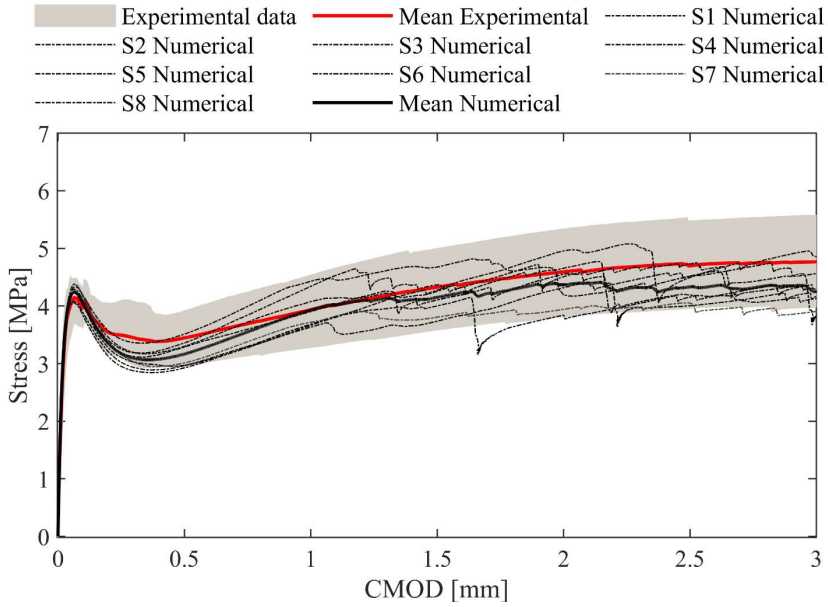

Figure 7.11 – MSFRC flexural tests calibration (LDPM 200 mm).

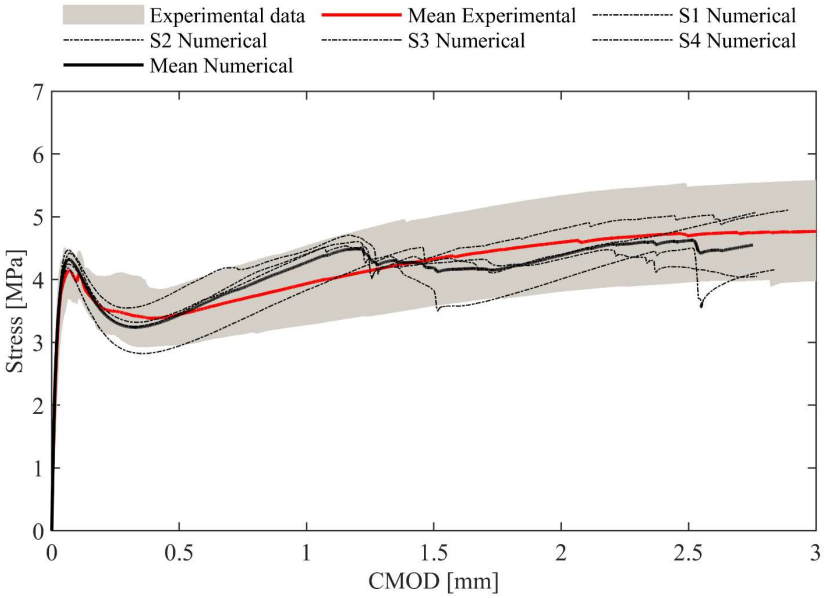

Figure 7.12 – MSFRC flexural tests calibration (LDPM 600 mm).

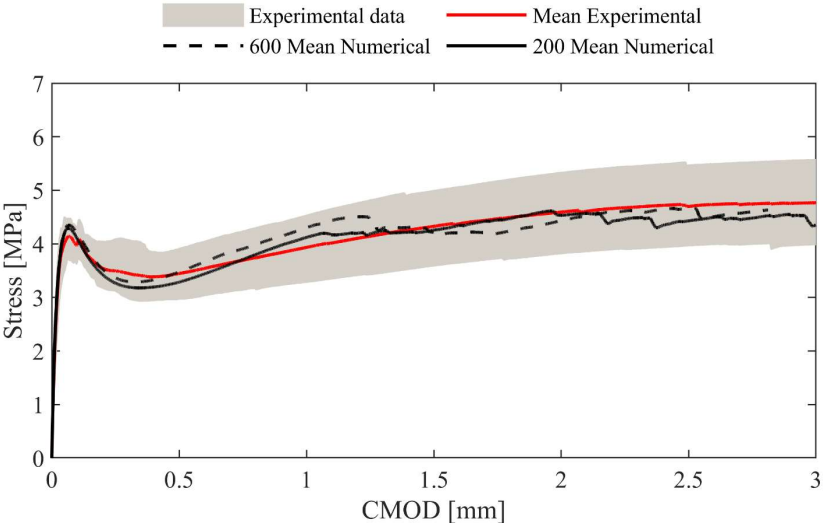

Figure 7.13 – MSFRC flexural tests calibration: influence of LDPM length.

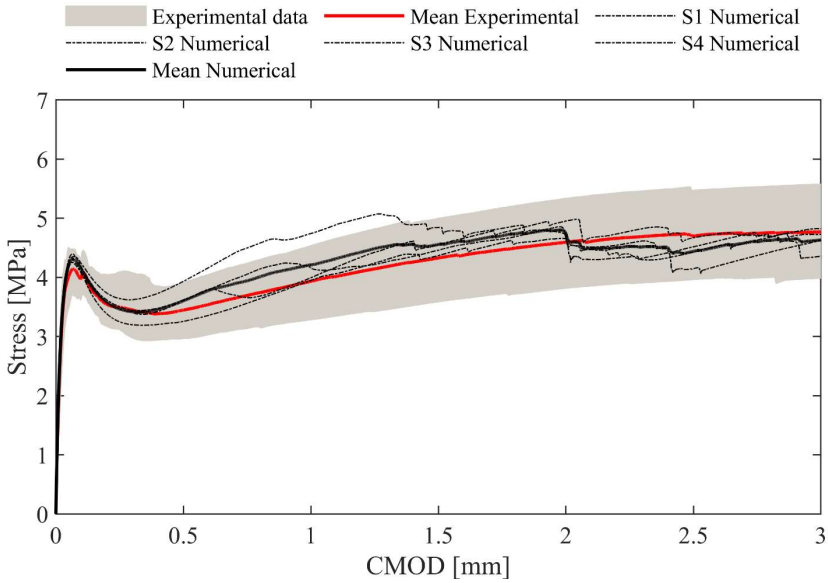

Figure 7.14 – MSFRC flexural tests calibration (Higher fibre modulus).

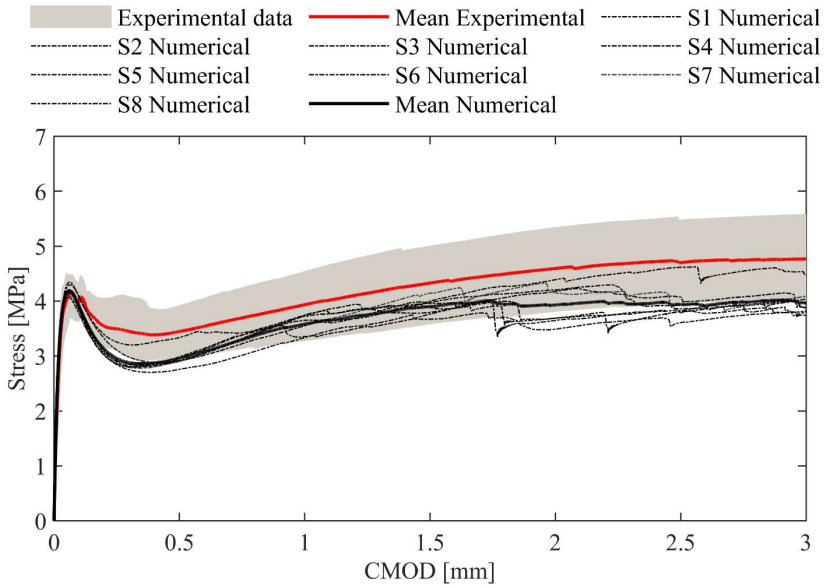

Figure 7.15 – MSFRC flexural tests calibration (Lower minimum aggregate size – 5mm).

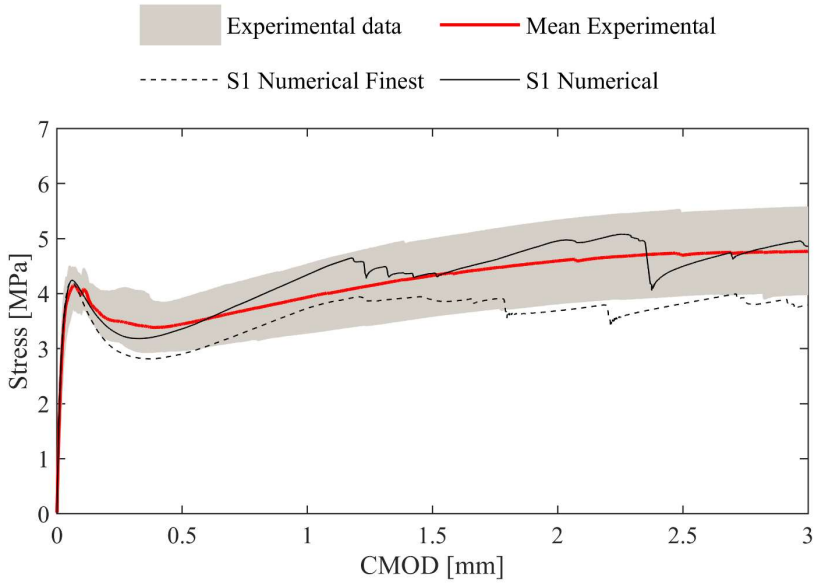

Figure 7.16 – MSFRC flexural tests calibration: comparison of one seed with 5 mm and 8 mm minimum aggregate size.

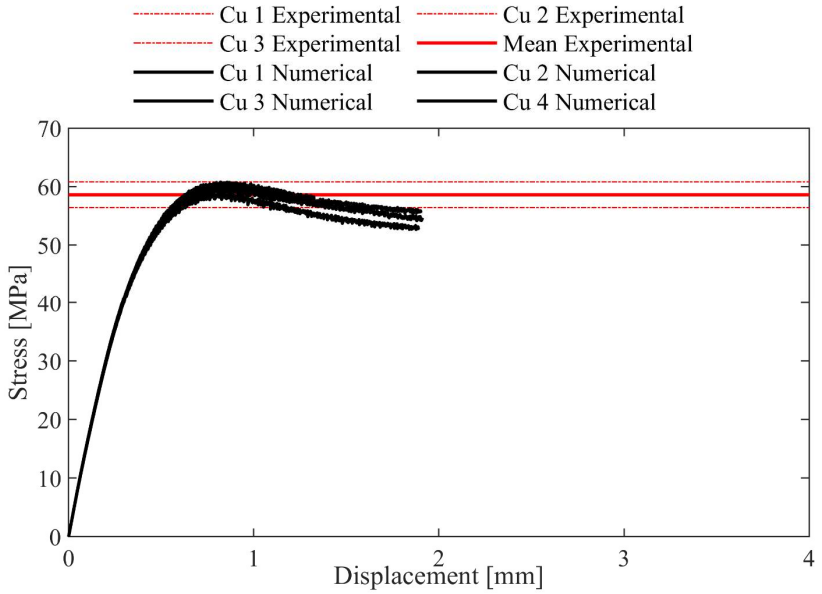

Figure 7.17 – MSFRC compressive tests tests calibration.

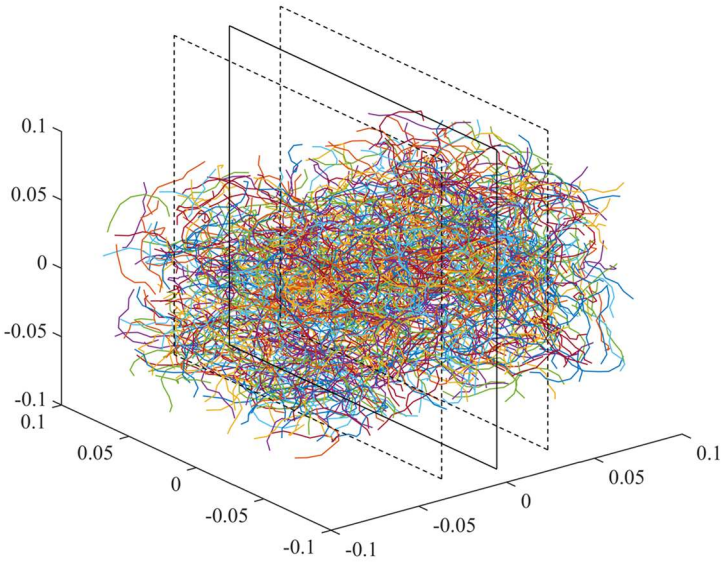

Figure 7.18 – Fibers generation and schematization of the numerical fibre count.

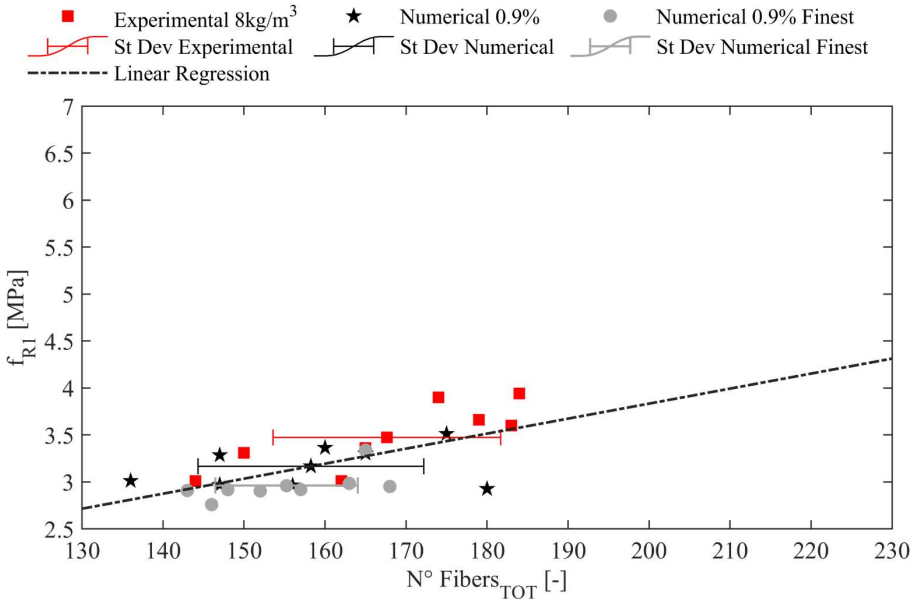

Figure 7.19 – MSFRC Fiber count versus f_{R1} residual flexural strength.

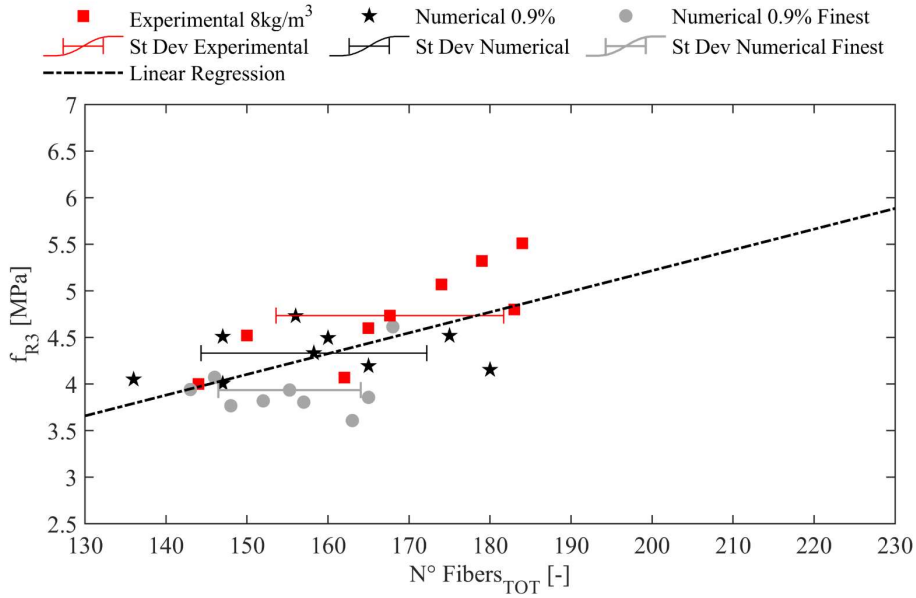

Figure 7.20 – MSFRC Fiber count versus f_{R3} residual flexural strength.

7.7. SHORT TERM BEHAVIOUR: MODEL VALIDATION

According to the remarks and observations drawn in the previous section, the model is validated on the experimental results of the MSFRC reinforced with a higher dosage of 10 kg/m^3 of the same fibers type using the parameters previously calibrated and collected in Table 7.8 for the LDPM constitutive law and Table 7.9 for the fibre-matrix interaction (LDPM-F).

The mean numerical curve (black solid lined) in Figure 7.21 shows a good agreement with the experimental results.

Moreover, the flexural tests are simulated also with the full LDPM approach extended to the entire specimen (Figure 7.22).

The peak compressive strength of the material is validated on the experimental results simulating cube compressive tests (Figure 7.23)

The comparison in presented also in terms of number of fibers in Figure 7.24 and Figure 7.25 respectively for the residual flexural strength values correspondent to 0.5 mm and 2.5 mm crack opening. The number of fibers numerically generated is in agreement with the experimental count and the linear regression elaborated on

experimental and numerical data confirms the dependence of the post cracking behaviour on the fibers contained onto the middle cracked section.

Table 7.8 – LDPM mechanical parameters used for the validation of the MSFRC model.

E_0 [GPa]	α [-]	σ_t [MPa]	l_t [mm]	σ_s/σ_t [-]	n_t [-]	σ_{C0} [MPa]
40	0.25	2.0	800	4.0	1.5	190
H_{c0}/E_0 [-]	k_{c0} [-]	k_{c1} [-]	k_{c2} [-]	μ_0 [-]	μ_∞ [-]	σ_{N0} [MPa]
0.4	2	1	5	0.35	0	600
d_0 [mm]	d_a [mm]	c [kg/m^3]	w/c [-]	n_F [-]	ρ_c [kg/m^3]	a/c [-]
8	15	400	0.46	0.5	2400	4.34

Table 7.9 – LDPM – F mechanical parameters used for the validation of the MSFRC model.

G_d [N/m]	τ_0 [MPa]	β [-]	k_{sp} [-]	k_{sn} [-]	σ_{uf} [MPa]	k_{rup} [-]
1.0	4.0	0.5	6.2	1.0	473	0.0
E_f [GPa]	l_f [mm]	d_f [mm]	V_f [%]	Tortuosity	Shape [-]	ρf [kg/m3]
3.3	54	0.81	1.1	0.6	crimped	910

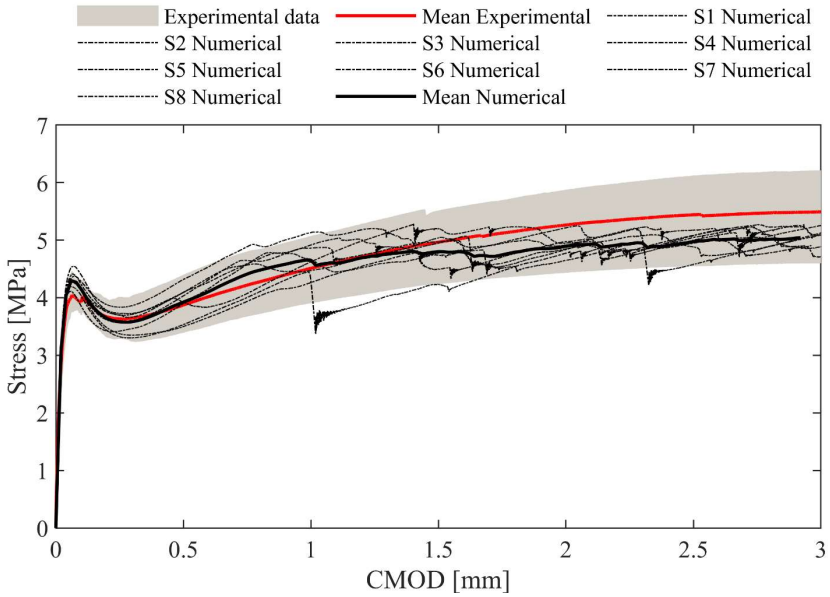

Figure 7.21 – MSFRC flexural tests validation (LDPM 200 mm).

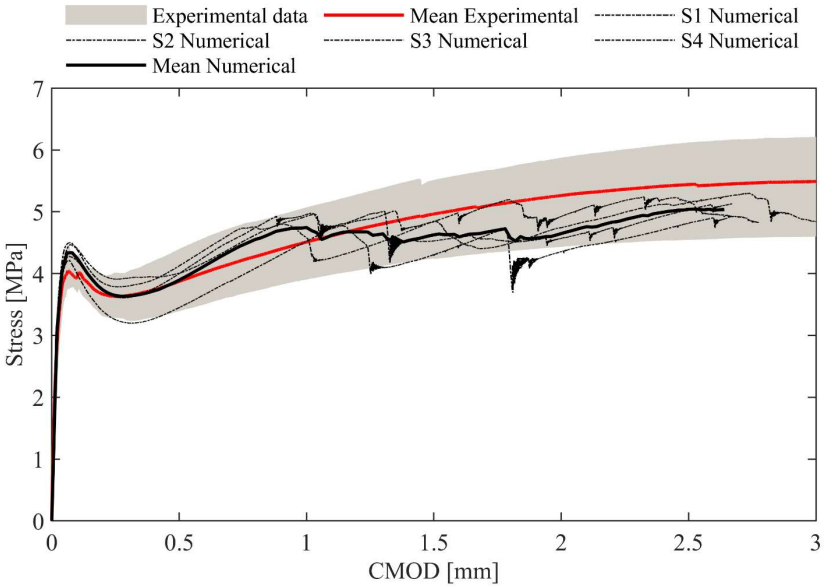

Figure 7.22 – MSFRC flexural tests validation (LDPM 600 mm).

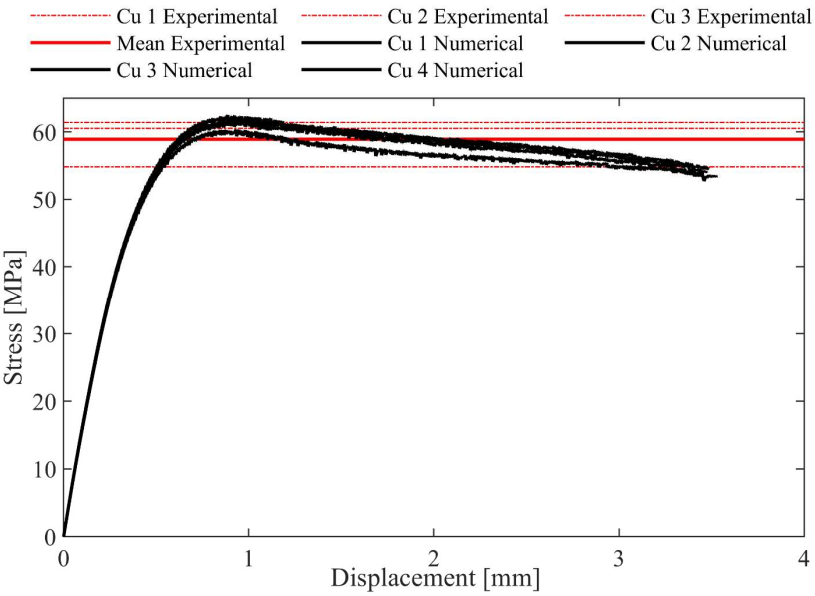

Figure 7.23 – MSFRC cube compressive tests validation.

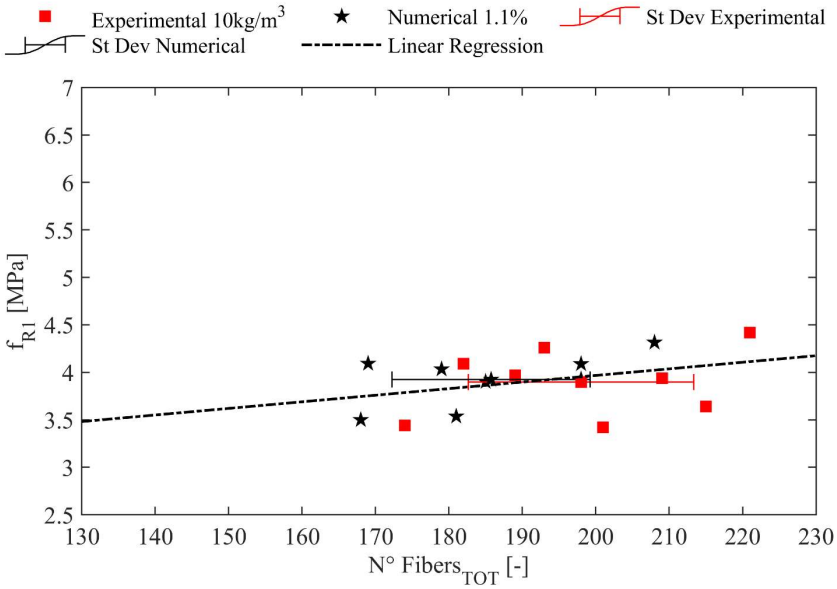

Figure 7.24 – MSFRC Fiber count versus f_{R1} residual flexural strength.

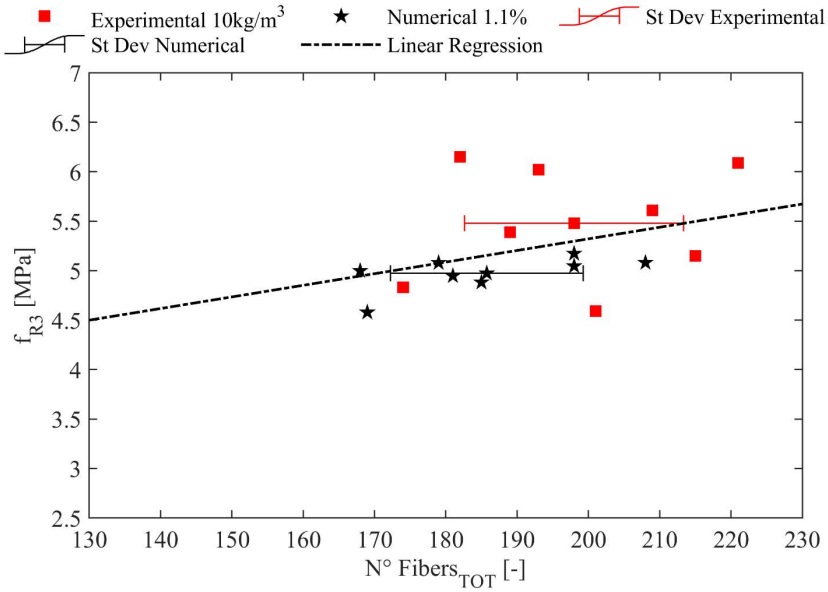

Figure 7.25 – MSFRC Fiber count versus f_{R3} residual flexural strength.

7.7.1. Influence of the preferential direction parameter

One of the innovative aspects of the present work is represented by the simulation of the fibers viscoelasticity and, since the viscoelastic deformations might be

influenced by their position in the matrix, the idea is to analyze a condition in which there are no specification about the preferential direction of their placement. For this reason, the flexural response calibrated with the previous parameters is simulated without considering this property actually being more significative in case of numerical model for structural elements, i.e. slabs.

Figure 7.26 and Figure 7.27 show the results of model calibrated and validated, respectively for 0.9% and 1.1% of fibers volume fraction, revealing a good calibration of the parameters also in case the fibers arrangement is only driven by the seed set in the code.

The preferential direction parameter is not considered when compressive tests on cube are simulated.

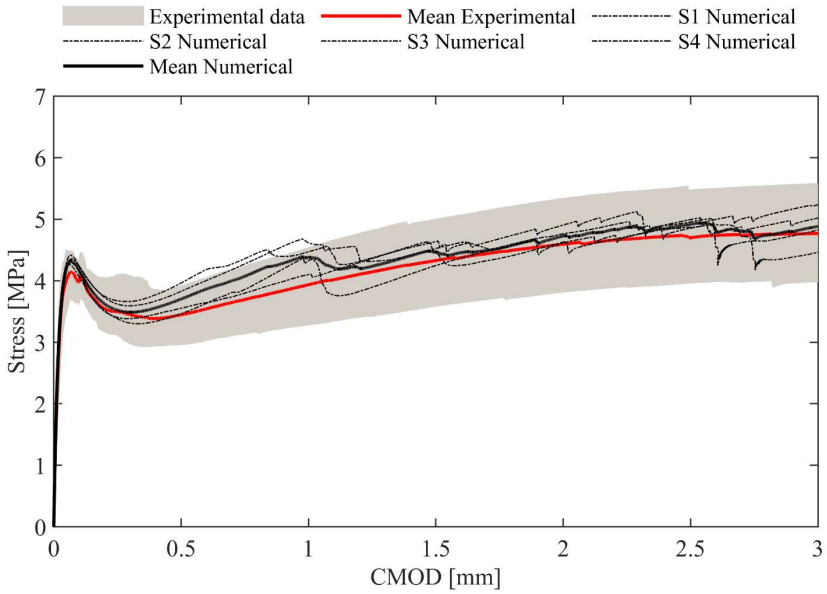

Figure 7.26 – MSFRC flexural tests validation without considering fibers preferential direction [0.9%].

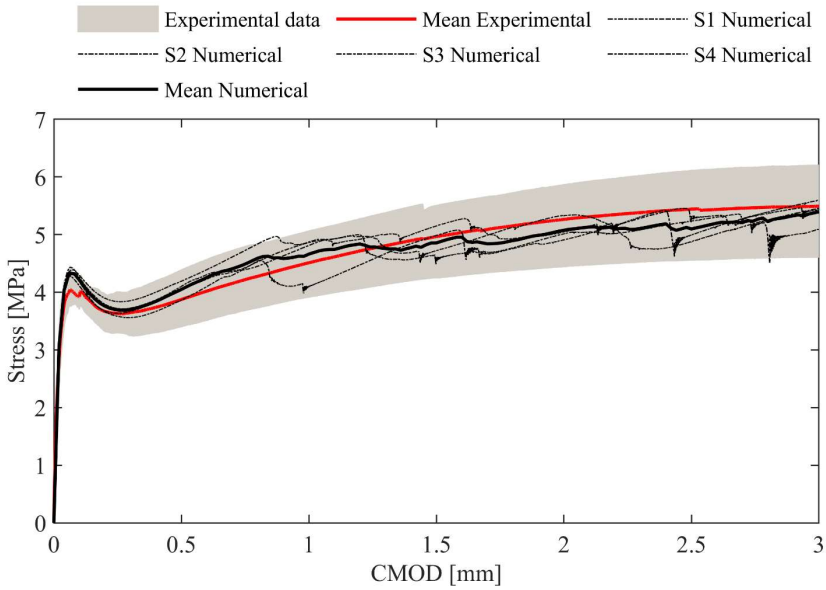

Figure 7.27 – MSFRC flexural tests validation without considering fibers preferential direction [1.1%].

7.7.2. Cracking process evolution

The present code makes possible to simulate and observe how the cracks gradually evolve colouring the corresponding facets according to the total crack opening values. This is an important aspect to consider since it could be a powerful mean by which many conditions are investigated, i.e. how the supports conditions affect tha cracks formation, that in the experimental analysis cannot be separated by other influencing factors. In order to represent the cracks configuration at a certain simulated crack opening, the values measured are plotted against the computational time step pointing the exact instants of time at which the information are extracted from the visualization program Paraview 5.6.0 (Figure 7.28, Figure 7.29, Figure 7.30).

Comparing Figure 7.31, Figure 7.32 and Figure 7.33 it is possible to drawn some considerations about how the cracking pattern is handled differently by plain and fibre reinforced concrete respectively with volume fractions of 0.9% and 1.1%.

The representations depict respectively the configuration at a measured CMOD numerical value of 0.5 mm for plain concrete and MSFRC with lower and higher

volume fraction where the total crack opening has a maximum value higher for plain concrete and slightly lower for the MSFRCs.

Indeed, as expected, the cracks are more diffused in case of fibre reinforced concrete rather than in case of plain concrete where the crack is more localized and the bridging effect is only due to the aggregates. The cracking pattern shown by the fibre reinforced concretes reflect the crack-bridging phenomenon since the residual strength gained.

The same evaluation can be made comparing the process zone of the two volume fractions, 0.9% and 1.1%, at measured crack openings of 1.5 mm (Figure 7.34 – Figure 7.35) and 2.5 mm (Figure 7.36 – Figure 7.37). The representations below emphasize the increment of the process zone extension with the fibre dosage.

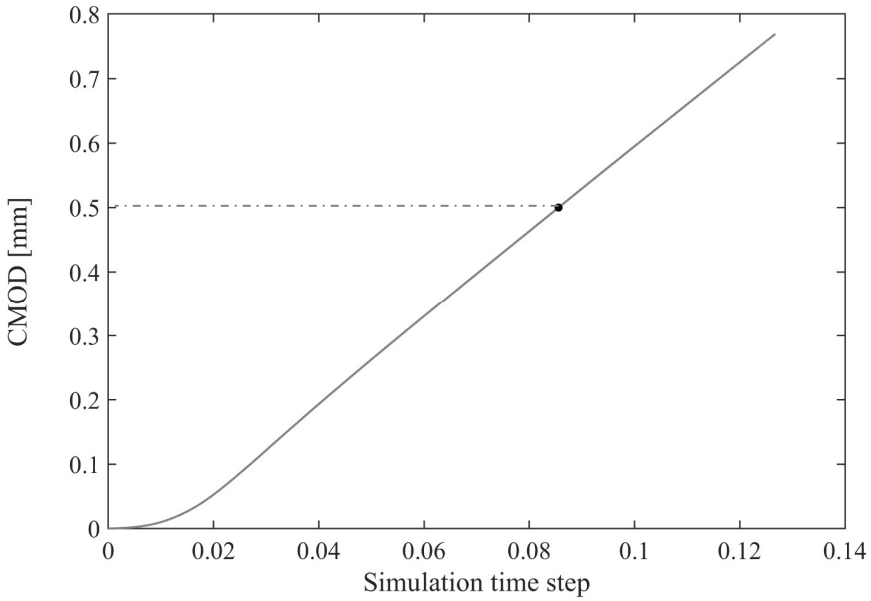

Figure 7.28 – Plain concrete TPB simulation (Seed 1) with LDPM length 600 mm: CMOD values versus computational time steps.

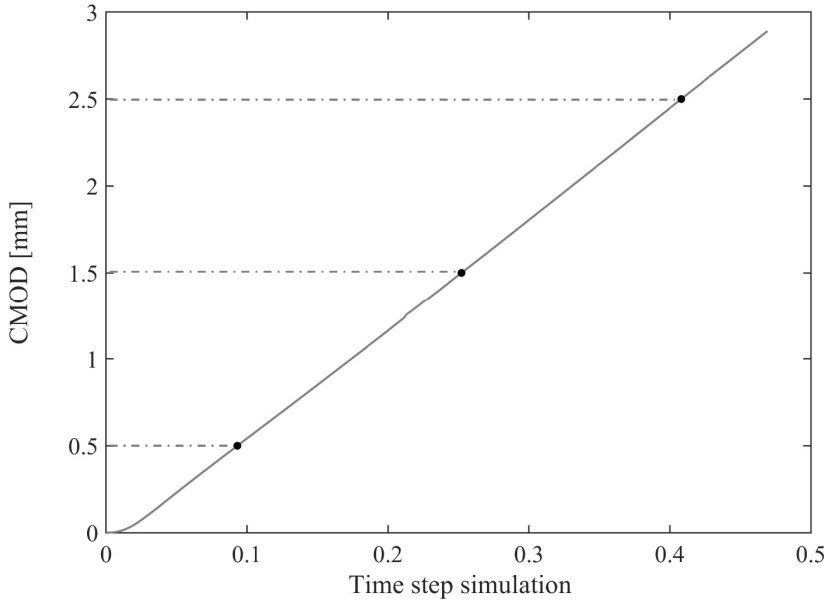

Figure 7.29 – MSFRC 0.9% volume fraction TPB simulation (Seed 1) with LDPM length 600 mm: CMOD values versus computational time steps.

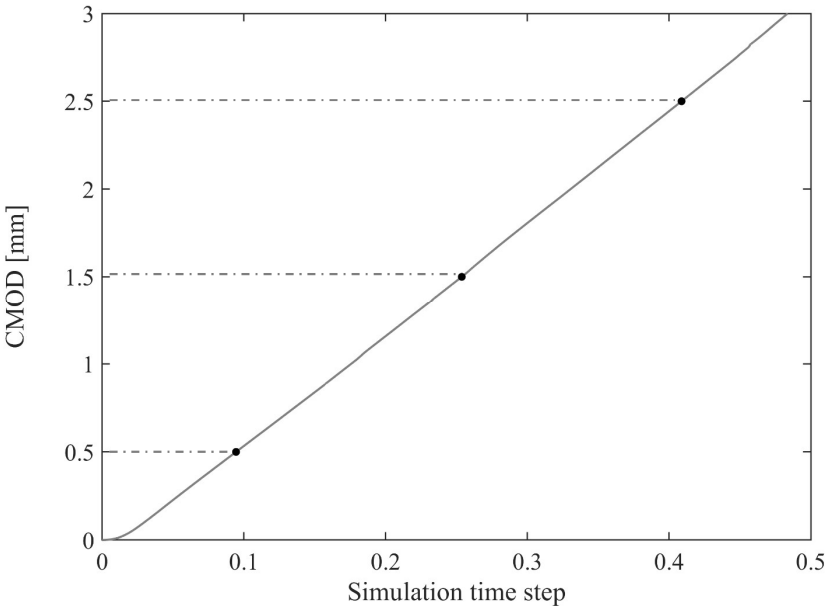

Figure 7.30 – MSFRC 1.1% volume fraction TPB simulation (Seed 1) with LDPM length 600 mm: CMOD values versus computational time steps.

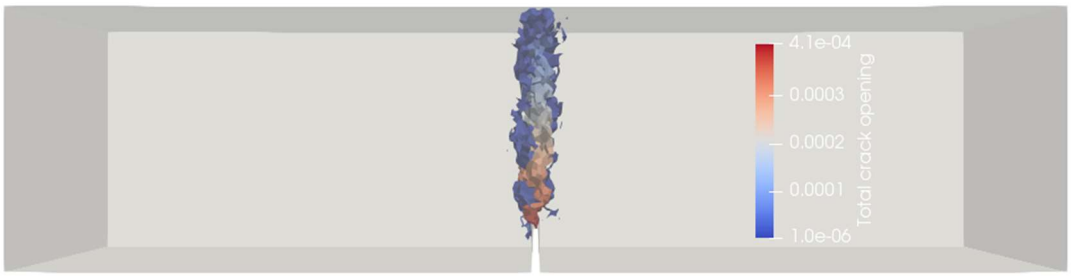

Figure 7.31 – Plain concrete cracking pattern at measured CMOD of 0.5 mm (LDPM 600 mm, Seed 1).

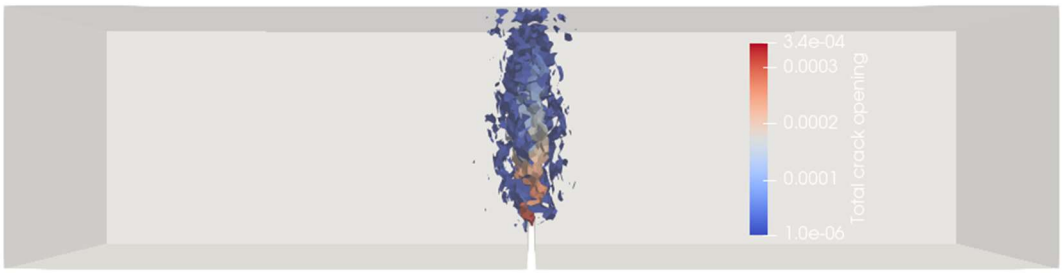

Figure 7.32 – MSFRC 0.9% cracking pattern at measured CMOD of 0.5 mm (LDPM 600 mm, Seed 1).

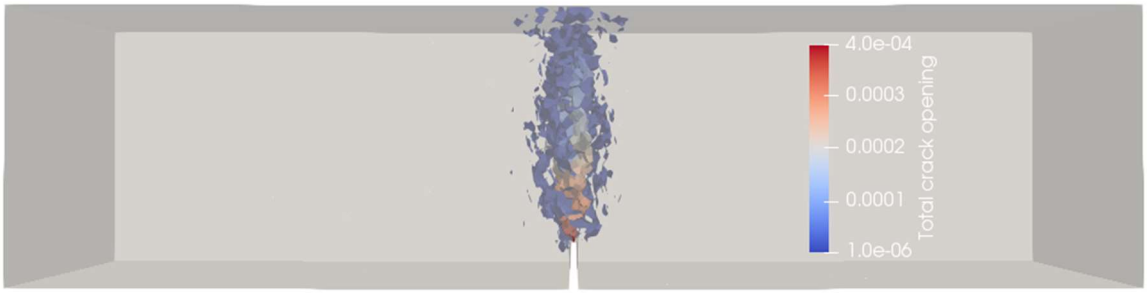

Figure 7.33 – MSFRC 1.1% cracking pattern at measured CMOD of 0.5 mm (LDPM 600 mm, Seed 1).

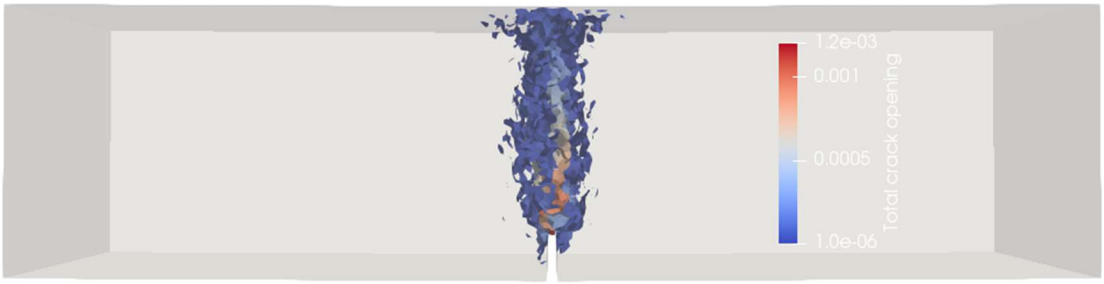

Figure 7.34 – MSFRC 0.9% cracking pattern at measured CMOD of 1.5 mm (LDPM 600 mm, Seed 1).

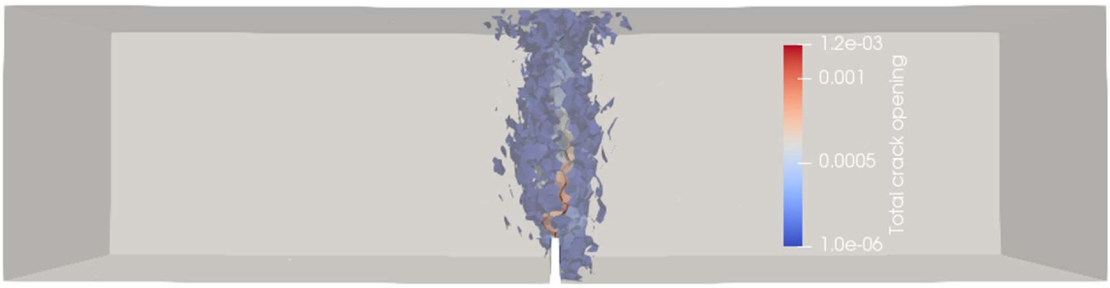

Figure 7.35 – MSFRC 1.1% cracking pattern at measured CMOD of 1.5 mm (LDPM 600 mm, Seed 1).

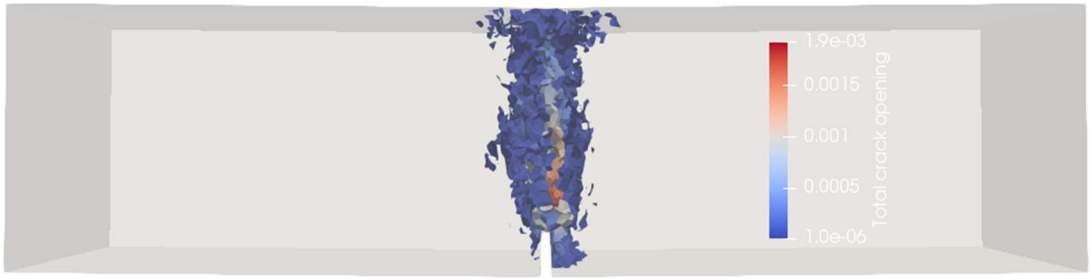

Figure 7.36 – MSFRC 0.9% cracking pattern at measured CMOD of 2.5 mm (LDPM 600 mm, Seed 1).

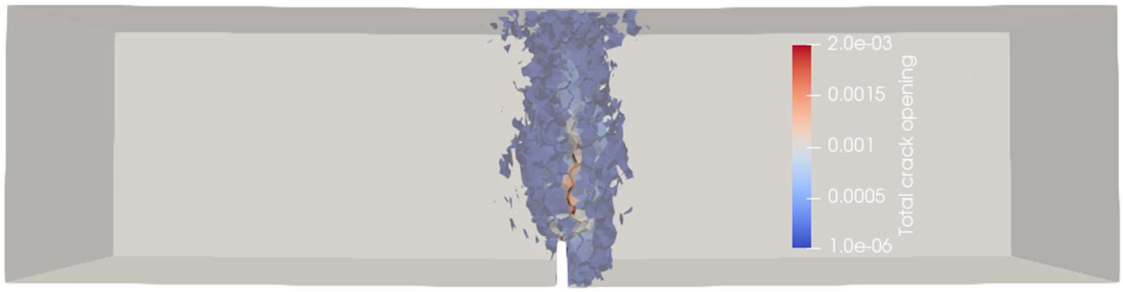

Figure 7.37 – MSFRC 1.1% cracking pattern at measured CMOD of 2.5 mm (LDPM 600 mm, Seed 1).

7.8. LONG TERM BEHAVIOUR: MODEL CALIBRATION

The large experimental campaign of creep tests performed (reported in chapter 6, section 6.4) produced a very wide database of results used to study in deep the creep behaviour of the MSFRC under different loading conditions. Besides the

experimental investigation, the results achieved represent the background for the numerical simulation of creep and shrinkage phenomena. The calibration procedure is structured according the following phases:

i. Refining of the LDPM static parameters on cube compressive tests and preloading phase of prisms under flexural load;
ii. Calibration of the shrinkage strain profile on shrinkage tests;
iii. Calibration of creep compressive parameters on cylinders creep compression;
iv. Calibration of the fibre viscoelasticity on fibre uniaxial creep tests;
v. Calibration of tensile creep deformations on results of uniaxial tensile tests on MSFRC.

The phases ii and iii consider a numerical model elaborated with no fibers addition with the aim of simulating the concrete matrix creep and shrinkage deformations.

The further step regards the simulation of the viscoelastic bond between fibre and matrix and the model validation on creep flexural experimental tests.

7.8.1. LDPM – F mechanical parameters definition

The pre-cracking phase of the material under flexural and uniaxial tensile tests revealed an increment of the peak strength respect to that characterized in the previous batches realized with 8 kg/m^3 and 10 kg/m^3 fibre dosages. For this reason, the elastic and inelastic numerical LDPM parameters are refined fitting the experimental flexural results, considering the pre-cracking stage, and compressive tests on cubic specimens where the peak strength is considered (Table 7.10). The fiber – concrete interaction considers the same parameters (Table 7.11).

The pre-cracking phase for the prisms is numerically simulated in displacement control, according to the experimental conditions, so that the specimen is prekcracked until a CMOD value of 0.5 mm and then unloaded. The numerical model considers an extension of the LDPM approach to the whole prism and considering three

different arrangement of fibers since the prisms tested under sustained load are three. The results show a good calibration of the pre-cracking flexural behaviour (Figure 7.38). The simulation of the loading and unloading stage in terms of crack opening is depicted in Figure 7.40 for CMOD value of 0.06 mm, 0.5 mm and 0.19 mm.

In addition, the peak compressive strength is calibrated on the cube tests (Figure 7.39).

Table 7.10 – LDPM mechanical parameters re-calibrated for the MSFRC viscoelastic model.

E_0 [GPa]	α [-]	σ_t [MPa]	l_t [mm]	σ_s/σ_t [-]	n_t [-]	σ_{C0} [MPa]
45	0.25	2.5	800	3.0	0.5	190
H_{c0}/E_0 [-]	k_{c0} [-]	k_{c1} [-]	k_{c2} [-]	μ_0 [-]	μ_∞ [-]	σ_{N0} [MPa]
0.4	2	1	5	0.35	0	600
d_0 [mm]	d_a [mm]	c [kg/m^3]	w/c [-]	n_F [-]	ρ_c [kg/m^3]	a/c [-]
8	15	400	0.46	0.5	2400	4.34

Table 7.11 – LDPM – F mechanical parameters for the MSFRC viscoelastic model.

G_d [N/m]	τ_0 [MPa]	β [-]	k_{sp} [-]	k_{sn} [-]	σ_{uf} [MPa]	k_{rup} [-]
1.0	4.0	0.5	6.2	1.0	473	0.0
E_f [GPa]	l_f [mm]	d_f [mm]	V_f [%]	Tortuosity	Shape [-]	ρf [kg/m3]
3.3	54	0.81	0.9	0.6	crimped	910

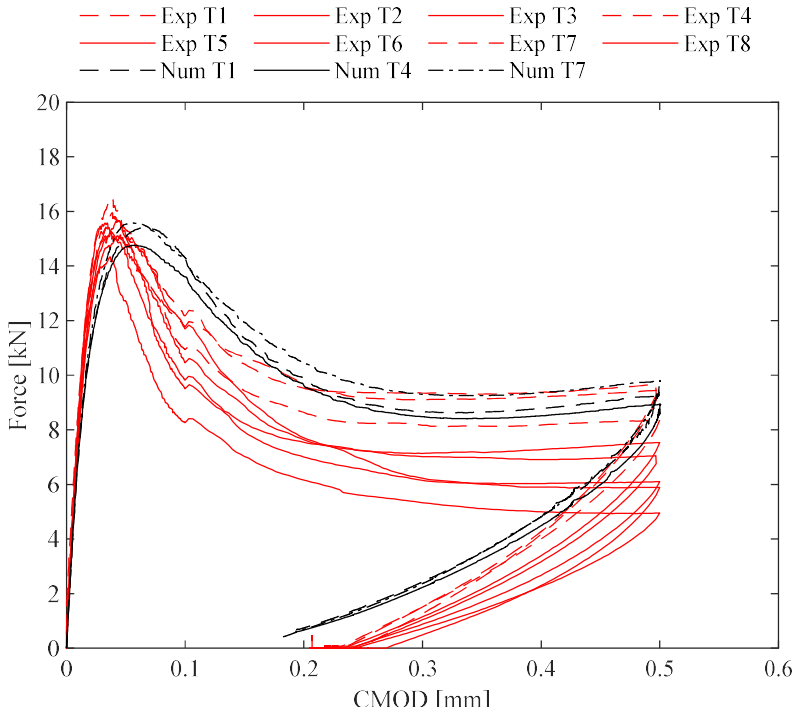

Figure 7.38 – MSFRC pre-loading phase simulation for three samples having three different fiber seeds (LDPM 600 mm).

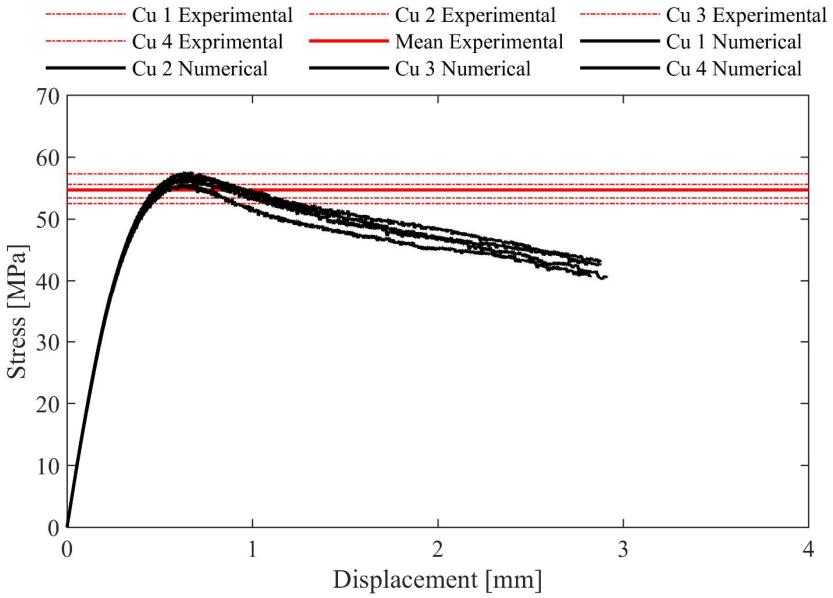

Figure 7.39 – MSFRC compressive tests for concrete characterization.

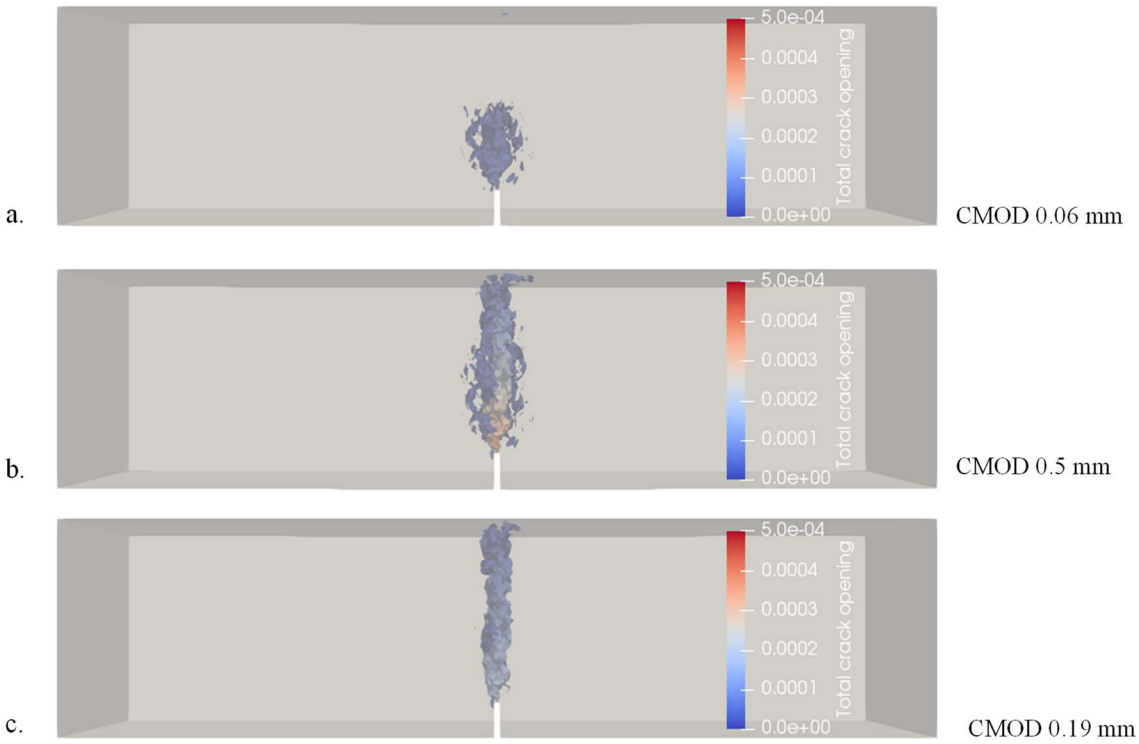

Figure 7.40 – MSFRC crack evolution during the preloading phase until a residual crack opening (LDPM 600mm).

7.8.2. Calibration procedure of time dependent phenomena

The previous procedure aimed at calibrating the mechanical parameters characterizing the LDPM and LDPM – F constitutive behaviour, is considered as the starting point since these parameters are then kept constant for the following phases. The visco-elastic and viscous behaviour of the material is calibrated following the phases 'i' to 'v' reported in section 7.8 trying to decouple the physical phenomena occuring in order to calibrate the parameters separately. In general, the perfect calibration should use several experimental test types, reported in Table 7.12, to fully describe the hygro-thermo-chemical reactions, the hygral and thermal strains and visco-elastic and viscous deformations occurring (Abdellatef et al., 2019). On one side it is impossible to decouple all phenomena since any of them act simoultaneously, and, on the other, a several number of tests should be performed.

The first four steps define the HTC model parameters: thermal conductivity tests determine the thermal transport properties, then the moisture content and the hydration evolution are to be calibrated separately and finally the step four, the calibration of the moisture transport phenomenon.

Once the previous parameters are calibrated, they are assumed in the next steps where the deformation tests are used to define the thermal and hygral deformations and, then, to define the visco-elastic and viscous strains. These are identified by testing samples under sustained loads.

In the present work, since no tests for the HTC model definition have been performed, the parameters are assumed starting from a dataset already calibrated for a concrete designed with almost the same mix design properties (Table 7.13).

The parameters reported in Table 7.14 are calibrated on the time – dependent deformations: α_h is determined on the shrinkage strain profile while the others on the creep compression tests. The value of α_T is better defined since the experimental tests are performed in non isothermal conditions, so the thermal expansion could be accurately described. ξ_1 is included in the set of visco-elastic parameters together with ξ_2 and n_α that are calibrated almost on the initial part of the creep compressive curve. Once they are defined, the parameters accounting for the viscous creep are calibrated, ξ_4 and k_1.

The definition of the fibrous reinforcement viscoelastic behaviour is based on the model described in section 7.5, where an easier approach is used since the non aging property of the polypropylene. As described before, the set of parameters need to be calibrated consists of three coefficients, α, β, the fractional exponential kernel coefficients and γ the rheological parameter. An initial set of parameters is assumed by fitting the experimental tensile creep curves on the single fibre tests by performing an iterative procedure trough an algorithm elaborated with Matlab™ code. The definition of starting values for the iterative procedure is based on the data reported by Golub et al. (Golub et al., 2008) for viscoelastic materials, i.e. aramid fibers and parapolyamide fibers and Sorzia (Sorzia, 2016) for polypropylene fibers (Table 7.15).

Then, the fitted values are used for the global model reproducing the viscoelastic creep of MSFRC cylinders under uniaxial tensile sustained load where the parameters are refined.

Table 7.12 – Calibration procedure of undamaged behaviour, adapted by (Abdellatef et al., 2019).

Mechanism to calibrate	Tests needed for uncoupled calibration	Parameters
1.Thermal transport	Thermal conductivity tests	c_t , λ_t
2.Moisture content	Sorption/desorption isotherms relevant to two different values of hydration degree with cement only and 2 other cases with silica fume (if present)	g_1, g_2, g_3
3.Hydration evolution	One adiabatic calorimetric test for cement only and another one with both cement and silica fume (if present)	A_{c1}, A_{c2}, η_c, A_{s1}, A_{s2}, η_s
4.Moisture transport	One drying test with relative humidity profile time/space history, or two tests with different relative humidity boundary conditions	D_0, D_1, n
5.Hygral deformation	Shrinkage and swelling tests of sealed samples	α_h
6.Thermal deformation	Thermal expansion and contraction tests	α_T
7.Aging visco-elastic behaviour	Apparent modulus of elasticity at three different loading ages for fully saturated or sealed samples	ξ_1, ξ_2, n_α
8.Basic viscous behaviour	Compliance function of fully saturated or sealed samples at 1 loading age	ξ_4
9.Drying viscous behaviour	Compliance function of drying samples at 1 loading age	k_1

Table 7.13 – Parameters used to simulate the chemical reactions, heat transfer and moisture transport in concrete.

Parameters (Units)	Value
A_{c1} (h^{-1} x 10^{7})	8.50
A_{c2} (x 10^{-7})	5
η_c (-)	7
A_{s1} (h^{-1} x 10^{7})	-
A_{s2} (x 10^{-7})	-
η_s (-)	-
c_t (kJ/kg°K)	1.2
λ_t (W/m°K)	2.8
D_0 (kg/mm h x10^{-9})	0.4
D_1 (kg/mm h x10^{-7})	15
n (-)	4.5
g_1 (-)	2.20
g_2 (-)	0.20
g_3 (-)	-

Table 7.14 – Parameters calibrated to simulate creep and hygro-thermal deformations.

Parameters (Units)	Value
α_h (x10^{-3})	1.19
α_T (x10^{-6})	5
ξ_1 (MPa^{-1} x 10^{-6})	1.3
ξ_2 (MPa^{-1} x 10^{-6})	0.42
ξ_4 (MPa^{-1} x 10^{-6})	2.
*n_α (-)	1.3
K_0 (MPa^{-2} sec^{-1} x 10^{-2})	2.34
K_1 (MPa/Kel x 10^{4})	0.001

*assumed

Table 7.15 – Parameters calibrated to simulate creep deformations of the fibre.

Parameters (Units)	Parameters set (Fibers tensile creep test)
α	-0.0098
β	0.0998
λ	0.0998

7.8.3. Shrinkage deformation calibration and validation

The shrinkage test is simulated considering the concrete matrix without fibers inclusion. The environmental conditions are simulated assigning two curves describing the evolution of temperature and relative humidity on time. They are defined considering the computational time. Figure 7.41a shows the temperature history assigned corresponding to the experimental conditions and, so, the increment of temperature, expressed in K, at 50 days and 178 days. Figure 7.41b reports the relative humidity profile that considers the 28 days of curing in water (100% humidity) and a gradual decrement until the 50% that represents the condition of the chamber where the experimental tests are performed. The application of the boundary conditions of temperature and humidity is simulated considering a sample size approximately 10 mm larger than the real: this strategy is adopted in order to not generate discontinuities on the specimen external faces.

The hygro thermo chemical phenomena can be visualize at different time steps: Figure 7.42 depicts the change of temperature on time according to the time step assigned with a focus on the temperature increment at 50 days (Figure 7.43) where the gradual increment can be appreciated.

Figure 7.44 illustrates the evolution of the humidity history selecting any instant of time: after the curing period of 28 days and the gradual diffusion of the new humidity condition.

Figure 7.45 shows the numerical model simulating the shrinkage deformations (black solid line) of one cylinder calibrated on the experimental results (red solid lines) of two cylinders in free loading conditions. The coefficient driving the hygral deformations, α_h, is defined using the data of the deformations gained during the first period of 100 days together with α_T value that defines the thermal deformation. The model is so validated on the remaining data until the end of the experimental test.

The results show a good prediction of the shrinkage strain on time.

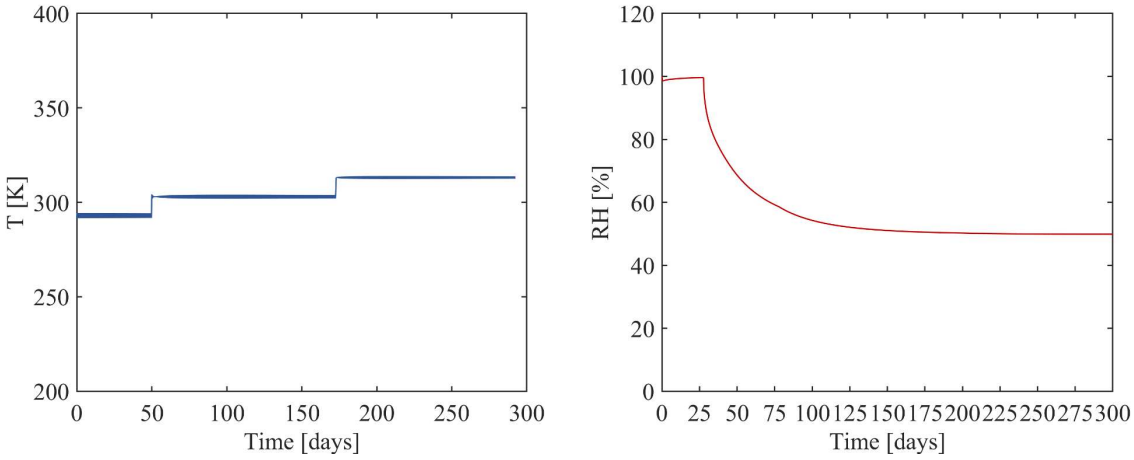

(a) (b)

Figure 7.41 – (a) Temperature Profile and (b) Relative humidity profile of HTC model simulated.

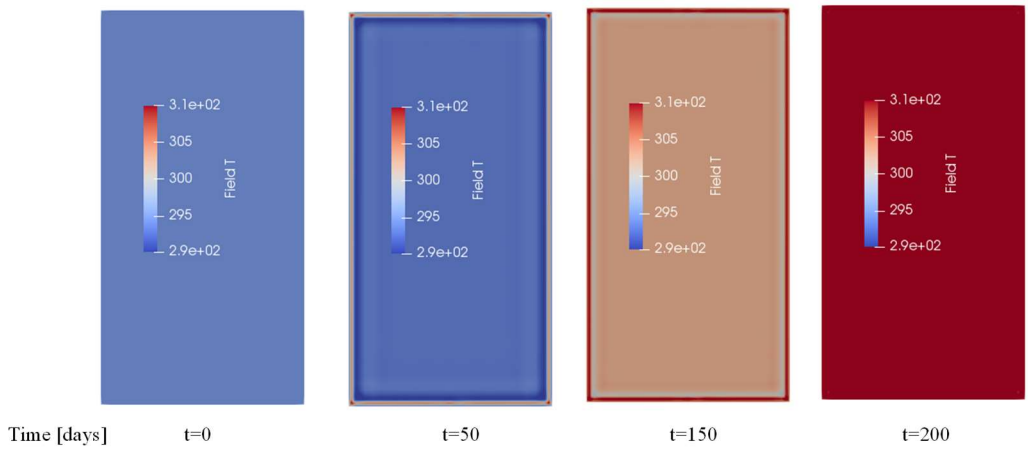

Figure 7.42 – Temperature changes and diffusion in the cylinder over time.

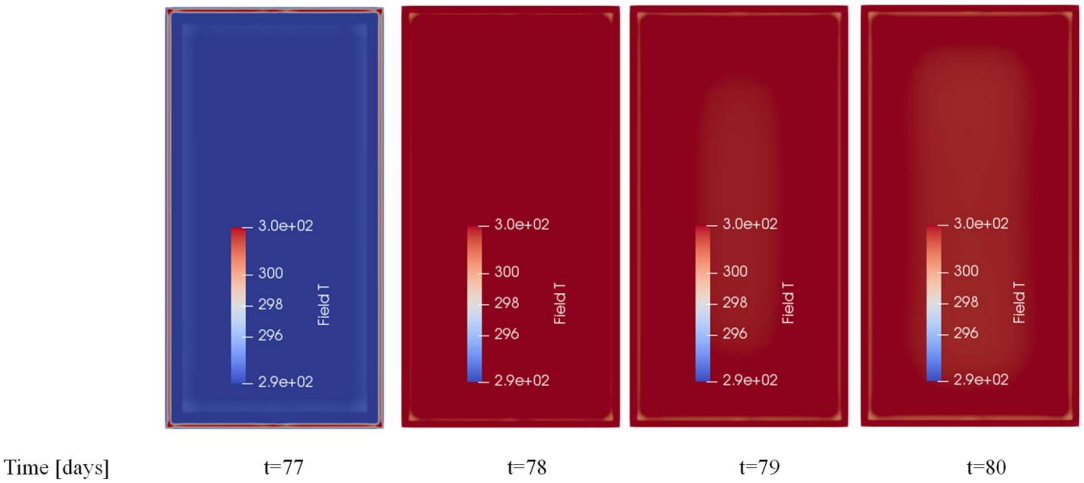

Figure 7.43 – Focus on the gradual application of temperature increment at 80 days (considering the curing period of 28 days).

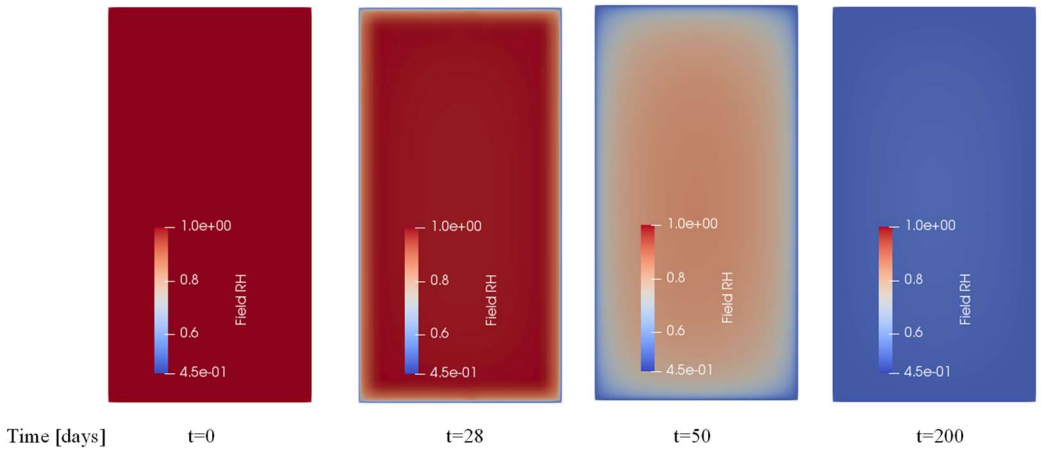

Figure 7.44 – Relative humidity evolution and diffusion in the cylinder over time.

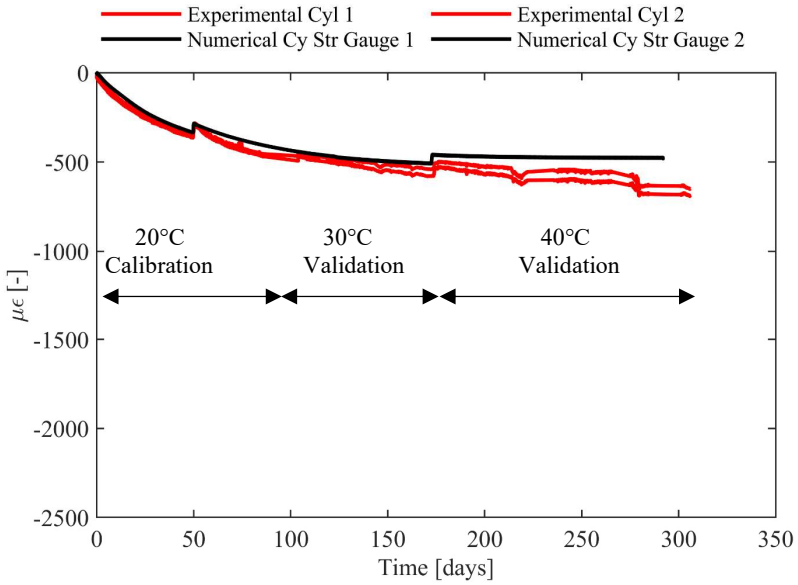

Figure 7.45 – MSFRC shrinkage strains: calibration and validation.

7.8.4. Creep compressive deformation calibration and validation

The previous parameters are kept fixed for the further steps, the definition of the visco-elastic and viscous creep is achieved by calibrating the remaining parameters, ξ_1, ξ_2, n_α, ξ_4 and k_1.

First the cylindrical peak compressive strength is defined, through simulations lasting few hours, in order to attest if the load applied during the experimental tests, 20% of the peak value, is consistent with the numerical peak strength exhibited by

the material with the parameters calibrated. Thus, the cylinders simulated are loaded with the same experimental value that is reliable for the peak strength resulted by the simulation (Figure 7.46).

The creep compressive test is simulated defining also the humidity and temperature history as for shrinkage tests (section 7.8.3). The conditions, as explained before, are simulated on a cylinder 10 mm larger than the real size (Figure 7.49 dark grey surface) while the loading condition is applied on the sample modelled with 150 mm diameter and 300 mm height.

The loading history is applied gradually: Figure 7.49 depicts the stress in unloaded conditions, during the loading phase and when the sample is fully loaded emphasizing the change of the stress state of the concrete particles.

The parameters, also for the present load condition, are calibrated on the data of the first period of 100 days and, then, validated on other part of the curve (Figure 7.48).

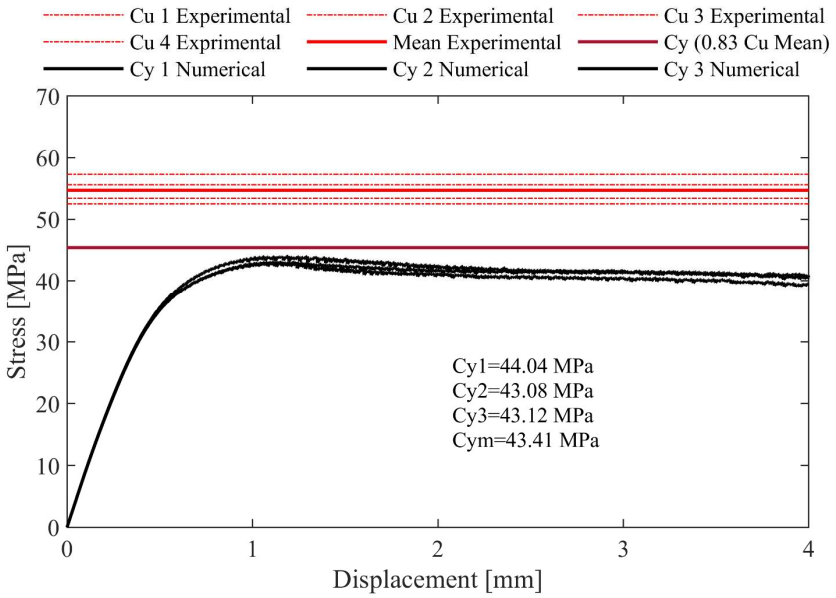

Figure 7.46 – MSFRC cylinders compressive strength estimation on the experimental cube compressive strength.

Figure 7.47 – Numerical simulation of compressive test on the MSFRC cylinders.

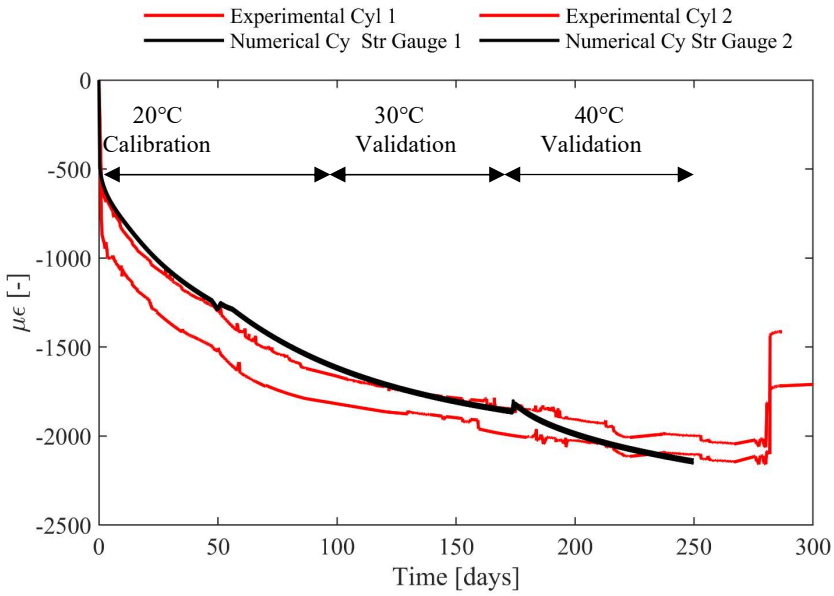

Figure 7.48 – MSFRC creep compressive strains: calibration and validation.

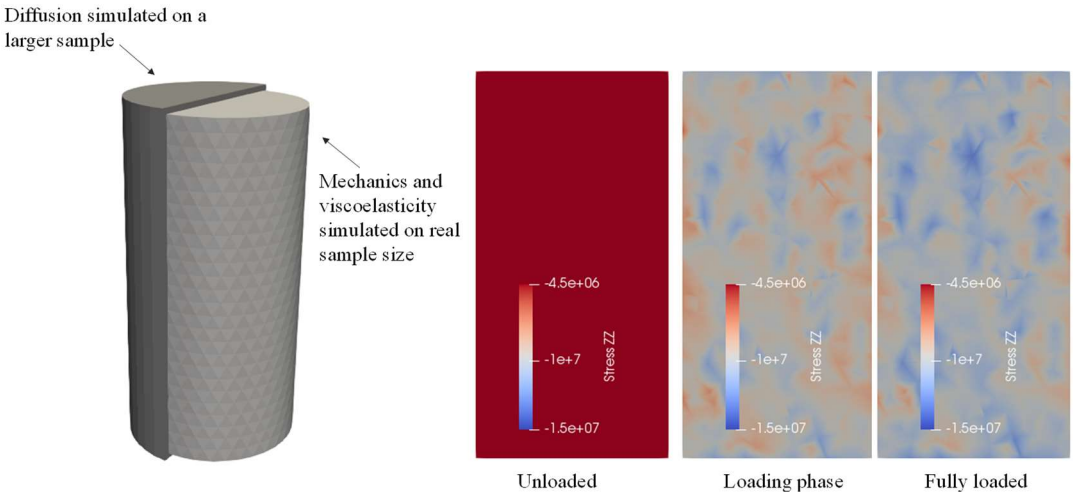

Figure 7.49 – MSFRC creep compressive mechanism simulated on the cylinder having real size and stress evolution (expressed in Pa) along the principal direction ZZ.

7.8.5. Fibre creep tensile deformation calibration

The estimation of the viscoelastic deformation exhibited by the polypropylene fibre is reported in Figure 7.50-Figure 7.51 where the set of parameters in Table 7.15 defines the curve. The viscoelastic behaviour is simulated for both load ratios, 20% and 40% loading, but the analytical model is fitted on the data achieved by the fibre at lower load during the first 50 days when the temperature is kept constant at 20 °C (Figure 7.52). Although the model under consideration does not consider the temperature influence and its variations, the prediction of the strain profile over time results accurate (Figure 7.53). The influence of the temperature variable should be account since the polymers mechanical long term behaviour is modified by this factor. In particular, the elastic modulus of a thermoplastic material decreases with the increment of time and temperature, the latter leads also to a decrement of the 'time to failure' (Smithers, 2014).

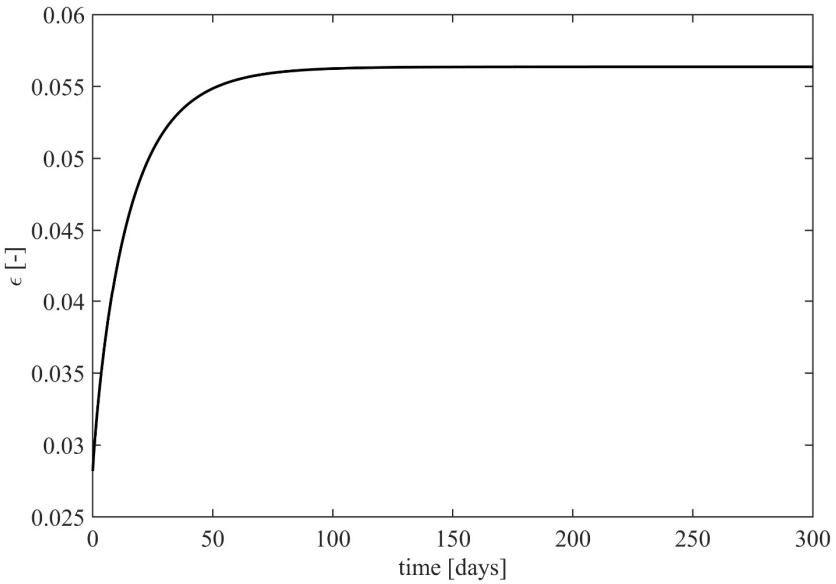

Figure 7.50 – Creep behaviour according to the analytical model (section 6.4.10) of the polypropylene fibre tested under a load equal to the 20% of the maximum experimental tensile strength.

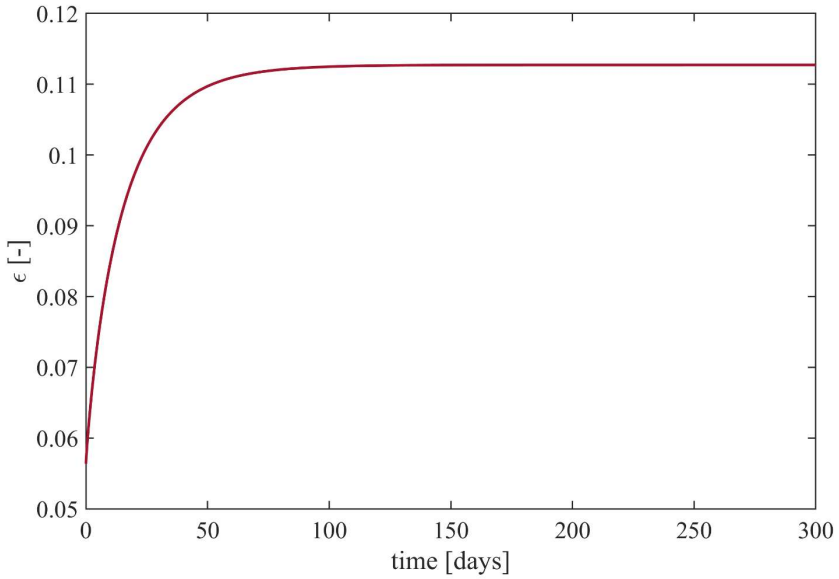

Figure 7.51 – Creep behaviour according to the analytical model (section 6.4.10) of the polypropylene fibre tested under a load equal to the 40% of the maximum experimental tensile strength.

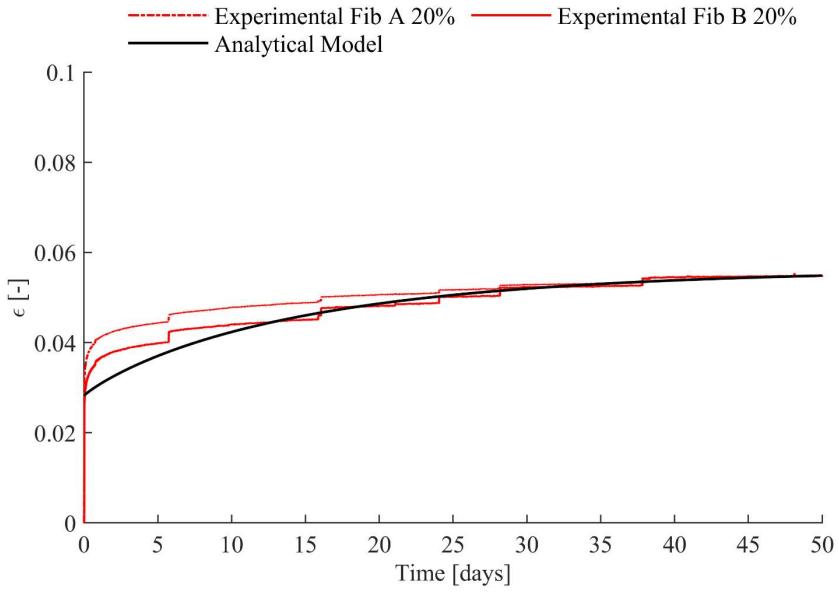

Figure 7.52 – Analytical model (section 6.4.10) fitting the experimental data of polypropylene fibre deformations under tensile creep load.

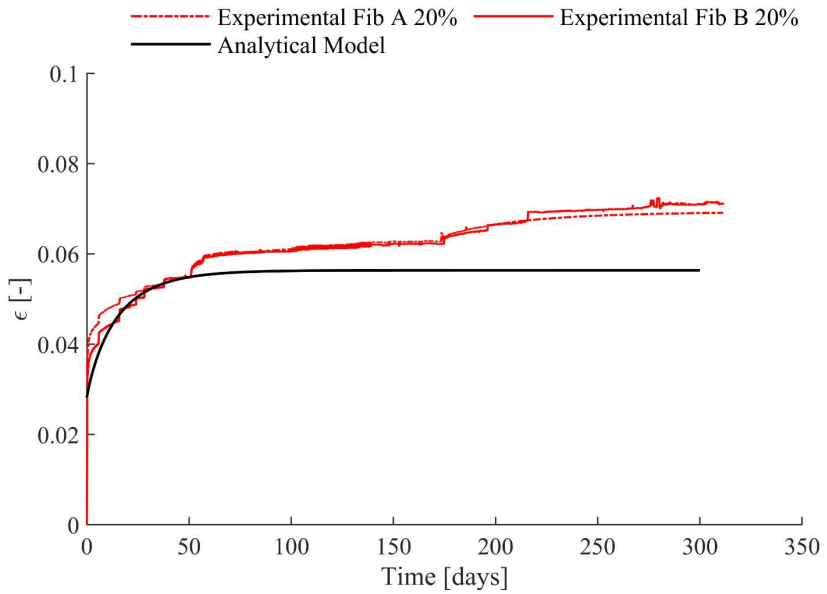

Figure 7.53 – Comparison between experimental data and numerical model prediction without accounting for temperature variations.

7.8.6. Uniaxial tensile creep deformation calibration

The parameters so calibrated are used for the simulation of a creep test under sustained load for notched cylinders. As in the experimental tests, the specimen is first pre-cracked and then the sustained load is applied modelling two square steel plates connected to the upper and lower face.

The notched specimen is modelled (Figure 7.54) according to the same dimensions of the samples used in the experiments.

The pre-cracking simulation has required a lot of accuracy in defining the displacement curve because it is crucial in the cracking pattern development as the cracks should start in the notched section. The rate displacement adopted in the numerical simulations is decisive for this aspect because a high rate might cause the crack formation close to the interface between the specimen and the plates modelled. Moreover, an important aspect is the application of the same boundary conditions as in the experimental procedure: the free rotations must be allowed to not generate additional stress. The compatibility of the results in this sense is verified by observing

the difference in displacements of four edge points of the upper steel plate and the cracks evolution that, as desired, result not uniform as Figure 7.55 shows.

The pre-cracked phase is simulated imposing a vertical displacement and generating a residual crack opening compatible to that exhibited experimentally. For each cylinder three seeds are generated, nine simulations in total, in order to consider the variability of fibers dispersion that is crucial for the present loading condition (Figure 7.56). The experimental fibre count is compared with the number of fibers generated by the code (Table 7.16) revealing a higher number.

The mechanism expected regards the viscoelastic fibre elongation and the interfacial slippage between fibre and matrix as responsible of the deformations gained.

The tensile creep tests are simulated first considering the elastic contribution of the fibre reinforcement (Figure 7.57) revealing a great discrepancy with the experimental results. Considering the viscoelastic contribution of the fibers (Figure 7.58) simulated for six seeds, as expected, the deformations obtained are characterized by a higher value. The comparison between the numerical response and the experimental curves are reported in Figure 7.59. The simulations consider the set of parameters in Table 7.15, where β is recalibrated on the experimental results considering the consistence with the elastic deformation when cylinders are loaded for the creep test.

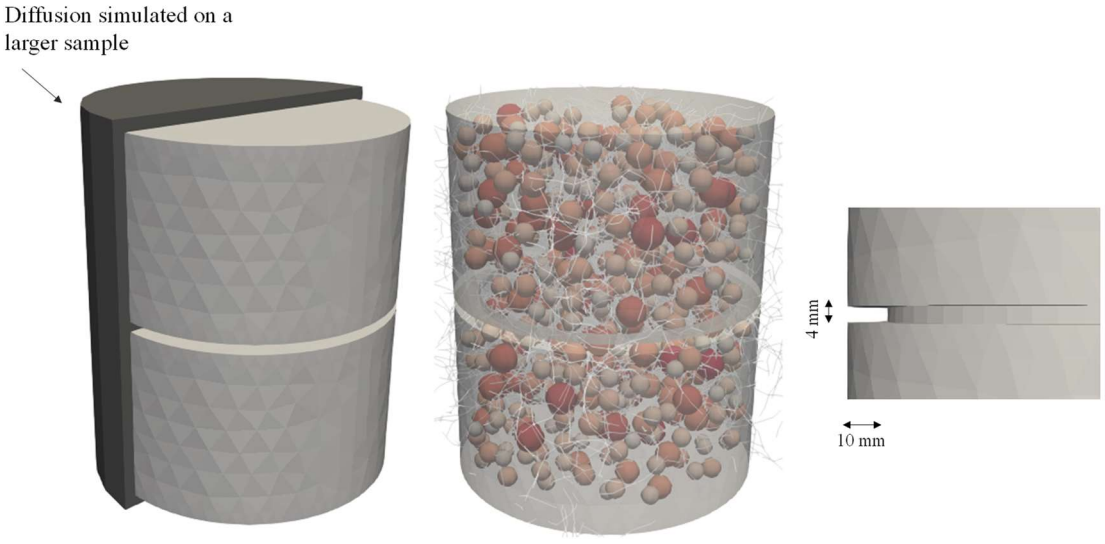

Figure 7.54 – MSFRC model of notched specimen for the mechanical and viscoelastic, viscous problem solution and unotched cylinder for the HTC model.

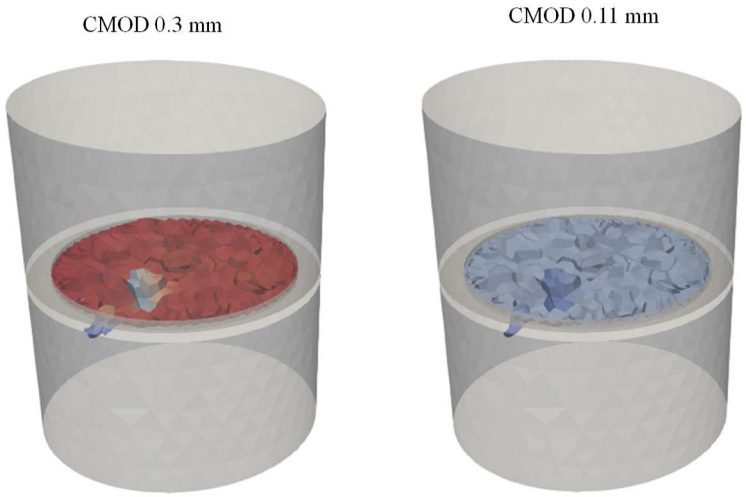

Figure 7.55 – MSFRC cylinders non uniform crack evolution during the simulated pre-cracking phase.

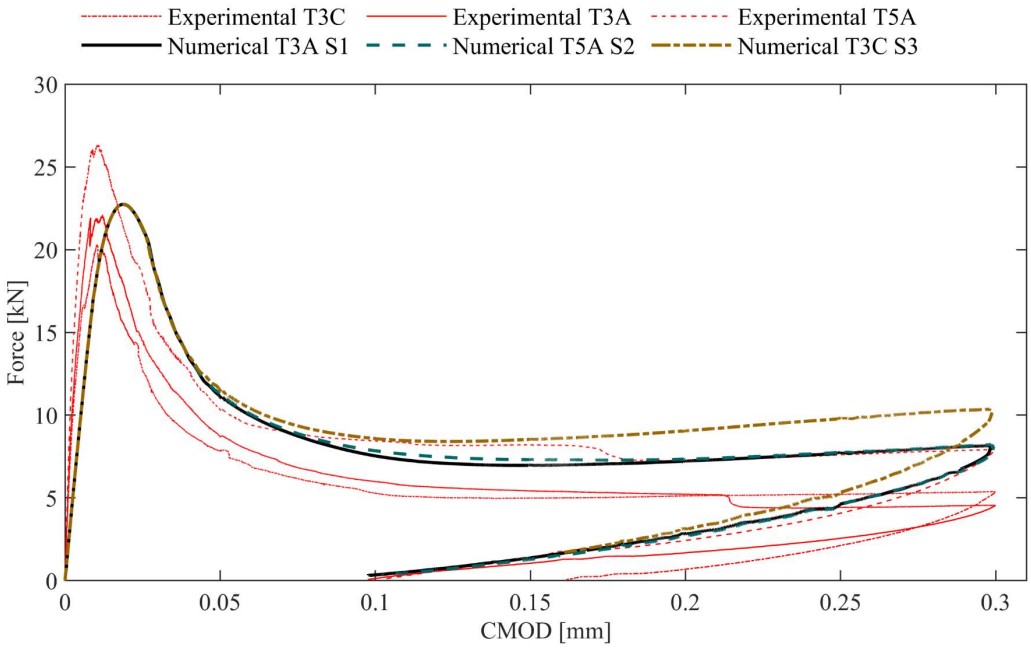

Figure 7.56 – Force – CMOD curves simulating the pre-cracking phase of MSFRC cylinders under uniaxial tensile load.

Table 7.16 – Experimental and numerical fibre count of cylinders tested under uniaxial sustained load.

Specimen ID	Fibre Count	
Experimental	Experimental	Numerical
T5A	75	100
T3A	59	105
T3C	80	108

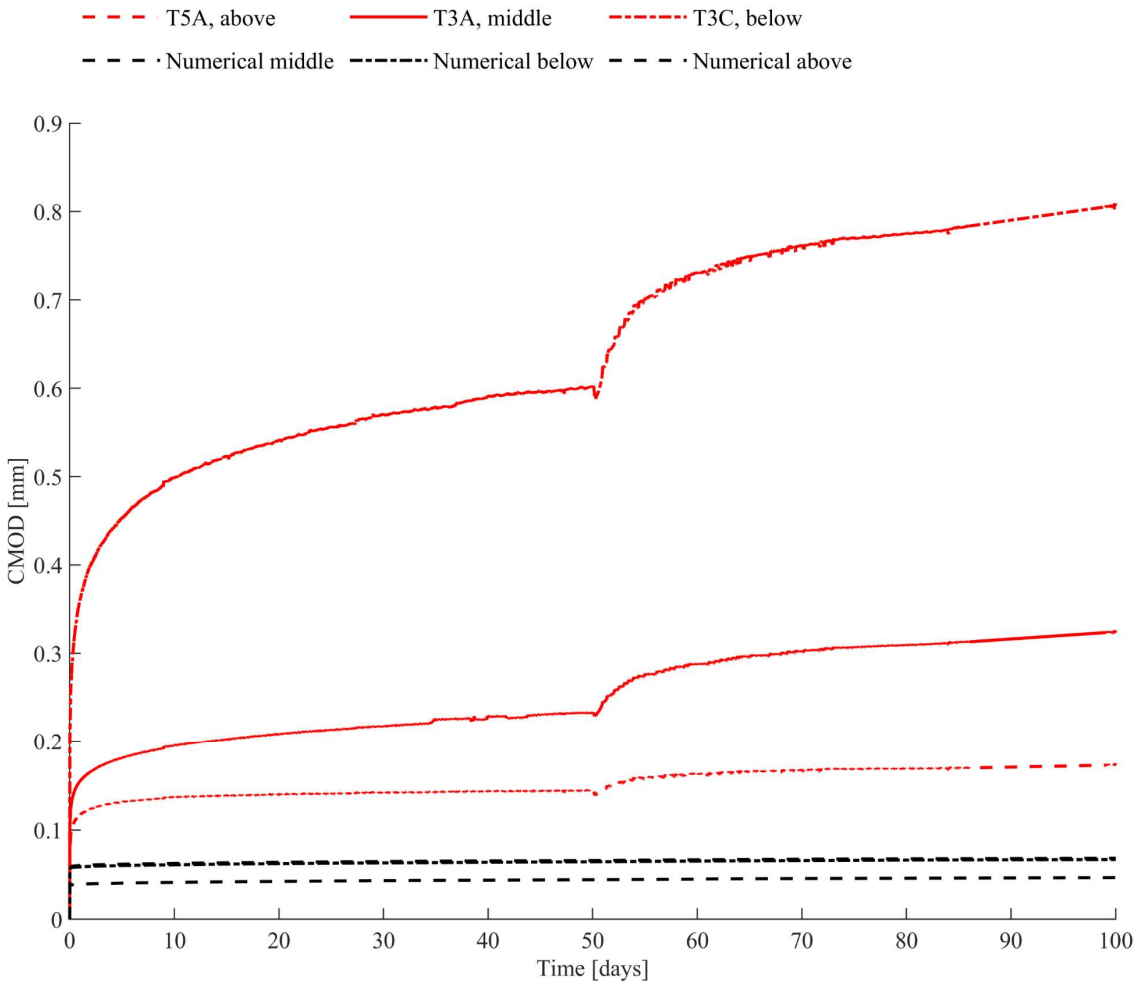

Figure 7.57 – Uniaxial tensile creep experimental tests (red curves) simulated with elastic fibers behaviour for data of 100 days.

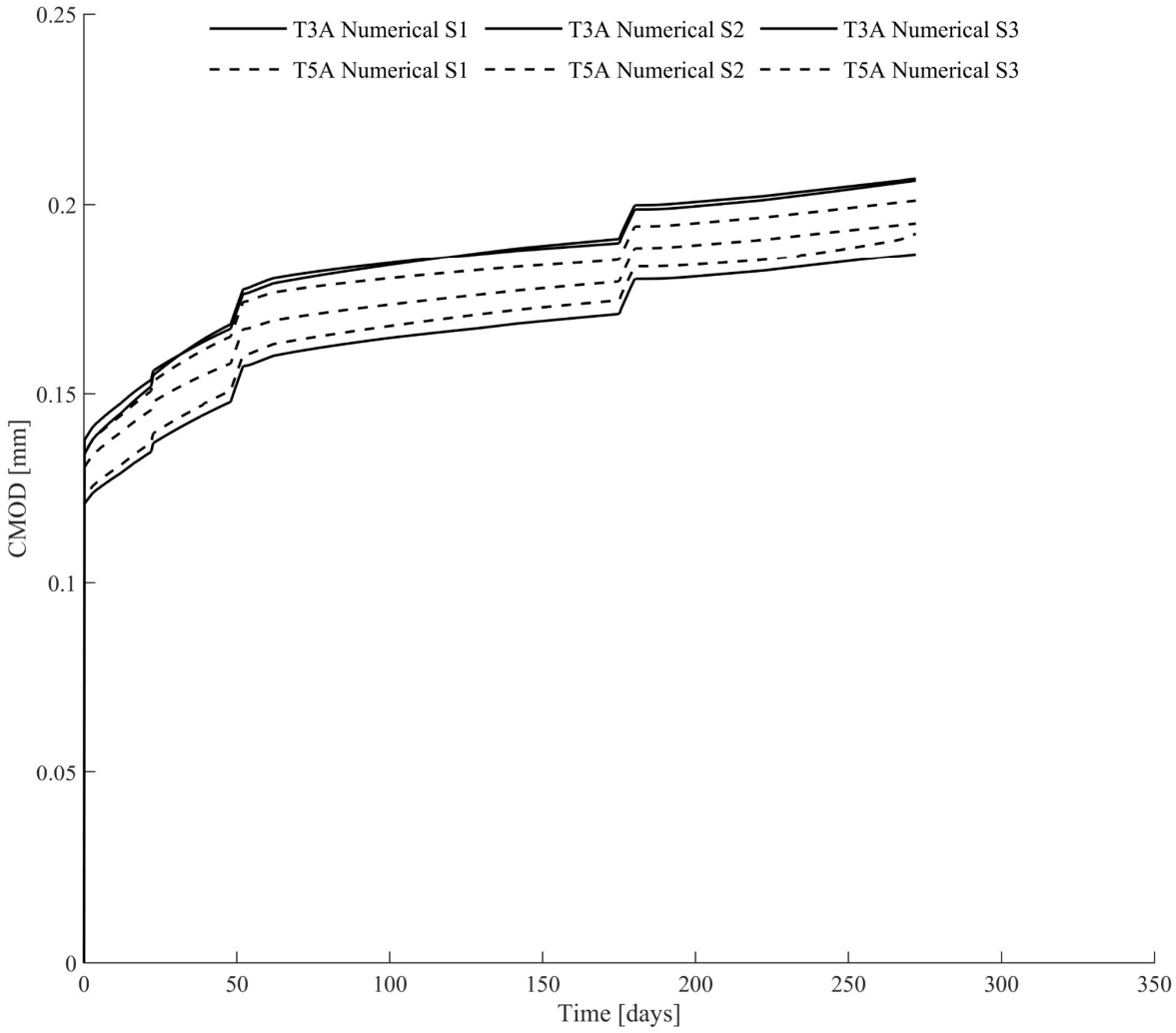

Figure 7.58 – Uniaxial tensile creep experimental tests simulated with viscoelastic fibers behaviour for alla data.

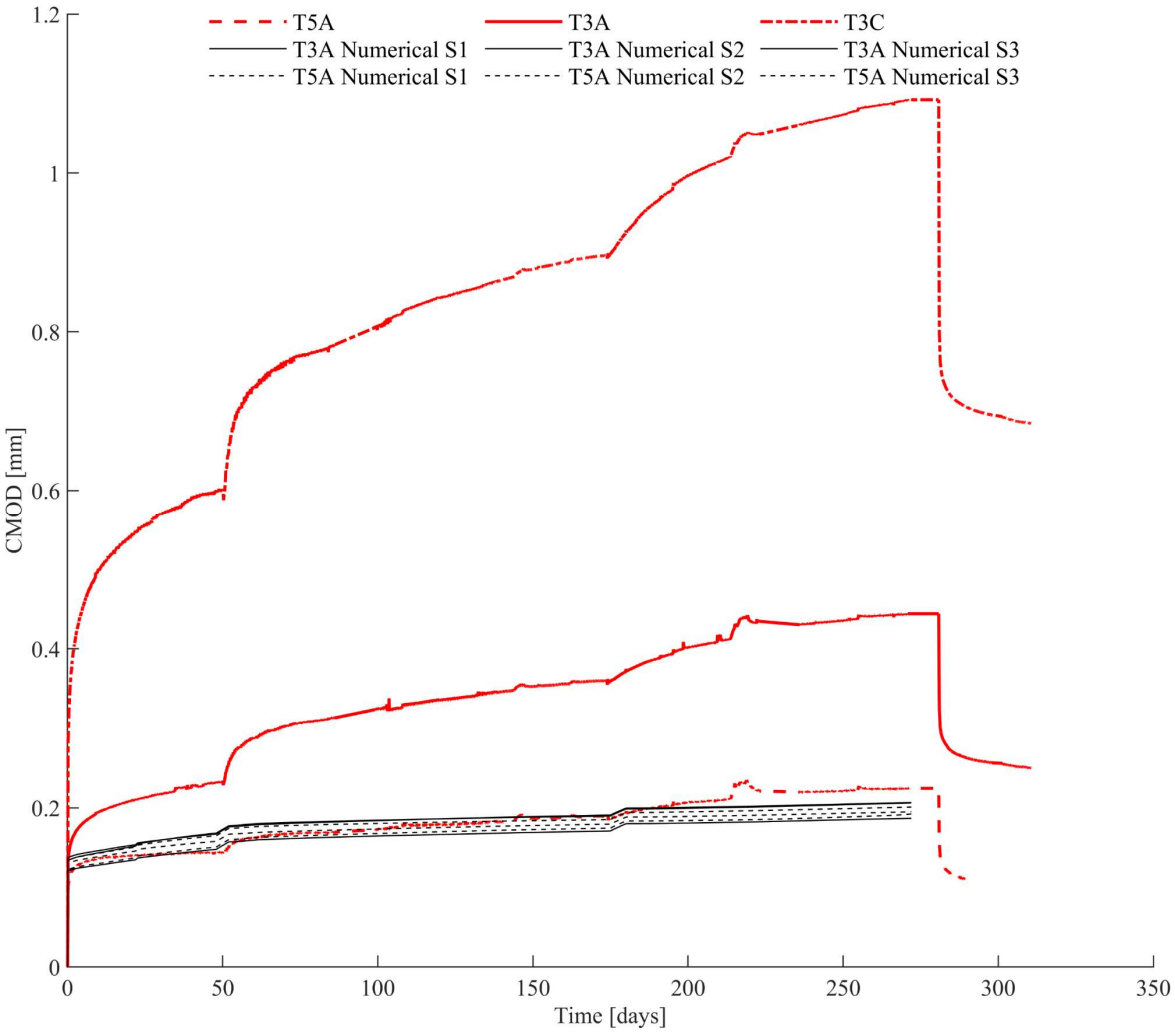

Figure 7.59 – Uniaxial tensile creep experimental tests simulated with viscoelastic fibers behaviour for alla data and compared with experimental data (red curves).

7.8.7. Concluding remarks

The last stage of the analysis here exposed represents an innovative aspect in the field of fibre reinforced concrete numerical approach because the MSFRC mechanical performance under sustained load is simulated as a composite material accounting for the viscoelastic fibre contribution. This aspect, crucial for polymers, is not the only responsible of the material deformation but the viscoelastic bond behaviour between fibre and matrix should be considered. This is demonstrated by the difference between the output of the numerical model and the experimental results. Despite the experimental tensile creep tests are different in terms of CMOD evolution, the numerical model was expected to simulate a deformation trend included in the scatter identified by the three cylinders. The element that should be also considered is that the higher experimental trend (cylinder T3C) is associated to a not uniform crack opening evolution and, so, a combined effect of pure tension and secondary moment. For this reason, the other two cylinders can be used as a reference for the model. In addition, the absence of viscoelastic bond inclusion in the numerical model can be addressed as the cause of the difference of deformations. Moreover, the load curve applied during the pre-cracking phase, in terms of vertical displacement, might influence the value of the residual crack opening and, so, the crack growth on time.

In this framework, the aspects that need to be investigated are:

a. The fibre orientation;
b. The number of fibers;
c. The viscoelastic bond between fibre and matrix.

CHAPTER 8

8. ROUND ROBIN OF CREEP TESTS ON STEEL AND MACRO-SYNTHETIC FIBRE REINFORCED CONCRETE

8.1. OUTLINE OF THE ROUND ROBIN TEST

Within the activities concerning the study of FRCs mechanical performance, the University of Bologna took part to a RRT, Round Robin Test, organized to test the same FRC with different methodologies and conditions. The principal aim is to investigate the differences in methodologies and how they affect the results. The initial phase, preceeding the experimental activity, consists of the agreement about the procedure and conditions to be performed by the partecipants. In the perspective of defining common guidelines about the creep test procedure, the analysis of the results produced by the RRT will represent the starting point for standard test procedure recommendations. In addition, a further analysis is performed on the results to detect the potential parameters affecting the long term response of FRCs that, together with the set-up and methodologies proposals, will form the state of the art of the present topic. Moreover, future investigations will use the present document as a starting point for validations of models. The international partecipants are 19, identified as laboratories:

Table 8.1 – Round Robin Test partecipants.

Lab ID	Institution	Country
1	Universitat Politècnica de València UPV	Spain
2	Universitat Politècnica de Catalunya UPC	Spain
3 – A	OTH Regensburg	Germany
*3 – B	University Innsbruck	Austria
4	BASF Construction Chemicals Italy	Italy
5	LEMIT-CIC and Facultad de Ingenierià UNLP	Argentina
6	Indian Institute of Technology Madras IITM	India
7	NV BEKAERT SA	Belgium
8	Tohoku University	Japan
*9	ArcelorMittal Fibres	Luxembourg
10	BBRI Belgium Building Research Institute	Belgium
11	**University of Bologna**	**Italy**
12	Universidade Federal de Rio de Janeiro	Brazil
13	École Polytechnique of Montrèal	Canada
*14	Politecnico di Milano	Italy
15	Sigma Béton CETU Centre for Tunnel Studies, MEDDE	France

16	Stellenbosch University	South Africa
17	TSE Technologies in Structural Engineering	Australia
18	VSH VersuchsStollen Hagerbach	Switzerland
*19	IBAC Aachen	Germany

The type of experimental tests are:

- flexural creep tests
- uniaxial tensile creep tests
- square and round panel tests.

They are performed on concrete reinforced with steel and macro-synthetic fibers. Among all data of the RRT, the analysis of flexural creep tests results are reported in the present part, on which is developed a statistical analysis of the parameters influencing the response.

8.2. EXPERIMENTAL CAMPAIGN

8.2.1. Materials

The concrete mix specifications in Table 8.2 represent the final and unique mix design used for both synthetic and steel fibers so that no additional variables to account for are added: the present admixture design has been agreed to achieve a concrete class strength of C35/45 with a standard compressive strength. The granulometry curve describing the aggregate assortment is depicted in Figure 8.1. The fibers type are selected, in terms of length and dosage, in order to reflect the real applications. It is important to specify that, for concrete reinforced with steel fibres, 50% of the first and second type have been mixed to have almost the same performance for the SFRC avoiding an additional variable to consider. The fibers used are reported in Table 8.3 where the geometrical and mechanical properties are listed: steel fibers are characterized by hooked-end profile while the macro-synthetic present a crimped shape.

Table 8.2 – Mix design specifications.

Component [kg/m^3]	Synthetic	Steel
Cement CEM I 42.5R	350	350
Water w/c=0.5	175	175
Aggregate 1 (12-20)	118	118
Aggregate 2 (6-12)	591	591
Sand 1	482	482
Sand 2	482	482
Sand 3	168	168
Superplasticizer	3.75	2.50
Fibres	10	30

Table 8.3 – Fibre geometry and mechanical properties.

Properties	Synthetic fibres	Steel fibres	
Provider	BASF	BEKAERT	ArcelorMittal
Brand	--	Dramix 3D 65-60 BG	HE 90/60
Fibre length [mm]	40	60	60
Wire diameter [mm]	0.76	0.90	0.90
Aspect ratio (l/d)	53	65	67
Tensile strength [MPa]	430	1160	1200
Young Modulus [MPa]	3400	210000	210000
	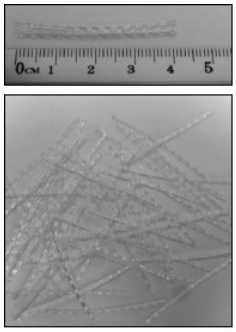	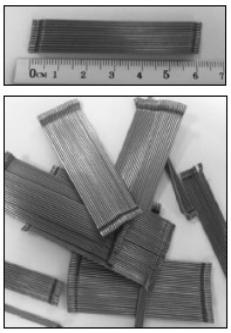	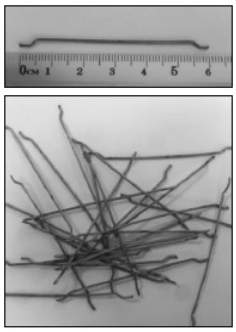

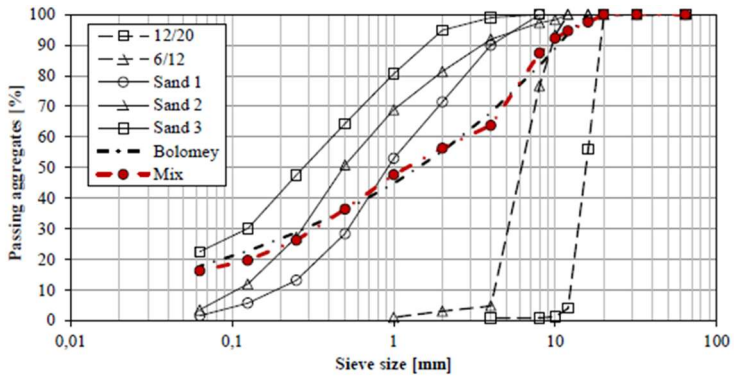

Figure 8.1 –Particle size distribution of concrete mix.

8.2.2. Specimens casting

The specimens are produced in an unique location, in a precast concrete plant equipped with industrial mixer and casting benches (Figure 8.2). Preliminar batches of 0.5 m^3 and 1.5 m^3 (MB-0 and SB-0) for each FRC type have been realized to test respectively the type of concrete and validate the casting procedures also checking the time taken, but they are not used for RRT creep tests.

The final batches, identified with codes M-B1, M-B2 for concrete containing macro-synthetic fibers and S-B1 and S-B2 for concrete containing steel fibers, are produced in four days.

The specimens are demoulded after one day and the moulds prepared for the new cast: all samples are numbered and identified so that, in case of anomalities and dispersion of results, it could have been traced back to the order and time of producing.

The samples are then sent to the respective international laboratory. In Table 8.4 are reported the specifications of the specimens produced in terms of type, size and reinforcement (M for macro-synthetic and S for steel fibers)

Figure 8.2 – Specimens preparation.

Table 8.4 – Specimens number produced.

Shape	Size [mm]	M-B1	M-B2	S-B1	S-B2	S-B0	Total
Prismatic S1	150x150x600	63	60	61	37	45	266
Prismatic S2	100x100x500	5	8	1	8	-	22
Prismatic S3	150x150x700	5	-	8	-	-	13
Square Panel	600x600x100	7	9	7	6	3	32
Round Panel	Ø800x75	2	2	-	-	-	4
Cylindrical	Ø150x300	30	28	30	20	6	114
Total		112	107	107	71	54	451

8.2.3. Mechanical characterization of Fibre Reinforced Concrete

Each batch has been mechanically characterized in terms of compressive strength, EN 12390-3 (2009), elastic modulus, EN 12390-13 (2013), and flexural residual strength according to EN 14651. The compressive strength achieved (Table 8.5), masured on cylindrical specimens, ranges from 30.8 MPa to 37.6 MPa observing an increment of the strength on time (tests have been done at 7, 28 days and at some intervals until 500 days). While the elastic modulus has a value between 28.6 GPa and 30.1 GPa (Table 8.5). Regarding the flexural response, although the different fibre reinforcement type, the mixes show almost the same post-peak performance with a higher scatter for post-peak response of steel fibre reinforced concrete. This

result could be motivated by the lower fibres number for steel reinforcement due to the higher density of steel rather than for macro-synthetic (Table 8.6).

Table 8.5 – Compressive strength and elastic modulus characterization.

Batch	Mean f_c [MPa]					E [GPa]
	~7 days	~28 days	~90 days	~300 days	~500days	~90 days
M-B1	30.53	33.93	37.87	40.11	42.18	28.63
M-B2	31.23	37.57	42.50	38.82	44.06	30.11
S-B0	31.23	37.70	-	-	-	-
S-B1	27.33	30.80	34.73	34.45	35.53	-
S-B2	30.77	36.17	37.90	38.59	-	29.63

Table 8.6 – Flexural peak and residual strength characterization for all batches.

Batch	7 days			28 days		
[MPa]	f_L	$f_{R,1}$	$f_{R,3}$	f_L	$f_{R,1}$	$f_{R,3}$
M-B1	3.12	1.86	3.06	3.65	2.37	3.57
M-B2	3.29	1.93	2.96	3.45	1.99	3.08
MSynthetic	3.20	1.90	3.01	3.53	2.15	3.28
S-B0	3.37	2.64	3.15	3.92	3.56	3.72
S-B1	3.15	1.88	2.34	3.44	2.80	3.00
S-B2	3.16	2.42	2.46	3.90	3.28	3.69
Steel	3.25	2.34	2.76	3.75	3.21	3.47

Batch	90 days			300 days			500 days		
[MPa]	f_L	$f_{R,1}$	$f_{R,3}$	f_L	$f_{R,1}$	$f_{R,3}$	f_L	$f_{R,1}$	$f_{R,3}$
M-B1	3.98	2.55	3.94	5.11	2.95	4.87	4.76	2.84	4.53
M-B2	3.92	1.92	2.97	5.45	3.06	4.64	4.96	2.42	3.63
MSynthetic	3.95	2.23	3.46	5.28	3.0	4.76	7.86	2.63	4.08
S-B0	3.82	2.77	2.77	4.56	3.35	3.79	4.27	3.85	4.10
S-B1	3.90	3.79	4.38	4.84	3.47	3.69	4.99	3.86	4.39
S-B2	3.99	3.52	3.98	4.78	3.78	4.01			
Steel	3.9	3.36	3.71	4.72	3.5	3.81	4.63	3.86	4.25

8.2.4. Creep flexural test procedure

An overview of the tests performed by each laboratory is reported in Table 8.7.

Table 8.7 – Type of test and number of specimens for each laboratory.

Creep Test	Laboratory									Tot
	1	2	3	4	5	6	7	8	9	
Flexural	12	12	6	6	12	6	6	6	-	86
Direct Tension	-	-	-	-	-	-	-	-	-	10
Square Panel	-	-	-	-	-	-	-	-	-	24
Round Panel	-	-	-	-	-	-	-	-	-	4

Creep Test	Laboratory										Tot
	10	11	12	13	14	15	16	17	18	19	
Flexural	8	6	4	2	-	-	-	-	-	-	86
Direct Tension	-	6	-	-	-	-	4	-	-	-	10
Square Panel	-	-	4	-	-	12	-	-	8	-	24
Round Panel	-	-	-	-	-	-	-	4	-	-	4

The analysis illustrated in the present section is performed on the results of creep flexural tests. There are no official recommendations which regulate the test procedure but it has been tried to mantain a common way of carrying them out following in principle the same procedure explained in chapter 6, section 6.4.8, performing three phases (Figure 8.3):

1. Pre-cracking test (O – D) at a rate of 0.05 mm/min up to a CMOD or deflection 0.5 mm and at a rate of 2 mm/min during the unloading stage;
2. Creep test under sustained load (D – H);
3. Post-creep failure test (H – end) where an initial hysteresis loop is performed until the creep load applied during the previous phase and then reloaded until failure (CMOD of 4 mm or equivalent deflection) at a rate of 0.2 mm/min.

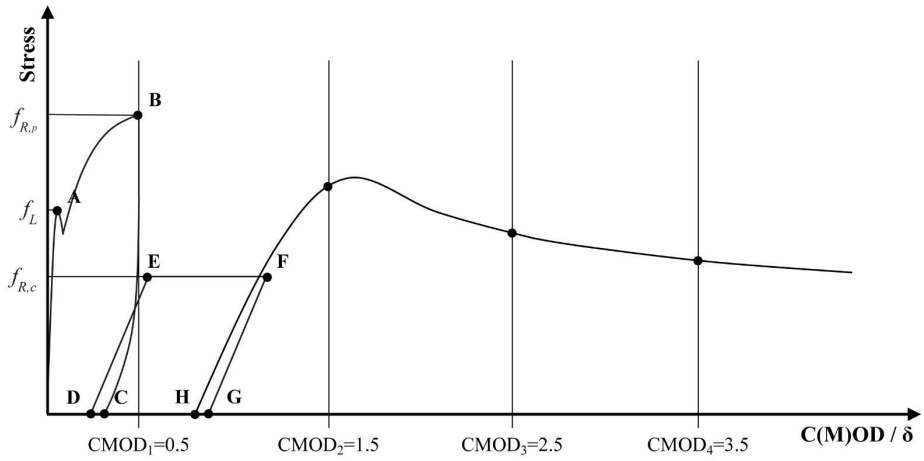

Figure 8.3 – Main phases of a creep test.

8.2.5. Differences between laboratories procedure

Although the procedure followed by each laboratory includes the three phases characterizing the flexural creep test, each partecipant did not adopted identical conditions but they adapt their own methodology referring to their national standards. The differences among all laboratories are collected in

Table 8.8 where the principle variable conditions are presented by:

- Size of the specimen (cross section tipically 150x150mm^2 except only one case, 75x150 mm^2 and a span length from 500mm to 700mm);
- Presence of notch;
- Type of deformation registered (CMOD or deflection);
- Number of specimens tested in the same test frame (from single to three samples configuration);
- Climate conditions monitored (temperature and humidity);
- Configuration in precracking and creep test (three or four point bending test);
- Boundary conditions of supports and load application supports;

– Loading time (time to apply the sustained load, if too fast or too slow, is supposed to influence the initial response and, so, the creep deformation evolution).

The mechanical characterization of the material properties in terms of peak (f_L) and residual flexural strength (f_{R1}) measured during the pre-cracking phase are taken into account as variables together with the creep index (I_c), defined as the ratio between the residual capacity at crack opening of 0.5 mm and the load applied during the creep test. The loading time values for all laboratories are reported in form of histograms (Figure 8.4) where the representation emphasizes the difference of values between laboratories. The mechanical parameters, the peak strength and residual strength, are reported in Figure 8.5 – Figure 8.6 dividing into steel and macro-synthetic fibers, reporting the mean values for each group. The values of the creep index are collected in the histograms in Figure 8.7.

The conditions listed before are represented as pie charts: In Figure 8.9 the type of supports are grouped considering the three degree of freedom, translation and rotation around x-axis and rotation around y-axis. If all of them are considered, the laboratories can be divided into four groups while, considering only the translation along x-axis, two groups are identified.

The type of configuration adopted during the pre-cracking and creep test, three or four point bending, identify three groups: some laboratories performed both phases according the same static scheme, while the remaining used the three point configuration furing the first phase performing the creep test in four point bending configuration (Figure 8.10). Figure 8.11 shows the percentage of partecipants who controlled temperature and humidity conditions in the ambient where the tests are performed.

Some possible creep frames are reproduced in Figure 8.12 – Figure 8.13 – Figure 8.14 – Figure 8.15 where the main differences, apart from those listed before, regard for example the position of the load, the number of specimens allocated in the frame, the type of instruments used for the deformation control.

Table 8.8 – Differences between all laboratories for properties and flexural creep test procedure.

Lab ID	Temperature Control	Humidity Control	Def Control	Support Type
1	Yes	Yes	CMOD	A
2	No	No	Deflection	A
3	Yes	Yes	Deflection	B
4	Yes	Yes	CMOD	A
5	Yes	No	CMOD	A
6	Yes	Yes	CMOD	A
7	No	No	Deflection	B
8	Yes	Yes	CMOD	B
10	Yes	Yes	CMOD	B
11	Yes	Yes	CMOD	A
12	Yes	Yes	CMOD	A
13	Yes	Yes	CMOD	A

Lab ID	Support Type	Pre-cracking Configuration	Creep Configuration	Notch	Size
1	A	Three	Four	Yes	150 150 600
2	A	Three	Four	Yes	150 150 600
3	B	Four	Four	No	150 150 500
4	A	Three	Four	Yes	150 150 600
5	A	Three	Four	Yes	150 150 600
6	A	Three	Four	Yes	150 150 700
7	B	Three	Three	Yes	150 150 600
8	B	Four	Four	Yes	150 150 600
10	B	Three	Three	Yes	150 150 600
11	A	Three	Four	Yes	150 150 600
12	A	Four	Four	Yes	150 150 600
13	A	Four	Four	Yes	75 150 700

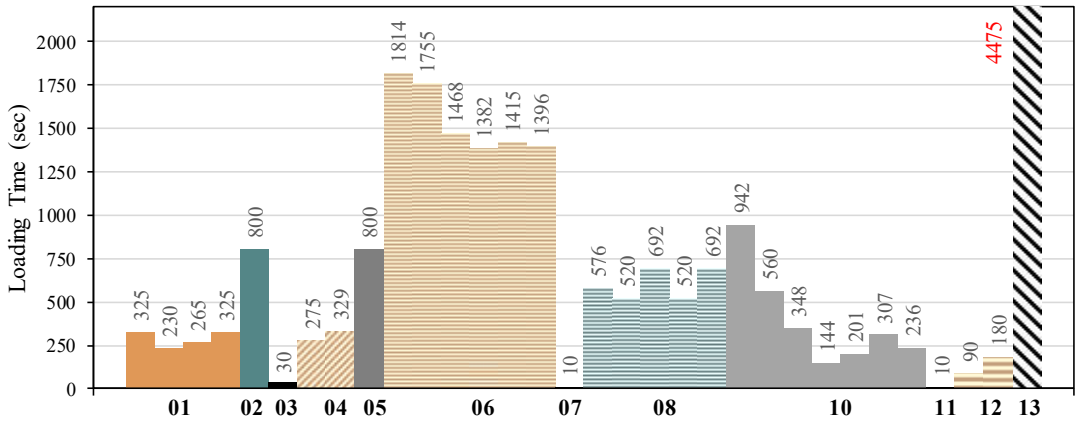

Figure 8.4 – Duration of the load application at the beginning of the creep test for all laboratories.

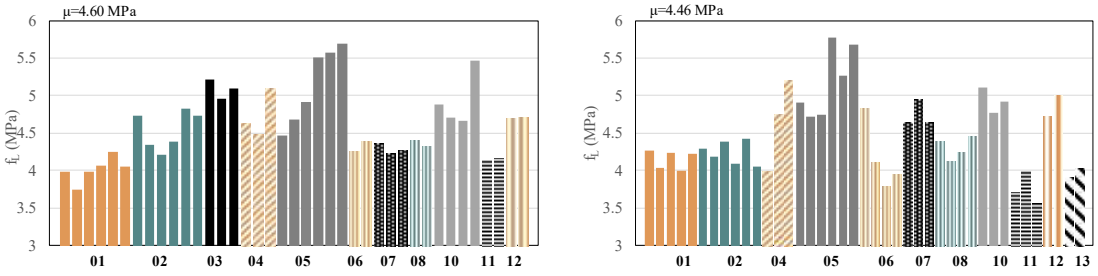

(a) (b)

Figure 8.5 – Flexural peak strength for all laboratories (a) Macro-synthetic and (b) Steel Fibers.

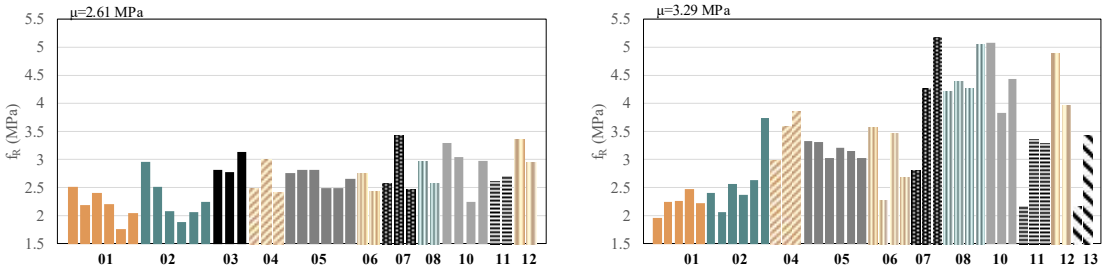

(a) (b)

Figure 8.6 – Flexural residual strength at CMOD/Deflection 0.5 mm for all laboratories (a) Macro-synthetic and (b) Steel Fibers.

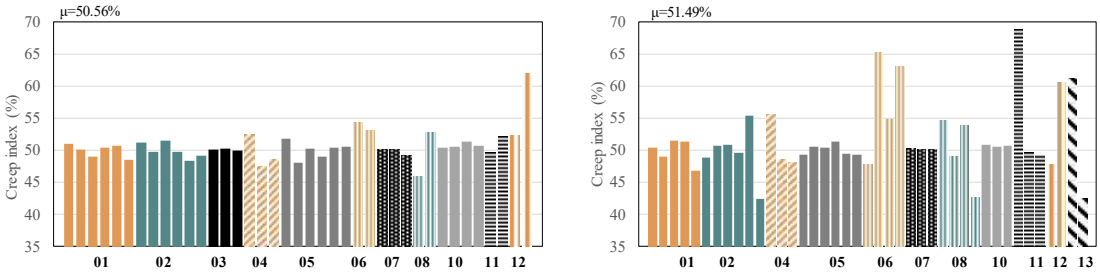

(a) (b)

Figure 8.7 – Creep Index for all laboratories (a) Macro-synthetic and (b) Steel Fibers.

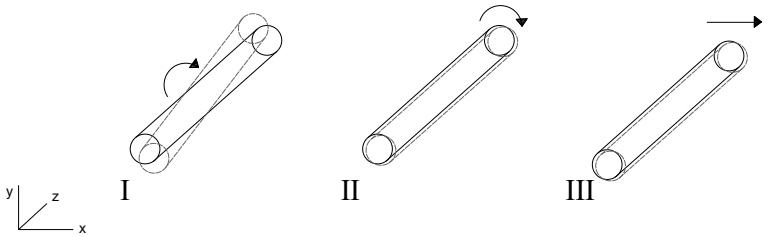

Figure 8.8 – Classification of the degrees of freedom of supports.

(a) (b)

Figure 8.9 – Type of supports classified considering (a) All degrees of freedom [I II III]; (b) Only the translation along the the X axis [III].

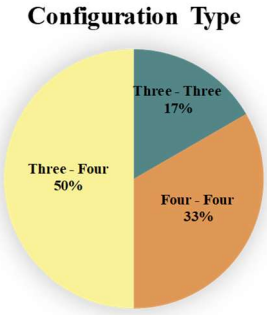

Figure 8.10 – Type of static configuration during pre-cracking and creep test.

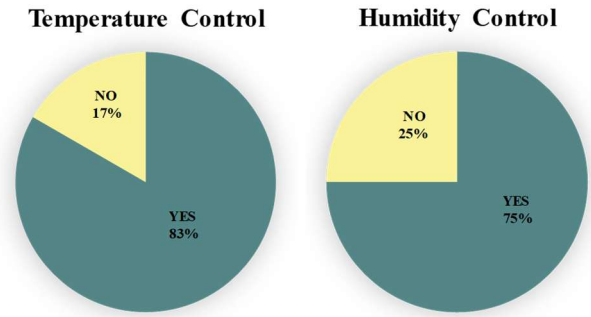

Figure 8.11 – Percentages of laboratories controlling Temperature and Relative Humidity.

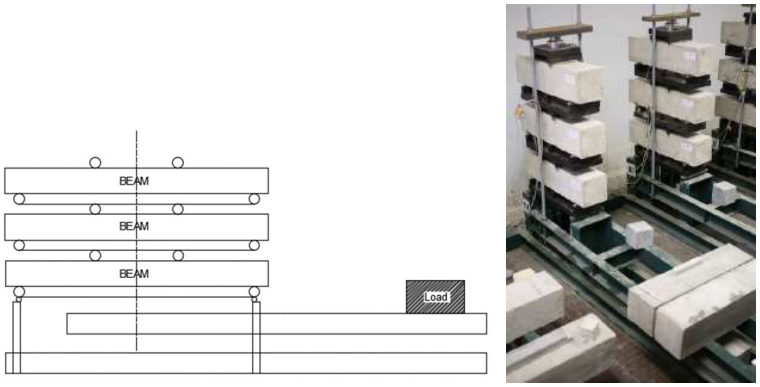

Figure 8.12 – Flexural creep test set-up adopted by LAB 1.

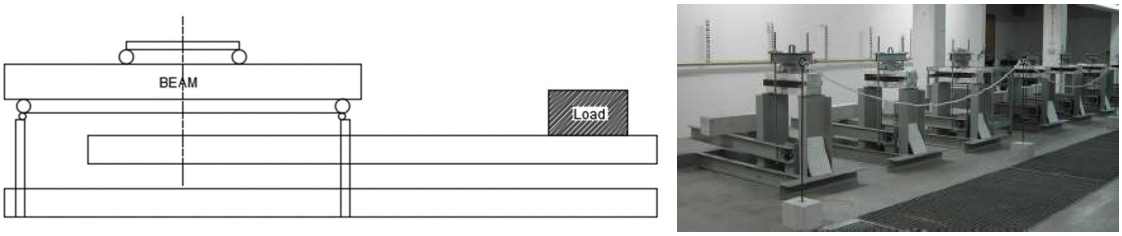

Figure 8.13 – Flexural creep test set-up adopted by LAB 3.

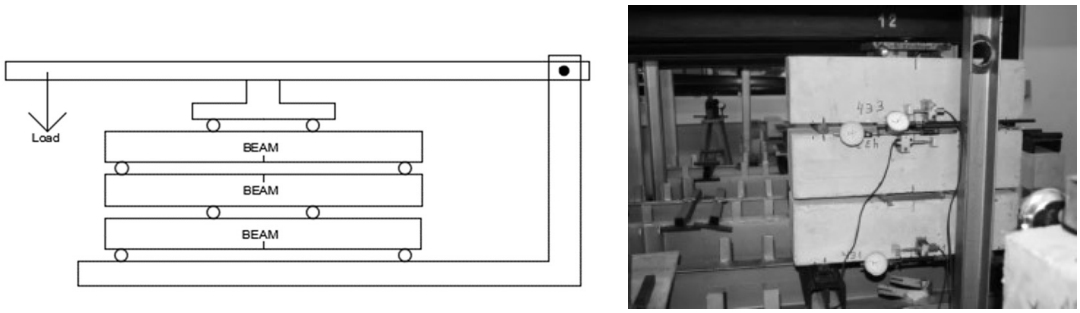

Figure 8.14 – Flexural creep test set-up adopted by LAB 5.

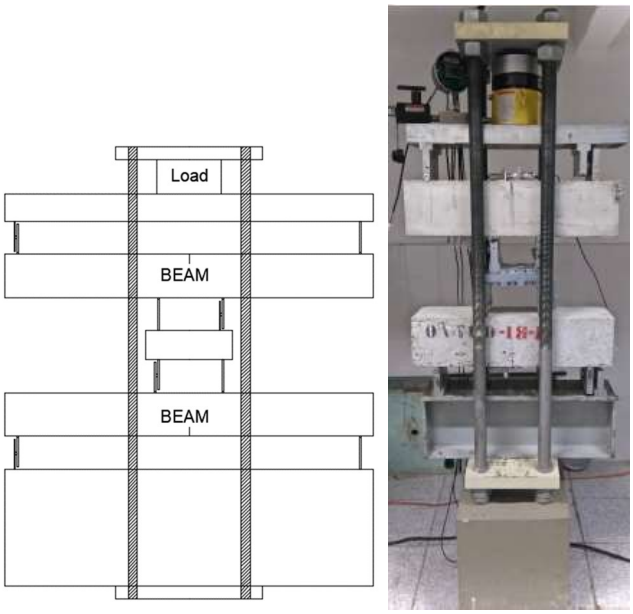

Figure 8.15 – Flexural creep test set-up adopted by LAB 12.

8.2.6. Flexural creep tests results

According to the RRT procedure, the creep deformations are reported by each participant, as the value measured at a precise instant of time: 0 (indicated with point E also later), 10 minutes, 30 minutes, 1, 2, 3, 5, 7, 14, 30, 60, 90, 120, 150, 180, 210, 240, 270, 300, 330, 360 days. The response of the creep flexural test is represented for all laboratories considering the mean curve of the specimens tested by each partecipant. The relation is presented in terms of creep coefficient that representes, as defined in section 5.1.1., an indicator of the long term deformation at a general instant

of time. It is calculated considering the deformation, CMOD or deflection, correspondent to the point E, for MS and S fibers (Figure 8.16Figure 8.17). In Figure 8.18Figure 8.19 the creep coefficient trend of the specimens tested at University of Bologna are reported. The first analysis is aimed at understanding how the initial deformation value, used in the calculation of the creep coefficient, might influence the differences among the laboratories. For this reason, the φ values are calculated with the initial deformation (point E), the value measured after 10 minutes (point E+10') and 30 minutes (point E+30'). The single values at a time of 360 days, the ultimate creep coefficient value, is reports for all laboratories, distinguished according to the fibre type (Figure 8.20 – Figure 8.25). Observing these representations two main differences can be traced: the creep coefficients of MS fibre reinforced concrete are higher than S fibre reinforced concrete and the former presents higher scattered results. The first observation can be due to the difference of fibre behaviour since the plastic material is affected more by creep phenomena and so the definition of the instantaneous deformation might be responsible of the results. Moreover, more detailed considerations are drawn in the following section after a statistical analysis involving the parameters previously discussed.

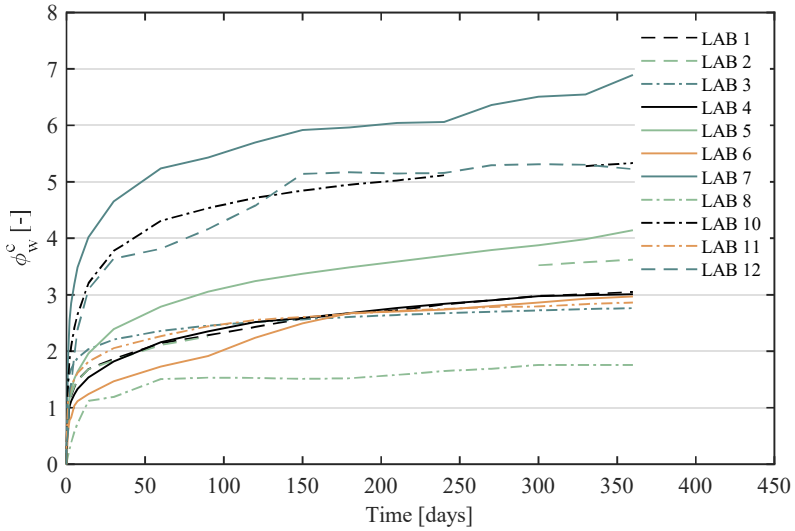

Figure 8.16 – Creep coefficient versus time for specimens with MS fibres for all laboratories.

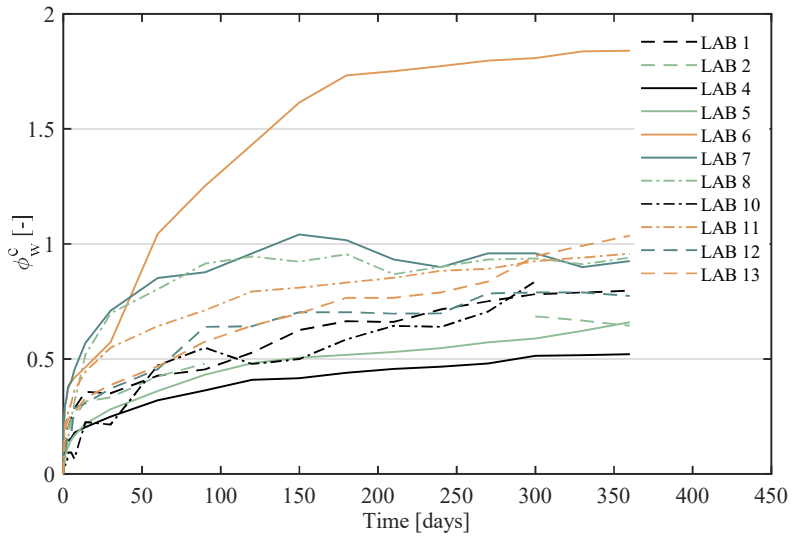

Figure 8.17 – Creep coefficient versus time for specimens with ST fibres for all laboratories.

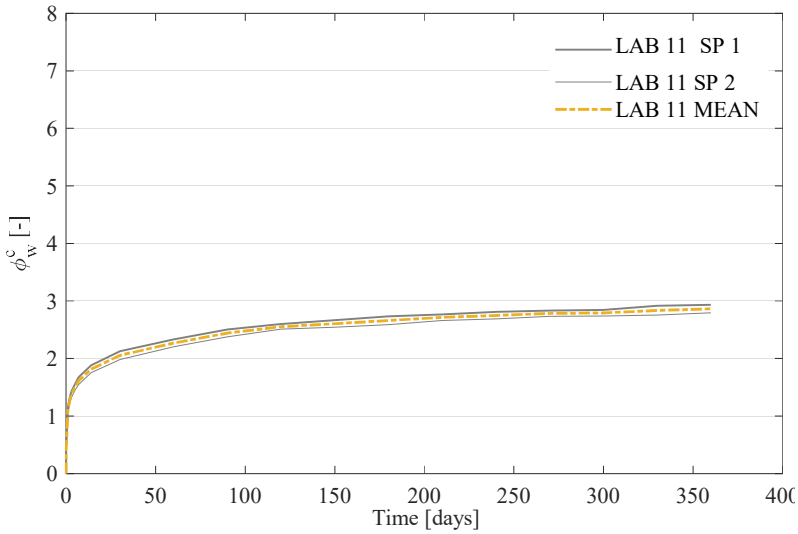

Figure 8.18 – Creep coefficient versus time for specimens with MS fibres for LAB 11 (University of Bologna).

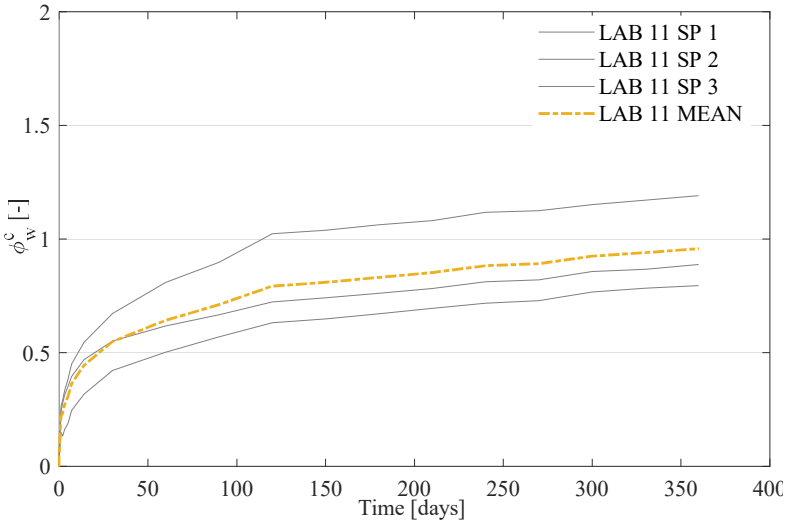

Figure 8.19 – Creep coefficient versus time for specimens with ST fibres for LAB 11 (University of Bologna).

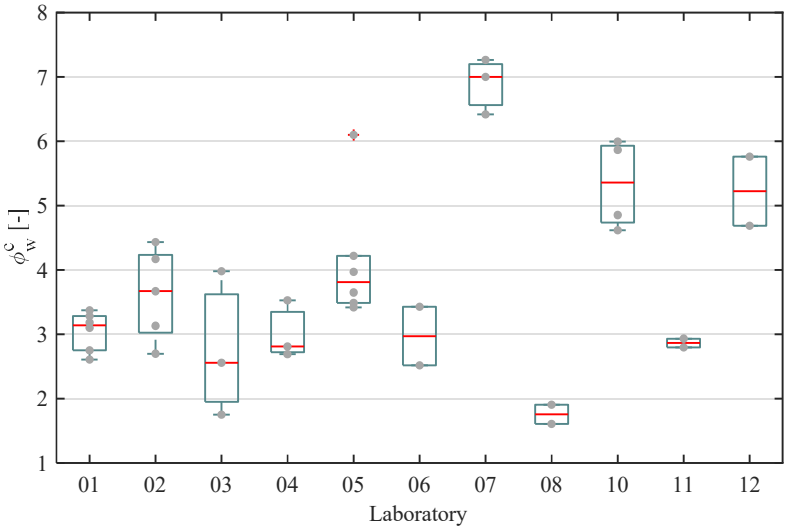

Figure 8.20 – Creep coefficient for MSFRC beams at t = 360 days considering $t_0 = t_E$.

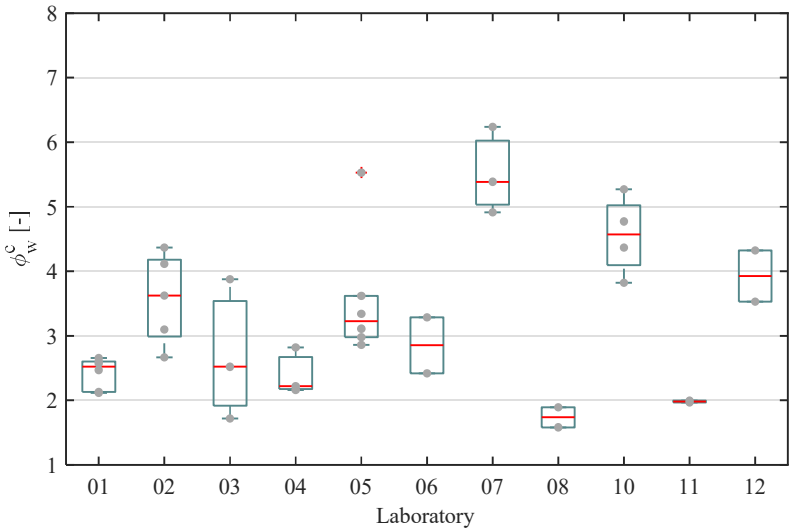

Figure 8.21 – Creep coefficient for MSFRC beams at t = 360 days considering $t_0 = t_E + 10'$.

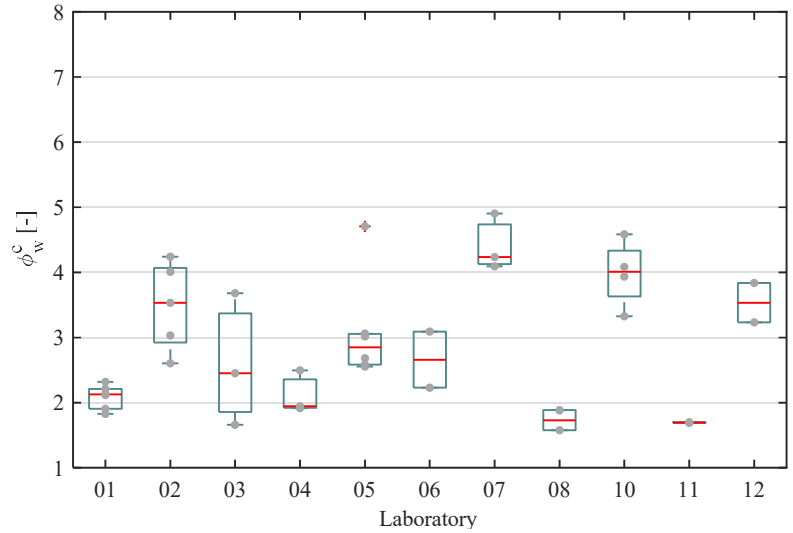

Figure 8.22 – Creep coefficient for MSFRC beams at t = 360 days considering $t_0 = t_E + 30'$.

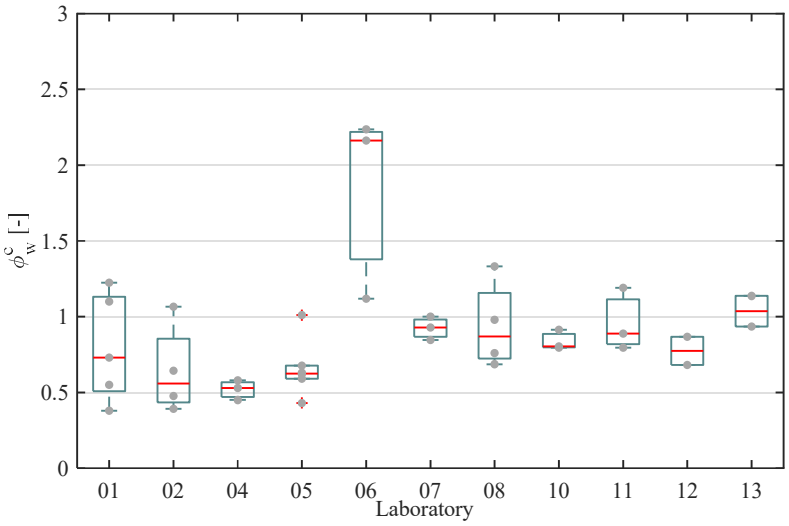

Figure 8.23 – Creep coefficient for SFRC beams at t = 360 days considering $t_0 = t_E$.

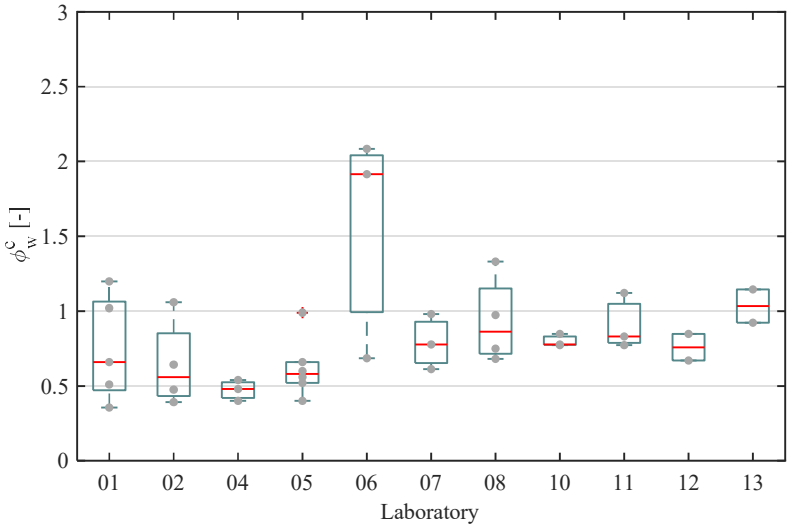

Figure 8.24 – Creep coefficient for SFRC beams at t = 360 days considering $t_0 = t_E + 10$'.

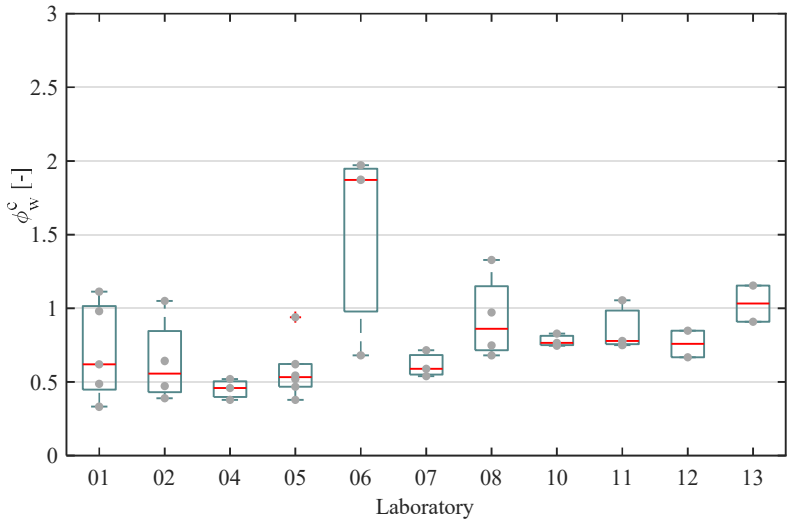

Figure 8.25 – Creep coefficient for SFRC beams at t = 360 days considering $t_0 = t_E + 30$'.

8.3. STATISTICAL ANALYSIS OF THE EFFECT OF TESTS CONDITIONS ON FLEXURAL CREEP RESPONSE

The evaluation of the possible factors influencing the experimental results in terms of creep coefficient is carried out by formulating a statistical analysis on the database of creep flexural test results using mixed effect nonlinear regression models, a statistical model incorporating fixed and random effects. The random effect represents the variable accounting for the variability of the single laboratory that could be not associated with the parameters correlated.

The model aims at establishing a mathematical relation between the creep coefficient and the qualitative and mechanical parameters described in section 8.2.5. The reliability of the statistical model elaborated can be achieved selecting the variables that do not present singularities otherwise the statistical significance might not be accurate. For this reason the following variables are considered:

i. f_L, peak strength;
ii. f_{R1}, residual strength for 0.5 mm crack opening or deflection;
iii. I_c, creep load ratio;

iv. Supports conditions, classified according to the blocked or allowed translation along the horizontal X axis;
v. Relative humidity control;
vi. Temperature control;
vii. Configuration in precracking and creep phase.

The loading time is a variable that is supposed to influence the response but, since the laboratory named '13', indicates a very high value, the statistical analysis could be compromised. For this reason the model considers the parameters listed, while in a second phase the loading time will be included in as a variable but not considering the data of this laboratory, in order to understand if the present variable appears significant.

8.3.1. Statistical model description

The fitting model has the mathematical form of a power law correlating the creep coefficient variable to the time as a function of the variables investigated:

$$\varphi_{ij}(t) = (\delta_j + c_0 + \sum_{k=1}^{N} c_k x_{kij} + \varepsilon_{ij}) \cdot (\frac{t}{t+a})^b \quad [8.1]$$

where c_0, a, b, c_i are the unknown regression coefficients on which the Anova[2] (Analysis of Variance) significance test is executed, δ_j is a random coefficient that includes the variability among laboratories indicating the deviation of the j-th laboratory from the general mean (mean of δ_j=0), x_{kij} is the value of the k-th parameter for the i-th specimen of the j-th laboratory and ε_{ij} represents the value of the i-th

[2] The ANOVA, analysis of variance, belongs to the inferential statistics techniques by which it is possible to compare two or more groups of data comparing the internal variability between the groups. The null hypothesis consists in the same origin or the same stochastic distribution of the data of all groups. Could be also used, but with less efficiency, when there are ordinal or continuous explanatory variables (it would be preferable to use the linear regression). The variance can be broken into two components, Variance within groups (or Variance within) and Variance between groups (Variance between). This distinction is made because some phenomena could be conditioned by the characteristics of each group to which they belong and the analysis of variance finds if there are differences between several groups. If there are no differences between groups, the variability is due to phenomena within the single group. The comparison aimed at understand that if the internal variability of each group is higher than that between groups, the variability is the results of only internal variable phenomena.

specimen of the *j*-th laboratory of a normal error term; N refers to the numer of variables correlated to the creep coefficient and listed before. The regression model considers qualitative and quantitative variables: the former are considered with their numerical value, i.e. f_R, f_L, I_c, while the qualitative variables, i.e. temperature control, support type, etc., are converted into binary variables so their value could be 0 or 1 according to the verification of the condition set as true in the code. In particular $x_1 = f_R$; $x_2 = f_L$; $x_3 = I_c$; $x_4 = 1$ if the temperature is controlled and 0 in the opposite case; $x_5 = 1$ if the supports do not allow the translation along the horizontal axis (see section 8.2.5, Figure 8.8), 0 in the opposite case; $x_6 = 1$ if the pre-cracking test is performed in three-point bending and four-point bending for creep, 0 otherwise; $x_7 = 1$ if the load condition of three-point bending is used for pre-cracking and creep test, 0 otherwise and $x_8 = 1$ if the humidity is controlled, otherwise 0. The same model is used to describe the creep coefficient calculated with the elastic deformation measured at three moments of time (points E, E+10', E+30'), to understand the effect of the elastic deformation adopted on the results. The analysis is carried out separately for steel and macro-synthetic fibers since the mechanical behaviour results different. This aspect results of great interest because plastic materials exhibit most of the elastic deformation during the loading phase and with higher rate than steel, so the identification of the elastic deformation is supposed to play an important role.

8.3.2. Results of the statistical analysis

The procedure followed is divided in three phases:

1. The regression model is fitted on all data identifying the outliers;
2. The regression model is fitted on the data not including the outliers;
3. The Anova test is performed on the regression coefficients.

The first evaluation (step 1) is based on the standardized residuals, the residuals divided by their standard deviation, where the values outside the boundaries represent the outlier data (Figure 8.26). Since the creep coefficient curve of each sample is described by a set of eighteen points, if all points lie outside the boundaries, that

sample is considered as outlier and not included in the dataset analysed in the step 2. The same evaluation is performed on MS and S fibres and the data highlighted with black boxes are those eliminated from the database (Figure 8.26 and Figure 8.28).

The curves fitted by the model, considering the instantaneous deformation, are reported in Figure 8.27 for synthetic fibers and in Figure 8.29 for steel fibers: the magenta line, that has higher or lower difference with a blue line indicates the fixed creep curve as the laboratories have no differences between them. The higher this difference, the more the single laboratory is supposed to be an outlier. The curves pointed with the arrows are those representing the data of each sample considered as outliers (step 1): one curve for the MSFRC, belonging to the laboratory 5 and three curves for the SFRC, one reported by the laboratory 5 and two of laboratory 6.

The regression model is so fitted on the database where the outliers are not included and the procedure is repeated on the creep coefficient calculate with the elastic deformation at the three time instant. The curves for synthetic fibers are reported in Figure 8.30, Figure 8.31, Figure 8.32, those for steel fibers in Figure 8.33, Figure 8.34, Figure 8.35. The model describes accurately the creep coefficient evolution for both materials.

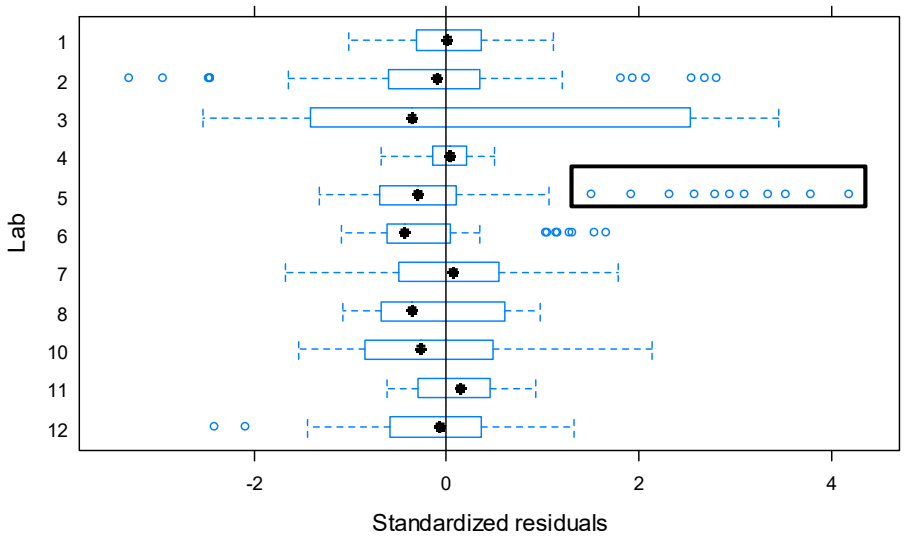

Figure 8.26 – Standardized residuals obtained from nonlinear regression on MS-FRC considering all data of the dataset and creep coefficient at $t_0 = t_E$.

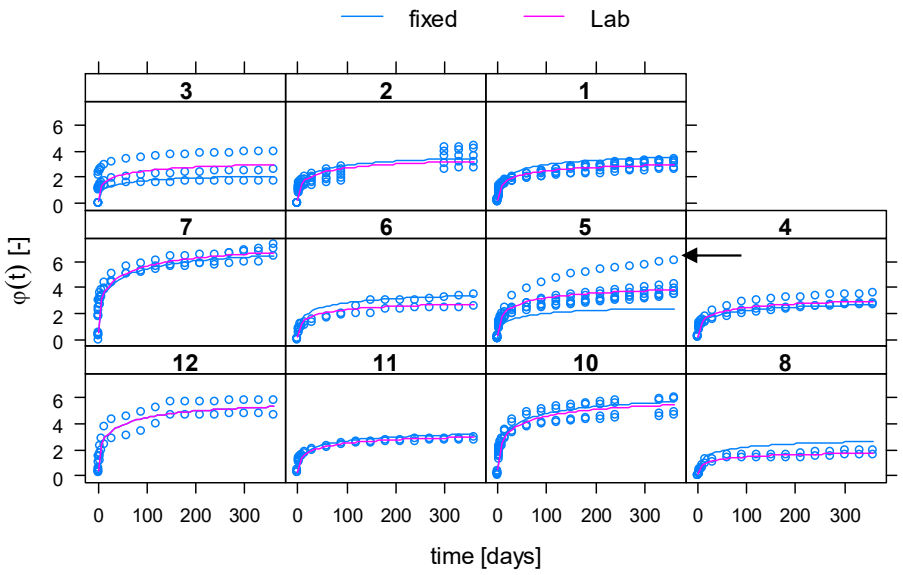

Figure 8.27 – Prediction of the creep coefficient of MSFRC specimens for each laboratory, considering $t_0 = t_E$.

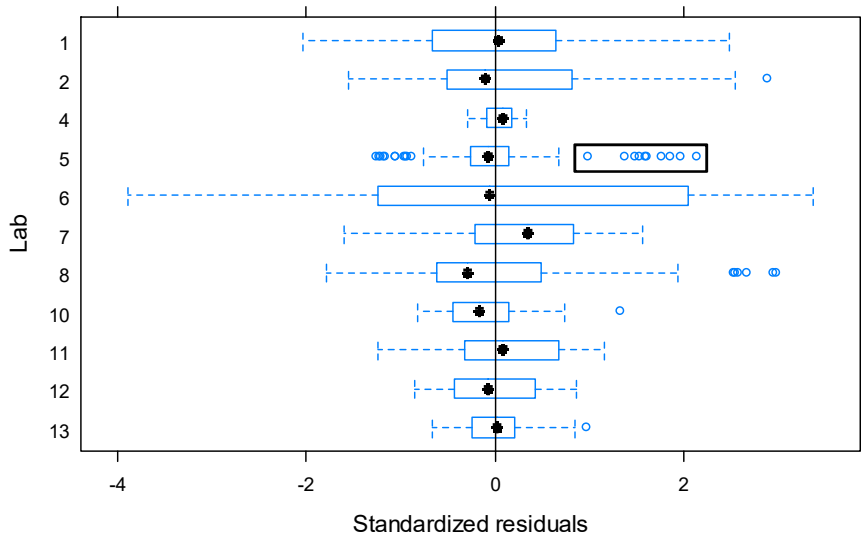

Figure 8.28 – Standardized residuals obtained from nonlinear regression on S-FRC considering all data of the dataset and creep coefficient at $t_0 = t_E$.

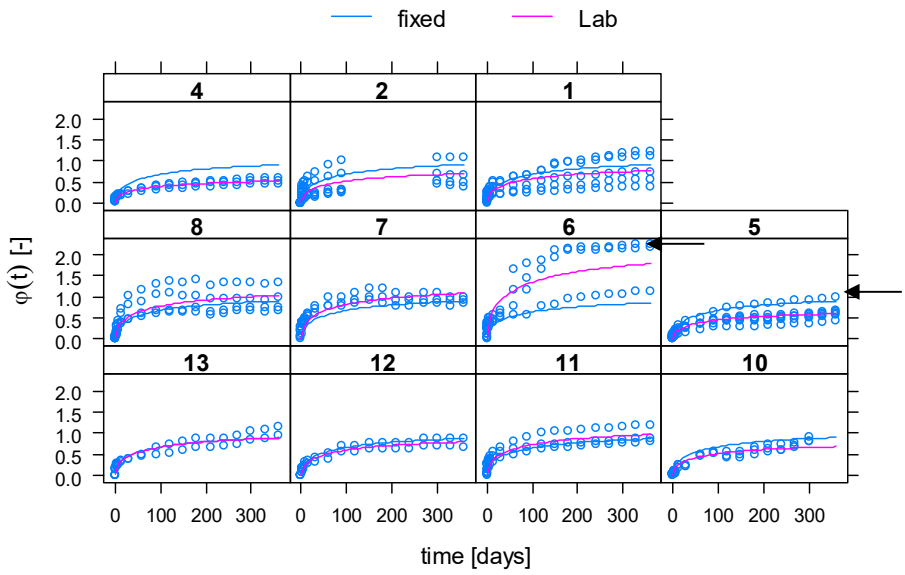

Figure 8.29 – Prediction of the creep coefficient of SFRC specimens for each laboratory, considering $t_0 = t_E$.

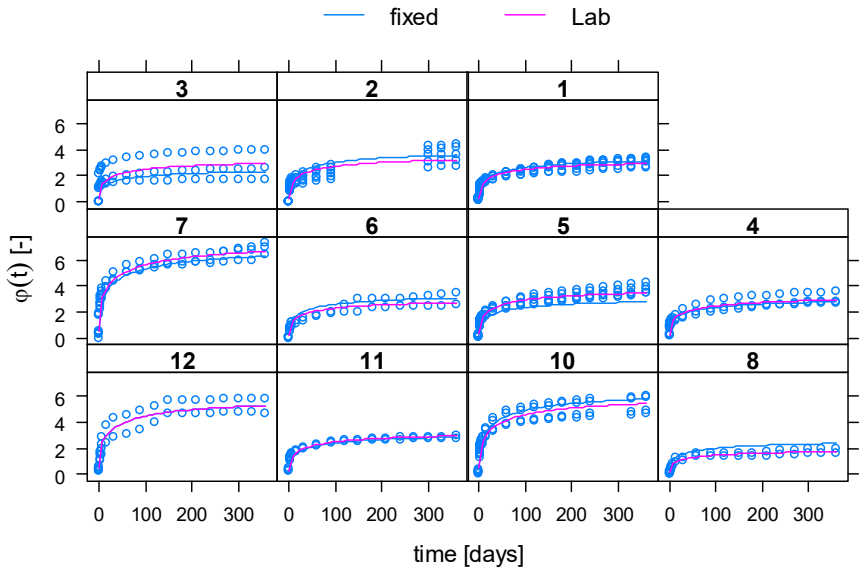

Figure 8.30 – Prediction of the creep coefficient of MSFRC specimens without outliers for each laboratory, considering $t_0 = t_E$.

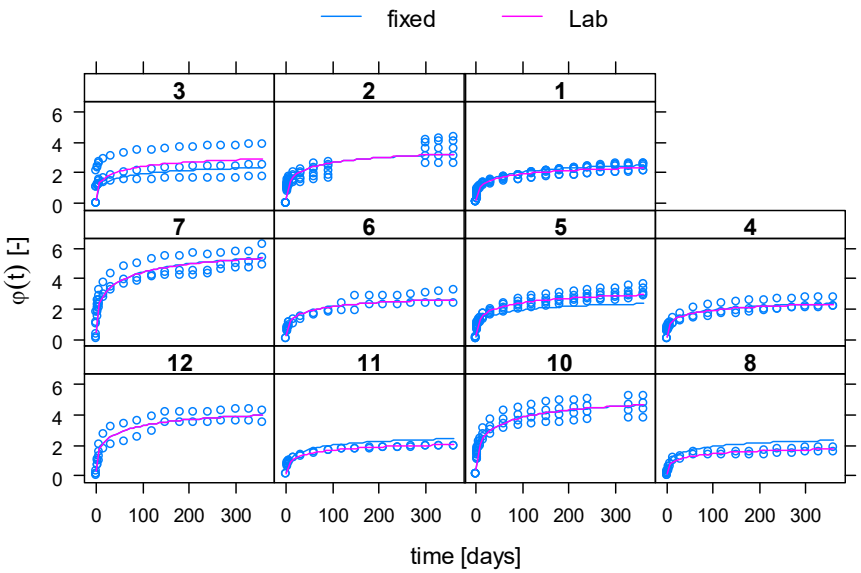

Figure 8.31 – Prediction of the creep coefficient of MSFRC specimens without outliers for each laboratory, considering $t_0 = t_E + 10'$.

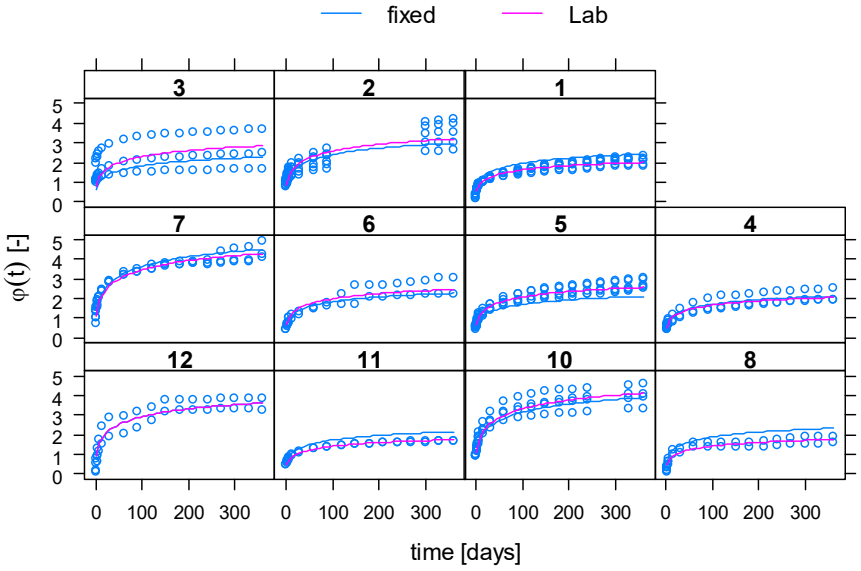

Figure 8.32 – Prediction of the creep coefficient of MSFRC specimens without outliers for each laboratory, considering $t_0 = t_E + 30'$.

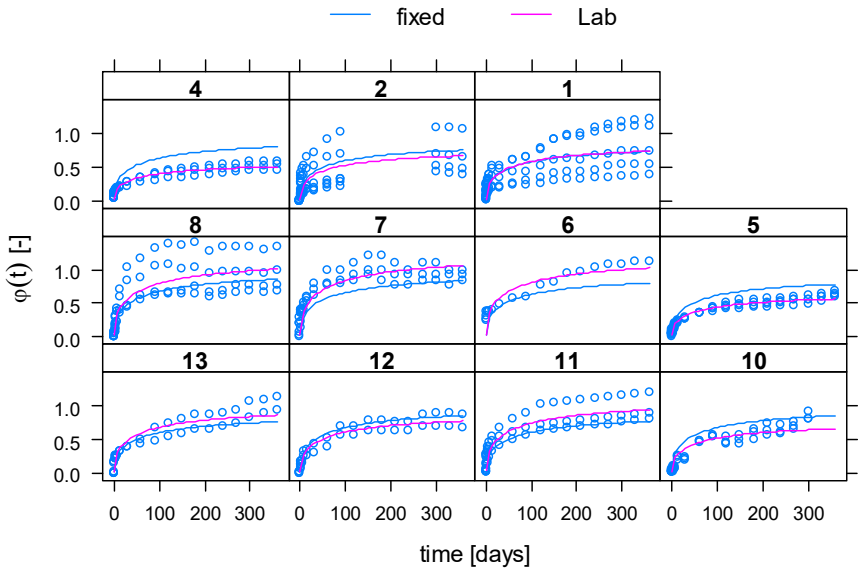

Figure 8.33 – Prediction of the creep coefficient of SFRC specimens without outliers for each laboratory, considering $t_0 = t_E$.

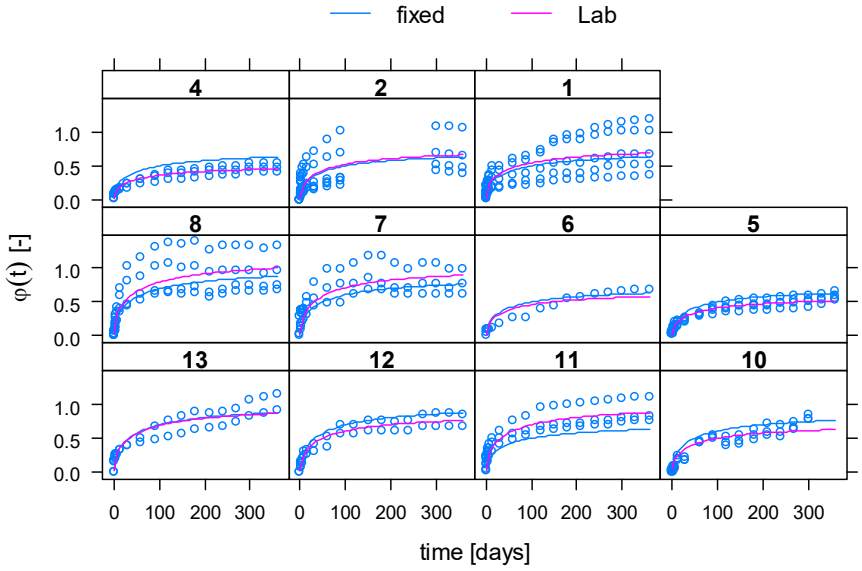

Figure 8.34 – Prediction of the creep coefficient of SFRC specimens without outliers for each laboratory, considering $t_0 = t_E + 10$'.

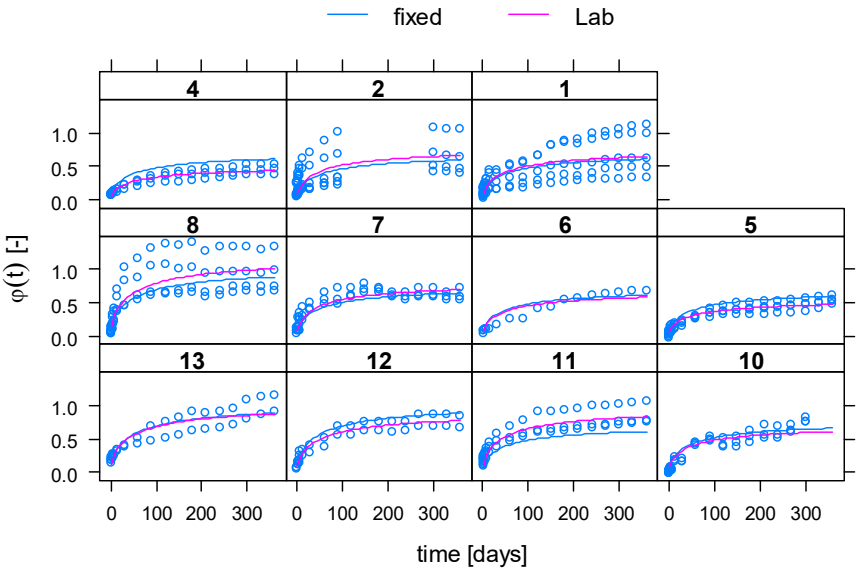

Figure 8.35 – Prediction of the creep coefficient of SFRC specimens without outliers for each laboratory, considering $t_0 = t_E + 30'$.

8.3.3. Analysis of the results

The creep coefficient curves are so fitted with the mathematical power law indicated in the previous section. On the regression parameters the significance test is performed in order to investigate which parameters result statistically significant for the creep deformation evolution, distinguishing into macro-synthetic and steel fibers. In Table 8.9 – Table 8.10 are reported the values of the parameters and the p-values output of the Anova test, respectively for MS and S fibers, considering the creep coefficient calculated with the instantaneous deformation and the delayed deformations, CMOD or deflection, at 10 and 30 minutes.

In light of data analysis, the variables showing a statistical significance on the macro synthetic fibre reinforced concrete long term behaviour are the mechanical parameters, residual flexural strength (f_R) and creep index (I_c), the climate control (T°C) and the configuration and type of supports. Relating the creep coefficient values to the residual strength the relation shows a decrement with the increment of

residual strength (Figure 8.36). The temperature is an environmental variable that affects concrete and polymers behaviour: it was expected, above all for MSFRCs, to be significant. The translational costraint seems to influence the response on time, only this degree of freedom is considered (section 8.2.5) as the movement more likely to happen. Considering the three creep coefficients, the significant parameters are maintained the same but obviously with different values.

Regarding concrete reinforced with steel fibres, the p-values indicate that the residual strength is the only parameter resulting significant on the instantaneous creep coefficient, while considering higher deformations, the type of configuration used during the pre-cracking and creep test appear to affect the creep deformations.

As a general concept, the residual strength is dependent strongly on the number of fibres crossing the cracked surface and, since the number of the steel fibres is lower than plastic, the first are arranged in a more casual way in the matrix and can vary more. This observation is confirmed by the coefficient of variation that is 28 % for the residual strength of SFRC and 15 % for MSFRC (considering also the outlier specimens, Table 8.11).

Regarding the two static configurations adopted for creep and pre-cracking tests, the three point bending creates a concentrated condition while the application of the load in four point bending configuration makes possible to distribute the maximum bending moment over a larger length: this might cause a different response of FRCs.

Analysing the relations between the creep coefficient and the residual strength for the two fibre types, a different trend is observed. The creep coefficient decreases with higher residual strength for MSFRC while shows a slight decrement in case of SFRC (Figure 8.37). Since the dependence of the residual capacity on the number of fibers, the relation between the creep coefficient and the fibers density is represented in Figure 8.39 reflecting the same trend of the residual strength with the creep coefficient increment. On the contrary, for creep coefficients related to steel fibers density, the linear regression trend suggests no remarkable relation. This difference can motivate the output of the significance test that indicates the residual strength

significance only for the instantaneous creep coefficient.

An observation that deserves attention regards the difference between the standard deviation 'between' and 'within' laboratories that is reduced considering a different initial deformation in the creep coefficients calculation. The data collected in Table 8.9 and Table 8.10 reveal that, for both FRCs reinforcement, the variability between groups is higher than that within: this suggests that the difference in the tests procedure (as the conditions performed) affects the results more than the internal variability due to the ordinary scatter in these experimental tests.

Figure 8.38 represents the random factor values for all laboratories, for synthetic and steel fibers: the major scatter of data is found for MSFRCs rather than SFRC. As described before the random factor is introduced in the model to account for the variability that cannot be motivated by the properties correlated and the box plot representation helps to point out the laboratories with the higher value and so assumed as outliers in the procedure adopted. The experimental tests on MS fibre reinforced concrete present more variability appearing more sensible to a variety of factors respect to steel fibre reinforced concretes.

Moreover, considering an instantaneous deformation delayed of 10 minutes and 30 minutes the variability of data is reduced, more for plastic fibres rather than steel. Even for steel, considering the crack opening or deflection at 30' the variance can be related to the internal variability of the data group, but in general the variance odds are more evident for synthetic fibres. For this reason, the identification of the proper deformation to consider in the calculation of the creep coefficient requires attention above all because a high portion of deformation is exhibit upon loading by plastics, so the viscoelasticity starts almost immediately.

The presence of several aspects to account for is the main reason why official recommendations regulating the behaviour of the fiber reinforced concrete analysis in a cracked state are required. In addition, the database generated by the present work will be published with the aim of representing a reference in the field of creep tests on FRCs.

Table 8.9 – Values of the model [8.1] parameters and their p-values for MSFRC.

	MS $t_0=t_E$		MS $t_0=t_E$+10'		MS $t_0=t_E$+30'	
	value	p-val.	value	p-val.	value	p-val.
c_0 [-]	1.97	<0.001	0.77	<0.001	3.77	<0.001
a [days]	184.68	<0.001	252.21	<0.001	358.34	<0.001
b [-]	0.26	<0.001	0.26	<0.001	0.26	<0.001
c_1 (f_R) [1/MPa]	-0.76	<0.001	-0.28	<0.001	-0.76	<0.001
c_2 (f_L) [1/MPa]	-	-	-	-	-	-
c_3 (Ic) [-]	0.07	<0.001	0.07	<0.001	0.04	0.001
c_4 (TC) [-]	-0.57	<0.001	-0.87	<0.001	-0.72	0.0004
c_5 (ST) [-]	3.00	<0.001	1.44	0.00	1.53	0.0008
c_6 (LC TF) [-]	-2.65	<0.001	-1.47	<0.001	-1.89	<0.001
c_7 (TC TT) [-]	3.80	<0.001	2.60	<0.001	1.90	<0.001
c_8 (HC) [-]	-	-	-	-	-	-
σ^2 between [-]	0.211	-	0.152	-	0.185	-
σ^2 within [-]	0.140	-	0.144	-	0.101	-

Table 8.10 – Values of the model [8.1] parameters and their p-values for SFRC.

	ST $t_0=t_E$		ST $t_0=t_E$+10'		ST $t_0=t_E$+30'	
	value	p-val.	value	p-val.	value	p-val.
c_0 [-]	0.71	<0.001	1.01	<0.001	1.00	<0.001
a [days]	200.20	<0.001	145.60	<0.001	136.30	<0.001
b [-]	0.36	<0.001	0.41	<0.001	0.45	<0.001
c_1 (f_R) [1/MPa]	0.07	0.002	-	-	-	-
c_2 (f_L) [1/MPa]	-	-	-	-	-	-
c_3 (Ic) [-]	-	-	-	-	-	-
c_4 (TC) [-]	-	-	-	-	-	-
c_5 (ST) [-]	-	-	-	-	-	-
c_6 (LC TF) [-]	-	-	-0.29	0.02	-0.32	0.011
c_7 (TC TT) [-]	-	-	-0.13	0.35	-0.26	0.034
c_8 (HC) [-]	-	-	-	-	-	-
s^2 between [-]	0.045	-	0.023	-	0.018	-
s^2 within [-]	0.023	-	0.025	-	0.023	-

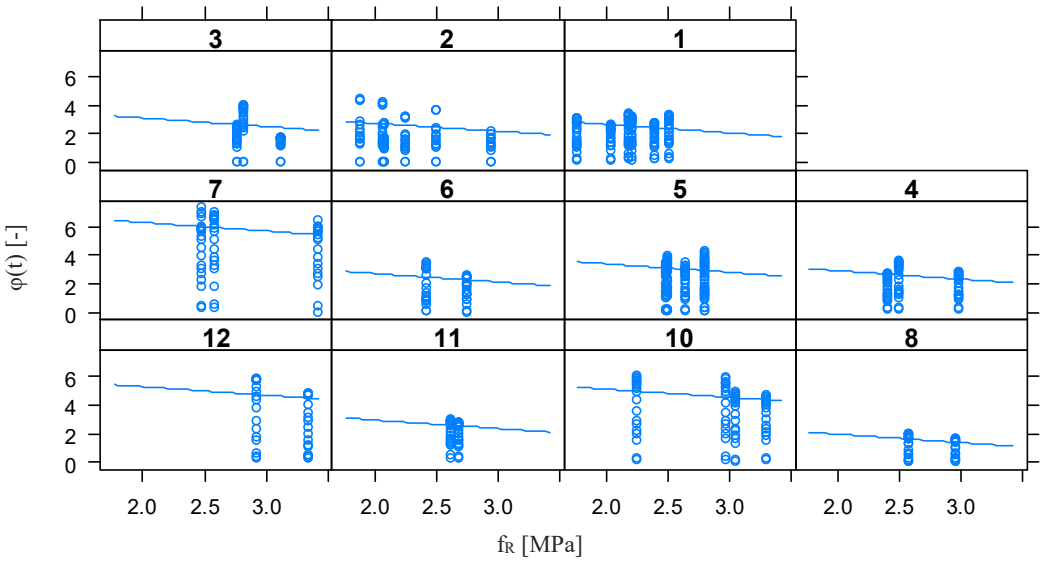

Figure 8.36 – Creep coefficient ($t_0 = t_E$) prediction versus residual strength for all laboratories for MSFRC.

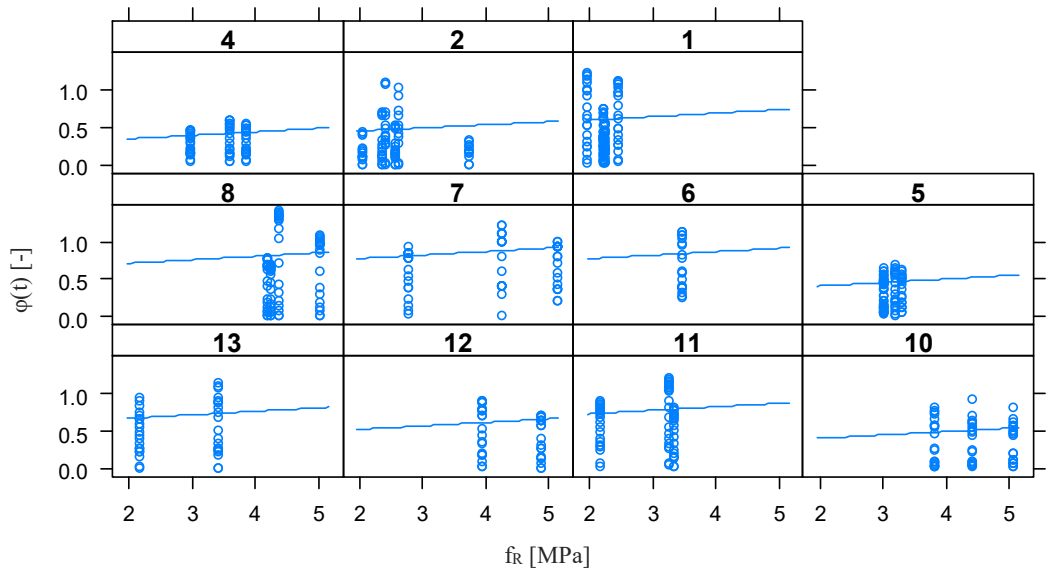

Figure 8.37 – Creep coefficient ($t_0 = t_E$) prediction versus residual strength for all laboratories for SFRC.

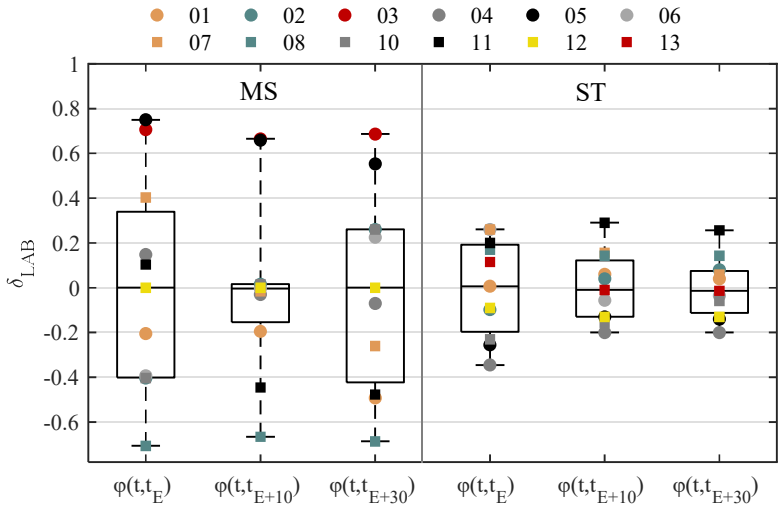

Figure 8.38 – Random factors for all laboratories, for creep coefficients at $t_0 = t_E$, $t_0 = t_E + 10'$, $t_0 = t_E + 30'$ – MS and S fibers.

Table 8.11 – Coefficient of Variation of the residual strength for MSFRC and SFRC.

	COV [%] MS Fibres	COV [%] ST Fibres
$f_{r,1}$	15%	27%
$f_{r,1}$ [without outliers]	15%	28%
f_L	12.2%	12.6%
f_L [without outliers]	12.3%	12.6%

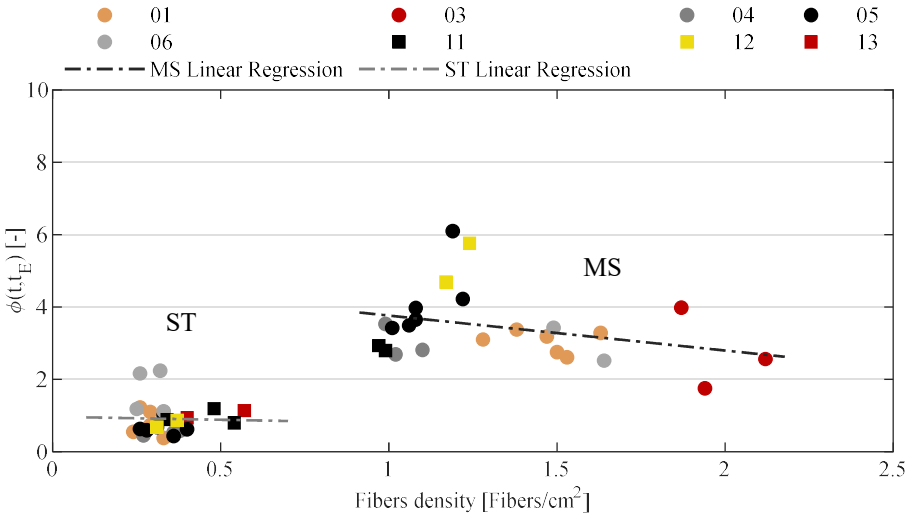

Figure 8.39 – Creep coefficients ($t_0 = t_E$) versus fibers density and linear regressions for MS and ST fibers.

Conclusions and Future developments

The research work presented in this thesis was focused on the experimental and numerical investigation of fibre reinforced concretes, under short and long term conditions.

The study starts with an experimental campaign aimed at characterizing the aspects affecting the interface between macro-synthetic crimped fibers and different mortar admixtures by means of pull-out tests. The analysis highlighted the influence of the type of matrix, in terms of mix design, on the failure process of the single fibre in terms of type and bond strength. The results produced made possible to calibrate a numerical one dimensional model able to simulate the pull-out failure of this fibre type and so the constitutive bond-slip law.

The experimental investigation is then perfomed at Macro-Synthetic Fibre Reinforced Concrete scale where the influence of concrete, fibre type and dosage on the material response is analysed in deep. The experiments revealed a high correlation between the residual strength of the material and the fibre dosage adopted, in particular with the number of fibers effectively crossing the cracked surface. Since different concrete admixtures have been tested, the results made possible to understand how the high dosage and the concrete strength interact: the compressive strength has no significant influence on the nominal flexural residual tensile strength. The experimental results produced are the starting point for the numerical model calibration determining a local stress-crack opening constitutive law able to describe properly the post-peak response of the material according to the fibre dosage considered. The fracture process activated in the composite derives from the mechanism developed at interface fibre-matrix: due to this, the characterization of the failure exhibited by the fibre during the pull-out tests has been decisive to understand what happens at a bigger scale.

In the field of synthetic reinforcement, the effect of micro fibers and optimized cementitious matrix are experimentally studied. The main purpose consisted of

designing admixtures where the cement is substituted in different proportions by a sustainable waste product (porcelain stoneware powder). The experimental results emphasized the possibility of optimizing the admixture using porcelain stoneware products realizing high performance fibre composites. Moreover, the effect of the optimization is measured also after a longer curing period, 60 days, and some admixtures featured an increment of compressive and flexural strength on time. This observation is drawn with the aim of understanding how the material tested might behave on time.

The aspect regarding the characterization of FRCs long term performance has represented the core of the second part of the research. First of all, a wide experimental campaign is performed where the behaviour of a fibre reinforced concrete with polypropylene crimped fibers is investigated testing the material in different loading conditions with the aim of separating the contributions interacting in the flexural state. Shrinkage, in unloaded conditions, and creep compressive tests, are performed: the deformations exhibited are ascribed mostly to the cementitious matrix. At the same time, the fibre viscoelastic behaviour has been investigated performing tensile tests on the single fibre. This has represented a challenging aspect since the complexities associated to the procedure of testing a filament under sustained load, assuring the undamaged condition of the sample and the proper calibration and application of the load. In addition, the bond between fibre and matrix, at a bigger scale, is simulated by applying uniaxial tensile sustained load on precracked cylinders whose deformations are given mostly by the viscoelastic nature of the fibre itself and the viscous slippage at the interface. It has to be specified that the type of fibers used is different from that characterized before but the principal aim of the research is the analysis of the mechanical response of the macro-synthetic fibers but not a comparison of the performance of the short and long term behaviour. In the framework of time dependent effects characterization, the results of a round robin experimental campaign of creep bending tests on macro-synthetic and steel fibre reinforced concretes, have been analysed. The principal aim would have been

the evaluation of the principal aspects influencing the creep deformations, considering the mechanical properties of the material and the testing procedure adopted. The purpose has been fulfilled performing a statistical analysis on the parameters of a multi regression model used to correlate the creep experimental behavior to the variables investigated. The results highlighted the influence of several aspects on the long term deformations for fibre reinforced concretes tested, especially in case of macro-synthetic fibers.

The aspect to emphasize is the lack of standardized methods and regulations in this field and, for this reason, the experimental analysis, supported by numerical studies, represent a good approach.

The numerical analysis sees the description of the macro-synthetic FRCs tested with a discrete theory, Lattice Discrete Particle Model, able to reproduce the hetereogeneity of the material in terms of concrete aggregates and fibers dispersion. A numerical predictive model of the short term response has been calibrated and validated, as the first part of the analysis. The time dependent phenomena are also simulated: the viscoelastic behaviour of concrete and polymeric fibers is calibrated on the basis of the experimental results. The numerical model reproduces also the conditions in which the experiments have been carried out: temperature, humidity, curing conditions and testing procedure.

However, the results highlighted the need of defining also the viscoelastic bond between fibre and matrix as the model is not able to reproduce completely the experimental behaviour if only the viscoelastic contribution of both constituents is calibrated. This means that, for the fibres tested, the viscoelastic deformation given by the slippage at the interface is remarkable. This conclusion is drawn first on the results of the experiments but also supported by the numerical investigation, of fundamental importance in this sense. The inclusion of the fibre with viscoelastic behaviour represents, therefore, the innovative aspect since the LDPM theory has been widely validated for only concrete mechanical behaviour simulations.

The innovative aspects of the present study concern the evaluation of the differences, in terms of mechanical performance, given by the different characteristics of the MSFRC components and the innovative set-up developed in the framework of the long term behaviour investigation. The numerical study included the calibration of the constitutive behaviour for local and global mechanical performance and a predictive model for the short term analysis of the MSFRC tested. In addition, the simulation of the time dependet phenomena is of great importance for the assessment of the contribution of each loading state condition occurring in the cracked state of the FRCs, representing also a starting point for the creep deformations prediction. As the adoption of the FRCs for the realization of different structural elements, as described in section 1.2.7 of the thesis, the mechanical characterization of the material performance has an important role in the design phase. Any applications can be suggested, aside from those already proposed, are the use of this composite material in precast elements or in some structural elements where it could be easier to place fibers instead of high amount of ordinary steel reinforcement. Above all, the control of the cracked state for reinforced concrete structures is one of the optimal use of the fibers and, so, of the composite material at issue.

The future works that can be done, on the basis of the conclusions presented, regard the experimental and numerical approaches. The experimental characterization of the bond behaviour of inclined fibers helps to detect the phenomena due to the different placement of fibers in the material matrix. Moreover, the experiments can be used to calibrate the parameter set in the numerical analysis and that account for these effects, desumed from the literature for the numerical simulations reported (as specified). The description of the interface behaviour with a 2-D and 3-D models, simulated as 1-D in the research exposed, represents a further development of the model calibrated.
The adoption of high performance composites as reinforcement of concrete elements, at a smaller scale, under flexural loads will be an application of the material characterized.

Since the fibre orientation plays an important role, the effect of the numerical parameters accounting the orientation, i.e. the preferential direction variation, will be detected especially for the time dependent phenomena simulations where it has not been considered.

The characterization of the bond between fibre-matrix with a viscoelastic constitutive law represents the next step of the research. The procedure will make use of the experimental tests of fibre pull-out under sustained load using the loading frame described in section 6.4.10.

The phenomena so calibrated will be validated on the creep deformations under flexural load conditions understanding how the calibration of uncoupled phenomena can predict the material performance in terms of creep deformations.

References

Abdallah, S., Fan, M., and Zhou, X. (2016). Effect of Hooked-End Steel Fibres Geometry on Pull-Out Behaviour of Ultra-High Performance Concrete. *International Journal of Civil, Environmental, Structural, Construction and Architectural Engineering*, *10*(12), 1599–1604.

Abdellatef, M., Boumakis, I., Wan-Wendner, R., and Alnaggar, M. (2019). Lattice Discrete Particle Modeling of concrete coupled creep and shrinkage behavior: A comprehensive calibration and validation study. *Construction and Building Materials*, *211*, 629–645.

ACI Committee 544. (2002). Report on Fiber Reinforced Concrete Reported by ACI Committee 544, *96*(Reapproved).

Aguado, A., Gàlvez, J. C., Fernandez-Ordònez, D., and De La Fuente, A. (2016). Sustainability evaluation of the concrete structures. In *II International Conference on Concrete Sustainability ICCS16*. Madrid, Spain.

Alvaro, V., Pascale, G., and Di Tommaso, A. (2007). *MATERIALI COMPOSITI A MATRICE CEMENTIZIA PER I RINFORZI STRUTTURALI*. Università di Bologna (Master Thesis, in Italian).

Amanjean, E. N., Mouret, M., and Vidal, T. (2019). Effect of design parameters on the properties of ultra-high performance fibre-reinforced concrete in the fresh state. *Construction and Building Materials*, *224*, 1007–1017.

Amin, N., Kirk, V., Garo, A., and Bijan, S. (2014). Drying shrinkage behaviour of fibre reinforced concrete incorporating polyvinyl alcohol fibres and fly ash. *Advances in Civil Engineering*, *2014*(2014), 1–10.

Arango, S., Taungua, E. G., Vargas, J. R. M., and Serna Ros, P. (2012). A comprehensive study on the effect of fibers and loading on flexural creep of SFRC. In *BEFIB2012 - Fibre reinforced concrete* (pp. 704–715). Guimarães, Portugal.

ASTM A 820. (1996). Specification for Steel Fibers for Fiber Reinforced Concrete.

ASTM C 1550. (2012). ASTM C1550-12 Standard Test Method for Flexural Toughness of Fiber Reinforced Concrete (Using Centrally Loaded Round Panel).

Aveston, J., Cooper, G. A., and Kelly A. (1971). Single and multiple fracture. In *The properties of fiber composites. Proceedings "National Physical Laboratory"* (pp. 15–26). Guilford, UK.

Babafemi, A. J. (2015). *Tensile Creep of Cracked Macro Synthetic Fibre Reinforced Concrete*. Stellenbosch University (PhD Thesis).

Bakker, A. (2006). Lecture 15 - Discrete Phase Modeling Applied Computational Fluid Dynamics Discrete phase modeling. *Computational Fluid Dynamics*.

Balaguru, P. N., and Shah, S. P. (1992). *Fiber Reinforced Cement Composites*. New York: McGraw Hill.

Barragan, B. E., Gettu, R., Martin, M. A., and Zerbino, R. L. (2003). Uniaxial tension test for steel fibre reinforced concrete—a parametric study. *Cement and Concrete Composites*, *25*(7), 767–777.

Barragán BE. (2002). *Failure and toughness of steel fiber reinforced concrete under tension and shear*. Universitat Politècnica de Catalunya.

Bartos, P. (1981). Review paper: Bond in fibre reinforced cements and concretes. *International Journal of Cement Composites and Lightweight Concrete*, *3*(3), 159–177.

Bartoš, P. (1980). Analysis of pull-out tests on fibres embedded in brittle matrices. *Journal of Materials Science*, *15*(12), 3122–3128.

Bažant, P. Z., Fellow, ASCE, and Xi, J. (1995). Continuous retardation spectrum for solidification theory of concrete creep. *Journal of Engineering Mechanics*, *121*(2).

Bažant, Z. P., and Oh, B. H. (1983). Crack band theory for fracture of concrete. *Materials and Structures*, *16*, 155–177.

Bentur, A., Mindess, S., and Vondran, G. (1989). Bonding in polypropylene fibre reinforced concretes. *International Journal of Cement Composites and Lightweight Concrete*, *11*(3), 153–158.

Bentur, A., Wu, S. T., Banthis, N., Baggott, R., Hansen, W., Katz, A., … Taerwe, L. R. (1996). Fibre-matrix interfaces. *High Performance Fibre Reinforced Cementitous Composites 2*, 149–191.

Bernard, E. (2004). Creep of cracked fibre reinforced shotcrete panels. *Shotcrete: More Engineering Developments*, 47–57.

Bernardi, P., Cerioni, R., and Michelini, E. (2012). Numerical modelling of the behaviour of SFRC elements in presence of multiple cracks. *Proceeding of the 8th RILEM Int. Symposium on Fibre Reinforced Concrete*, 219–220.

Betterman, L. R., Ouyang, C., and Shah, S. P. (1995). Fiber-matrix interaction in microfiber-reinforced mortar. *Advanced Cement Based Materials*, *2*(2), 53–61.

Blanco, A., Pujadas, P., De La Fuente, A., Cavalaro, S., and Aguado, A. (2013). Application of constitutive models in European codes to RC-FRC. *Construction and Building Materials*, *40*, 246–259.

Bowling, J., and Groves, G. W. (1979). The debonding and pull-out of ductile wires from a brittle matrix. *Journal of Materials Science*, *14*(2), 431–442.

Bozza, M. CALCESTRUZZI STRUTTURALI AD ALTA RESISTENZA (Report).

Brandt, A. M. (1985). On the optimal direction of short metal fibres in brittle matrix composites. *Journal of Materials Science*, *20*(11), 3835–3841.

Brühwiler, E., and Denarié, E. (2008). Rehabilitation of concrete structures using Ultra-High Per- formance Fibre Reinforced Concrete. *The Second International Symposium on Ultra High Performance Concrete*, (1), 1–8.

BS EN 14651-2005. (2005). Test method for metallic fibred concrete — Measuring the flexural tensile strength (limit of proportionality (LOP), residual). *British Standard Institution*, *3*, 1–17.

Budiansky, B., Hutchinson, J., and Evans, A. G. (1986). Matrix fracture in fiber-reinforced ceramics. *Journal of Mech.Phys. Solids*, *34*(2), 167–189.

Buratti, N., and Mazzotti, C. (2015). Experimental tests on the effect of temperature on the long-term behaviour of macrosynthetic Fibre Reinforced Concretes. *Construction and Building Materials*, *95*, 133–142.

Buratti, N., Mazzotti, C., and Savoia, M. (2011). Post-cracking behaviour of steel and macro-synthetic fibre-reinforced concretes. *Construction and Building Materials*, *25*(5), 2713–2722.

Buratti, N., Vinciguerra, A., Mazzotti, C., and Bignozzi, M. C. (2018). Calcestruzzi fibrorinforzati ad altissime prestazioni contenenti materie prime seconde. In *Italian Concrete Days Giornate aicap 2018*.

Böhni, H. (2005). *Corrosion in Reinforced Concrete Structures*. Woodhead Publishing Ltd and CLC Press LLC.

Cascardi, A., Micelli, F., and Aiello, M. A. (2017). An Artificial Neural Networks model for the prediction of the compressive strength of FRP-confined concrete circular columns. *Engineering Structures*, *140*, 199–208.

Cavalaro, S. H. P., and Aguado, A. (2015). Intrinsic scatter of FRC: an alternative philosophy to estimate characteristic values. *Materials and Structures/Materiaux et Constructions*, *48*(11), 3537–3555.

Chamis, C. C. (1972). *Mechanics of Load Transfer At the Fiber - Matrix Interface*.

Chasioti, S. G., and Vecchio, F. J. (2017). Effect of fiber hybridization on basic mechanical properties of concrete. *ACI Structural Journal*, *114*(3), 375–384.

Chiu, Y.-C., Panchmatia, P., and Sivaram, A. (2011). *Analysis of Fracture Energy: Comparative Study of PCC and FRC*. West Lafayette, Indiana,US.

Choun, Y. S., and Park, H. K. (2015). Containment performance evaluation of prestressed concrete containment vessels with fiber reinforcement. *Nuclear Engineering and Technology*, *47*(7), 884–894.

Claisse, P. A., Cabrera, J. G., and Hunt, D. N. (2001). Measurement of porosity as a predictor of the durability performance of concrete with and without condensed silica fume. *Advances in Cement Research*, *13*(4), 165–174.

CNR-DT 204/2006. (2008). Istruzioni per la Progettazione , l ' Esecuzione ed il Controllo di Strutture Consiglio Nazionale delle Ricerche.

Collepardi, S., and Troli, R. (2013). PRINCIPI GENERALI SUI CALCESTRUZZI FIBRORINFORZATI. *Enco Journal*, 1–17.

Coppola, L., and Buoso, A. (2013). Il calcestruzzo fibrorinforzato: risultati di una campagna sperimentale su spritz-beton rinforzati con fibre in acciaio, vetro e polipropilene sperimentale. *Enco Journal*, 18–26.

Cosenza, E., Manfredi, G., and Realfonzo, R. (2002). Development length of FRP straight rebars. *Composites Part B: Engineering*, *33*(7), 493–504.

Cox, H. L. (1952). The elasticity and strength of paper and other fibrous materials. *British Journal of Applied Physics*, *3*(3), 72–79.

CSLP (Consiglio Superiore dei Lavori Pubblici). (2019). Linea guida per l'identificazione, la qualificazione, la certificazione di valutazione tecnica ed il controllo di accettazione dei calcestruzzi fibrorinforzati FRC (Fiber Reinforced Concrete).

Cunha, V. M., Barros, J. A. O., and Sena-cruz, J. (2010a). *Pullout behavior of hooked-end steel fibres in self-compacting concrete*. Guimarães, Portugal.

Cunha, V. M., Barros, J. A. O., and Sena-cruz, J. (2010b). *Pullout behavior of hooked-end steel fibres in self-compacting concrete*.

Cusatis, G., Mencarelli, A., Pelessone, D., and Baylot, J. (2011). Lattice Discrete Particle Model (LDPM) for failure behavior of concrete. II: Calibration and validation. *Cement and Concrete Composites*, *33*(9), 891–905.

Cusatis, G., Pelessone, D., and Mencarelli, A. (2011). Lattice Discrete Particle Model (LDPM) for failure behavior of concrete. I: Theory. *Cement and Concrete Composites*, *33*(9), 881–890.

D.M. 17 Gennaio 2018. (2018). Norme Tecniche per le costruzioni (NTC2018). *Ministry of Infrastructure and Transportation, Rome.*

Darwin, D., Barham, S., Kozul, R., and Luan, S. (2001). Fracture energy of high-strength concrete. *ACI Materials Journal*, *98*(5), 410–417.

Del Prete, C., Buratti, N., Manzi, S., and Mazzotti, C. (2019). Macro-synthetic fibre reinforced concrete: influence of the matrix mix design on interfacial bond behaviour. In *IOP Conference Series: Materials Science and Engineering*. Prague, CZ Republic.

Di Maida, P., Radi, E., Sciancalepore, C., and Al., E. (2015). Pullout behavior of polypropylene macro-synthetic fibers treated with nano-silica. *Construction and Building Materials*, *85*, 39–44.

Di Prisco, M., Colombo, M., and Dozio, D. (2013). Fibre-reinforced concrete in fib Model Code 2010: Principles, models and test validation. *Structural Concrete*, *14*(4), 342–361.

Di Prisco, M., Ferrara, L., Colombo, M., and Mauri, M. (2004). On the identification of SFRC constitutive Law in uniaxial tension. In *Proceedings of sixth RILEM symposium on fibre-reinforced concretes (BEFIB 2004)* (pp. 827–836).

Di Prisco, M., Plizzari, G., and Vandewalle, L. (2011). Calcestruzzo fibrorinforzato nel nuovo codice modello fib, 1–10.

Dupont, D., and Vandewalle, L. (2002). Characterisation of steel fibre concrete with a r–e relation. In *Proceedings of the 4th international PhD symposium in civil engineering* (pp. 108–114).

Easley, T. C., Faber, K. T., and Shah, S. P. (2010). Use of a Crack-Bridging Single-Fiber Pullout Test to Study Steel Fiber/Cementitious Matrix Composites. *Journal of the American Ceramic Society*, *82*(12), 3513–3520.

Eligehausen, R., Popov, E., and Bertero, V. (1983). *Local bond stress–slip relationships of deformed bars under generalized excitations*. Berkeley.

Euclid Chemical. (2018). *Technical Bulletin FC-1* (Vol. 3).

Fehling, E., Bunje, K., and Leutbecher, T. (2007). Design Relevant Properties of Hardened Ultra High Performance Concrete, Ultra High Performance Concrete (UHPC). In *Int. Symp. on Ultra High Performance Concrete* (pp. 327–338). Kassel.

Ferrara, L., Shyshko, S., and Mechtcherine, V. (2012). Predicting the Flow-Induced Dispersion and Orientation of Steel Fibers in Self-Consolidating. In *BEFIB2012 - Fibre reinforced concrete* (pp. 1–12).

fib Bulletin 28. (2004). *Environmental design - State-of-the-art*.

fib Bulletin 71. (2013). *Integrated Life Cycle Assessment of Concrete Structures*.

Findley, W. N., J.S., L., and K., O. (1976). *Creep and Relaxation of Nonlinear viscoelastic materials*. (North-Holland Publishing Company, Ed.).

Focacci, F., Nanni, A., Fellow, ASCE, and E. Bakis, C. (2000). Local bond-slip relationship for FRP reinforcement in concrete, *4*, 24–31.

Foote, R., Mai, Y. W., and Cotterell, B. (1985). Process size and crack growth measurements in fibre cements. Fibre reinforced concrete properties and applications. *American Concrete Institute*, 55–70.

Garcia, V. J., Márquez, C. O., Zúñiga-Suárez, A. R., Zuñiga-Torres, B. C., and Villalta-Granda, L. J. (2017). Brazilian Test of Concrete Specimens Subjected to Different Loading Geometries: Review and New Insights. *International Journal of Concrete Structures and Materials*, *11*(2), 343–363.

Ghersi, A. (2012). *Il cemento armato*. (D. Flaccovio, Ed.) (II).

Golub, V. P., Fernati, P. V., and Lyashenko, Y. G. (2008). Determining the parameters of the fractional exponential heredity Kernels of linear viscoelastic materials. *International Applied Mechanics*, *44*(9).

Grauers, M. (2000). *Rational production and improved working environment through using self compacting concrete*. Lulea University of Technology.

Groth, P. (2000). *Fibre Reinforced Concrete – Fracture Mechanics Methods Applied on Self-Compacting Concrete and Energetically Modified Binders.* Luleå University of Technology, Sweden.

Hajek, P. (2019). Concrete Structures for Sustainable and Resilient Built Environment. In *SSCS19* (pp. 5–11). Lecco.

Hameed, R., Turatsinze, A., Duprat, F., and Sellier, A. (2009). Metallic Fiber Reinforced Concrete : Effect of Fiber Aspect Ratio on the Flexural Properties. *ARPN Journal of Engineering and Applied Sciences*, *4*(5), 67–72.

Hillerborg, A. (1985). The theoretical basis of a method to determine the fracture energy GF of concrete. *Matériaux et Constructions*, *18*(4), 291–296.

Hillerborg, A., Modéer, M., and Petersson, P. E. (1976). Analysis of crack formation and crack growth in concrete by means of fracture mechanics and finite elements. *Cement and Concrete Research*, *6*, 773–782.

Houshyar, S., Shanks, R. A., and Hodzic, A. (2005). Tensile creep behaviour of polypropylene fibre reinforced polypropylene composites. *Polymer Testing*, *24*(2), 257–264.

Hsueh, C. H. (1992). Requirements of frictional debonding at fiber/matrix interfaces for tough ceramic composites. *Composites Engineering*, *2*(8), 655–663.

IEA - International Energy Agency. (2018). *Global Energy and CO2 Status Report*. Paris, France.

Illston, J. M. (1965). The creep of concrete under uniaxial tension. *Magazine of Concrete Research*, *17*(51), 77–84.

Imbabi, M. S., Carrigan, C., and McKenna, S. (2012). Trends and developments in green cement and concrete technology. *International Journal of Sustainable Built Environment*, *1*(2), 194–216.

Imechanica.org. (n.d.). Compositi a fibre corte.

ISO 9277:2010. (2010). Determination of the specific surface area of solids by gas adsorption — BET method.

Jackson, R. B., Le Quéré, C., Andrew, R. M., Canadell, J. G., Peters, G. P., Roy, J., and Wu, L. (2017). Warning signs for stabilizing global CO2 emissions. *Environmental Research Letters*, *12*(11).

Jansson, A., Löfgren, I., Gylltoft, K., and Thomas. (2008). Design methods for fibre-reinforced concrete: a state-of-the-art review.

Jewell, R. B., Mahboub, K. C., Robl, T. L., and Bathke, A. C. (2015). Interfacial bond between reinforcing fibers and calcium sulfoaluminate cements: Fiber pullout characteristics. *ACI Materials Journal*, *112*(1), 39–48.

Jin, C., Buratti, N., Stacchini, M., Savoia, M., and Cusatis, G. (2016). Lattice discrete

particle modeling of fiber reinforced concrete: Experiments and simulations. *European Journal of Mechanics, A/Solids*, *57*, 85–107.

Jiràsek, M., and Bazant, Z. P. (2002). *Inelastic Analysis of Structures*. Wiley.

JSCE. (2004). *Recommendations for design and construction of ultra-high strength fiber reinforced concrete structures (Draft)*.

Karihaloo, T. (2001). Effect of type and volume fraction of aggregate on the fracture properties of concrete. *Fracture Mechanics of Concrete and Concrete Structures, Recent Advances in Fracture Mechanics of Concrete*, 123–129.

Khabaz, A. (2016). Performance evaluation of corrugated steel fiber in cementitious matrix. *Construction and Building Materials*, *128*, 373–383.

Kooiman, A. G. (2000). *Modelling steel fibre reinforced concrete for structural design*. Delft University of Technology.

Krenchel, H. (1964). *Fibre Reinforcement – Theoretical and practical investigations of the elasticity and strength of fibre-reinforced materials*. Technical University of Denmark.

Kusterle, W. (2009). Viscous material Behavior of Solids - Creep of Polymer FiberReinforced Concrete. In *'th Central European Conference on Concrete Engineering* (pp. 95–99).

Lerch, J. . O., Rooyen, A. S. V., and Boshoff, W. P. (1999). The influence of mixing on the single-fibre performance of macro synthetic fibre reinforced concrete. *Cement and Concrete Research*, *103*, 130–139.

Leung, C. K. Y., and Geng, Y. (1995). EFFECT OF LATERAL STRESSES ON FIBER DEBONDING/ PULL-OUT, *5*(95).

Li, V. C., and Stang, H. (1997). Interfacial property characterization and Strengthening Mechanisms in Fiber Reinforced Cement Based Composites. *Advanced Cement Based Materials*, *6*(1), 1–20.

Li, V. C., Stang, H., and Krenchel, H. (1993). Micromechanics of crack bridging in fibre-reinforced concrete. *Materials and Structures*, *26*(8), 486–494.

Li, V. C., Wang, Y., and Backer, S. (1990). Effect of inclining angle, bundling and surface treatment on synthetic fibre pull-out from a cement matrix. *Composites*, *21*(2), 132–140.

Lim, T. Y., Paramsivam, P., and Lee, S. (1987). Bending behaviour of steel–fiber concrete beams. *ACI Journal*, *84*, 286–298.

Lin, Z., Kanda, T., and Li, V. C. (1999). On interface property characterization and performance of fiber-reinforced cementitious. *Concrete Science and …*, *1*, 173–174.

Lin, Z., and Li, V. C. (1997). Crack bridging in fiber reinforced cementitious composites with slip-hardening interfaces. *Journal of the Mechanics and Physics of Solids*, *45*(5),

763–787.

Liu, J., Li, C., Liu, J., Yang, Z., and Cui, G. (2012). Pullout behavior of polyvinyl alcohol fiber from cementitious matrix during plastic state. *8th RILEM International Symposium on Fibre Reinforced Concrete: Challenges and Opportunities (BEFIB 2012)*, 480–488.

Löfgren, I. (2005). *Fibre-reinforced concrete for industrial construction - A fracture mechanics approach to material testing and structural analysis*. *Doktorsavhandlingar vid Chalmers Tekniska Hogskola*.

Lok, T. S., and Xiao, L. (1998). Tensile behaviour and moment–curvature relationship of steel fibre reinforced concrete. *Mag Concr Res*, *50*(4), 359–368.

Maidl, B. R. (1995). *Steel fibre reinforced concrete*. Berlin: Ernst and Sohn.

Marangi, P. (2010). *Computational Modeling of Fiber Reinforced Concrete With Application to projectile penetration*. Università degli Studi di Bologna (Master Thesis).

Marfia, S. (2007). *Modellazione del calcestruzzo fibrorinforzato*. Università degli Studi di Roma "Tor Vergata."

Markovic, I., Walraven, J. C., and Mier, J. V. (2004). Tensile behaviour of high performance hybrid fibre concrete. In *Proceedings of the 5th International Symposium on Fracture Mechanics of Concrete and Concrete Structures* (pp. 1–8).

Markovich, I., Van Mier, J. G. M., and Walraven, J. C. (2001). Single fiber pullout from hybrid fiber reinforced concrete 1. *Heron*, *46*(3), 191–200.

McKinley, J. D. (1996). *Extracting pattern from scattered data - applicability of artificial neural networks to the interpretation of bearing capacity data*. (U. of C. Department of Engineering, Ed.).

Mier, J. G. M., and Vliet, M. R. A. (1999). Experimentation, numerical simulation and the role of engineering judgement in the fracture mechanics of concrete and concrete structures. *Construction and Building Materials*, *13*, 3–14.

Mobasher, B., and Barsby, C. (2011). Flexural Design of Strain Hardening Cement. *2nd International RILEM Conference on Strain Hardening Cementitious Composites*, 53–60.

Mohammad, A. M., and Ozgur, E. (2017). Statistical models for mechanical properties of UHPC using response surface methodology. *Computers and Concrete*, *19*(6), 673–681.

Morton, J., and Groves, G. W. (1974). The cracking of composites consisting of discontinous ductile fibres in a brittle matrix - effect of fibre orientation.

Mouton, C. J. (2012). *Investigating the tensile creep of steel fibre reinforced concrete*. Stellenbosch University.

Naaman, A. E. (1992). F i b e r pullout and b o n d s l i p . experimental validation ii:, *117*(9), 2791–2800.

Naaman, A. E., and Reinhardt, H. W. (2006). Proposed classification of HPFRC composites based on their tensile response. *Materials and Structures*, *39*(5), 547–555.

Nammur, G., and Naaman, A. E. (1986). Bond stress model for fiber reinforced concrete based on bond stress-slip relationship. *ACI Materials Journal*, *1*, 45–57.

NF P 18-470. (2016). Concrete — Ultra-high performance fibre-reinforced concrete — Specifications, performance, production and conformity.

Ostrowski, K., Sadowski, Ł., Stefaniuk, D., Wałach, D., Gawenda, T., Oleksik, K., and Usydus, I. (2018). The Effect of the Morphology of Coarse Aggregate on the Properties of Self-Compacting High-Performance Fibre-Reinforced Concrete. *Materials*, *11*(8), 1372. https://doi.org/10.3390/ma11081372

Otsuka, K., and Date, H. (2000). Fracture process zone in concrete tension specimen. *Engineering Fracture Mechanics*, *65*, 111–131.

P.P. Li, Q.L. Yu, C.P. Chung, H. J. H. B. (2017). Mix design and performance evaluation of ultra-high performance concrete (UHPC) with basalt aggregate. In *6th International Conference on Non-Traditional Cement and Concrete, June 19–22, 2017*. Brno, Czech Republic.

Plizzari, G. (2008). Il calcestruzzo fibrorinforzato per le applicazioni strutturali, 1–72.

Plizzari, G., Cangiano, S., and Alleruzzo, S. (1997). The fatigue behaviour of cracked concrete. *Fatigue and Fracture of Enginwring Materials and Structures*, *20*(8), 1195–1206.

Rabtnov, Y. N. (1948). Equilibrium of an elastic medium with after-effect. *Journal of Applied Mathematics and Mechanics*, *12*, 53–62.

Ramous, E., Festa, D., and Bernardo, E. (2010). *Complementi di scienza e tecnologia dei materiali*.

Redon, C., Li, V. C., Wu, C., Hoshiro, H., Saito, T., and Ogawa, A. (2001). Measuring and Modifying Interface Properties of PVA Fibers in ECC Matrix. *Journal of Materials in Civil Engineering*, *13*(December), 399–406.

RILEM TC 162-TDF. (2000). RILEM TC 162-TDF : Test and design methods for steel fibre reinforced concrete, *33*(March), 75–81.

Rinaldi, Z., Grimaldi, A., and Galli, G. (2004). Ductility of RC Beams Reinforced With FRC. *13th World Conference on Earthquake Engineering*, (131), 2–9.

Robins, P., Austin, S., Chandler, J., and Jones, P. (2001). Flexural strain and crack width measurement of steel-fibre-reinforced concrete by optical grid and electrical gauge methods. *Cement and Concrete Research*, *31*(5), 719–729.

Rossi, L., and Pascale, G. (2007). *CARATTERIZZAZIONE MECCANICA DI*

CALCESTRUZZI FIBRORINFORZATI CON FIBRE D'ACCIAIO. Università degli Studi di Bologna (Master Thesis, in Italian).

Roumaldi, J. P., and Batson, G. B. (2008). Mechanics of Crack Arrest in Concrete.

Rozovskii, M. I. (1961). Some features of elastic media with memory. *Izv. AN SSSR*, *2*, 30–36.

Russo, E. (2011). Calcestruzzi ad altissime prestazioni :proprietà e comportamento meccanico.

Saeed, K. (2012). *Review of Recycled Aggregate Concrete Till 2012*.

Sakata, K., and Shimomura, T. (2004). Recent progress in research on and evaluation of concrete creep and shrinkage in Japan. *Journal of Advanced Concrete Technology*, *2*(2), 133–140.

Sarbini, N. N., Ibrahim, I. S., and Saim, a. a. (2012). Assessment on The Mechanical Performance of Steel Fibre Reinforced Concrete using Fibres Geometrical Factor. *8th RILEM International Symposium on Fibre Reinforced Concrete*, (August 2016).

Shah, S. P. (1988). Theoretical Model for Predicting the Performance of fiber Reinforced Concrete. *Journal of Ferrocement*, *18*(3), 263–284.

Smithers, R. (2014). Why Plastic Products Fail.

Sorelli, L. G., and Meda, A. and Plizzari, G. . (2005). Bending and uniaxial tensile tests on concrete reinforced with hybrid steel fibers. *Journal of Materials in Civil Engineering*, *17*(5), 519–527.

Sorelli, L. G., Meda, A., and Plizzari, G. A. (2005). Bending and uniaxial tensile tests on concrete reinforced with hybrid steel fibers. *Journal of Materials in Civil Engineering*, *17*(5), 519–527.

Sorzia, A. (2016). Modelling of Creep and Stress Relaxation Test of a Polypropylene Microfibre by Using Fraction-Exponential Kernel. *Modelling and Simulation in Engineering*, *2016*, 1–7.

Spasojević, A. (2008). *Structural Implications of Ultra-High Performance Fibre-Reinforced Concrete in Bridge Design*. ÉCOLE POLYTECHNIQUE FÉDÉRALE DE LAUSANNE.

Stang, H., and Krenchel, H. (1993). Micromechanichs of crack bridging in fibre-reinforced concrete. *Materials and Structures*, *26*, 486–494.

Stang, H., Li, V. C., and Krenchel, H. (1995). Design and structural applications of stresscrack width relations in fibre reinforced concrete. *Materials and Structures*, *28*, 210–219.

Stang, H., Li, Z., and Shah, S. P. (1990). Pull-out problem: stress versus fracture mechanical approach. *Journal of Engineering Mechanics*, *116*(10), 2136–2150.

Stang, H., and Shah, S. P. (1991). Characterization of interfacial Bond in FRC Materials. *Toughening Mechanism in Quasi Brittle Materials*, 507–527.

Taengua, E. G., Arango, S., Martì-Vargas, J. R., and Serna, P. (2014). Flexural creep of steel fiber reinforced concrete in the cracked state. *Construction and Building Materials*, *65*, 321–329.

Taheri, M., Barros, J. A. O., and Salehian, H. (2012). a Design Model for Fibre Reinforced Concrete Bending Elements With Longitudinal Pre-Stressed Steel and Frp Bars, 1–12.

Tang, C. S., Li, J., Wang, D. Y., and Shi, B. (2016). Investigation on the interfacial mechanical behavior of wave-shaped fiber reinforced soil by pullout test. *Geotextiles and Geomembranes*, *44*(6), 872–883.

Tavano, S., and Berra, M. (1985). Malte cementizie speciali con fumo di silice. *Rapporto Interno Enel*.

Tayeh, B. A., Abu Bakar, B. H., Megat Johari, M. A., and Voo, Y. L. (2013). Utilization of ultra-high performance fibre concrete (UHPFC) for rehabilitation a review. *Procedia Engineering*, *54*, 525–538.

Tijssens, M. G. A., Sluys, L. J., and Giessen, van der. (2001). Simulation of cementitious composites with explicit modeling of microstructural features,. *Engineering Fracture Mechanics*, *68*, 1245–1263.

Tscharnuter, D., Jerabek, M., Major, Z., and Pinter, G. (2012). Uniaxial nonlinear viscoelastic viscoplastic modeling of polypropylene. *Mech Time-Depend Mater*, *16*, 275–286.

Tuberosa, B., Troiani, E., Sangiorgi, S., Scafè, M., and Marabini, P. (2012). Proprietà meccaniche a trazione di compositi polimerici rinforzati con fibre lunghe di carbonio di interesse per il settore automotive.

Tue, N. V., Simsch, G., Schneider, H., and Schmidt, D. (2004). Bearing Capacity of Stub Columns made of NSC, HSC and UHPC confined by a Steel Tube. In *Proceedings of the International Symposium on Ultra High Performance Concrete* (pp. 339–350). Kassel.

UNI EN 12350-2:2019. (2019). Prova sul calcestruzzo fresco - Parte 2:Prova di abbassamento al cono.

UNI EN 12350-3:2019. (2019). Prova sul calcestruzzo fresco - Parte 3:Prova di Vébé.

UNI EN 12350-5:2019. (2019). Prova sul calcestruzzo fresco - Parte 5: Prova di spandimento alla tavola a scosse.

UNI EN 12390-13:2013. (2013). Prova sul calcestruzzo indurito - Parte 13: Determinazione del modulo di elasticità secante in compressione.

UNI EN 12390-3:2009. (2009). Prove sul calcestruzzo indurito - Parte 3:Resistenza alla compressione dei provini.

UNI EN 12390-3:2019. (2019). Prove sul calcestruzzo indurito - Parte 3:Resistenza alla compressione dei provini.

UNI EN 12390-6:2010. (2010). Prove sul calcestruzzo indurito - Parte 6:Resistenza a trazione indiretta dei provini.

UNI EN 13263-1:2009. (2009). Fumi di silice per calcestruzzo - Parte 1: Definizioni, requisiti e criteri di conformità.

UNI EN 14721:2007. (2007). Metodo di prova per calcestruzzo con fibre metalliche - Misurazione del contenuto di fibre nel calcestruzzo fresco e nel calcestruzzo indurito.

UNI EN 14889-1:2006. (2006). Fibre per calcestruzzo - Parte 1: Fibre di acciaio - Definizioni, specificazioni e conformità.

UNI EN 1916:2004. (2004). Tubi e raccordi di calcestruzzo non armato, rinforzato con fibre di acciaio e con armature tradizionali.

UNI EN 197-1:2011. (2011). Cemento - Parte 1: Composizione, specificazioni e criteri di conformità per cementi comuni.

UNI EN 206:2016. (2016). Calcestruzzo - Specificazione, prestazione, produzione e conformità.

Vandewalle, L., Nemegeer, D., Balazs, L., Barr, B., Bartos, P., Banthia, N., Brandt, A., Criswell, M., Denarie, F., Di Prisco, M., Falkner, H., Gettu, R., Gopalaratnam, V., Groth, P., et al. (2001). RILEM TC 162-TDF: Test and design methods for steel fibre reinforced concrete - Uni-axial tension test for steel fibre reinforced concrete. *Materials and Structures*, *34*(235), 3–6.

Vasanelli, E., Micelli, F., and Aiello, M. A. (2014). Influence of matrix grade on the mechanical behaviour of fibre-reinforced concrete. *Proceedings of the Institution of Civil Engineers - Construction Materials*, *167*(5).

Vasanelli, E., Micelli, F., Aiello, M. A., and Plizzari, G. (2013). Long term behavior of FRC flexural beams under sustained load. *Engineering Structures*, *56*, 1858–1867.

Vasanelli, E., Micelli, F., Aiello, M. A., and Plizzari, G. (2014). Crack width prediction of FRC beams in short and long term bending condition. *Materials and Structures*, *47*, 39–54.

Vrijdaghs, R., Di Prisco, M., and Vandewalle, L. (2016). Creep of cracked polymer fiber reinforced concrete under sustained tensile loading. In *9th International Conference on Fracture Mechanics of Concrete and Concrete Structures FraMCoS-9* (pp. 1–9). Berkley.

Vrijdaghs, R., Di Prisco, M., and Vandewalle, L. (2017). Short-term and creep pull-out behavior of polypropylene macrofibers at varying embedded lengths and angles from a concrete matrix. *Construction and Building Materials*, *147*, 858–864.

WA, E., JM, R., and EP., K. (2004). Modelling non-linear behaviour of steel fibre reinforced concrete. In *6th International RILEM Symposium on Fibre Reinforced*

Concretes (pp. 837-846). RILEM Publications SARL. (pp. 837–846).

Wang, Y., Li, V. C., and Backer, S. (1988). Modelling of fibre pull-out from a cement matrix. *International Journal of Cement Composites and Lightweight Concrete*.

Wu, K. R., Chen, B., Yao, W., and Zhang, D. (2001). Effect of coarse aggregate type on mechanical properties of high-performance concrete. *Cement and Concrete Research*, *31*(10), 1421–1425.

Y., S., and Shah, S. P. J. (1993). Matrix Cracking and Interface Debonding in Fiber-Reinforced Cement -Matrix Composites. *Advanced Cement Based Materials*, *1*(2), 55–66.

Yang, E.-H., Wang, S., Yang, Y., and Li, V. C. (2007). Fiber-Bridging Constitutive Law of Engineered Cementitious Composites. *Journal of Advanced Concrete Technology*, *6*(1), 181–193.

Yin, S., Tuladhar, R., Collister, T., Combe, M., Nagaratnam, S., and Deng, Z. (2015). Post-cracking performance of recycled polypropylene fibre in concrete. *Construction and Building Materials*, *101*, 1069–1077.

Yoo, D. Y., and Banthia, N. (2016). Mechanical properties of ultra-high-performance fiber-reinforced concrete: A review. *Cement and Concrete Composites*, *73*, 267–280.

Yoo, D. Y., Kim, S., Park, G. J., Park, J. J., and Kim, S. W. (2017). Effects of fiber shape, aspect ratio, and volume fraction on flexural behavior of ultra-high-performance fiber-reinforced cement composites. *Composite Structures*, *174*, 375–388.

Yoshida, N., Matsunami, Y., Nagayama, M., and Sakai, E. (2010). Salt weathering in residential concrete foundations exposed to sulfate-bearing ground. *Journal of Advanced Concrete Technology*, *8*(2), 121–134.

Zdenek, P. B., Fellow, ASCE, and Yunping, X. (1995). Continuous retardation spectrum for solidification theory of concrete creep. *Journal of Engineering Mechanics*, *121*(2).

Zdenek, P. B., and Yunping, X. (1994). Drying creep of concrete: constitutive model and new experiments separating its mechanisms. *Materials and Structures*, *27*(1), 3–14.

Zerbino, R. L., and Barragan, B. E. (2012). Long-term behavior of cracked steel fiber-reinforced concrete beams under sustained loading. *ACI Materials Journal*, *109*(2), 215–224.

Zerbino, R., Monetti, D. H., and Giaccio, G. (2019). Creep behaviour of cracked steel and macro-synthetic fibre reinforced concrete. *Materials and Structures*, *49*(8), 3397–3410.

Zerguini, A., and Rossi, P. (2003). Post-cracking behaviour in uniaxial tension of Metallic Fiber-Reinforced Concrete (MFRC): Experimental study of scale effects. *Bulletin Des Laboratoires Des Ponts et Chaussées*, *242*, 67–75.

Zhao, G., Di Prisco, M., and Vandewalle, L. (2013). Experimental Research and Numerical Simulation of Post-Crack Creep Behavior of SFRC Loaded in Tension. In

Ninth International Conference on Creep, Shrinkage, and Durability Mechanics (CONCREEP-9) (pp. 340–347).

Zhao, G., Verstrynge, E., Di Prisco, M., and Vandewalle, L. (2012). Investigation on Single Fiber Pullout and Interfacial Debonding Mechanisms With Acoustic Emission Techniques, 1–11.

Zhao, Q., Y., J., Guoqing, G., Jinyang, J., and Xiaochen, L. (2016). Effect of fiber types on creep behavior of concrete. *Construction and Building Materials*, *105*, 416–422.

Zollo, R. F. (1997). Fiber-reinforced concrete: An overview after 30 years of development. *Cement and Concrete Composites*, *19*(2), 107–122.

Sitography

gabrielecherubin.wordpress.com

https://it.mathworks.com/help/simbio/ug/what-is-nonlinear-mixed-effects-modeling.html

https://it.wikipedia.org/wiki/Analisi_della_varianza

domusweb.it

pinterest.ru

pinterest.com

aehistory.wordpress.com

indiamart.com

danteer.com

Acknowledgements

I never thought I'd get to this point and, since verba volant scripta manet, if I am writing something it means that it is really happening.

The research developed has been carried out at University of Bologna in the Department of Civil, Chemical, Environmental and Material Engineering (DICAM), in collaboration with the Institute of structural engineering, Christian Doppler Laboratory of Boku University in Vienna who provided me the means to develope the numerical study here described.

First of all I would like to thank Prof. Claudio Mazzotti and Prof. Nicola Buratti, they have been my guide in these years of study and work: from them I learned rigor, passion and motivation.Thanks also go to Prof. Marco Savoia one of the head of the working team which I belong to.
I would like to acknowledge who guided me in the research activity during my period abroad in Vienna, Prof. Roman Wan-Wendner, Prof. Jan Vorel and the working team, Ioannis, Marco, Lisa, Gilda, Michele, Lisa, Kresimir and Stefan.

My family plays the most important role for me, my father and mother are the people I love most in the world. My sister Francesca is my half from which only physical distance separates me. Their support is my strength.

In these years I have met some wonderful people. Lidia, my colleague, my traveling companion, my friend and my support. As everyone says it is not easy to find someone with whom to make such a beautiful relationship immediately, but perhaps neither I nor you are 'someone'. Said, who with his privacy has, however, opened his heart and I love him too much. Vittoria, the girl all pepper and very sweet. I have always asked myself how would have been without them, but I cannot find the answer. My thanks go to all my colleagues I met as soon as I arrived and to those with whom I share my days still, Diego, Giacomo, Milena, Marta, Francesca, Jessica, Simonetta, Silvia, Mirco, Cristian, Elena, Marco. The newest, Noemi, Elena, Matteo and Lucia.

A huge thanks goes to my CIRI colleagues especially, Alessandro, Anna T., Anna V., Andrea, Valentina, Dit, Michele, Simone who guided me from the beginning when I just started my research. Their experience has been a very important guidance in these three years, hoping to continue working together.
Luca, Irene, Matteo, Giulia, Achille and Luciano with whom I shared my days during the last period.

I shared these three years with my Valentina, my flatmate, my friend, my 'gio'.
One of my most beautiful experiences during these years has been the research period in Vienna. I have the most beautiful memories inside my heart with the people I have left, Gilda, Michele, Lorenzo, Marta, Giorgia, Nasti, Carlotta and Lisa.

Not in order of importance, my best friends, Anna and Mari, our friendship has exceeded and exceeds any limit. You are and always will be my number one fan and the people I would always fight for.

Finally, I thank myself for having learned the art of perseverance.

Ringraziamenti

Non avrei mai pensato di arrivare a questo punto e, dal momento che verba volant scripta manet, se sto scrivendo qualcosa significa che sta davvero accadendo.

La ricerca sviluppata è stata condotta presso l'Università di Bologna nel Dipartimento di Ingegneria Civile, Chimica, Ambientale e dei Materiali (DICAM), in collaborazione con l'Istituto di ingegneria strutturale, Christian Doppler Laboratory dell'Università Boku di Vienna che mi ha fornito i mezzi per sviluppare lo studio numerico qui descritto.

Innanzitutto vorrei ringraziare il Prof. Claudio Mazzotti e il Prof. Nicola Buratti, sono stati la mia guida in questi anni di studio e lavoro: da loro ho imparato rigore, passione e motivazione. Grazie anche al Prof. Marco Savoia parte importante del gruppo di lavoro a cui appartengo.

Vorrei ringraziare chi mi ha guidato nell'attività di ricerca durante il mio periodo all'estero a Vienna, il Prof. Roman Wan-Wendner, il Prof. Jan Vorel e il gruppo di lavoro, Ioannis, Marco, Lisa, Gilda, Michele, Lisa, Kresimir e Stefan .

La mia famiglia svolge il ruolo più importante per me, mio padre e mia madre sono le persone che amo di più al mondo. Mia sorella Francesca è la mia metà dalla quale solo la distanza fisica mi separa. Il loro supporto è la mia forza.

In questi anni ho incontrato delle persone meravigliose. Lidia, la mia collega, la mia compagna di viaggio, la mia amica e il mio sostegno. Come dicono tutti, non è facile trovare qualcuno con cui intrattenere immediatamente una relazione così bella, ma forse né io né te siamo "qualcuno". Said, che con la sua privacy ha, tuttavia, aperto il suo cuore e lo amo troppo. Vittoria, la ragazza tutta pepe e molto dolce. Mi chiedo sempre come sarebbe stato non averli conosciuti, ma ancora non riesco a rispondermi. I miei ringraziamenti vanno a tutti i miei colleghi che ho incontrato appena arrivata e a quelli con cui condivido ancora i miei giorni, Diego, Giacomo, Milena, Marta, Francesca, Jessica, Simonetta, Silvia, Mirco, Cristian, Elena, Marco. Ed i più recenti, Noemi, Elena, Matteo e Lucia.

Un ringraziamento enorme va soprattutto ai miei colleghi CIRI, Alessandro, Anna T., Anna V., Andrea, Valentina, Dit, Michele, Simone che mi hanno guidato fin dall'inizio

quando ho appena iniziato la mia ricerca. La loro esperienza è stata una guida molto importante in questi tre anni, nella speranza di continuare a lavorare insieme. Luca, Irene, Matteo, Giulia, Achille e Luciano con cui ho condiviso i miei giorni durante l'ultimo periodo.

Ho condiviso questi tre anni con la mia Valentina, la mia coinquilina, la mia amica, la mia 'gio'.

Una delle mie esperienze più belle in questi anni è stata il periodo di ricerca a Vienna. Ho i ricordi più belli incisi nel mio cuore con le persone che mi son rimaste dentro, Gilda, Michele, Lorenzo, Marta, Giorgia, Nasti, Carlotta e Lisa.

Non in ordine di importanza, le mie migliori amiche, Anna e Mari, la nostra amicizia ha superato e supera ogni limite. Siete e sarete sempre le mie fan numero uno e le persone per le quali avrei sempre lottato.

Infine, ringrazio me stessa per aver imparato l'arte della perseveranza.

Appendix A.1

Mix design specifications of pull-out experimental campaign.

SPECIMEN ID	MIX DESIGN		
	Water [Kg]	Cement [Kg]	Sand [Kg]
(2/5) G0A-P1	0.79	1.97	3.86
(2/5) G0A-P2	0.79	1.97	3.86
(2/5) G0B-P1	0.79	1.97	3.86
(2/5) G0B-P2	0.79	1.97	3.86
(2/5) G0C-P1	0.79	1.97	3.86
(2/5) G0C-P2	0.79	1.97	3.86
(2/5) G01A-P1	0.63	1.57	4.61
(2/5) G01A-P2	0.63	1.57	4.61
(2/5) G01B-P1	0.63	1.57	4.61
(2/5) G01B-P2	0.63	1.57	4.61
(2/5) G01C-P1	0.63	1.57	4.61
(2/5) G01C-P2	0.63	1.57	4.61
(2/5) G1A-P1	0.86	1.91	3.73
(2/5) G1A-P2	0.86	1.91	3.73
(2/5) G1B-P1	0.86	1.91	3.73
(2/5) G1B-P2	0.86	1.91	3.73
(2/5) G1C-P1	0.86	1.91	3.73
(2/5) G1C-P2	0.86	1.91	3.73
(2/5) G2A-P1	0.69	1.53	4.49
(2/5) G2A-P2	0.69	1.53	4.49
(2/5) G2B-P1	0.69	1.53	4.49
(2/5) G2B-P2	0.69	1.53	4.49
(2/5) G2C-P1	0.69	1.53	4.49
(2/5) G2C-P2	0.69	1.53	4.49
(2/5) G3A-P1	0.57	1.28	5
(2/5) G3A-P2	0.57	1.28	5
(2/5) G3B-P1	0.57	1.28	5
(2/5) G3B-P2	0.57	1.28	5
(2/5) G3C-P1	0.57	1.28	5
(2/5) G3C-P2	0.57	1.28	5
(2/5) G4A-P1	0.92	1.84	3.62
(2/5) G4A-P2	0.92	1.84	3.62
(2/5) G4B-P1	0.92	1.84	3.62

(2/5) G4B-P2	0.92	1.84	3.62
(2/5) G4C-P1	0.92	1.84	3.62
(2/5) G4C-P2	0.92	1.84	3.62
(2/5) G5A-P1	0.74	1.49	4.38
(2/5) G5A-P2	0.74	1.49	4.38
(2/5) G5B-P1	0.74	1.49	4.38
(2/5) G5B-P2	0.74	1.49	4.38
(2/5) G5C-P1	0.74	1.49	4.38
(2/5) G5C-P2	0.74	1.49	4.38
(2/5) G6A-P1	0.62	1.25	4.89
(2/5) G6A-P2	0.62	1.25	4.89
(2/5) G6B-P1	0.62	1.25	4.89
(2/5) G6B-P2	0.62	1.25	4.89
(2/5) G6C-P1	0.62	1.25	4.89
(2/5) G6C-P2	0.62	1.25	4.89
(2/5) G7A-P1	1.04	1.73	3.40
(2/5) G7A-P2	1.04	1.73	3.40
(2/5) G7B-P1	1.04	1.73	3.40
(2/5) G7B-P2	1.04	1.73	3.40
(2/5) G7C-P1	1.04	1.73	3.40
(2/5) G7C-P2	1.04	1.73	3.40
(2/5) G8A-P1	0.85	1.42	4.16
(2/5) G8A-P2	0.85	1.42	4.16
(2/5) G8B-P1	0.85	1.42	4.16
(2/5) G6B-P2	0.85	1.42	4.16
(2/5) G8C-P1	0.85	1.42	4.16
(2/5) G8C-P2	0.85	1.42	4.16
(2/5) G9A-P1	0.72	1.2	4.69
(2/5) G9A-P2	0.72	1.2	4.69
(2/5) G9B-P1	0.72	1.2	4.69
(2/5) G9B-P2	0.72	1.2	4.69
(2/5) G9C-P1	0.72	1.2	4.69
(2/5) G9C-P2	0.72	1.2	4.69

Appendix A.2

Results of the Pull-out experimental campaign: Force, Mean compressive strength and failure type specified for each sample.

Legend:

R Ruptured Fibre

S Slipped Fibre

RS Mixed mode failure type I (more pronounced)

RSS Mixed mode failure type II (less pronounced)

ID SAMPLE	CEM I 42.5							
	Embedded length 20 mm				Embedded length 25 mm			
	Force [N]	Bond Strength [MPa]	Rcm [MPa]	Failure type	Force [N]	Bond Strength [MPa]	Rcm [MPa]	Failure type
G/H0 A-1	269	4.67	36	RS	269	3.74	58	RSS
G/H0 A-2	234	4.06	36	R	260	3.61	58	R
G/H0 B-1	273	4.74	36	R	293	4.07	58	R
G/H0 B-2	300	5.21	36	R	232	3.22	58	S
G/H0 C-1	276	4.79	36	R	313	4.35	58	R
G/H0 C-2					311	4.32	58	R
G/H01 A-1	249	4.32	46	R	255	3.54	48	R
G/H01 A-2	269	4.67	46	R	290	4.03	48	R
G/H01 B-1	260	4.51	46	R	277	3.85	48	R
G/H01 B-2	247	4.29	46	R	290	4.03	48	R
G/H01 C-1	269	4.67	46	R	249	3.46	48	RS
G/H01 C-2					253	3.51	48	R
G/H1 A-1	269	4.67	53	R	250	3.47	45	S
G/H1 A-2	263	4.57	53	R	213	2.96	45	S
G/H1 B-1	258	4.48	53	R	234	3.25	45	S
G/H1 B-2	280	4.86	53	R	200	2.78	45	RS
G/H1 C-1	249	4.32	53	S	250	3.47	45	R
G/H1 C-2	249	4.32	53	R	278	3.86	45	R
G/H2 A-1	271	4.7	43	R	269	3.74	42	R
G/H2 A-2	258	4.48	43	RSS	277	3.85	42	R
G/H2 B-1	267	4.63	43	R	126	1.75	42	S
G/H2 B-2	268	4.65	43	R	217	3.01	42	S

G/H2 C-1	252	4.37	43	RS	203	2.82	42	R
G/H2 C-2	237	4.11	43	R	264	3.67	42	R
G/H3 A-1	280	4.86	41	RSS	301	4.18	38	R
G/H3 A-2	280	4.86	41	RS	298	4.14	38	R
G/H3 B-1	279	4.84	41	R	250	3.47	38	R
G/H3 B-2					244	3.39	38	S
G/H3 C-1	294	5.1	41	R	260	3.61	38	R
G/H3 C-2	267	4.63	41	RSS	320	4.44	38	RSS
G/H4 A-1	262	4.55	54	S	241	3.35	44	S
G/H4 A-2	274	4.76	54	RSS	281	3.9	44	R
G/H4 B-1	230	3.99	54	R	227	3.15	44	S
G/H4 B-2	333	5.78	54	R	240	3.33	44	S
G/H4 C-1	294	5.1	54	R	178	2.47	44	S
G/H4 C-2	210	3.65	54	S	237	3.29	44	S
G/H5 A-1	275	4.77	46	RSS	218	3.03	37	S
G/H5 A-2	223	3.87	46	S				
G/H5 B-1	322	5.59	46	R	191	2.65	37	S
G/H5 B-2	271	4.7	46	S	237	3.29	37	S
G/H5 C-1	262	4.55	46	S	302	4.19	37	R
G/H5 C-2	277	4.81	46	R	287	3.99	37	S
G/H6 A-1	265	4.6	42	RSS	192	2.67	33	RSS
G/H6 A-2	238	4.13	42	S	232	3.22	33	R
G/H6 B-1	281	4.88	42	RSS	252	3.5	33	R
G/H6 B-2	250	4.34	42	S	234	3.25	33	S
G/H6 C-1	263	4.57	42	S	284	3.94	33	R
G/H6 C-2	216	3.75	42	S	271	3.76	33	R
G/H7 A-1	144	2.5	44	S	167	2.32	35	S
G/H7 A-2	158	2.74	44	S	193	2.68	35	S
G/H7 B-1	181	3.14	44	S	149	2.07	35	S
G/H7 B-2	217	3.77	44	S	122	1.69	35	S
G/H7 C-1	179	3.11	44	S	245	3.4	35	S
G/H7 C-2					140	1.94	35	S
G/H8 A-1	237	4.11	42	S	192	2.67	31	S
G/H8 A-2	202	3.51	42	S	212	2.94	31	S
G/H8 B-1	225	3.91	42	S	165	2.29	31	S
G/H8 B-2	220	3.82	42	S	153	2.12	31	S
G/H8 C-1	232	4.03	42	R	252	3.5	31	S
G/H8 C-2	239	4.15	42	S	228	3.17	31	S
G/H9 A-1	213	3.7	40	S	196	2.72	28	S
G/H9 A-2	263	4.57	40	S	209	2.9	28	S
G/H9 B-1	229	3.98	40	R	171	2.37	28	S
G/H9 B-2	256	4.44	40	S	178	2.47	28	S
G/H9 C-1	304	5.28	40	R	290	4.03	28	R
G/H9 C-2	289	5.02	40	R	219	3.04	28	S

ID SAMPLE	CEM I 52.5							
	Emb 20				Emb 25			
	Force (N)	Bond Strength (MPa)	Rcm (MPa)	Failure type	Force (N)	Bond Strength (MPa)	Rcm (MPa)	Failure type
G/H0 A-1	294	5.1	70	R	277	3.85	49	R
G/H0 A-2	293	5.09	70	R	301	4.18	49	R
G/H0 B-1	298	5.17	70	R	291	4.04	49	R
G/H0 B-2	296	5.14	70	R	326	4.53	49	R
G/H0 C-1	303	5.26	70	R	238	3.31	49	R
G/H0 C-2	310	5.38	70	R	295	4.1	49	R
G/H01 A-1	229	3.98	63	S	310	4.3	39	R
G/H01 A-2					299	4.15	39	R
G/H01 B-1	277	4.81	63	RSS	305	4.24	39	R
G/H01 B-2	231	4.01	63	RSS	257	3.57	39	R
G/H01 C-1	302	5.24	63	R	293	4.07	39	R
G/H01 C-2	273	4.74	63	S	234	3.25	39	S
G/H1 A-1	316	5.49	53	R	296	4.11	59	R
G/H1 A-2	243	4.22	53	S	316	4.39	59	R
G/H1 B-1	253	4.39	53	R	314	4.36	59	R
G/H1 B-2	259	4.5	53	S	289	4.01	59	R
G/H1 C-1					273	3.79	59	R
G/H1 C-2	321	5.57	53	R	301	4.18	59	R
G/H2 A-1	297	5.16	56	R	270	3.75	48	R
G/H2 A-2	315	5.47	56	R	289	4.01	48	R
G/H2 B-1	316	5.49	56	R	266	3.69	48	RS
G/H2 B-2	316	5.49	56	R	283	3.93	48	R
G/H2 C-1					273	3.79	48	R
G/H2 C-2	259	4.5	56	RSS	301	4.18	48	R
G/H3 A-1	326	5.66	38	R	196	2.72	43	RSS
G/H3 A-2	259	4.5	38	RSS	309	4.29	43	R
G/H3 B-1					304	4.22	43	R
G/H3 B-2	234	4.06	38	R	259	3.6	43	RSS
G/H3 C-1	317	5.5	38	R				
G/H3 C-2	262	4.55	38	R	315	4.37	43	R
G/H4 A-1	282	4.9	55	S	236	3.28	49	S
G/H4 A-2	317	5.5	55	R	276	3.83	49	R
G/H4 B-1	314	5.45	55	R	293	4.07	49	R

G/H4 B-2	284	4.93	55	R	288	4	49	R
G/H4 C-1	259	4.5	55	S	244	3.39	49	R
G/H4 C-2	273	4.74	55	S	297	4.12	49	R
G/H5 A-1					274	3.8	51	R
G/H5 A-2	251	4.36	43	R	270	3.75	51	RSS
G/H5 B-1	264	4.58	43	R	312	4.33	51	R
G/H5 B-2	265	4.6	43	R	298	4.14	51	R
G/H5 C-1					219	3.04	51	S
G/H5 C-2	303	5.26	43	R	250	3.47	51	R
G/H6 A-1					292	4.05	51	R
G/H6 A-2	273	4.74	34	R	260	3.61	51	R
G/H6 B-1	245	4.25	34	RSS	275	3.82	51	RS
G/H6 B-2	253	4.39	34	S	313	4.35	51	R
G/H6 C-1	259	4.5	34	RSS	303	4.21	51	R
G/H6 C-2	264	4.58	34	R	319	4.43	51	R
G/H7 A-1	216	3.75	39	S	283	3.93	43	S
G/H7 A-2	213	3.7	39	S	270	3.75	43	R
G/H7 B-1	182	3.16	39	S	264	3.67	43	RS
G/H7 B-2	218	3.78	39	S	251	3.49	43	R
G/H7 C-1					254	3.53	43	S
G/H7 C-2					232	3.22	43	S
G/H8 A-1	198	3.44	39	S	267	3.71	45	S
G/H8 A-2	209	3.63	39	S	257	3.57	45	S
G/H8 B-1	223	3.87	39	S	312	4.33	45	S
G/H8 B-2	217	3.77	39	S	252	3.5	45	S
G/H8 C-1					312	4.33	45	S
G/H8 C-2					205	2.85	45	S
G/H9 A-1	195	3.38	36	S	279	3.87	42	R
G/H9 A-2	270	4.69	36	S	285	3.96	42	S
G/H9 B-1	251	4.36	36	R	326	4.53	42	S
G/H9 B-2	267	4.63	36	R	261	3.62	42	S
G/H9 C-1					235	3.26	42	R
G/H9 C-2					231	3.21	42	R

Appendix B

Mix design specifications of High Performance Sustainable Concrete experimental campaign.

Mix ID	C [kg/m^3]	P [kg/m^3]	SF [kg/m^3]	Sand [kg/m^3]	SP [l/m^3]	PVA [kg/m^3]	H_2O TOT [l/m^3]
H1	420.0	630.0	0.0	933.4	29.2	30.0	240.7
H2	840.0	210.0	0.0	980.0	29.2	30.0	241.4
H3	420.0	367.5	262.5	929.7	29.2	30.0	240.6
H4	577.5	210.0	262.5	940.6	31.7	30.0	240.8
H5	630.0	420.0	0.0	967.6	25.0	30.0	241.2
H6	420.0	498.8	131.3	935.9	27.5	30.0	240.7
H7	708.8	210.0	131.3	974.4	25.0	30.0	241.3
H8	498.8	288.8	262.5	927.5	33.3	30.0	240.6
H9	564.4	354.4	131.3	958.4	25.0	30.0	241.1
H10	420.0	630.0	0.0	990.3	44.2	30.0	204.8
H11	840.0	210.0	0.0	1043.4	41.7	30.0	205.7
H12	420.0	367.5	262.5	986.6	44.2	30.0	204.8
H13	577.5	210.0	262.5	999.7	45.8	30.0	205.0
H14	630.0	420.0	0.0	1031.0	37.5	30.0	205.5
H15	420.0	498.8	131.3	1005.9	37.5	30.0	205.1
H16	708.8	210.0	131.3	1048.8	33.3	30.0	205.8
H17	498.8	288.8	262.5	1001.9	41.7	30.0	205.0
H18	564.4	354.4	131.3	1021.9	37.5	30.0	205.4
H19	462.4	693.6	0.0	741.4	14.2	30.0	289.0
H20	924.9	231.2	0.0	797.1	12.5	30.0	289.9
H21	462.4	404.6	289.0	715.5	22.5	30.0	288.6
H22	635.8	231.2	289.0	734.8	22.5	30.0	288.9
H23	693.6	462.4	0.0	771.4	12.5	30.0	289.5
H24	462.4	549.1	144.5	730.7	17.5	30.0	288.9
H25	780.3	231.2	144.5	774.7	14.2	30.0	289.6
H26	549.1	317.9	289.0	738.2	17.5	30.0	289.0
H27	621.4	390.2	144.5	754.8	15.0	30.0	289.2
H28	377.6	566.4	0.0	1078.8	56.7	30.0	196.8
H29	755.1	188.8	0.0	1160.0	41.7	30.0	198.1
H30	377.6	330.4	236.0	1103.9	45.8	30.0	197.2
H31	519.2	188.8	236.0	1137.0	39.2	30.0	197.8
H32	566.4	377.6	0.0	1139.0	41.7	30.0	197.8
H33	377.6	448.4	118.0	1127.3	37.5	30.0	197.6
H34	637.2	188.8	118.0	1156.1	37.5	30.0	198.1
H35	448.4	259.6	236.0	1120.4	42.5	30.0	197.5
H36	507.4	318.6	118.0	1141.7	37.5	30.0	197.9
H37	480.0	720.0	0.0	710.1	30.0	30.0	269.4

H38	960.0	240.0	0.0	802.6	15.0	30.0	270.8
H39	480.0	420.0	300.0	714.6	26.7	30.0	269.4
H40	660.0	240.0	300.0	734.6	26.7	30.0	269.8
H41	720.0	480.0	0.0	749.9	25.0	30.0	270.0
H42	480.0	570.0	150.0	732.0	20.8	30.0	269.7
H43	810.0	240.0	150.0	773.0	19.2	30.0	270.4
H44	570.0	330.0	300.0	718.1	29.2	30.0	269.5
H45	645.0	405.0	150.0	750.3	20.8	30.0	270.0
H46	377.6	566.4	0.0	1050.3	20.8	30.0	243.1
H47	755.1	188.8	0.0	1107.5	15.0	30.0	244.0
H48	377.6	330.4	236.0	1055.7	17.5	30.0	243.2
H49	519.2	188.8	236.0	1069.2	18.3	30.0	243.4
H50	566.4	377.6	0.0	1082.2	16.7	30.0	243.6
H51	377.6	448.4	118.0	1059.6	16.7	30.0	243.3
H52	637.2	188.8	118.0	1092.7	15.0	30.0	243.8
H53	448.4	259.6	236.0	1065.8	16.7	30.0	243.4
H54	507.4	318.6	118.0	1078.3	15.0	30.0	243.6
H55	360.0	540.0	0.0	1154.4	29.2	30.0	212.0
H56	720.0	180.0	0.0	1205.3	25.0	30.0	212.8
H57	360.0	315.0	225.0	1162.1	25.0	30.0	212.1
H58	495.0	180.0	225.0	1177.1	25.0	30.0	212.3
H59	540.0	360.0	0.0	1185.3	25.0	30.0	212.5
H60	360.0	427.5	112.5	1163.7	25.0	30.0	212.1
H61	607.5	180.0	112.5	1191.2	25.0	30.0	212.6
H62	427.5	247.5	225.0	1169.6	25.0	30.0	212.2
H63	483.8	303.8	112.5	1177.5	25.0	30.0	212.3
H64	462.4	693.6	0.0	862.9	25.0	30.0	233.7
H65	924.9	231.2	0.0	914.2	25.0	30.0	234.6
H66	462.4	404.6	289.0	858.8	25.0	30.0	233.7
H67	635.8	231.2	289.0	878.0	25.0	30.0	234.0
H68	693.6	462.4	0.0	888.5	25.0	30.0	234.2
H69	462.4	549.1	144.5	860.8	25.0	30.0	233.7
H70	780.3	231.2	144.5	896.1	25.0	30.0	234.3
H71	549.1	317.9	289.0	868.4	25.0	30.0	233.8
H72	621.4	390.2	144.5	878.4	25.0	30.0	234.0
H73	420.0	630.0	0.0	848.1	25.0	30.0	276.1
H74	840.0	210.0	0.0	894.7	25.0	30.0	276.8
H75	420.0	367.5	262.5	844.4	25.0	30.0	276.0
H76	577.5	210.0	262.5	861.8	25.0	30.0	276.3
H77	630.0	420.0	0.0	871.4	25.0	30.0	276.4
H78	420.0	498.8	131.3	846.2	25.0	30.0	276.0
H79	708.8	210.0	131.3	878.3	25.0	30.0	276.6

H80	498.8	288.8	262.5	853.1	25.0	30.0	276.1
H81	564.4	354.4	131.3	862.2	25.0	30.0	276.3